



Grant Agreement No.: 226479

SafeLand

Living with landslide risk in Europe: Assessment,
effects of global change, and risk management strategies

7th Framework Programme
Cooperation Theme 6 Environment (including climate change)
Sub-Activity 6.1.3 Natural Hazards

Deliverable D4.3

Creation and updating of landslide inventory maps, landslide deformation maps
and hazard maps as input for QRA using remote-sensing technology

Work Package 4.2 – Remote-sensing technologies for landslide detection,
monitoring and rapid mapping

Deliverable Leader: CNRS

Revision: 2 – Approved

September 2011

Rev.	Deliverable Responsible	Controlled by	Date
0	CNRS	ITC	20/04/2011
1	CNRS	UNISA	07/06/2011
2	CNRS	NGI	05/09/2011



SUMMARY

The mapping of existing landslides in a given area is typically one of the first workings steps toward a further hazard and risk assessment. Already for several decades aerial photographs have been a commonly used data source to support inventory mappings and more recently several remote sensing technologies have emerged as useful tools for the mapping, characterization and monitoring of landslides. Radar interferometry, laser scanning, photogrammetry and advanced image analysis techniques are reaching maturity to support and enhance traditional field observation at the local and especially at the regional level.

This document provides an overview of innovative remote techniques that are relevant for the creation and updating of landslide inventories and landslide deformation maps. Emphasis is given to advanced technologies targeting a higher accuracy and degree of automation for the derivation of relevant variables such as spatial extent, volumes, activity, structural units and deformation rates. Recent developments of such techniques within the SafeLand project and in sister projects of collaborating institutions are discussed and demonstrated with various summaries of recently finished and ongoing case studies. The techniques are grouped by the employed data types including passive optical images, radar imagery, high-resolution topographic data and also examples for the synergetic use of multi-modal data.

The second part of the deliverable is dedicated to the role of remote sensing for collecting information on predisposing factors and elements at risk. It comprises a comprehensive overview of available techniques for collection topographic data and spatial information related to the geological setup, soils, land cover and elements at risk. Interesting studies which adopt such information for the creation of hazard and risk maps are highlighted.

Strategies for remote sensing based updating of inventories and related databases, as well as open questions for the linkage of remote sensing and QRA are discussed in the final section of the document.

This document was elaborated as a deliverable for the SafeLand project (EC-FP7), which targets the development and application of innovative tools for risk assessment and management for landslides. The deliverable benefited of

contributions from landslide and remote-sensing researchers of 12 European research institutions and was compiled by the Centre National de la Recherche Scientifique (*Institut de Physique du Globe de Strasbourg, IPGS/EOST*) at the University of Strasbourg.

To quote this document:

SafeLand deliverable 4.3, 2011. *Creation and updating of landslide inventory maps, landslide deformation maps and hazard maps as inputs for QRA using remote-sensing technology*. Edited for the SafeLand European project by Stumpf, A., Malet, J.-P. and Kerle, N. Available at <http://www.safeland-fp7.eu>

Note about contributors

The following organisations contributed to the work described in this deliverable:

Lead partner responsible for the deliverable:

Centre National de la Recherche Scientifique (CNRS)
Institut de Physique du Globe de Strasbourg (IPGS/EOST)

Deliverable prepared by:

André Stumpf (CNRS), Jean-Philippe Malet (CNRS), Norman Kerle (ITC)

Partner responsible for quality control:

Università degli studi di Salerno (UNISA)
Dario Peduto

Contributors:

- i. Analisi e Monitoraggio del Rischio Ambientale (AMRA Scarl)
G. Fornaro
- ii. Bureau de Recherches Géologiques et Minières (BRGM)
D. Raucoules, M. de Michele
- iii. Centre National de la Recherche Scientifique (CNRS)
*J. Travelletti, J.-P. Malet, C. Delacourt, P. Allemand, J. Schmittbuhl,
R. Toussaint, A. Mathieu, O. Maquaire, C. Lissak, S. Rothmund*
- iv. Faculty for Geo-information Sciences and Earth Observation (ITC)
A. Stumpf, N. Kerle, B. Krol, T. Martha, K.A. Razak, C.J. van Westen
- v. Geological Survey of Austria (GSA)
R. Supper
- vi. Geological Survey of Norway (NGU)
J.F. Dehls, T. Oppikofer
- vii. Geological Survey of Slovenia (GeoZS)
M. Carman

- viii. Joint Research Centre (JRC)
M. Van Den Eeckhaut, J. Hervás

- ix. Università degli studi di Firenze (UNIFI)
*V. Tofani, P. Lu, S. Segoni, N. Casagli, F. Catani, F. Cigna, S. Bianchini,
G. Righini, C. Proietti*

- x. Università degli studi di Salerno (UNISA)
L. Cascini, D. Peduto

- xi. Universitat Politècnica de Catalunya (UPC)
J. Gili, J. Moya

- xii. Université de Lausanne (UNIL)
C. Michoud, A. Abellán, M.-H. Derron, M. Jaboyedoff

CONTENTS

1. INTRODUCTION.....	14
2. HISTORICAL OVERVIEW.....	16
2.1. OBSERVATIONS OF GROUND DEFORMATION.....	16
2.2. ELABORATION OF LANDSLIDE INVENTORIES.....	18
2.3. COLLECTION OF HAZARD AND RISK RELATED INFORMATION	20
3. LANDSLIDE INVENTORY INFORMATION ACQUIRED FROM REMOTE-SENSING TECHNIQUES	22
3.1. INTERPRETATION OF PASSIVE OPTICAL IMAGERY (VISIBLE AND INFRA-RED).....	22
3.1.1. DATA ACQUISITION	22
3.1.2. DATA ANALYSIS	24
A. <i>Visual interpretation of single and stereoscopic images.....</i>	<i>24</i>
B. <i>Image classification with semi-automated pixel-based methods.....</i>	<i>25</i>
C. <i>Image classification with semi-automated object-oriented methods.....</i>	<i>26</i>
D. <i>Correlation of optical images.....</i>	<i>26</i>
3.1.3. INNOVATIVE CASE STUDIES.....	27
<i>Random Forests and object-oriented analysis for landslide mapping from very high resolution imagery.....</i>	<i>28</i>
<i>Digital correlation of optical images for landslide monitoring and detection on regional scale.....</i>	<i>37</i>
<i>Image correlation of terrestrial photographs for landslide monitoring.....</i>	<i>43</i>
<i>Object-oriented analysis of unmanned aerial vehicle (UAV) imagery for mapping and monitoring of landslide surface features.....</i>	<i>55</i>
3.2. INTERPRETATION OF RADAR IMAGERY.....	66
3.2.1. DATA ACQUISITION	66
3.2.2. DATA ANALYSIS	68
A. <i>Surface change detection with classical SAR Interferometry (DinSAR) methods.....</i>	<i>68</i>
B. <i>Surface change detection with advanced SAR Interferometry (A-DInSAR, PS-INSAR) methods.....</i>	<i>70</i>
C. <i>Correlation of high resolution SAR images.....</i>	<i>70</i>
3.2.3. INNOVATIVE CASE STUDIES.....	71
<i>Persistent Scatterers hotspot and clustering analysis for detection of slow-moving landslides.....</i>	<i>72</i>
<i>Updating landslide inventory maps in mountain areas by means of Persistent Scatterer Interferometry.....</i>	<i>80</i>
<i>A-DInSAR data analysis towards slow-moving landslide characterization.....</i>	<i>90</i>
<i>Use of short baseline InSAR for regional and local rockslide mapping</i>	<i>98</i>
3.3. INTERPRETATION OF DIGITAL ELEVATION MODELS	105
3.3.1. DATA ACQUISITION	105
3.3.2. DATA ANALYSIS	109

A.	<i>Visual interpretation of DEMs and multi-temporal DEMs</i>	109
B.	<i>Sediment budget analysis and displacement analysis with multi-temporal DEMs differencing</i>	110
C.	<i>Surface change detection from LiDAR point clouds analysis methods</i>	110
D.	<i>Semi-automatic object- and raster-based landslide mapping using morphological features</i> ...	111
3.3.3.	INNOVATIVE CASE STUDIES	112
	<i>Airborne laser scanning of forested landslides characterization: terrain model quality and visualization</i>	113
	<i>Application of differential ALS for landslide inventory mapping in forested areas: The test site of Gschliefgaben</i>	128
	<i>Airborne LiDAR for detailed mapping of landslide features under sparse vegetation coverage: the Villerville-Cricqueboeuf landslide</i>	137
	<i>Landslide Volumetric Analysis Using Cartosat-1-Derived DEMs</i>	146
	<i>Image correlation of TLS (Terrestrial Laser Scanning) data for landslide monitoring</i>	157
	<i>Object oriented mapping of landslides under dense vegetation cover using LiDAR derivatives</i>	168
3.4.	MULTI-SENSOR DATA ANALYSIS METHODS	178
3.4.1.	DATA FUSION.....	178
3.4.2.	INNOVATIVE CASE STUDIES	179
	<i>Object-oriented change detection for landslide rapid mapping</i>	180
	<i>Combination of airborne & terrestrial LiDAR for the structural analysis of landslides</i> ..	190
	<i>Segment Optimization and Data-Driven Thresholding for Knowledge-Based Landslide Detection by Object-Based Image Analysis</i>	201
	<i>Synergetic use of UAV-based optical remote-sensing and Terrestrial LiDAR for landslide monitoring</i>	214
4.	REMOTE-SENSING DATA AS INPUT FOR QUANTITATIVE HAZARD AND RISK ASSESSMENT	226
4.1.	DIRECT USE OF REMOTE-SENSING INFORMATION FOR HAZARD ANALYSIS	226
4.1.1.	BACK-ANALYSIS OF PAST LANDSLIDES	226
4.1.2.	INITIATION OF DETAILED INVESTIGATIONS AND CONTINUOUS MONITORING	227
4.1.3.	HAZARD ASSESSMENT IN EMERGENCY SITUATIONS.....	228
4.2.	INDIRECT USE OF REMOTE-SENSING INFORMATION FOR HAZARD AND RISK MODELS	229
4.2.1.	REMOTE-SENSING INVENTORY MAPS AS INPUTS TO HAZARD MODELS	229
4.2.2.	REMOTE-SENSING DISPLACEMENT AND VOLUME MAPS AS INPUTS TO HAZARD MODELS	231
4.2.3.	REMOTE-SENSING DERIVED PREDISPOSING FACTORS MAPS AS INPUTS TO HAZARD MODELS	234
	A. <i>Topographic data and derivatives</i>	234
	B. <i>Lithology, Structure, Faults</i>	240
	C. <i>Soils</i>	243
	D. <i>Land cover information</i>	248
4.2.4.	REMOTE-SENSING DERIVED ELEMENTS AT RISK MAPS AS INPUTS TO RISK MODELS	251
	A. <i>Elements at risk in the landslide hazard context</i>	251

B. Inventorization of EaR.....	252
4.3. REMOTE-SENSING DERIVED DATA FOR MODEL ASSESMENT AND VALIDATION.....	258
4.3.1. REMOTE-SENSING FOR THE ASSESSMENT OF SUSCEPTIBILITY/HAZARD MAPS AT REGIONAL- LOCAL SCALE.....	259
4.3.2. REMOTE-SENSING FOR THE ASSESSMENT OF SITE-SPECIFIC PHYSICALLY-BASED MODELS ...	263
5. DISCUSSION	265
5.1. UPDATING STRATEGIES OF REMOTE-SENSING PRODUCTS	265
5.1.1. FOR EVENT-BASED LANDSLIDE INVENTORY MAPPING	265
5.1.2. FOR LONG-TERM LANDSLIDE MONITORING AT HOT SPOT AREAS	269
5.1.3. FOR HAZARD AND RISK ASSESSMENT.....	272
5.2. REINFORCING THE LINKS BETWEEN QRA AND REMOTE SENSING.....	272
6. CONCLUSION.....	275
6. REFERENCES	275

List of acronyms

ALOS: Advanced Land Observing *Satellite*
A-DInSAR: Advanced DInSAR
ALS: Airborne Laser scanning
ANN: Artificial Neural Networks
ASTER GDEM: ASTER Global Digital Elevation Model
ASTER: Advanced Spaceborne Thermal Emission and Reflection Radiometer
CCD: Charge Coupled Device
COTS: Commercial Off-The-Shelf
CVA: Change Vector Analysis
DEM: Digital Elevation Models
DGPS: Differential Global Positioning System
DIC Digital Image Correlation
DInSAR: Differential Interferometric SAR
DN: Digital Number
DSGSD: Large Deep-Seated Gravitational Deformations
DSM: Digital Surface Models
DTM: Digital Terrain Models
EaR: Elements At Risk
EASA: European Aviation Safety Agency
EROS: Earth Resources Observation Systems
ERS: European Remote-sensing Satellite
ESA: European Space Agency
ESP: Estimation of Scale Parameter tool
FFT: Fast Fourier Transform
FNEA: Fractal Net Evolution Approach
GB-InSAR: Ground-Based Synthetic Aperture Radar Interferometry
GCP: Ground Control Point
GIS: Geographic information Systems
GLCM: Grey Level Co-occurrence Matrix
GLONASS: Globalnaja Nawigazionnaja Sputnikowaja Sistema
GNSS: Global Navigation Satellites Systems
GPS: Global Positioning Systems
HRDEM: High Resolution Digital Elevation Models
HRI: Hierarchical Robust Interpolation
ICP: Iterative Closest Points
IDW: Inverse Distance Weighted
IFSAR: Interferometric SAR
IMU: Inertial Measurement Units
InSAR: Interferometric SAR
IRS: Indian Remote-sensing Satellite
ISRO: Indian Space Research Organisation
Landsat TM: Landsat Thematic Mapper
LiDAR: Light Detection And Ranging

LOS: Line-Of-Sight

LSSM: Least Squares Surface Matching

MLC: Maximum Likelihood Classification

MODIS: Moderate Resolution Imaging Spectroradiometer

NCC: Normalized Cross-Correlation

NDVI: Normalized Difference Vegetation Index

NOAA-AVHRR: National Oceanic and Atmospheric Administration Advanced Very High Resolution Radiometer

OBIA: Object-Based Image Analysis

OOA: Object-Oriented Analysis

PCA: Principal Component Analysis

PID: Proportional Integral Differential

PSI: Persistent Scatterer Interferometry

PS-InSAR: Permanent Scatterer InSAR

PTD: Progressive TIN Densification

QRA: Quantitative Risk Assessment

RF: Random Forest

RFM: Rational Function Models

RMSE: Root Mean Square Error

ROI_PAC: Repeat Orbit Interferometry PACkage

RPC: Rational Polynomial Co-efficients

RXD: Reed-Xiaoli Detector

SAM: Spectral Angle Mapper

SAR: Synthetic Aperture Radar

SIFT: Scale-Invariant Feature Transform

SOP: Segmentation Optimization Procedure

SPOT: Satellite Pour l'Observation de la Terre

SRTM: Shuttle Radar Topography Mission

SVM: Support Vector Machines

TIN: Triangulated Irregular Network

TLS: Terrestrial Laser Scanning

TOF: Time of Flight

TOP: Terrestrial Optical Photogrammetry

TRMM: Tropical Rainfall Measurement Mission

UAV: Unmanned Aerial Vehicles

VHR: Very High Resolution

List of figures (figures from case studies not included)

Figure 1: VHR satellite images at Nova Friburgo / south-east Brazil recorded before and after heavy rainfalls that triggered thousands of landslides at January 12, 2011 (Copyrights: Google Earth, Geoeye Company).	22
Figure 2: Medium resolution images of rainfall triggered landslides at the same region as in Figure 1 recorded by NASA EO-1 ALI at 10 m resolution (Copyright: NASA).	23
Figure 3: Exemplary light-weight UAV systems. Right: Voyager G8 RR (http://www.sensor-asia.net/wp-content/uploads/2010/12/IMG_1389.jpg) , Left: Open-Source multicopter systems [Niethammer et al., 2009]	24
Figure 4: Raw SAR image with the return amplitude signal (left) and phases (right) of Bam area in Iran, December 2003 (free Envisat data, shown in the SafeLand deliverable 4.1).	66
Figure 5: The ground displacement, as a landslide, influences the phase shift of a Radar returned signal. The way of the signal on the Slave SAR image is longer than the way of the signal on the Master image, due to the displacement created by the rotational landslide. This additional distance produces a phase shift that can be detected and interpreted as an active area on susceptibility maps (SafeLand deliverable 4.1).....	68
Figure 6: Interferogram of the "La Valette" landslide processed with two SAR scenes acquired by the ERS-tandem mission (temporal baseline: 1 day). The detected phase decay (one fringe: 28 mm) is due to displacements detected along the line of sight [from Squarzoni et al., 2003].....	69
Figure 7: (a) Velocity map for the Inyltshik glacier in Kyrgyzstan for a three month period as derived from Maximum Likelihood texture tracking on ENVISAT-ASAR[Erten et al., 2009]. (b) 2D surface velocity field of the Aletsch glacier derived with the spectral diversity technique on L-band airborne SAR images[Prats et al., 2009].	71
Figure 8: a) LiDAR DSM (resolution 25 cm),, b) photogrammetric DSM (GSD 8 cm, resolution 25 cm), c) photogrammetric DSM (GSD 20 cm, resolution 25 cm) c) DMC DOM (20 cm GSD), [modified from Haala et al., 2010]	105
Figure 9: Left: Intercomparison between interferometric DSM derived from SRTM (90 m) and TANDEM-X (12 m), Source: DLR, Right: Hillshade representation of a airborne IFSAR DSM (3.4m)	106

Figure 10: Two meters HRDEM of the ski resort of Verbier (Valais, Switzerland) processed from an ALS point cloud (MNT-MO © CC-GEO-VS)..... 107

Figure 11: Left: Digital Surface Model (DSM), including vegetation canopy. Right: filtered Digital Elevation Model (DEM), for the same area. Obviously, morphological features are more visible on the DEM than on the DSM..... 108

Figure 12: A: Landslides in a hillshade representation of a airborne LiDAR DTM [Van Den Eeckhaut et al., 2007]. B: Visibility of landslide-induced surface cracks in a airborne LiDAR DTM after vegetation filtering [Razak et al., 2011b]..... 108

Figure 13: 3D rasterized model of a rockface with scree deposits generated from terrestrial LiDAR point clouds.[Abellán et al., 2010] 109

Figure 14: Relationship between the mean slope by LiDAR point-cloud spacing and resulting topographic raster [Chow and Hodgson, 2009]. 234

Figure 15: Derivative of a DEM and extracted fault lines [Gloaguen et al., 2007]..... 241

Figure 16: Locations and heights of buildings in landslide prone areas as extracted from a high-resolution ALS dataset. 88.6% of the buildings were correctly detected and the map includes only 10% false positives [Razak et al., 2011a]. 256

Figure 17: Existing roads (yellow lines in A) and ALS-derived road network (red lines in B) overlaid on the topographic openness with elevation variation [Razak et al., 2011a]. 256

Figure 18: a) Building footprint extraction for parts of Tegucigalpa, Honduras, and b) three segmentation and classification levels. Small objects, such as cars, are gradually removed in the rule-based classification stage, while at level 3 only whole buildings as semantic groups remain. (Source: Kerle 2011, unpublished material) 257

Figure 19: Total fractional cloud cover annual averaged from 1983-1990 according to the database of the International Satellite Cloud Climatology Project (ISCCP). 266

Figure 20: Abstract types of two-dimensional object changes and typical significance in the context of event-based landslide mapping. In reality the abstract types may often overlap or occur in parallel at different parts of a landslide. 267

Figure 21: Example for changes in surface texture indicating the occurrence of a landslide while the color information remains very similar. 267

Figure 22: Object-oriented backdating and updating for the construction of time series maps representing temporal and spatial changes. Spurious effects of mismatches (slivers) between reference objects can be addresses by defining a minimum mapping width [figure from *McDermid et al.*, 2008]. 268

Figure 23: Average revisit time (in days) across the world for the Sentinel-1 constellation: Two satellites in 12-day repeat orbits with 250 km swath widths. The blue around the equator reflects the 3-day revisit period, improving towards the poles. Source: ESA bulletin 131 - august 2007 271

1. INTRODUCTION

Data products of earth observing systems are increasingly available with higher spatial and temporal resolution and offer new opportunities for the detection, mapping, and characterization and monitoring of unstable slopes. They also reveal important environmental information about triggering factors, preconditioning factors and the exposed elements at risk to be integrated in the assessment of related hazards and risks. In the light of advancing remote-sensing technologies, image analysis methods and risk assessment strategies, the development of a framework for landslide hazard assessment that integrates the new sensor types and related analysis methods is a challenging task.

► According to the guidelines provided by JTC-1 [*Fell et al.*, 2008] **landslide inventory maps** may provide the following three categories of landslide related information plus one additional category which is concerned with metadata on the sources of information:

- **Basic:** Location (absolute and relative to topographic, geomorphological, geological and hydrological features), Type of movement, Volume (or area), Time of triggering/activation.
- **Intermediate:** Delineation and morphometric description of different landslide parts (crown elevation, toe elevation, length, width, height difference, slope, volume, orientation, azimuth, depth of surface rupture), historical information on landslide activity (reactivation, displacement rates), historic information on the past evolution of the land use.
- **Advanced:** Detailed geotechnical data and information on reactivation with high-temporal and spatial resolution for the definition of geotechnical conditions and model validation.
- **Metadata:** Information on the methods applied to derive each parameter, including statements on the accuracy/scale or certainty of the measurement

► **Deformation maps** are remote-sensing products that on its own already provide valuable information for the delineation of hazardous zone and in some cases even the prediction of failures. However, the JTC-1 guidelines recommend the inclusion of landslide activity in the inventory. This is supported by the view that activity maps are typically a further refinement of existing landslide inventory maps [*Metternicht et al.*, 2005] and recent examples that show the synergies arising when classical inventories are combined with remotely sensed displacement maps [*Cascini et al.*, 2009; 2010].

Chapter 2 provides a brief outline of the limitations of traditional techniques and datasets used for the observation of ground deformation, landslide inventory mapping and the gathering of hazard and risk related information. It provides the reader with an overview on the most important contributions of remote-sensing to QRA and links to further SafeLand deliverables that detail the advantages and limitations of innovative observation technologies.

Chapter 3 is the main part of this document and accommodates innovative case studies that illustrate how different remote-sensing technologies (described in detail in deliverable D4.1) can be applied to create and update inventory maps including deformation rates. It thereby reflects the latest research activities of the institutions collaborating in the Work Package 4.2 for such applications at regional and local scales. The chapter is organized by the main relevant remote-sensing data-types, which are images from passive systems, images from active microwave sensors, and digital elevation models that can originate from stereo-photogrammetry, LiDAR and other remote-sensing observations. A synthetic overview of the relevant remote-sensing systems and analysis methods is provided in the beginning of each section, whereas we refer to deliverable D4.1 for an in-depth review the processing methods and to deliverable D4.5 for an evaluation of the most advanced techniques. The final sub-chapter 3.5 highlights the potential added value of combining observations from multiple sensors and presents case studies which essentially benefited from the integration of multi-modal data.

Chapter 4 provides detailed information on the potential and practical use of remote-sensing derived datasets for landslide hazard and risk assessment. This includes not only observations of the landslide itself and but also a detailed overview of remote-sensing methods that can yield information on predisposing factors and elements at risk. The chapter attempts to provide input for the activities of WP2.3 by highlighting remote-sensing as an important source for the collection and updating of spatial data needed for QRA, and reviews studies which integrated remote-sensing data in landslide hazard and risk assessments.

In **Chapter 5**, strategies and challenges in the use remote-sensing technology for event-based inventory updating, for long-term landslide monitoring at known hot spot areas and for the updating of related spatial databases are discussed. Updating landslide information, but also hazard related information (described in Chapter 4), typically becomes an urgent necessity directly after major events. Appropriate updating frequencies may depend on many factors such as technological and monetary restrictions but also on the occurrence frequency and potential impacts. Therefore it is emphasized that the results of a QRA should be used to prioritize particular spatial and temporal subsets.

2. HISTORICAL OVERVIEW

2.1. OBSERVATIONS OF GROUND DEFORMATION

[UNIFI]

The measurement of superficial displacements induced by a slope movement often represents the most effective method for defining its behavior, allowing the observation of response to triggering factors and the assessment of effectiveness of corrective measures [Farina *et al.*, 2006].

Different techniques (see also SafeLand deliverable D4.1. Part A) are available for measurements of the ground displacements, starting from the traditional inclinometers, extensometers, topographic surveys, until more recent applications such as global positioning systems (GPS), aerial photogrammetry [Angeli *et al.*, 2000; Corominas *et al.*, 2000; Kääb and Vollmer, 2000; Malet *et al.*, 2002; van Westen and Getahun, 2003].

Remote-sensing images represent a powerful tool to measure landslide displacement as they offer a synoptic view that can be repeated at different time intervals and that is available at various scales.

The conventional ground-based techniques used in the observation of ground deformations are affected by some limitations that reduce their effectiveness (i.e. quality of the results) or their applicability range (variety of circumstances in which their employ is possible). One of the major issues in using traditional methods is that their application typically yields limited temporal and/or spatial resolution. Most of these drawbacks can be overcome employing more advanced remote-sensing techniques.

Traditional methodologies usually rely on instruments that measure one or more physical features of the terrain in a limited portion of space. Assessments over large areas require consequently either the installation of networks composed by many instruments, or the accomplishment of a field work in which many measures are performed at many discrete points. As a result, when working over large areas, the costs and the time needed to gather the required amount of data may increase dramatically. This point is very important, as cheapness is commonly considered one of the main advantages of traditional techniques, but this judgment can be considered as scale-dependent: even the most up to date remote-sensing techniques may become more affordable, for applications in very large areas

Traditional techniques are affected by evident limitations also in terms of the time interval they can investigate. For this reason, traditional techniques produce shortest temporal series of data, limited to the data in which the instrumentation was first installed or used in a field survey. The beginning of the observations is obviously subsequent to the installation of the instrumentation or the performing of the field survey: no data can be retrieved for antecedent periods. On the contrary for many remote-sensing techniques data provider can also deliver information relative to preceding periods. Thus, the studied period can be extended before the beginning of the study itself.

Furthermore, traditional techniques are usually employed directly on the landslides and thus, their effectiveness may be compromised by environmental factors (extensometers may be broken by sudden accelerations). This means that the measurements may prematurely and accidentally come to an end.

The strict need to be on site may bring other limitations, such as the need of carrying on site heavy equipment, the necessity of electrical power, the overcoming of natural obstacles, the obtainment of bureaucratic permissions. Some of these limitations become particularly crucial when time is a factor (in emergency scenarios); to this end, it should be also considered that a minimum lead-time is always constituted by the time needed to gather the equipment (and personnel) and for travelling to the site of study. Conversely, the employment of the most recent remote-sensing techniques allows being immediately operative and in many cases the possibility of performing back-monitoring allows to regain the lost time.

The techniques traditionally used in the observation of ground deformations are usually invasive and, compared to the emerging remote-sensing techniques, they could be affected by other limitations in the post processing phase. As an instance, some techniques require calibration data or post-elaboration to remove systematic errors or to correctly calibrate the measures and in order to relate measured parameters (elastic, electrical, etc) to soil/rock properties. In addition, the results may be sometimes difficult to interpret without the cooperation of other geoscientists (geologists, geomorphologists, geotechnical engineers, hydro-geologists, glaciologists, etc).

Despite the many advantages, remote-sensing techniques suffer a limitation that can be considered critical in the study of landslides: they are capable of observing only the behavior of the surface of the ground and therefore they can evaluate only superficial deformations, while deep displacements cannot be observed (the sliding surface cannot be identified). As a consequence, remote-sensing and traditional on-site technologies can be considered complementary: their joint use grants the most reliable assessments on ground deformation. To sum up, the main disadvantages of the techniques traditionally employed to assess ground deformations are:

- A single instrument provides information about a limited portion of ground.
- For reasons of time and costs, traditional techniques are not suitable when working at large scales.
- Back monitoring is not possible.
- Instrumentation may be damaged by environmental factors or by the landslide itself
- Restriction of travelling to be on the study site with instrumentation and with electrical power.
- Need for calibration data, post-processing elaborations and expert interpretation.

In the last years many examples have demonstrated the usefulness of remote-sensing for landslide ground deformation measurements by means of both optical images [*Casson et al.*,

2005; Delacourt et al., 2004; Yamaguchi et al., 2003], spaceborne radar [Berardino et al., 2003; Colesanti et al., 2003; Farina et al., 2006; Meisina et al., 2007; Singhroy and Molch, 2004; Strozzi et al., 2010] or the integration of traditional ground-based and remote-sensing [Meisina et al., 2007; Tofani et al., 2010; Yin et al., 2010].

2.2. ELABORATION OF LANDSLIDE INVENTORIES

[ITC+CNRS]

Though testimony of landslides can be found in scientific and religious texts throughout centuries before present days, systematic mapping surveys have only been conducted since the beginning of the 20th century and Howe [1909] is often mentioned as the one first differentiated landslide mappings on regional scale. Remarkable early attempts for country wide landslide mappings were reported from Sweden [STATENS-JÄRNVGARS, 1922] and documented for the former Czechoslovakia [Rybár et al., 1965] whereas mapping relied mainly on field surveys by experts. An often cited study of inventory mapping on regional scale is the work of Jones et al., [1961] conducted along the Columbia River because it was one of the first that resulted in a hazard assessment and served as input for statistical evaluations. From the literature alone it remains difficult to reconcile which study first integrated remote-sensing information for mapping purposes but it can be stated that black and white aerial photographs was the first medium used. Though several European countries provide access to archived aerial photographs dating back to until the 1930s, favorable material (in terms of image quality and coverage) seems more commonly available only after 1950 and states an important source to reconcile map historic activity. During the 60s and 70s more and more regional inventories were prepared especially by the U.S. Geological Survey [Wieczorek et al., 2005] and at the end of the 70s the visual interpretation aerial photographs has already been considered as the most useful accurate, and cost-effective remote-sensing technique for landslide inventory mapping [Rib and Liang, 1978]. Modern digital aerial sensors provide better spectral and spatial resolution as early panchromatic photographs and stereoscopic visualization (or pseudo 3D views) enhances the image understanding but the basic principles of visual interpretation remain similar. Already Varnes [1984] noted that the resulting inventories depends highly on the particular image interpreter and the experts understanding of the respective ground conditions. The subjectivity of manually elaborated inventories and associated problems for susceptibility and hazard assessment have been put forward in various papers [Brardinoni et al., 2003; Fiorucci et al., in press; Galli et al., 2008; Mantovani et al., 1996; Wills and McCrink, 2002] but to this point there is no satisfactory solution to this issue.

A combination of field surveys and visual interpretation to date remains the most frequently followed approach in scientific studies [Hovius et al., 1997; Huang and Li, 2009] and the elaboration of inventory maps by administrative bodies [Hervás and Bobrowsky, 2009]. Despite its time-consuming and labor intensive nature, results not only include a large degree of subjectivity, but also incur the risk of omissions due to limited site access or aerial

survey campaigns only being mounted with some delay after a given event. Due to historically rather larger intervals between field surveys and acquisition of aerial photographs, the term landslide inventory is most commonly understood as a snapshot of an area at a certain point of time, whereas in some cases statements on the activity and a coarse differentiation of the particular landslide types might be possible from remote-sensing data alone [Mantovani *et al.*, 1996]. Such inventories may at best provide suitable input to susceptibility models but are not sufficient input to assess the landslide hazard.

Attempts to employ satellite imagery for landslide inventory mapping were already made in the 1970s. The spatial resolution of optical systems at that time (SPOT, LANDSAT) provided only limited utility for detailed mappings. Among several technological innovations the enhanced spatial (and temporal) resolution of optical very-high resolution (VHR) satellite imagery is probably the most significant for the elaboration of landslide inventory maps. The increased availability of such datasets opens the door for the elaboration of multi-temporal landslide inventories, whereas relatively few studies so far addressed the development and application of efficient image classification and change detection methods to exploit the image type for landslide mapping [Hervás *et al.*, 2003; Nichol and Wong, 2005; Park and Chi, 2008]. Rau *et al.* [2007] recently demonstrated that optical VHR imagery can provide observation of landslide with high temporal frequency. On the one hand this potentially yields to multi-temporal inventories that are necessary for hazard assessment and on the other hand softens the conceptual border between inventory mapping and monitoring.

Passive optical sensors (see also SafeLand deliverable D4.1. PartA) have particular advantages for the spatial location and extent observation of catastrophic failures after major events. It has been demonstrated in several studies [Coe *et al.*, 1997; Kerle, 2002] that stereo-view imagery from aerial and spaceborne sensors is suitable to generate multi-temporal DSM from which landslide volumes can be deduced. While most of such studies focused on the detailed investigation of individual landslides Tsutsui *et al.* [2007] demonstrated recently that detection and volume estimation of landslide are in principle possible also on regional scale using stereo-photogrammetric and LiDAR (Light detection and ranging) technology (see also SafeLand deliverable D4.1. Part B). To present day the airborne LiDAR surveys of larger areas are still relative cost-intensive and provide accuracies that yield regional inventories with reliable volume information only for relative large displaced volumes [Burns *et al.*, 2010; Tsutsui *et al.*, 2007]) or for rather local event reconstruction [Scheidl *et al.*, 2008]. Visual and semi-automatic interpretation of single airborne LiDAR acquisitions became more common for the elaboration of regional inventories [Jaboyedoff *et al.*, 2010] and widened the viewing window of remote-sensing to investigate also landslides under forest [Van Den Eeckhaut *et al.*, 2007].

Generally, the exploding number of new space and airborne platforms (from micro-satellites to unmanned aerial vehicles, UAV) enables and unprecedented observation frequency and especially the advance of interferometric synthetic aperture radar (SAR) techniques [Farina *et al.*, 2006; Roering *et al.*, 2009] leads to a change in our view of

landslide inventories, moving from a static maps to dynamic digital inventories and constantly updated collections of hazard and risk related information

2.3. COLLECTION OF HAZARD AND RISK RELATED INFORMATION

[ITC+CNRS]

Beyond the observation of the landslides remote-sensing yields important data on the triggering and pre-disposing factors. With an increasing spatial and temporal resolution of remote-sensing products also the information that can be gathered about elements at risk is not only restricted to spatial extent and location anymore.

Digital elevation models (DEM) and their derivatives became an indispensable source for hazard and risk assessment and at latest since the release of the SRTM data in 2003 are available for most of the globally relevant regions (in terms of landslide risks). The cost-free available ASTER GDEM, though often not as accurate as SRTM, has brought significant enhancements in terms of spatial resolution. For higher resolution DEMs (sub 10m) which are generally desirable for landslide hazard analysis [van Westen *et al.*, 2008] the user can today choose among a great variety of potential sources (stereo-photogrammetry, airborne LiDAR, interferometric DEMs) whereas such datasets become increasingly available for entire countries (airborne LiDAR in Denmark and Switzerland).

Remote-sensing has played an important role in the development of modern geological maps. According to Lillesand and Kiefer, [1987] the first photographs taken from an airplane, for geologic mapping were recorded in 1913 and their interpretive use became widespread until the beginning of the 1940s. In the following decades it became an important tool for the mapping of geological lineaments, geomorphological studies and petroleum exploration, whereas more quantitative approaches for rock type characterization were only possible after the advent of multispectral spaceborne and hyperspectral airborne sensors in the 1980s. Although, at least in Europe geological mappings can be considered as complete, remote-sensing still provides an important source for geological information, especially in regions with sparser geospatial databases. A frequent application became the manual mapping of lineaments as a factor map in susceptibility assessment [Gómez and Kavzoglu, 2005; Pradhan *et al.*, 2006] whereas there are also efforts to map such structural features automatically [Karnieli *et al.*, 1996; Mavrantza and Argialas, 2008].

The mapping and monitoring of landcover and land use changes has always been one of the key tasks of remote-sensing and might be regarded as the best studied application of multispectral satellite remote-sensing. Various cases indicate that changing land cover and land use influence the frequency and magnitude of mass wasting processes [Glade, 2003; Meusburger and Alewell, 2008; 2009]. Considering the current prognoses of the global effects of climate change and urbanization past and present imagery is one of the few sources to reliably quantify land use and land cover changes.

As far as shallow landslides are concerned the geotechnical and hydrological characteristics of the soils are of great importance. Although, there exists a considerable body of literature on the remote-sensing of soils with the earliest publication dating back to the 1970s [Anderson and Croft, 2009] till the present day rather traditional soil maps are used as input into landslide hazard assessment. Some success was achieved for remotely analysis of soil salinity, mineralogical compositions of soils or surface permeability but in general the upscaling of laboratory measurements remains difficult [Lagacherie *et al.*, 2008]. The most promising advances have been made in the measurement of soil moisture with passive and active microwave sensors and first attempts to integrate such data were made recently [Ray *et al.*, 2010]. Although, several methods for the predictive modeling of soil depth have been proposed [Kuriakose *et al.*, 2009; Tesfa *et al.*, 2009] and soil depth is generally considered as a crucial factor for shallow landslides an integration of remote-sensing, soil depth and landslide hazard has yet not been demonstrated.

The relative temporal constancy of the mentioned pre-disposing factors may be one factor that makes their integration into landslide hazard assessment much more common than more dynamical triggering factors, which are mainly heavy rainfall and earthquakes. Driven by major advances in radar technologies the first real weather radar sensors developed short after the second world war period [Whiton *et al.*, 1998] and among other measurement systems for rainfall the secondary use of GPS [Bevis *et al.*, 1992] is one of the most remarkable developments. Falling more into the field of early warning than into hazards assessment a large number of studies have been dedicated to the elaboration of rainfall thresholds for given areas. Only few propose remotely sensed rainfall estimates such as TRMM to feed predictive models [Chang *et al.*, 2008; Hong and Adler, 2008] whereas on the other hand it has been demonstrated that at least ground observations are feasible to evaluate landslide hazard for different rainfall return periods [Dai and Lee, 2003].

Due to the advances in interferometry [Massonnet *et al.*, 1993] and digital image correlation [Van Puymbroeck *et al.*, 2000] observations of co-seismic displacement are now possible over large areas. In terms of hazard assessment resulting maps are valuable for the understanding of fault geometry and rupture processes [Shen *et al.*, 2009] that directly affect the landslide distribution patterns. However, for the integration of ground shaking intensities in probabilistic susceptibility models such as suggested by Lee *et al.*, [2008] station records remain indispensable.

One of the most active areas in photogrammetry and computer vision during the last decade has been the automatic extraction of man-made structures [Gruen *et al.*, 1997], potential elements at risk. Initially especially optical data was used to locate elements at risk whereas high resolution elevation models and imagery can nowadays be integrated to reveal detailed 3D information of an object [Haala and Kada, 2010]. Also where sophisticated 3D data is not available and a suitable database of exposure and vulnerability of elements at risk does not exist remote-sensing methods are useful to supplement ground observations [Ebert *et al.*, 2009; Hofmann *et al.*, 2008].

3. LANDSLIDE INVENTORY INFORMATION ACQUIRED FROM REMOTE-SENSING TECHNIQUES

3.1. INTERPRETATION OF PASSIVE OPTICAL IMAGERY (VISIBLE AND INFRA-RED)

3.1.1. Data acquisition

[ITC+CNRS]

An overview of the main operational and near-future optical sensor systems has been provided in D4.1 (35ff, 41ff, 44ff) and only VHR satellites and UAVs are highlighted here again since they provide the most significant technological advances for inventory mapping on regional scale. VHR satellite images can be acquired directly from space agencies, private satellite operators or their respective distributors, whereas due to U.S. regulations the highest publically available resolution from spaceborne sensors is at present 50cm. For change detection application there are generally large archives of medium resolution imagery available and the availability of suitable VHR imagery from earlier time steps is enhancing constantly. In cases of limited access to professional datasets is consumer geographic information systems (GIS) platforms such as operated by Google and Microsoft provide VHR imagery of various time steps and nearly global coverage and may provide a useful additional source for mapping [Van Den Eeckhaut *et al.*, 2010].

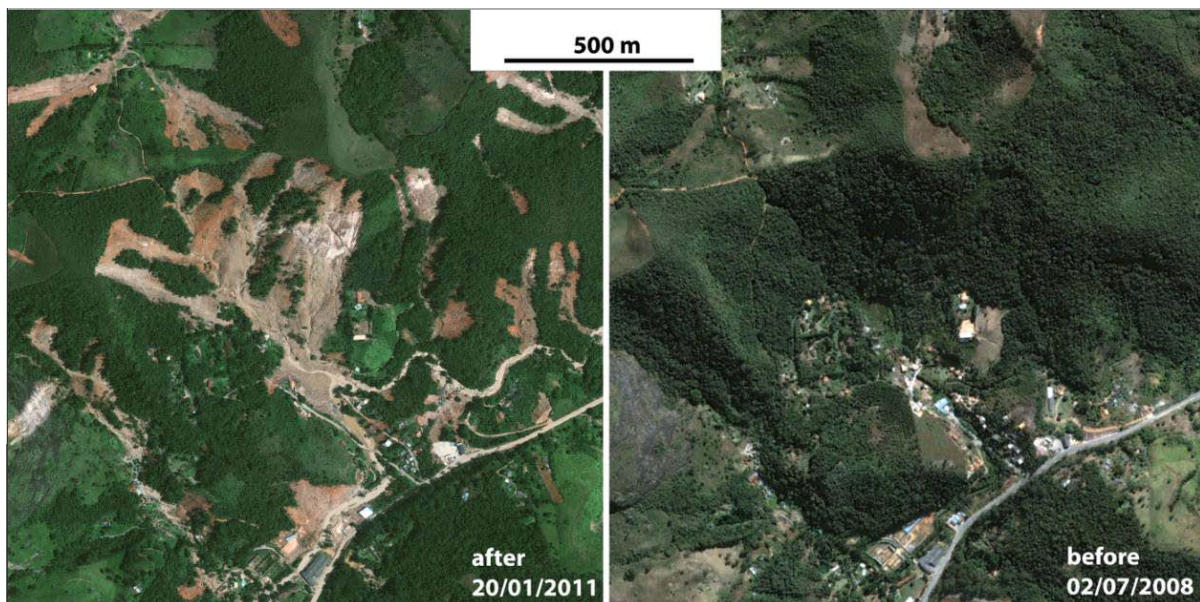


Figure 1: VHR satellite images at Nova Friburgo / south-east Brazil recorded before and after heavy rainfalls that triggered thousands of landslides at January 12, 2011 (Copyrights: Google Earth, Geoeye Company).



Figure 2: Medium resolution images of rainfall triggered landslides at the same region as in Figure 1 recorded by NASA EO-1 ALI at 10 m resolution (Copyright: NASA).

The number of available UAVs exploded in recent years and from low-cost systems equipped with consumer-grade cameras [Niethammer *et al.*, forthcoming] to fully integrated systems including near-infrared cameras, positioning systems and laser scanning devices [Nagai *et al.*, 2009] a great diversity of systems became available [Eisenbeiss, 2010].

The main advantages of image acquisition with UAVs are low-costs and their temporal very flexible employment. An examples from Taiwan [Chou *et al.*, 2010] illustrate how small platforms can be used to acquire images shortly after a given event and reports from China suggest that after the Wenchuan earthquake in 2008 at least 50 UAVs were involved in the monitoring of the disaster situation [Li, 2010]. The operation of UAVs below cloud cover provides another advantage above spaceborne sensors, whereas on the other hand rainfall and high wind speeds may prohibit the employment of light-weight systems.

For UAVs weighting more than 150 kg the European Aviation Safety Agency (EASA) is currently elaborating regulations. Below that weight national legislation should apply but since most EU countries do not yet have agreed on a clear legislation the operation of UAVs remains a grey zone in many cases. In Germany for example operating UAVs weighting less than 25 kg and flying below 300m is relatively unproblematic as long as they fly in the line of sight of the pilot and do not enter restricted airspace.



Figure 3: Exemplary light-weight UAV systems. Right: Voyager G8 RR (http://www.sensor-asia.net/wp-content/uploads/2010/12/IMG_1389.jpg) , Left: Open-Source multicopter systems [Niethammer et al., 2009]

3.1.2. Data analysis

A. Visual interpretation of single and stereoscopic images

[GeoZS]

Image interpretation enables detection, identification, measurement and/or evaluation the significance of environmental and cultural objects, patterns and spatial relationships in an image. Targets on aerial photographs or imagery (in tones of grey in B/W photography and in color / false colour photography in different colours/hues) may be any feature or object which can be observed in an image, has a form and can be distinguishable from other features around it in the image. Visibility of objects in the images varies due to the inherent characteristics of the objects and the quality of the aerial photography or imagery. When the same feature is photographed from two different positions with overlap between successive images, a stereo-model giving the three-dimensional view of the feature can be seen under a stereoscope. This valuable information cannot be obtained from a single print. Since giving adequate consideration to all aspects of a terrain depends on an interpreter's ability to integrate such elements to defined objectives, visual interpretation is considered as deductive process, where the identification of certain key features leads to the recognition of others.

Though there are some general guidelines for landslide specific [Rib and Liang, 1978; Soeters and Van Westen, 1996] no unified approach exists for the techniques or the methodology of visual image interpretation. It depends on kind of information to be interpreted, accuracy of the results to be obtained, the reference level of the person executing the interpretation, kind and type of imagery or photographs available, instruments available,

scale and other requirements of the final map, external knowledge available and any other sensory surveys that have been or will be made in the near future in the same area.

For landslide mapping image interpretation is commonly applied on scales between 1:10000 and 1: 50000 and generally three different analysis are used: (1) monocular in the case of satellite imagery and photographic enlargements, (2) stereoscopic for vertical and near vertical aerial photographs, SPOT as well as IRS-IC stereo-imagery and (3) densitometric for quantitative analysis using densitometers and for identifying terrain features. Such analysis is now carried out using digital image processing systems and GIS environments.

B. Image classification with semi-automated pixel-based methods

[JRC]

Semi-automated pixel-based methods include unsupervised and supervised classification, as well as change detection. We refer to sections 4.4 and 4.5 of D4.1 for a detailed overview and relevant references.

Unsupervised classification and clustering techniques can be used to obtain a first overview of the inherent structure of a given dataset. This technique does not need a sample, but the obtained classes must usually be interpreted and labeled by the user. Typically the user defines the number of targeted classes and a clustering algorithm assigns pixels to the different classes according to their position in a multivariate space. Many different algorithms using different similarity measures have been proposed.

A detailed overview of supervised classification techniques can be found in section 4.4 of D4.1. Maximum Likelihood Classification (MLC), Minimum Distance Classification and Mahalanobis Classifier are most commonly used. Important are also Markov Random Fields as this method takes into account the lack of contextual information, starts from the assumption that the class value of a pixel is to some degree conditional independent to its neighborhood and allows removing outliers. Finally, there are non-parametric models such as Linear Discriminators, Support Vector Machines (SVM), Artificial Neural Networks (ANN) and Random Forests. While these methods mainly used digital number (DN) of multispectral bands, also indices such as NDVI, DEM derivatives, and externally prepared vector layers (of flow accumulation and stream networks) or shadow masks have been employed. Some studies also investigated the use of image texture for pixel-based supervised classification to overcome the limitations of spectral information alone (case-study 2 in D4.1). Including texture information, especially Haralick texture features such as GLCM entropy, enables enhancing class separability and the accuracy of the classification.

If multi-temporal imagery of a given area can be provided, change detection is a promising approach for landslide mapping and monitoring. Despite the great variety of proposed approaches, change-detection methods usually comprise a modelling phase and a subtraction phase. While there is no general agreement on the best available method differencing, PCA, Change Vector Analysis (CVA) and Post-Classification Comparison are at present most frequently used.

C. Image classification with semi-automated object-oriented methods

[ITC+CNRS]

Especially with high resolution imagery the use of image segmentation proved to be beneficiary for many applications including landslide inventory mapping. Proposed approaches share the involvement of image segmentation techniques and the exploitation of spatial context and mainly focus on the mapping after catastrophic slope failures. Three main groups can be differentiated: expert-written rulesets, change detection, machine-learning and unsupervised clustering techniques.

The first studies that involved image segmentation for landslide mapping were based on expert-written rule sets [Barlow *et al.*, 2003; Barlow *et al.*, 2006]. If such rule sets are properly adjusted to the particular scene they may yield spatial location and landslide [Martha *et al.*, 2010a] type but the degree of automation is very low.

Given the availability of suitable pre- and post-event images are available change detection methods proved to be a suitable tool especially of post-disaster mapping. Multitemporal information can be exploited with object change detection [Lu *et al.*, in press; Park and Chi, 2008] whereas the analysis of change vectors helps to eliminate false positives and image segmentation provides coherent spatial units that help to suppress change noise. One difficulty arises from the selection of appropriate thresholds to distinguish between change and non-change areas. Though methods for spatial and spectral matching of multi-temporal images advanced considerably in recent years, VHR imagery recorded with different illumination conditions or view angles may in many cases still pose unsolvable problems for change detection.

Proposed machine-learning techniques [Stumpf and Kerle, accepted] and more traditional supervised classification techniques [Moine *et al.*, 2009] are already applicable using post-event imagery only. They require a set of training samples and benefit from the inclusion of topographic datasets. Considering the great diversity of sensor systems and landslide processes such semi-automatic techniques potentially offer a high flexibility but further research is needed to assure their robustness in real world applications.

D. Correlation of optical images

[CNRS]

Crippen and Blom [1991] were among the first to introduce correlation of optical images into geosciences as a tool to measure surface displacement and migration of dunes. They proposed to use the maximum correlation coefficient (correlation peak) of the grey values of two images in order to locate homologous displaced patches and achieved subpixel precision by bilinear interpolation of the original images to a finer resolution. Since this time, several algorithms (operating in the spatial domain and in the frequency domain Debella-Gilo and Kääh, 2011, [Debella-Gilo and Kääh, 2011; Leprince *et al.*, 2007) have been proposed to enhance precision, accuracy and robustness of the correlation and to define quantitative indicators of the uncertainty. The result of the correlation analysis, typically a full field

measurement of the displacement, contains a considerable amount of data compared with classical instrumentations and sensors (extensometers, fissurometers, inclinometers, GPS, strain gauges).

So far, image correlation techniques have been applied only on aerial and satellite images (SPOT, QuickBird, OrbView, EROS) for the creation of landslide displacement maps [Casson *et al.*, 2003; Delacourt *et al.*, 2007; Leprince, 2008], whereas the use of image correlation on terrestrial images has not been as popular for permanent landslide monitoring as in other application field such as in solid and fluid mechanics or for the monitoring of ice glaciers [Fallourd *et al.*, 2010] or volcanoes [Honda and Nagai, 2002].

Because of the remarkable sensitivity of the technique, the same type of method can be applied over a wide range of scales, from high-resolution satellite imagery (typically 2.5 to 5 m spatial resolution) to airborne and UAV very-high resolution imagery (from 0.5 to 2.5 m spatial resolution) and terrestrial ultra-high resolution images (less than 0.5 m spatial resolution). Recent works imply the development of sub-pixel displacement determination, the use of multi-modal images, and the introduction of feature semantics in the correlation. A major issue in applying image correlation for landslide analysis is to obtain sufficiently patterned images and very precise co-registration. When using image pairs acquired from the same position, only in-plane displacement can be retrieved, and one of the main challenges is therefore to use sequences of images from several angles of views in order to provide relevant information for the extraction of full three dimensional displacements (stereo-correlation). A second challenge lies in the inversion of mechanically significant properties from the displacement signal, such as the macro-scale rheology of the displaced material and the opening of cracks and fissures for brittle material.

3.1.3. Innovative case studies

The following section demonstrates the use of optical data via short summaries of four recently published or submitted research works carried out within SafeLand or through sister projects.

Random Forests and object-oriented analysis for landslide mapping from very high resolution imagery

Application: Landslide inventory mapping

Technique: Passive optical space- and airborne sensors

Main references: Stumpf, A. & N. Kerle (2011): Object-oriented mapping of landslide using Random Forests

Contributors: ITC (Stumpf, A., N. Kerle), CNRS (J. P. Malet)

Abstract

The increasing availability of very high resolution (VHR) remote-sensing images reveals new opportunities for the cartography of landslides in risk management and disaster response. Object-oriented image analysis has become one of the key-concepts to better exploit additional spatial, spectral and contextual information. The multitude of additional object attributes calls for the use of advanced data mining and machine learning tools to identify the most suitable features and handle the non-linear classification task. In this study we used the Random Forest algorithm for the selection of useful features and object classification in the context of landslide mapping. A workflow for image segmentation, feature extraction, feature selection and classification was developed and tested with multi-sensor optical imagery from four different test sites. Due to class imbalance and class overlap between landslide area and non-landslide areas the classifier can be heavily biased towards over and under prediction of the affected areas. This is a not uncommon issue for many real-world applications and a procedure to estimate a well-adjusted class ratio from the training samples was designed and tested. A number of potentially useful object metrics is evaluated and it is demonstrated that topographically guided texture measures provide significant enhancements. Employing 20 % of the image objects for training accuracies between 73.3 % and 87.1 % were achieved at four different test sites.

Keywords: landslide mapping; VHR satellite images; image segmentation; object-oriented image analysis; Random Forest

1. Introduction

Comprehensive landslide inventories are the most commonly used source for quantitative landslide hazard and risk assessment at regional scales [van Westen *et al.*, 2006]. Such inventories are also an important tool to address related concerns, such as to explore and quantify the role of landslides in the evolution and sediment budget of mountainous landscapes [Malamud *et al.*, 2004]. Manual interpretation of aerial photographs and field work to date remains the most frequently followed approach for the elaboration of inventory maps in scientific studies and by administrative bodies. Despite its time-consuming and labor intensive nature, however, results still include a large degree of subjectivity and may vary considerably among different authors [Galli *et al.*, 2008].

A number of recent events in China (2008), Italy (2009), Haiti (2010), and Brazil (2011) illustrate that the short-term availability of comprehensive VHR satellite images and strongly contrast the lack of reliable machine-aided mapping workflows. Proposed workflows for the analysis of optical data largely focused on the signals of individual pixel [Borghuis *et al.*, 2007; Nichol and Wong, 2005] or require the adjustment of hard coded thresholds for object classification [Barlow *et al.*, 2006; Lu *et al.*, in press; Martha *et al.*, 2010a]. Based on

samples, image segmentation and the Random Forest (RF) [Breiman, 2001] algorithms this study elaborates and tests a workflow feature selection and classifier training for landslide mapping on images from variety of state-of-the-art optical sensors.

2. Data and Methods

The analysed VHR imagery comprised an aerial photograph, IKONOS, Quickbird and Geoeye-1 of recently sites at France, China, Italy and Haiti, respectively (Figure 1). Furthermore topographic datasets were available from various sources and conformable resampled to a resolution of 10m. Reference data was available through landslide inventories elaborated from field work and the interpretation of various VHR remote-sensing datasets.

Image segmentation was performed on all images within eCognition 8 on 15 different scales considering spectral information and at each scale 96 object attributes including color, texture, shape and topographic derivatives were calculated. To evaluate their importance for a correct classification all landslide objects and equal amount of non-landslide objects were sampled and the RF-based feature selection approach described in *Diaz-Urriarte and Alvarez de Andres* [2006] was applied. In order to evaluate the classifier performance and the effects of feature reduction 20% of the landslide objects and an equal number of non-landslide objects were randomly sampled from the entire populations to train RFs [Liaw, 2010], once with the full feature set and once with the selected subsets.

In order to obtain a nearly balanced rate of commission and omission errors the training sample was again iteratively sub-divided. During various iterations the 20% of landslide objects were randomly sampled from the original training data. Starting with an initially balanced ratio β_i of non-landslide and landslide objects the ratio was increased by 0.1 after each iteration (bootstrap re-sampling). The underlying assumption was that a class ratio that provides a balanced error rates on the resampled subsets (β_n) of the original training samples would also serve to enhance the error balance for the entire population. The classifier performance was tested after each iteration on the remaining subsets of original training data and the ratio which provided the best balance was adopted to resample the entire training data. An overview of the complete workflow is also provided in Figure 2.

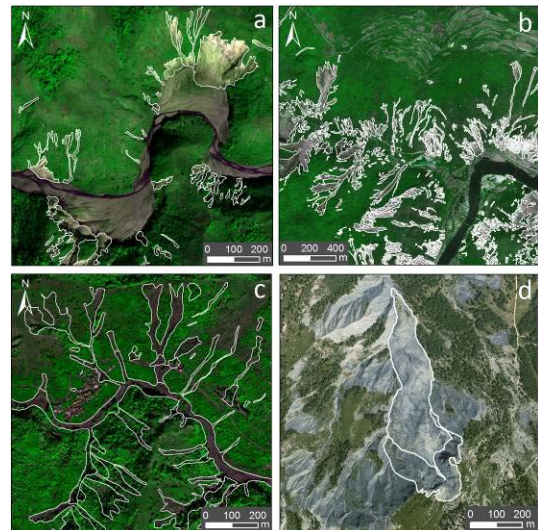


Figure 1: Analyzed subsets at the different test sites. a) Haiti, b) Wenchuan, c) Messina, d) Barcelonnette area. White outlines indicate the landslide areas.

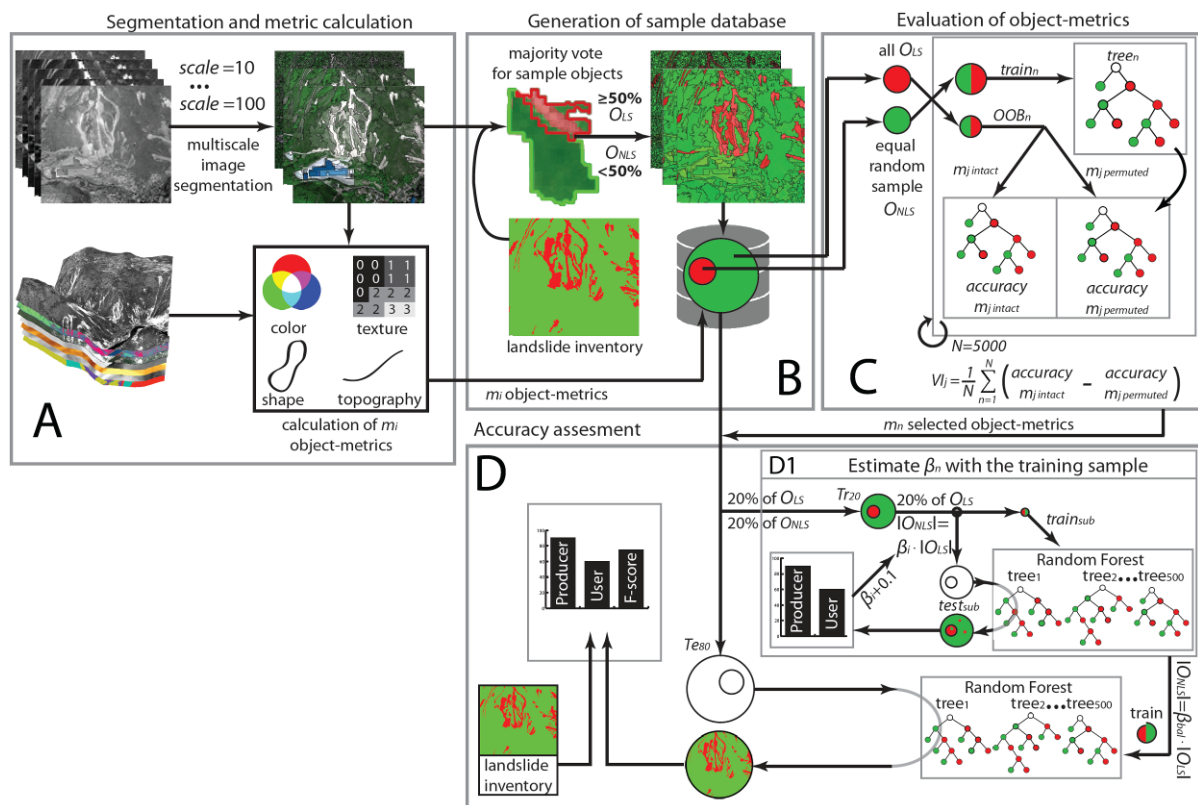


Figure 2: Overview of the processing steps followed in this study. **A**: The images were segmented at 15 different scale factors, and at each scale a number of object-metrics (m_i) was calculated. **B**: Based on the landslide inventory all segments can either be assigned as landslides (O_{LS}) or non-landslide objects (O_{NLS}). **C**: A balanced subset ($|O_{LS}| = |O_{NLS}|$) was repeatedly ($N=5000$) split into a training sample ($train_n$) and an out-of-bag test sample (OOB_n). The OOB_n sample was classified with the decision tree ($tree_n$) built from $train_n$. Sequentially, and one at a time, each object-metric m_j used in $tree_n$ was randomly permuted within the OOB_n sample. The respective decrease of the classification accuracy was measured and the variable importance (VI) of each m_j calculated as the average decrease from 5000 trees. $VI_j = \frac{1}{N} \sum_{n=1}^N (accuracy_{m_j \text{ intact}} - accuracy_{m_j \text{ permuted}})$. **D**: 20% of the image objects (Tr_{20}) and all selected object-metrics m_n were employed for the training of the RFs. **D1**: An iterative procedure was adopted to estimate the ratio of O_{LS} and O_{NLS} (β_n) in the training sample that leads to balanced error rates. In the first iteration 20% of O_{LS} and an equal number of O_{NLS} ($\beta_i=1$) were randomly sampled from Tr_{20} ($train_{sub}$) to train a RF. The remainder ($test_{sub}$) was sent through the RF in order to assess user's and producer's accuracies. The next iteration started with $\beta_i+0.1$ and the complete procedure was repeated until $\beta_i=7$. β_{bal} was determined as the β_i that led to the smallest difference between user's and producer's accuracies. **D**: The estimated β_{bal} was applied to the complete $train$ set, which was subsequently used to train the final RF. Accuracies in terms of correctly classified areas and objects were finally assessed with the remaining 80% test set (Te_{80}).

3. Results

3.1. Feature selection

Color, topographic variables and topographically guided versions of Haralick's original texture measures [Haralick, 1973] were ranked with a high variable importance at all test sites and different segmentation scales. On average only about one third of the pre-selected metrics were detected as useful. The ranking of less important features and especially the overall number selected varies considerably among the different test sites and in dependency of the segmentation scale (Figure 3). Shape metrics provide generally very little additional information. At larger scales and segmentation scales shape indices provide some discriminant power but cannot compensate the loss of fidelity of that a coarser segmentation causes for other features.

A RF classifier trained with 20% of all landslide objects and an equal number of non-landslide objects yielded higher accuracy in the classification of unseen image objects if a reduced feature space was adopted. This was observed for all test sites and a representative subset of tested segmentation scales.

3.2. Estimate of optimal class-balance β_n from the training samples

For all cases we observed a strong over prediction of landslide areas if a class-balanced training sample ($\beta_i=1$) was employed. Through random resampling of the original training data into further subsets training and test sets (20/80) with altering class distribution were created. Iteratively increasing the ration on non-landslide objects in the training sample, it was possible to monitor the effects of the changing class distribution on user's and producer's accuracies for the test set (Figure 4). The estimated class ratios (β_n) were then applied for the entire training set (20% of all data per site) and the overall performance of the classification was assessed on the remaining test data (80% of the data).

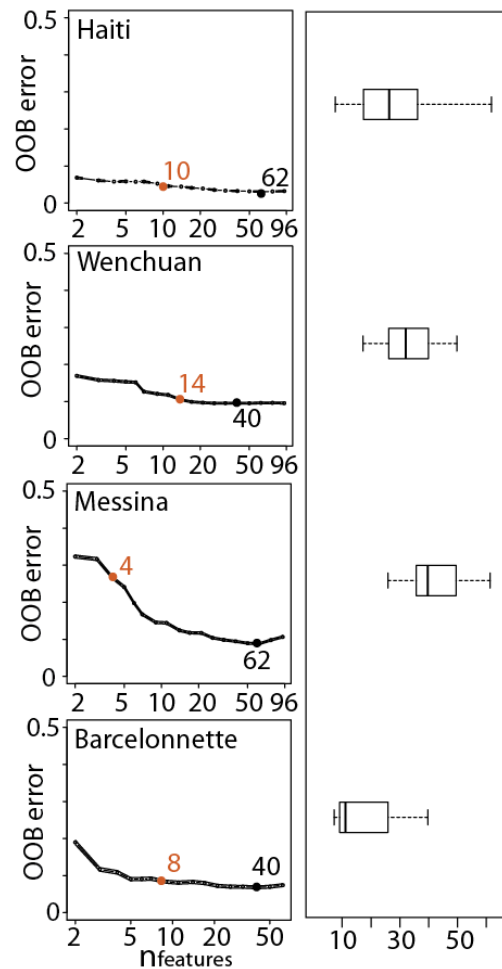


Figure 3: Feature selection history at the four test sites with the smallest segmentation scale. The out-of-bag (OOB) error is an error estimate intrinsic to the Random Forest approach [see Breiman, 2001]. The black dot indicates the variable combination with the smallest OOB error. The brown dot highlights the highest ranked texture measure with the respective rank. Boxplots indicate the variability of the number of selected features among all 15 segmentation scales.

As the estimated βn were in all cases below the natural class imbalance not all non-landslide objects initially subsampled for training could be used in the training set at once. However, they can be adopted to create several (here 50) βn -adjusted training sets with slightly different characteristics which yields a further estimate of the accuracy variability. Although, βn -estimates did not solve the problem entirely they provided a significantly better balance between user's and producer's accuracies than could be achieved with the natural class distribution or an ad hoc balanced training sample. The induced variance of non-landslide objects in the training sample demonstrated very little influence on the stability of the achieved accuracy.

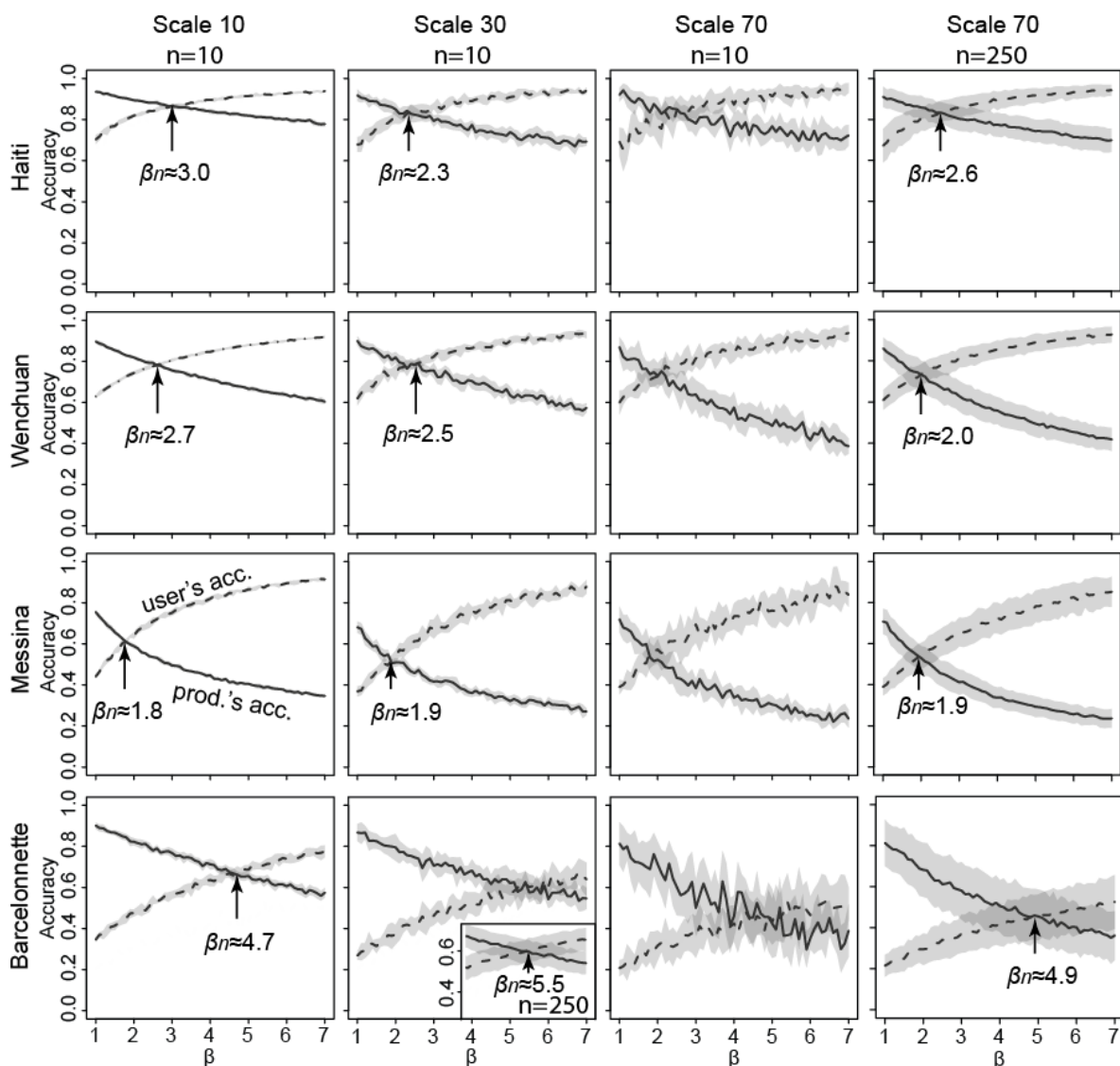


Figure 4: Estimates of the class balance (βn) that lead to a balance of the mean user's (dashed black line) and mean producer's accuracies (full black line) from iterative resampling of the training data. The means of the accuracies for each β were calculated from 10-fold bootstrap replicate runs ($n=10$). The grey margins show the corresponding standard deviations. For learning curves with high variance additionally figures from 250 bootstrap replicate runs ($n=250$) are presented.

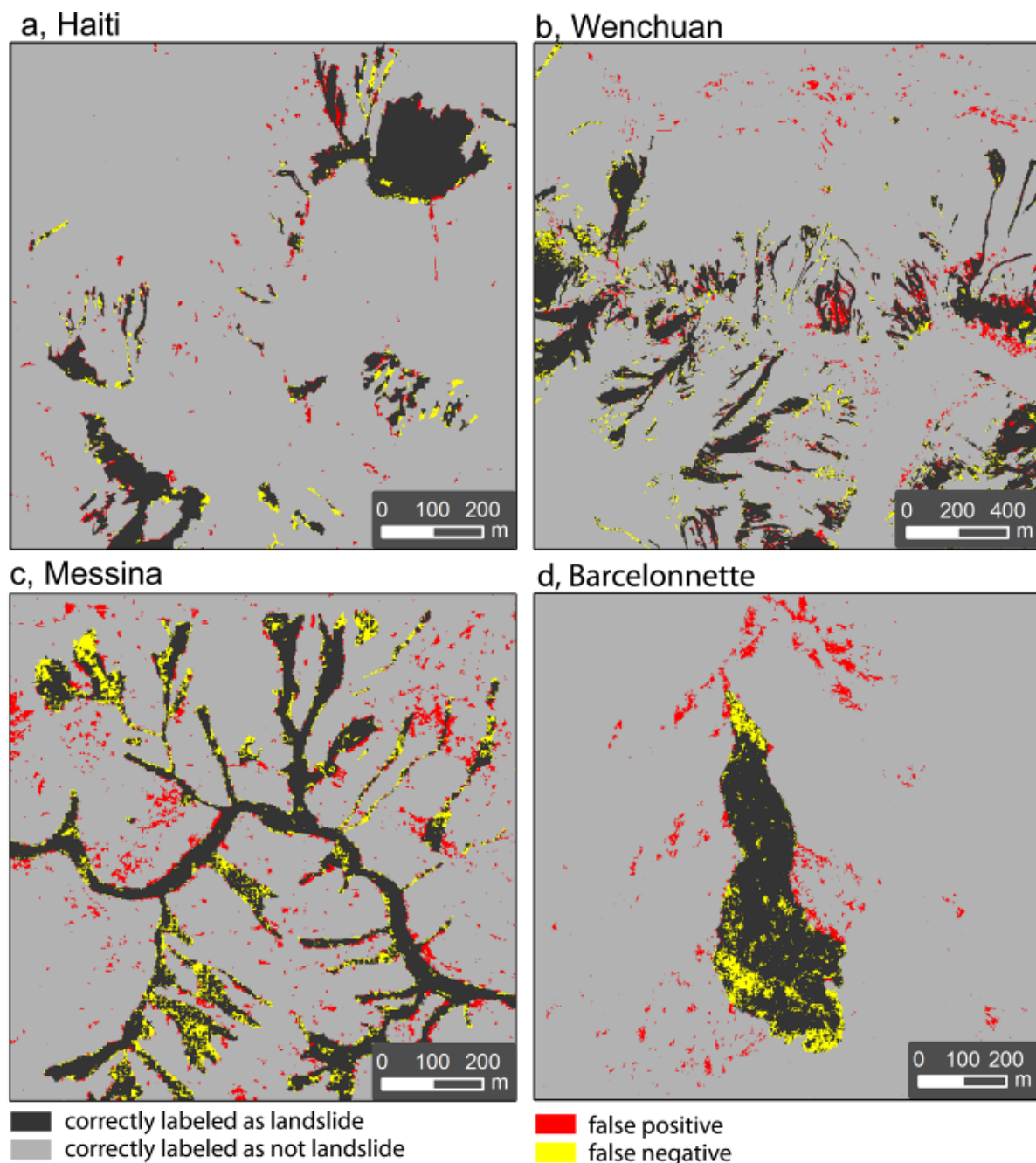


Figure 5: Results with a segmentation scale of 10, after feature selection and balancing of the error rates as indicated in Table 4 at a, Haiti b, Wenchuan c, Messina and d, Barcelonnette. Correctly classified areas include the samples used for training.

4. Results and Discussion

Among several factors that influence the correct recognition of affected areas feature selection as well as class-imbalance and –overlap were analyzed in this study. RF-based feature reduction enhanced the classifier performance in terms of accuracy and speed. Additional features resulting from image segmentation such as texture and auxiliary topographic data are

capable to considerably reduce confusion. Classifier performance may be benchmarked with a desired predefined producer's accuracy [Brenning, 2009], whereas balanced error rates we considered as rather desirable for landslide inventory mapping because over- or under-prediction would lead to systematic over- and under-estimation of the hazard. A procedure to adjust the class balance in the training sample was designed and helped to enhance to improve the balance of user's and producer's accuracy significantly. In summary, the RF classifier provided relatively high accuracies of up to 87% for the test sites Haiti and Wenchuan, while in the case of Messina the best model reached an accuracy of 73% (Figure) Those figures are in a similar range as the results of other recent studies on landslide mapping from optical imagery [Barlow *et al.*, 2006; Lu *et al.*, in press; Martha *et al.*, 2010a].

Table 1: Accuracy assessment for all test sites at three exemplary segmentation scales. RFs (ntrees = 500), trained with 20% of the landslide objects (OLS) and β_n -fold amount of non-landslide objects (ONLS) were tested. The mean accuracies and their standard deviations were derived from 50 replicate runs. The best result for each test site is indicated with bold numbers.

	Scale	β_n	user's accuracy	producer's accuracy	F_{area}	F_{obi}	β_n -adjusted training sample		
							O _{LS}	O _{NLS}	% all objects
Haiti	10	3.0	0.888 ±0.001	0.857 ±0.002	0.871 ±0.001	0.897 ±0.001	4512	13536	11.7
	30	2.3	0.828 ±0.012	0.871 ±0.009	0.849 ±0.007	0.883 ±0.003	564	1297	12.8
	70	2.6	0.885 ±0.011	0.724 ±0.013	0.7961 ±0.007	0.885 ±0.005	149	387	14.3
Wenchuan	10	2.7	0.813 ±0.001	0.811 ±0.001	0.812 ±0.001	0.805 ±0.001	6535	17645	17.0
	30	2.5	0.812 ±0.004	0.771 ±0.005	0.791 ±0.002	0.803 ±0.002	570	1425	17.4
	70	2.0	0.777 ±0.009	0.753 ±0.011	0.765 ±0.006	0.799 ±0.006	125	250	16.5
Messina	10	1.8	0.729 ±0.003	0.746 ±0.002	0.737 ±0.001	0.730 ±0.001	6135	11043	10.8
	30	1.9	0.690 ±0.012	0.609 ±0.009	0.647 ±0.004	0.592 ±0.004	663	1260	11.3
	70	1.9	0.643 ±0.020	0.598 ±0.013	0.620 ±0.008	0.605 ±0.011	125	238	11.9
Barcelonnette	10	4.7	0.778 ±0.01	0.780 ±0.005	0.779 ±0.004	0.765 ±0.002	1810	8507	10.8
	30	5.5	0.747 ±0.021	0.759 ±0.018	0.752 ±0.010	0.674 ±0.008	237	1304	10.1
	70	4.9	0.633 ±0.056	0.886 ±0.023	0.733 ±0.035	0.653 ±0.027	46	226	8.9

Though the quantities of employed samples are not always explicitly mentioned [Barlow *et al.*, 2006; Borghuis *et al.*, 2007; Nichol and Wong, 2005], most proposed solutions depend on the availability of some sort of training area to adjust the method. Once the samples are provided, the framework presented in this paper has the potential to run fully automated with different image types, and liberates the user from the selection of appropriate features and thresholds.

It can be observed that larger segmentation scales, yielding to larger objects with higher intra-object variance, are accompanied by a loss of accuracy. For the cases Messina and Wenchuan this has to be attributed to an increasing mismatch between the boundaries of the image objects and the reference objects (expressed by decreasing F_{area} in Table 1). For the test sites Messina and Barcelonnette large segmentation scales also decreases the classifier performance (expressed by decreasing F_{object} in Table 1).

Though, the particular performance of the presented supervised framework will vary for different ground conditions and input datasets, the robust performance of the workflow in the tested cases raises confidence in its utility of landslide mappings on regional scale. Further observations (not presented here) indicate that importance of different features varies in dependency of the segmentation scale and hence further improvements might possible considering evidence hierarchically among different scales. However, to the best of our knowledge a clear conceptual framework for such a multi-scale classification is still missing. More research is needed to test available machine learning tools on further datasets (multi-temporal datasets), on regional scale and under the consideration of user interaction.

References

- Barlow, J., S. Franklin, and Y. Martin (2006), High spatial resolution satellite imagery, DEM derivatives, and image segmentation for the detection of mass wasting processes, *Photogrammetric Engineering and Remote-sensing*, 72(6), 687-692.
- Borghuis, A. M., K. Chang, and H. Y. Lee (2007), Comparison between automated and manual mapping of typhoon-triggered landslides from SPOT-5 imagery, *International Journal of Remote-sensing*, 28, 1843–1856.
- Breiman, L. (2001), Random Forests, *Machine Learning*, 45(1), 5-32.
- Brenning, A. (2009), Benchmarking classifiers to optimally integrate terrain analysis and multispectral remote-sensing in automatic rock glacier detection, *Remote-sensing of Environment*, 113 239–247.
- Diaz-Uriarte, R., and S. Alvarez de Andres (2006), Gene selection and classification of microarray data using random forest, *BMC Bioinformatics*, 7(1), 3.
- Galli, M., F. Ardizzone, M. Cardinali, F. Guzzetti, and P. Reichenbach (2008), Comparing landslide inventory maps, *Geomorphology*, 94(3-4), 268-289.
- Haralick, R. M., K. Shanmugam and I. H. Dinstein (1973), Textural features for image classification., *IEEE Transactions on Systems, Man and Cybernetics*, 3(6), 610-621.
- Liaw, A. (2010), randomForest: Breiman and Cutler's random forests for classification and regression, Version 4.5-36.
- Lu, P., A. Stumpf, N. Kerle, and N. Casagli (accepted), Object-oriented change detection for landslide rapid mapping, *IEEE Geoscience and Remote-sensing Letters*.
- Malamud, B. D., D. L. Turcotte, F. Guzzetti, and P. Reichenbach (2004), Landslide inventories and their statistical properties, *Earth Surface Processes and Landforms*, 29(6), 687-711.
- Martha, T., N. Kerle, C. J. van Westen, and K. Kumar (2010), Characterising spectral, spatial and morphometric properties of landslides for semi-automatic detection using object-oriented methods, *Geomorphology*, 116(1-2), 24-36 .
- Nichol, J., and M. S. Wong (2005), Satellite remote-sensing for detailed landslide inventories using change detection and image fusion, *International Journal of Remote-sensing*, 26(9), 1913 - 1926.
- van Westen, C. J., T. W. J. van Asch, and R. Soeters (2006), Landslide hazard and risk zonation—why is it still so difficult?, *Bulletin of Engineering Geology and the Environment*, 65(2), 167-184.

Digital correlation of optical images for landslide monitoring and detection on regional scale

Application: Landslide mapping and monitoring

Technique: Multi-modal optical images

Main references: Delacourt, C., P. Allemand, E. Berthier, D. Raucoules, B. Casson, P. Grandjean, C. Pambrun, and E. Varel (2007): Remote-sensing techniques for analysing landslide kinematics: a review

Contributors: ITC (A. Stumpf), BRGM (D. Raucoules, M. de Michele, C. Delacourt)

Abstract

Digital image correlation has become an important technique for the detection and monitoring of surface displacements. The short text provides an overview of currently available techniques and recent studies that applied DIC on optical images for landslide monitoring.

Keywords: DIC, detection and monitoring of surface displacement

During the last decade DIC has been tested and validated for the monitoring of glacier flows, the measurement of coseismic slip, volcanic ground deformation, dune migration and landslide surface displacement. A number of improvements have been achieved through enhanced algorithms for correlation and interpolation and determination the location of corresponding points in two images with sub-pixel precision. The theoretical precision of the measurement can therefore reach between 1/16 [Debella-Gilo and Käüb, 2011] or 1/20 of a pixel [Leprince *et al.*, 2007a]. The actual accuracy of the measurements however depends on several factors such as the spatial and temporal resolution of the available imagery, the magnitude and coherency of the displacement, the accuracy of the underlying DEM, and not at least the proper co-registration of the multi-temporal images (Table 2).

On regional scale DIC has been applied in a multitude of studies to measure coseismic slip and deformation which is typically coherent over larger areas [Leprince *et al.*, 2007a]. Although, such regional measurements in some cases revealed slope failures as a signal de-correlation (Fig. 1) the method targets rather the detection and measurement of the displacement of slow moving landslide.

Table 2: Overview of options for the measurement of ground displacement from optical sensors [modified after Delacourt *et al.*, 2007]

	Optical sensor			
	Satellite	Aerial	Remote-controlled	Fixed Camera
Measurement Type	2 D horizontal displacement or 3D if DEMs available			
Spatial Resolution	0.6 m to 80 m	0.5 m to 2 m	< mm to 1 m	~ cm to ~ m
Accuracy	~1/5 to 1 pixel	~ 1 - 3 pixels	A few pixels	1/5 pixel
Swath	10 x 10 km to 60 x 60 km	5 x 5km	10 x 10 m to 300 x 300 m	10 x 10 m to 1 x 1 km
Temporal resolution	~30 days and less	> 5 years	On request	1 s to 1 day
Archive	SPOT1-4 (1986); IRS-1C, 1D, etc. (1995) SPOT5 (2002); IKONOS (1999); QUICKBIRD (1999); ALOS (2006), etc.	since 1950s	recently – locally a few years	recently - locally a few years
Major references	[Berthier <i>et al.</i> , 2006; Berthier <i>et al.</i> , 2005; Gonzalez <i>et al.</i> , 2010; Kääh, 2002; 2005; Leprince, 2008; Scambos <i>et al.</i> , 1992; Scherler <i>et al.</i> , 2008; Tseng <i>et al.</i> , 2009]	[Ayoub <i>et al.</i> , 2009; Casson <i>et al.</i> , 2003; Debella-Gilo and Kääh, 2011; Delacourt <i>et al.</i> , 2004; Delacourt <i>et al.</i> , 2009; Kääh, 2002; Michele and Briole, 2007]	???	[Arattano and Marchi, 2000] Travelli <i>et al.</i> 2011 (this document)

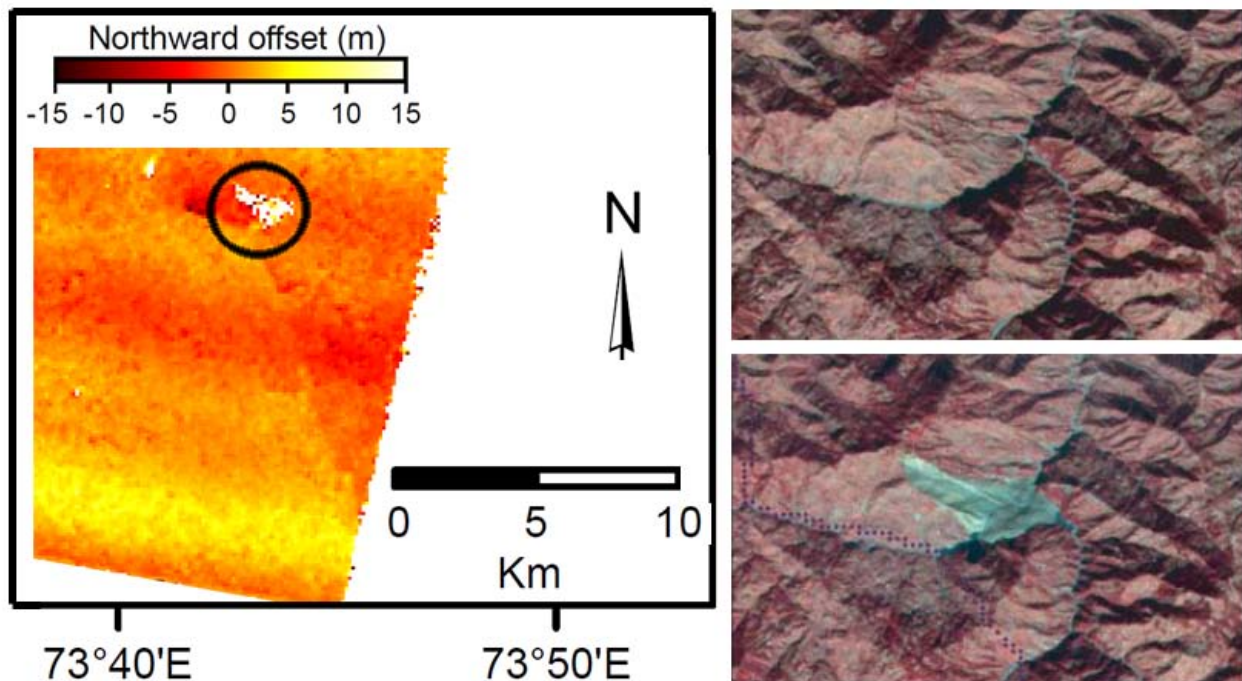


Figure 1: Left: Decorrelation signal (black circle) in the northward component of the coseismic offset field from the 2005 Kashmir earthquake derived from ASTER images. Right: Before and after images showing the area where the landslide occurred [modified after Leprince, 2008]

Although, relatively user friendly software to perform DIC with aerial and spaceborne images became available [Leprince *et al.*, 2007b], there are still rather few studies that applied the method to measure the surface displacement of landslides from airborne or satellite images [Casson *et al.*, 2005; Debella-Gilo and Kääh, 2011; Delacourt *et al.*, 2009; Kääh, 2002; Tseng *et al.*, 2009; Yamaguchi *et al.*, 2003] most of them working with individually developed algorithmic implementations. As indicated in Table 2 there are several potentially sources for recent imagery and in most areas such investigation could in principal benefit from large image archives available. In many cases this potentially enables the analysis of the displacement history over several decades and may provide important information to understand the failure mechanism and hence associated hazards and risk. Probably one of the most detailed investigations in this direction has been undertaken by Casson *et al.* [2005] who measured the average surface displacement of the La Clapière landslide from aerial photographs over time period of more than two decades. In combination with mutitemporal DEM it was further possible to reconstruct changes in the geometry and velocity of the slip with time.

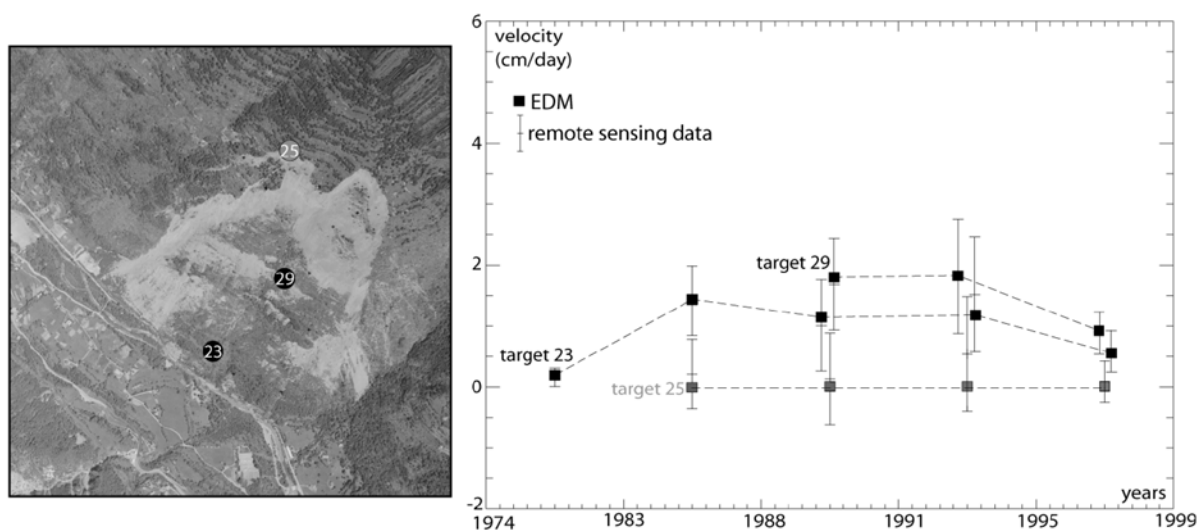


Figure 2: Comparison of remote-sensing derived displacement vectors with ground measurements at the La Clapière landslide [Casson *et al.*, 2005]

The only currently available example for the application of DIC in landslide detection and monitoring on a regional scale was presented by Delacourt *et al.*, [2007] for the Barcelonnette area in southern France (2). It demonstrates that the method is not only applicable for the detailed monitoring of individual sites but may also provide additional information on the landslide activity for the creation and updating of landslide inventories on regional scale.

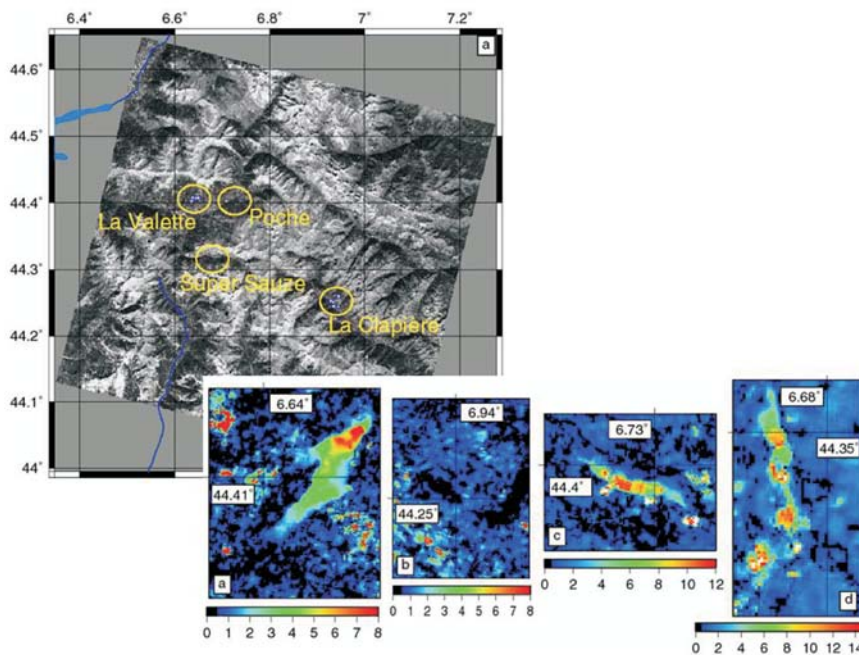


Figure 3: Example for the application of DIC for the detection and measurement of landslide-induced displacement at regional scale a) “La Valette” mudslide, b) “La Clapière” landslide (difficult to discriminate), c) “Poche” mudslide and d) “Super Sauze” mudslide [Delacourt *et al.*, 2007].

As noted above only two recent studies provide some comparison of different DIC implementations [Debella-Gilo and Käab, 2011; Haug *et al.*, 2010] and a comprehensive benchmarking and transparent presentation of available algorithms would facilitate the choice of the optimal methods. As the measurable displacement is directly a function of the pixel size of the input image more efforts are still needed to test the techniques on recently launched VHR spaceborne sensors (WorldView, Geoeye). Such sensors generally also provide multispectral information which might be useful to identify and filter out surface types that are known to introduce mismatches in DIC results (homogenous textured forests). New X-band radar satellites now also deliver images with resolution suitable for DIC and corresponding techniques are summarized in section 3.3.2 C.

Delacourt *et al.* [2007] emphasized the potential of fixed cameras and UAVs for acquiring imagery with any desired temporal frequency. A comprehensive literature review revealed no example where multitemporal UAV-acquired imagery has been used for a correlation-based measurement of displacement. The possibility to visually track landslide surface features from multitemporal UAV images has been confirmed by Niethammer *et al.*, [forthcoming] whereas the applicability of DIC on the fully co-registered images still needs to further elaboration. On the other hand, a study on DIC from terrestrial fixed cameras carried out by Travelletti *et al.* [2010] at the SafeLand test site Super Sauze yielded accurate and detailed maps of the landslides surface motion (this section).

References

- Arattano, M., and L. Marchi (2000), Video-derived velocity distribution along a debris flow surge, *Physics and Chemistry of the Earth, Part B: Hydrology, Oceans and Atmosphere*, 25(9), 781-784.
- Ayoub, F., S. Leprince, and J.-P. Avouac (2009), Co-registration and correlation of aerial photographs for ground deformation measurements *ISPRS Journal of Photogrammetry and Remote-sensing*, IN PRESS.
- Berthier, E., H. Björnsson, F. Pálsson, K. L. Feigl, M. Llubes, and F. Rémy (2006), The level of the Grímsvötn subglacial lake, Vatnajökull, Iceland, monitored with SPOT5 images, *Earth and Planetary Science Letters*, 243(1-2), 293-302.
- Berthier, E., H. Vadon, D. Baratoux, Y. Arnaud, C. Vincent, K. L. Feigl, F. Rémy, and B. Legrésy (2005), Surface motion of mountain glaciers derived from satellite optical imagery, *Remote-sensing of Environment*, 95(1), 14-28.
- Casson, B., C. Delacourt, and P. Allemand (2005), Contribution of multi-temporal remote-sensing images to characterize landslide slip surface. Application to the La Clapière landslide (France), *Nat. Hazards Earth Syst. Sci.*, 5(3), 425-437.
- Casson, B., C. Delacourt, D. Baratoux, and P. Allemand (2003), Seventeen years of the "La Clapière" landslide evolution analysed from ortho-rectified aerial photographs, *Engineering Geology*, 68(1-2), 123-139.
- Debella-Gilo, M., and A. Käab (2011), Sub-pixel precision image matching for measuring surface displacements on mass movements using normalized cross-correlation, *Remote-sensing of Environment*, 115(1), 130-142.
- Delacourt, C., P. Allemand, B. Casson, and H. Vadon (2004), Velocity field of the "La Clapière" landslide measured by the correlation of aerial and QuickBird satellite images, *Geophys. Res. Lett.*, 31.
- Delacourt, C., D. Raucoules, S. L. Mouélic, C. Carnec, D. Feurer, P. Allemand, and M. Cruchet (2009), Observation of a Large Landslide on La Reunion Island Using Differential Sar Interferometry (JERS and Radarsat) and Correlation of Optical (Spot5 and Aerial) Images, *Sensors*, 9(1), 616-630.
- Delacourt, C., P. Allemand, E. Berthier, D. Raucoules, B. Casson, P. Grandjean, C. Pambrun, and E. Varel (2007), Remote-sensing techniques for analysing landslide kinematics: a review, *Bulletin de la Societe Geologique de France*, 178(2), 89-100.
- Gonzalez, P. J., M. Chini, S. Stramondo, and J. Fernandez (2010), Coseismic Horizontal Offsets and Fault-Trace Mapping Using Phase Correlation of IRS Satellite Images: The 1999 Izmit (Turkey) Earthquake, *Geoscience and Remote-sensing, IEEE Transactions on*, 48(5), 2242-2250.
- Haug, T., A. Käab, and P. Skvarca (2010), Monitoring ice shelf velocities from repeat MODIS and Landsat data – a method study on the Larsen-C ice shelf, Antarctic Peninsula, and 10 other ice shelves around Antarctica, *The Cryosphere*, 4(2), 161-178.
- Käab, A. (2002), Monitoring high-mountain terrain deformation from repeated air- and spaceborne optical data: examples using digital aerial imagery and ASTER data, *ISPRS Journal of Photogrammetry and Remote-sensing*, 57(1-2), 39-52.
- Käab, A. (2005), Combination of SRTM3 and repeat ASTER data for deriving alpine glacier flow velocities in the Bhutan Himalaya, *Remote-sensing of Environment*, 94(4), 463-474.
- Leprince, S. (2008), *Monitoring Earth Surface Dynamics With Optical Imagery*, 252 pp, California Institute of Technology, Pasadena.
- Leprince, S., S. Barbot, F. Ayoub, and J. P. Avouac (2007a), Automatic and Precise Orthorectification, Coregistration, and Subpixel Correlation of Satellite Images, Application to Ground Deformation Measurements, *Geoscience and Remote-sensing, IEEE Transactions on*, 45(6), 1529-1558.
- Leprince, S., F. Ayoub, Y. Klinger, and J.-P. Avouac (2007b), Co-Registration of Optically Sensed Images and Correlation (COSI-Corr): an Operational Methodology for Ground Deformation Measurements, in *Geoscience and Remote-sensing Symposium*, edited, pp. 2700–2702, Institute of Electrical and Electronics Engineers, Barcelona, Spain.
- Michele, M. d., and P. Briole (2007), Deformation between 1989 and 1997 at Piton de la Fournaise volcano retrieved from correlation of panchromatic airborne images, *Geophysical Journal International*, 169(1), 357-364.
- Niethammer, U., M. R. James, S. Rothmund, J. Travelletti, and M. Joswig (forthcoming), Very high spatial resolution monitoring of the Super-Sauze landslide with an UAV-based remote-sensing technique, *Engineering Geology*.
- Scambos, T. A., M. J. Dutkiewicz, J. C. Wilson, and R. A. Bindshadler (1992), Application of image cross-correlation to the measurement of glacier velocity using satellite image data, *Remote-sensing of Environment*, 42(3), 177-186.

- Scherler, D., S. Leprince, and M. R. Strecker (2008), Glacier-surface velocities in alpine terrain from optical satellite imagery--Accuracy improvement and quality assessment, *Remote-sensing of Environment*, 112(10), 3806-3819.
- Travelletti, J., J. P. Malet, J. Schmittbuhl, R. Toussaint, M. Bastard, C. Delacourt, P. Allemand, and D. B. van Dam (2010), Multi-temporal terrestrial photogrammetry for landslide monitoring, paper presented at Mountain Risks: Bringing Science to Society, 2010., Florence, Italy.
- Tseng, C.-H., J.-C. Hu, Y.-C. Chan, H.-T. Chu, J.-F. Lee, J.-Y. Wei, C.-Y. Lu, and M.-L. Lin (2009), Non-catastrophic landslides induced by the Mw 7.6 Chi-Chi earthquake in central Taiwan as revealed by PIV analysis, *Tectonophysics*, 466(3-4), 427-437.
- Yamaguchi, Y., S. Tanaka, T. Odajima, T. Kamai, and S. Tsuchida (2003), Detection of a landslide movement as geometric misregistration in image matching of SPOT HRV data of two different dates, *International Journal of Remote-sensing*, 24(18), 3523-3534.

Image correlation of terrestrial photographs for landslide monitoring

Application: Landslide monitoring

Technique: Passive optical ground-based sensors

Main references: Travelletti, J., C. Delacourt, P. Allemand, J.-P. Malet, J. Schmittbuhl, R. Toussaint, M. Bastard (in press, IJPRS): Correlation of multi-temporal ground-based images for landslide monitoring: application, potential and limitations.

Contributors: CNRS (J. Travelletti, J.-P. Malet, J. Schmittbuhl, R. Toussaint)

Abstract

The objective of this work is to present a low-cost methodology to monitor the displacement of continuously active landslides from ground-based optical images analyzed with a normalized Image Correlation technique. The performance of the method is evaluated on a series of images acquired on the Super-Sauze landslide (South French Alps) over the period 2008-2009. The image monitoring system consists in a high resolution optical camera installed on a concrete pillar located on a stable crest in front of the landslide and controlled by a datalogger. The data are processed with a cross-correlation algorithm applied on the full resolution images in the acquisition geometry. Then, the calculated 2D displacement field is ortho-rectified with a back projection technique using a high resolution DEM interpolated from Airborne Laser Scanning (ALS) data. The heterogeneous displacement field of the landslide is thus characterized in time and space. The performance of the technique is assessed using as reference differential GPS surveys of a series of benchmarks. The sources of error affecting the results are then discussed. The strongest limitations for the application of the technique are related to the meteorological, illumination and ground surface conditions inducing partial or complete loss of coherence among the images. Small changes in the camera orientation and the use of a mono-temporal DEM are the most important factors affecting the accuracy of the ortho-rectification of the displacement field. Because the proposed methodology can be routinely and automatically applied, it offers promising perspectives for operational applications like, for instance, in early warning systems.

Keywords: image cross-correlation, image matching, landslide, time-lapse photography, displacement monitoring

1. Introduction

In the last decades, the development of ground-based platforms for landslide monitoring at the local scale provided many advantages over spaceborne and airborne platforms despite a shorter spatial coverage [Corsini *et al.*, 2006]. The geometry and frequency of acquisitions are more flexible and adaptable to any type of local environment. Furthermore, the installation of the monitoring system is generally relatively easy. In addition ground-based platforms are permanent installations that allow a continuous monitoring [Casagli *et al.*, 2004; Delacourt *et al.*, 2007].

Three main categories of ground-based remote-sensing techniques are used in landslide monitoring: Ground-Based Synthetic Aperture Radar Interferometry (GB-InSAR), Terrestrial Laser Scanning (TLS) and Terrestrial Optical Photogrammetry (TOP). Here only a state-of-the-art of the application of TOP to landslide is given; detailed reviews of the application of GB-InSAR and TLS to landslides can be found in Tarchi *et al.* [2003], Jaboyedoff *et al.* (2010), and Monserrat & Crosetto [2008].

TOP is a very cost-effective technique with implementation, operating and equipment costs much lower than GB-InSAR and TLS. The technique consists in acquiring digital optical images represented using a matrix of intensity values (brightness) recorded at each pixel of the Charge Coupled Device (CCD) of the camera. While aerial images are acquired on overhead photographs from an aircraft, TOP uses RGB images acquired from a spot very close to the ground [Jiang *et al.*, 2008]. In the last decades, camera self-calibration and analytical processing techniques allow the use of non-metric cameras and of simplified camera calibration algorithms to compute digital elevation models using the principle of stereoscopic views [Mikhail *et al.*, 2001; Jiang *et al.*, 2008]. In the current state, the application of terrestrial images for landslide monitoring is mostly related to the production of DEMs for image ortho-rectification and sediment budget analysis [Pesci *et al.*, 2004; Cardenal *et al.*, 2008], and more recently to the characterization of the slope morpho-structure [Lim *et al.*, 2005; Sturzenegger & Stead, 2009].

Using correlation techniques, two-dimensional displacement fields can be derived by tracking objects in two images acquired at different time. So far, image correlation techniques have been applied only on aerial and satellite images (SPOT, QuickBird, OrbView, EROS) for the creation of landslide displacement maps [Casson *et al.*, 2003; Delacourt *et al.*, 2004; LePrince *et al.*, 2008]; the use of image correlation on terrestrial images has not been as popular for permanent landslide monitoring as in other application field such as in solid and fluid mechanics for the characterization of the deformation pattern of soil/rock samples [White *et al.*, 2003; Chambon *et Schmittbuhl*, 2003; Küntz *et al.*, 2005] or for the monitoring of other natural processes such as ice glaciers [Corripio *et al.*, 2004; Fallourd *et al.*, 2010; Maas *et al.*, 2008] or volcanoes [Honda & Nagai, 2002]. Only Delacourt *et al.* [2007] demonstrated an efficient application of TOP for landslide monitoring which consisted in the determination of the landslide boundaries and in the qualitative estimation of the spatial variability of displacement at the La Clapière landslide (French Alps) with an image acquisition system installed at 1 km-distance.

Generally, the 2D displacements (in pixel) evaluated by the correlation algorithm have an accuracy of about 0.2 pixel [Casson *et al.*, 2005; Delacourt *et al.*, 2007] in the image plane, corresponding to an accuracy of millimeters to several centimeters for distances of about 100 m in the local coordinate system [Kraus & Waldhäusl, 1994].

The major sources of errors affecting the displacement calculations and thus potentially limiting the efficiency of TOP for an operational landslide monitoring can be classified in two groups: (i) the parameters affecting the Image Correlation computation and (ii) the external parameters influencing the ortho-rectification procedure. The objective of this work is therefore to evaluate the potential and the limitations of TOP for the permanent monitoring of landslide using Digital Image Correlation (DIC) techniques.

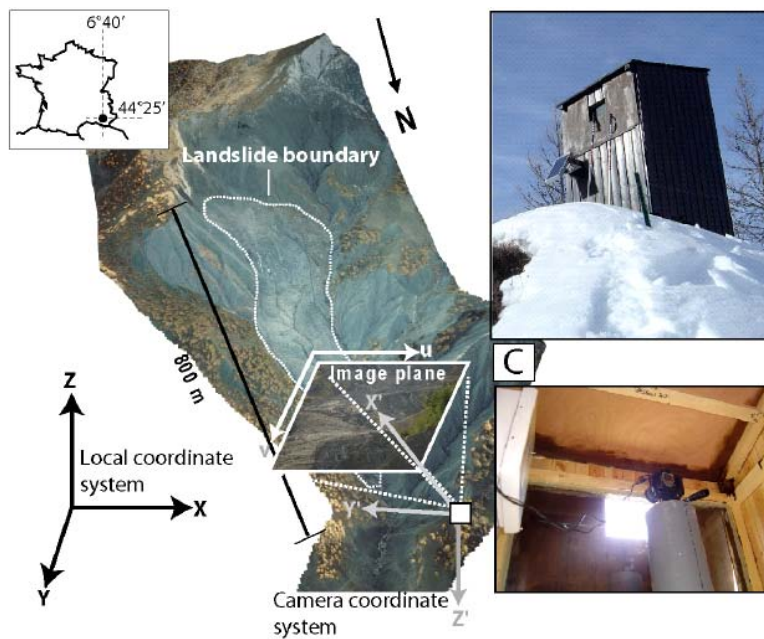


Figure 1: View of the Super-Sauze landslide towards the south with the different coordinate systems used in the georeferencing procedure and location of the camera monitoring system.

2. Data and Methods

The steps in the data processing workflow consist in (1) correlating the images by pairs in their original acquisition geometry to prevent any loss of information, and (2) ortho-rectifying the calculated displacement fields using a high-resolution digital elevation model interpolated from airborne LiDAR data. The daily images presenting the best ground texture contrast and the most homogeneous lightening are selected based on expert judgment.

The development of the method has been carried out on images acquired at the toe of the Super-Sauze mudslide (South French Alps; *Malet, 2003*) for the period 2008-2009 by a remote camera monitoring system. This instrumentation consists in a low-cost D70 Nikon non-metric reflex digital camera installed on a concrete pillar located on a stable crest in front of the landslide at a distance of 300 m from the lower part and 900 m from the main scarp (Fig. 1). The acquisition system is controlled by a datalogger (Campbell CR10) and the power is provided by a 40 W solar panel. The characteristics of the acquisition are presented in Table 2. Each four days, four images are acquired at 11:00, 12:00, 13:00 and 14:00 GMT in order to increase the probability of having at least one image with good meteorological conditions. Each photograph (6 Mb) is stored in a native file format to avoid any loss of information. As reference measurements, landslide displacements are also currently monitored by Differential Global Positioning System (DGPS) and Terrestrial Laser Scanning (TLS).

The 2D displacement field is obtained by correlating two optical images acquired at different time. The image correlation technique is based on the automatic identification of identical texture patterns within an image by maximizing a correlation function [*Lewis, 1995; Baratoux*

et al., 2001; *Debella-Gilo & Kääb*, 2010]. Its principle adapted for landslide kinematics analysis is described in *Delacourt et al.* [2007]. Visible ground features have to be superimposed on two successive images on stable parts located outside the landslide. On the areas affected by landslide movements, the visible and recognizable features are shifted by the displacements. In order to quantify the ground displacements, a correlation window is defined on a reference (often the oldest) image. The corresponding window is searched in a pre-defined explored area belonging to the second image. The starting point of this explored area is the expected position of the window as if no displacement occurred between two acquisitions. The process is repeated for each pixel of the reference image. The Euclidean distance between the reference point and the matching point represents the displacement magnitudes in the image plane. By modifying the zone of interest, it is then possible to determine the displacements at various positions within the images (Fig. 2). It is important to note that the normalized cross-correlation technique cannot track objects that start to rotate significantly or are affected by important perspective distortions [*Lewis*, 1995].

A sub-pixel hierarchical correlation technique is used [*Chambon*, 2003]. The RGB images are first converted in gray-scale images on which a 3x3 pixel Sobel convolution matrix is applied to highlight the ground surface texture. The gradient values are then correlated [*Chambon*, 2003]. Four successive degradations of the image resolution are applied following a pyramidal approach for changing the physical size of the correlation window and of the explored area by down-sampling the gradient values of the full resolution image [*D'Antone*, 1995; *Kumar & Banerjee*, 1998; Fig. 2]. The optimum sizes of the correlation window (16x16 pixels) and of the explored area (32x32 pixels) were identified with a trial and error procedure. These parameters are constant during the correlation computation. The correlation starts with the lowest resolution image in order to determine the largest displacements. Then the location of the pixel with the maximum cross-correlation value is used as the centre of the zone of interest for the next correlation step at a higher resolution. The spatial location of the maximum correlation value in the highest resolution image is thus progressively better estimated (Fig. 4). Ignoring high resolution information at the first computational step decreases the probability to reach a local minima of the correlation function and, consequently, to obtain wrong matches in the correspondence solutions [*Aloui & Ibn-Elhaj*, 2009]. In addition, this approach ensures a higher probability of reliable correlation peak detection [*Anandan et al.*, 1993]. The sub-pixel displacement is computed after the correlation at the highest resolution image. An iterative procedure is used to find the maxima of the correlation function interpolated with a bi-parabolic formula and with a maximization procedure based on the simplex method [*Chambon*, 2003].

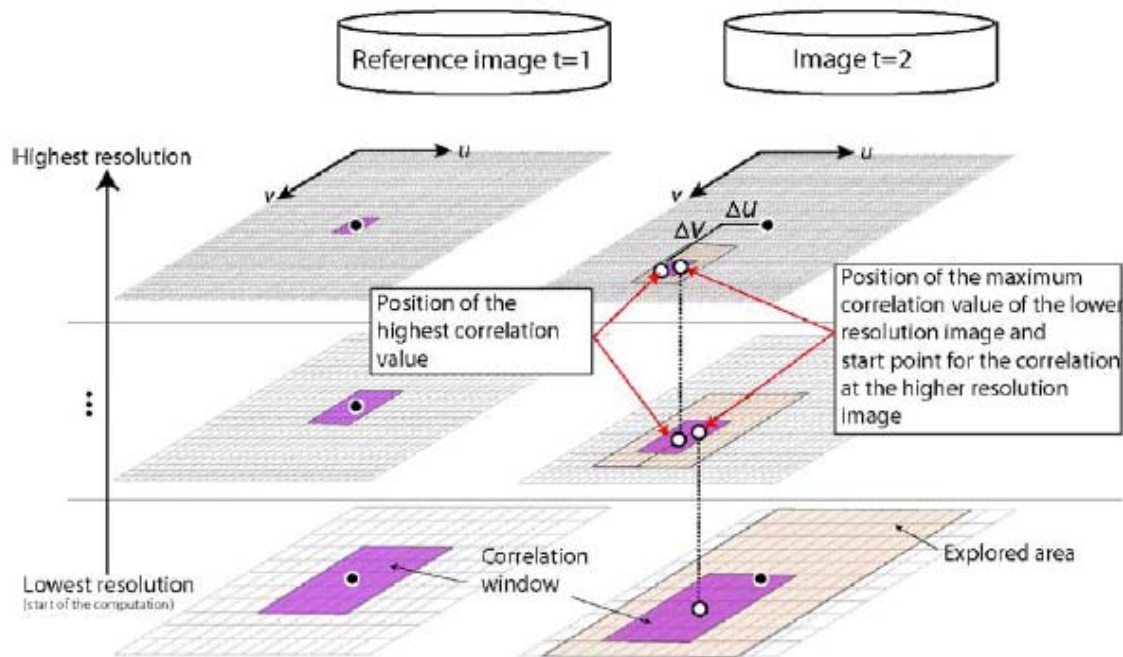


Figure 2: Principle of the normalized hierarchical image correlation. The correlation computation starts from the lowest resolution to the highest resolution by keeping constant the size of the correlation window and the explored area, while their physical size is decreasing. At each higher resolution level, the explored area is centered on the pixel with the highest t correlation value of the previous resolution level. The estimate of the position of the maximum correlation value is thus increased.

The correlation results consist in matrices of displacements Δu and Δv along the u - and v -axes in the image plane with their associated correlation index (Fig. 4). Because the pixel size is not constant in the image due to the oblique acquisition, the displacements field correlated in the image plane cannot be directly interpreted in terms of metric displacements. Therefore an ortho-rectification procedure is necessary for a quantitative analysis of the displacement fields.

3. Results

3.1. Displacement maps of the landslide

A set of images over the period May–July 2008 is used to illustrate the potential of the technique for the characterization of the kinematics during an acceleration period triggered by high rainfall amounts and a fast melting of the snow cover.

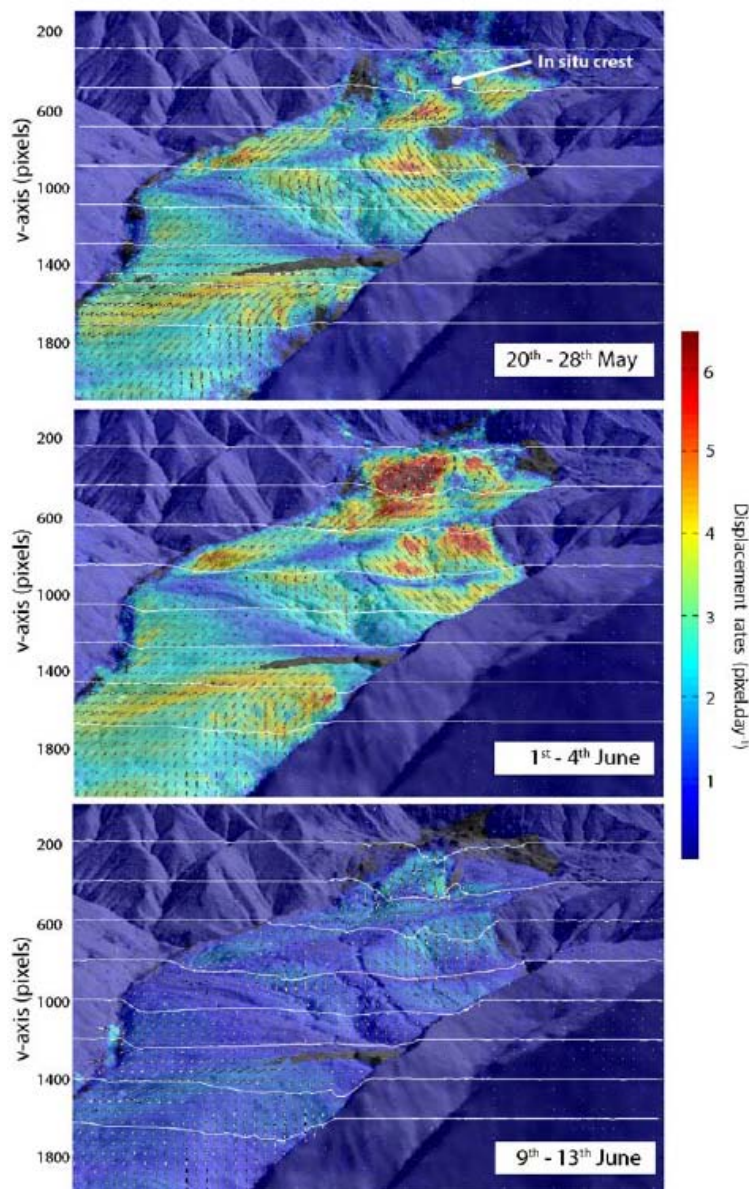


Figure 3: Displacement rates amplitude (color) and displacement direction (arrows) in the image plane and cumulated displacements along 8 profiles crossing the landslide over the period the 20th May to the 25th June 2008. In order to highlight the displacement direction, the arrow length is normalized in each image.

Figure 3 shows an example of displacement rate (in $\text{pixel}\cdot\text{day}^{-1}$) of the ground surface in the image plane derived from image pairs of 20–28 May, 1–4 June and 9 June–13 June. The reference is the image of 20 May. The contrast in displacement rates between the landslide area and the stable area gives confidence on the calculated velocity field. One can notice that the pattern of displacement rate is heterogeneous spatially and temporarily. The upper part of the landslide displays the highest velocities ranging from 1 to 7 $\text{pixels}\cdot\text{day}^{-1}$ while the lower part displays velocities of less than 4 $\text{pixels}\cdot\text{day}^{-1}$. No quantitative comparisons can be carried out at this stage because the pixel sizes vary strongly in the image. From the 20 May to the 13 June, cumulated displacements up to 110 pixels are observed in the upper part. The maximum of displacement rate is observed around the 1st June. Then the landslide decelerates to

displacement rate of about 1 pixel.day^{-1} .

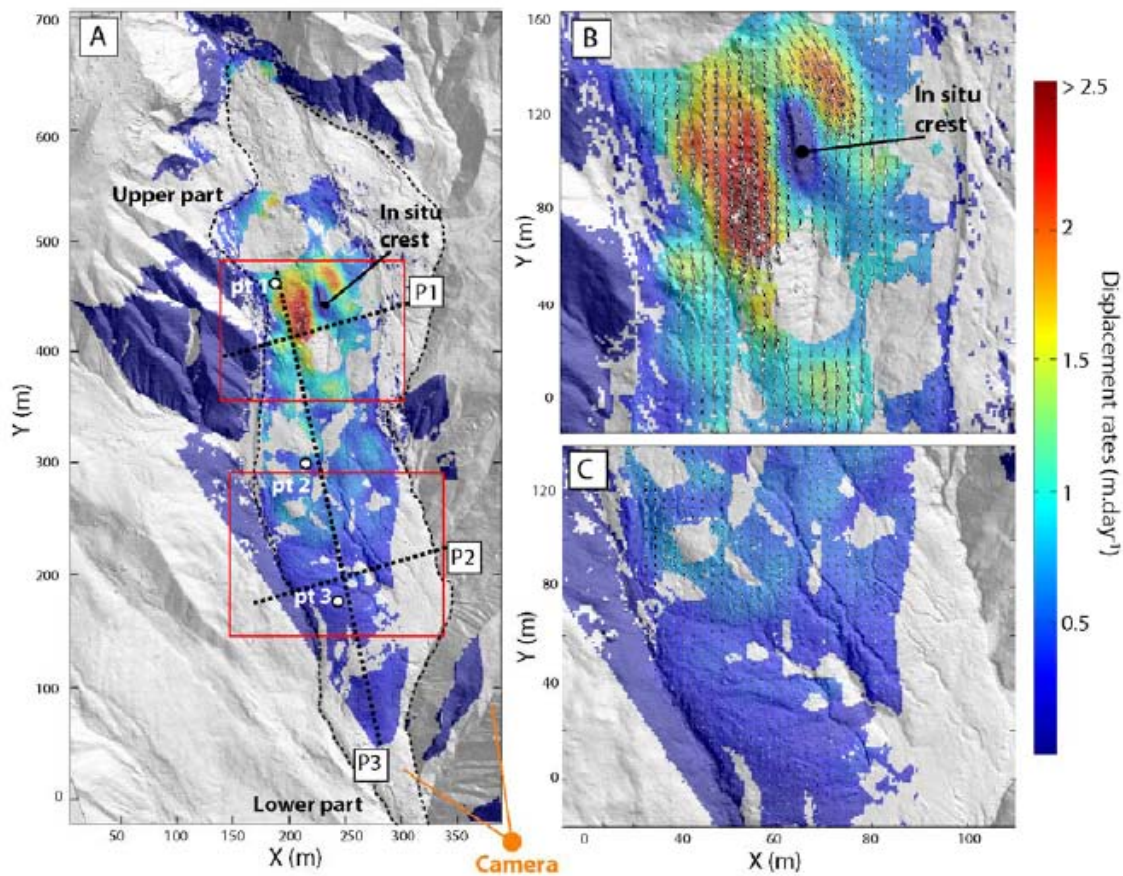


Figure 4: Displacement rates map for the period 1st – 4th June 2008. (A) Displacement rates observed on the whole landslide. The profiles P1, P2 and P3 refer to Fig. 5 and the locations pt1, pt 2 and pt 3 refer to Fig. 6. (B) Details on the displacement rates and displacement direction of the velocity amplitude and direction in the upper part. (C) Details on the displacement rates and displacement direction in the lower part.

Some local specific displacement patterns are also clearly highlighted; for instance, the presence of a stable *in-situ* crest located in the landslide body is perfectly identified in the correlated images.

Figure 4 presents the amplitude of the 3D ortho-rectified displacement rates for the period 1st June– 4th June in the local coordinate system. The difference of kinematics among the upper (until 3 m.day^{-1}) and the lower (until 1 m.day^{-1}) parts becomes more evident than in the image plane. The geometrical effect induced by the presence of the stable *in-situ* crest on the landslide kinematics is also clearly pointed out. The temporal evolution of the displacement rates is illustrated with two transversal and one longitudinal profiles on Figures 5 and 6. The difference of displacement rates between the upper and the lower part of the landslide is particularly pointed out.

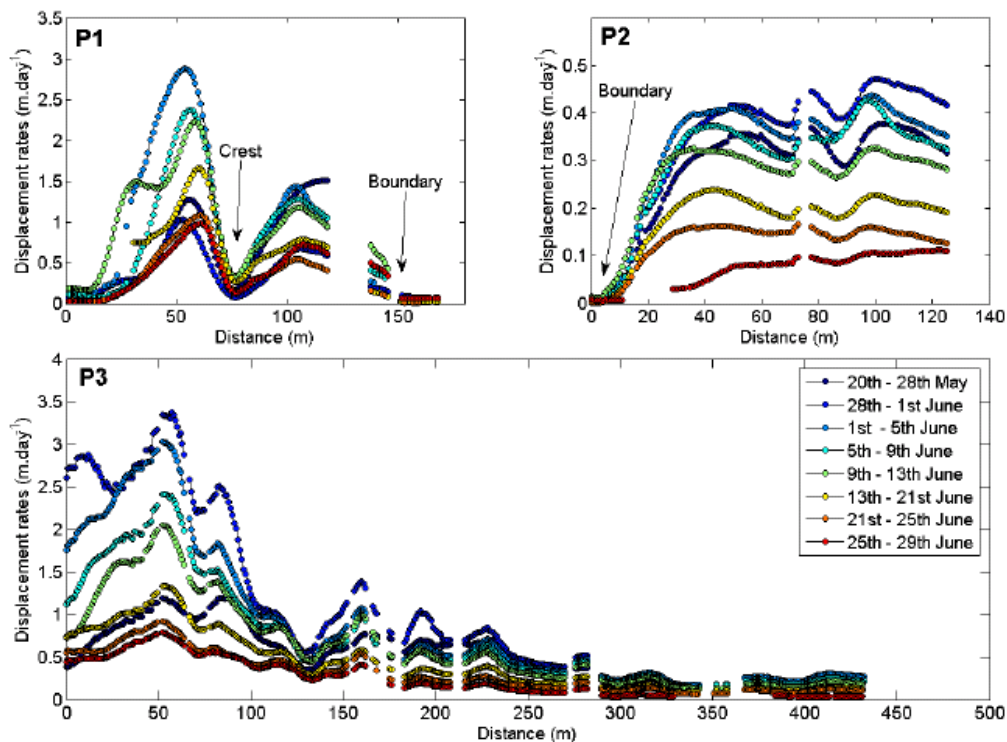


Figure 5: Displacement rates profiles in the upper (P1), the medium (P2) and the lower (P3) part of the landslide. The location of the profiles is indicated in Fig. 4.

The precision of the computed displacements is assessed by performing a null hypothesis on the stable areas [Berthier *et al.*, 2005; Casson *et al.*, 2003]. Only the points with a correlation coefficient $r > 0.8$ are taken into account. In the image plane coordinate system, the average errors μ range from 0.5 to 0.9 pixel with standard deviations σ of 0.3 to 1.2 pixel for the image pairs between the 20 May and the 25 June. In the local coordinate system, the average errors μ range from 0.03 m to 0.11 m with standard deviations σ of 0.10 to 0.31 m for the image pairs between the 20 May and the 25 June.

3.2. Comparisons with dGPS displacement measurements

In order to estimate the accuracy and validate the calculated displacements, comparisons with independent and more accurate geodetic technique is necessary. Sixty benchmarks distributed in the stable parts and on the landslide body were monitored by DGPS with a horizontal and a vertical average accuracy of ± 0.02 m and ± 0.05 m. In total, 219 DGPS measurements are available for the period 2008–2009. In order to validate the displacements computed in the image plane, the DGPS benchmarks are projected in the image plane using the collinearity equations [Bonneval 1972, Kraus & Waldhüsel, 1998]. The pixel displacements derived from the image correlation are then averaged in a perimeter of 16 pixels around each benchmark. The results are presented in Figure 6A. A correlation coefficient of $r = 0.98$ is found between DGPS measurements and Image Correlation, and an average relative accuracy of 11% is determined (Fig 6C). In order to validate the metric displacements in the local coordinate system, the ortho-rectified displacements are averaged in an area of 4 m^2 around each benchmark and compared with the DGPS displacements. A correlation coefficient of

$r=0.95$ is found (Fig. 11B), and an average relative accuracy of 20% is determined (Fig. 6D).

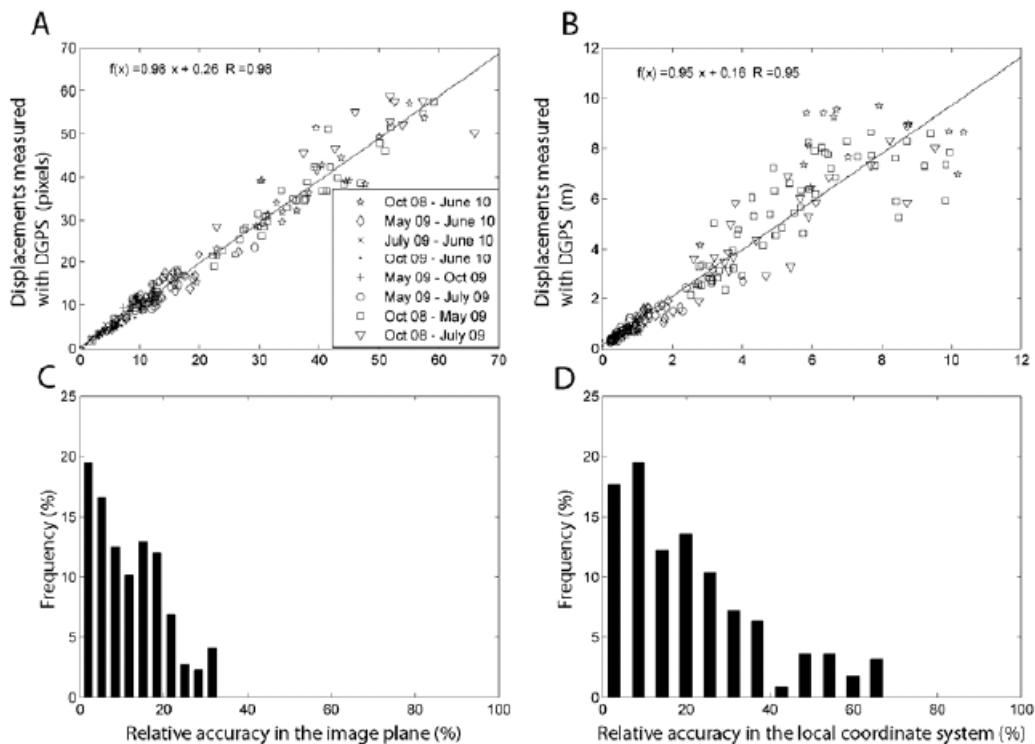


Figure 6: Assessment of the accuracy of the Image Correlation technique. Relationships between the displacements observed by Image Correlation and the displacements observed by DGPS on sixty benchmarks in the image plane (A) and in the local coordinate system (B). Relative accuracy of the Image Correlation technique in the images plane (C) and in the local coordinate system (D).

4. Discussion and Conclusion

The potential of multi-temporal correlation of ground-based images for landslide monitoring has been assessed using the dataset available on the Super-Sauze landslide (South French Alps). A methodology to compute displacement rates both in the image plane coordinate system and in the local coordinate system has been proposed.

The results demonstrated clearly the potential and the limitation of this technique by identifying the heterogeneous displacement field, in space and in time, of the landslide. The camera monitoring allowed to characterize displacements up to 3 m.day^{-1} during an acceleration period, and displacement of about 0.02 m.day^{-1} computed over the period July to September (the less active period). The results are in good agreement with previous knowledge on the landslide kinematics and are in very good agreement with benchmark displacements measured by DGPS.

For objects located in a range of 300 to 900 m from the camera location, this study showed that the pixel size can vary from 0.005 to 0.04 m^2 according to the resolution of the image (2000x3008 pixels) and the angle of incidence of the line of sight. The orientation of the line of sight (depending on the location and orientation of the camera) to the ground surface has to

be considered before installing a permanent monitoring system. Areas of low incidence angles ($< 5^\circ$) are very sensitive to small movements of the camera. Therefore, the angle should be the most perpendicular as possible to the mean displacement vector of the landslide. 3D displacements of less than 0.04 m and 0.06 m in the lower part of the landslide and 0.09 m and 0.11 m in the u and v -directions are difficult to measure over a period of four days without a sub-pixel correlation algorithm.

The strongest limitations are independent of the acquisition system and are related to the meteorological and illumination conditions (Fig. 7) and the ground surface changes inducing partial or complete loss of coherence between pairs of images. During the winter season (from November to May), the presence of snow impedes reliable correlation results and excessive ground deformations between two consecutive years impede valid displacement measurements even if the images are acquired during the same solar time. The small changes in the camera orientation and the use of a constant DEM are the most important parameters that affect the accuracy of the ortho-rectification of the displacement field. A regular acquisition of multi-temporal DEMs through airborne or terrestrial laser scanning or stereoscopic photogrammetric views is believed to be a priority to significantly improve the accuracy of the technique. The errors induced by the sub-pixel correlation algorithm are thus insignificant compared to the influences of the other parameters cited previously.

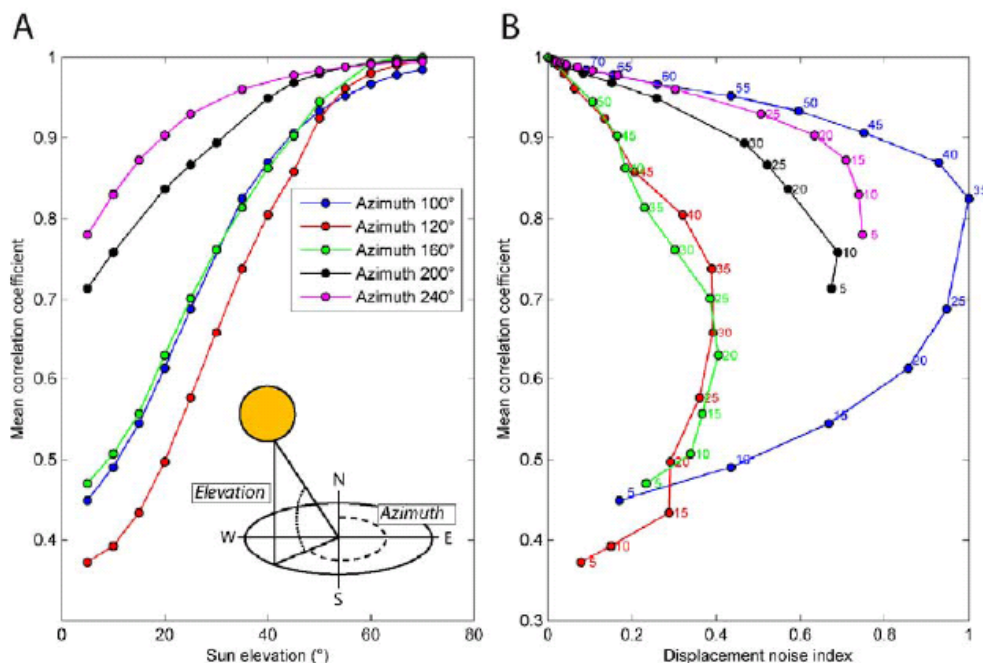


Figure 7: Results of the correlation on the synthetic shaded relief images. (A) Influence of illumination conditions as a function of the sun elevation and azimuth on the mean correlation coefficient. (B) Relationship between displacement noise index and correlation coefficient. The values near the dots correspond to the sun elevation angles.

The results demonstrate that Image Correlation techniques implemented in permanent

monitoring system is particularly interesting for monitoring landslides characterized by annual pluri-decimeteric displacements. In addition, this low cost technique is a very suitable alternative for inaccessible landslides or areas without access to power supply. Furthermore, because the proposed methodology does not require GCPs except for determining the external orientation of the camera and for combining displacement pattern observed in image pairs acquired over two years, the methodology can be routinely and automatically applied to new pairs of images. Therefore this study offers very promising perspectives for operational applications which can be potentially integrated in an early warning system by considering additional efforts in direct data transmission. Finally, inversion of the displacement field could be developed to characterize the macroscopic rheological properties of the landslide material.

References

- Alaoui El. M. I., & Ibn-Elhaj E. (2009). A robust hierarchical motion estimation algorithm in noisy image sequences in the bispectrum domain. *Signal Image and Video Processing*, 3, 291-302.
- Anandan, P., Bergen, R.J., Hanna, K.J., & Hanna, K.J. (1993). Hierarchical model-based motion estimation. In L. Sezan, (Eds.), *Image Sequence Analysis*. Kluwer, Dordrecht.
- Baratoux, D., Delacourt, C., & Allemand, P. (2001). High-resolution digital elevation models derived from Viking Orbiter images: Method and comparison with Mars Orbiter Laser Altimeter Data. *Journal of Geophysical Research*, 106, 32927-32941.
- Berthier, E., Vadon, H., Baratoux, D., Arnaud, Y., Vincent, C., Feigl, K. L., Rémy, F., & Legrésy B. (2005). Surface motion of mountain glaciers derived from satellite optical imagery. *Remote-sensing of Environment*, 95, 14-28.
- Bonneval, H., (1972). Levés topographiques par photogrammétrie aérienne. In Eyrolles (Eds.), *Photogrammétrie générale: Tome 3, Collection scientifique de l'Institut Géographique National*, Paris, France.
- Casagli, N., Farina, P., Leva, D., & Tarchi, D. (2004). Application of ground-based radar interferometry to monitor an active rock slide and implications on the emergency management. In E. Kluwer (Eds.), *The NATO Advanced Research Workshop*, Celano, Italy.
- Casson, B., Baratoux, D., Delacourt, D., & Allemand, P. (2003). "La Clapière" landslide motion observed from aerial differential high resolution DEM. *Engineering. Geology*, 68, 123-139.
- Casson B., Delacourt C., & Allemand, P. (2005). Contribution of multi-temporal sensing images to characterize landslide slip surface – Application to the La Clapière Landslide (France). *Natural Hazards and Earth System Sciences*, 5, 425-437.
- Cardenal, J., Mata, E., Perez-Garcia, J.L., Delgado, J., Andez, M.A., Gonzalez, A., Diaz-de-Teran, J.R. (2008). Close Range Digital Photogrammetry Techniques applied to Landslide Monitoring. International Archives of the Photogrammetry, *Remote-sensing and Spatial Information Sciences*. Vol XXXVII. Part B8.
- Chambon G. (2003). Caractérisation expérimentale du frottement effectif des zones de faille. PhD Thesis. Université Paris XI Orsay, ENPC..
- Chambon, G., & Schmittbuhl, J. (2003). Shear with comminution of a granular material: Microscopic deformations outside the shear band. *Physical Review E*, 68, 1-8.
- Corripio, J.G. (2004). Snow surface albedo estimations using terrestrial photography. *International Journal of Remote-sensing*, 25(24), 5705-5729.
- Corsini, A., Farina P., Antonello G., Barbieri M., Casagli N., Coren F., Guerri L., Ronchetti F., Sterzai P., & Tarchi D. (2006). Space-borne and ground-based SAR interferometry as tools for landslide hazard management in civil protection. *International Journal of Remote-sensing*, 27, 2351 - 2369.
- D'Antone, I. (1995). Hierarchical correlation for track finding. *Nuclear Instrument and Methods in Physics Research*, 356, 476-484.
- Debella-Gilo M., & Käab A. Sub-pixel precision image matching for measuring surface displacements on mass movements using normalized cross-correlation. *Remote-sensing of Environment* (2010).
- Delacourt, C., Allemand P., Casson B., & Vadon H. (2004). Velocity field of the "La Clapière" landslide measured by the correlation of aerial and Quick-Bird satellite images. *Geophysical. Research Letters*, 31, 1-

5.

- Delacourt, C., Allemand, P., Berthier, E., Raucoules, D., Casson, B., Grandjean, P., Pambrun, C., & Varel, E. (2007). Remote-sensing techniques for analysing landslide kinematics: a review. *Bulletin de Société Géologique*, 178, 89-100.
- Fallourd, R., Vernier, F., Friedt J.-M., Martin, G., trouvé, E., Moreau, L. & Nicolas, J.-M. (2010). Monitoring temperate glacier with high resolution automated digital cameras – Application to the Argentière Glacier. in: Paparoditis N., Pierrot-Deseilligny M., Mallet C. & Tournaire O. (Eds.), IAPRS, Vol. XXXVIII, Part 3B, Saint-Mandé, France., 1-23.
- Honda, K., & M. Nagai (2002), Real-time volcano activity mapping using ground-based digital imagery, *ISPRS Journal of Photogrammetry and Remote-sensing*, 57,1-2, 159-168.
- Jaboyedoff, M., Oppikofer T., Abellan A., Derron M.-H., Loye A., Metzger R., & Pedrazzini A. (2010). Use of LiDAR in landslide investigations: a review. *Natural Hazards*. doi 10.1007/s11069-010-9634-2
- Jiang, R., Jauregui, D.V., & White, K. (2008). Close-range photogrammetry applications in bridge measurement: Literature review. *Measurement*, 41, 823-834.
- Kraus, K. & Waldhäusl, P., (1994). *Photogrammetry, Fundamentals and Standard processes*. vol 1. Hermès (editor), Paris.
- Kumar, S., & Banerjee, S., (1998). Development and application of a hierarchical system for digital particle image velocimetry to free-surface turbulence. *Physics of Fluids*, 10, 160-177.
- Küntz, M., Jolin, M., Bastien, J., Perez F., & Hild, F. (2007). Digital image correlation analysis of cracks behavior in a reinforced concrete beam during a load test. *Canadian journal of civil engineering*, 33, 1418-1425.
- LePrince, S., Berthier, E., Ayoub, F., Delacourt, C., & Avouac, J.- P. (2008). Monitoring Earth Surface Dynamics With Optical Imagery. *Eos*, 89, 1-5.
- Lewis, J.P., (1995). Fast normalized cross-correlation. *Vision Interface*, 120-123.
- Lim, M., Petley, D.N., Rosser, N.J., Allison, R.J., Long, A.J. & Pybus, D. (2005). Combined digital photogrammetry and time-of-flight laser scanning for monitoring cliff evolution. *The Photogrammetric Record*, 20, 109-129.
- Malet, J.-P. (2003). Les glissements de type écoulement dans les marnes noires des Alpes du Sud. Morphologie, fonctionnement et modélisation hydromécanique. PhD Thesis in Earth Sciences, Université Louis Pasteur, Strasbourg.
- Maas, H.-G., Schwalbe, E., Dietrich, R., Bäessler, M., & Ewert, H. (2008). Determination of spatio-temporal velocity fields on glaciers in West- Greenland by terrestrial image sequence analysis. *IAPRS*, XXXVII, Part B8 Beijing, China, 1419-1424.
- Mikhail, E., Bethel, J. S., & McGlone, J. C. (2001). *Introduction to Modern Photogrammetry*, Hardcover (edition), New-York.
- Monserrat, O., & Crosetto, M. (2008). Deformation measurement using terrestrial laser scanning data and least squares 3D surface matching. *ISPRS Journal of Photogrammetry and Remote-sensing*, 63, 142-154.
- Pesci A., Baldi B., Bedin A., Casula G., Cenni N., Fabris M., Loddo F., Mora P., & Bacchetti M. (2004). Digital elevation models for landslide evolution monitoring: application on two areas located in the Reno River Valley (Italy). *Annals of Geophysics*, 47, 1339-1353.
- Sturzenegger, M., & Stead, D. (2009). Close-range terrestrial digital photogrammetry and terrestrial laser scanning for discontinuity characterization on rock cuts. *Engineering Geology*, 106, 163-182.
- Tarchi, D., Casagli, N., Fanti, R., Leva, DD., Luzi, G., Pasuto, A., Pieraccini, M., & Silvano, S. (2003). Landslide monitoring by using ground-based SAR interferometry: an example of application to the Tessina landslide in Italy. *Engineering Geology*, 68,15-30.
- White, D. J., Take, W. A. & Bolton, M. D., (2003). Soil deformation measurement using particle image velocimetry (PIV) and photogrammetry. *Géotechnique*, 53, 619-631.

Object-oriented analysis of unmanned aerial vehicle (UAV) imagery for mapping and monitoring of landslide surface features

Application: Landslide characterization and monitoring

Technique: Passive optical airborne sensors

Main references: Stumpf, A., U. Niethammer, S. Rothmund, A. Mathieu, J.-P. Malet, N. Kerle, M. Joswig (2011): Object-oriented analysis of unmanned aerial vehicle (UAV) imagery for mapping and monitoring of landslide surface features

Contributors: ITC (A. Stumpf, N. Kerle), CNRS (J.P. Malet, A. Mathieu)

Abstract

The surface features of active landslides reveal important insights into the pattern of deformation and influence hydrological processes that determine the behavior of the landslide. Especially, tension cracks and fissures may modify the pore-water response considerably and their integration into hydrological models can yield more reliable kinematic forecasts and estimates of the hazard level. Systematic mappings of the distribution and evolution of fissures and cracks have been difficult in the past, whereas the recent wide-spread of low-cost Unmanned Aerial Vehicles (UAVs) provides an efficient solution to acquire imagery with sufficient spatial and temporal resolution.

This study focuses on the adaption and application of advanced object-oriented image analysis techniques to UAV imagery with ground resolutions of 5-10 cm and thereby targets an efficient semi-automatic mapping and characterization of geomorphological features.

Multi-temporal VHR optical images of the Super Sauze landslide (South French Alps) were acquired with an UAV for the period 2008-2010 and reveal the pattern and development of geo-indicators of landslide activity. Especially, surficial fissures are expressions of the distribution of stress and strain within the landslide and proxies for analyzing the kinematics and rheology of the material.

The highly textured landslide surface (composed of blocks of different sizes, of small gullies and open channels, and of lobes) creates a challenging domain for the application of automated fissure detection. Based on algorithms for edge detection, morphological filtering, texture analysis, image segmentation and shape analysis, an image processing chain that enables the semi-automated mapping of surface fissures is proposed. Knowledge on the geomorphological processes is incorporated in the workflow to efficiently distinguish the different structures.

The processing chain results in multi-temporal maps for the abundance and density of fissures, The high image resolution also allows mapping the vegetation patterns and characterizing the relative distribution of gravel sizes at the surface via windowed measurements of the grey values entropy. In general the semi-automatic analysis of the UAV imagery provides a cost-efficient, objective and transparent way for the monitoring of hazardous sites and geomorphological features in general.

Keywords: image cross-correlation, image matching, landslide, time-lapse photography, displacement monitoring

1. Introduction

The observation of surface characteristics of slopes and rockwalls is an important approach to gather information about their internal states. Surface features in general reveal important information about the past and present patterns of deformation and displacement and their observation and interpretation can contribute to a better understanding of the underlying processes and related hazards [*Fleming and Johnson, 1989; McCalpin, 1984; Parise, 2003*]. More specifically detailed mapping and analysis of structural discontinuities is a powerful

tool to identify and characterize of potentially unstable areas [Günther *et al.*, 2004; Hoek and Bray, 1981; Jaboyedoff *et al.*, 2004; Matheson, 1983; Priest, 1993; Selby, 1993] and surface fissures may serve as a geo-indicator for initial failure states [Abramson *et al.*, 2001; Chowdhury and Zhang, 1991; Petley *et al.*, 2006].

The surface characteristics also modify hydrological processes such as infiltration and drainage patterns, which in turn influence the ground-water system and the kinematic response of the landslide to hydrological events [Malet *et al.*, 2003; Malet *et al.*, 2005; van Asch *et al.*, 2009]. Especially, tension cracks and fissures may modify the infiltration and pore-water response considerably and their integration into physically-based models may yield more reliable kinematic forecasts and estimates of the hazard level [Baum and Fleming, 1991; Corominas *et al.*, 2002; Iverson, 2000; Lindenmaier *et al.*, 2005; Malet *et al.*, 2005; van Beek and van Asch, 1999].

Mappings at the detail of surface fissures and other, similar scaled surface characteristics require extensive field surveys [comp. Fleming *et al.*, 1999; Meisina, 2006] which quickly become unfeasible for the systematic and repeated production of maps over larger area.

The recent wide-spread availability of VHR images especially from low-cost Unmanned Aerial Vehicles (UAVs) now provides an efficient solution to acquire imagery of landslides with spatial and temporal resolution that may allow detailed monitoring of surface features [Niethammer *et al.*, in press]. Airborne images from UAVs and such with comparable resolutions have been used in numerous geoscientific studies such as the monitoring of vegetation dynamics or crops [Berni *et al.*, 2009; Dunford *et al.*, 2009; Hardin and Jackson, 2005; Laliberte and Rango, 2009; Lucieer *et al.*, 2010], and geomorphological and soil surface processes [Carbonneau, 2010; Carbonneau *et al.*, 2006; Corbane *et al.*, 2008; Graham *et al.*, 2010; Marzloff and Ries, 2007; Puech *et al.*, 2009; Raclot, 2006], whereas their potential use for the for the monitoring of landslides still needs to be further explored.

This study focuses on the adaption and application of advanced object-oriented image analysis techniques to analyses UAV imagery with ground resolutions of 5-10 cm and thereby targets a semi-automatic mapping of surface fissures and other geomorphological relevant features.

2. Data and Methods

Niethammer *et al.*, [2009] used a low-cost quad-copter UAV to acquire images of the Super Sauze mudslide at several dates (Fig. 1). It has been demonstrated that the acquired images allow the photogrammetric generation of topographic models, and also relationships between observable fissure structures and mechanical processes have been previously discussed by Niethammer *et al.* [in press]. The same authors carried out a visual interpretation of images acquired in October 2008 to map surface fissures at four different locations of the landslide and suggested that multi-temporal maps of the fissures would provide valuable input for the understanding of the landslide dynamics. However, the manual mapping of the numerous structures for an entire landslide and/ or multiple time-steps is a tedious work. To make the

mapping more efficient and explore potential relationships between the image features and geomorphological processes we used the eCognition software environment to design an automated mapping workflow.

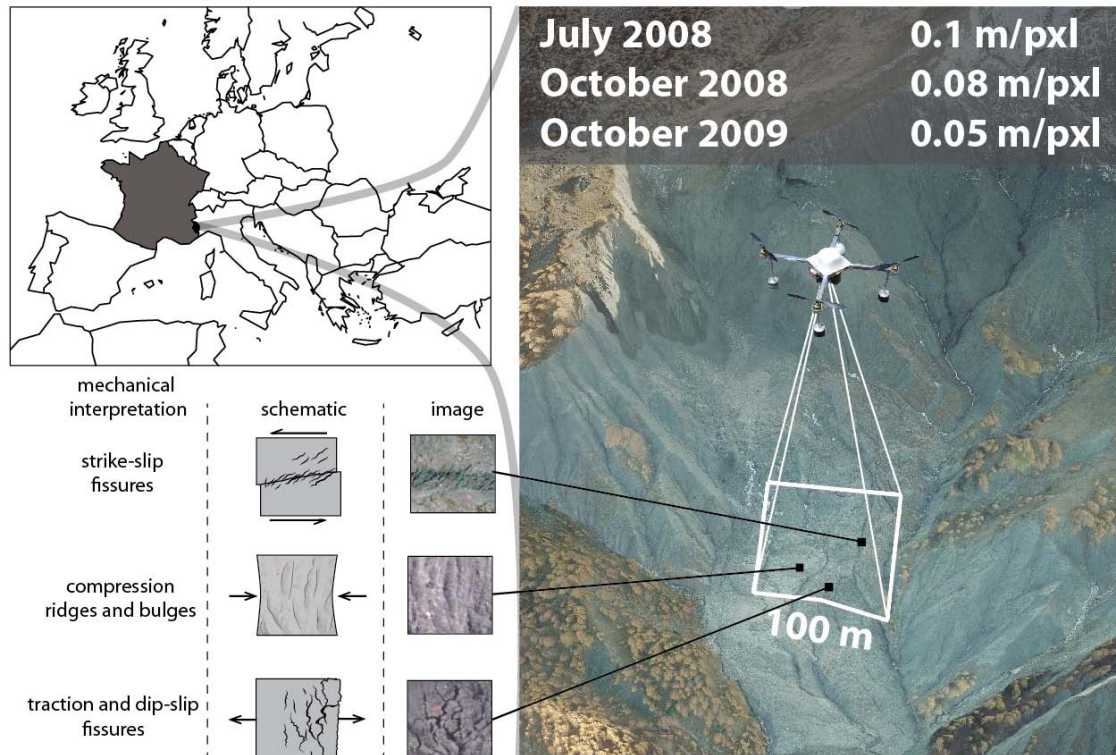


Figure 1: Location of the Super Sauze mudslide and detailed fissure patterns that can be observed in the acquired images.

2.1. Fissure mapping workflow

An overview of the mapping workflow is provided in Figure 3. The starting point is the extraction of linear elements based on the grey-value gradients within the image. The adopted line extraction tool [Trimble, 2011] is a steerable canny-like [Canny, 1986] edge detector including several parameters that can be tuned towards the linear elements of interest. Among other parameters the user can define the length, width and border width of the features of interest, their angle of orientation and the maximum similarity of the line to the border, which defines the sensitivity to changes in grey values (Figure 2a). As illustrated in Figure 2b the definition of the length and boundary width can be used to scale the line extraction toward certain size on linear elements.

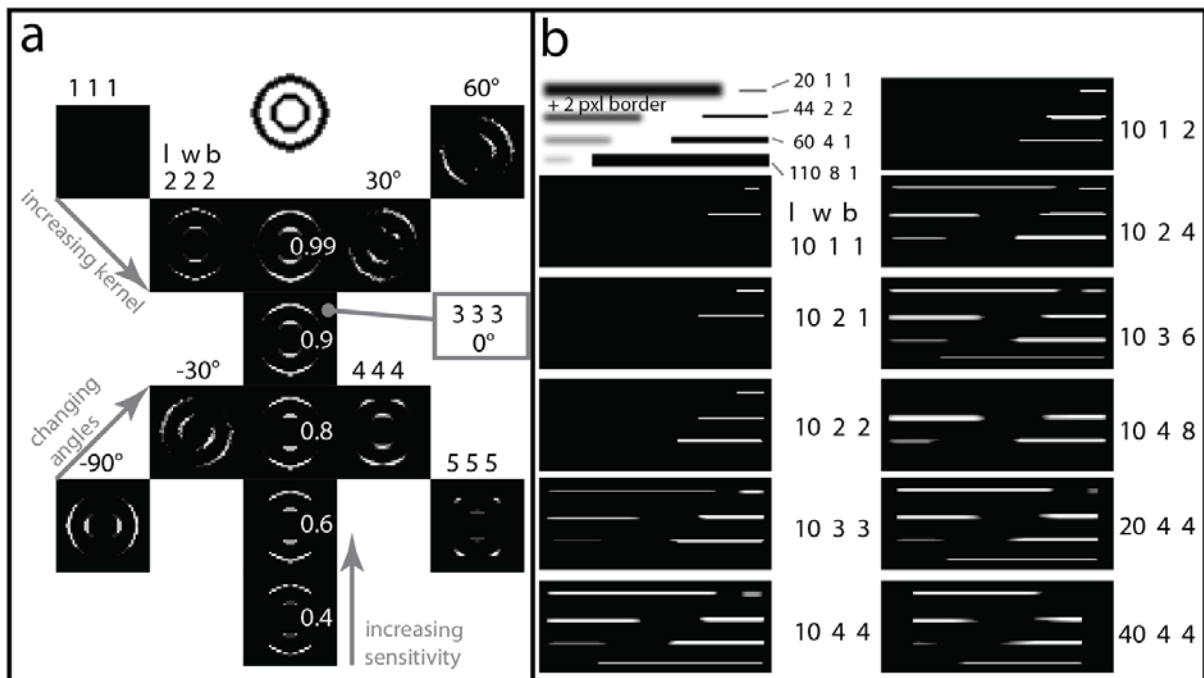


Figure 2: Effects of changing parameters in the line extractor on the resulting gradient images. a, Effects of homogeneously changing kernel (l =line length, w =line width, b =border width), changing angles and increasing sensitivity on a circular test patch. b, Effects kernel changes according to different line widths (w), lengths (l) and border widths (b) on a linear test patch.

According to field observations and previous reports [Grandjean *et al.*, 2007; Niethammer *et al.*, in press] the dimensions of fissures in clay-rich landslide may vary between 0.1 - 0.4 m in width, and from dm to several meters in length. Those values provided some boundary conditions for the parametrization of the line extraction, which after several trials were fixed at 0.2 m line width (boundary-width=2x line width) and a length of 0.8 m. Further inputs for the line extractor are the variance of the image and the selection between dark lines (negative gradient) and bright lines (positive gradient). In this work we focus on the extraction of dark linear elements corresponding to open fissures at the surface. The sensitivity was kept at the default of 0.9. The exclusion of certain fissure orientation a priori is not desired in the given case and hence the extraction was run iteratively at all angles (stepwidth = 5°) and the resulting gradient images were summed up into a single layer. An automatic histogram-based thresholding on the resulting layer is subsequently used to generate candidate objects for fissures (Fig. 3b). The documentation of the proprietary software does not provide details on the implemented thresholding methods. However, in a comparison of the thresholds with those obtained from 17 different thresholding methods implemented in the OpenSource image processing software Fiji (<http://pacific.mpi-cbg.de>), the rather traditional method after Otsu [1979] yielded the same results in all tested cases.

Fissure areas demonstrated a high heterogeneity of grey values and homogenous image patches ($GLCM_{Mean} < 0.2$) were excluded (Fig. 3c). A significant amount of false detections was induced by vegetated patches and shadows. The green to brownish color of the vegetation corresponds to a relatively low ratio of the blue channel. Consequently vegetation appears as dark patches when the blue channel is divided by the sum of all channels. For summer month with active vegetation the ratio of the green channel was implemented as an additional optional stop to verify the results and Otsu's thresholding method was then applied on both bands to classify vegetation (Fig. 3d). A number of further criteria were used to suppress patches smaller than $0.2m^2$, with a strong elongation and very low values in the green channel (< 120) from the vegetation class. Consequently, all fissure candidates that completely overlapped or shared 15% of their border with the mapped vegetation were excluded as false positives.

Images recorded with direct sunlight on the surface show a high contrast of the fissures but also feature several shaded zones induced by the micro- and macro-topography of the landslide surface. An empirical threshold was found for the grey values in the red channel (< 110) to classify shadows and all line candidates which were found to be located in the shadowed areas ($> 33\%$ of the direct surrounding shadowed) were excluded. The observed fissures are presumably induced by kinematic discontinuities and corresponding stress fields in the moving mass and are typically concentrated in a local neighborhood. We attempted to address this issue in a subsequent step

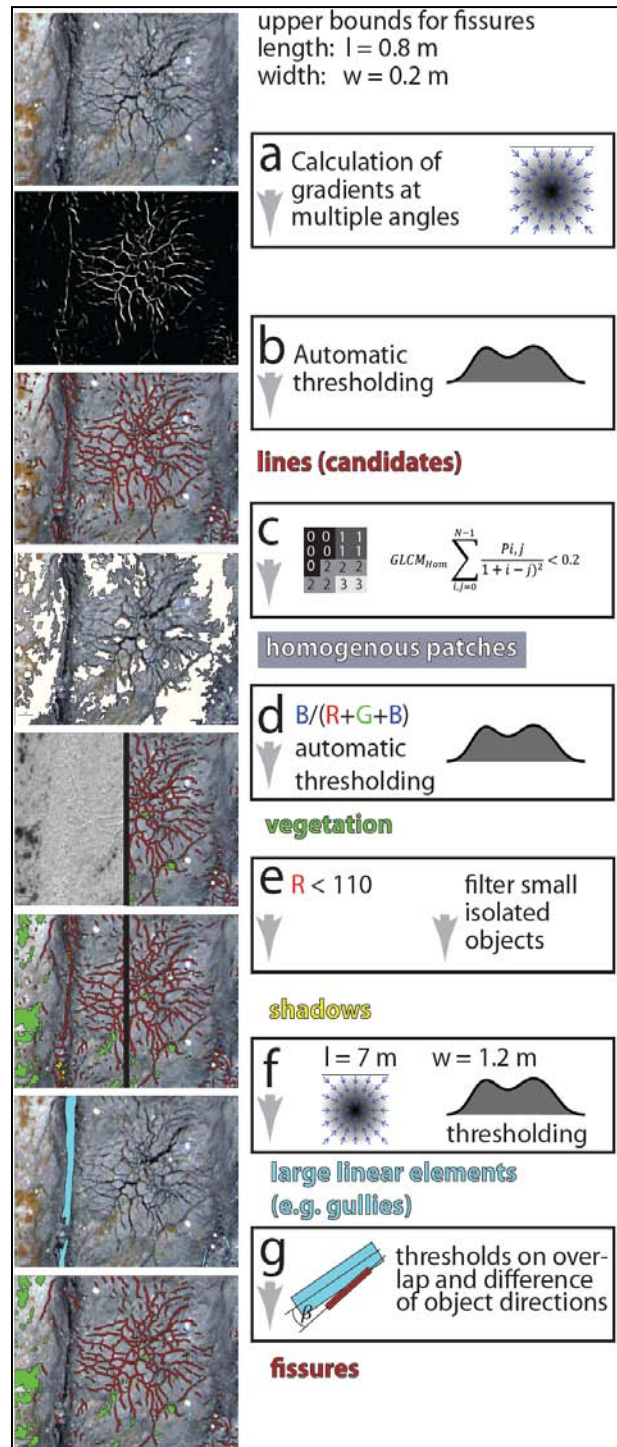


Figure 3: Generalized methodological flowchart for the mapping of fissures and elimination of false positives.

excluding all linear features smaller than the initially defined 0.8 m, and without any other fissures in a surrounding of half this distance (Fig. 3f).

In the final step of the workflow false positives that originate from larger linear structures such as gullies or the borders of the moving mass were addressed. For this purpose the line extractor was parameterized toward this larger features (length = 7m, width = 1.2 m) and those larger lines were classified in the same way as previously the fissure candidates. The larger linear features were linked with overlapping fissure candidates and empirical thresholds were determined to distinguish between false positives that actually belong to larger structures (> 20% of the area fall into the larger structure, difference in the main direction of the angles < 25°) and actually existent fissures (Fig. 3f).

3. Results and Discussion

The workflow was structured and parameterized as described above and applied to UAV images from three different time steps. The resulting maps are displayed in Fig. 4 and provide detailed information about the location and size of individual fissures and vegetation patches as well as their overall spatial patterns. To evaluate the obtained results the map obtained for July 2008 was compared qualitatively to an expert map based on field mapping and image interpretation for the same time step. It can be observed that especially for highly fissured areas both maps provide very similar spatial patterns (highlighted with bright outlines in Fig. 4 b) but it also must be noted that the automated mapping detects a substantially greater amount of relatively small linear features. The generally smaller size (length) and higher number of fissures resulting from the automated approach indicates a different degree of generalization when compared to the expert map. Furthermore it should be considered that the accuracy of both mappings is a priori unknown, and that higher localization uncertainties have an especially strong impact on the overlap of two quasi-line datasets. Creating a 0.2 m buffer on the lines

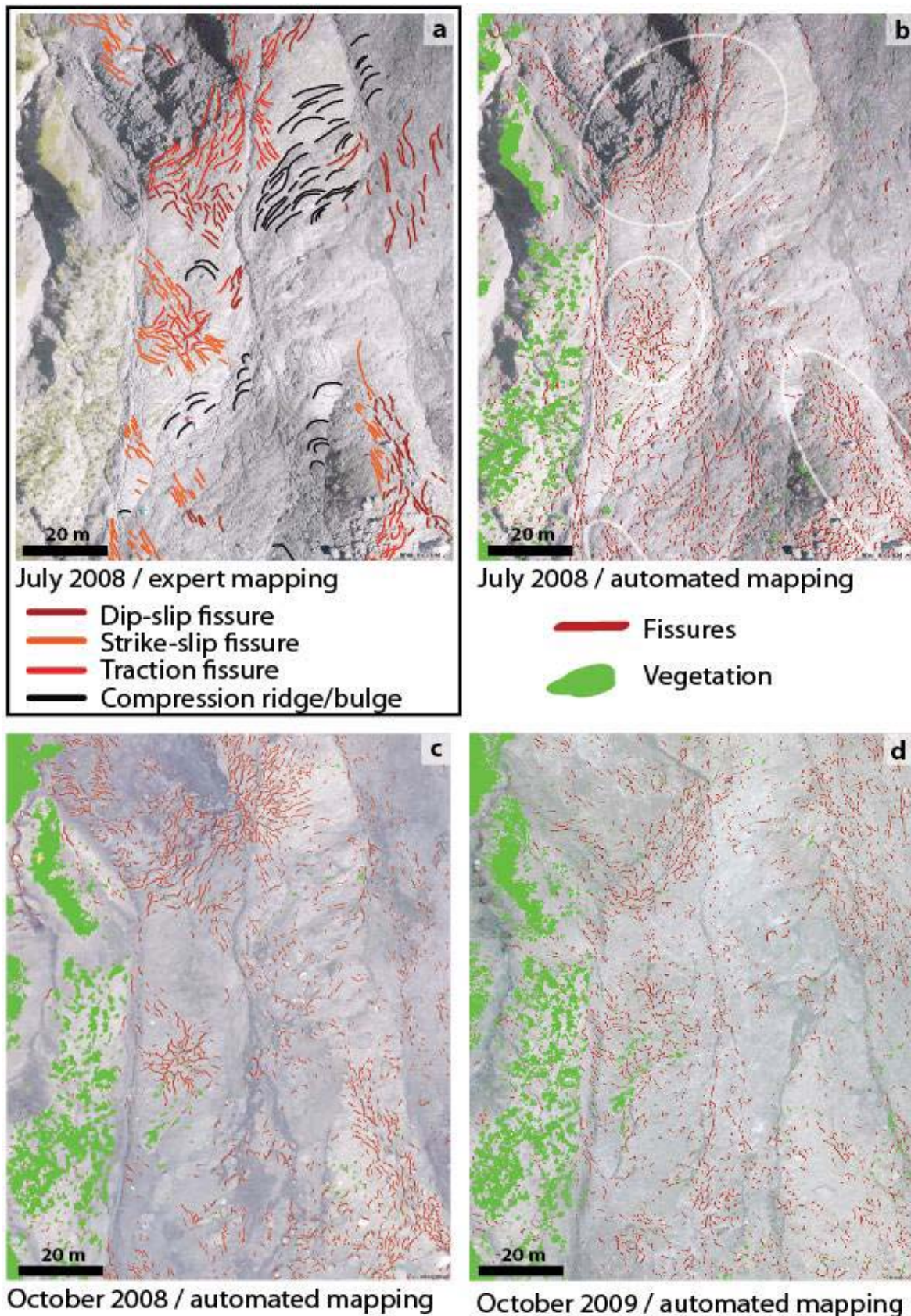


Figure 4: (a) Expert map of surface fissures based on field work and photo-interpretation in July 2008. (b-d), Results of the automated mapping of the vegetation and surface fissures for July 2008 and two further time-steps.

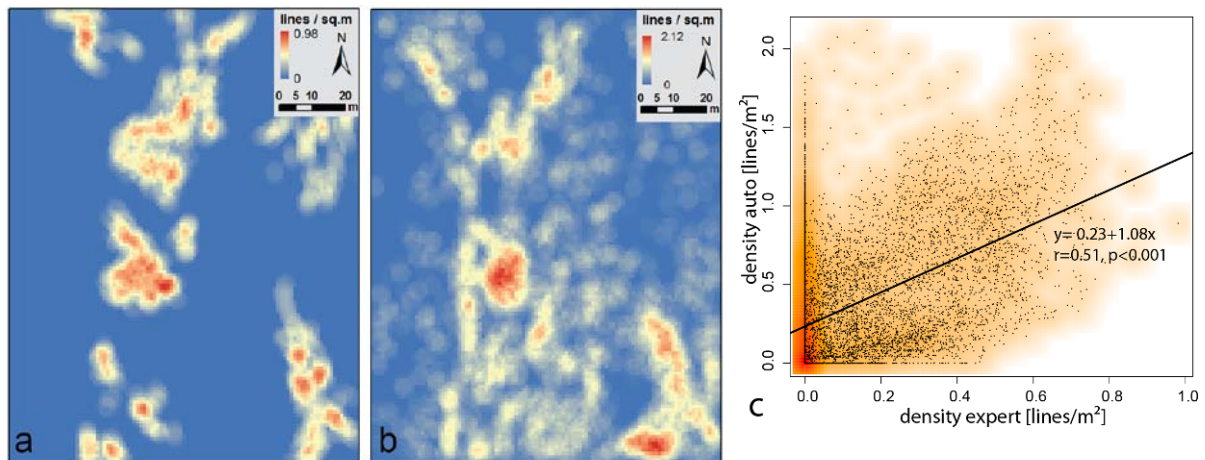


Figure 5: Comparison between the fissure density maps obtained for the July 2008 from the expert mapping (a) and the automated mapping (b).

provided from the expert resulted in measures for completeness and correctness lower than 30% with the polygons from the automated mapping. For a further quantitative comparison of the results we considered calculation of density maps which were derived using a circular kernel with a diameter of 3m. Fig. 5 shows that results from both maps correlate to some degree, whereas the scattering of the density values (Fig. 5c) also illustrate that the results still comprise considerably uncertainties.

4. Conclusion and Perspectives

The current version of automated mapping workflow is relatively sensitive to small linear features resulting in a generally higher number and density of detected fissures. This appears to be partially the result of true over-detection, which appears generally more pronounced in strongly illuminated images (July 2008), but also of different levels of generalization compared to the expert mapping. Although, the sensitivity of the line extractor is adjusted according to overall image variance, further normalization techniques should be tested to better account for variable illumination conditions among the different time steps. In this context it might also be helpful to include also optional steps to allow user interaction for sampling, where the sample could serve for prescreening of potentially fissured areas and an adjustment of hardcoded thresholds according to image and sample statistics.

Further efforts are also needed to implement parameters that allow for the scaling of the resulting maps, and simple heuristics to enhance the connectivity of neighboring lines (Fig. 6)

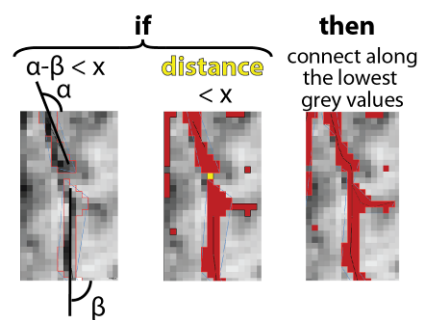


Figure 6: Example for simple heuristics to enhance network connectivity.

are important in this context, since they would allow to interpolate between fractured linear elements and exploit further information inherent in the network.

Beside quantitative differences between the two mappings it is worth highlighting also a few qualitative differences. An expert mapping allows to distinguish among different fissure types that reflect different mechanical processes (Fig. 4a), and a similar automated classification could be achieved by relating the main direction of the fissures to topographic information. The expert map also highlighted several compression ridges, which are visible as linear structures in the image but would need a differently structured workflow.

Though further enhancements and tests are needed to increase the accuracy of the results and the robustness of the method, it was possible to demonstrate that an automated mapping workflow can yield detailed maps of surface fissures and other surface features. On the selected images the workflow runs within 8-12 minutes and produces not only map of the fissures (including fissure width in integer pixel values) but also maps the vegetated areas. UAVs provide a cost-efficient option to acquire images with ultra-high spatial resolution and open a new window for geomorphological studies. As the technical design of the platforms and sensors advances and such image types become more commonly available, further studies are needed to better explore the types of information that can be extracted. Key issues thereby will be synergetic combination of image features, spatial context and knowledge of the physical processes.

References

- Abramson, L. W., T. S. Lee, S. Sharma, and G. M. Boyce (2001), Slope stability and stabilization methods, edited, p. 736, Wiley.
- Baum, R. L., and R. W. Fleming (1991), Use of longitudinal strain in identifying driving and resisting elements of landslides, *Geological Society of America Bulletin*, 103, 1121-1132.
- Berni, J. A., P. J. Zarco-tejada, L. Suárez, and E. Fereres (2009), Thermal and Narrowband Multispectral Remote-sensing for Vegetation Monitoring From an Unmanned Aerial Vehicle. , *IEEE Transactions on Geoscience and Remote-sensing*, 47, 722-738.
- Canny, J. (1986), A Computational Approach to Edge Detection, *Ieee T Pattern Anal*, 8(6), 679-698.
- Carbonneau, P. (2010), High spatial and temporal resolution monitoring of glacial and periglacial processes using Unmanned Aerial Vehicles project 2009-116. Project Summary Report *Rep.*, 6 pp, Department of Geography, Durham University.
- Carbonneau, P. E., S. N. Lane, and N. E. Bergeron (2006), Feature based image processing methods applied to bathymetric measurements from airborne remote-sensing in fluvial environments., *Earth Surface Processes and Landforms*, 31, 1413-1423.
- Chowdhury, R. N., and S. Zhang (1991), Tension cracks and slope failure. , in *International Conference In Slope Stability Engineering: developments and applications. Proceedings of an international conference*, edited by R. J. Chandler, pp. 27-32, Institution of Civil Engineers, Isle of Wight.
- Corbane, C., D. Raclot, F. Jacob, J. Albergel, and P. Andrieux (2008), Remotely sensed soil surface characteristics with a multiscale object oriented approach, *Catena*, 75, 308-318.
- Corominas, J., J. Moya, and M. Hürlimann (2002), Landslide rainfall triggers in the Spanish eastern Pyrenees in *4th EGS Plinius Conference on Mediterranean Storms*, edited, Universitat de les Illes Balears (Spain), Mallorca, Spain.
- Dunford, R., K. Michel, M. Gagnage, H. Piegay, and M. L. Tremelo (2009), Potential and constraints of Unmanned Aerial Vehicle technology for the characterization of Mediterranean riparian forest., *International Journal of Remote-sensing*, 30, 4915-4935.
- Fleming, R. W., and A. M. Johnson (1989), Structures associated with strike-slip faults that bound landslide

- elements, *Engineering Geology*, 27(1-4), 39-114.
- Fleming, R. W., R. L. Baum, and M. Giardino (1999), Map and Description of the Active Part of the Slumgullion Landslide, Hinsdale County, Colorado, U.S. Geological Survey, p.36.
- Graham, D. J., A.-J. Rollet, H. Piégay, and S. P. Rice (2010), Maximizing the accuracy of image-based surface sediment sampling techniques, *Water Resour. Res.*, 46(W02508), 15.
- Grandjean, G., J.-P. Malet, A. Bitri, and O. Méric (2007), Geophysical data fusion by fuzzy logic for imaging the mechanical behaviour of mudslides, *Bulletin de la Societe Geologique de France*, 178(2), 127-136.
- Günther, A., A. Carstensen, and W. Pohl (2004), Automated sliding susceptibility mapping of rock slopes, *Natural Hazards and Earth System Sciences* 4, 95-102.
- Hardin, P., and M. Jackson (2005), An unmanned aerial vehicle for rangeland photography, *Rangeland Ecology & Management*, 58, 439-442.
- Hoek, E., and J. W. Bray (1981), *Rock Slope Engineering*, London.
- Iverson, R. M. (2000), Landslide triggering by rain infiltration, *Water Resour. Res.*, 36(7), 1897-1910.
- Jaboyedoff, M., F. Baillifard, F. Philipposian, and J. D. Rouiller (2004), Assessing fracture occurrence using "weighted fracturing density": a step towards estimating rock instability hazard, *Nat. Hazards Earth Syst. Sci.*, 4(1), 83-93.
- Laliberte, A., and A. Rango (2009), Texture and scale in object-based analysis of subdecimeter resolution unmanned aerial vehicle (UAV) imagery, *IEEE Transactions on Geoscience and Remote-sensing*, 47(3), 761-770.
- Lindenmaier, F., E. Zehe, A. Dittfurth, and J. Ihringer (2005), Process identification at a slow-moving landslide in the Vorarlberg Alps, *Hydrological Processes*, 19(8), 1635-1651.
- Lucieer, A., S. A. Robinson, and D. Turner (2010), Using an unmanned aerial vehicle (UAV) for ultra-high resolution mapping of Antarctic moss beds *Rep.*, 14 pp, University of Wollongong.
- Malet, J.-P., A.-V. Auzet, O. Maquaire, B. Ambroise, L. Descroix, M. Esteves, J.-P. Vandervaere, and E. Truchet (2003), Soil surface characteristics influence on infiltration in black marls: application to the Super-Sauze earth flow (southern Alps, France), *Earth Surface Processes and Landforms*, 28(5), 547-564.
- Malet, J. P., T. W. J. van Asch, R. van Beek, and O. Maquaire (2005), Forecasting the behaviour of complex landslides with a spatially distributed hydrological model, *Nat. Hazards Earth Syst. Sci.*, 5(1), 71-85.
- Marzloff, I., and J. B. Ries (2007), Gully monitoring in semi-arid landscapes., *Zeitschrift fuer Geomorphologie* 51(4), 405-425.
- Matheson, G. D. (1983), Rock Stability Assessment in Preliminary Site Investigations – Graphical Methods *Rep.*, Transport and Road Research Laboratory, Crowthorne.
- McCalpin, J. (1984), Preliminary age classification of landslides for inventory mapping, in *21st Annual Engineering Geology and Soils Engineering Symposium*, edited, pp. 99-111, Moscow, Idaho.
- Meisina, C. (2006), Characterisation of weathered clayey soils responsible for shallow landslides, *Nat. Hazards Earth Syst. Sci.*, 6(5), 825-838.
- Niethammer, U., S. Rothmund, and M. Joswig (2009), UAV-based remote-sensing of the slow-moving landslide Super-Sauze, paper presented at International Conference Landslide Processes: from geomorphologic mapping to dynamic modelling, CERG Editions, Strasbourg, February 6 to 7, 2009.
- Niethammer, U., M. R. James, S. Rothmund, J. Travelletti, and M. Joswig (in press), UAV-based remote-sensing of the Super-Sauze landslide: Evaluation and results, *Engineering Geology, In Press, Accepted Manuscript*.
- Otsu, N. (1979), A Threshold Selection Method from Gray-Level Histograms, *IEEE Transactions on Systems, Man and Cybernetics*, 9(1), 62-66
- Parise, M. (2003), Observation of surface features on an active landslide, and implications for understanding its history of movement, *Nat. Hazards Earth Syst. Sci.*, 3(6), 569-580.
- Petley, D., S. Dunning, N. Rosser, and A. B. Kausar (2006), Incipient Landslides in the Jhelum Valley, Pakistan Following the 8th October 2005 Earthquake, in *Disaster Mitigation of Debris Flows, Slope Failures and Landslides*, edited, pp. 47-55, Universal Academy Press, Inc., Tokyo, Japan.
- Priest, S. D. (1993), *Discontinuity analysis for rock engineering*, Chapman & Hall, London, UK.
- Puech, C., N. Thommeret, B. Kaiser, J. S. Bailly, A. Jacome, F. Rey, and N. Mathys (2009), MNT à très haute résolution dans les modelés fortement disséqués : des données aux tests d'application, *Géomorphologie: Relief, Processus, Environnement* 2, 141-152.
- Raclot, D. (2006), Remote-sensing of water levels on floodplains: a spatial approach guided by hydraulic unctoning., *International Journal of Remote-sensing*, 27, 2553-2574.

- Selby, M. J. (1993), *Hillslope materials and processes*, 445 pp., Oxford University Press, Oxford, UK.
- Trimble (2011), *eCognition Developer 8.64.0 Reference Book*, 410 pp., Trimble Documentation, München, Germany
- van Asch, T. W. J., L. P. H. van Beek, and T. A. Bogaard (2009), The diversity in hydrological triggering systems of landslides., paper presented at The First Italian Workshop on Landslide, Napoli, Italy 8- 10 June.
- van Beek, L., and T. van Asch (1999), A combined conceptual model for the effects of fissure-induced infiltration on slope stability, in *Process Modelling and Landform Evolution*, edited by S. Hergarten and H. Neugebauer, pp. 147-167, Springer Berlin / Heidelberg.

3.2. INTERPRETATION OF RADAR IMAGERY

3.2.1. Data acquisition

Active microwave sensors, also called Radar, use electromagnetic waves of wavelengths from 1 mm to 1 m artificially emitted by antennas. These technologies have been developed for about one hundred years, but this is in late 1940's that, for military reconnaissance purposes, major advances were achieved [Woodhouse, 2006]. Then, the first civilian application at a large scale was setup to map the Panama's province of Darien, acquiring Radar mosaic images of a 20'000 km² ground area that has never been photographed before due to a permanent and dense fog [Lillesand *et al.*, 2008]. Even if first environmental remote-sensing applications were performed from aerial platforms, today the majority of the Radar images are acquired from spaceborne platforms. Indeed, the fly and the trajectory of the platform have to be as stable as possible and perfectly knew (reasonable in a satellite, not yet from airplane) to perform Synthetic Aperture Radar (SAR) images [Wiley, 1954].

SAR images are now the raw data of each Radar-based environmental application, with a ground resolution from 30 m (Envisat platform) to 1 m for the last generation of devices (TerraSAR-X platform). Usually, spaceborne sensors are emitting radio waves in the bands X, C and/or L, according to regulations of the International Telecommunication Union. Then waves are back-scattered by the Earth's surface and sensors record the amplitude and the phase shift of the returned signal (Figure 4). Thus the complex image (amplitude and phase) acquired constitutes the raw level of data on which main of remote-sensing algorithms are processed.

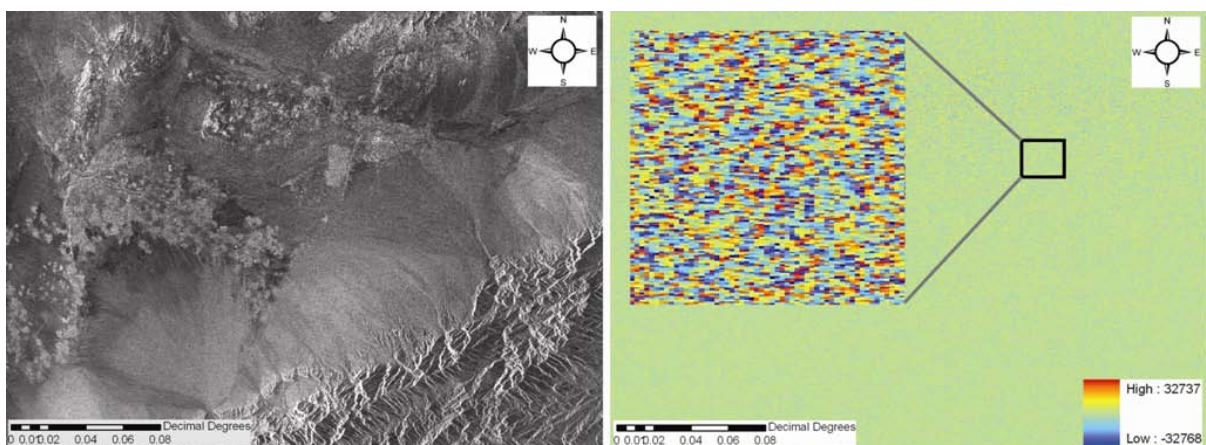


Figure 4: raw SAR image with the return amplitude signal (left) and phases (right) of Bam area in Iran, December 2003 (free Envisat data, shown in the SafeLand deliverable 4.1).

The longer the wavelength is, the worse the accuracy is both in terms of spatial resolution and measurement precision, but better are the penetration capacity and the stability

of the returned signal with respect to environmental changes. Today, in 2011, the mostly used images are acquired by seven platforms operated by the Canadian, European, German, Italian and Japan space agencies (resp. CSA, ESA, DLR, ASI and Jaxa). The main characteristics of these systems are resumed within the Table 3.

Table 3: Main key features of the seven most used systems for civil Radar environmental applications.

	ERS 1&2	Envisat	ALOS	TerraSAR-X	Radarsat-2	COSMO SkyMed
Operator	ESA	ESA	Jaxa	DLR & infoterra GmbH.	CSA & MDA Ltd.	ASI
Band	C	C	L	X	C	X
Repeat period (days)	35	35	46	11	24	16
Geometric resolution (m)	30	30 to 150	10 to 100	1.1 to 18..5	3 to 100	1
Look Angle (°)	21.1-25.9	15-45	7.9-60	10-60	20-49	20-60
Mean Swath Width (km)	80 to 102.5	100	40 to 70	10 x 5 to 100 x 150	20 to 100	10 to 200
Mean Altitude (km)	784	800	692	514	802	619
On	17.07.1991 & 20.04.1995	01.03.2002	24.01.2006	15.06.2007	14.12.2007	08.06.2007
Off	10.03.2000 (ERS1)	-	-	-	-	-
Documentation	earth.esa.int/ers	envisat.esa.int	www.jaxa.jp/projects/sat/alos/ind_ex_e.html	www.infoterra.de/terrasar-x-satellite	www.asc-csa.gc.ca/eng/satellites	www.cosmo-skymed.it

The principles Radar technologies and applications are described in many publications, books and encyclopedias. About the radar imaging part used in environmental and Earth sciences, *Massonnet and Feigl*, [1998], *Hanssen* [2001], *Woodhouse* [2006], *Lillesand et al.* [2008] or the SafeLand deliverable 4.1 [*Michoud et al.*, 2010] provide worthy introductions and overviews.

3.2.2. Data analysis

A. Surface change detection with classical SAR Interferometry (DinSAR) methods

[UNIL]

As already noted, InSAR techniques were originally used to produce topographic maps. Then, in 1985, Massonnet [1985] published a technical report on the possibility to map temporal changes of the Earth's surface, "removing the signal of the topography" inside interferometric scenes. He applied for the first time the concept of Differential InSAR for ground displacement detection. Indeed, as described in details in the SafeLand deliverable 4.1 [*Michoud et al.*, 2010], DInSAR techniques aim to compare the phase shift of returned signals of two SAR images of a same area acquired from two different point of view and/or at different times. Its main application is to detect and quantify small ground displacements (Figure 5). More information about theoretical considerations is available in *Massonnet and Feigl* [1998], *Lauknes* [2004], *Catani et al.* [2005], *Colesanti and Wasowski* [2006], *Woodhouse* [2006], *Ferretti et al.*[2007] and is summarized in the SafeLand deliverable 4.1 [*Michoud et al.*, 2010].

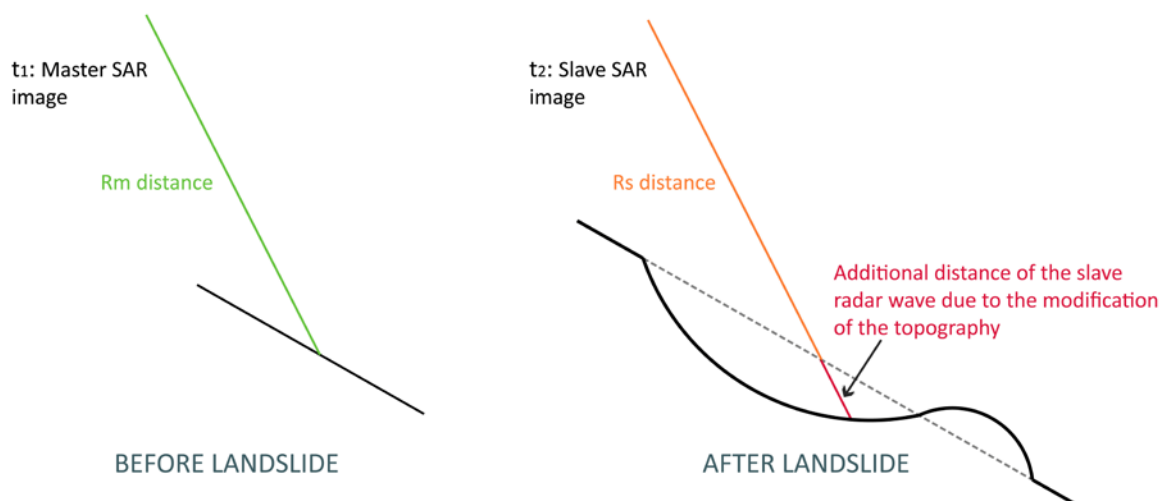


Figure 5: the ground displacement, as a landslide, influences the phase shift of a Radar returned signal. The way of the signal on the Slave SAR image is longer than the way of the signal on the Master image, due to the displacement created by the rotational landslide. This additional distance produces a phase shift that can be detected and interpreted as an active area on susceptibility maps (SafeLand deliverable 4.1).

First DInSAR studies applied to changes in the Earth's Surface concerned co-seismic field displacements [Massonnet *et al.*, 1993] and post-seismic readjustments [Massonnet *et al.*, 1996] induced by the 1992 Lander's earthquake (California), where the authors were able to detect movements of 28 mm along an active fault, during the three years that followed the seismic event. Later, Fruneau [1996] and Carnec *et al.* [1996] presented two monitoring studies of the temporal displacement evolution of the "La Clapière" landslide (France) using simple SAR interferometric pairs. Afterwards, Squarzoni *et al.* [2003] were able to assess the movements of the "La Valette" mudslide (France) during nine years thanks to archived Radar scenes (Figure 6). Then, Singhroy and Molch [2004] advised to use DInSAR techniques to support field survey in case of large rockslides, because precursory deformations were visible on interferometric pairs processed prior to a major rock fall.

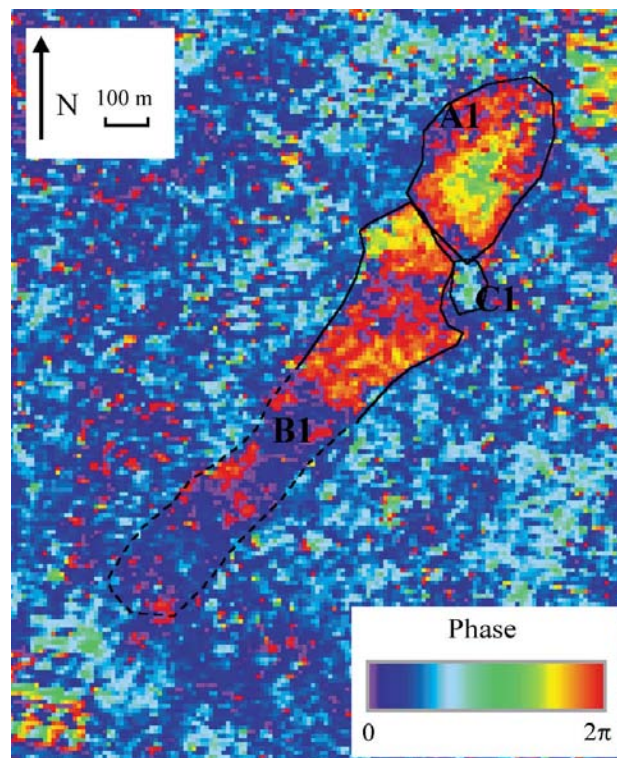


Figure 6: Interferogram of the "La Valette" landslide processed with two SAR scenes acquired by the ERS-tandem mission (temporal baseline: 1 day). The detected phase decay (one fringe: 28 mm) is due to displacements detected along the line of sight [from Squarzoni *et al.*, 2003].

Even if these studies showed very promising results, they all find major limitations, mainly caused by temporal decorrelations [Massonnet and Feigl, 1998] and atmospheric artefacts [Zebker *et al.*, 1997]. Then, since Ferretti *et al.* [1999; 2000] and the development of the Permanent Scatterer technique, all Advanced InSAR methods use now a large multi-stack of SAR images in order to overcome those limits, providing more accurate and reliable results.

B. Surface change detection with advanced SAR Interferometry (A-DInSAR, PS-INSAR) methods

[UNISA]

The analysis of slow-moving landslide phenomena has been proven to be valuably enhanced by the use of remote-sensing data such as those acquired by space-borne Synthetic Aperture Radar (SAR). This contribution is further enhanced via the development of innovative algorithms – such as those adopted for multipass Differential Interferometric Synthetic Aperture Radar (DInSAR) image processing (A-DInSAR, PS-INSAR) – which allows, even over large areas, the retrieval of around 20-year displacements of the topographic surface at fairly affordable costs. The scientific literature is rich of case studies showing how these techniques can turn out to be useful in furnishing input data for i) the landslide characterization (detection of unmapped phenomena [Casini *et al.*, 2010; Farina *et al.*, 2006]; ii) the check of the boundaries and of the state of activity, see [Canuti *et al.*, 2004; Casini *et al.*, 2008; Farina *et al.*, 2006] iii) the monitoring at different scales of both the phenomena and the structure/infrastructures interacting with the affected areas [Casini *et al.*, 2008; Farina *et al.*, 2006]. The potential of the use of DInSAR data is testified by their increasing diffusion, as recently recorded worldwide with several different applications (European Space Agency's (ESA) projects MASMOV, ALPS, SLAM, TERRAFIRMA, etc.). This growth is remarkable in Italy, where a pioneering project (Piano Straordinario di Telerilevamento Ambientale) was launched in 2002 (Italian Law 179/2002), as well as in the Campania region (southern Italy) thanks to the PODIS-TELLUS project (2008). Both projects were set up to enhance the availability of DInSAR data and promote their use in the field of land management.

C. Correlation of high resolution SAR images

[BRGM]

Recently launched X-band radar satellites are capable to acquire images at sub-metric resolutions (TerraSAR-X and Cosmo-Skymed) equivalent to those provided by optical sensors widely used for image correlation (Spot 5, Quickbird, etc.). In this context, the SAR data has become an interesting alternative to optical data for image correlation techniques applied to ground surface deformation. For a given study site High Resolution SAR data can be obtained with coherent acquisition modes and orbital configuration, and with reliable temporal resolution since the image acquisition is relatively independent from local weather conditions. Among the currently available techniques for the correlation of SAR images we can distinguish between speckle tracking [Gray *et al.*, 2001], Isolated Point Scatterer (IPS) [Serafino, 2006], normalized cross-correlation (NCC) [Strozzi *et al.*, 2002] and Maximum Likelihood texture tracking [Erten *et al.*, 2009; Harant *et al.*, 2011]. Another available technique is the spectral diversity technique [Prats *et al.*, 2009; Scheiber and Moreira, 2000]

but requires a coherent set of SAR scenes to create interferograms. To the best of our knowledge the technique has not yet been applied in the context of landslide but provided promising results for the monitoring of glacier kinematics (Figure 7).

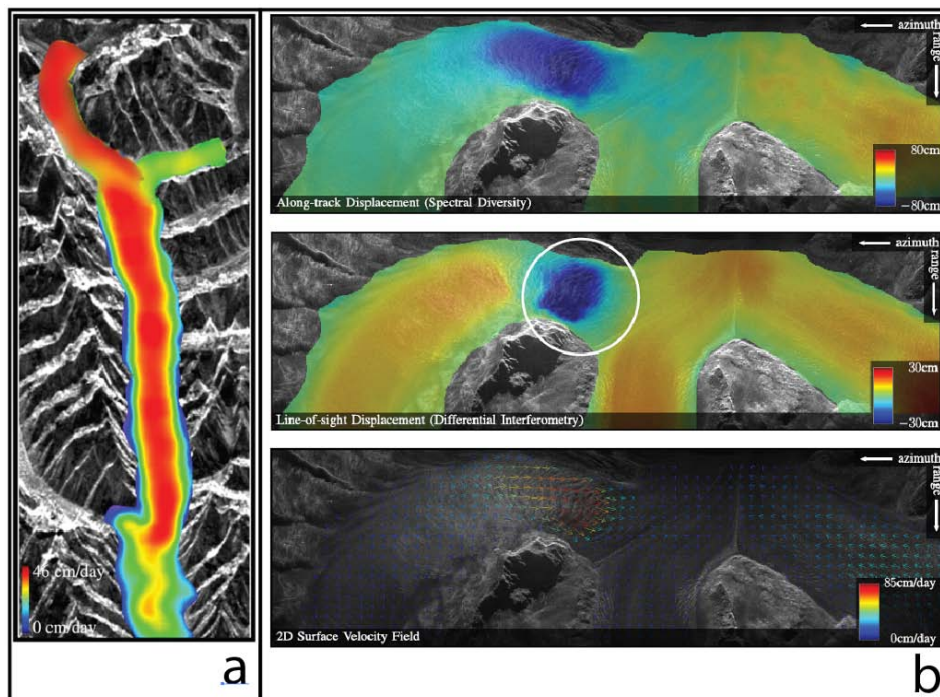


Figure 7: (a) Velocity map for the Inyltshik glacier in Kyrgyzstan for a three month period as derived from Maximum Likelihood texture tracking on ENVISAT-ASAR[Erten *et al.*, 2009]. (b) 2D surface velocity field of the Aletsch glacier derived with the spectral diversity technique on L-band airborne SAR images[Prats *et al.*, 2009].

3.2.3. Innovative case studies

The following section demonstrates the use of radar imagery via short summaries of five recently published or submitted research works carried out within SafeLand or through sister projects.

Persistent Scatterers hotspot and clustering analysis for detection of slow-moving landslides

Application: Landslide hotspot mapping

Technique: Active spaceborne SAR sensors

Main references: Lu, P., F. Catani, N. Casagli and V. Tofani (2009): Hotspot analysis of Persistent Scatterers (PS) for slow-moving landslides detection.

Contributors: UNIFI (P. Lu, F. Catani, N. Casagli, V. Tofani)

Abstract

SAR interferometry (InSAR) has already shown its significance for landslide mapping. However, temporal decorrelation and atmospheric disturbances limit the usefulness of traditional differential InSAR techniques. The recently developed Persistent Scatterers (PS) technique removes the temporal decorrelation and atmospheric artifacts by generating radar benchmarks derived from a multi-interferogram analysis of SAR images. PS are suitable for investigating slow moving landslides because they are able to detect ground displacements with the accuracy of millimeters. However, because of the large number of PS that can be identified, the effective extraction of information useful for landslide studies from this technique sometimes remains difficult. With the aim of mapping landslides rapidly and (semi-)automatically, we perform the hotspot analysis on the PS present within the Arno river basin (Italy) using spatial statistics approach. We process 4 years (2003-2006) of RADARSAT SAR images within the basin so as to identify slow moving landslides and meanwhile update the existing landslide inventory. We apply the G_i^* statistics in our study for the local test on PS datasets. We use the velocity of PS as the weighting factor and calculate the G_i^* index for each single PS. The result indicates that both high positive and low negative G_i^* values express the clustering of relatively rapid mass movements. The high positive values suggest movement towards the sensor along the satellite Line-of-Sight (LOS) whereas the low negative values imply movement away from the sensor. Moreover, we employ the kernel function for PS density estimation based on the G_i^* values. The output is the hotspot map which emphasizes the existing mass movement. We consider that our methodology offers an innovative tool for extracting useful information from PS, thus providing an effective way of landslide rapid mapping.

Keywords: landslide hotspot mapping; InSAR, Persistent Scatterers

1. Introduction

Remote-sensing is useful for landslide studies. SAR interferometry (InSAR) is an important branch of remote-sensing [Bamler & Hartl 1998]. It is valuable for landslide mapping and monitoring [Corsini *et al.* 2006]. Combined with both amplitude and phase parameters, an interferogram can be generated with the radar images of the same area. After unwrapping interferogram fringes, it is capable to detect ground movement with millimetric accuracy [Massonnet & Feigl 1998]. However, the usefulness of traditional differential InSAR (DInSAR) techniques is limited by factors such as temporal decorrelation and atmospheric disturbances [Fruneau *et al.* 1996, Massonnet & Feigl 1998, Kimura & Yamaguchi 2000, Ferretti *et al.* 2001]. The Persistent Scatterers (PS) technique is a recently developed InSAR approach. It is patented by the Politecnico di Milano and is commercially available through the POLIMI spin-off company Tele-Rilevamento Europa (TRE). PS technique produces radar benchmarks derived from a multi-interferogram analysis of SAR images. The temporal decorrelation and atmospheric artifacts can be meanwhile estimated and removed (Ferretti *et*

al. 2001). Some successful cases have shown the suitability of PS for investigating slow moving landslide [Colesanti et al. 2003, Casagli et al. 2005, Farina et al. 2006].

However, the effective extraction of useful information from this technique for landslide studies is sometimes difficult due to the large number of PS that can be present, thereby entailing long interpretation times. In the places where there are a lot of stable reflectors such as buildings and bared rocks, the PS density is higher than 500 PS/km². Large number of PS calls for an efficient approach of data processing. Still, with the quick development of new SAR sensors and efforts of increasing PS density, the PS data is expected to be updated more frequently with higher density. Thus, an effective approach of data interpretation is needed.

With the intention of developing an effective procedure for landslide mapping from PS, we introduce a spatial statistical approach on the PS analysis, choosing the Arno river basin (Italy) as the study area. The aim is to employ PS processed from 4 years (2003-2006) of RADARSAT SAR images to identify slow moving landslides within the basin. We consider this spatial statistics approach as an effective way for landslide mapping, thus providing an innovative approach for the rapid extraction of useful information from PS.

2. Study area

The Arno river basin is located in the central Italy (Fig. 1). The total area of the whole basin is about 9130 km². The basin is across of Apennines chain. As a result, 7190 km² of the basin is situated in the mountainous and hilly area. The basin is very susceptible to landslides. More than 27,000 landslides were mapped. The affected landslide area is more than 800 km². These landslides are dominated by earth slides and flows (about 74%) as well as shallow landslides and creeps [Catani et al. 2005a, Farina et al. 2006]. Most of these slide movements are slow and intermittent, accompanied with accelerations due to the prolonged and intensive rainfall. The concentration of precipitation periods also accounts for the landslides activity transition from dormant to active [Catani et al. 2005b]. More than 16,000 civil buildings, 460 industrial areas and 350 km roads are affected by landslides. In addition, ca. 6 billions Euro losses are expected in the upcoming 30 years [Catani et al. 2005b].

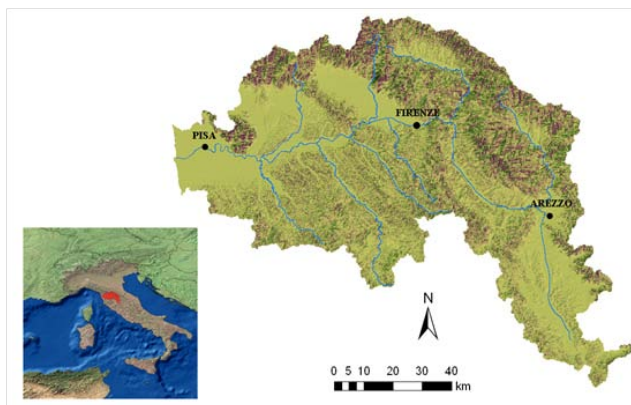


Figure 1. The location of the Arno river basin

Figure 1. Location of the Arno River Basin

3. Methodology

3.1. Persistent Scatterer Interferometry

PS technique is a long-term multi-image interferometric approach. A series of interferometric SAR images are referred to a unique master acquisition. PSInSAR is able to overcome the main disadvantages of DInSAR (temporal decorrelation and atmospheric disturbances). The temporal decorrelations can be removed by using long temporal series of SAR images along the same satellite orbit. Also, the atmospheric disturbances can be estimated so as to remove the produced artifacts [Ferretti *et al.* 2001]. The interferometric phase is analyzed on a pixel-by-pixel approach. With the generation of multi-interferograms, stable radar benchmarks can be identified based on the coherence map. The output of PS technique is a set of sub-pixel points with high coherence corresponding to phase stable radar targets. These targets include man-made structures (buildings, dams and bridges) and natural reflectors (bared rocks). The velocity of each single PS can be estimated by performing the statistical analysis on the amplitudes of the electromagnetic returns. The detailed description of PS can be found in Ferretti *et al.* [2000, 2001].

A PS dataset of 4 years of RADARSAT images spanning from March 2003 to January 2007 is available for the Arno river basin. The data have been processed by TRE on behalf of the Arno river basin Authority. Since the acquisition circle is 24 days, more than 46 RADARSAT images are utilized for PSInSAR analysis. These images are captured in the beam mode of S3, which gives the incidence angle ranging between 30 and 37 degrees. The used track number of RADARSAT for the basin is 54 for descending and 247 for ascending images. These two tracks cover about 6300 km², approximately 70% area of the whole basin. Totally more than 700,000 PS are identified. The density of ascending PS is 54 PS/ km² and the density of descending data is 59 PS/ km². The PS located within the flat area is then masked so as to only focus on the movement in mountainous and hilly areas.

3.2. Hotspot and clustering analysis

The purpose of the hotspot and clustering analysis is to identify concentrations of high velocity PS. The analysis is based on the two statistics approaches: Getis-Ord G_i^* statistics and kernel density estimation.

3.2.1 Getis-Ord G_i^* statistics

The Getis-Ord G_i^* statistics is a kind of local spatial statistics which represents the association up to a specified distance. In the study we apply G_i^* statistics to evaluate the spatial clustering of neighboring PS. The G_i^* index is defined as follows [Getis & Ord 1996]:

$$G_i^*(d) = \frac{\sum_j w_{ij}(d)x_j - W_i^* \bar{x}}{s^* \left\{ \left[(nS_{1j}^*) - W_i^{*2} \right] / (n-1) \right\}^{0.5}} \quad (1)$$

While in the Equation 1,

$$W_i^* = \sum_j w_{ij}(d) + w_{ij}, \quad S_{1j}^* = \sum_j w_{ij}^2 \quad \text{and} \quad s^{*2} = \frac{\sum_j x_j^2}{n} - \bar{x}^2.$$

$w_{ij}(d)$ is the spatial weights vector. It is defined within the searching distance d from the PS whose velocity is x . Each single PS is at a site i with its neighbors j within the distance d . In the study, all the PS are treated as the same weight, namely 1.

In order to define the searching distance of d , for each pixel (10m) of the DTM of the Arno river basin, both the shortest path to a channel ($d1$) and the ridge ($d2$) are calculated based on steepest descent direction. The searching distance of each pixel (d_i) is calculated as the mean value of $d1$ and $d2$, simulated as a measure of landslide length along the slope. The estimation of the searching distance d is based on the mean value of all DTM pixels. In the case of the Arno River basin, the searching distance d is 114m compared with a DTM of 10m resolution.

We apply the G_i^* statistics in our study and perform the local test on PS datasets. We choose the velocity of PS as the weighting factor and calculate G_i^* index for each single PS. The G_i^* index measures concentrations of high velocity PS for the entire study area. The larger (positive) the G_i^* index is, the more intense the clustering of high velocity values, with the PS moving direction towards Line-of-Sight (LOS) of the satellite. The smaller (negative) the value is, the more intense the clustering of low velocity values (negative), with the PS moving direction away from LOS.

3.2.2 Kernel density estimation

The following procedure is to estimate PS density using kernel calculation. The kernel density estimation [Silverman 1986] uses a kernel estimator which is defined as:

$$f(x) = \frac{1}{nh} \sum_{i=1}^n K\left(\frac{x - X_i}{h}\right) \quad (2)$$

where h is the window width, $x - X_i$ is the distance to each PS i . K is the quadratic kernel function defined as:

$$K(x) = \frac{3}{4}(1 - x^2), |x| \leq 1$$

$$K(x) = 0, x > 1$$

We employ this kernel function for PS density estimation, choosing the previous derived G_i^* index as the weight. The output is a smooth density map adding the values of kernel function. It indicates the existing hotspot of high velocity mass movement.

4. Result and discussion

Figure 2 shows one part of the hotspot map derived from the same SAR image frame. The area is within the Arno river basin covering the Pistoia-Prato-Firenze and the Mugello basin. Both the ascending (Fig 2a) and descending (Fig 2b) hotspot map are displayed based the result of kernel density estimation. Clustering of positive velocity PS (moving towards LOS) is rendered with blue hotspot while clustering of negative velocity PS (moving away from LOS) is rendered with red color. The deeper color it displays, the more intense clustering of higher velocity PS. The radius of the hotspot implies the dimension of the potential landslide-affected area. Figure 3 is the hotspot map with the overlay of both ascending and descending hotspot map. The magenta areas are the combination of red and blue hotspots. They indicate the different moving directions of PS from different ascending and descending orbits. Still, the deep blue and deep red hotspot indicate the same moving directions detected from the ascending and descending PS.

The clustering of high velocity PS is able to detect landslide considering LOS of satellite and down-slope landslide movement can especially be detected from PS moving away from sensor. According to the previous studies and existing landslide inventory map, some of the detected hotspots are confirmed to be the mass movements resulting from slow moving landslides. Hence, the hotspot map is expected to be an important source for the following study of landslide inventory updating. However, detection errors exist when such mass movement is related to other geophysical processes that PS can identify. The major errors are attributed to uplift and ground subsidence. Moreover, the hotspot sometimes shows the limitations in separating landslide movement from other geo-processes. For example, if an area is subject to both landslide and subsidence, the hotspot analysis possibly only yields the result of one big hotspot. This hotspot however fails to separate these two kinds of mass movement. Such problems are mainly resulted from the current limitations of PS technology for detailed interpretation of mass movement.

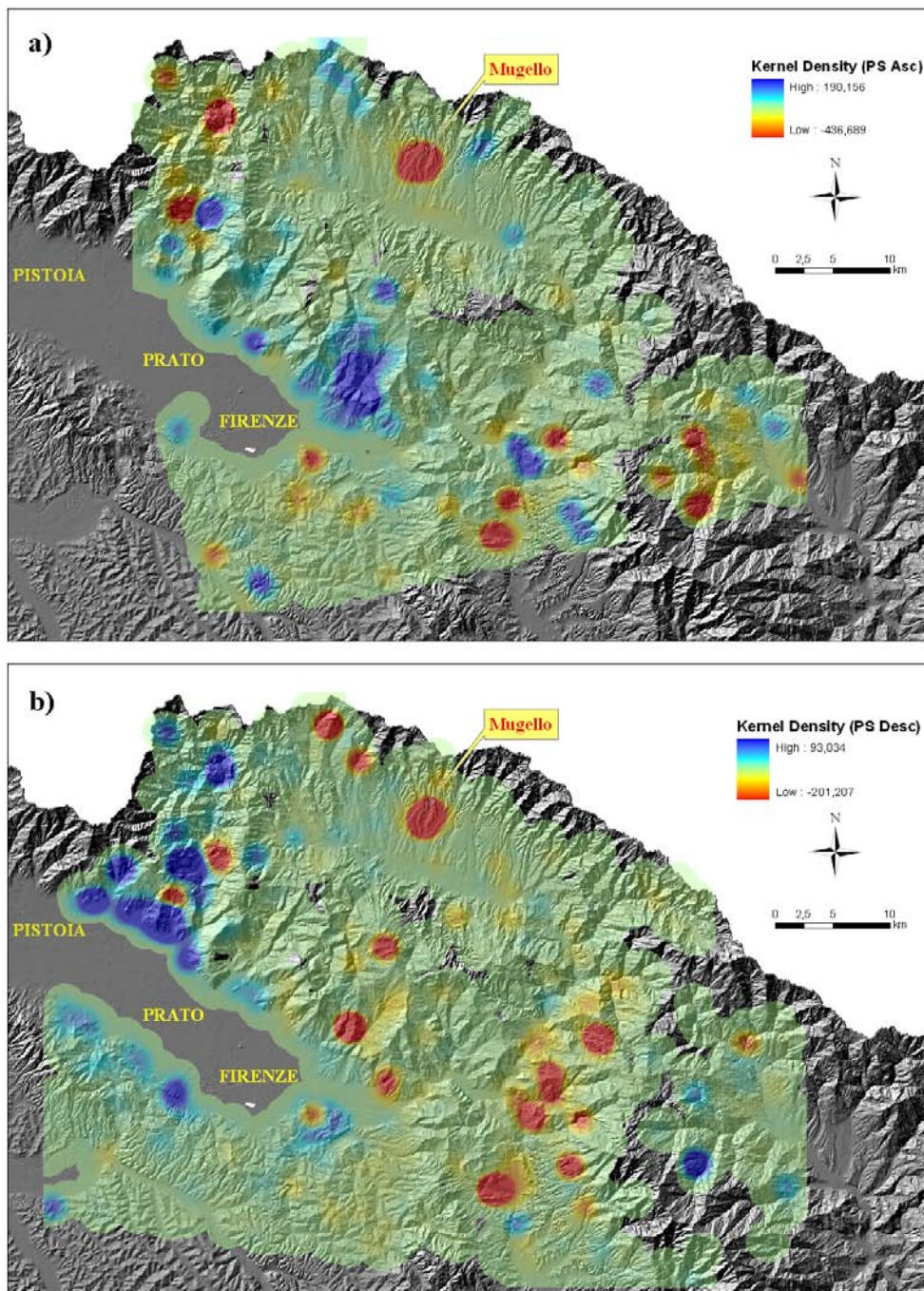


Figure 2. Part of the hotspot map of the Arno river basin, including the Pistoia-Prato-Firenze and Mugello basin area: a) hotspot map derived from kernel density estimation using ascending RADARSAT PS; b) hotspot map derived from kernel density estimation using descending RADARSAT PS. Red Hotspot (low negative kernel density) indicates the clustering of high velocity PS moving away from LOS whereas blue hotspot (high positive kernel density) implies the clustering of high velocity PS moving towards LOS.

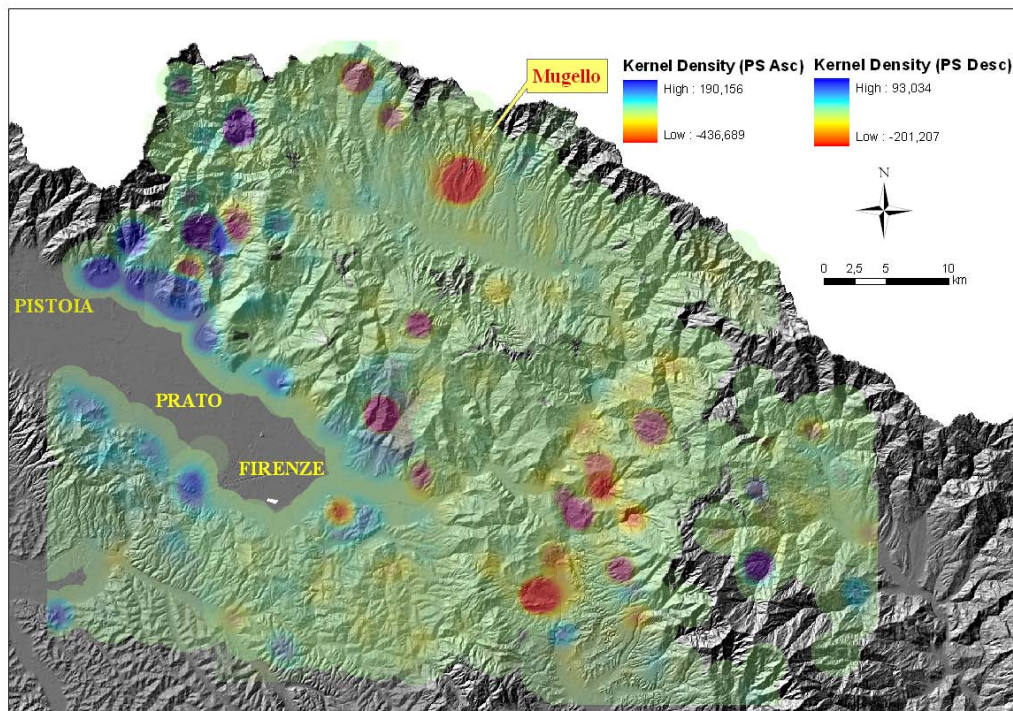


Figure 3. The hotspot map overlaid with ascending and descending data. The magenta hotspot indicates the clustering of high velocity PS detected by both ascending and descending PS, with one moving direction away from LOS and another moving towards LOS. The deep red and blue hotspots imply the clustering of high velocity PS detected by both ascending and descending data, with the same moving direction along LOS.

References

- Bamler, R. & Hartl, P. 1998. Synthetic aperture radar interferometry. *Inverse Problems* 14: 1-54.
- Casagli, N., Guerri, L., Righini, G., Ferretti, A., Colombo, D. & Prati, C. 2005. Integrated use of PS and very high resolution optical images for supporting landslide risk management. *URSI, Symposium on Microwave Remote-sensing of the Earth, Oceans, Ice and Atmosphere, 20-21 April 2005, Ispra, Italy*.
- Catani, F., Farina, P., Moretti, S., Giovanni, N. & Strozzi, T. 2005a. On the application of SAR interferometry to geomorphological studies: estimation of landform attributes and mass movements. *Geomorphology* 66: 119-131.
- Catani, F., Casagli, N., Ermini, L., Righini, G. & Menducci, G. 2005b. Landslide hazard and risk mapping at catchment scale in the Arno River basin. *Landslides* 2: 329-342.
- Colesanti, C., Ferretti, A., Prati, C. & Rocca, F. 2003. Monitoring landslides and tectonic motions with the Persistent Scatterers Technique. *Engineering Geology* 68: 3-14.
- Corsini, A., Farina, P., Antonello, G., Barbieri, M., Casagli, N., Coren, F., Guerri, L., Ronchetti, F., Sterzai, P. & Tarchi, D. 2006. Space-borne and ground-based SAR interferometry as tools for landslide hazard management in civil protection. *International Journal of Remote-sensing* 27: 2351-2369.
- Farina, P., Colombo, D., Fumagalli, A., Marks, F. & Moretti, S. 2006. Persistent Scatterers for landslide investigations: outcomes from the ESA-SLAM project. *Engineering Geology* 88: 200-217.
- Ferretti, A., Prati, C. & Rocca, F. 2000. Non-linear subsidence rate estimation using Persistent Scatterers in Differential SAR interferometry. *IEEE Transactions on Geoscience and Remote-sensing* 38: 2202-2212.

- Ferretti, A., Prati, C. & Rocca, F. 2001. Persistent Scatterers in SAR interferometry. *IEEE Transactions on Geoscience and Remote-sensing* 39: 8-20.
- Fruneau, B., Achache, J. & Delacourt, C. 1996. Observation and modeling of the Saint-Etienne-de-Tinee landslide using SAR interferometry. *Tectonophysics* 265(3): 181-190.
- Getis, A. & Ord J.K. 1996. Local spatial statistics: an overview. In John Wiley and Sons (eds), *Spatial Analysis: Modeling in a GIS Environment* : 261.
- Kimura, H. & Yamaguchi, Y. 2000. Detection of landslide areas using satellite radar interferometry: *Photogrammetric Engineering and Remote-sensing* 66(3): 337-344.
- Massonnet, D. & Feigl, K. L. 1998. Radar interferometry and its application to changes in the earth's surface. *Reviews of Geophysics* 36(4): 441-500.
- Silverman, B.W. 1986. In CRC Press (eds), *Density Estimation for Statistics and Data Analysis*. ISBN 0412246201, 9780412246203

Updating landslide inventory maps in mountain areas by means of Persistent Scatterer Interferometry

Application: Landslide hotspot mapping

Technique: Satellite radar sensors

Main references: Cigna, F., S. Bianchini, G. Righini, C. Proietti, and N. Casagli (2010): Updating landslide inventory maps in mountain areas by means of Persistent Scatterer Interferometry (PSI) and photo-interpretation: Central Calabria (Italy) case study

Contributors: UNIFI (F. Cigna, S. Bianchini, G. Righini, C. Proietti, N. Casagli)

Abstract

Conventional methods used to detect slope instability and map geomorphologic processes, especially in mountain areas, can benefit from remote-sensing analyses, optical and radar satellite data. We illustrate the contribution of Persistent Scatterer Interferometry (PSI) and photo-interpretation for the updating of pre-existing landslide inventory maps in mountain areas, through the case study of Central Calabria, located in southern Italy with an extension of 4,470 km². We used 108 ENVISAT ascending images (20 m ground resolution) acquired in 2003-2009 and processed with the PSP (Persistent Scatterer Pairs) technique, 1 optical image acquired by SPOT satellite (2.5 m resolution), and digital orthophotos with 1 m resolution covering the whole investigated area. All these data were integrated and combined with additional ancillary information (topographic, geological and land use maps). 980 landslides (23.9% of pre-existing inventory) were updated by means of PSI information and 64 new landslides were also detected. The state of activity and the intensity of these landslides were also updated and/or evaluated, showing that 22% and 2% of the updated inventory include active (919 landslides) and reactivated (93 landslides) phenomena respectively. The outcomes of the integrated radar-interpretation and photo-interpretation methodology for Central Calabria and its operative usefulness for civil protection authorities represented a valuable proof of the reliability of this approach for updating landslide inventory maps in mountain areas at regional scale.

Keywords: landslide; Persistent Scatterers; state of activity; landslide inventory

1. Introduction

Many urban settlements in mountain regions are developed without taking into account landslide hazards and their potential consequences on local population [*Schuster and Fleming, 1986*]. Proper identification and mapping of such phenomena, together with a good urban planning, facilitate the mitigation of geological risks and the reduction of damages and economic impacts.

In mountain regions, the use of ground-based instrumentation is not always economically and practically suitable to perform a systematic control of natural phenomena, because of both huge extension and inaccessibility of the investigated areas. Radar and optical remote-sensing techniques represent therefore a valuable tool for landslide identification and mapping, which are fundamental activities for landslide hazard and risk assessment.

In the last years, many different InSAR (Synthetic Aperture Radar Interferometry) techniques for measuring ground deformations have been developed and experimented to analyze different geological processes and dynamics, such as land subsidence, slow moving

landslides, tectonic motions, and volcanic activity [Massonnet and Feigl, 1998; Singhroy et al., 1998; Ferretti et al., 2001; Hilley et al., 2004; Salvi et al., 2004; Bürgmann et al., 2006]. Multi-temporal InSAR analyses (Persistent Scatterer Interferometry, PSI), integrated and coupled with *in situ* investigations and surveys together with photo-interpretation, can successfully support conventional landslide studies at local and regional scale, thanks to the measurement and monitoring of ground deformations with millimetre accuracy and also the reconstruction of the history of deformations of the investigated areas [Farina et al., 2008; Casagli et al., 2009; Cigna et al., 2010a, 2010b].

We present an integrated methodology for the updating of pre-existing landslide inventory maps in mountain areas, based on the combination of thematic maps (topographic, geological, land use maps) and optical (orthophotos and optical satellite images) data with multi-temporal ground deformation measures extracted by means of multi-pass InSAR. We discuss potentials and limitations of this approach through an application to the test site of Central Calabria, located in southern Italy. This region is extensively affected by slow landslides threatening urban settlements and consequently fits very well the potentials of radar analyses.

2. Central Calabria (Italy)

2.1 Geological and geomorphologic background

The investigated area is the central part of the Calabria peninsula in Italy and includes part of the provinces of Cosenza, Catanzaro, Crotona and Vibo Valentia, with a total area of 4,470 km². Most of the outcropping basement is composed of Hercynian and Alpine crystalline and metamorphic allochthonous complexes, with associated Eocene and Lower Neogene sedimentary sequences [Van Dijk et al., 2000]. Along the internal side of the Calabrian Arc, Mesozoic carbonate rocks similar to the Apennine allochthonous units crop out in windows below this basement. The contact between the basement units is overlapped at a low angle, obliterated by successive high-angle faults. Terrigenous Tertiary sequences are present as remains along the over-thrust contacts between these basement units and also as tectonic wedges along the fault zones at a higher angle. All these rocks are crossed by a complex group of high-angle faults, which can be organized in major systems and patterns, partly correlated to transcurrent faulting [Van Dijk et al., 2000]. The geological structure is characterized by low-angle thrusts, dissected by high-angle faults with oblique movement components [Guerricchio, 2004]. The geomorphologic setting is characterized by widespread slope movements. In particular, several slow moving slides and complex slide-flows can be recognized and, secondarily, severe erosion and superficial rapid slope movements. Earth slides involve metamorphic rocks and earth flows affect Pliocene deposits. Moreover, landslides generally show recent morphologies, indicative of new activations. Along the eastern border of the Coastal Chain, large-scale and deep-seated gravitational landslides can also be recognized [Iovine et al., 2006].

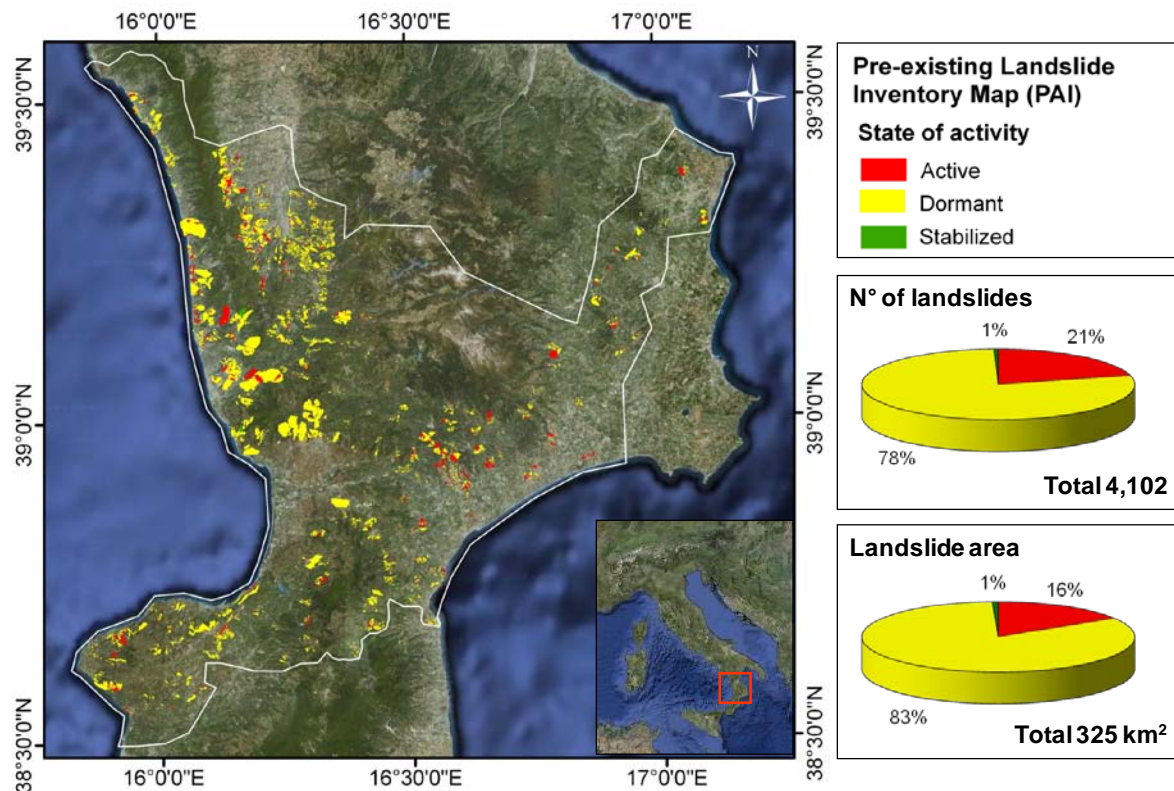


Figure 1: Pre-existing landslide inventory for the area of Central Calabria (Italy) displayed on a Google Earth map (left). Main statistics for the pre-existing inventory are summarized inside the pie charts (right).

2.2 Pre-existing landslide inventory map

The official landslide inventory map available for Central Calabria is part of the Hydrogeological Setting Plan (PAI, *Piano di Assetto Idrogeologico*) of Calabria Region, published in 2006 and distributed by the Regional River Basin Authority. Inside the investigated area, a total of 4,102 landslides are mapped, 861 (21%) of which are classified as active, 3,220 (78%) as dormant and 21 (1%) as stabilized (the reference year is 2006). Landslides cover an area of 325 km², corresponding to 7.3% of the whole territory (Figure), and the main landslide typologies are represented by rotational slides and flows [Cigna *et al.*, 2010a]. The inventory of the PAI can be integrated also with the information from the IFFI (*Inventario dei Fenomeni Franosi in Italia*, Landslide Inventory in Italy) inventory, a national landslide database published in 2007. Both these sources of information (PAI and IFFI) are based on aerial photo-interpretation, field surveys and collection of local databases mapped on a reference scale of 1:10,000.

3. Landslide inventory map updating

3.1 Methods

The methodology relies on the updating of a pre-existing landslide inventory database by means of the integration of very high resolution optical images (orthophotos and IKONOS, SPOT, QuickBird satellite images) with other thematic data (topographic, geological, land use maps), combined with ground displacement measurements provided by a Persistent Scatterer Interferometry (PSI) analysis. In particular, the methodological approach uses the ‘radar-interpretation’ [Farina *et al.*, 2008] and photo-interpretation methods and it is based on the possibility of extending and assigning a spatial meaning to the point-wise ground displacement measurements provided by the PSI technique, through the interpretation of aerial and satellite optical imagery and other ancillary data.

The contributions of this integrated analysis to the updating of pre-existing inventories consist in the following facets [Cigna *et al.*, 2010a]: i) detection of geomorphologic phenomena not emerged from conventional field analyses or bibliographic studies; ii) verification or modification of landslide boundaries; iii) assessment of representative ground deformation rate for each phenomenon; iv) definition of state of activity; v) assessment of main direction of displacements (reconstruction of vertical and horizontal EW deformation components, combining ascending and descending data – if available).

3.2 Input data

The different types of input data that are necessary to perform the updating of a pre-existing landslide inventory map through this integrated analysis, can be grouped in two categories: ancillary and PSI data.

3.2.1 Ancillary data

Ancillary data generally include thematic maps (topographic, geomorphologic, geological and land use maps) and optical images (both aerial and satellite data).

In particular, for the Central Calabria test site we collected the following ancillary data:

- 1:25,000 topographic map distributed by IGM (Military Geographic Institute) and 1:10,000 map from the Regional Cartographic Center (RCC);
- Digital Terrain Model (DTM) with 20 m spatial resolution;
- Regional geological map at 1:25,000 scale, distributed by RCC;
- Digital colour orthophotos from Volo Italia 2000 (not stereo), with 1 m resolution;
- SPOT multispectral image acquired in 2005 with 2.5 m resolution;
- CORINE Land Cover map [Perdigao and Annoni, 1997] at 1:50,000 scale (the 3rd classification level was used), published in 2000 and distributed by ISPRA (*Istituto Superiore PRotezione Ambiente*).

3.2.2 PSI data

Today many archives of SAR images are available, including both historical data acquired since the early '90s (ERS1/2 images) and images from currently operating SAR satellites (ENVISAT, RADARSAT1/2), spanning a time interval of more than 17 years. However, the choice of the best radar data stacks for a given test site is mainly driven by the spatial and temporal coverage of these data in the investigated area. As well as for SAR data, many different PSI techniques are available today to process multi-temporal SAR data stacks; among which, the Permanent Scatterers (PSInSAR; *Ferretti et al.*, [2001]), the PSP (Persistent Scatterer Pairs; *Costantini et al.*, [2000]) and the SBAS (Small BAseline Subset; *Berardino et al.*, [2002]) approach.

For the Central Calabria test site we used 108 ENVISAT ASAR (Advanced SAR) images acquired along ascending orbits in 2003-2009 and distributed in 3 different frames. SAR data were processed by e-GEOS (an ASI/Telespazio Company) by means of the PSP technique, providing 348,874 Persistent Scatterers (PS) in the whole area, with a mean target distribution of 78 PS/km² [*Cigna et al.*, 2010a]. For each PS, the following measures were extracted:

- geographic coordinates (latitude, longitude and elevation), with meter precision;
- average LOS (Line Of Sight) displacement rate in 2003-2009, with a precision of about 1 mm/yr (depending on the number of available images, the phase stability of each PS and its distance from the reference point);
- 2003-2009 displacement time series (i.e. LOS displacement at each acquisition), with millimetre (mm) precision.

3.3 Updating procedure

Following our methodology, the updating of the pre-existing landslide inventory database is obtained through the integration of traditional photo-interpretation with the radar-interpretation approach. This methodology has been recently developed and validated by the scientific community (PREVIEW and Terrafirma projects; [*Casagli et al.*, 2008, *Cigna et al.*, 2010a, *Pancioli et al.*, 2008, *Righini et al.*, 2008, *Herrera et al.*, 2009]). The entire process, including the analysis and interpretation of all the available data, is carried out in a Geographic Information System (GIS) environment.

In general, the updating of a pre-existing landslide inventory can lead to the identification of new landslides, the modification of boundaries of pre-mapped phenomena and the assessment (or updating) of their state of activity [*WP/WLI*, 1993] and landslide intensity [*Cruden and Varnes*, 1996], integrating qualitative (state of activity) and quantitative information (intensity; here defined in terms of movement velocity) of each phenomenon.

Monoscopic and stereoscopic photo-interpretation of aerial photos and satellite optical images are the conventional tools for the identification and mapping of ground instabilities, allowing the recognition of geomorphologic evidences and indicators of movement (anomalies in vegetation coverage) and the shape of unstable areas [*Soeters and van Westen*, 1996]. For the

Central Calabria, we interpreted one colour orthophoto (Volo Italia) and one satellite image (SPOT) using the monoscopic photo-interpretation approach and the multispectral analysis respectively [Cigna *et al.*, 2010a].

In order to evaluate the state of activity and intensity of the phenomena covered by the PSI data, we used an activity matrix and an intensity scale (Figure 2), defined in terms of PS average yearly velocity and based on the information coming from the pre-existing inventory map of the investigated area (i.e. PAI, 2006) and from ENVISAT ascending PSI data (2003-2009). Representative ground displacement values in 2003-2009 for each landslide are determined through the analysis of spatial distribution and frequency of PSI data inside its boundaries. These values are then compared to some deformation thresholds (2 and 10 mm/yr in the LOS direction, away or towards the satellite) and combined with the landslide information extracted from the pre-existing inventory to determine the state of activity (reactivated, active, dormant, stabilized) and intensity (negligible, extremely slow, very slow) of each phenomenon (Figure 2).

Activity Matrix

ENVISAT data (2003-2009)

		$V < 2 \text{ mm/yr}$	$V \geq 2 \text{ mm/yr}$
Pre-existing Landslide Inventory (PAI 2006)	Stabilized	Stabilized	Reactivated
	Dormant	Dormant	Reactivated
	Active	Active	Active
	New Landslide	Dormant	Active

Intensity Scale

ENVISAT data (2003-2009)

$V < 2 \text{ mm/yr}$	$V = 2-10 \text{ mm/yr}$	$V > 10 \text{ mm/yr}$
Negligible	Extremely slow	Very slow

Figure 2: Activity matrix and intensity scale based on ENVISAT PSI measures and the information from the pre-existing landslide inventory of Central Calabria (Italy).

The deformation thresholds used inside the activity matrix and intensity scale are site-specific values and they are empirically determined taking into account the characteristics of each application, typology of landslides affecting the investigated area, PSI data, LOS direction, measurement accuracy, distance from the reference point. Generally, the use of the activity matrix is performed through a conservative approach; in other words, the previous state of activity of dormant or active landslides is not lowered (to stabilized or dormant, respectively) even if PSI data register slow movement rates (lower than 2 mm/yr, away or towards the

satellite), unless field evidences and in situ monitoring data confirm an actual lowering of activity (Figure 2).

The interpretation of PSI information, supported by the analysis of the geomorphologic evidences through photo-interpretation, can lead to two main conditions (Figure 2):

- Presence of PS data outside the previous mapped areas, resulting in:
 - new landslide detection, when significant PS velocities, and also geological and geomorphologic evidences suggest the presence of a landslide;
 - no additional landslide detection, when geomorphologic and geological setting and/or the PS velocity distribution do not confirm the presence of a landslide (other geological processes such subsidence or erosion, may also induce significant deformations).
- Presence of PS data within the already mapped landslides, resulting in:
 - confirmation of the state of activity when the inventory information is in agreement with PS data;
 - change of the state of activity when the inventory information is not in agreement with PS data;
 - Change of landslide boundaries, when PS data suggests the enlargement (or reduction) of the already mapped area.

3.4 Results

An overview of the updated landslide inventory map for the Central Calabria test site is shown in Figure 4. The updated landslide inventory provides not only the spatial distribution of slow moving landslides – represented as polygons – but also their temporal characteristics (i.e. state of activity and intensity) [Cigna *et al.*, 2010a].

The radar-interpretation of ENVISAT PSI data gave spatial and temporal information for 980 landslides (23.9%) of the pre-existing inventory (PAI), updating the boundaries and/or state of activity of 144 phenomena and confirming the spatial and temporal characteristics of 836 phenomena (Table 4). The analysis also allowed us to map 64 new landslides, corresponding to 1.5% of the updated inventory (Table 5). The updated map totally includes 4,166 phenomena, corresponding to an area of 334 km² (Figure 4). The distribution of the state of activity and intensity in the updated inventory (Figure 3) highlights that 229 and 93 of the updated phenomena were active or reactivated in 2009 respectively, for a total of 919 active (continuous) landslides in the whole updated inventory (corresponding to 60.3 km²; 18%) and a total of 93 reactivated phenomena (i.e. 22.6 km²; 7%). Dormant and stabilized landslides are 3,136 (i.e. 248.7 km²; 74%) and 18 (i.e. 2.2 km²; 1%) respectively (Figure 4).

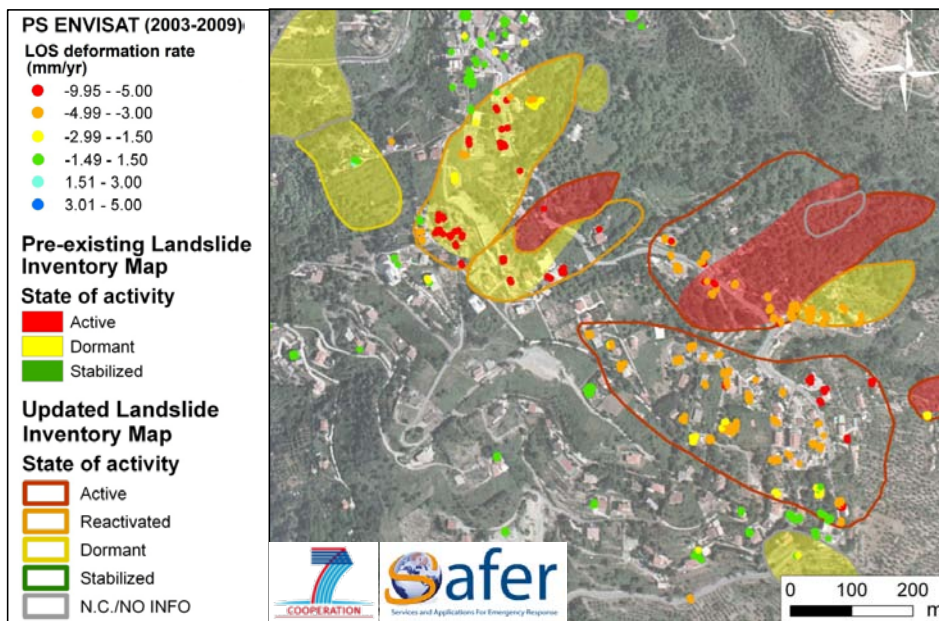


Figure 3: Updating of the pre-existing landslide inventory map for the Central Calabria (Italy): example for the area of Catanzaro. PSI data (2003-2009), pre-existing (2006) and updated (2009) inventories are displayed on the 2000 orthophoto. N.C. and NO INFO designate, respectively, landslides with insufficient number or complete absence of PS within the already mapped area.

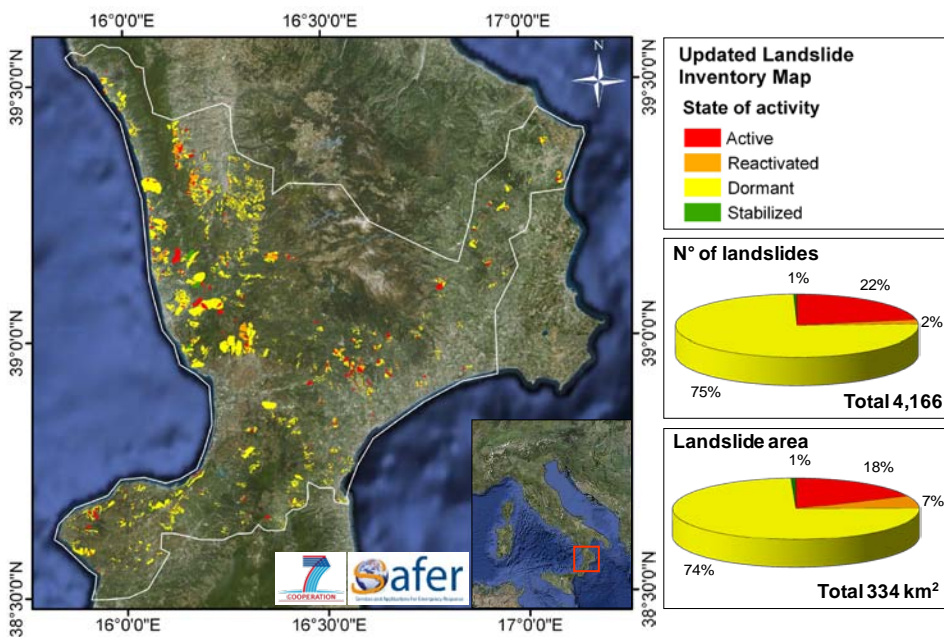


Figure 4: Updated landslide inventory map for the area of Central Calabria (Italy) overlapped on a Google Earth map (left). Main statistics for the updated inventory are summarized inside the pie charts (right).

Table 4: Landslide distribution for the pre-existing inventory map (2006).

Landslides	N°	Pre-existing Inventory
		%
Updated	980	23.9
N.C.*	321	7.8
NO INFO**	2,801	68.3
Total	4,102	100

* Not sufficient number of PS

** Absence of PS within already mapped landslide

Table 5: Landslide distribution for the updated inventory map (2009).

Landslides	N°	Updated Inventory
		%
Updated	980	23.5
New	64	1.5
N.C. + NO INFO*	3,122	74.9
Total	4,166	100

* Not sufficient number of PS and/or absence of PS within the already mapped landslides

4. Discussion

In the application for Central Calabria, the use of photo-interpretation turned out to be a useful contribution for landslide mapping in particular in hilly and mountainous environments, where a low density of radar targets was identified. On the other hand, radar-interpretation contribution was more suitable for most of the landslides involving urban areas and the road network, for which the reliability of PSI was higher but photo-interpretation was strongly limited by the dense urban fabric [Cigna *et al.*, 2010a].

The presence of highly vegetated areas frequently led to a lack of PSI measures (due to the absence of good radar reflectors). Thus, PSI data did not give any additional information on 321 landslides (7.8% of the PAI) due to an insufficient number of PS (N.C.), and on 2,801 landslides (68.3% of the PAI) due to the complete absence of PS within the already mapped landslides (NO INFO; (Table 4 and Table 5). In these cases, we did not change the spatial and temporal information of the original inventory.

By using ENVISAT PSI data, or other data with similar acquisition frequency (i.e. 1 image per month), the applicability of this integrated approach for the investigation of landslide processes is limited to extremely slow ($v < 16$ mm/yr) and very slow phenomena (16 mm/yr $< v < 1.6$ m/yr), as defined by Cruden & Varnes in 1996. However, the availability of new SAR missions with higher temporal frequency, such as TerraSAR-X and COSMO-SkyMed (i.e. 3-4 acquisitions per month), allows today the opening of new perspectives and scenarios also for the analysis of faster phenomena.

5. Conclusions

The outcomes of this study for the test site of Central Calabria provided valuable results, demonstrating the suitability of this integrated method for the updating of landslide inventory maps using radar remotely sensed data for detection and mapping of slow moving landslides. Its operative usefulness for civil protection authorities represents a valuable proof of the

reliability of this approach for application in mountain areas and at regional or local scale. However, vegetated areas often prevent reflective targets to be identified as PS; moreover, fast moving phenomena usually decrease or even compromise also the functioning of PSI analyses.

The analysis for Central Calabria opens new perspectives for the future exportability of this methodology in different and various geomorphologic environments (tropical, high mountains etc.), as an effective tool to improve risk management activities and focus planning resources according to distribution and intensity of landslide hazard.

References

- Berardino, P., Fornaro, G., Lanari, R. & Sansosti, E. 2002. A new algorithm for surface deformation monitoring based on Small Baseline Differential SAR Interferograms. *IEEE Trans. Geosci. Remote Sens.* 40(11): 2375-2383.
- Bürgmann, R., Hilley, G., Ferretti, A. & Novali, F. 2006. Resolving vertical tectonics in the San Francisco Bay Area from Permanent Scatterer InSAR and GPS Analysis. *Geology* 34: 221-224.
- Casagli, N., Cigna, F., Del Conte, S. & Liguori, V. 2009. Nuove tecnologie radar per il monitoraggio delle deformazioni superficiali del terreno: casi di studio in Sicilia. *Geologi di Sicilia*, XVII, 3: 17-27.
- Casagli, N., Colombo, D., Ferretti, A., Guerri, L. & Righini, G. 2008. Case Study on Local Landslide Risk Management During Crisis by Means of Remote-sensing Data. *Proc. First World Landslide Forum, Tokyo, Japan*, 125-128.
- Cigna F, Bianchini S, Righini G, Proietti C, Casagli N (2010) Updating landslide inventory maps in mountain areas by means of Persistent Scatterer Interferometry (PSI) and photo-interpretation: Central Calabria (Italy) case study. In: Malet JP, Glade T, Casagli N (eds) *Mountain Risks: Bringing Science to Society*, Proc. International Conference, CERIG Editions, Florence, Italy, November 24-26, 2010, pp 3-9
- Cigna, F., Del Ventisette, C., Liguori, V. & Casagli, N. 2010. InSAR time-series analysis for management and mitigation of geological risk in urban area. *Proc. IGARSS 2010*, Honolulu, Hawaii, USA.
- Costantini, M., Iodice, A., Magnapane, L. & Pietranera, L. 2000. Monitoring terrain movements by means of sparse SAR differential interferometric measurements. *Proc. IGARSS 2000*, Honolulu, Hawaii, USA. 3225-3227.

A-DInSAR data analysis towards slow-moving landslide characterization

Application: landslide mapping and characterization

Technique: A-DInSAR

Main references: Cascini et al., 2008, 2009, 2010, 2011.

Contributors: UNISA (L.Cascini, D. Peduto)

Abstract

Uncertainties related to the characterization and mapping of slow-moving landslides can be partly overcome by integrating conventional techniques with remote-sensing data, such as Advanced Differential SAR Interferometry (A-DInSAR). However, standardized procedures for the interpretation and the confident use of A-DInSAR data, according to landslide zoning developments, have not been fully investigated and validated, although algorithms for image processing have become more and more sophisticated. This research addresses a new methodology for the use of A-DInSAR data in landslide analyses at different scales via the integration of remote-sensing data with simple geomorphological models and geometric considerations. The methodology is tested inside a well documented area in Central-Southern Italy where an advanced dataset consisting of base and thematic maps is available.

Keywords: landslide characterization, A-DInSAR.

1. Introduction

Displacement data can be profitably used to characterize both the boundaries and the state of activity of slow-moving landslide phenomena. To this aim, the measurements need to be efficient in terms of time and budget especially when dealing with analyses over large areas. In this regard, the use of advanced satellite techniques, which involve data achieved by Synthetic Aperture Radar (SAR) [Gabriel et al. 1989], can turn out to be extremely useful. In particular, the differential Advanced SAR interferometry (A-DInSAR) can complement with traditional topographic techniques to obtain a comparable accuracy of ground surface displacements while being less expensive and time consuming. However, the application of A-DInSAR techniques to the analysis and mapping of landslide phenomena is a relatively new and still challenging topic and only few successful case studies are discussed in the scientific literature [Berardino et al., 2003; Colesanti and Wasowski, 2006; Hilley et al., 2004; Cotecchia, 2006; Farina et al., 2006, Wasowski et al., 2008; Cascini et al., 2010].

The present research is aimed to overcome some of the current difficulties by introducing a new methodology for multipass A-DInSAR data interpretation in areas for which a proper geomorphological and topographic knowledge is available.

The methodology [Cascini et al., 2010, 2011] is essentially based on the integration of information concerning landslide features and related ground displacements and is tested at both medium (i.e. 1:25,000 scale according to Fell et al., 2008) and large scales (i.e. 1:5,000

scale, *Fell et al.*, 2008) within a sample area in the territory of National Basin Authority of Liri-Garigliano and Volturno (NBA-LGV) rivers (Central-Southern Italy).

2. Data and Methods

In the present test case thirty-three images (track 308 - frame 2765), acquired over descending orbits of the European Remote-sensing (ERS-1, ERS2) satellite systems, spanning the time interval from March 1995 until February 2000, have been processed at both low-(pixel spacing of 40x40 m) and full-resolution (pixel spacing of 10x10m) [*Fornaro et al.*, 2009a] e b).

Main goals of the analysis are : a) tackling the limit related to the one dimensional projection in the Line Of Sight (1D LOS projection) of a deformation that can actually occur in all three dimensions [*Rocca*, 2003; *Manzo et al.*, 2006]; b) correctly addressing the ambiguity of phase measurements which implies that it is extremely difficult to detect LOS displacement rates exceeding 8 – 10 cm/yr, thus limiting the use of A-DInSAR data only to landslides ranging from extremely to very slow phenomena according to the velocity classification of *Cruden and Varnes* [1996].

The selected dataset covers an area belonging to the northern portion of NBA-LGV in Central-Southern Italy (Fig. 1) for which both base and thematic maps were available at 1:25,000 scale. These maps were produced in 2001 within the PSAI project (Piano Stralcio per l'Assetto Idrogeologico).

The test area has an extension of 489 km² and includes eleven municipalities, belonging to two Regions (Lazio and Abruzzo) (Fig. 1). The geological map highlights that the bedrock mainly consists of Upper Miocene arenaceous units mantled by Quaternary Age superficial deposits, characterized by talus and alluvial fans. Landslide phenomena are widespread all over the area (covering around 5% of the whole territory) as it can be noticed in the available landslide inventory map at 1:25,000 scale, derived from aerial photographs and surface surveys.

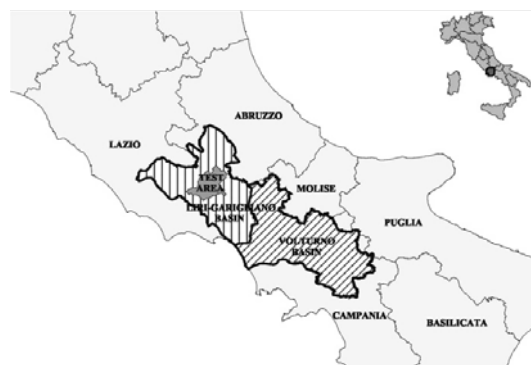


Figure 1: Location of the study area

In the study area a total number of 897 slow-moving landslides are mapped [*Peduto*, 2008; *Cascini et al.*, 2009]; according to *Varnes* [1978] they are classified as: 204 rotational slides, 238 earth flows, 78 rotational slides-earth flows, 336 creeps, 33 earth flows - creeps, 8 deep-seated gravitational movements. On the basis of geomorphological criteria, three different

states of activity are distinguished for these landslides, defined as follows: “active” (including active, reactivated and suspended), “dormant” and “inactive” (relict) phenomena [Cruden and Varnes, 1996]. The selected landslide typologies exhibit a significant predominance of dormant phenomena (428) on active ones (92).

The adopted methodology is described in the framework of Figure 2 [Cascini *et al.*, 2011]. In particular, the first step of the analysis consists of the generation of the a priori A-DInSAR landslide visibility map [Cascini *et al.*, 2009]. This can allow distinguishing in advance whether an area is expected to be visible from space-borne SAR sensors, thus driving data-users through the image dataset selection.

Once SAR images have been processed, a procedure for 1D-LOS A-DInSAR data projection can be implemented to generate the advanced A-DInSAR landslide velocity map (for a detailed description see [Cascini *et al.*, 2010] which results from the integration of information on the sensor acquisition geometry, the observed scene and the kinematics of the landslide phenomenon. According to the extension of the area to be investigated and the purposes of the analysis these maps can then be used in analyses either at medium (1:100,000 to 1:25,000) or large (1:25,000 to 1:5,000) scale.

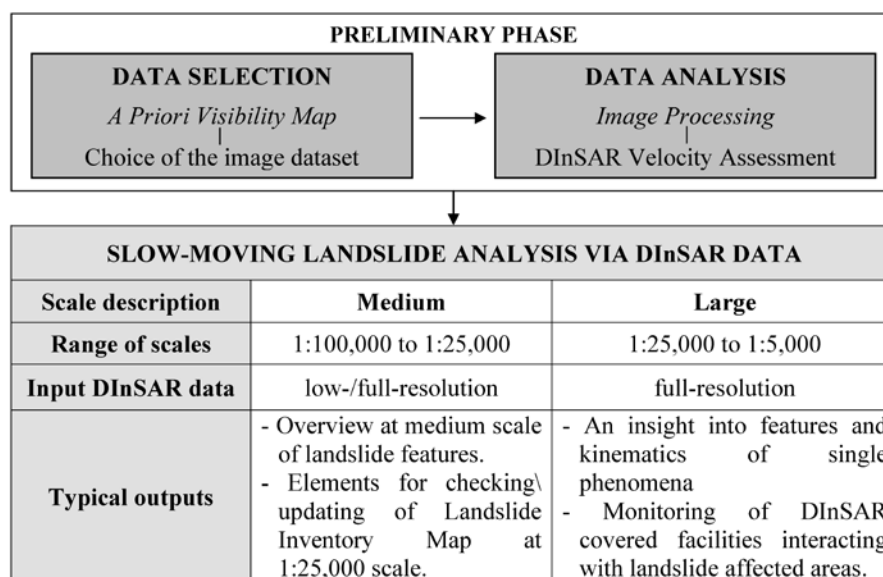


Figure 2: Framework for the use of A-DInSAR data in analyses of slow-moving landslide phenomena at different scales [after Cascini *et al.*, 2011].

Analyses at medium scale via low/full- resolution A-DInSAR data furnish an overview of landslide characterization (state of activity) together with elements for the checking\updating of Landslide Inventory Maps at 1:25,000 scale [Cascini *et al.*, 2009, 2010].

Conversely, analyses at large scale via full- resolution A-DInSAR data provide an insight into features and kinematics of single phenomena and help the analysis of the behaviour of A-DInSAR covered structures [for more details see Cascini *et al.*, 2010, 2011].

3. Results

The first step of the analysis concerned the generation of an advanced low-resolution A-DInSAR landslide velocity map at 1:25,000 scale in order to analyse rotational slides, earth flows and rotational slides-earth flows, whose total amount is 553; 185 (around 33%) of those resulted covered by A-DInSAR data.

The map was generated starting from low-resolution A-DInSAR velocity values, a DEM at 1:25,000 scale and introducing simplified geomorphological schemes [Cascini *et al.*, 2010], which take into account the landslide geometrical features suggested by Cruden and Varnes [1996].

According to these criteria the advanced low-resolution A-DInSAR landslide velocity map was generated for the whole study area highlighting that almost 84% of the A-DInSAR covered dormant landslides (144) exhibit evidence of no-movement. On the other hand, the percentage of active landslides (25) with moving coherent A-DInSAR pixels is about 24%, on the average [Cascini *et al.*, 2008]. An example is reported with reference to the municipalities of Frosinone and Torrice (Lazio Region) in Figure 3 where very few moving low-resolution A-DInSAR pixel are detected over an area of about 3 km x 6 km where dormant phenomena prevail.

Within this area, the directions of movement (see the four red arrows), derived by modeling the available 1D LOS A-DInSAR data, seem congruent with the assumption of the geomorphological schemes (downward along slope direction).

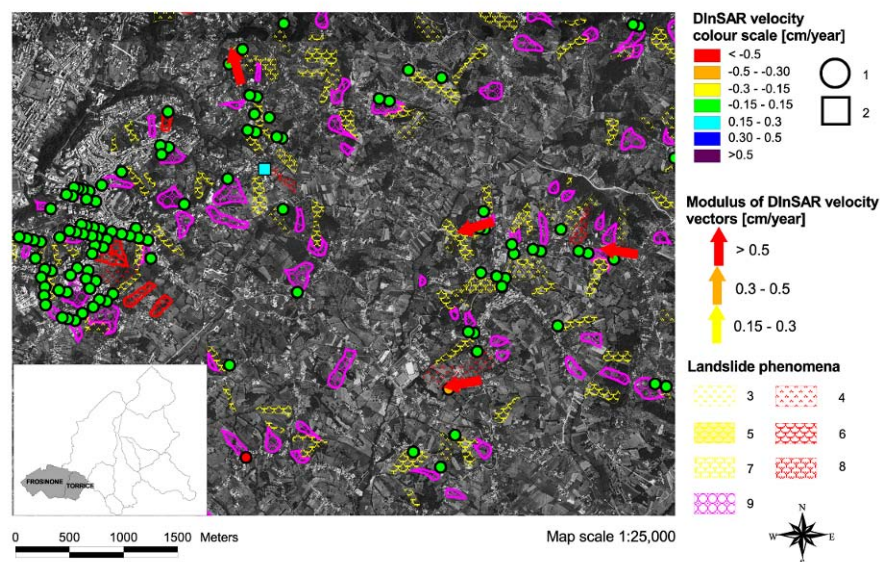


Figure 3: An example of advanced low-resolution A-DInSAR landslide velocity map for the municipality of Frosinone and Torrice (Lazio Region, Italy). 1) Not moving A-DInSAR coherent pixel or on flat areas; 2) A-DInSAR coherent pixel moving on vertical direction; 3) dormant rotational slide; 4) active rotational slide; 5) dormant earth flow; 6) active earth flow; 7) dormant rotational slide–earth flow; 8) active rotational slide–earth flow; 9) creep phenomenon [modified after Cascini *et al.* 2010].

The advanced low-resolution map can be also used for the detection of new landslide phenomena by extending the analysis of moving/not moving coherent pixels on those portions of the territory mapped as hollows in the geomorphological map at 1:25,000 scale [Cascini *et al.*, 2009]. These zones (1263 within the study area) are characterized by geomorphological settings quite similar to landslide-affected areas, also exhibiting the same landslide predisposing factors. The proposed procedure allowed the detection of 63 hollows where a clear evidence of movement was recorded; this can provide elements for a check/update of the landslide inventory map that represents the starting point for the landslide risk analysis as described in Fell *et al.* [2008].

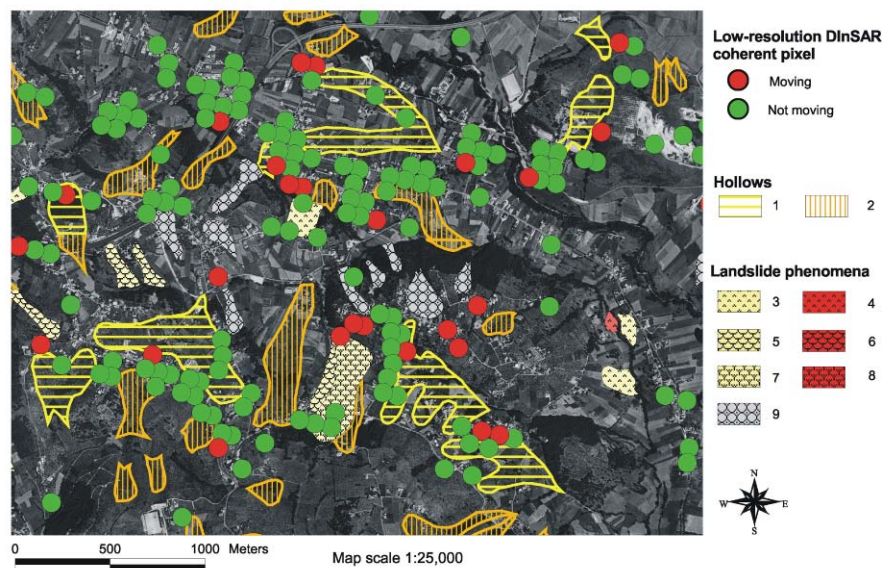


Figure 4: An example of low-resolution moving A-DInSAR coherent pixel detection within portions of the territory mapped as hollows. (1) Hollow with moving A-DInSAR coherent pixel; (2) hollow not covered or with not-moving A-DInSAR coherent pixel; (3) dormant rotational slide; (4) active rotational slide; (5) dormant earth flow; (6) active earth flow; (7) dormant rotational slide-earth flow; (8) active rotational slide-earth flow; (9) creep phenomenon [Cascini *et al.*, 2009].

Analyses of landslide phenomena at more detailed scale (i.e. 1:5,000) can exploit full-resolution A-DInSAR data. Accordingly, full-resolution A-DInSAR data were processed via tomographic analysis [Fornaro *et al.*, 2009b] with reference to an area of 64 km² corresponding to the municipalities of Frosinone and Torrice.

In this research work full-resolution A-DInSAR data pursued two main goals: the preliminary analysis of landslide features (i.e. check of mapped boundaries; detection of ground displacement out of mapped areas); an insight into different kinematic behaviour characterizing different portions of the same phenomenon. For sake of brevity, hereafter only the first issue is discussed with regard to an example in Torrice and Frosinone urban areas; the second issue, addressed via the case study of La Consolazione landslide, is described in details in Cascini *et al.* [2010].

Following the flowchart in Figure 2 the advanced full-resolution A-DInSAR landslide velocity map was generated at a scale of 1:5,000. In order to check possible changes in landslide boundaries, the entire full-resolution coherent pixel dataset was projected including pixels out of the mapped landslides and assuming translational movements along the steepest slope direction. Examples of the results obtained are shown in Figure 5 where evidences of movements both inside and outside the landslide boundaries can be noticed. Particularly, special attention is worth being paid to full-resolution A-DInSAR coherent pixels exhibiting mean velocity values exceeding 0.3 cm/year within two dormant earth flows (labelled with letters A and D) and creep zones (labelled with letters B and C) as well as the areas framed with the circle and the square, respectively.

With reference to the zone framed with the circle, a cross check via the geomorphological map shows that the buildings in the area were built on an hollow on which the A-DInSAR data show evidences of movement for the period 1995-2000.

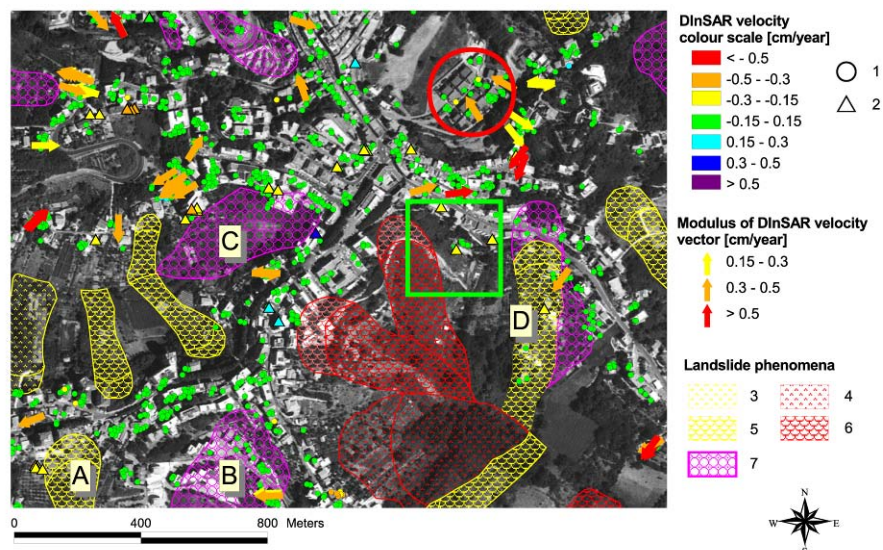


Figure5: Overview of advanced full-resolution A-DInSAR landslide velocity map for a portion of the municipality of Frosinone (Lazio Region, Italy). 1) Not moving A-DInSAR coherent pixel or on flat areas; 2) not projected translational displacement owing to high condition number; 3) dormant rotational slide; 4) active rotational slide; 5) dormant earth flow; 6) active earth flow; 7) creep phenomenon [Cascini *et al.*, 2010].

The area framed by a rectangle highlights the presence of moving full-resolution A-DInSAR coherent pixels in proximity of a landslide classified as active earth flow in the landslide inventory map at a scale of 1:25,000. In this case a more detailed analysis [see Cascini *et al.*, 2010] was possible thanks to the availability of a map of the phenomenon, drawn at 1:5,000 scale by the NBA-LGV technicians. The superimposition of full-resolution A-DInSAR data on this enhanced inventory map points out that the moving coherent pixel falls within the portion actually moving and suggests the retrograding movement towards the top of the hill. This last example clearly shows how full-resolution A-DInSAR data can be useful in addressing investigations on both the state of activity and the spatial evolution of landslide

phenomena. In addition, the full-resolution A-DInSAR data reliability must be necessarily checked via thematic and topographic maps at large scale (i.e.1:5,000), see *Cascini et al.*, [2010].

4. Discussion and Conclusion

In the last decade the use of remote-sensing data derived from A-DInSAR techniques has increasingly grown, even though some problems still arise in the analysis of slow-moving landslides. Starting from current limits of A-DInSAR technique to landslide applications, the present research work introduces an innovative procedure that allows a significant improvement of the common 1D LOS velocity maps.

The first step of the procedure consists of the generation of the a priori A-DInSAR visibility map to forecast the visibility of slopes on the basis of their aspect and inclination, vegetation cover and the presence of buildings/infrastructures. The second step allows the development of advanced A-DInSAR landslide velocity maps via the joint use of a DEM and simplified geomorphological schemes at both 1:25,000 and 1:5,000 scales.

The methodology is applied in an area, of around 500 km², which is hilly, vegetated and scarcely urbanised. Although the covered phenomena are around 34% of the total, using a descending dataset only, the proposed procedure for low/full-resolution A-DInSAR data highlights perspectives of application to check/update landslide inventory maps at different scale over areas of unprecedented extension.

In conclusion the results obtained seem particularly appealing also considering that ultimate sensors (TerraSAR-X, COSMO/SKYMED, Sentinel, etc) will provide enhanced monitoring capability due to a significant increase in the spatial resolution, three times higher data acquisition frequency and an increase in the sensitivity to temporal decorrelation via the reduction of the wavelength.

References

- Berardino, P., Costantini, G., Franceschetti, G., Iodice, L., Pietranera, L., Rizzo, V. (2003). Use of differential SAR interferometry in monitoring and modelling large slope instability at Matera (Basilicata, Italy). *Engineering Geology*, 68 (1–2), 31–51.
- Cascini L., Fornaro G., Peduto D. (2010). Advanced low- and full-resolution A-DInSAR map generation for slow-moving landslide analysis at different scales. *Engineering Geology*, 112 (1-4), 29-42, doi:10.1016/j.enggeo.2010.01.003.
- Cascini L., Fornaro G., Peduto D. (2009). Analysis at medium scale of low-resolution A-DInSAR data in slow-moving landslide-affected areas. *ISPRS Journal of Photogrammetry and Remote-sensing*, 64(6), 598-611. doi:10.1016/j.isprsjprs.2009.05.003
- Cascini L., Ferlisi S., Fornaro G., Peduto D. (2011). The use of A-DInSAR techniques to analyse ground deformations and related effects to buildings in urban areas. Submitted to IS-SEOUL 2011, 5th International Symposium on deformation characteristics of geomaterials, Seoul, South Korea, 31 August - 3 September 2011.
- Cascini L., Ferlisi S., Peduto D., Pisciotta G., Di Nocera S., Fornaro G. (2008). Multitemporal A-DInSAR data

- and damages to facilities as indicators for the activity of slow-moving landslides. In: *Landslides and Engineered Slopes. From the Past to the Future*. Chen Z., Zhang J., Li Z., Wu F., Ho K. (eds.). Proceeding of the 10th International Symposium on Landslides and Engineered Slopes, 30 June-4 July 2008, Xi'an (China), Taylor and Francis Group, London. Vol. II, pp. 1103-1109. ISBN 978-0-415-41196-7.
- Colesanti, C., Wasowski, J. (2006). Investigating landslides with space-borne Synthetic Aperture Radar (SAR) interferometry. *Engineering Geology*, 88, 173–199.
- Cotecchia, V. (2006). The Second Hans Cloos Lecture. Experience Drawn from the Great Ancona Landslide of 1982. *Bulletin of Engineering Geology and the Environment*, vol. 65. Springer-Verlag, pp. 1–41.
- Cruden, D.M., Varnes, D.J. (1996). Landslide Types and Processes. In: Turner, A.K., Schuster, R.L. (Eds.), *Landslides, Investigation and Mitigation*, Transportation Research Board Special Report 247, Washington D.C, pp. 36–75.
- Farina, P., Colombo, D., Fumagalli, A., Marks, F., Moretti, S. (2006). Permanent Scatterers for landslide investigations: outcomes from the ESA-SLAM project. *Engineering Geology*, 88, 200–217.
- Fell, R., Corominas, J., Bonnard, C., Cascini, L., Leroy, E., Savage, W.Z. (2008). Guidelines for landslide susceptibility, hazard and risk zoning for land-use planning. *Engineering Geology*, 102 (3–4), 99–111.
- Fornaro, G., Pauciuolo, A., Serafino, F. (2009a). Deformation monitoring over large areas with multipass differential SAR interferometry: a new approach based on the use of spatial differences. *International Journal of Remote-sensing*, 30 (6), 1455–1478.
- Fornaro, G., Reale, D., Serafino, F. (2009b). Four-dimensional SAR imaging for height estimation and monitoring of single and double scatterers. *IEEE Transactions on Geoscience and Remote-sensing*, 47 (1), 224–237.
- Gabriel, K., Goldstein, R.M., Zebker, H.A. (1989). Mapping small elevation changes over large areas: differential interferometry. *Journal of Geophysical Research*, 94.
- Hilley, G.E., Burgelman, R., Ferretti, A., Novali, F., Rocca, F. (2004). Dynamics of slowmoving landslides from Permanent Scatterer Analysis. *Science*, 304, 1952–1955.
- Manzo, M., Ricciardi, G.P., Casu, F., Ventura, G., Zeni, G., Borgstrom, S., Berardino, P., Del Gaudio, C., Lanari, R. (2006). Surface deformation analysis in the Ischia Island (Italy) based on spaceborne radar interferometry. *Journal of Volcanology and Geothermal Research*, 151, 399–416.
- Peduto D. (2008). Analysis of ground deformations related to subsidence and landslide phenomena via A-DInSAR techniques. Ph.D. Thesis (In English). University of Salerno, Italy, May 2008.
- Rocca, F. (2003). 3D Motion recovery with multi-angle and/or left right Interferometry. Proc. 3rd International Workshop on ERS SAR Interferometry (FRINGE 2003), Frascati (Italy), 2–5 December 2003. ESA SP-550, available also online: http://earth.esa.int/fringe03/proceedings/posters/62_roca.pdf (accessed July 13, 2009).
- Varnes, D.J. (1978). Slope movements. Types and processes. In: Schuster, R.L., Krizek, R.J. (Eds.), *Landslides: Analysis and Control*. Special Report, vol. 176, pp. 11–35. National Academic of Sciences, Transportation Research Board, Washington.
- Wasowski, J., Casarano, D., Bovenga, F., Refice, A., Nutricato, R., Nitti, D.O. (2008). Landslide-prone Towns in Daunia (Italy): PS Interferometry-based Investigation. In: Chen, et al. (Ed.), *Landslides and Engineered Slopes*. Taylor & Francis Group, London. ISBN: 978-0-415-41196-7, pp. 513–518

Use of short baseline InSAR for regional and local rockslide mapping

Application: Rockslide inventory mapping

Technique: Active microwave sensor

Main references: Lauknes et al., 2010: Detailed rockslide mapping in northern Norway with small baseline and persistent scatterer interferometric SAR time series methods; Henderson et al., 2011: A structural, geomorphological and InSAR study of an active rock slope failure development

Contributor: NGU (J.F. Dehls)

Abstract

Differential synthetic aperture radar interferometry (InSAR) provides a method for efficiently mapping ground movements over tens of thousands of square kilometers. The European Space Agency's archive of satellite radar scenes, acquired since 1992, provides an invaluable resource when performing an initial assessment of a new study area. Experience in northern Norway has shown that there is a very good correlation between ground velocities mapped using InSAR and landslide activity mapped in the field. In this case study, we present the results of an analysis performed in Troms county, in northern Norway. Images from the ERS-1 and ERS-2 satellites were processed using the short baselines subset algorithm. Numerous rockslides were identified and subsequently examined in the field. The Gamanjinni rockslide is just one example of these. Structures mapped in the field agree remarkably well with variations in the surface velocity mapped using InSAR.

Keywords: rockslide mapping; interferometry, InSAR

1. Introduction

Like most remote-sensing techniques, differential synthetic aperture radar interferometry (InSAR) facilitates the mapping of large geographic areas within a relatively short time. In the case of InSAR, the result is a map of relative surface movements with respect to the position of the sensor. In this case study, we present the use of the European Space Agency's archive of radar images to identify rockslides in relatively remote areas of Norway (Figure 1).

Synthetic Aperture Radar (SAR) is a microwave imaging system. It uses microwaves, which can penetrate clouds. By comparing multiple SAR images, we are able to measure changes in travel time as a function of the satellite position and time of acquisition. This allows us to generate Digital Elevation Models (DEM). Changes not related to topography include those due to changes atmosphere and topography between acquisitions.

If the topography for an area is known, two images can be used to measure deformation ranging from centimetres to metres. Smaller deformations, however, are not easy to distinguish from atmospheric effects using just two images. If we use many images (15 or more), however, we can take advantage of the differences in spatial and temporal correlation to distinguish between deformation and atmospheric effects. We can do this if we assume that atmospheric effects have a high degree of spatial correlation but are almost random in time,

whereas the deformation we are looking for will have much higher temporal correlation [Ferretti *et al.*, 2001].

Over the last years, several algorithms have been developed to do this type of analysis. In this case example, we have used an improved version of the small baselines (SBAS) algorithm [Berardino *et al.*, 2002; Lauknes *et al.*, 2011].

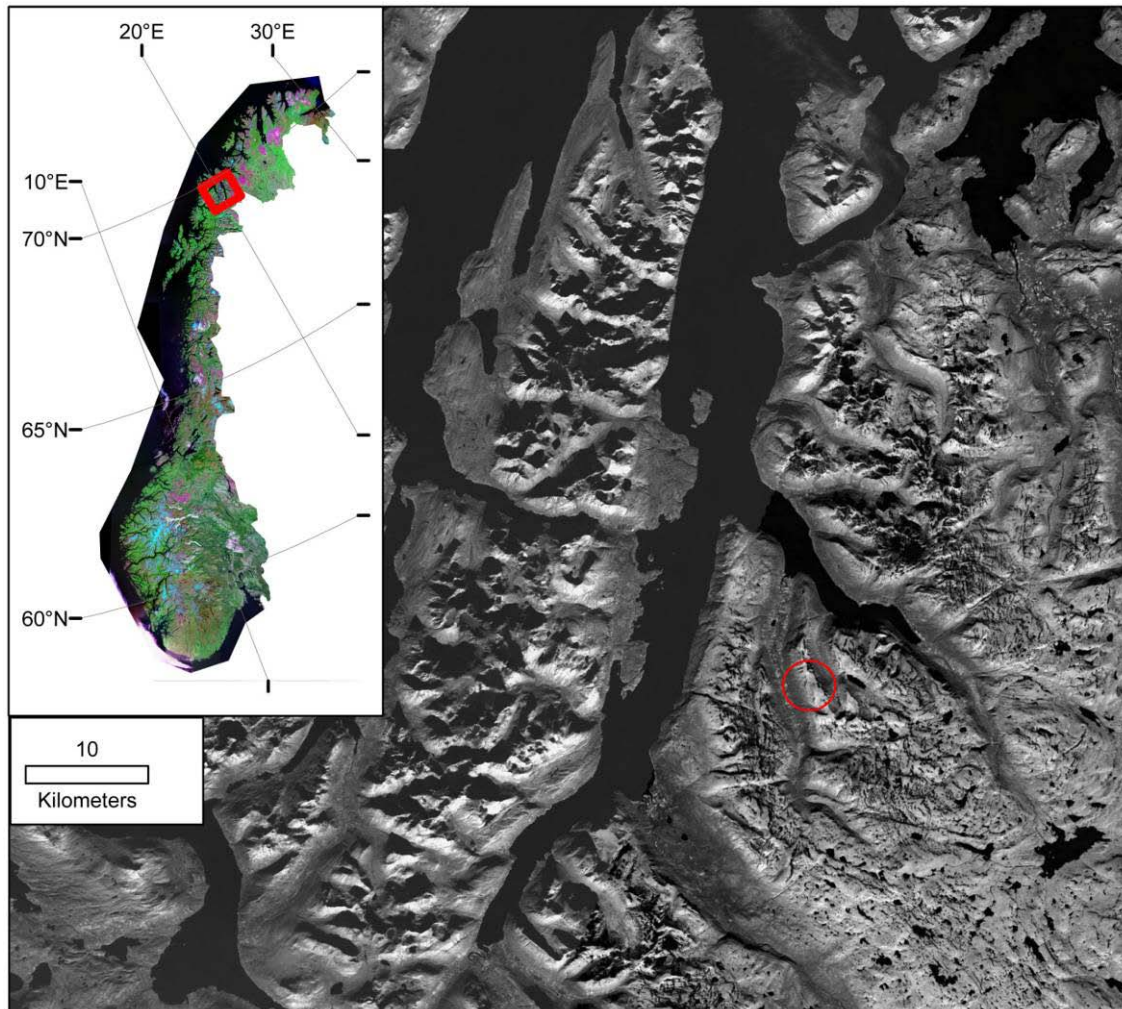


Figure 1: Location of the study area. The Lyngen peninsula is located in Troms county, in Northern Norway. This image shows the average intensity of the SAR images used for this study. The red circle shows the location of the Gamanjuni rockslide, discussed below.

2. Data and Methods

The data used were acquired by the ERS-1 and ERS-2 satellites between 1992 and 1999. All (19) snow-free scenes were used. These scenes were used to generate 60 interferograms with a maximum perpendicular baseline of 300 m and a maximum temporal separation of four years. The ERS satellites have an operating wavelength of 5.66 cm, and the radar looks to the right (west) with an angle of approximately 23.5° from the vertical. The radar is only sensitive to displacement changes with a component in the radar line-of-sight (LOS) direction.

From the 60 interferograms, a common set of pixels was chosen that were above a preset coherence threshold in a selected fraction of the interferograms (Figure 2.). Since interferometric phase measurements are observed modulo 2π , the interferograms must be spatially ‘unwrapped’ to determine absolute phase values. This was done using the SNAPHU program [Chen and Zebker, 2001]. After phase unwrapping, all pixels were referenced to a selected (assumed stable) reference pixel with high coherence. For each interferogram, an orbital phase ramp as well as phase delay due to tropospheric stratification was estimated and removed. DEM error, atmospheric phase screen and deformation were then estimated using the technique outlined in *Lauknes et al.*, [2011].

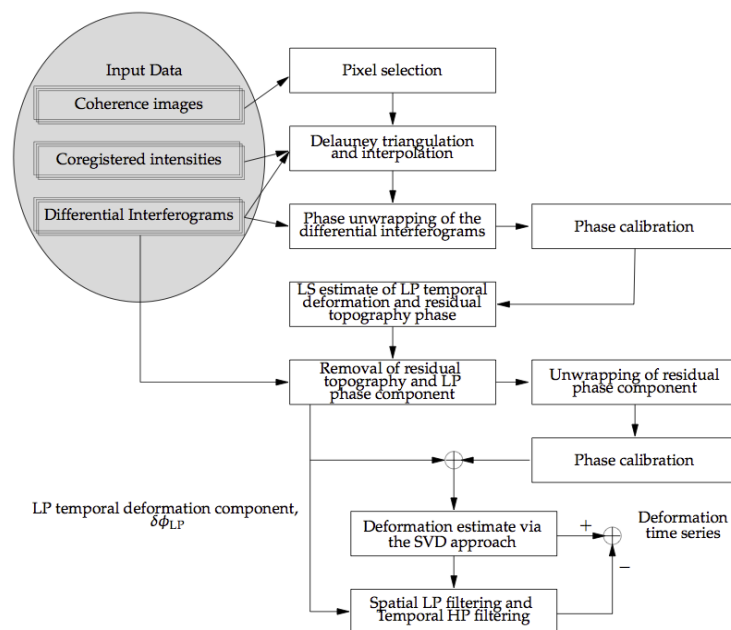


Figure 2: Outline of the processing steps used in the InSAR analysis. The input data consisted of 60 radar scenes from the ERS-1 and ERS-2 satellites. A detailed description of the method can be found in *Lauknes et al.*, 2011.

3. Results

3.1 Regional findings

Numerous unstable rock slopes were identified within the study area (Figure 3). Some of these were known previously, but many were only confirmed in the field after the InSAR analysis was completed. In all cases, there was a good degree of correlation between mapped structures in the field and surface velocities measured using the images. The tectonic significance of the regional uplift trend is discussed in *Osmundsen et al.*, [2009].

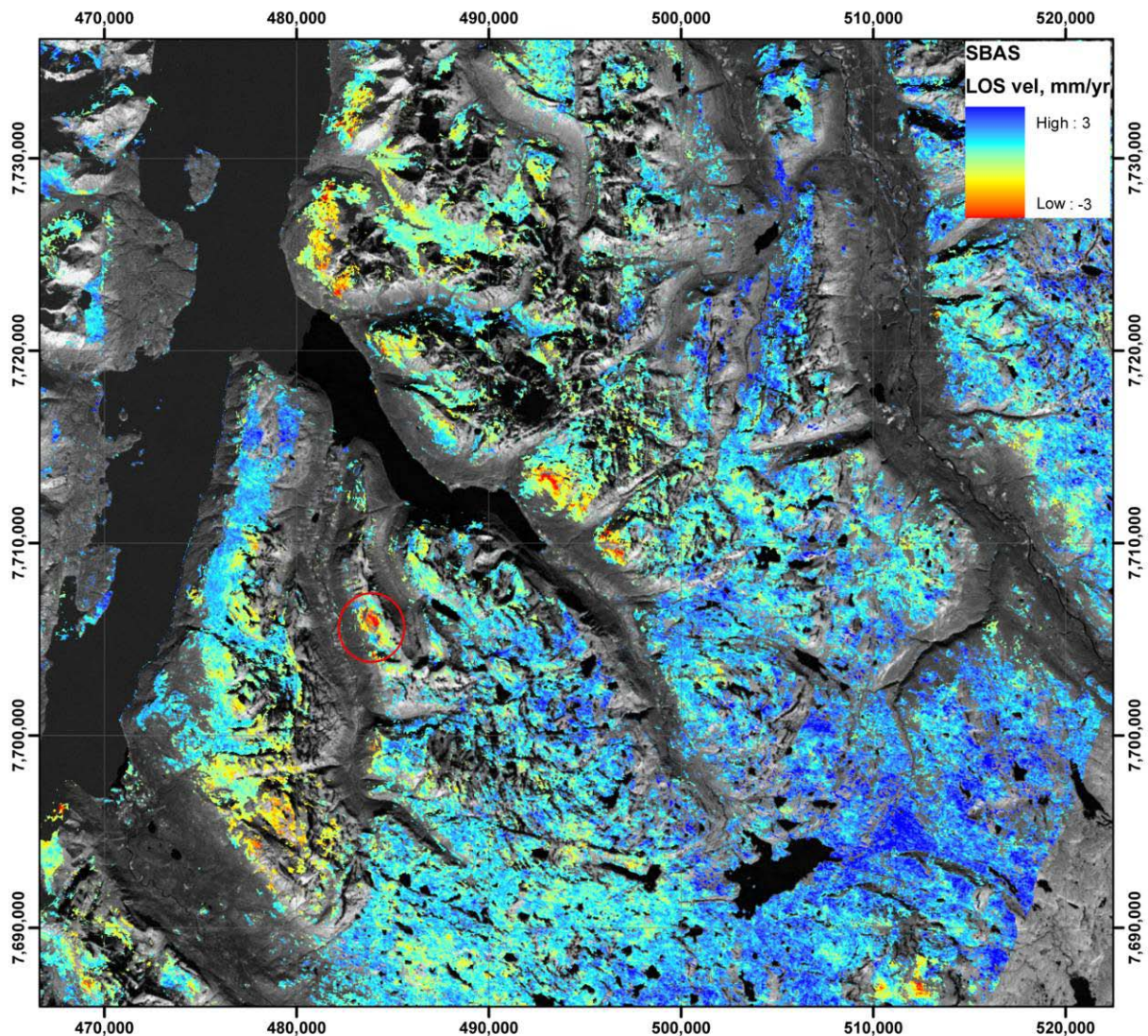


Figure 3: Average line-of-sight velocity between 1992 and 1999 determined using the SBAS method. Red areas represent areas which are moving away from the satellite. Since the line-of-sight is only 23° from vertical, these can be either slope-parallel movements, vertical movements or something in between. Gamanjinni rockslide is highlighted by the red circle.

3.2. Gamanjinni rockslide

One of the unstable rock slopes identified in the study is the Gamanjinni rockslide. The rockslide is situated on the eastern flank of the N-S valley of Manndalen. The Gamanjinni site lies almost directly on the crest of a regional anticline, with the back-wall on the immediate east-dipping limb of the anticline and the active block on the downslope, west-dipping limb. On top of the bedrock rests an up to one metre thick block field, with individual blocks varying in size from a few centimetres up to a few tens of centimetres.

There is a remarkable spatial coincidence of the structures observed independently from the aerial photo analysis and the detailed pattern of the InSAR data (Figure 4). The spatial extent of the InSAR movement area fits very well with the area delimited by Scarp A and Scarp B. There is some evidence for segmentation of the sliding block into smaller blocks along secondary extensional fractures. A Basal Sliding Plane (BSP) is observed with a 20-30° dip towards the valley floor to the west. The BSP is sub-parallel to, and appears to utilise, the shallow west-dipping foliation. The presence of fresh talus slopes at the front and sides of the block, and particularly in the vicinity of extensional structures within the block, suggests that active shearing occurs along this basal plane.

4. Discussion and Conclusion

Using these bounding-structures of the Gamanjuni rockslide, together with the estimated depth to the sliding plane, we estimate an approximate volume for the unstable block of 23 million m³, making this site one of the larger potential rockslides in Norway. The paucity of extensional structures within the block strongly suggests the possibility of a single catastrophic failure. A large river runs in the bottom of the valley which could be blocked and dammed by a rockslide of this size.

Gamanjuni is just one of several similar rockslides along the same ridge in the Manndalen valley. In addition, numerous unstable rock slopes have been identified in the neighbouring slopes, such as the south side of Kåfjord and the west side of Lyngenfjord. One of the rockslide along Lyngenfjord, called Nordnes, has been monitored for several years now using many ground-based systems due to the hazard it represents [Nordvik *et al.*, 2010]. However, the costs involved in similar monitoring of all the unstable slopes identified during this study would be prohibitive. New existing and planned satellites have the ability to acquire relatively frequent images. By installing artificial corner reflectors (visible also during the winter) and acquiring regular SAR images, it should be possible to determine if and when any of these landslides needs closer, ground-based monitoring.

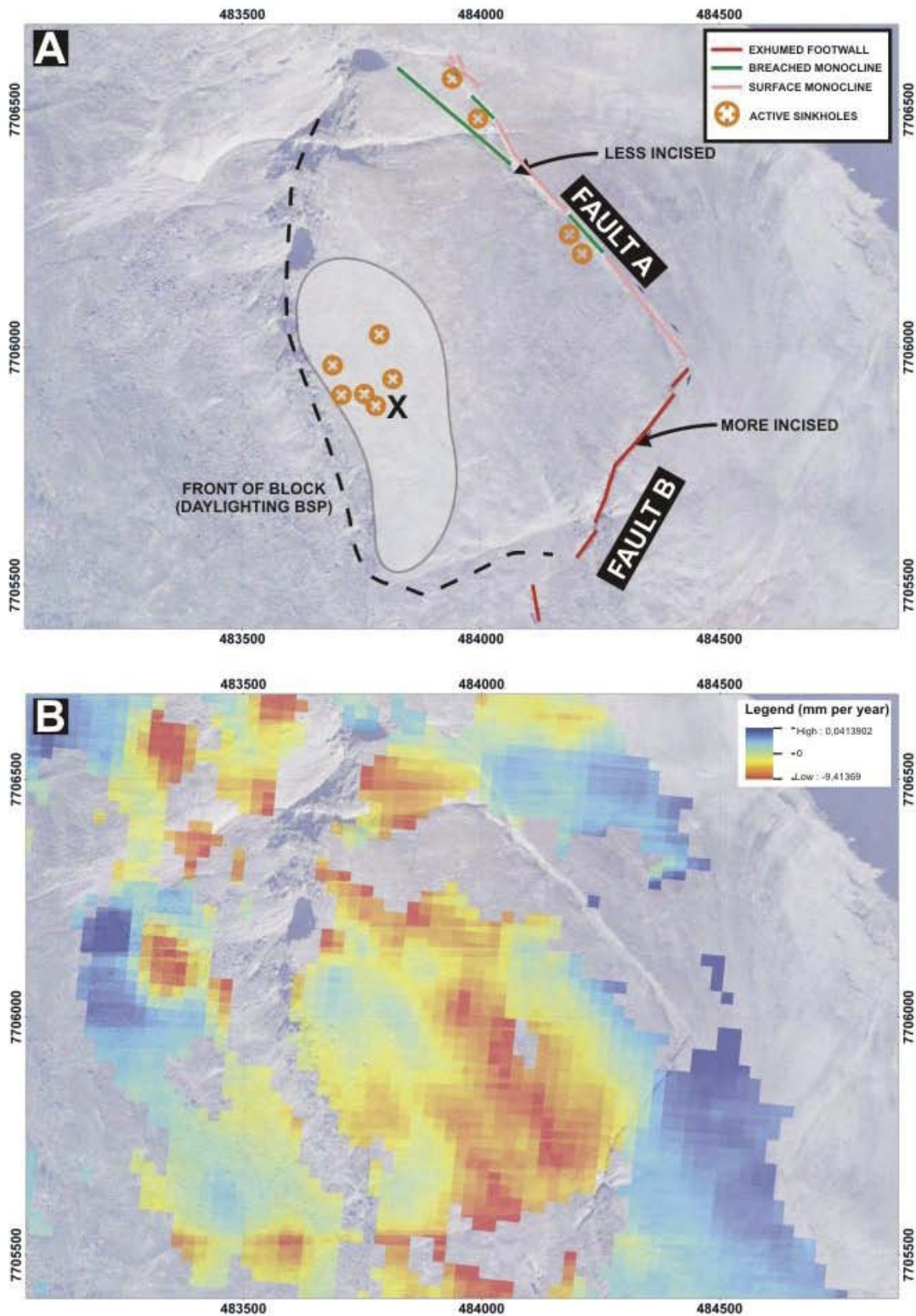


Figure 4: From Henderson et al., 2009. The upper figure shows a simplified geological interpretation overlain on an orthophoto of the Gamanjanni rockslide. The lower figure shows the average line-of-sight velocity between 1992 and 1999 for the area.

References

- Berardino, P., G. Fornaro, R. Lanari, and Sansosti, E. (2002), A new algorithm for surface deformation monitoring based on small baseline differential SAR interferograms, *IEEE Transactions on Geoscience and Remote-sensing*, 40(11), 2375-2383.
- Chen, C. W., and Zebker, H. A. (2001), Two-dimensional phase unwrapping with use of statistical models for cost functions in nonlinear optimization, *J Opt Soc Am A*, 18(2), 338-351.
- Ferretti, A., C. Prati, and Rocca, F. (2001), Permanent scatterers in SAR interferometry, *IEEE Transactions on Geoscience and Remote-sensing*, 39(1), 8-20.
- Henderson, I.H.C., Lauknes, T.R., Osmundsen, P.T., Dehls, J.F., Larsen, Y., and Redfield, T.F. (2011), A structural, geomorphological and InSAR study of an active rock slope failure development, *Geological Society of London Special Publications*, 351, 185-199.
- Lauknes, T. R., A. Piyush Shanker, J. F. Dehls, H. A. Zebker, I. H. C. Henderson, and Larsen, Y. (2010), Detailed rockslide mapping in northern Norway with small baseline and persistent scatterer interferometric SAR time series methods, *Remote-sensing of Environment*, 114(9), 2097-2109.
- Lauknes, T. R., H. A. Zebker, and Y. Larsen (2011), InSAR Deformation Time Series Using an L1Norm Small-Baseline Approach, *IEEE Transactions on Geoscience and Remote-sensing*, 49(1), 536-546.
- Nordvik, T., L. H. Blikra, E. Nyrnes, and Derron, M. H. (2010), Statistical analysis of seasonal displacements at the Nordnes rockslide, northern Norway, *Engineering Geology*, 114(3-4), 228-237.
- Osmundsen, P. T., I. Henderson, T. R. Lauknes, Y. Larsen, T. F. Redfield, and Dehls, J. F. (2009), Active normal fault control on landscape and rock-slope failure in northern Norway, *Geology*, 37(2), 135-138.

3.3. INTERPRETATION OF DIGITAL ELEVATION MODELS

3.3.1. Data acquisition

[ITC+CNRS+UNIL]

Sources for topographic data can be grouped into those freely available to the public and datasets which are usually associated with costs. SRTM [Jarvis *et al.*, 2008] and the ASTER GDEM [ASTER-GDEM-VALIDATION-TEAM, 2009] are two sources which are available without costs, globally and at resolution up to 30 m. For scientific studies and administrative hazard zonation an access to the countries topographic maps may furthermore be possible in most cases without significant costs. While such datasets provide valuable auxiliary information for the interpretation of other data types they are typically too coarse for detailed mappings of inventory relevant variables. Higher resolution information is generally associated with additional costs which are typically related to the required resolution and the areal extent. Among available remote-sensing methods for the acquisition of digital elevation models it can be distinguished between stereophotogrammetry, Radar-based models and LiDAR derived topographic data. The most traditional source is certainly the construction of DSMs with stereophotogrammetric image matching. On the one hand large historic archives of stereo views are available and on the other hand modern satellites (SPOT, Cartosat-1, ALOS and WorldView-1/2) and aerial sensors (e.g.UAV) continue to collect up-to-date datasets. The highest resolution of photogrammetric DSM from spaceborne images is at present 2 m [Poli *et al.*, 2010] and a comparison of different sensors is currently under way [Reinartz *et al.*, 2010]. Due to enhanced sensors and stereo matching algorithms the results of stereophotogrammetric processes (Fig. 5 b-c) are still among the most precise and accurate methods to acquire topographic data [Haala *et al.*, 2010].

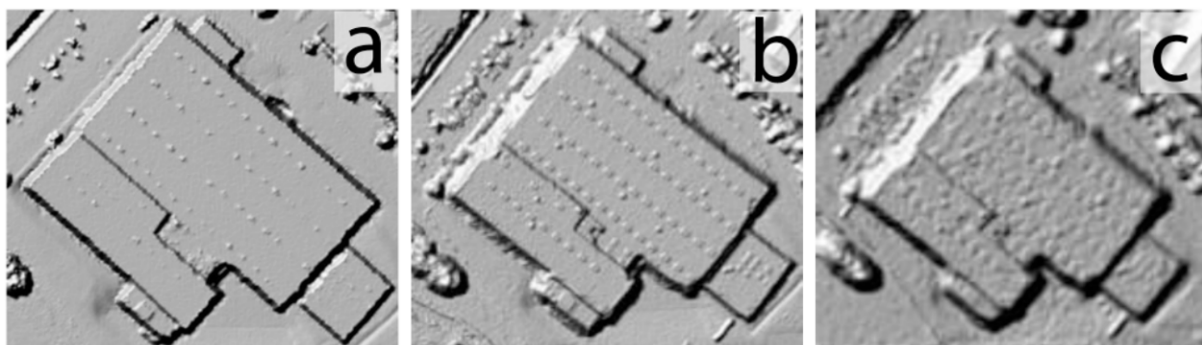


Figure 8: a) LiDAR DSM (resolution 25 cm), b) photogrammetric DSM (GSD 8 cm, resolution 25 cm), c) DMC DOM (20 cm GSD) [modified from Haala *et al.*, 2010]

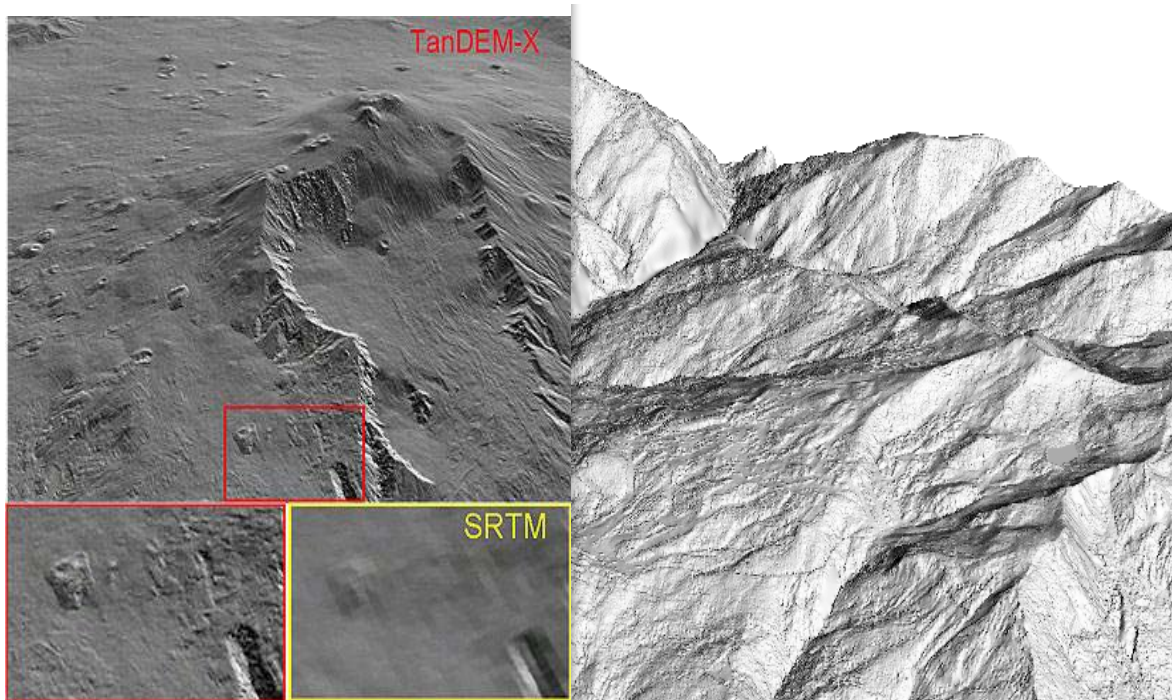


Figure 9: Left: Intercomparison between interferometric DSM derived from SRTM (90 m) and TANDEM-X (12 m), Source: DLR, Right: Hillshade representation of a airborne IFSAR DSM (3.4m)

At latest since the successful SRTM mission, interferometric SAR (IFSAR) has proved it's capability to yield accurate topographic datasets over wider areas. For European territories DSMs derived from airborne IFSAR are available with a ground resolution of 3-4 m and the TANDEM-X satellite constellation will soon provide a global topographic dataset with a resolution of 12 m and a relative vertical accuracy of less < 2 m [Krieger *et al.*, 2007]. However, it also has to be considered that the X-Band interferometry cannot penetrate most surfaces and ground under vegetation cannot be observed directly.

LASERS (Light Amplification by Stimulated Emission of Radiation) are active optical sensor that emit series of pulses of highly collimated, coherent, monochromatic (optical wavelength range), directional and in phase electromagnetic radiation. After first experiences in 1965 [Shepherd, 1965] and major improvements in the 1990's, lasers mounted on airborne platforms (airplanes or helicopters), also called Airborne Laser Scanning (ALS), can now produce High Resolution Digital Elevation Models (HRDEM) at regional scales [Petrie and Toth, 2009]. As a consequence, ALS is now a remarkable technique for topography mapping (Figure 10) and is widely used in Geosciences for landslides detection, characterization and monitoring.

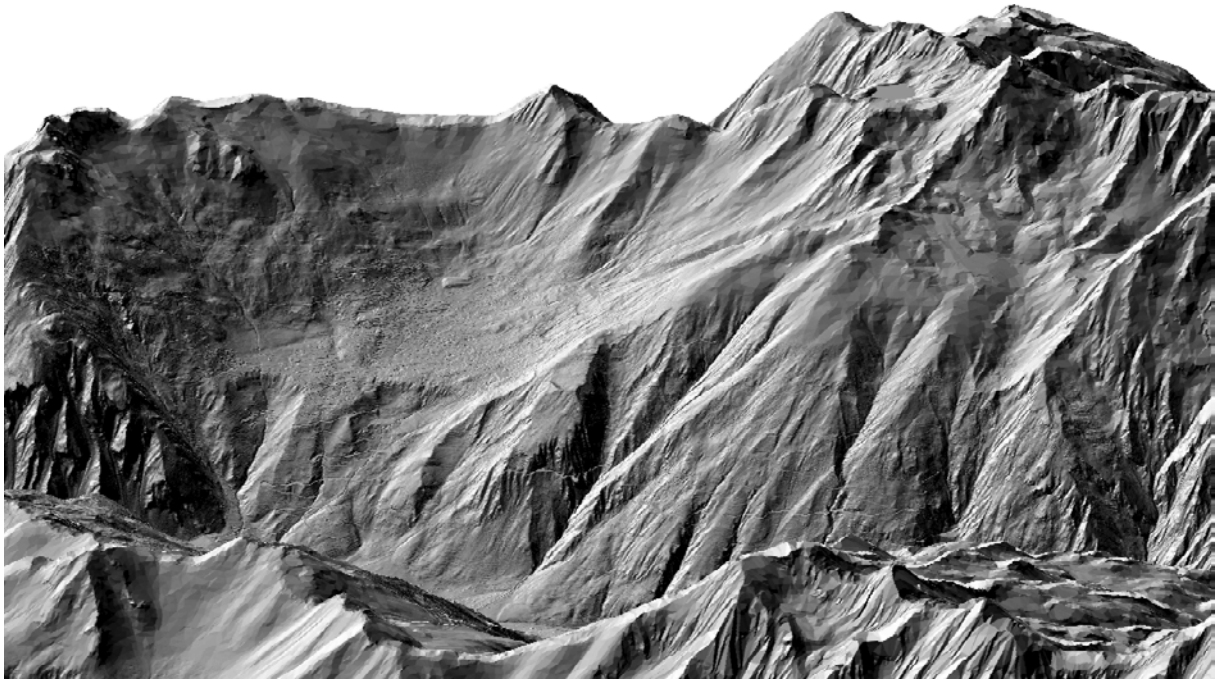


Figure 10: two meters HRDEM of the ski resort of Verbier (Valais, Switzerland) processed from an ALS point cloud (MNT-MO © CC-GEO-VS).

Basically, on an airborne platform, three components are used:

1. a LiDAR (Light Detection and Ranging) which emits laser pulses and records the time of flight (TOF) of the back-scattered pulses;
2. a set of at least two GNSS antennas (Global Navigation Satellites Systems) which record the coordinates of the LiDAR at any time;
3. an IMU (Initial Measurement Unit) which record the roll, pitch and yaw angles of the platform according to three fixed orthogonal axes.

So, as the LiDAR knows its position, its direction of sight and the TOF of each emitted laser pulses, it is possible to reconstruct the surface in 3D, post-processing millions points clouds. The resolution is basically function of the altitude, the velocity of the platform and the scanning frequency [Shan and Toth, 2009]. Usual ALS point densities are 1-2 point m^{-2} . For natural hazard purposes, it is generally more convenient to filter out vegetation and non-natural structures from point clouds, in order to work on geomorphologic surfaces. Indeed, as shown in the following figure, geomorphological features are much more obvious on a “cleaned” elevation surface than on a raw surface.

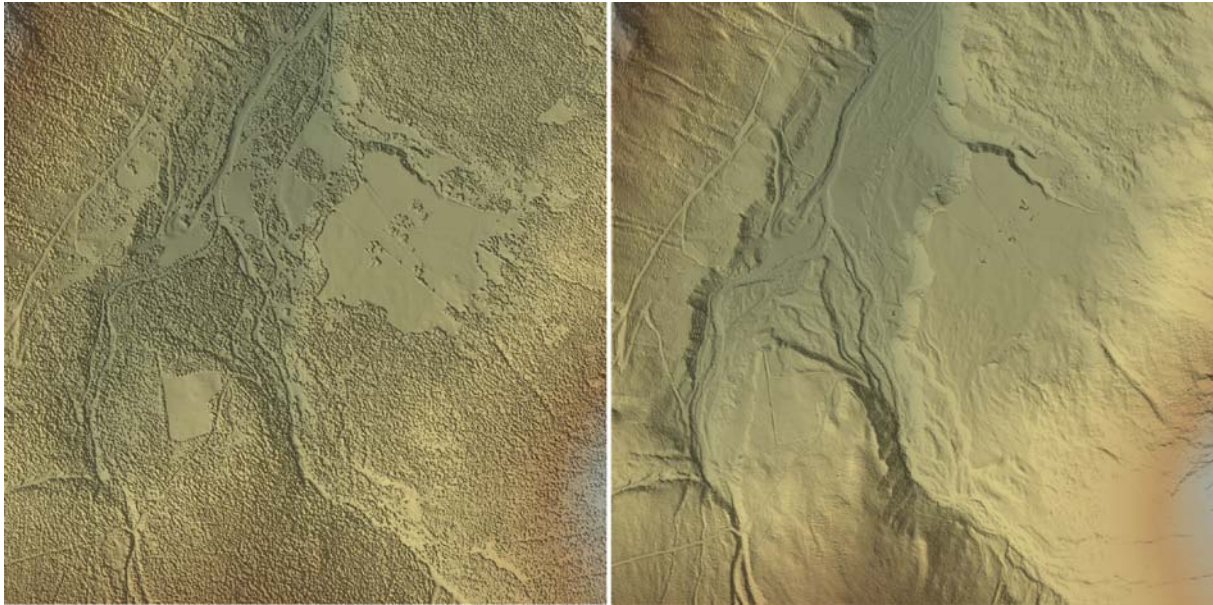


Figure 11: Left: Digital Surface Model (DSM), including vegetation canopy. Right: filtered Digital Elevation Model (DEM), for the same area. Obviously, morphological features are more visible on the DEM than on the DSM.

To find more information on theoretical considerations of ALS, we recommend the SafeLand deliverable 4.1 [Michoud *et al.*, 2010], as well as Shan and Toth [2009] or Vosselman and Maas [2010].

In some European countries Airborne LiDAR datasets are already available with national scale, resolution higher than 1 m and vertical accuracies that are typically in the range of decimeters. Beside the high resolution the advantage of LiDAR lies especially in the possibility to observe the ground also under relatively dense vegetation (Figure 12). If more detailed observations and higher accuracies are required terrestrial LiDAR is at present the most precise instrument for the acquisition of topographic information (Figure 13) on local scale.

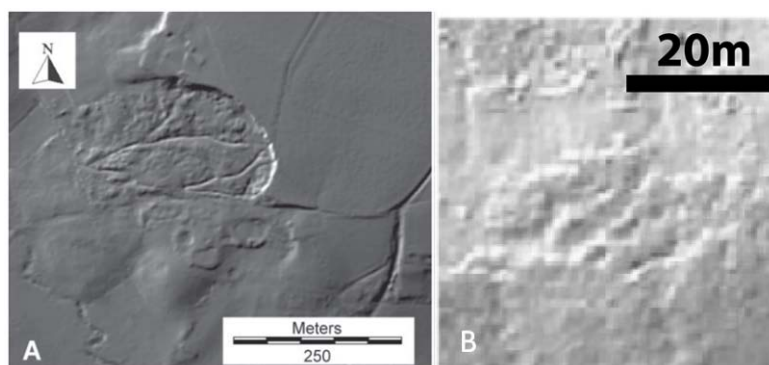


Figure 12: A: Landslides in a hillshade representation of a airborne LiDAR DTM [Van Den Eeckhaut *et al.*, 2007]. B: Visibility of landslide-induced surface cracks in a airborne LiDAR DTM after vegetation filtering [Razak *et al.*, 2011b]

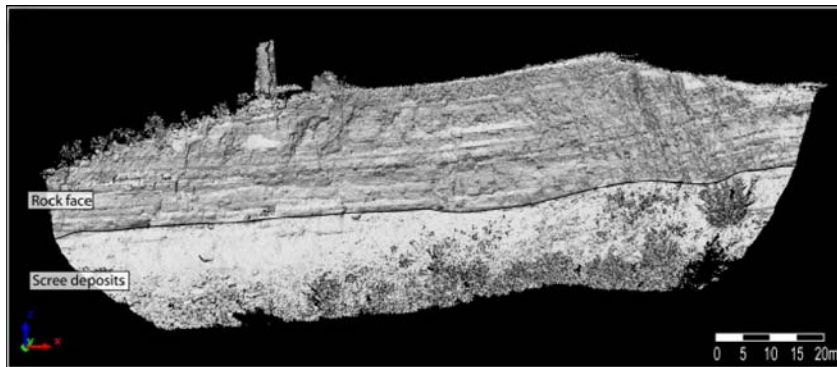


Figure 13: 3D rasterized model of a rockface with scree deposits generated from terrestrial LiDAR point clouds [Abellán *et al.*, 2010]

3.3.2. Data analysis

A. Visual interpretation of DEMs and multi-temporal DEMs

[JRC]

A detailed overview and relevant references are provided in sections 3.5 and 4.3 of D4.1. For identification, mapping, classification and prediction of landslides DEMs are indispensable. DEMs and their derivatives have been widely used for landslide hazard mapping at regional scale for a long time. However, their use regained popularity since the increasing availability of high resolution DEMs (HRDEMs). The latter can be produced through stereo pairing of aerial photographs or passive optical imagery or from active radar interferometric techniques and terrestrial or airborne laser scans (see section 4.3 of D4.1). The visualization of the HRDEMs can be highly improved by using hillshade maps or draping over VHR orthophotos (section 4.3.2 of D4.1). For landslide inventory mapping also DEM-derivatives such as slope, shaded relief and surface roughness maps are important. The identification of landslides on DEM-derivative maps is based on the recognition of landslide characteristics (main scarps, reverse slopes, convex landslide feet) and alterations of the drainage system (Case study 7 in D4.1).

Comparison of multitemporal DTMs is typically carried out by a simple subtraction. Whereas the subtraction between two epochs cannot provide the overall volume of the displaced mass, this difference allows an estimation of the volume of the uplifted and subsided parts of the terrain between the two epochs. Hence, this technique is only useful for large landslides with considerable vertical change in the topography. While for the past mainly photogrammetric elaborated DTMs are used, for the last decade DTMs from other sources such as airborne LiDAR scans, or WorldView-1, Quickbird and Ikonos stereopairs are available. Rather than being derived from the same data type, the accurate alignment of the DTMs through the identification of homologous points on non-moving terrain parts is important, and effects of vegetation and changes of vegetation have to be considered. Apart from the depth of vertical displacement, also the velocity of the landslide determines whether

comparison of multitemporal DTMs is useful, as due to the frequency of aerial surveys this method is mostly suitable for slow moving landslides only.

B. Sediment budget analysis and displacement analysis with multi-temporal DEMs differencing

[ITC]

Height differences between DTMs from at least two different time steps can be measured to picture the displaced volumes. While the differencing of the DTMs is a relatively simple operation that can be applied to any DTM, results and accuracy of the volume estimates may vary considerably among different inputs [Kerle, 2002]. Elevation models derived from stereo-photogrammetry typically include heights of the canopy which needs to be considered because the vegetation is typically removed during catastrophic slope failures [Martha et al., 2010c]. Variable accuracies of the input DTMs at different surface textures, slope angles and sun angle elevations also needs careful consideration [Martha et al., 2010b; Tsutsui et al., 2007]. Corrections of vegetation heights are unnecessary if all surface heights correspond to real ground points and the inputs are consequently digital terrain models [Dewitte et al., 2008]. In the DTM difference image of catastrophic slope failures and slow moving landslides typically generate zone of depletion and zones of accumulation. Interpreting the extent and the spatial arrangement of those zones can provide constrains on the possible failure mechanism and complement the volume estimates.

However, the resolution of the input DTM needs to be chosen in relationship to the scale of the process at hand. DTMs generated from new generation sensors such as WorldView - 1/2 and Geoeye-1 still needs to proper evaluation and most spaceborne products offer only sufficient detail to investigate large scale slope failures. Aerial images offer an interesting alternative especially for the reconstruction of historic mass balances, whereas the most advanced and accurate topographic models and consequently volume estimates can be currently derived from TLS and ALS [Favalli et al., 2010].

C. Surface change detection from LiDAR point clouds analysis methods

[CNRS]

LiDAR technology provides high-resolution point clouds of the topography and, when repeated datasets are available, has several applications in terms of deformation and displacement monitoring [Abellán et al., 2010; Gordon et al., 2001; Jaboyedoff et al., 2009c; Oppikofer et al., 2008; Teza et al., 2007; Travelletti et al., in review; Travelletti et al., 2008]. It is mainly used to create accurate and precise Digital Elevation Models (which are 2.5D representations of the topography) or virtual 3D scenes of point clouds. The density mainly depends on the position of the sensor and of the platform (decimetric to centimetric resolution for ALS and centimetric to millimetric resolution for TLS).

For a multi-temporal analysis of LiDAR DEMs and/or LiDAR point clouds, the critical issue is the alignment of the point cloud whose accuracy will determine the range of

deformation and displacement that can be monitored [Jaboyedoff *et al.*, 2010; Travelletti *et al.*, in review]. Point clouds alignment consists in a registration by a visual identification of homologous points and an optimization of the alignment either by the Iterative Closest Points (ICP) algorithm [Besl and McKay, 1992] or by the Roto-Translation technique [Teza *et al.*, 2007]. The choice of the alignment procedure depends on the quality of the point clouds and the requested accuracy. Another critical issue is the accurate filtering of the vegetation in order to represent the real ground morphology (and thus the texture in the DEMs) at the surface.

In order to compute differences (elevation changes, displacement, and deformation), several procedures can be applied on the aligned point clouds. Most of the procedures are based on the compilation of either 1) vectors between two points (or areas) or 2) distances between two data sets (point to surface comparison) either in a user-defined direction or as shortest distance between the two surfaces. This difference calculation allows for the computation of volume differences, as is discussed by different authors [Bitelli *et al.*, 2004; Chen *et al.*, 2006; Dewitte *et al.*, 2008; Mueller and Loew, 2009]. Monitoring surface displacements in rock slopes is simpler than in soil slides because the displacements can be considered as rigid body transformations [Monserat and Crosetto, 2008], and thus the real landslide movement can be decomposed as a combination of translations and rotations. In order to avoid any hypothesis on the rheology of the displaced material, correlation of slope gradient images constructed from the LiDAR DEMs can be applied by measuring displacements of characteristic pixels that occur between image acquisitions, using either FFT-based or direct cross correlation-based algorithms [Travelletti *et al.*, in press]. With such technique, sub-pixel accuracy can be obtained by using advanced statistical techniques.

D. Semi-automatic object- and raster-based landslide mapping using morphological features

[JRC]

In contrast to the relatively high number of studies that used visual interpretation of DEMs and multi-temporal DEMs for extracting landslides from detailed topographic data such as LiDAR (section 3.4.2 A) only few studies have attempted to develop computer-aided methods. The visual identification of landslides features on remote-sensing images is based on the recognition of landslide characteristics and alterations of the drainage system, and semi-automated methods try to translate this expert knowledge in an objective landslide classification method.

Previous attempts of automatic landslide identification have been carried out in a pixel-based analysis. McKean and Roering [2004] have applied various surface roughness filters using LiDAR-derived DEMs to map deep-seated landslide sites, based on the notion that landslide surfaces are rougher due to the appearance of cracks, benches and scars. Roering *et al.*, 2005 [2005] used slope and curvature maps to distinguish old landslides with subdued morphology from steep and dissected terrain and valley floors. Glenn *et al.* [2006]

employed the standard deviation of elevation differences from a hypothetical spline plain, semivariograms, and fractal dimensions to characterize the mechanisms of deep-seated slides. Using different filter size allowed them to define different landslide activity stages. Also *Kasai et al.* [2009] characterized geomorphic features of deep-seated landslides at various stages of evolution and activity. They combined the LiDAR-derived Eigenvalue Ratio filter and slope angle, and assessed relationships between the ranges of filter values and actual surface features.

Section 3.4.3 contains a case-study on ongoing research to semi-quantitatively identify old vegetated landslides, not detectable from passive optical images, using OOA and LiDAR derivatives [*Van Den Eeckhaut et al.*, 2011]. Previous studies have proven the potential of OOA and passive optical remote-sensing data (see section 4.8 of D4.1) for semi-automatic creation of inventories of active landslides. Yet, DEMs have only been used in the second step, the classification. The case-study of [*Van Den Eeckhaut et al.*, 2011] starts from the hypothesis that OOA might provide better results than pixel-based methods when using high resolution topographical data, because OOA rests upon two interrelated methodological steps: (1) segmentation or regionalization of pixels, if necessary on different scales, into meaningful, homogeneous objects that reduce the noise inherent in pixel-based analysis [*Blaschke*, 2010]; and (2) rule-based classification incorporating spectral, textural, morphometric and contextual landslide features. The case-study goes into more detail compared to *van Asselen and Seijmonsbergen* [2006], which used LiDAR derivatives for both the segmentation and classification phase of geomorphological mapping. Their classification included slopes with mass movement, but they did not focus on single landslides as this was too difficult.

3.3.3. Innovative case studies

The following section demonstrates the use of high resolution DEMs via short summaries of six recently published or submitted research works carried out within SafeLand or through sister projects.

Airborne laser scanning of forested landslides characterization: terrain model quality and visualization

Application: Landslide mapping and characterization

Technique: Airborne LiDAR

Main reference: Razak, K.A., M.W. Straatsma, C.J. van Westen, J. P. Malet and S. M. de Jong (2011): Airborne laser scanning of forested landslides characterization: terrain model quality and visualization

Contributors: ITC (K. A. Razak, M.W. Straatsma, C.J. van Westen), CNRS (J.-P. Malet)

Abstract

Mapping complex landslides under forested terrain requires an appropriate quality of digital terrain models (DTMs), which preserve small diagnostic features for landslide classification such as primary and secondary scarps, cracks, and displacement structures (flow-type, rigid-type). Optical satellite imagery, aerial photographs and synthetic aperture radar images are less effective to create reliable DTMs under tree coverage. Here, we utilized a very high density airborne laser scanning (ALS) data, with a point density of 140 points m² for generating a high quality DTM for mapping landslides in forested terrain in Barcelonnette region, South French Alps. We quantitatively evaluated the preservation of morphological features and qualitatively assessed the visualization of ALS-derived DTMs. We presented a filter parameterization method suitable for landslide mapping and compared it with two default filters from the hierarchical robust interpolation (HRI) and one default filter from progressive TIN densification (PTD) method. The results indicate that the vertical accuracy of the DTM derived from the landslide filter is about 0.04 m less accurate than that from the PTD filter. However, the landslide filter yields a better quality of the image for the recognition of small diagnostic features as depicted by expert image interpreters. Several DTM visualization techniques were compared for visual interpretation. The openness map visualized in a stereoscopic model reveals more morphologically relevant features for landslide mapping than the other filter products. We also analyzed the minimal point density in ALS data for landslide mapping and found that a point density of more than 6 points m² is considered suitable for a detailed analysis of morphological features. This study illustrates the suitability of high density ALS data with an appropriate parameterization for the bare-earth extraction used for landslide characterization and identification in forested terrain.

Keywords: Airborne laser scanning; Forested landslides; Automatic bare-earth extraction; Landslide filter; Landslide visualization; Barcelonnette region

1. Introduction

Over the last few years, Airborne Laser Scanning (ALS) became available and is used to map landslide morphology and estimate landslide activity in areas that are partly or completely covered by dense vegetation [Sekiguchi and Sato, 2004; Van Den Eeckhaut et al., 2005, 2007; Glenn et al., 2006; Schulz, 2007]. The ability of ALS to penetrate the forest canopy and its independence of solar incidence angle makes ALS superior to image-based photogrammetric techniques for acquiring a high resolution digital terrain model (DTM) in forested terrain [Kraus, 2007] and the high spatial resolution of ALS outperforms the use of synthetic aperture radar (SAR). The interpretability of landslides depends on the quality of the DTM. Reported vertical accuracies of vegetated and sloping terrains vary between 0.20 and 2.00 m [Huisling and Gomes Pereira, 1998], 0.26 m for deciduous forests (Hodgson and Bresnahan,

2004), 0.57 m [Kraus and Pfeifer, 1998], 0.31 m for coniferous forest [Reutebuch et al., 2003] and 0.31 m for shrub and conifer trees [Wang and Glenn, 2009]. So far no detailed assessment on DTMs has been carried out to reveal the suitability of ALS and derived DTMs to accurately map landslide-morphological features.

Filtering of ground points from the ALS point cloud is an important step in the accurate geomorphologic mapping of landslides. Generally, ALS-derived DTMs have been used to characterize landslide morphology and activity [McKean and Roering, 2004; Glenn et al., 2006; Kasai et al., 2009]. Several algorithms have been developed for DTM extraction from ALS point clouds [Sithole and Vosselman, 2004]. In spite of the ability to automatically classify ground points and non-ground points, complex scenarios such as the preservation of discontinuities (steep slopes), vegetation on slopes, low vegetation and influence of outliers (multi-path errors or hit off objects) still require further improvement of the filtering algorithms [Sithole and Vosselman, 2004] and some manual editing is often carried out by the data provider. The selection of the appropriate filtering algorithm depends on the type and complexity of the landscape [Sithole and Vosselman, 2004; James et al., 2007]. An optimal method for landslide inventory mapping is currently not known. Especially, the preservation of important landslide characteristics, such as scarps, cracks, rock blocks, deposition lobes, ponds, hummocky topography, and back-tilted slope surface, while removing vegetation is a challenging task.

In this study two DTM filters (hierarchical robust interpolation, progressive TIN densification) are tested on a very high ALS data with more than 140 points m⁻² with respect to the preservation of geomorphological features of forested landslides.

The second part of this study evaluates various visualization methods of an ALS derived DTM representing a large complex landslide, whereas different visualization techniques discussed in the literature are qualitatively assessed by different image interpretation experts.

2. Study Area

The Bois Noir landslide (Fig. 1) is located on the south-facing slope of the Barcelonnette Basin in the South French Alps, 2.5 km to the south-east of Jausiers (Alpes-de-Haute-Provence, France). The area is characterized by irregular topography with slope gradients ranging between 10 and 35° [Thiery et al., 2007] and the site is covered by *Pinus Nigra* (black pine tree) which is the dominant species. Geology at the study area is characterized by a 15-m thick top layer of morainic colluvium, underlain by autochthonous Callovo-Oxfordian black marls as present in the northern part of Bois Noir landslide [Maquaire et al., 2003]. The southern part of Bois Noir is characterized by outcrops of limestone in the summit crest and is characterized by steep slopes of up to 70°, with extensive scree slopes.

The hummocky topography is inherited from the different phases of the Quaternary glaciation [Hippolyte and Dumont, 2002]. The Bois Noir slope segment is characterized by a dry and mountainous Mediterranean climate with strong inter-annual rainfall variability (annual rainfall may vary between 400 and 1400 mm). These predisposing geomorphic and climatic

factors explain the development of the slope by rotational or translational shallow landslides which usually affect the uppermost two to six meters [Thiery *et al.*, 2007].

We focussed on a small and most active part of the 24 ha of the Bois Noir slope segment (Fig. 1A) to limit data volumes and to optimize the scale of visualisation.

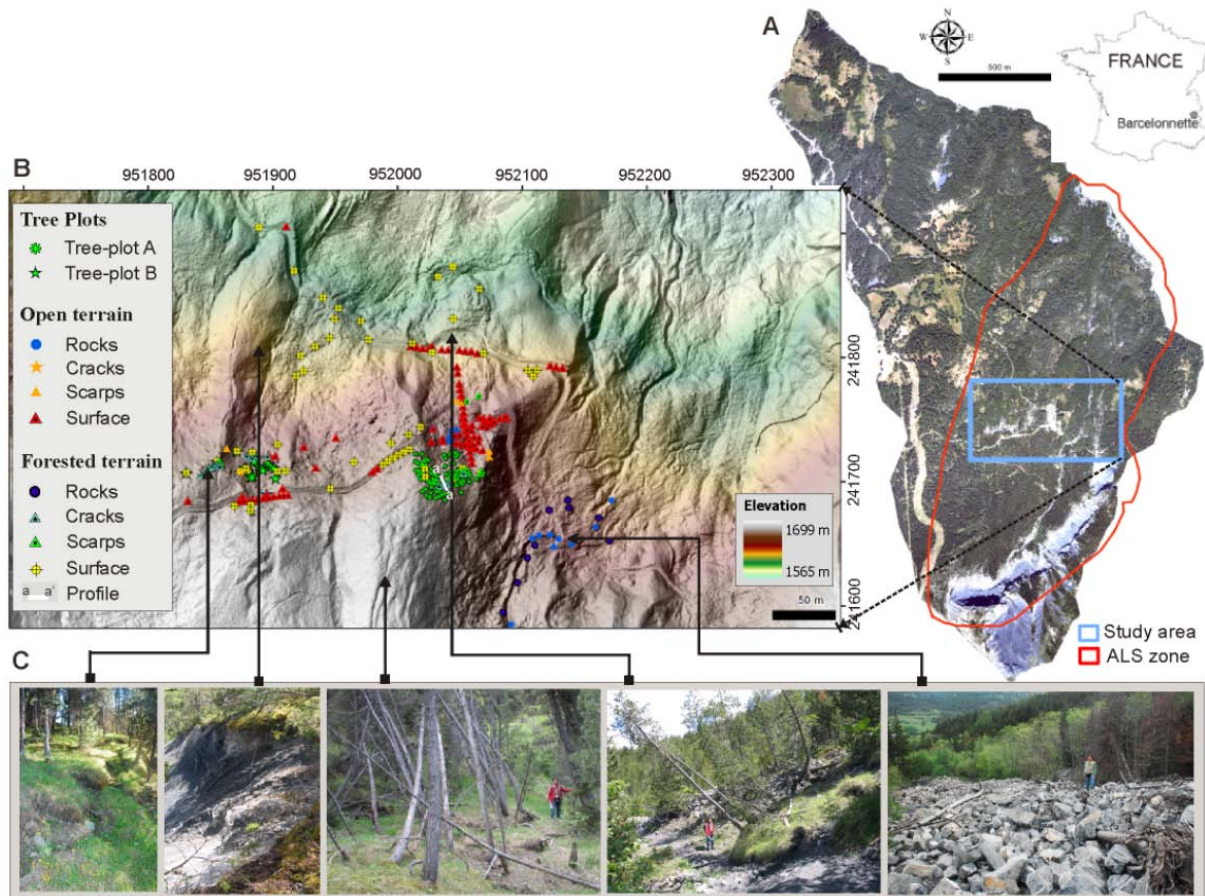


Figure 1: Location of the study area at Bois Noir landslide in the Barcelonnette Basin (South French Alps). A) Orthophoto of study area and ALS zone in 2009. B) Map showing validation points measured in different geomorphological features and trees over forested and open terrain. C) Photographs of representative landslide features in the study area.

3. Methods

3.1. Data collection

The ALS campaign was carried in July 2009, using a helicopter flying about 300 m above the ground. In order to increase the point density seven flight lines were flown resulting in 50 million points. Using only last pulse measurements resulted in point density of 140 points m^{-2} , which is still far above any commercial application of ALS data.

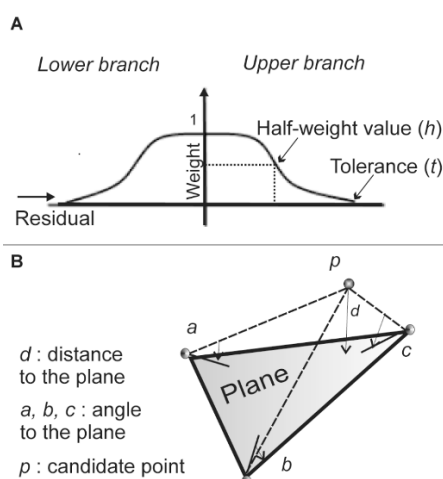
During a field campaign in June 2009, 332 points were collected using a total station and a Leica differential GPS system 1200 with two geodetic base stations. Further details of the point acquisition are provided in Razak *et al.* [2011].

3.2. Quantitative assessment of landslide DTM accuracy

In this study, we evaluated two common filters for bare-earth extraction [Sithole and Vosselman, 2004]: hierarchical robust interpolation (HRI) and progressive TIN densification (PTD). Both filters execute automatically without manual editing and work on point clouds directly without gridding the data.

3.2.1. Parameterization of Hierarchical Robust Interpolation

Pfeifer et al. [2001] proposed the HRI approach to filter the point cloud on three different hierarchical levels. Each level corresponds to an increase in resolution and comprises four steps to extract ground points: thin out, filter, interpolate, and sort out/classify. In the thin out step, the original data are thinned out to a low density point cloud. A grid is overlaid over the point cloud and for each cell, the lowest or most central point is chosen. In the filter step, a DTM is determined by applying the method of Kraus and Pfeifer [1998], which works by iteratively computing a local average. Weights are based on the residual value relative to the



DTM in the previous iteration. The weight function gives a low weight to points with a large residual and high weight to points with a small residual. Fig. 2A shows a schematic diagram of a weight function which is determined by half of its maximum value at h and the weight function is cut off at tolerance, t .

Fig. 2: Parameterization of Hierarchical Robust Interpolation (HRI) and Progressive TIN Densification (PTD) method. A) Weight function of HRI method, showing the half-weight value (h) and tolerance (t) for residual calculation. B) Triangle of identified ground points indicates angles (a, b, c) and distance to the plane (d) of PTD method.

We propose an iterative approach based on the HRI method, which we will refer to as the landslide filter. This filter is capable of dealing with the complexity of terrain, especially in a rugged forested area for landslide mapping. Besides that, we used two predefined parameterizations embedded in SCOP++, called as a HRI-default filter and a forest filter in this study. The different parametrization schemes of the filters are shown in Table 1.

3.2.2. Parameterization of Progressive TIN Densification

The PTD method was developed by Axelsson [2000]. PTD is an iterative approach where in each iteration, points are added to the existing TIN if they are below predefined thresholds. The thresholds are determined on the basis of the angle points (a, b, c) of the TIN facets and the distance (d) to the plane (Fig. 2B). The procedure to add candidate points (p) to the TIN is done continuously until all points exceed the thresholds. Parameterization of PTD consists of the selection of the maximum slope degree of the study area, the lowest points in a large grid, the maximum number of iterations for distance and angle to the plane, and threshold for the edge length. Since the PTD method is sensitive to below terrain blunders points 0.5 m lower

than any neighbouring point within a 5 m radius) were first removed. We set the maximum slope angle to 86° , the iteration angle to 10° , and the distance to the plane to 1.5 m. For the iteration angle, the edge length was set to less than 5 m in order to avoid adding unnecessary points and to reduce the use of memory and computation time. These choices are based on point density and terrain characteristics over the study area.

Table 1. Parameterization of weight functions, thinning output and buffer zones for the landslide filter, forest filter and HRI-default filter.

Step/filter	Filter step – weight function				Thin out step Cell size (m)	Classify step Buffer zone (m)
	Upper branch		Lower branch			
	Half-weight value (m)	Tolerance (m)	Half-weight value (m)	Tolerance (m)		
<i>First hierarchy</i>						
Landslide filter						
1st Scheme	0.80	2.40	–	3.60	3	0.45
2nd Scheme	0.56	1.68	–	2.52	3	0.20
3rd Scheme	0.40	1.20	–	1.80	3	0.10
Forest filter	0.80	2.40	–	3.60	6	0.45
HRI-default filter	0.80	2.40	–	3.60	3	0.45
<i>Second hierarchy</i>						
Landslide filter						
1st Scheme	0.30	0.90	1.20	1.20	2	0.45
2nd Scheme	0.21	0.63	0.84	0.84	2	0.20
3rd Scheme	0.15	0.45	0.60	0.60	2	0.10
Forest filter	0.30	0.90	1.20	1.20	3	0.45
HRI-default filter	0.30	0.90	1.20	1.20	2	0.45
<i>Third hierarchy</i>						
Landslide filter						
1st Scheme	0.15	0.30	0.23	0.45	0.25	0.45
2nd Scheme	0.11	0.30	0.16	0.45	0.25	0.20
3rd Scheme	0.08	0.30	0.11	0.45	0.25	0.10
Forest filter	0.15	0.30	0.23	0.45	0.25	0.45
HRI-default filter	0.15	0.30	0.23	0.45	0.25	0.45

3.2.3. Quantitative error assessment

The vertical accuracy of the different DTMs was first determined by computing *RMSE* (root mean square error) between field points and the corresponding DTM points. The effect on the spatial representation of the four different DTM filters was assessed by computing the differences between the results from the landslide filter and the other filters. The last quality aspect evaluated is the density analysis of filtered points. The point density of the ground points is computed based on the average number of points within one square meter.

3.3. Qualitative assessment of DTM interpretability

The qualitative assessment of the ALS-derived DTMs produced by the different ALS filtering parameterization was carried out in two ways. Firstly, we assessed the interpretability of geomorphological features on a hybrid DTM. A hybrid DTM consists of a regular grid, intermeshed with break lines, form lines, border lines and spot heights (SCOP++, 2008). Such DTMs have been used in many landscape studies, [Hollaus *et al.*, 2006; Szekely *et al.*, 2009]. We assessed the interpretability of cracks, scarps, rock blocks, depletion zones and accumulation zones.

Secondly, we asked three expert interpreters to evaluate the interpretability of the different DTMs. The DTMs were provided to the expert image interpreters without informing them on the applied filtering methodology. The evaluation was done on the basis of a stereoscopic model and shaded relief images. The interpretability of different DTMs was rated based on the degree of morphological appearance and a landslide inventory map was created using DTM that was rated highest. The image interpretation was done using a screen visualization technique with 3D anaglyph glasses. A landslide map indicates the outlines of geomorphological units, roads, cracks, drainage network, and landslide activity.

3.3.1. Visualisation in 2D

The interpretability of the images depends on the DTM visualization techniques. Here we compare four different visualization techniques based on a gridded DTM with 0.25 m cell size, namely shaded relief map [Horn, 1981], color composite map [Smith and Clark, 2005], openness map [Yokoyama et al., 2002], and red relief image [Chiba et al., 2008].

3.3.2. Visualization in 3D

Two types of 3D visualization were also produced and evaluated. Firstly, Static stereoscopic models [Smith and Clark, 2005] were created using the shaded relief, the openness map and the DTM. Secondly, a dynamic 3D point cloud visualization [Vosselman and Klein, 2010] was used.

3.4. Analysis of ALS point density for landslide recognition

The ALS data enabled the acquisition of extremely dense point clouds over the landslide area. To assess the influence of the point density on the interpretability of the ALS data eight artificially thinned datasets were produced by grouping points in local neighborhoods of 0.25, 1, 3, 5, 7, 9, 11 and 13 m. The eight datasets had average point density in between 1.69 and 27.20 points m⁻² and were used to create a 1 m resolution DTM by using a natural neighbour interpolation technique. The original DTM and the eight thinned ALS-derived DTMs were given to expert-image interpreters for suitability assessment. Diagnostic morphological features have been referred for this assessment in order to examine the suitability of ALS point density for landslide recognition. This assessment is informative for the users who want to order and use the ALS data for mapping landslides beneath vegetation.

3. Results

3.1. Quantitative assessment

The vertical accuracy of the four produced DTMs varies between 0.28 and 0.87 m compared to the field data and depends on the different morphological features and the applied filters (Table 2). For all morphological features the PTD filter outperforms the filters based on HRI

with *RMSE* being lower than that for the best HRI parameterization by 0.02 to 0.04 m. The landslide filter shows the best results of the different HRI parameterizations. The errors for cracks and scarps are lower when no vegetation is present, but for rock blocks *RMSE* values are comparable between the open and forested terrain. The original point density of last pulse data was 140 points m⁻².

The point density of the ground points varies between 22 points m⁻² and 76 points m⁻² depending on the filters (Table 3). The point density of the filtered data using parameterization of the landslide filter is about 52 points m⁻², and 64% of the point cloud was filtered out during the automatic filtering process. In contrast, point density analysis of the PTD method shows that the ALS points were reduced by 85% after the filtering process.

The differences between the DTMs generated by the landslide filter and the other filters were computed to evaluate the spatial effect of the different filters (Fig. 3). The major height difference between the landslide and PTD filters mostly occurs over the zone of depletion as depicted in the two subset area in Fig. 3A. It shows that the landslide filter preserves small scale morphological features on such areas better than the PTD filter.

Table 2: Quantitative assessment of the vertical accuracy of morphological landslide features with different filter parameterization. Units are in meters.

	Cracks		Scarps		Rocks		Ground surface	
	Number of points	RMSE	Number of points	RMSE	Number of points	RMSE	Number of points	RMSE
<i>Open terrain</i>								
Landslide filter	5	0.33	5	0.40	18	0.33	94	0.34
Forest filter		0.33		0.39		0.39		0.35
HRI-default filter		0.33		0.87		0.41		0.35
PTD filter		0.29		0.36		0.32		0.31
<i>Forested terrain</i>								
Landslide filter	35	0.38	12	0.51	9	0.38	53	0.33
Forest filter		0.38		0.51		0.37		0.34
HRI-default filter		0.38		0.51		0.38		0.34
PTD filter		0.35		0.50		0.31		0.28

Table 3: Point density of ALS ground points extracted using four different filters.

	ALS data input (million points)	Filtered ground points (Average points m ⁻²)
Landslide filter		
First scheme	35.1	75
Second scheme	19.2	68
Third scheme	18.9	53
Forest filter	35.1	76
HRI-default filter	35.1	75
PTD filter	35.1	22

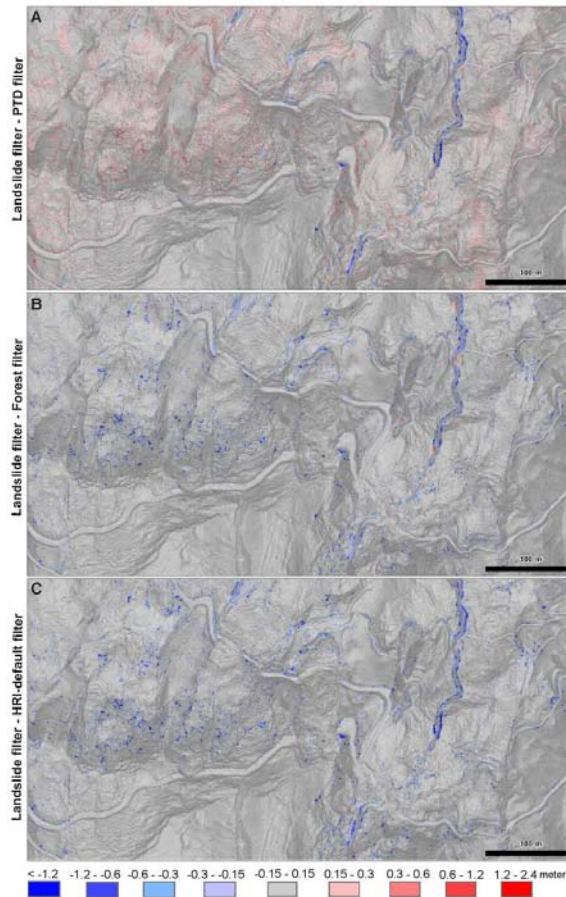


Fig. 3: Height differences between terrain models generated from the landslide filter- and A) PTD filter, B) forest filter and C) HRI-default filter. Positive values indicate that the DTM from the landslide filter is higher than the one from the other filter.

3.1. Qualitative assessment of ALS-derived DTMs

The qualitative analysis on the generated DTMs by different filtering parameter settings was carried out based on shaded relief images of the hybrid DTM model as shown in Fig. 4. Fig. 4A presents an area with a number of shallow cracks in the terrain. Each of the filters is capable of identifying the cracks although the HRI-default filter and the forest filter still show some vegetation that was not properly filtered out. Fig. 4B indicates that the landslide and PTD filters are slightly better in eliminating trees compared to the other two filters. The accumulation zones in the complex landslide can be recognized on each of the filter products. The displaced material and the disrupted road are seen on the subset images (Fig. 4C). In Fig. 4D, the landslide filter shows slightly better results than the other filters for an escarpment area. However, as can be seen in Fig. 4E, the trade-off for the good performance is that both the landslide and PTD filters are worse for detecting isolated rock blocks in the area. The PTD filter also shows a smoothing effect due to insufficient ground points over the tested area.

4.3. Expert interpretation of DTMs

The three experts on image interpretation that evaluated the results from the various filters agree that the ALS-derived image generated using the landslide filter was the best for

landslide interpretation. The PTD-derived DTM shows less information over the deposition and accumulation zones, whereas, the forest and HRI-default filters do not completely filter out the trees.

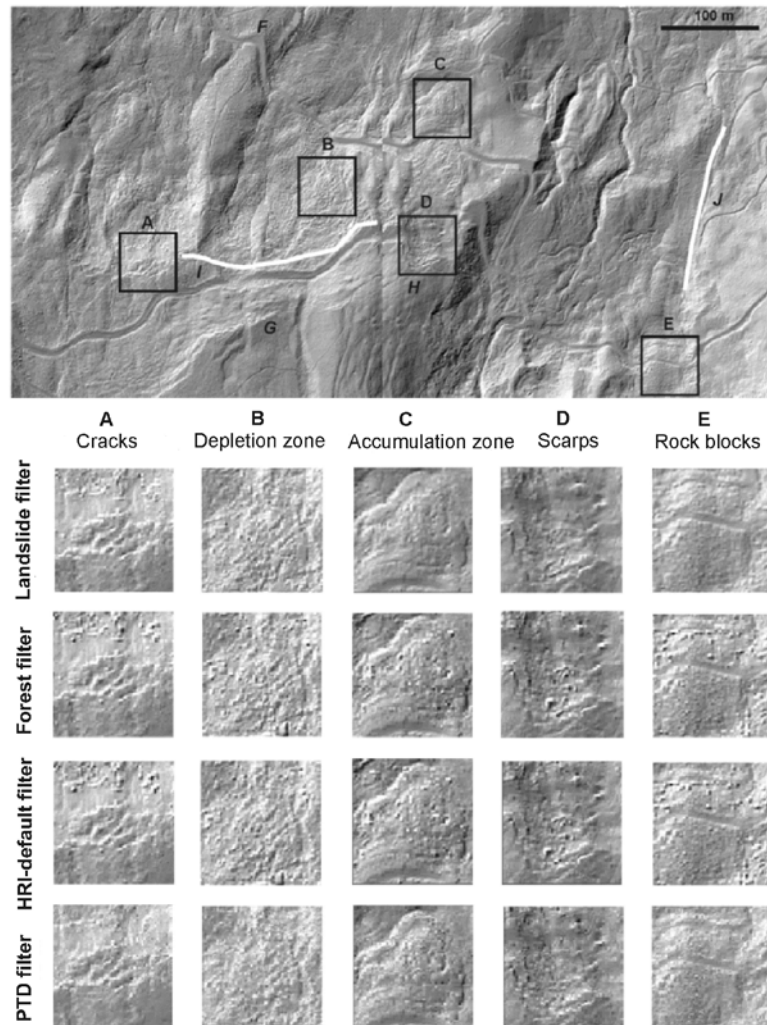


Figure 4. Examples of the representation of the shaded relief images from hybrid DTM models from the four filters for different landslide features. See text for explanation.

For the experts it was generally possible to identify several landslide specific features, to determine the landslide type and to evaluate the relative age of different features [see *Razak et al.* 2011 for further details].

A complete geomorphological interpretation of the sample area is presented in Fig. 5. One of the questions that remained after interpreting the images is whether a number of ridge features (*F* and *G* in Fig. 4) have a structural geological control (for instance showing the bedding or the main local discontinuity of the underlying rocks) or are related to older landslide features. Given the importance of landslides in the area and the relatively large depth of the landslide features, it is more likely that these ridges are related to larger scale instability that can only be interpreted well when looking at the image of the entire Bois Noir landslide slope segment. Also the relationship between the most recent landslide activity and larger scale instability

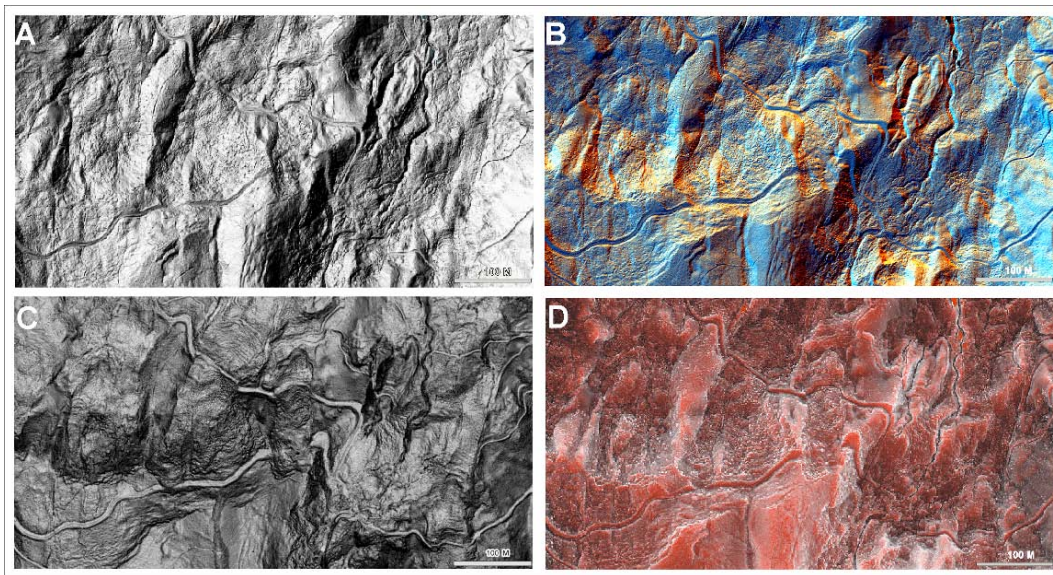


Figure 6: Illustrations of the various visualization methods used for landslide interpretation. A) Shaded relief map. B) Color composite map. C) Openness map. D) Red relief image map.

4.5. ALS point density on landslide recognition

The thinned out datasets ranged from a point density of 1.69 to 27.20 points m^{-2} . Fig. 7 shows a detail of the Bois Noir area, visualized as openness images. The experts all agreed that the thinned dataset could be used to recognize the major geomorphological indicators of landslide activity. However, in order to differentiate the minor relief, recognize individual landform and properly assess the landslide activity, point densities at level 1–3 are required.

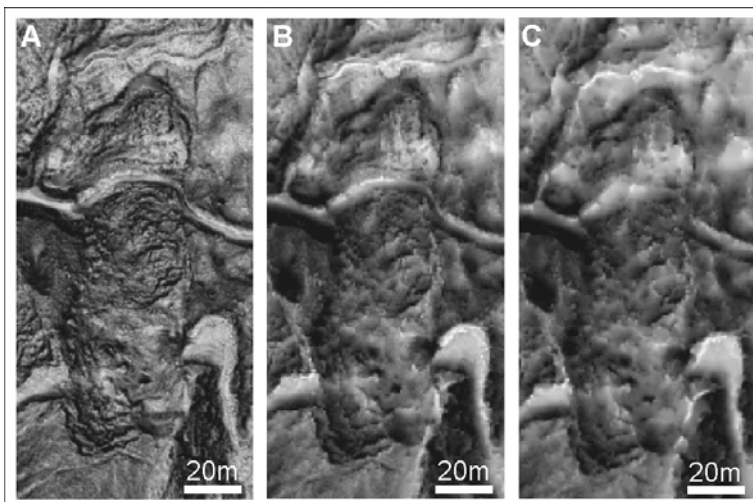


Fig. 7: Three examples of an openness map made from different point densities. A) Original dataset. B) Thinned level 3. C) Thinned level 8

5. Discussion and conclusions

In this study, we evaluated absolute accuracy of an ALS-derived DTMs and its suitability of various types for mapping landslides and for identifying morphological features of landslides. The vertical accuracy of the DTM varied between 0.28 and 0.36 m for the PTD filter. The accuracy depends on the types of geomorphological features. Our results are an improvement

in accuracy compared to the previous studies that reported 0.57 m [Kraus and Pfeifer, 1998] and 0.46 m [Hodgson et al., 2003] vertical error over forested area. Reutebuch et al., [2003] and Wang and Glenn [2009] reported similar results for sloping forested terrain. The PTD filter yielded slightly lower RMSE than the landslide filter: about 0.28 and 0.33 m for morphological preservation and elimination of the trees, respectively. However, the landslide filter shows a better visualization for landslide recognition as depicted by expert image interpreters.

The ALS-derived DTM offers a significant improvement for landslide recognition and classification in forested terrain, as compared to optical images. Small morphological features, such as cracks, lateral ridges, pressure ridges and step wise morphology are clearly recognizable and gives the image interpreter unprecedented detail. Also the type of landslide is easily recognized from the detailed DTM. The trade-off between the four different filters is that trees were properly filtered out in the landslide and PTD filters, but rock blocks and the edges of incised channels are also filtered out. The HRI-default and forest filters maintained more of the trees, rock and channel edges. This trade-off is not shown in the accuracy assessment, but only showed up while interpreting the gridded DTM. This suggests that the HRI method with landslide filter parameterization would be a good method for DTM extraction of forested landslides, but that a separate filter should be applied when there is an interest in rock blocks and step edges.

The assessment of landslide activity was more difficult using just the DTM. This could be done much better if two ALS datasets were available from two different periods. Vegetation characteristics are important indicators of activity and these are normally obtained from aerial images. However, also with a high density ALS data the distribution pattern of irregular trees can be a good indicator for assessing landslide activity. The shape of the tree stem and the orientation of the tree may also be influenced by landslides. Back-tilting of trees indicate a rotational slide, whereas bended stems indicate slow motion of the top soil. These topics are currently being investigated.

While the RMSE values differed little between the filters, the method of visualisation had a large effect on the interpretability of the landslide. Stereoscopic model was used to visualize the landslides. The 3D view of the landscape gives a much stronger impression of the landscape dynamics than any of the monoscopic images. The interpretability of the 3D point cloud visualization was also less attractive than the stereo image due to the varying point densities across the area. For vegetation assessment the raw point cloud would be superior as at such a high point density the shape of the tree is clearly recognizable. The openness image showed most of the details in the area. It has a more natural view than the composite image and has the added advantage that the openness can be combined in a stereoscopic view as it is monochromatic. Shaded relief images proved less attractive due to the dependence on solar angle and the loss of detail in the end result.

The required point density for landslide interpretation depends on the purpose of the study. Gross morphological features of landslides are easily distinguished at a point density of 1.69 points m^{-2} . Detailed analysis of morphological features requires a point density more than

5.69 points m⁻². However for vegetation analysis, a very high density ALS data are preferable to enable detailed characterization of the shape of tree stems and branches [Bucksch and Lindenbergh, 2008].

This study has shown the quality of an ALS-derived DTM for landslides mapping under a dense forest canopy. The generation of a detailed landslide inventory in forested terrain is considered important for landslide hazard assessment. This method should also be suitable in tropical areas where the re-vegetation of landslides proceeds rapidly. Furthermore, the vegetation characteristics, particularly on irregular trees extracted from high density ALS data could be used to assess the landslide activity beneath densely vegetated area. Follow up work is planned for landslides occurring in a forested tropical area with a case study in Malaysia.

References

- Axelsson, P., 2000. DEM generation from laser scanner data using adaptive TIN models. *International Archives of Photogrammetry and Remote-sensing* 35, 110-117.
- Brardinoni, F., Slaymaker, O., Hassan, M.A., 2003. Landslide inventory in a rugged forested watershed: a comparison between air-photo and field survey data. *Geomorphology* 54, 179-196.
- Bucksch, A., Lindenbergh, R., 2008. CAMPINO – a skeletonization method for point cloud processing. *ISPRS Journal of Photogrammetry and Remote-sensing* 63, 115-127.
- Chiba, T., Kaneta, S.I., Suzuki, Y., 2008. Red relief image map: new visualization method for three dimensional data. In: *The International Archives of the Photogrammetry, Remote-sensing and Spatial Information Sciences* vol. XXXVII, Part B2. Beijing, 1071-1076.
- Glenn, N.F., Streutker, D.R., Chadwick, J., Glenn, D.J., Thackray, G.D., Dorsch, S.J., 2006. Analysis of LiDAR-derived topographic information for characterizing and differentiating landslide morphology and activity. *Geomorphology* 73, 131-148.
- Hippolyte, J.C., Dumont, T., 2002. Identification of quaternary thrusts, folds and faults in a low seismicity area: examples in the Southern Alps (France). *Terra Nova* 12, 156-162.
- Hodgson, M.E., Jensen, J.R., Schmidt, L., Schill, S., Davis, B., 2003. An evaluation of LiDAR- and IFSAR-derived digital elevation models in leaf on conditions with USGS Level 1 and Level 2 DEMs. *Remote-sensing Environment* 84, 295-308.
- Hodgson, M.E., Bresnahan, P., 2004. Accuracy of airborne LiDAR-derived elevation: empirical assessment and error budget. *Photogrammetric Engineering & Remote-sensing* 70, 331-339.
- Hollaus, M., Wagner, W., Eberhofer, C., Karel, W., 2006. Accuracy of large-scale canopy heights derived from LiDAR data under operational constraints in a complex alpine environment. *ISPRS Journal of Photogrammetry and Remote-sensing* 60, 323-338.
- Horn, B.K.P., 1981. Hill shading and the reflectance map. *Proc. IEEE* 69(1), 14-47.
- Huising, E.J., Gomes Pereira, L.M., 1998. Errors and accuracy estimates of laser data acquired by various laser scanning systems for topographic applications. *ISPRS Journal of Photogrammetry and Remote-sensing* 53, 245-261.
- James, L.A., Watson, D.G., Hansen, W.F., 2007. Using LiDAR data to map gullies and headwater streams under forest canopy: South Carolina, USA. *Catena* 71, 132-144.
- Kasai, M., Ikeda, M., Asahina, T., Fujisawa, K., 2009. LiDAR-derived DEM evaluation of deep-seated landslides in a steep and rocky region of Japan. *Geomorphology* 113, 57-69.
- Kraus, K., Pfeifer, N., 1998. Determination of terrain models in wooded areas with airborne laser scanner data. *ISPRS Journal of Photogrammetry and Remote-sensing* 53, 193-203.
- Kraus, K., 2007. *Photogrammetry*, 2nd ed. Walter de Gruyter, Berlin.

- Lopez Saez, J., Corona, C., Stoffel, M., Astrade, L., Berger, F., Malet, J.-P. (submitted). Dendrogeomorphic reconstruction of past landslide reactivation with seasonal precision: Bois Noir landslide, southern French Alps. *Geomorphology*, 25 p (submitted in August 2010).
- Maquaire, O., Malet, J.-P., Remaitre, A., Locat, J., Klotz, S., Guillon, J., 2003. Instability conditions of marly hillslopes: towards landsliding or gullyng? The case of the Barcelonnette Basin, South East France. *Engineering Geology* 70, 109-130.
- McKean, J., Roering, J., 2004. Objective landslide detection and surface morphology mapping using high-resolution airborne laser altimetry. *Geomorphology* 57, 331-351.
- Nichol, J.E., Shaker, A., Wong, M.S., 2006. Application of high-resolution stereo satellite images to detailed landslide hazard assessment. *Geomorphology* 76, 68-75.
- Pfeifer, N., Stadler, P., Briese, C., 2001. Derivation of digital terrain models in the SCOP++ environment. OEEPE workshop on airborne laserscanning and interferometric SAR for detailed digital elevation models, Stockholm, Sweden.
- Prokesova, R., Kardos, M., Medvedova, A., 2010. Landslide dynamics from high-resolution aerial photographs: A case study from the Western Carpathians, Slovakia. *Geomorphology* 115, 90-101.
- Reutebuch, S.E., McGaughey, R.J., Anderson, H.E., Carson, W.W., 2003. Accuracy of a high-resolution LiDAR terrain model under a conifer forest canopy. *Canadian Journal of Remote-sensing* 29, 527-535.
- Rott, H., 2009. Advances in interferometric synthetic aperture radar (InSAR) in earth system science. *Progress in Physical Geography* 33, 769-791.
- Schulz W.H., 2007. Landslide susceptibility revealed by LIDAR imagery and historical records, Seattle, Washington. *Engineering Geology* 89, 67-87
- SCOP++, 2008. The SCOP++ software manual, IPF, <http://www.inpho.de/>TU Vienna and INPHO GmbH, Germany.
- Sekiguchi, T., Sato., H.P., 2004. Mapping of micro topography using airborne laser scanning. *Landslides* 3, 195-202.
- Sithole, G., Vosselman, G., 2004. Experimental comparison of filter algorithms for bare-earth extraction from airborne laser scanning points clouds. *ISPRS Journal of Photogrammetry and Remote-sensing* 59, 85-101.
- Smith, M.J., Clark, C.D., 2005. Methods for the visualization of digital elevation models for landform mapping. *Earth Surface Processes and Landforms* 30, 885-900.
- Szekely, B., Zamolyi, A., Drahanits, E., Briese, C., 2009. Geomorphic expression of neotectonic activity in a low relief area in an Airborne Laser Scanning DTM: A case study of the Little Hungarian Plain (Pannonian Basin). *Tectonophysics* 474, 353-366.
- Thiery, Y., Malet, J.-P., Maquaire, O., 2004. Observation on the activity of the Bois Noir landslide. Internal Report, EC-FP5 Alarm Project, Brussels, 10 p.
- Thiery, Y., Malet, J.-P., Sterlacchini, S., Puissant, A., Maquaire., 2007. Landslide susceptibility assessment by bivariate methods at large scales: Application to a complex mountainous environment. *Geomorphology* 92, 38-59.
- Vallet, J., Skaloud, J., 2004. Development and experiences with a fully digital handheld mapping system operated from a helicopter. In: *The International Archives of Photogrammetry, Remote-sensing and Spatial Information Sciences* vol. XXXV, Part B5. Istanbul, 791-797.
- Van Den Eeckhaut, M., Poesen, J., Verstraeten, G., Vanacker, V., Moeyersons, J., Nyssen J., Van Beek, L.P.H., 2005. The effectiveness of hillshade maps and expert knowledge in mapping old deep-seated landslides. *Geomorphology* 67, 351-363.
- Van Den Eeckhaut, M., Poesen, J., Verstraeten, G., Vanacker, V., Nyssen, J., Moeyersons, J., Van Beek, L.P.H., Vandekerckhove, L., 2007. Use of LIDAR-derived images for mapping old landslides under forest. *Earth Surface Processes and Landforms* 32, 754-769.
- Van Westen, C.J., Castellanos, E., Kuriakose, S.L., 2008. Spatial data for landslide susceptibility, hazard, and vulnerability assessment: An overview. *Engineering Geology* 102, 112-131.

- Van Westen, C.J., Lulie Getahun, F., 2003. Analyzing the evolution of the Tessina landslide using aerial photographs and digital elevation models. *Geomorphology* 54, 77-89.
- Vosselman, G., Klein, R., 2010. Visualisation and structuring of point clouds. In: Vosselman, G., Maas, H.G. (Eds.), *Airborne and Terrestrial Laser Scanning*. Whittles Publishing, ISBN 978-1904445-87-6, pp. 43-79.
- Wang, C., Glenn, N.F., 2009. Integrating LiDAR intensity and elevation data for terrain characterization in a forested area. *IEEE Geosciences and Remote-sensing Letters* 6, 463-466.
- Yokoyama, R., Shirasawa, M., Pike, R.J., 2002. Visualizing topography by openness: a new application of image processing digital elevation models. *Photogrammetric Engineering & Remote-sensing* 68, 257-265.

Application of differential ALS for landslide inventory mapping in forested areas: The test site of Gschliefgraben

Application: Landslide inventory mapping

Technique: Differencing of airborne LiDAR DEMs

Main references: unpublished material

Contributors: GSA (I. Baron, R. Supper)

Abstract

This study demonstrates the application of multi-temporal airborne laser scans (ALS) for the monitoring of a highly active landslide and related remedial works. ALS surface models of the Gschliefgraben landslide were acquired for five different time steps between April 2007 and September 2009. Derived terrain models and high resolution aerial photographs were interpreted in combination with differential surface models for a detailed tracking of the vertical displacement and the general evolution of stable and unstable areas. ALS is shown to be an efficient tool for the investigation of landslides, especially in forested and inaccessible areas. A detailed geomorphic analysis of the terrain models enables to recognize individual slope failures and their deposits and to distinguish the active slides and earthflows from inactive areas.

Keywords: OOA, disaster support, feature extraction, K-means cluster analysis, segmentation, India.

1. Introduction

The Gschliefgraben site is one of the most prominent and extensively studied slope failures in Central Europe. It comprises a large complex of geologically controlled slides, earth flows, topples, rockfalls and deep-seated gravitational deformations in the Gschliefgraben valley and along the slopes of the Northern Calcareous Alps. In late November 2007, an earth flow of about 3.8 million m³ of colluvial mass was reactivated in the central and western parts of the valley. The displacement velocity was up to 4.7 m/day at the beginning. Consequently, in frame of the first emergency measures, 55 buildings had to be evacuated. Recently, the Gschliefgraben landslide has been a test site of the European FP7 project SafeLand where new techniques have been tested for rapid mapping monitoring and effective early warning, consisting of, e.g., airborne and ground-based geophysical surveys and the GEOMON4D (continuous geoelectrics) and DMS (automatic inclinometer) monitoring systems.

Landslide inventory map was a basic input for the interpretations of geophysical data. Due to large dimensions of the area, dense forest and complexity of the mass movement phenomena, the landslide inventory was based on analysis of high resolution digital terrain models from (DTM) differential airborne laser scans (ALS) and orthophotographs.

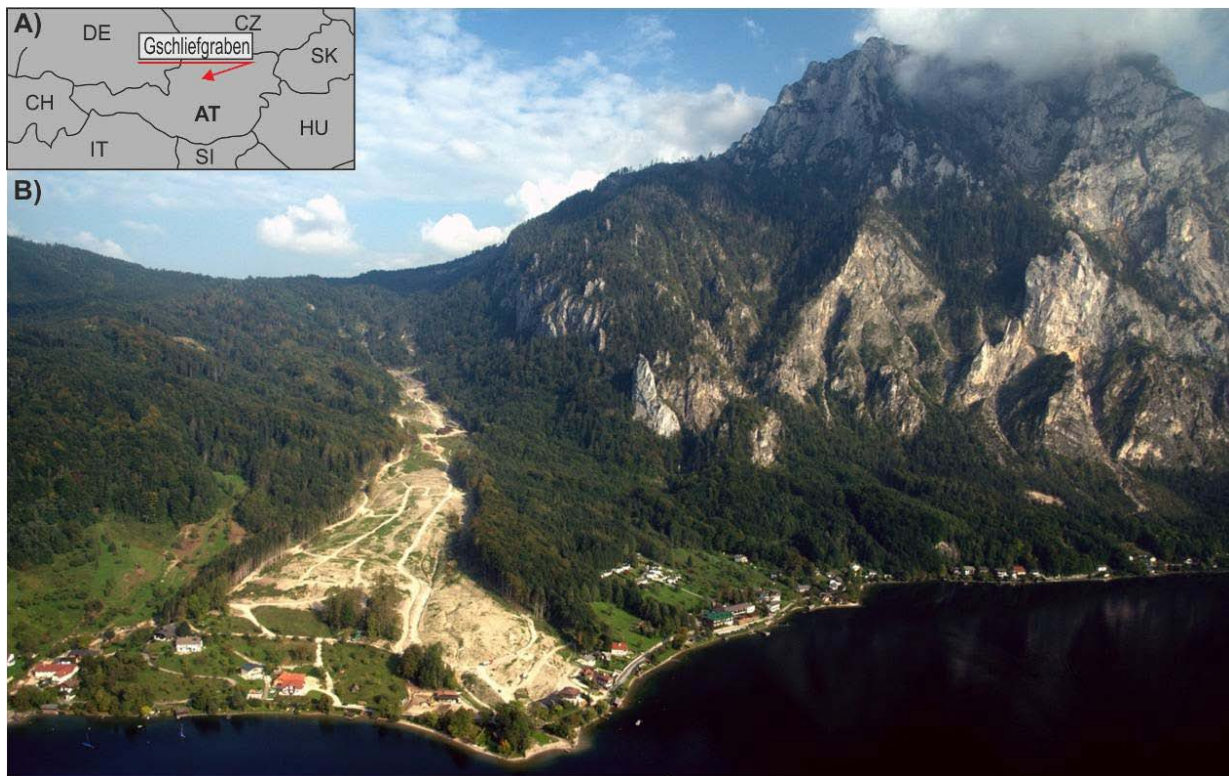


Fig. 1: General setting of the Gschlifgraben site: A) Position within Austria, B) Airborne photo of the Gschlifgraben valley and Mt. Traunstein from the west (Photo by: R. Supper, 2009).

2. Geological and Geomorphic settings

The area of Gschlifgraben is a 2.85 km long and 0.85 km wide valley along the foot of the Northern Calcareous Alps (Fig. 1) south of the town of Gmunden. The front of the Northern Calcareous Alps there forms a steep cuesta with the summit at Mt. Traunstein (1,691 m a.s.l.). The valley is divided into small sub-parallel catchments; its topography is strongly controlled by complicated tectonics and a very complex lithology, as well as by mass wasting that has been active here since the end of the last glacial period.

The surveyed area of Gschlifgraben covered three main geological units with completely different lithology and geological structure, i.e.: (i) Northern Calcareous Alps and the “Marginal Nappe” (NCA), (ii) Ultrahelveticum (UHV) and (iii) the Rhenodanubian Flysch Zone (RFZ).

The NCA unit (Triassic-Cretaceous age) is generally composed of densely fractured, diversely stratified, steeply dipping and frequently faulted competent brittle rock. Dolomite and Limestone are the most abundant rock types. The substrate is highly permeable and the joints often have a character of opened cracks. Generally this unit shows the highest electrical resistivity and the lowest content of radioactive elements.

The UHV unit (Cretaceous-Lower Tertiary age) comprises tectonically strongly deformed variegated marl, claystone, nummulitic limestone, sandstone, arcose etc. This unit is the most incompetent one in the study area. The material contains a relatively high fraction of swelling

clay minerals. Moreover the soft rocks are intensively tectonically fragmented. The rocks of the UHV are locally quite permeable (fractured sandstone, limestone etc.), however impermeable zones prevail. Tectonic joints use to be filled with secondary or tectonic clay. Due to these facts, this zone shows a relatively low resistivity, and a high U, K and Th content.

The RFZ (Cretaceous age) is built up mostly with slate, shale, cemented marl and sandstone of different thickness. The alteration of competent vs. incompetent and permeable vs. impermeable rocks exhibit high local contrast resulting in a distinct local contrast of resistivity and U, K, and Th content.

The main mass wasting processes are represented by sliding and flowing in the central part, which is built up mostly of the UHV unit. The UHV emerge here in a form of the tectonic window between the RFZ and the NCA. On the other hand, falling, toppling, and spreading are the most characteristic types of mass movement in the eastern and southern marginal areas of the Gschlifgraben valley along NCA, where hard rock dominates (dolomite, limestone, cemented Pleistocene breccia). At some places, great portions of the NCA and the below situated RFZ and UHV units are subject to Deep-seated Gravitational Deformations in a rather initial evolution stage.

3. Data and Methods

A set of 5 high-resolution Airborne Laser Scan (ALS) scenes, which were taken at different times in April 2007, January, February, March and September 2008 (Tab. 1), represented the ground surface topography of Gschlifgraben just before, during, and after the major recent landslide event of winter 2007/08.

Table 1: Parameters of the ALS campaigns in the site of Gschlifgraben

Date	Ordering party	Company	Sensor	Resolution [mm]	Flight Height [m]	Processing by
2007-04-05	GeoL	Topscan	ALTM 2050, 3100	~20	1000	Topscan
2008-01-03	WLV	Diamond sensing	Airborne Riegl LMS – Q 560	20	650	Area-Vermessung ZT-GmbH
2008-02-11	WLV	Diamond sensing	Airborne Riegl LMS – Q 561	20	650	Area-Vermessung ZT-GmbH
2008-04-28	GeoL	Topscan	ALTM 3100	~20	1000	Topscan
2008-09-05	WLV	Diamond sensing	Airborne Riegl LMS – Q 561	20	650	Area-Vermessung ZT-GmbH

Note: WLV – Austrian Service for Torrent and Avalanche Control, GeoL – Abteilung Geoinformation und Liegenschaften, Upper Austria

Slope gradient maps in inverted greyscale (“pseudo-hillshade”), derived from the ALS Digital Terrain Model (DTM) were applied for visual inspection of the area. Such slope-gradient maps have a much better and more comprehensive performance of the ground topography than the classical hillshade maps representing only one illumination azimuth (Fig. 2). Although the vertical orientation of individual slopes on such a map could be difficult to be determined, the advantages of its expressivity prevailed. This small disadvantage was eliminated by applying contour lines. The recent activity state of individual slope failures (since 2000) was assessed by analysing bare surfaces on orthophotos from 2000 (Fig. 3, application GoogleEarth) and 2008, by analysing differential ALS DTM in ArcGIS software, and by comparing individual “pseudo-hillshades”. The ALS analysis was complemented with field inspections and field geomorphic, structural and engineering-geological mapping.

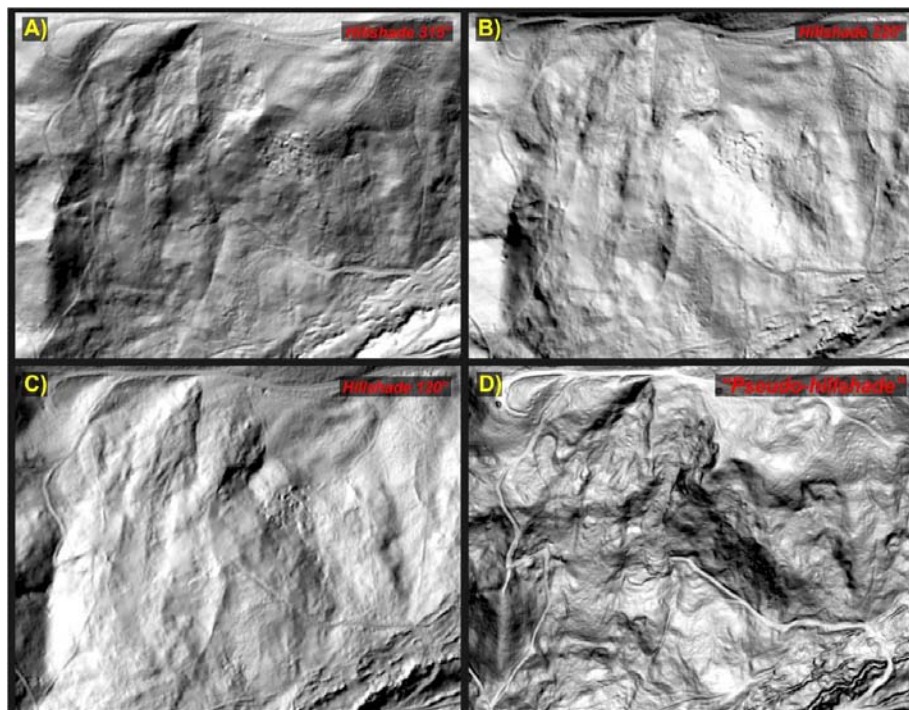


Fig. 2: Comparison of hillshade DTM with different azimuths of illumination (A-C), and the slope-gradient map in inverted greyscale, the “pseudo-hillshade” (D). Each of the frames covers the same area 512 m wide.

4. Results

The detailed geomorphic analysis of the ALS DTMs and orthophotos enabled (i) recognizing individual slope failures and their deposits and (ii) distinguishing the active slides and earthflows from the dormant (inactive) and old ones (Fig. 4, Fig. 5). These observations were compiled in a form of the landslide inventory map (Fig. 7). In total, the study area was affected by morphologically expressive mass movements at more than 50 % (Tab. 2). The mass-movement phenomena in the area include different types of landslides at different volumes, evolutionary stages and activity level, forming a complicated complex. Due to the

limited time available, limited scale and complexity of slope failures, the inventory could only deal with a rough classification. Shallow and deep-seated slides (slumps), their transitions to earthflows, earthflows alone, fallen boulders or sagged slopes and toppled rock towers were the most abundant landslide types. At relatively large portion of the valley, individual bodies of dormant (inactive) rather small scale earthflows and slumps were not distinguishable from each other. Thus they were grouped together as the category “5” (Fig. 7). The active slides and earthflows (active between 2000 and 2008) were distinguished well and they had affected about 5 % of the study area (Tab. 2, Fig 7).



Fig. 3: The activity of the earthflow complex between 2000 and 2008 was assessed based on the identification of bare surfaces on set of orthophotos. The orthophotos are superimposed on the ALS pseudo-hillshade.

Also the major recent landslide event in winter 2007/08 and subsequent remedial works were well documented by the differential ALS. The main recent earthflow mobilized older mass-movement deposit in the central and lower western part of the Gschlifgraben valley. Distinct subsidence in the upper earthflow portion, as well as the uplift of about 14 m in the

accumulation zone was identified (Fig. 5A). The remedial works comprised of distinct material removal from the active earthflow, managed by the Austrian Service for Torrent and Avalanche Control Survey (WLV Austria) in spring and summer 2008 (Fig. 5B).

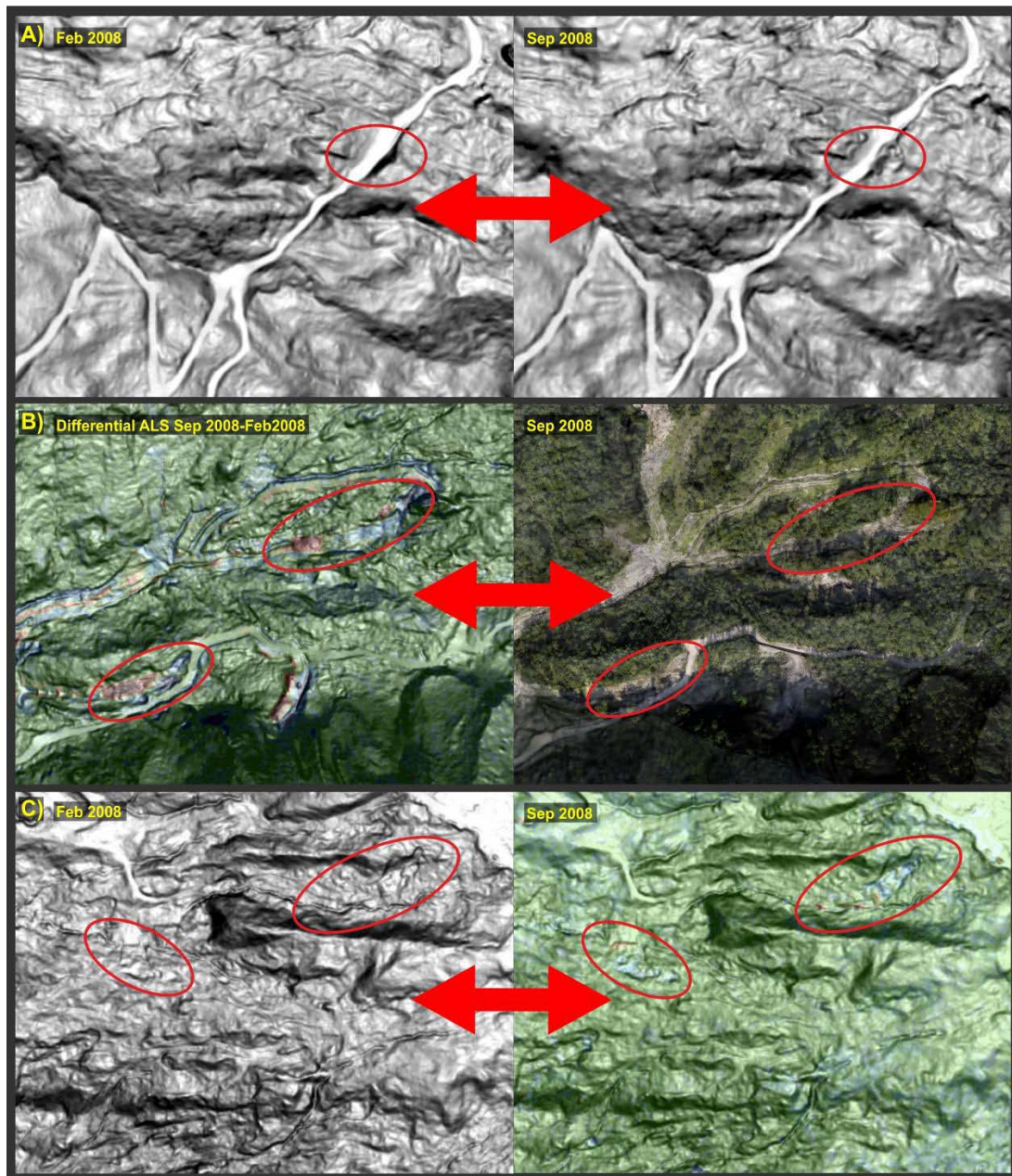


Fig. 4: A more-detailed activity assessment of landslides was based on differential ALS, which had the best expressivity, as evidenced by comparison of A) two separate ALS pseudo-hillshades taken in different time, B) differential ALS model and the orthophoto, and C) pseudo-hillshade and superimposed differential ALS model.

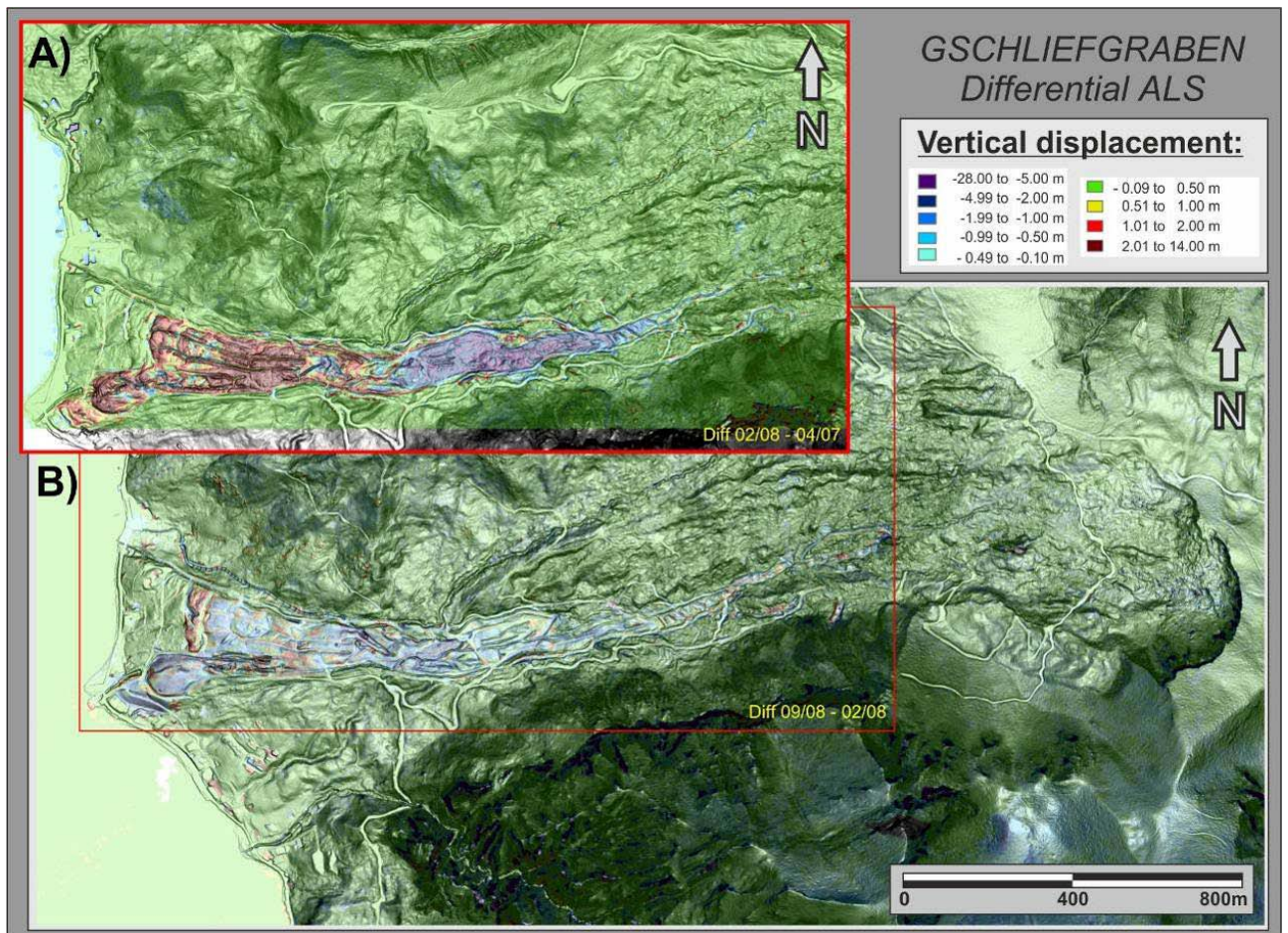


Fig. 5: Two differential ALS scenes highlight mass transport due to (A) the major recent landslide event in winter 2007/08 and (B) latter remedial works comprising of distinct material removal from the active earthflow (below). The presented individual ALS surveys took place in April 2007, February 2008 and September 2008.

Table 2: Review of the spatial extent of different landslide types vs. total area.

Index	Type	Area [km ²]	Area [%]
0	Stable area	2,17	48,69
1	Active landslides	0,01	0,30
2	Active earthflows	0,21	4,77
3, 4, 5	Inactive landslides and earthflows	1,20	27,05
6	Old landslide	0,85	19,18
	Total:	4,45	100,00

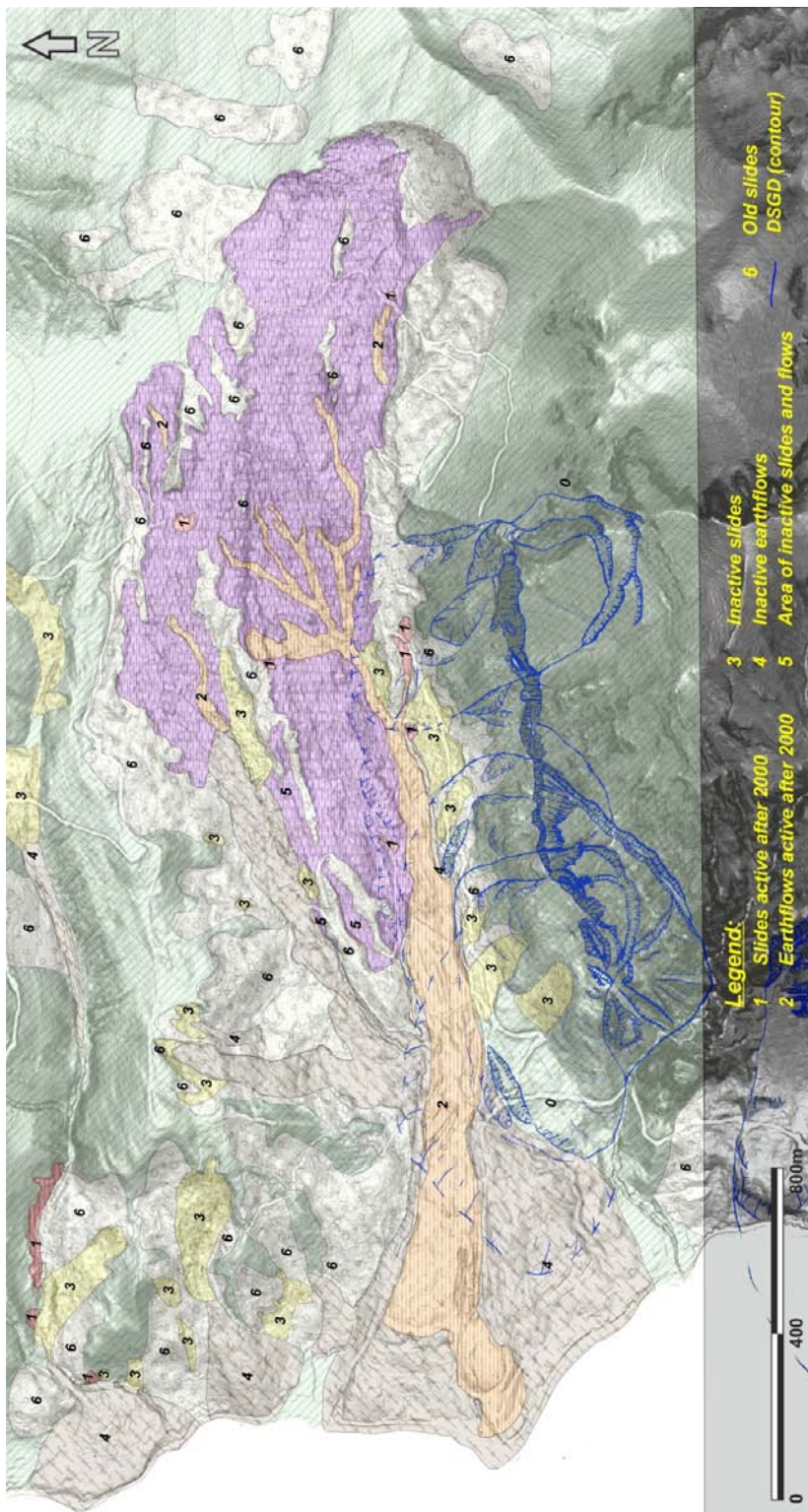


Fig. 6: Landslide inventory map of the area of Gschlifgraben. Slope failures comprise more than 50 % of the area, even the Deep-seated Gravitational Deformations (blue contours) were not included in the summary. The map served as an input for interpreting the airborne geophysical data.

5. Conclusion

The results proved high efficiency of ALS derived detailed digital terrain models in determining landslide phenomena, even in forested and inaccessible areas. The detailed geomorphic analysis of the ALS DTMs and different time-lapse orthophotos from the Gschliefgraben site enabled us to recognize individual slope failures and their deposits and to distinguish the active slides and earthflows from the dormant (inactive) and old ones. Those results were compiled in form of the landslide inventory map. This map then served as an essential base for interpreting the airborne geophysical data.

Acknowledgements

The authors would like to acknowledge the excellent close cooperation with the Austrian Service for Torrent and Avalanche Control (WLV), Section Upper Austria – especially to Wolfgang Gasperl and Harald Gruber – and to Centro Servizi di Geingegneria, Ricaldone (Italy), and ZT Büro Moser/Jaritz, Gmunden (Austria).

Airborne LiDAR for detailed mapping of landslide features under sparse vegetation coverage: the Villerville-Cricqueboeuf landslide

Application: Landslide mapping

Technique: Airborne LiDAR

Main references: Lissak, C., O. Maquaire and J.-P. Malet (in review): Characterization of the complex morpho-structure of a rotational landslide by combining airborne and ground-based methods.

Contributors: CNRS (O. Maquaire, C. Lissak, J.-P. Malet)

Abstract

The purpose of this work is to present a methodology based on the combination of high-resolution ALS data, field surveys and geometrical modeling to propose a detailed geomorphological map of the Villerville coastal landslide, which is further used for hazard assessment. The survey has been conducted in April 2010, and consisted in detailed field mapping, filtering of the original ALS point clouds datasets to underline the ground-based morphology hidden by the vegetation, combination of all the information in a morphodynamic map. The methodology is presented by illustrating the complex morphology of the landslide to explain the features important to delineate for the hazard assessment, and describe the limits of the method.

Keywords: ALS data, field geomorphological mapping, vegetation filtering, morphodynamic map

1. Introduction

Mapping complex landslides under vegetated terrain requires an appropriate quality of digital terrain models (DTMs), which preserve small-size features for landslide classification such as primary and secondary scarps, grabens, depletion zones, and displacement structures [Kraus & Pfeifer, 1998; Sekiguchi & Sato, 2004]. Optical satellite imagery and aerial photographs are less effective to create reliable DTMs under vegetation coverage [Nichol *et al.*, 2006; Razak *et al.*, 2011].

This work presents a simple method to map detailed features by combining extensive field surveys and the use of a very high density airborne laser scanning (ALS) data, with a point density of ca. 60 points/m² for generating a high quality DTM. The method has been developed for the coastal landslides of Villerville-Cricqueboeuf at which some areas are inaccessible because of the dense coverage of bushes.

2. Data and Methods

2.1. History of development of the landslide and objective of the mapping

In Normandy, along the Calvados coast, 50 km of cliffs are partly and periodically affected by landslides for several centuries. On the eastern side, the 12 km long Pays d'Auge section between Trouville-sur-Mer and Honfleur, has been particularly affected [Maquaire, 2000].

Two spectacular landslides are investigated: the "Fosses du Macre" and the "Cirque des Graves" landslides near the municipality of Villerville-Cricqueboeuf (Fig. 1).

On 10-11 January 1982, a major landslide completely or partially destroyed thirty houses and damaged the road in several places (subsidence of ca. 10 cm). Deformations of the slope consisted in subsidence grabens divided by subvertical scarps varying from some tens of centimetres to over one or two meters. At the top, the crown of the landslide consists of a 3 m high scarp. The disturbances at the Cirque des Graves were much greater than at the 'Fosses du Macre'. After the rapid acceleration phase, the deceleration of the movements lasted about two weeks. Three reactivations have been observed since the first failure:

- during the night of the 12/13 February 1988, the crisis caused several damage, and extended the main scarp laterally as well as uphill and downhill. A rise in the beach dislodged the jetty and the breakwaters. The major movements occurred principally at the Fosses du Macre.
- at the end of January or beginning of February 1995 (the precise date of onset is unknown), major displacements occurred. This crisis caused a recession of the landslide crown. Again, the major movements principally occurred at the Fosses du Macre.
- on 23-24 March 2001, after several weeks of warning signs such as the opening of cracks in two houses, a recession and a subsidence of the main scarp occurred. Due to the recession, several houses are now located very close to the main scarp and are menaced at short time. Deformations of the rock platform were observed as for the February 1988 landslide and jetty and breakwaters were dislodged. Again, the major movements principally occurred at the Fosses du Macre. At the Cirque des Graves, subsidences are also observed on the road.

The objective of the work is to produce a detailed geomorphological map of the landslide by explicitly mapping all relevant morphological features testifying of landslide movement (such as scarps, grabens, depletion zones, counter slopes, undulating areas) as a first step for a further geometrical modeling of the landslide sub-surface and a qualitative assessment of the hazard.



Figure 1: Morphology and ortho-photographs of the Villerville-Cricqueboeuf landslides in 2010 (Left: Fosses du Macre landslide; Right; Cirque des Graves landslide).

2.2. Data acquisition and processing methods

2.2.1 Acquisition of Airborne Laser Scanning (ALS) data

The ALS campaign was carried in April 2010 at a period of relatively low vegetation coverage (absence of leaf on the trees, presence of bushes), using a helicopter flying about 300 m above the ground. An airborne hand-held laser scanning system provided by the Helimap company was used. This system has been developed specifically for the mapping over complex areas [Vallet and Skaloud, 2004]. A RIEGL VQ-480 laser scanner with a pulse repetition rate of up to 300 kHz was used to record full waveform laser data. Positioning was done using a Topcon Legacy GGD capable of tracking GPS and GLONASS positioning satellites. The orientation of the aircraft was determined using the iMAR FSAS inertial measurement unit. In order to increase the point density seven flight lines were flown resulting in 100 million points. We used last pulse data that amounted to 45 million points with a mean point density of 60 points.m⁻² on average, which is still far above any commercial application of ALS data.

2.2.2 Vegetation filtering of ALS datasets

The TLS datasets were processed and analyzed using the Scop++ software [Pfeifer et al., 2001; SCOP++, 2008]. Vegetation filtering was carried out by using the hierarchical approach (HRI Hierarchical Robust Interpolation) originally proposed by Pfeifer et al. [2001]. The HRI method has the capability to automatically extract points belonging to the ground surface and classify the non-ground points into several classes such as buildings, vegetation and low points [Pfeifer et al., 2009]. A detailed description of the approach and its evaluation

for landslide mapping can be found in *Razak et al.* [2011]. In this study, the mesh size for the filtering was fixed at 0.30 m and the minimum height at 0.15 m.

2.2.3 Vertical accuracy of the DTM

The vertical accuracy of the DTM (interpolated with an Inverse Distance Weighted function) has been first determined by computing the *RMSE* (Root Mean Square Error) between field points (measured by dGPS or tacheometry) and the DTM. RMSE was calculated for forested and open terrain.

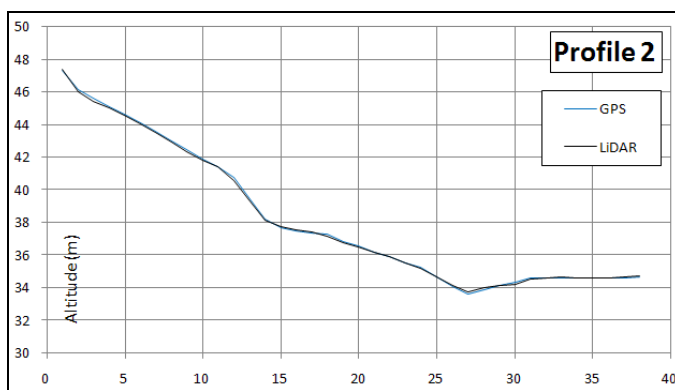


Figure 2: Comparison of the profile 2 between interpolation of GPS and LiDAR survey.

In open terrains, the average difference in *Z* is of 0.04 m with a standard deviation of 0.01 m. In forested terrain, the comparison was carried out by the comparison of multiple profiles along the slope because of the important filtering. Several profiles were acquired by total stations measurements in the field (Fig. 2) and compared to extracted profiles from the LiDAR DTM (Fig. 7): on these profiles, the average difference in *Z* is of 0.41 m with a standard deviation of 0.12 m.

3. Results

3.1. Identification and mapping of the main morphological features

A first geomorphological map was produced from field surveys (observations and positioning of significant points or topographical profiles by DGPS, etc...) and analysis of various existing documents [*Flageollet & Helluin*, 1984; 1987], postcards and ancient aerial oblique photographs, etc... The morphological mapping has been undertaken by extracting relevant information from an ortho-photograph of 2006 and a topographical map of 1976 (1/2000). The digitalization of contour lines (equidistance 1m) has been used to construct a DEM using an Inverse Distance Weighted (IDW) interpolation method.

The particular and complex morphology of the Villerville-Cricqueboeuf landslides consists in a succession of scarps and benches with counter slopes. The legend of the final map includes the following morphological key information relevant for hazard assessment. The main

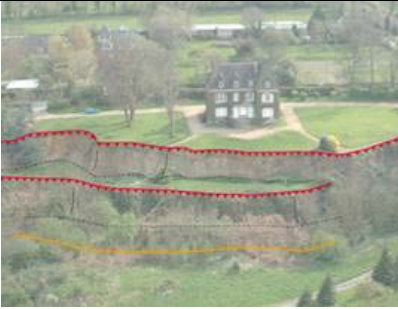







morphological features (Table 1) have been recognized in the field at some sub-areas within the landslide body. This field surveys allow to locate precisely the minor forms (not identifiable on the documents) such as tension cracks, open fractures with or without difference of level, minors scarps emerged after the last reactivation or non-visible on the orthophotograph due to vegetation cover.

3.2. Methodology for morphological mapping with the use of ALS data

The proposed methodology consists in successive steps:

- Qualification of the Digital Elevation Model (DEM) derived from LiDAR data interpolation; to define the altimetric and planimetric accuracy,
- Production of an hillshade map to visualize a pseudo relief map (with several illumination angles) and a slope orientation map,
- Extraction of the drainage network,
- Interpretation of the documents to map landslide features, with a digitization in a GIS.

Table 1: Landslide features to be extracted from the ALS point clouds.

Landslide feature	Photographs	Legend
<p>• <u>Scarps</u> This feature is sub divided into 3 classes (major, secondary and minor scarps)</p>		<p>Height of scarps</p> <ul style="list-style-type: none">  > 5 m Major scarp  [2-5] m Secondary scarp  < 2 m Minor scarp  Break of slope  Counter slopes
<p>• <u>Cracks and fissures</u> This feature is defined as the main opened cracks observed with or without any difference altitude in altitude.</p>		
<p>• <u>Counter slopes and talwegs</u> This feature is defined according to the surface hydrology (permanent or temporary flows, ponds, wetlands and poorly drained soils).</p>		

- Superficial slides and mudflows

This feature is defined according to presence of highly saturated areas at the surface, and the presence of recent lobes without any vegetation coverage.



Several shaded relief maps were interpolated to highlight the contour and the morphology of the landslides (Fig. 3).

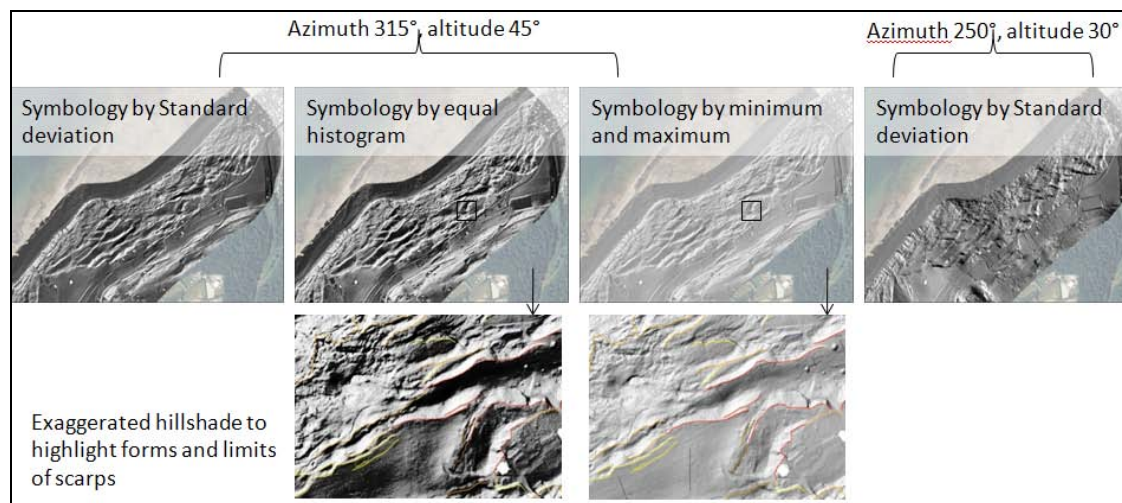


Figure 3: Example of different hillshade maps produced for the interpretation by considering different illumination angles.

3.3. Detailed geomorphological map at 1:500 scale

The LiDAR DTM allows to construct a detailed morphological map. On Figures 4 and 5, a comparison among a previous map produced at a lower scale with a contour line-interpolated DTM of 1976 illustrates the gain in detection of relevant surface features. If the major scarps were already mapped, the local morphology of the features were undetectable in some areas covered by dense shrub vegetation.

For instance, the ALS datasets allows to identify a succession of secondary scarps and to better discriminate the boundaries among the unstable and stable areas within the landslide (Fig. 5).

The ALS DTM allowed to locate minor geomorphological features resulting from the 'recent' activity of the landslide (Fig. 4, 5). The field observations have clarified some specific

questions such as the presence of opened fractures, but most of these detailed forms were not visible due to the particularly dense canopy which has been filtered with the HRI approach. The ALS DTM highlights the progressive 'decomposition' of the lower parts of the landslide in many different small slumps and panels (Fig. 11).

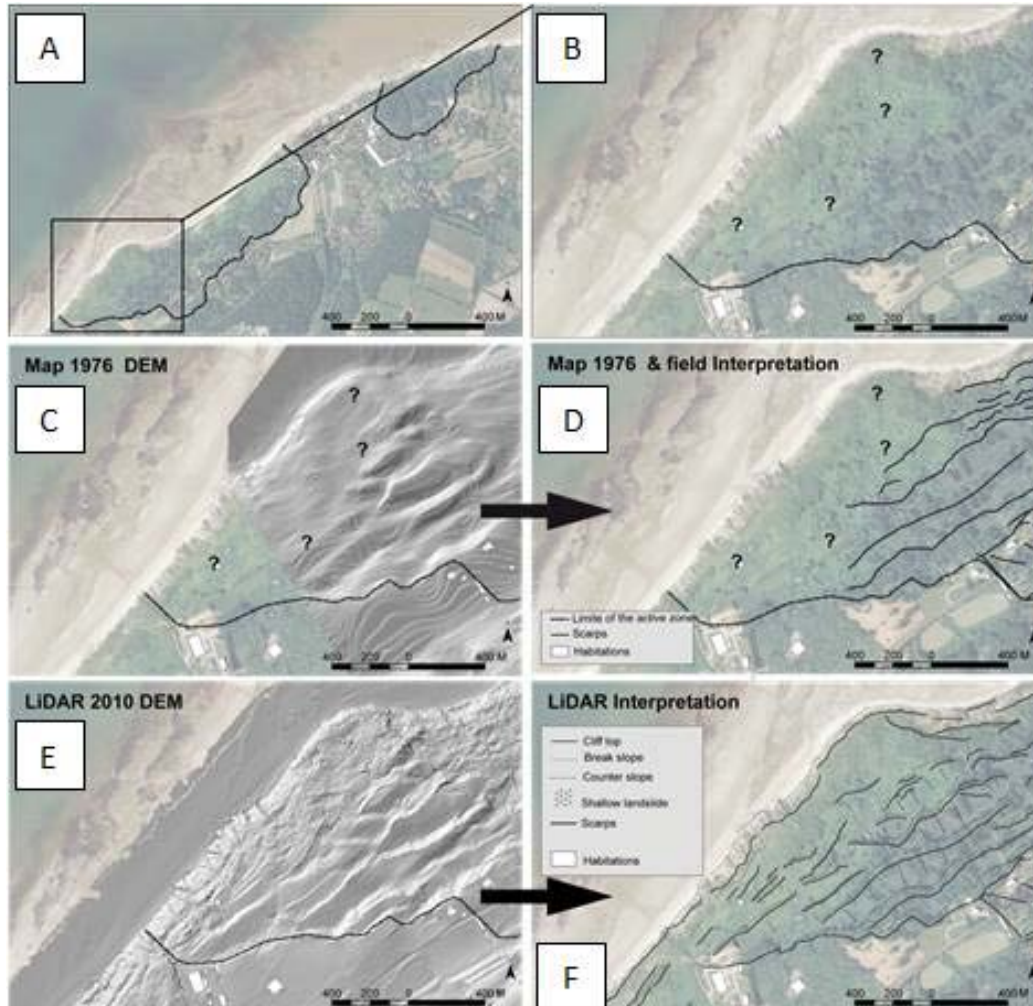


Figure 4: Comparison between the low resolution DTM from the morphological map of 1976 and the ALS-derived DTM in a forested area (Villerville landslide). A, B) Location of the landslide sub-areas with difficult interpretations; C) Extract of the low resolution DEM; D) Derived morphological interpretation from the 1976 map and field surveys to highlight the major morphological features with many unaccessible areas, E) ALS-derived DTM ; F) Interpretation of morphological features from the ALS data.

4. Discussion and Conclusion

In this study, we evaluated the suitability of using an ALS-derived DTM for mapping landslides and for identifying morphological features of landslides. The accuracy of the landslide DTM based on ALS data has been characterized, and a methodology using different sources of information and different visualisation techniques has been proposed to interpret the detailed landslide features. The vertical accuracy of the DTM is the open terrain id very

good (< 0.04 m) while it is 0.42 m in the ofrested terrain where a HRI filter has been used to filter the vegetation coverage.

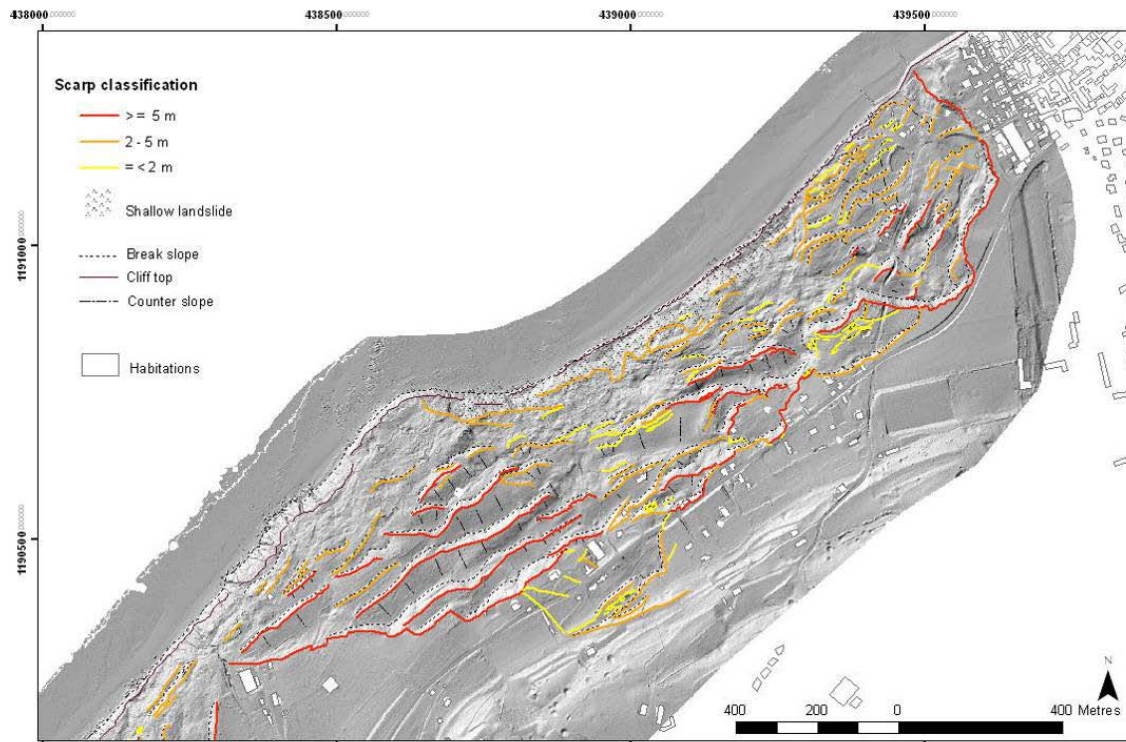


Figure 5: Main morphological features of the Villerville (Cirque des Graves) landslide

References

- Flageollet, J.-C., Helluin, E. 1984. Formations quaternaires et zonage des risques de glissements de terrain à Villerville et Cricqueboeuf (Calvados). In: *Actes du Colloque "Mouvements de terrain"*, Documents du BRGM, N° 83, Ed. BRGM, Orléans, pp. 41-46.
- Flageollet, J.-C., Helluin, E. 1987. Morphological investigations of the sliding areas along the coast of Pays d'Auge, near Villerville, Normandy, France. In: *Proceedings of the 1st International Conference on Geomorphology*, Vol. 1, pp. 477-486.
- Kraus, K., Pfeifer, N., 1998. Determination of terrain models in wooded areas with airborne laser scanner data. *ISPRS Journal of Photogrammetry and Remote-sensing* 53, 193-203.
- Maquaire, O. 2000. Effects of groundwater on the Villerville-Cricqueboeuf landslides. Sixteen years of survey (Calvados, France). In: Bromhead, E., Dixon, N., Ibsen, M.-L. (Eds.): *Landslides in Research, Theory and Practice. Proceedings of the 8th International Symposium on Landslides*, Cardiff, Wales, T. Telford, London, Vol. 2, pp. 1005-1010.
- Nichol, J.E., Shaker, A., Wong, M.S., 2006. Application of high-resolution stereo satellite images to detailed landslide hazard assessment. *Geomorphology* 76, 68-75.
- Pfeifer, N., Mandlbürger, G., 2009. LiDAR data filtering and DTM generation. In: Shan, J., Toth, C.K. (Eds.), *Topographic Laser Ranging and Scanning: Principles and Processing*. CRC / Taylor & Francis, pp. 307-333.
- Pfeifer, N., Stadler, P., Briese, C., 2001. Derivation of digital terrain models in the SCOP++ environment. OEEPE Workshop on Airborne Laser scanning and Interferometric SAR for detailed digital elevation models, Stockholm, Sweden.

Razak, K.A., Straatsma, M.W., van Westen, C.J., Malet, J.-P., de Jong, S.M. 2011. Airborne laser scanning of forested landslides characterization: terrain model quality and visualization. In: *Geomorphology : an international journal of pure and applied geomorphology*, 126 (2011)1-2 pp. 186-200.

SCOP++, 2008. The SCOP++ software manual, IPF, <http://www.inpho.de>/TU Vienna and INPHO GmbH, Germany.

Sekiguchi, T., Sato., H.P., 2004. Mapping of micro topography using airborne laser scanning. *Landslides* 3, 195-202.

Vallet J, Skaloud J 2004 Development and experiences with a fully-digital handheld mapping system operated from a helicopter. In: *The International Archives of the Photogrammetry, Remote-sensing and Spatial Information Sciences*, Istanbul, Vol. XXXV, Part B5.

Landslide Volumetric Analysis Using Cartosat-1-Derived DEMs

Application: Landslide volume estimation

Technique: Stereophotogrammetry from passive optical spaceborne sensors

Main references: Martha, T. R., Kerle, N., Jetten, V., van Westen, C.J. and Vinod Kumar, K. (2010): Landslide Volumetric Analysis Using Cartosat-1-Derived DEMs

Contributors: ITC (T. Martha, N. Kerle, C.J. van Westen)

Abstract

Monitoring of landscape changes can lead to the identification of environmental hotspots, improved process understanding, and provide means for law enforcement. Digital elevation models (DEMs) derived from stereoscopic satellite data provide a systematic, synoptic framework potentially useful to support these issues. Along-track high resolution stereoscopic data, provided with rational polynomial co-efficients (RPC), are ideal for fast and accurate extraction of DEMs due to reduced radiometric difference between images. In this study, we assess the suitability of data from the relatively new Cartosat-1 satellite to quantify large-scale geomorphological changes, using volume estimation of the 2007 Salna landslide in the Indian Himalayas as a test case. The depletion and accumulation volumes, estimated as $0.55 \times 10^6 \text{ m}^3$ and $1.43 \times 10^6 \text{ m}^3$, respectively, showed good match with the volumes calculated using DEMs generated from manually extracted spot height data, also for DEMs generated only with RPCs and without GPS points. The result showed that these data can provide an important input for disaster management activities.

Keywords: Volume estimation, Cartosat-1, landslide, disaster management

1. Introduction

Volumetric analysis has the potential to monitor and quantify also large-scale events, and can be useful in implementing proper risk management strategies or to enforce environmental regulations. For example, reliable information on material volume can help government agencies to estimate the value of contract and number of days required to clear the debris from transportation routes in case of a landslide [Jaiswal and van Westen, 2009], or the amount of material required to reclaim the land in case of open-pit mining as a mandatory requirement under a mine control act [Townsend et al. 2009]. In the past such assessments have typically been done through time-consuming field measurements, although those tend to suffer from difficulties in establishing accurate baseline topography. Photogrammetric techniques have been increasingly used because of their capability to rapidly reconstruct the 3D topography from aerial photographs [Kerle 2002; Dewitte and Demoulin 2005; Kääh 2002] and, provided such data exist for different time periods, allow objective change detection. More recently, civilian Earth observation satellites have offered stereoscopic data with sufficient spatial resolution to allow aerial data to be effectively replaced [Tsutsui et al. 2007; Radhika et al. 2007; Martha et al. 2010; Zhang and Gruen 2006]. In addition, new generation satellites such as Cartosat-1 have considerable advantages over airborne stereo imagery, due to their high periodicity, synoptic view, high data quality, relatively low cost, and quick extraction of digital surface models (DSM) using rational function models (RFM) [Martha et al. 2010; Baltsavias et al. 2008].

Cartosat-1, launched by Indian Space Research Organisation (ISRO) in 2005, is a global mission planned for cartographic mapping, urban studies and disaster management [NSRC]. It carries two cameras, PAN-aft and PAN-fore with -5° and $+26^\circ$ viewing angles, respectively, acquiring images of a 900 km^2 area ($12\,000 \times 12\,000$ pixels) with a gap of 52 seconds. The ground sampling distance of Cartosat-1 is 2.5 m, and the base to height (B/H) ratio is 0.62. Detailed specifications of Cartosat-1 are provided in NSRC. Data from Cartosat-1 are 10 bits and provided with rational polynomial co-efficients (RPCs) for photogrammetric processing and extraction of 3D information using RFM. In principle, therefore, Cartosat-1 data are well suited for fast and accurate 3D surface reconstruction, although in practice there can be potential problems due to shadow, occlusion and steep slopes depending on the terrain [Martha et al. 2010; Baltasvias et al. 2008]. With Cartosat-1 acquiring along-track data, image matching is less problematic than for across-track images due to reduced radiometric variation between the two images of a stereo pair [Radhika et al. 2007]; however, factors such as valley orientation, sun elevation angle and poor texture frequently hinder accurate extraction of elevation data [Martha et al. 2010]. We addressed some of these problems through SAT-PP photogrammetric software, especially developed for high resolution satellite data and which previously demonstrated the ability to process such stereoscopic data due to its superior image matching algorithm [Zhang and Gruen 2006], compared to other commercial off-the-shelf (COTS) software types [Martha et al. 2010].

In this study we tested the utility of Cartosat-1 data for quantitative volume analysis based on cut and fill assessment, an established method for estimating the volume of large landslides [Kerle 2002; Tsutsui et al. 2007; Chen et al. 2005]. We used the 2007 Salna landslide in the Indian Himalayas as a test case, which offers a great challenge to automatic DEM extraction due to steep slopes and large topographic shadows [Martha et al. 2010]. Previous studies have demonstrated the utility of DEMs extracted from satellite data for monitoring topographic changes due to glacial melting [Surazakov and Aizen 2006; Käab 2002], landslides [Tsutsui et al. 2007], and rehabilitation planning of coal mining areas [Loczy et al. 2007]. The purpose of this paper is to assess if Cartosat-1 derived DEMs are sufficiently accurate to quantify such changes and to monitor compliance with related legislation.

1.1. Landslide Volume Estimation for landslide hazard assessment

Some of the major earthquakes that have created several deep-seated landslides in the recent past are the Kashmir earthquake in India and Pakistan in October 2005 and the Sichuan earthquake in China in May 2008. Apart from direct damage landslides also contribute sediments to river systems and create siltation problems in reservoirs, reducing their capacity for hydro power generation. They also have the potential to create artificial lakes by blocking river courses, thus generating potential flash floods in down-stream areas [Dunning et al. 2007; Wang et al. 2009]. Knowledge of failure volumes is also critical for more accurate understanding of the landslide process [Scott et al. 2005] and the preparation of susceptibility maps, which show potential areas of future landslide occurrences. For example, landslide

susceptibility maps will be more accurate if volume, instead of area of the landslide, is used to calculate weights of the terrain parameters. *Okura et al.* [2003] showed how the volume of a landslide directly affects its travel distance, while *Dai and Lee* [2001] demonstrated that frequency-volume relationships can be used to predict rainfall induced landslides. Traditionally, failure volumes have been estimated by measuring landslide dimensions (length, width and depth) on the ground, using assumptions about the shape of the landslide [*Cruden and Varnes* 1996]. Such ground-based methods may provide accurate volume figures, though are time-consuming, error-prone and at times not possible due to terrain inaccessibility. Pre- and post-failure topographic maps can also be used for calculating the landslide volume using change detection techniques. However, topographic maps are typically not updated immediately after the event, or lack sufficient accuracy [*Kerle* 2002]. In order to overcome these problems, stereophotogrammetry with multi-temporal satellite images and aerial photographs provide a feasible solution to estimate landslide extents and volumes.

2. Test area

The test area is located in one of the landslide prone areas in the Himalayas. Its centre coordinates are 30° 23' 38" N and 79° 12' 42" E. It is located in the Nagol Gad (River) sub-catchment in the High Himalayas in the Uttarakhand state of India (Fig. 1). Nagol Gad is a part of Alaknanda catchment, which witnessed several major co-seismic landslides during the Chamoli earthquake in March 1999 and it lies very close to the main central thrust [*Barnard et al.* 2001]. Rocks exposed in this area are banded quartzite on the crown, and quartzite interbedded with mica schist at the toe of the landslide. However, the landslide investigated for this volumetric analysis was triggered by heavy rainfall in July 2007. It occurred near the Salna village in the Chamoli district of Uttarakhand state. The landslide-affected area is completely exposed to sun in both pre- and post-landslide images (Fig. 2a and 2b). The general topography is steep, with slopes ranging from 18° to 63°. The elevations of the crown and tip of the landslide are 1636 m and 1261 m, respectively. The Salna landslide is a translational rock slide, which means that the failure has taken place along a planar surface of rupture. Its length (crown to tip) is 530 m, with a maximum width at the centre of the landslide of 260 m (Fig. 1a). Although there were no fatalities, the major road connecting the surrounding area with Chamoli town was blocked for several months, causing hardship to local population and damage to the regional economy.

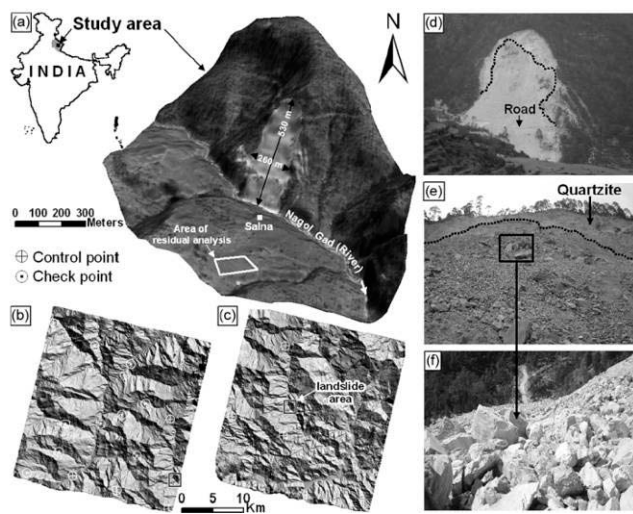


Figure 1: Location map of the study area. (a) Three-dimensional perspective view of the Salna landslide with the Cartosat-1 image draped over a DEM, (b) and (c) pre- and post-landslide DEMs, respectively, showing the distribution of control and check points, (d) field photograph showing the synoptic view of the landslide, (e) view of the quartzite bedrock exposed in (the area above the black dotted line) the scarp, and a part of the zone of accumulation as seen from the temporarily constructed road, and (f) large angular boulders with large voids in between, signaling a volume increase during deposition.

3. Methods

3.1. DEM Generation

Two sets of stereoscopic Cartosat-1 data, acquired on 06 April 2006 (pre-landslide) and 16 December 2007 (post-landslide), were processed using SAT-PP software. Compared to established COTS photogrammetric packages, SAT-PP has an improved image matching algorithm based on combined matching results of feature points, grid points and edges, leading to superior results also in steep terrain [Zhang and Gruen 2006]. Digital surface models (DSMs) with 10 m grid size were generated using RPCs determined from the RFM and provided by the data vendor. RFM is a generic sensor model and is used as an alternative to physical sensor models for block orientation of the stereo-image pair. RPCs are terrain independent, and require refinement with ground control points (GCPs) at block level to increase the absolute geo-location accuracy of DSMs [Baltsavias *et al.* 2008]. Therefore, we used six GCPs with good planimetric and vertical distribution to refine the orientation result of the RFM (Fig. 1b) [Baltsavias *et al.* 2008]. The GCPs were collected in a differential GPS (DGPS) survey using a dual frequency (L1 and L2) Leica 520 receiver. The standard deviation of the errors of elevation, longitude and latitude of the points surveyed range between 0.10 m to 0.46 m, 0.04 m to 0.15 m and 0.04 m to 0.21 m, respectively.

The necessity of high DEM accuracy for an elevation change analysis has been emphasized by previous researchers [Kerle 2002], [Van Niel *et al.* 2008]. Kerle [2002] showed how especially the combination of errors in the vertical accuracy of photogrammetrically derived DEMs and the landslide thickness typically being the smallest dimension readily combine to substantial uncertainty. Errors in elevation difference can either result from mis-registration of the pre- and post-event DEMs [Van Niel *et al.* 2008], or from low spatial accuracy resulting from sun illumination and valley orientation with reference to the satellite track [Martha *et al.*

2010]. Along-track satellite data such as Cartosat-1 offer improved results of image matching due to reduced radiometric variation between images of a stereo pair [Radhika *et al.* 2007]. However, distortion of feature geometry due to steep terrain and variable viewing angle of Cartosat-1 has compromised some of these advantages. This problem can be overcome using SAT-PP software, which relies on a robust point, grid and feature based image matching technique [Zhang and Gruen 2006]. Topographic shadow in mountainous area is another problem that creates inaccuracies in a DEM. SAT-PP is also capable of generating the adequate number of match points required for an accurate DEM generation for relatively small shadow areas; however, large shadows still remain a problem [Martha *et al.* 2010; Zhang and Gruen 2006].

In an earlier study we assessed the absolute accuracy of the pre-landslide DEM using 10 independent check points obtained from the DGPS survey, resulting in vertical and planimetric root mean square error (RMSE) as 2.31 m and < one meter, respectively [Martha *et al.* 2010]. In addition, spatial accuracy of the pre-landslide DEM was estimated by a drainage line comparison method, wherein drainage lines were used as a proxy to estimate the error due to spatial auto-correlation in the absence of a very accurate reference DEM [Martha *et al.* 2010]. Subsequently, refinement of the orientation result of post-landslide RFM was done by using three GCPs common in the overlap area (Fig. 1c). Thus, both the DEMs are brought to the same spatial framework. However, to verify the vertical and co-registration accuracies of two DEMs, a residual analysis was carried out between the two DEMs in an area adjacent to the landslide (Fig. 1a). This area is unvegetated and no morphological changes have occurred during the observation period. The residual analysis shows a vertical mean and standard deviation of errors as 0.11 m and 0.06 m, and the same errors for planimetry as 0.09 m and 0.05 m, respectively. The low error indicates that both DEMs are co-registered properly and have a good vertical accuracy relative to each other. Therefore, any change in height can be attributed to morphological changes such as occurrence of landslides, and subsequently the volume can be calculated.

3.2. Volumetric analysis

As volume calculation must be based on the actual pre- and post-landslide terrain surfaces, vegetation that may have covered the area before failure, or that was possibly retained during the landslide, must be corrected for, as it forms part of the photogrammetric surfaces. Accurate estimation of vegetation height has previously been shown to be challenging [Kerle 2002]. In the area of the Salna landslide mainly chir trees, a pine variety typical in the Himalayas, are found. The height of some of the uprooted and standing trees (in the adjacent area) was measured on the ground. This height, in conjunction with the height of the trees measured through manual interpretation of stereo images was used to create a non-uniform vegetation height surface (Fig. 2d). Total 74 trees (7 from ground and 67 from stereo image) with an 11.87 m mean height, and 19.67 m and 4.29 m as maximum and minimum heights, respectively were used for the creation of the vegetation height surface. Subsequently, this

surface was subtracted from the automatically generated pre-failure DSM, and a vegetation-corrected 10 m digital terrain model (DTM) was created. Vegetation correction was not required for the post-failure DSM since trees were completely uprooted. After vegetation correction area and volume of the Salna landslide were calculated by subtracting the post-landslide DTM from the pre-landslide DTM, using the cut and fill operation in ArcGIS. This operation summarizes areas and volumes of change using surfaces of a given location at two different time periods, and identifies regions of surface material removal, addition and no change.

4. Results and Discussion

The Salna landslide was triggered due to excessive rainfall, and the pre-landslide Cartosat-1 image already showed the existence of small active landslides in that area (Fig. 2a). The slope length of the main scarp below the crown of the landslide is approximately 50 m (Fig. 2c). This landslide completely buried the road with material displaced from the crown part. The new road (Fig. 1b), which was temporarily constructed to allow traffic to resume is now positioned 62 m outward from its previous location, and the shape of the road is convex outward (Fig. 2d), indicating the deposition of a large amount of material and development of a hummocky structure. Similarly, the Nagol Gad (River) was pushed 25 m to its right bank by the landslide (Fig. 2d).

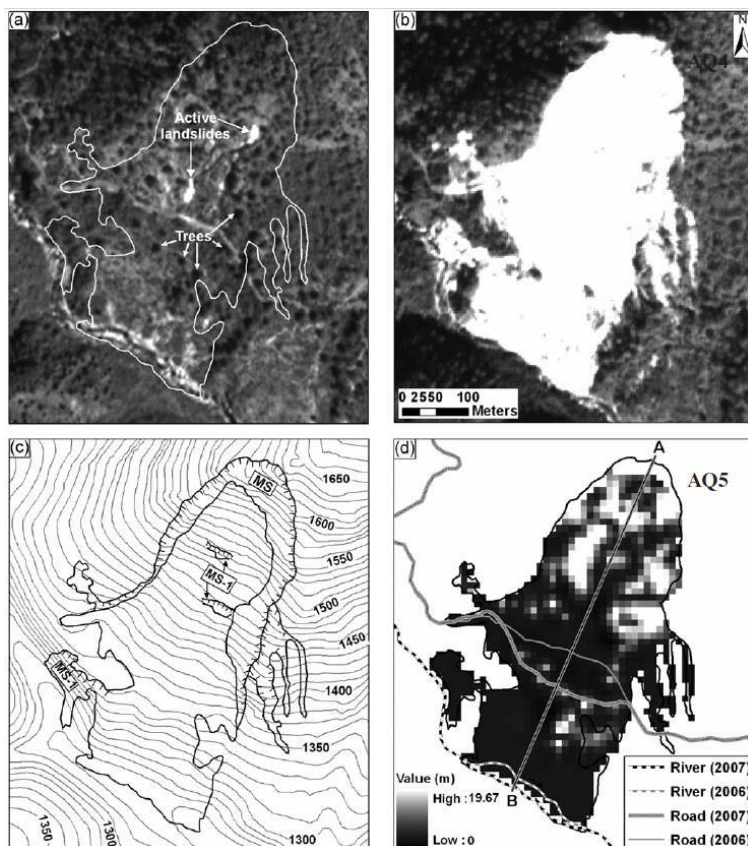


Figure 2: Salna landslide. (a) Cartosat-1 orthoimage of April 6, 2006, showing the prelandslide area outlined in white. It was a distressed zone with the presence of two minor landslides acting as a precursor to the main event. (b) Cartosat-1 orthoimage of December 16, 2007, showing the landslide that occurred in July 2007. (c) Post-landslide map showing the (MS) main scarp and (MS-1) minor scarps. (d) Non-uniform vegetation-height surface created by the interpolation of heights measured from 74 trees and post-landslide effects. The new road now has a convex outward shape, and the original river was pushed outward due to the deposition of debris at the foothill region. The profile along A–B is shown in Fig. 3.

Fortunately, no damming of the river occurred due to the landslide. Debris mainly composed of boulders of banded quartzite is seen in the zone of accumulation (Figs.1c and 1d). From the profile (Fig. 3) and from the extent of the volume gain (Fig. 4b) it is clear that the area of the zone of depletion is less than the area of the zone of accumulation, indicating expansion, or bulking, of material after the displacement due to fragmentation of the bed rock.

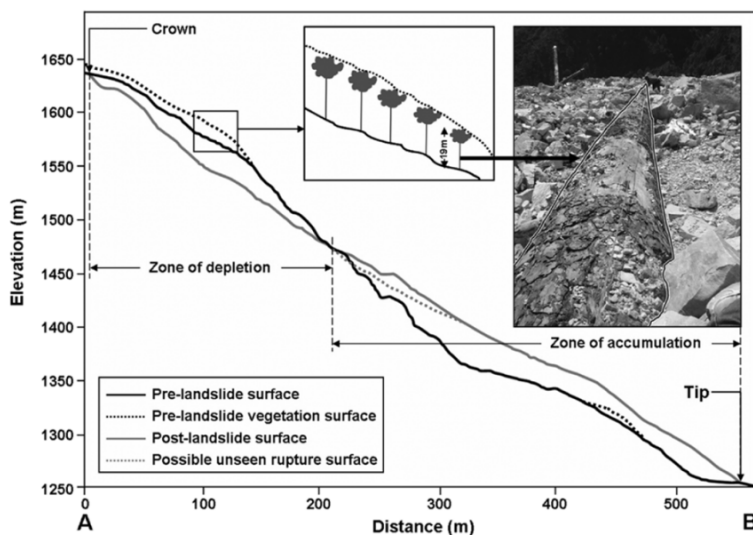


Figure 3: Pre- and post-failure surface profile from the crown to tip of the landslide. The gray dotted line shows the possible extension of the surface of rupture over which debris is temporarily deposited. The heights of some of the chir pine trees were measured on the ground (e.g., an uprooted tree in the inset photograph).

The elevation change map shows that maximum deposition of material has taken place at a height of approximately 1420 m (Fig. 4a). The cut and fill volumes, i.e. the volumes of depleted and accumulated material, were estimated as $0.55 \times 10^6 \text{ m}^3$ and $1.43 \times 10^6 \text{ m}^3$, respectively (Table I). Also, the area of the zone of depletion is smaller than the area of zone of accumulation, due to lateral spreading of the broken rock fragments (Fig. 4b).

So far, we have estimated the landslide volume from DEMs derived with the use of additional GCPs. However, the need for field-measured control points severely undermines the utility of satellite data for rapid and independent post-landslide assessment. To assess the dependency of accurate volume estimation on additional field-mapped GCPs, we also created DEMs only with the RPCs provided with Cartosat-1 data. Such a step is reasonable, as additional GCPs primarily affect the absolute accuracy of the DEM, and less the relative elevation value distribution. Nevertheless, the effect of integrating two such relative surfaces for accurate change assessment was unknown. Table I shows that the estimated volume values based on RPC-only DEMs fall to within 1–3% of the GCP-supported DEM values, indicating that the volume figures are less sensitive to GCPs support than expected.

The bulking factor (ratio of volume gain to volume loss) of 2.60 (Table I) is comparable to previously reported values for similar events, such as the bulking following the flank collapse of Casita volcano, Nicaragua studied by Scott *et al.* [2005]. The bulking of Salna landslide is due to two factors: 1) incomplete separation of loss area from gain area, due to which material is still lying at the bottom of the hidden rupture surface [van Westen and Getahun 2003], which is impossible to be constructed from post-failure stereo data (Fig. 3); and 2) poor

sorting of large and angular broken quartzite rock fragments (Fig. 1d) created by the translational rock slide, leading to a possible overestimation of the gain volume. However, the estimated volume can be considered realistic, since the post-landslide surface was generated shortly (approximately five months) after the occurrence of the landslide, suggesting limited deposition material loss due to surface erosion and further remobilization.

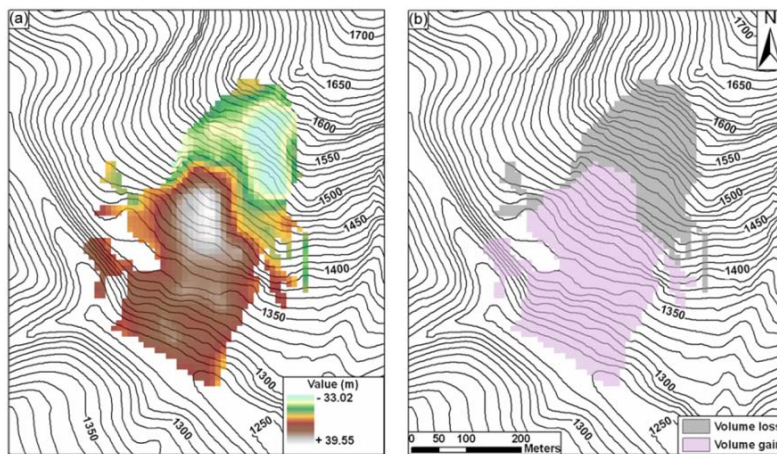


Figure 4: Volumetric analysis of the Salna landslide. (a) Elevation difference due to landslide with negative values showing the lowering of surface and positive values showing the rising of the surface after the event. (b) Extent of the volume loss and volume gain, which corresponds to the zones of depletion and accumulation, respectively.

4.1. Accuracy assessment of volume

The global accuracy of the DEM has been verified by independent check points. Assessment of accuracy of volume is a challenge, particularly with only limited reference data, i.e. without a dense network of ground check points for both pre- and post-landslide affected area. Due to the absence of detailed verification data for the relatively small landslide area (i.e. part of the large DEMs for which accuracy has been checked), we manually extracted spot heights [Kerle 2002], identifying 85 and 129 points from the pre- and post-failure datasets, respectively, using StereoAnalyst in ERDAS Imagine, and compared the volume obtained from spot height data with the automatic results (Table I). The number of points is sufficient for a reliable comparison since they were collected with particular emphasis on break-in-slope and scarp areas, leading to a surface that models the actual failure area well. Spot heights from the pre-failure image were collected by selectively measuring ground elevations in between trees, thus eliminating the need for further vegetation correction, and directly on the failure and deposition surfaces in the post-failure image. These points were interpolated using the TOPOGRID algorithm in ArcGIS to derive reference DTMs [Wise 2007].

Table 1: Quantitative comparison of volumes

DEM type	Volume loss (10^6 m^3)		Volume gain (10^6 m^3)		Bulking
	Before vegetation correction	After vegetation correction	Before vegetation correction	After vegetation correction	
DEM (with GCP)	0.77	0.55	1.34	1.43	2.60
DEM (without GCP)	0.76	0.54	1.31	1.41	2.61
DTM (spot height)	0.67		1.26		1.88

5. Conclusion

Updated elevation data are essential for identifying areas of large-scale topographic changes for disaster management or enforcement of environmental legislation. The purpose of this study was to assess the potential of a new generation of space borne sensors to provide DEMs for the quantification of landscape changes. In this study, DEMs with 10 m grid size corresponding to two different time periods, generated from Cartosat-1 data using digital photogrammetric methods, were used to quantify large-scale topographic changes resulting from a landslide. Following photogrammetric conventions, we generated DEMs with a grid size equivalent to 3–4 times of the ground sampling distance. With some data types, such as from SPOT5, higher resolutions can be achieved, for example the 2.5 m resolution DEMs produced by *Tsutsui et al.* [2007], using super resolution processing [*Latry and Rouge 2003*]. Interestingly, the previously reported requirement for additional GCPs [*Baltsavius et al. 2008*] was found to be of lesser importance, allowing us to create surfaces with comparable relative accuracy also without such field-based measurements. This requires actual co-registration of pre- and post-failure DSMs rather than use of absolute coordinates. This means that RPCs alone are sufficient for the estimation of volume, thus freeing rapid post-failure volume assessment entirely from field data requirements, although refinement of the RFM orientation result is required to improve the absolute geo-location accuracy necessary for cartographic applications. Knowledge on pre-failure topography is crucial for accurate estimation of volume [*Kerle 2002*]. Cartosat-1 was launched in 2005, and its data were systematically acquired, providing substantial archives of images for major parts of the world. Availability of post-failure datasets from Cartosat-1 shortly after the event then enabled us to do rapid volume estimation. The cut and fill volumes derived from automatic DEMs showed reasonably good match with the reference volume derived from DEMs generated using manually extracted spot height data. This indicates that a 10 m DEM from Cartosat-1 data can be effectively used for large scale elevation change and volumetric analysis such as for a deep-seated landslide. The information on landslide volume can effectively be used to establish magnitude-frequency relationship for quantitative estimation of landslide hazard. However, the volume values calculated based on manually extracted spot heights shows deviations of about +17% and -12% for the volume loss and gain areas, respectively, resulting

also in a bulking factor that is 27% lower than based on automatic DEMs with GCPs. This indicates that where vegetation cover is not uniform, as was the case at Salna, instead of a constant vegetation elevation surface to correct pre- and post-failure DSMs it is preferable to construct a more accurate vegetation layer based on multiple evidence, such as the tree trunk length measured in the field, but also extrapolation from the height of trees left standing in adjacent areas.

This study showed that Cartosat-1 data have the potential to derive volume information critical for disaster assessment, in principle without any additional GPS field measurement, provided that any present vegetation artifacts are removed from the DEMs used in the change assessment. It must also be noted that, with landslide thickness, i.e. z , typically being the smallest dimension, elevation errors resulting from photogrammetric artifacts or inaccurate DSM-to-DTM correction will have a correspondingly large consequence on volume calculations. Quantitative estimation of similar large-scale changes in the landscape, due to open-pit mining and urban waste disposal, although not shown in this study, can in principle also be done with Cartosat-1 derived DEMs since they require multi-temporal DEMs similar to the ones used in this study.

References

- Baltsavias, E., Kocaman, S., Wolff, K. 2008. Analysis of Cartosat-1 images regarding image quality, 3D point measurement and DSM generation, *The Photogrammetric Record*, vol. 23, no. 123, pp. 305-322.
- Barnard, P.L., Owen, L.A., Sharma, M.C., Finkel, R.C. 2001. Natural and human-induced landsliding in the Garhwal Himalaya of northern India, *Geomorphology*, vol. 40, no. 1-2, pp. 21-35, 2001/9.
- Chen, R.-F., Chan, Y.-C., Angelier, J., Hu, J.-C., Huang, C., Chang, K.J., Shih, T.-Y. 2005. Large earthquake-triggered landslides and mountain belt erosion: The Tsaoling case, Taiwan. *Comptes Rendus Geosciences*, vol. 337, no. 13, pp. 1164-1172.
- Cruden, D., Varnes, D.J. 1996. Landslide types and processes, *Landslides Investigation and Mitigation. Special Report 247*, A. K. Turner and R. L. Schuster, eds., pp. 36-75, Washington D.C.: Transportation Research Board, National Academy of Sciences.
- Dai, F.C., Lee, C.F., 2001. Frequency-volume relation and prediction of rainfall-induced landslides," *Engineering Geology*, vol. 59, no. 3-4, pp. 253-266.
- Dewitte, O., Demoulin, A. 2005. Morphometry and kinematics of landslides inferred from precise DTMs in West Belgium. *Natural Hazards and Earth System Sciences*, vol. 5, no. 2, pp. 259-265, 2005.
- Dunning, S.A., Mitchell, W.A., Rosser, N.J., Petley, D.N. 2007. The Hattian Bala rock avalanche and associated landslides triggered by the Kashmir Earthquake of 8 October 2005. *Engineering Geology*, vol. 93, no. 3-4, pp. 130-144.
- Jaiswal, P., van Westen, C.J. 2009. Estimating temporal probability for landslide initiation along transportation routes based on rainfall thresholds. *Geomorphology*, vol. 112, no. 1-2, pp. 96-105.
- Kääb, A. 2002. Monitoring high-mountain terrain deformation from repeated air- and spaceborne optical data: examples using digital aerial imagery and ASTER data. *ISPRS Journal of Photogrammetry and Remote-sensing*, vol. 57, no. 1-2, pp. 39-52, 2002/11.
- Kerle, N. 2002. Volume estimation of the 1998 flank collapse at Casita volcano, Nicaragua: A comparison of photogrammetric and conventional techniques, *Earth Surface Processes and Landforms*, vol. 27, no. 7, pp. 759-772.
- Latry, C., Rouge, B. 2003. Super resolution: quincunx sampling and fusion processing. In: *Geoscience and Remote-sensing Symposium*, pp. 315-317.
- Loczy, D., Czigany, S., Dezso, J., Gyenizse, P., Kovacs, J., Nagyvaradi, L., Pirkhoffer, E. 2007. Geomorphological tasks in planning the rehabilitation of coal mining areas at Pecs, Hungary. *Geografia Fisica E Dinamica Quaternaria*, vol. 30, no. 2, pp. 203-207.
- Martha, T.R., Kerle, N., van Westen, C.J., Jetten, V., Vinod Kumar, K. 2010. Effect of sun elevation angle on DSMs derived from Cartosat-1 data. *Photogrammetric Engineering and Remote-sensing*.

- NRSC. Cartosat-1 data user's handbook, http://www.nrsc.gov.in/IRS_Documents/Handbook/cartosat1.pdf.
- Okura, Y., Kitahara, H., Kawanami, A., Kurokawa, U. 2003. Topography and volume effects on travel distance of surface failure. *Engineering Geology*, vol. 67, no. 3-4, pp. 243-254, 2003/1.
- Radhika, V.N., Kartikeyan, B., Gopala Krishna, B., Chowdhury, S., P.K., S. 2007. Robust Stereo Image Matching for Spaceborne Imagery," *IEEE Transactions on Geoscience and Remote-sensing*, vol. 45, no. 9, pp. 2993-3000.
- Scott, K.M., Vallance, J.W., Kerle, N., Macías, J.L., Strauch, W., Devoli, G., 2005. Catastrophic precipitation-triggered lahar at Casita volcano, Nicaragua: occurrence, bulking and transformation. *Earth Surface Processes Landforms*, vol. 30, pp. 59-79,
- Surazakov, A.B., Aizen, V.B. 2006. Estimating volume change of mountain glaciers using SRTM and map-based topographic data. *IEEE Transactions on Geoscience and Remote-sensing*, vol. 44, no. 10, pp. 2991-2995.
- Townsend, P.A., Helmers, D.P., Kingdon, C.C., McNeil, B.E., de Beurs, K.M., Eshleman, K.N. 2009. Changes in the extent of surface mining and reclamation in the Central Appalachians detected using a 1976-2006 Landsat time series. *Remote-Sensing of Environment*, vol. 113, no. 1, pp. 62-72, 2009.
- Tsutsui, K., Rokugawa, S., Nakagawa, H., Miyazaki, S., Cheng, C.T., Shiraishi, T., Yang, S.D. 2007. Detection and volume estimation of large-scale landslides based on elevation-change analysis using DEMs extracted from high-resolution satellite stereo imagery. *IEEE Transactions on Geoscience and Remote-sensing*, vol. 45, no. 6, pp. 1681-1696.
- Van Niel, T.G., McVicar, T.R., Li, L., Gallant, J.C., Yang, Q. 2008. The impact of misregistration on SRTM and DEM image differences, *Remote-Sensing of Environment*, vol. 112, no. 5, pp. 2430-2442.
- van Westen, C.J., Lulie Getahun, F. 2003. Analyzing the evolution of the Tessina landslide using aerial photographs and digital elevation models. *Geomorphology*, vol. 54, no. 1-2, pp. 77-89, 2003/8/15.
- Wang, F., Cheng, Q., Highland, L., Miyajima, M., Wang, M., Yan, C. 2009. Preliminary investigation of some large landslides triggered by the 2008 Wenchuan earthquake, Sichuan Province, China. *Landslides*, vol. 6, no. 1, pp. 47-54.
- Wise, S.M. 2007. Effect of differing DEM creation methods on the results from a hydrological model. *Computers and Geosciences*, vol. 33, pp. 1351-1365.
- Zhang, L., Gruen, A. 2006. Multi-image matching for DSM generation from IKONOS imagery. *ISPRS Journal of Photogrammetry and Remote-Sensing*, vol. 60, no. 3, pp. 195-211.

Image correlation of TLS (Terrestrial Laser Scanning) data for landslide monitoring

Application: Landslide monitoring

Technique: Passive ground-based sensors

Main references: Travelletti, J., Delacourt, C., Malet, J.-P. (in review): Multi-date correlation of Terrestrial Laser Scanning data for the characterization of landslide kinematics.

Contributors: CNRS (J. Travelletti, C. Delacourt, J.-P. Malet)

Abstract

This work presents a simple method to obtain 3D deformation and displacement maps from repeated TLS acquisitions by taking full advantage of the geometric information available in consecutive point clouds. The performance of the method is tested on TLS datasets acquired at the toe of the Super-Sauze landslide (South French Alps) from October 2007 to May 2010.

The method is based on the simplification of a 3D matching problem in a 2D matching problem by using a 2D statistical normalized cross correlation function. The point clouds are first filtered from vegetation and co-registered in a common local coordinate system by aligning the TLS acquisitions on stable parts in the surrounding of the landslide. A perspective projection is then applied to project and interpolate the 3D point clouds on a 2D regular grid perpendicular to the viewing direction. In order to emphasize the relief morphology projected in the 2D grid, the 2D gradient of the distance separating the point clouds from the TLS location is computed and then correlated. Then, a re-projection of the correlated displacements in the 3D local coordinate system allows to reproduce the 3D displacement field and to compute the strain field.

The results indicate that amplitudes of displacement smaller than the spatial resolution of the TLS point clouds are detectable with low noise data. Comparisons with the 3D amplitudes of displacement computed (1) with the Iterative Closest Point algorithm and (2) with DGPS observations of benchmarks indicate an average accuracy of the method of 4 cm.

Keywords: terrestrial laser scanning, point clouds, image correlation, landslide, displacement monitoring

1. Introduction

In the last few years, automatic matching algorithms applicable to Terrestrial Laser Scanning (TLS) data have started to be developed because of their capability to fully exploit all the geometric information available in the point clouds. The objective of these techniques is to find correspondences among typical features or objects located in multi-temporal point clouds assuming that the tracked object has a constant geometry in time and/or a perfectly rigid behaviour. The Iterative Closest Point method [ICP; *Besl and McKay*, 1992] and the Least Squares 3D Surface Matching methods [LSSM, *Gruen and Akca*, 2005] are among the most used algorithms for the automatic characterization of 3D displacement fields. Their application to landslide monitoring has been demonstrated by *Teza et al.* (2008), *Monserrat and Crosetto* [2008] and *Oppikofer et al.* [2009]. *Teza et al.* [2007] presented an automatic calculation method using an ICP-based piecewise alignment method. In addition to sensor-based technical limitations (instrumental errors, point resolution, laser beam divergence), they pointed out the problem of three limiting factors affecting the calculation of the displacements, such as the presence of shadow zones (unscanned areas), important soil

deformation and growth of vegetation.

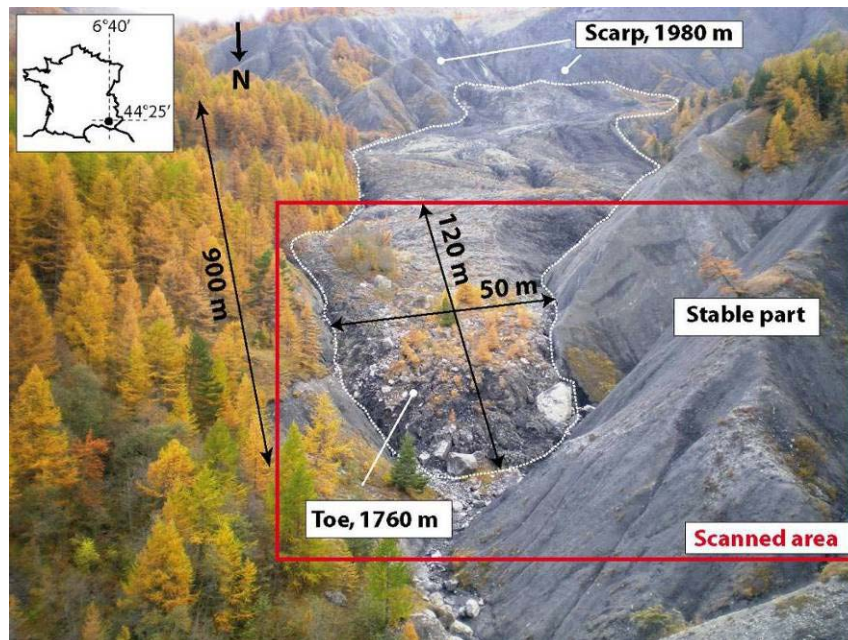


Figure 1: View of the Super-Sauze landslide from the TLS base station. The picture (18 Oct. 2008) corresponds to the plan perpendicular to the viewing direction of the laser scan. The toe of the landslide and the stable part are included in the scanned area.

The objective of this work is to propose a simple method to measure the 3D displacement field of a slow-moving clayey landslide, and derive displacement and deformation maps from repeated TLS acquisitions. The method is based on the application of a normalized cross-correlation function in order to exploit the complete geometrical information available in the point clouds. The hypothesis is that for objects scanned from a unique view point, simple 2D correlation functions (largely used in digital photogrammetry analyses) can be applied on multi-temporal point clouds and yield the same range of accuracy than complex and time-consuming 3D Surface Matching algorithms. Numerous examples demonstrated the efficiency of such type of statistical function to detect the displacement field of landslides from satellite and aerial optical images [Casson *et al.*, 2003; Delacourt *et al.*, 2004; LePrince *et al.*, 2008], but only a few work has been carried out to apply this approach to TLS point clouds [Travelletti *et al.*, 2008; Schwalbe *et al.*, 2008].

The performance of the method is tested on datasets acquired at the toe of the Super-Sauze mudslide (South French Alps) over a period of three years (October 2007 - May 2010). First, the principles of the method are presented. Second, the application to the landslide dataset is detailed and the performance is evaluated among other measures of displacement. Finally, a strain analysis is applied in order to define the deformation and displacement regime of the landslide, and identify some possible controlling factors.

2. Data and Methods

2.1 Study site

The Super-Sauze landslide has developed in Callovo-Oxfordian black marls of the Barcelonnette basin (Alpes-de-Haute-Provence, France) (Fig. 1). In the 1960s, the area was affected by deep and shallow failures in the scarp area. The collapsed material composed of rocky panels progressively transformed into a silty sandy matrix integrating marly fragments of heterogeneous size through successive drying/wetting and freeze/thaw cycles [Malet, 2003]. In the late 1970s, the mobilized material started to accumulate in the gullies. From the 1970s until today, the landslide is gradually covering the torrential stream located downstream with typical range of velocity between 1 to 3 cm.d⁻¹ and acceleration peak until 40 cm.d⁻¹ in the spring season [Malet *et al.*, 2002]. In 2007, the landslide extent over a distance of 900 m between an elevation of 1980 m at the crown and 1760 m at the toe with an average width of 135 m and a average slope of 25°. The total volume is estimated at 560,000 m³ [Travelletti and Malet, 2011].

The displacements are currently monitored by Differential Global Positioning System surveys (DGPS), an automatic system of optical photographs [Travelletti *et al.*, in press] and TLS acquisitions. The landslide ground surface nearly free of vegetation is particularly adapted for TLS monitoring.

2.2 Data acquisition

For this study, the monitoring of the toe was realized with a long-range terrestrial laser scan Optech ILRIS-3D, which principle is based on the time-of-flight distance measurements using an infrared laser [Slob and Hack 2004]. Ten acquisitions were acquired between October 2007 and May 2010 for the same base station at an average distance of 100 m from the landslide toe. At this distance, the laser diameter on the ground surface is estimated between 3 cm and 5 cm.

2.3 Methodology

The approach is based on the reduction of a 3D matching problem in a 2D matching problem by using a 2D statistical normalized cross correlation function. The point clouds are co-registered in a common local coordinate system following the method used in Oppikoffer *et al.* [2009]. Each TLS acquisition is aligned on the stable parts of the landslide composed of a rough topography made of crests and gullies whose morphology is preserved during the whole acquisition period (Fig. 1). After a first manual matching, the ICP algorithm is used to refine the alignment quality with a final 3D error of 4 cm (Fig. 2). For the absolute georeferencing, a georeferenced Airborne Laser Scanning (ALS) point cloud acquired in October 2007 was used as a reference. The TLS point clouds were aligned as single point

clouds on the stable parts in the ALS point cloud. The co-registration accuracy of the sequential point clouds is thus not affected by the georeferencing accuracy estimated to an average error of 1 cm and a standard deviation of 14 cm.

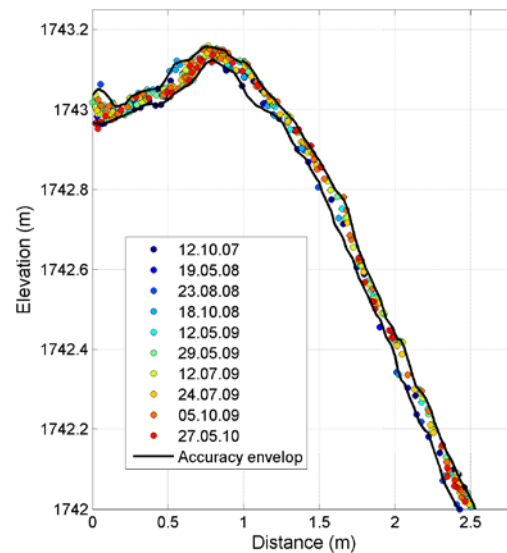


Figure 2: Profile across the point clouds showing the co-registration quality.

The type of representation of the topographical surface is of paramount importance to the detection of displacements of the landslide. Because the correlation function gives good results when the input data contains regions of rapidly varying pixel information [Duffy and Hughes-Clarke, 2005], the norm of the 2D gradient in u and v directions of the distance between the point clouds and the TLS station is calculated for emphasizing the morphology of the landslide toe. The generated images are then converted in grey-scale values (16 bits) and are used as inputs for the correlation step to compute the 2D displacement field in the plane perpendicular to the viewing direction of the laser scan. A projective transformation [Kraus and Waldhäusl, 1994] was used to project gradient raster in a plane perpendicular to the viewing direction of the laser scan.

2.3.3. Determination of the displacement field by TLS image correlation

The correlation principle consists in recognizing identical intensity distribution patterns in a correlation window in two images to determine the displacement of the center of the window by maximizing a normalized cross correlation function [Chambon, 2003; Hild, 2003]. The size of the correlation window is a compromise between the desired accuracy and the spatial resolution of the displacement field [Delacourt et al., 2007]. In this work, a correlation window of 30 pixels produced the most uniform vector field over the entire image. This correlation window corresponds to a ground surface varying between 0.5 m^2 and 3.5 m^2 . A sub-pixel correlation [Press et al., 1997; Chambon, 2003] is also used to detect displacements magnitudes below the limit fixed by the points spacing of 3 cm.

The result of the correlation corresponds to the displacements Δu and Δv along the u -axis and v -axis with their coefficient correlation value representing the matching quality. The displacements Δu and Δv are then reprojected in 3D displacements in the local coordinate system.

2.3.4. Determination of the strain field by TLS image correlation

The analyses of the displacement field do not exhaust a kinematics analysis and is therefore supported by a strain analysis used to highlight areas in the landslide toe with different behaviors. Because the magnitude of the horizontal displacements represents on average 93% of the magnitude of the 3D displacement, the 2D Cauchy's strain tensor E was used assuming small deformation [Pollard and Fletcher, 2010, Pan et al., 2009].

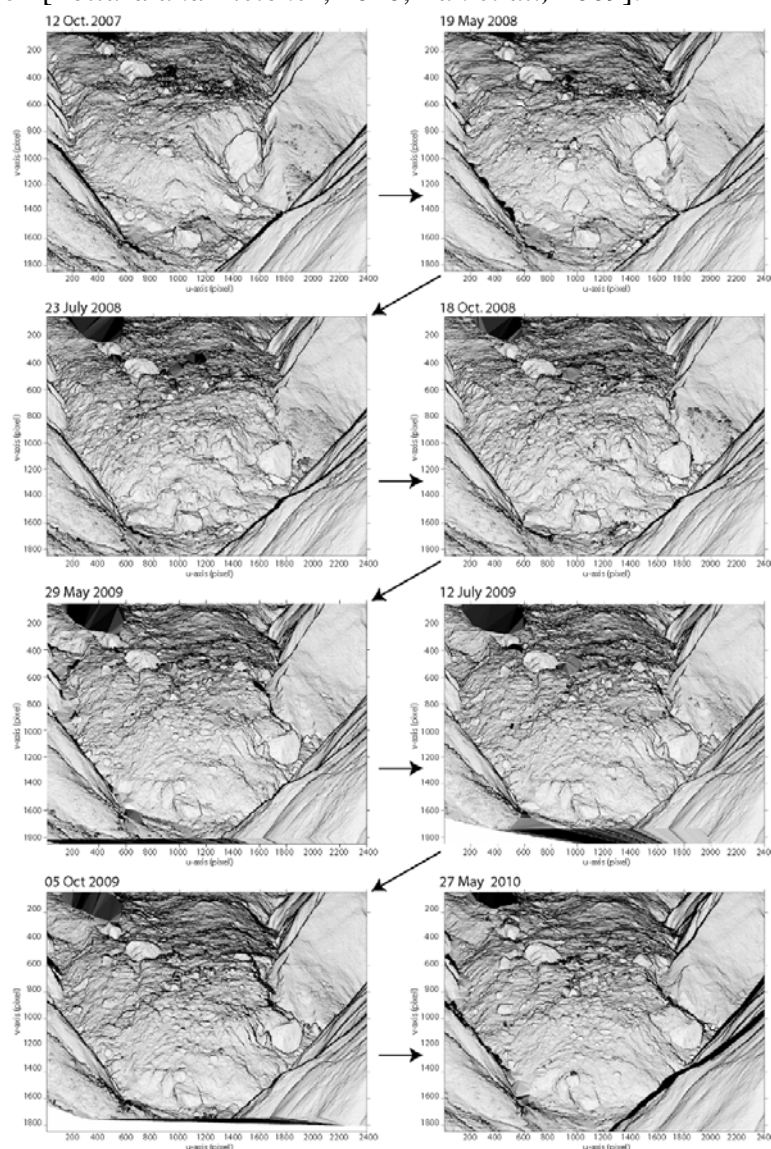


Figure 3: Images derived from the gradient calculation on the TLS point clouds. The morphology of the landslide toe is very well represented and the progression of the landslide toe is also particularly highlighted. The grey-scale images are then correlated.

3. Results

3.1. Displacement maps of the landslide

The displacements are generally well reproduced for all periods of acquisition. The contrast in displacement between the landslide area and the stable area gives confidence on the calculated displacement field. Four acquisitions periods (October 2007 - May 2008, July 2008 - October 2008, October 2008 - May 2009, July 2009 - October 2009) are presented to illustrate both the performance of the approach and the behavior of the landslide (Fig. 4). Conservation of surface texture is well fulfilled in the periods characterized with low displacement rates, especially between July and October (Fig. 4A). For the period July-October 2008, displacements between 0.5 and 1.5 m are observed, thus corresponding to an average displacement rate of 0.6 to 1.7 cm.day⁻¹. The displacement field displays significant spatial heterogeneities. The largest displacements are detected in the front of the toe where the terrain slope increases. The detachment of a toe compartment is also highlighted in the front. The same period of the following year (July-October 2009) displays a very different kinematics both in terms of magnitude and spatial distribution. Displacements are shorter and range from 0.1 m at the front of the landslide toe to 0.6 m in the upper part of the toe, thus corresponding to an average displacement rate of 0.1 to 0.8 cm.day⁻¹.

3.2. Comparison and validation of the displacements

Two methods are used to validate the computed displacements. Five rigid blocs distributed on the landslide toe are identified in the point clouds of each TLS acquisition (Fig. 5A). The triangulated blocs of the first TLS acquisition are aligned on their corresponding triangulated blocs in the second TLS acquisition using the ICP method. The results of the comparisons between the displacement obtained with the ICP method and those derived from the correlation are synthesized in Fig. 5B. The displacements derived from both methods are in very good agreement ($r^2 = 0.99$) with an average error and a standard deviation of 2 cm.

The second method consists in comparing the obtained displacements with a Differential Ground Positioning System surveys (DGPS) on the same blocks (horizontal and vertical accuracy of 0.02 m and 0.05 m). The displacements perfectly correlate ($r^2 = 0.99$). A mean error and a standard deviation of 0.04 m and 0.03 m are determined (Fig. 5C). This results show that the error due to the co-registering is about 3 cm.

3.3. Strain analysis

The strain field derived from the acquisition over the periods of July - October 2008 and 2009 is used to illustrate the kinematics of the toe. The first step consists in determining the accuracy of the computed strain field. Therefore, a null hypothesis is performed on the stable areas assuming that the strain error in these parts is similar to the strain error in the landslide. The accuracy analysis on the stable parts shows that more than 90% of the surface strain and

shear strain ranges between $\pm 2.10^{-3}$ which is therefore considered as the lowest interpretable value.

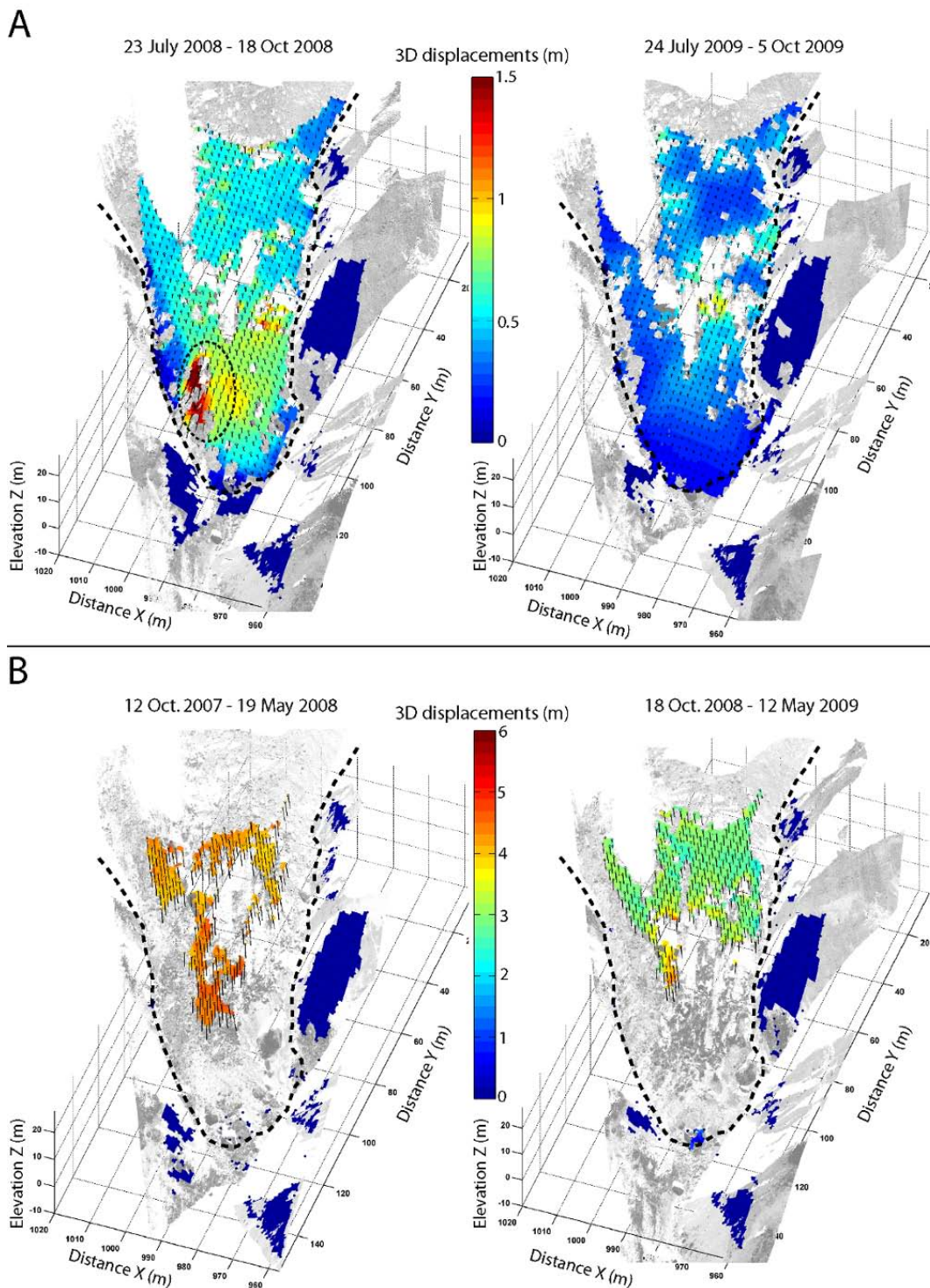


Figure 4: 3D displacements field obtained by TLS measurements related to the acquisition periods of (A) July - October of the years 2008 and 2009 and (B) the periods of October - May of the years 2007 and 2008. The dashed circle indicates the detachment of compartment at the front of the toe. The displacement maps are draped on their corresponding point clouds (intensity values).

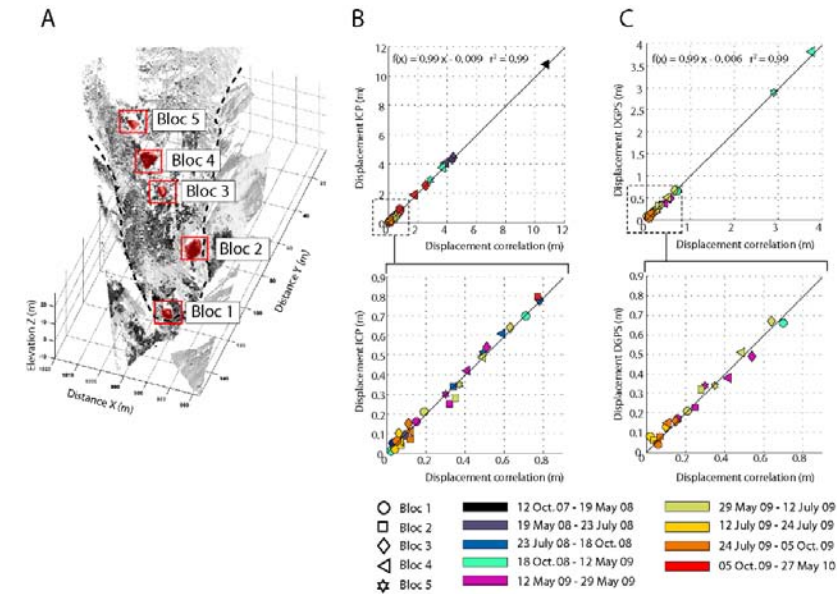


Figure 5: Comparison and validation of the displacements obtained by correlation with the ICP method and DGPS monitoring A) locations of the blocs in the point cloud, B) comparison with the ICP method and C) comparison with the DGPS monitoring.

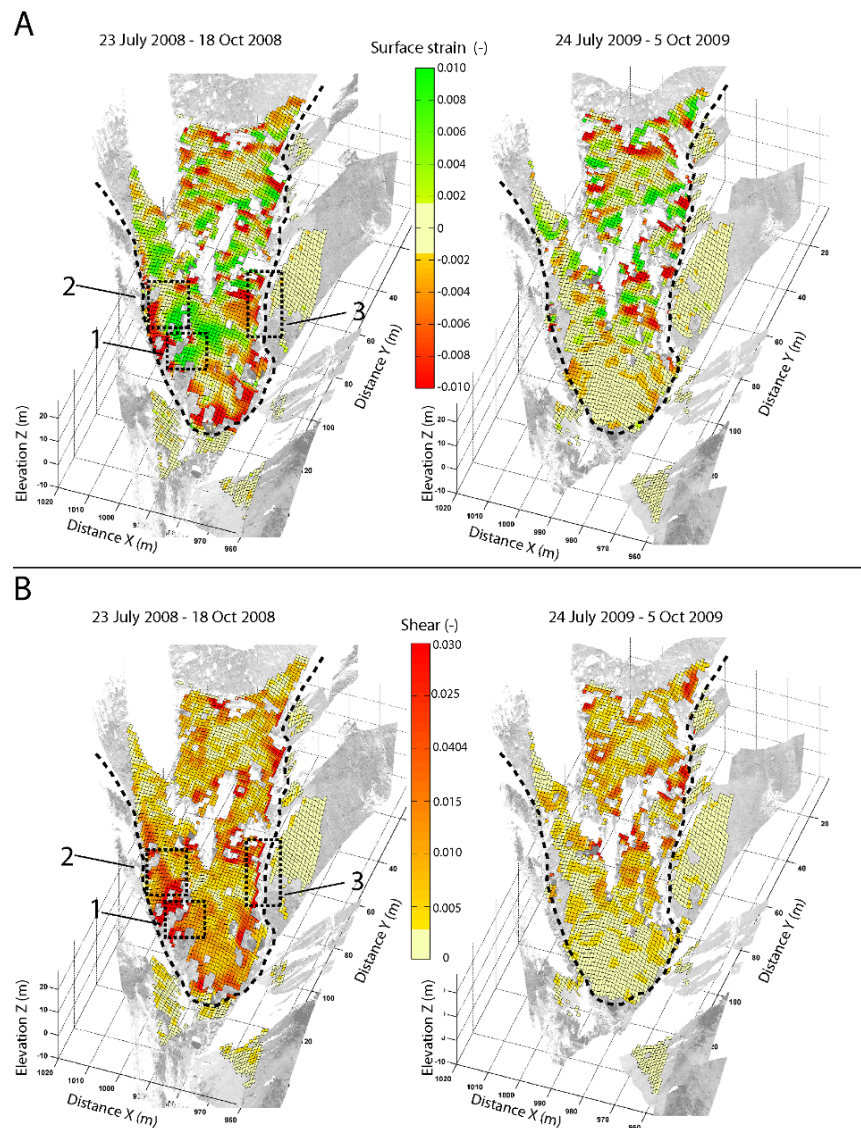


Figure 6: Strain field obtained by TLS measurements related to the acquisition periods of July – October of the years 2008 and 2009. Maps of the Surface strain (positive value mean extension) (A) and shear strain (B). The dashed squares refer to Fig. 7. The strain maps are draped on their corresponding point clouds (intensity values).

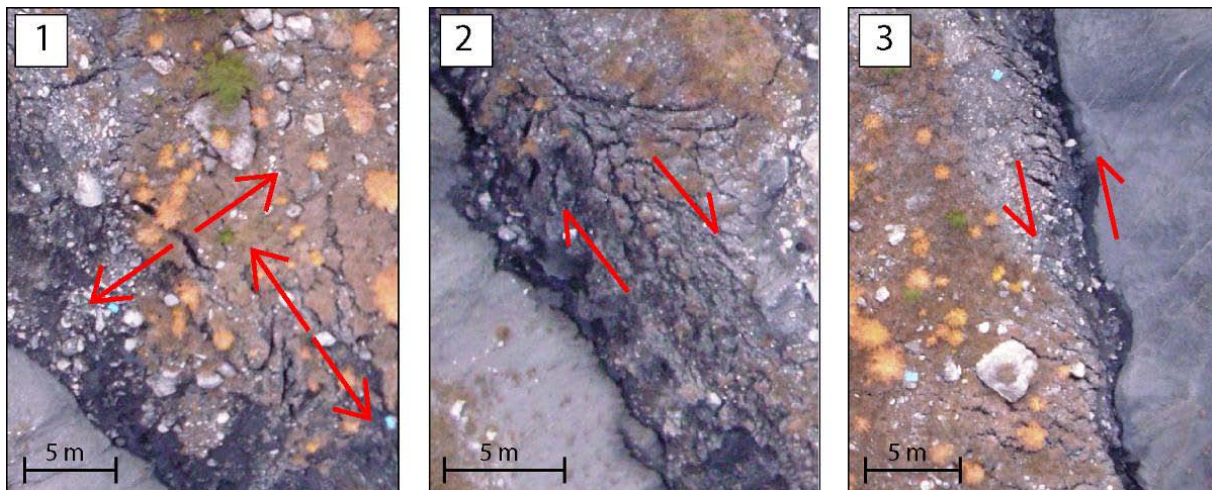


Figure 7: Tensile fracture (1) and shear fracture (2, 3) observed in the front of the toe (block 4 in Figure 7) on an orthophotograph acquired in October 2008 by *Niethammer et al.* [2010]. The location of the pictures is indicated on Figure 6.

The strain analysis allows to discriminate areas under extension or compression affected by shearing (Fig. 6). Note that because of the finite size of the correlation window and the strain window, a significant smoothing of the strain fields is introduced, associated with a spatial spreading of the structures. The upper part of the toe is characterized by a succession of approximately parallel bands (width of 5 to 10 m) in compression and extension whose main orientation is perpendicular to the sliding direction (Fig. 6A). Except at the proximity of the stable part, the upper part is not affected by important shearing (Fig. 6B). The location of the compression and extension zone changes from 2008 to 2009, thus suggesting a displacement of these areas with the landslide material. The behavior of the toe front is very different considering the year 2008 or the year 2009. In 2008, extension is observed, thus inducing compression in the material located in the very front of the toe near the boundary of the landslide (Fig. 6A). The consequence of this extension results in the development of tensile fissures identifiable on the field (Fig. 7). The toe front is also affected by important shearing concentrated along the landslide boundary. The important shear magnitude in these areas is confirmed by very persistent shear and tensile fissures affecting the landslide material (Fig. 7). In 2009, the deformation affecting the toe front is less important than in the previous year because the displacements in that part are very low and uniform.

4. Discussion and Conclusion

This work presents a simple approach to derive the 3D displacement field from consecutive TLS acquisition by fully exploiting the geometrical information contained in the point clouds. This method provides an alternative to complex 3D matching algorithms since the implementation of 2D correlation algorithms is much simpler and time consuming. In the case of landslide characterized without excessively dense vegetation cover, the proposed approach

has been demonstrated to be an accurate method for the determination of the 3D displacements. The error related to the approach itself is negligible compared to the instrumental and co-registering errors. The strongest limitation of the approach is due to the development of strong deformation between two TLS acquisition.

The kinematics of the toe of the Super-Sauze landslide could be determined. The obtained displacements are in perfect agreement with the displacements computed with the ICP algorithm and the displacements derived from a DGPS survey. The 2D strain analyse allowed to detect different kinematics patterns in the landslide toe. These patterns are in good agreement with the observed fissuring.

The approach would be particularly adapted for slow deformation of rock instabilities, because the plastic deformations of the objects (rock compartments) are less important than in soils. In addition the stress can be derived from the strain analysis if an elastic constitutive behaviour of the material is assumed, typically in pre-failure stage. Additional efforts are also still necessary to adapt the method to different acquisition configurations. Finally, the proposed approach can be setup in an automatic routine that can be potentially used in permanent monitoring systems.

References

- Besl, P., McKay, N., 1992. A method for registration of 3-D shapes. *IEEE Trans Pattern Anal Mach Intell*, 14, 239-256.
- Casson, B., Delacourt, C., Allemand, P., 2005. Contribution of multi-temporal sensing images to characterize landslide slip surface – Application to the La Clapière landslide (France). *Natural Hazards and Earth System Sciences* 5, 425–437.
- Chambon, G., 2003. Caractérisation expérimentale du frottement effectif des zones de faille. Ph.D. Thesis. Université Paris XI Orsay, ENPC.
- Delacourt, C., Allemand, P., Casson, B., Vadon, H., 2004. Velocity field of the “La Clapière” landslide measured by the correlation of aerial and Quick-Bird satellite images. *Geophysical. Research Letters*, 31, 1-5.
- Delacourt, C., Allemand, P., Berthier, E., Raucoules, D., Casson, B., Grandjean, P., Pambrun, C., Varel, E., 2007. Remote-sensing techniques for analysing landslide kinematics: a review. *Bulletin de Société Géologique*, 178(2), 89-100.
- Duffy, G. P., Hughes-Clarke, J. E., 2005. Application of spatial cross correlation to detection of migration of submarine sand dunes. *Journal of Geophysical Research*, 110, 1-11.
- Gruen, A., Akca, D., 2005. Least squares 3D surface and curve matching. *ISPRS Journal of Photogrammetry and Remote-sensing*, 59 (3), 151–174.
- Hild, F., 2003. Mesure de champs de déplacement par corrélation d’images et applications en mécanique des solides. Notes de cours, IPSI. Laboratoire de Mécanique et Technologie, CNRS-UMR 8535, Université Paris 6, France.
- Kraus, K., Waldhäusl, P., 1994. *Photogrammetry, Fundamentals and Standard processes*. vol 1. Hermès (Eds.), Paris.
- LePrince, S., Berthier, E., Ayoub, F., Delacourt, C., Avouac, J.- P. 2008. Monitoring earth surface dynamics with optical imagery. *Eos*, 89, 1-5.
- Malet, J.-P. 2003. Les glissements de type écoulement dans les marnes noires des Alpes du Sud. Morphologie, fonctionnement et modélisation hydromécanique. Ph.D. Thesis, Université Louis Pasteur, Strasbourg.
- Monserrat, O., Crosetto, M., 2008. Deformation measurement using terrestrial laser scanning data and least squares 3D surface matching. *ISPRS Journal of Photogrammetry*, 61(1), 142-154.
- Niethammer, U., Rothmund, S., James, M. R., Travelletti, J., Joswig, M. 2010. UAV-based remote-sensing of landslides. *International Archives of Photogrammetry, Remote-sensing and Spatial Information Sciences*, Vol. XXXVIII, Part 5 Commission V Symposium, Newcastle upon Tyne, UK.

- Oppikofer, T., Jaboyedoff, M., Blikra, L. H., Derron, M. H., Metzger, R. 2009. Characterization and monitoring of the Aknes rockslide using terrestrial laser scanning. *Natural Hazards and Earth System Sciences*, 9, 1003-1019.
- Pan, B., Asundi, A., Xie, H., Gao, J. 2009. Digital image correlation using iterative least squares and pointwise least squares for displacement field and strain field measurements. *Optics and Lasers in Engineering*, 47, 865-874.
- Pollard, D., Fletcher, C. 2010. *Fundamentals of Structural Geology*. Cambridge University Press (Eds.), Cambridge.
- Press, W.H., Flannery, B.P., Teukolsky, S.A., Vetterling, W.T. 1997. *Numerical Recipes in C, The Art of Scientific Computing*, Second Edition, Cambridge Univ. Press, New York
- Prokop, A., Panholzer, H., 2009. Assessing the capability of terrestrial laser scanning for monitoring slow moving landslides. *Natural Hazards and Earth System Sciences*, 9, 1921–1928.
- Schwalbe, E., Maas, H.-G., Dietrich, R., Ewert, H., 2008. Glacier velocity determination from multi temporal terrestrial long range scanner point clouds. *ISPRS - The International Archives of Photogrammetry, Remote-sensing and Spatial Information Sciences*. Vol. XXXVII, Part B5, Beijing 2008.
- Slob, S., Hack, R. 2004. 3D Terrestrial Laser Scanning as a new field measurement and monitoring technique. In: Hack, R., Azzam, R., Charlier, R. (Eds), *Engineering geology for infrastructure planning in Europe: A European perspective*. Springer, Berlin. *Lecture notes in Earth Sciences*, 104, pp. 179-189.
- Teza, G., Galgaro, A., Zaltron, N., Genevois, R., 2007. Terrestrial laser scanner to detect landslide displacement fields: a new approach. *International Journal of Remote-sensing*, 28(16), 3425-3446.
- Teza, G., Pesci A., Genevois, R., Galgaro, A., 2008. Characterization of landslide ground surface kinematics from terrestrial laser scanning and strain field computation. *Geomorphology*, 97, 424-437.
- Travelletti, J., Oppikofer, T., Delacourt, C., Malet, J.-P., Jaboyedoff, M., 2008. Monitoring landslide displacements during a controlled rain experiment using a long-range terrestrial laser scanning (TLS). *ISPRS - The International Archives of the Photogrammetry, Remote-sensing and Spatial Information Sciences*. Vol. XXXVII. Part B5, pp. 485–490
- Travelletti, J., Malet, J-P. 2011. Characterization of the 3D geometry of flow-like landslides: a methodology based on the integration of multi-source data. *Engineering Geology* (in press).
- Travelletti, J., Delacourt, C., Toussaint, R., Allemand, P., Malet J.-P. Schmittbuhl, J., Bastard, M. 2011 (in press). Correlation of multi-temporal ground-based images for landslide monitoring: application, potential and limitations. *International Journal of Photogrammetry & Remote-Sensing* (in press).

Object oriented mapping of landslides under dense vegetation cover using LiDAR derivatives

Application: Landslide inventory mapping

Technique: Active optical airborne LiDAR

Main references: Van Den Eeckhaut, M., J. Hervás, N. Kerle, R. Supper (in prep):

Contributors: JRC (M. Van Den Eeckhaut, J. Hervás); ITC (N. Kerle); GSA (R. Supper)

Abstract

This case-study presents preliminary results of the application of object-oriented segmentation and classification using LiDAR derivatives. The aim of this contribution is to highlight the possibilities of using this combination for recognition and classification of landslides in densely vegetated areas where spectral data do not allow accurate landslide inventory mapping. The test area is the Flemish Ardennes (Belgium) where deep-seated landslides are located on soil-covered hillslopes. A relatively qualitative approach based on expert-knowledge is presented. The results obtained show that object-oriented analysis using LiDAR derivatives (such as slope gradient, curvature and difference in elevation) and edge detection allows recognition and characterization of profound morphologic properties of deep-seated landslides. Main scarp, landslide boundary and landslide segments were successively classified. Based on length/width characteristics and presence of reverse slopes the landslides were further categorized as rotational or complex slides. Future results will focus on improving the segmentation and automating of the classification procedure.

Keywords: landslide mapping; LiDAR; object-oriented image analysis, conceptualisation, vegetated landslides

1. Introduction

Light Detection and Ranging (LiDAR) and its wide range of derivative products has recently become a powerful tool in landslide research, particularly for landslide identification and landslide inventory mapping. Since the availability of LiDAR, shaded-relief, slope, surface roughness and contour maps, and other derivatives have regained popularity, especially for landslide inventory mapping in forested areas [Schulz, 2004; Van Den Eeckhaut *et al.*, 2007; Haneberg *et al.*, 2009].

In contrast to the many studies that use expert-based analysis of LiDAR derivatives to identify landslides, only few studies have attempted to develop computer-aided methods for extracting landslides from LiDAR data [McKean and Roering, 2004; Booth *et al.*, 2009]. Promising results were obtained with surface roughness parameters. All these automated attempts have been carried out in a pixel-based analysis. However, with high resolution topographical data such as LiDAR, object-based or object-oriented analysis (OOA) might provide better results. OOA rests upon two interrelated methodological steps: (1) segmentation or regionalization of pixels into meaningful, homogeneous objects, that reduce the noise more and more confronted with in a pixel-based analysis and that facilitate a multi-scale analysis [Blaschke, 2010]; and (2) rule-based classification incorporating spectral, textural, morphometric and contextual landslide features. It is clear that the quality of the segmentation largely controls the classification.

OOA has gained increased attention for (semi-)automated landslide identification from passive optical airborne and satellite sensor data [Barlow *et al.*, 2003, Martha *et al.*, 2010; *subm.*; Lu *et al.*, *in press*; Stumpf and Kerle, *subm.*]. These studies have proven the potential for creation of inventories of recent landslides of different types. Yet, Digital Elevation Models (DEMs) have only been used in the second step, the classification.

The identification of old vegetated landslides, not detectable from passive optical images, has not been investigated so far. Van Asselen and Seymonsbergen [2006] used LiDAR derivatives in an OOA for semi-automated geomorphological mapping. Their classification included slopes with mass movement. They did not focus on individual landslides as separation of individual landslides of different types was difficult.

The objective of this study is to test OOA for landslide inventory mapping using LiDAR data only for both the segmentation and classification steps. As such we enter in the field of geomorphometry. More specifically, we will exploit the profound morphologic manifestation of old, densely vegetated landslides to semi-automatically map their extent using LiDAR derivatives, and we will outline the pros and cons of the methodology. We focus on two study areas, i.e. the Flemish Ardennes (Belgium) and Vorarlberg (Austria). As this study is ongoing, we only present preliminary results of the first study area. The Flemish Ardennes is a hilly region characterised by loose tertiary lithology (alternation of clays and more sandy lithology) affected by more than 200 landslides [Van Den Eeckhaut *et al.*, 2007; case-study 7 in D4.1].

2. Data and Methods

2.1. Data

The LiDAR data (AGIV, 2005) used in this study are similar to the data used for a smaller study area by Van Den Eeckhaut *et al.* [2007]. Flights took place in 2001 and 2002. An Azimuth Aeroscan small footprint (30 cm) multi-return LiDAR system with a pulse rate of 15 kHz and vertical accuracy (RMSE) of 4 cm was used. Laser pulses were sent at equal intervals within 600 m wide swaths with average pulse density of 1 per 4 m². The last return from each pulse was assumed to be from the soil surface, although this was not always the case. Terrascan software was used by the vendor for the production of the bare earth DTM, and a manual check followed. The data have a point density of at least 1 per 20 m², a horizontal accuracy below 15 cm and an average vertical accuracy that depends on vegetation height, decreasing from 7 cm for freshly cut lawn to 20 cm for pastures and forests [GIS-Vlaanderen, 2003]. From the LiDAR point data, a Triangulated Irregular Network (TIN) was derived which was then converted to a Digital Terrain Model (DTM) with a 2 m resolution and after low pass filtering (kernel size 3) different LiDAR-derivatives were produced. LiDAR derivatives of different order can be used. However, higher order derivative maps are more and more deviating from human conceptualization [Minar and Evans, 2008]. Therefore the derivatives evaluated in this study (Table 1) are focussing on the lower order maps which the human brain also uses for delineating landslide boundaries and classifying landslide parts.

Table 1: Maps used in the study

Map	Additional information
Image layer (2 m x 2 m resolution)	
DTM (m)	
Slope gradient (%)	
Plan- and profile curvature (°)	
Edge_slope	Map obtained through edge detection (pixel min/max filter in eCognition) on Slope gradient map
Edge_slopecl	Expert-based classification of Edge_slope map
Dif_DTM_DTMki (m) with i=15, 25, 50, 75	Difference between original DTM and DTMki with DTMki: raster map where each grid cell represents the mean value of a moving window with kernel size ki with i=15, 25, 50, 75 (best result was obtained with i=50)
Thematic layer (vector map)	
River	Derived from the DTM using the hydrology toolbox in ArcGIS

2.2. Conceptualization of landslides and translation to OOA

The ultimate benchmark of OOA is human perception [Lang, 2009]. Our visual sense of any kind of object is a common experience, yet not always easy to communicate and even more difficult to translate in rule sets. Hence, (semi-)automated classification of landslides, almost always represents an attempt to replicate subjective landslide recognition (Martha et al., 2010). Stumpf et al. (subm.) provide an overview of image object features previously used in OOA-based landslide inventory studies. Most of these features are not solely characteristic for landslides, and many are related to passive optical images (i.e. spectral information, texture) making them not very useful in a LiDAR oriented approach where the focus should be put on identification of geomorphometric features. Figure 1 contains the conceptualization of landslides including old deep-seated rotational/translational slides with a flow characteristic (i.e. complex slides) and rotational slides, landslide-free terrain (mainly cropland and pastures) and possible false positive landslides (road-and riverbanks and field borders). The ultimate objective is to find a classification ruleset based on the listed characteristics.

Translation of the landslide concept in eCognition starts with segmentation. Different segmentation procedures are available, but so far landslide studies mainly used multiresolution segmentation. Also we use this procedure, but in combination with Contrast Split segmentation (Fig. 1), which segments an image or image object into regions with high and low values. It is based on a threshold that maximizes the contrast between the resulting objects and low objects, where a possible range of the threshold can be predefined by the user. The scale factor is one of the most important factors influencing the segmentation [Drăguț et al., 2010] and recently several procedures for objective selection of appropriate scales for multiresolution segmentation have been suggested. Drăguț et al. [2010] created the estimation of scale parameter tool (ESP) that allows estimating the scale parameter for segmentation of

one image. Other attempts for optimization of scale are suggested by *Martha et al.* [accepted] and *Stumpf et al.* [accepted]. Up to now, we used ESP as it fast and straight forward.

The segmentation and classification procedure was calibrated for a 10 km² test area in the Flemish Ardennes. It was then applied to the 50 km² area surrounding the test area (Fig. 2). For the test and validation area, the existing landslide inventory map obtained through visual inspection of LiDAR derivative maps and field surveys [*Van Den Eeckhaut et al., 2007*] contains subsequently 4 and 14 rotational slides, 10 and 16 complex slides, 4 and 6 possible slides (less clear geomorphic manifestation) and 2 and 15 shallow slides. The latter are not taken into account in this study.

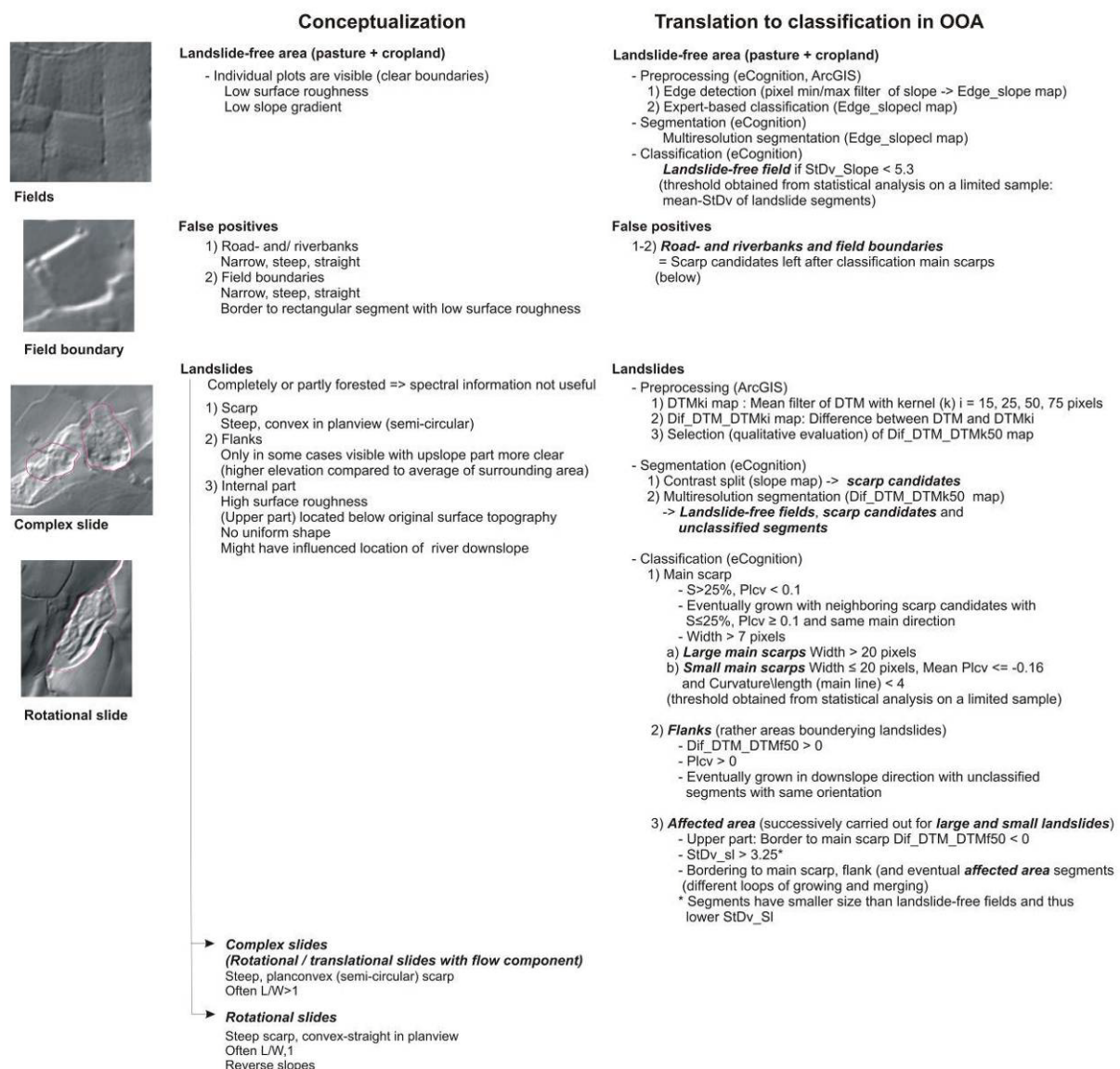


Figure 1: Human conceptualization of landslides and translation to object oriented analysis (S: slope gradient, StDv_Slope: standard deviation of slope gradient; Plcv: plan curvature)

3. Results

3.1. Landslide identification

Figure 1 shows the procedure followed for segmentation and classification. First, landslide-free agricultural fields were extracted. The segmentation procedure for this included detection of edges on the slope map and subsequent multiresolution segmentation using the resulting map (Edge_slopecl). Then, a sample of landslide-free field and landslide-affected segments was analysed and segments with a standard deviation of slope gradient below 5.3. (i.e. mean - standard deviation calculated for sample of landslide-affected segments) were found to be landslide-free fields.

For extraction of landslides, the most clear landslide characteristics, the main scarps, were extracted first, then the flanks and finally the landslide-affected area. Contrast split segmentation of the slope map was carried out to separate steep (classified scarp candidates) from flatter terrain. The flatter terrain in this map was subsequently split with multiresolution segmentation of the Dif_DTM_DTMk50 map (Table 1) and the river map (Fig. 2).

Main scarp segments were extracted from scarp candidates using their concave planform. As individual scarps could consist of several segments a growing procedure was subsequently used. Based on their width, large and small main scarp segments were separated because during the calibration procedure more false positives were obtained for smaller main scarps.

Compared to main scarps, the morphologic manifestation of flanks is much less clear. No appropriate procedure has been found for segmentation of flank candidates yet, and thus the focus was not put on landslide flanks itself but on segments bordering the sides of the landslides. Especially for the upper part of the landslide, these segments are located above the surrounding segments (i.e. have mean Dif_DTM_DTMk50 > 0). However, for rotational slides also segments of reverse slope meet this criterion. This had to be taken into account when classifying the landslide-affected area. The latter was started from the main scarp (first the large and subsequently the small) in downslope direction. The procedure consists of a succession of loops of procedures 'grow', 'merge' and 'find enclosed by'. Finally, the unclassified segments were classified as landslide-free field. The results obtained are shown Figure 2.

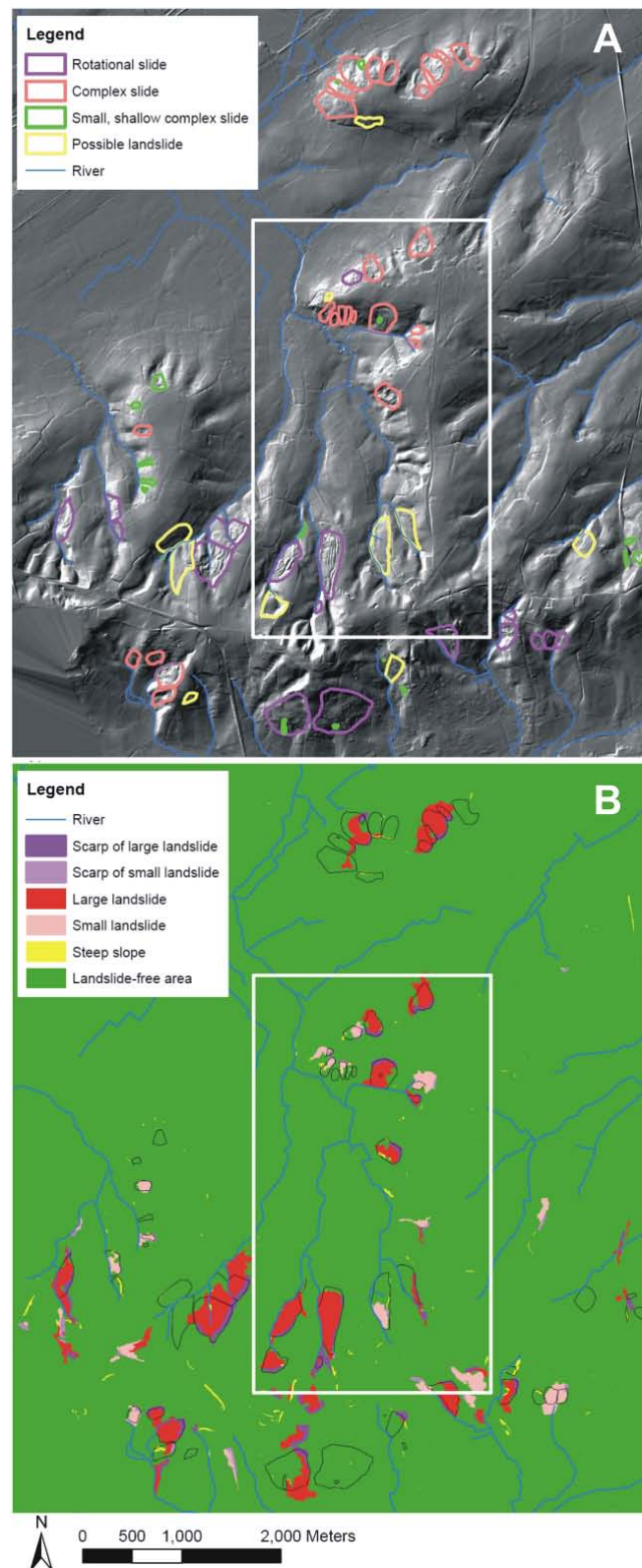


Figure 2: Test (with rectangular) and validation area in the Flemish Ardennes: (A) The shaded relief map is overlain with the expert-based landslide inventory map (LiDAR data © AGIV); (B) Preliminary landslide inventory obtained with OOA.

3.2. Accuracy assessment

Accuracy assessment can be carried out by comparing the landslide inventory obtained with OOA with the expert-based inventory (Fig. 2). No difference in accuracy was found for the calibration and validation area. The rotational slides in the central south of the study area are for example in agreement with the expert-based inventory. The two large complex slides in the south, however, are not identified with OOA. Their surface morphology is probably too subdued and affected by anthropogenic interventions (construction of houses and roads in the lower deforested part of the landslides).

For both complex and rotational slides the extent of about 70% of the landslides were correctly identified (Table 2). These results are in the same order as the results obtained by *Martha et al.* [2010]. False negatives (unidentified landslides) are always landslides for which the main scarp was not correctly identified. In most cases the main scarps were initially identified as scarp candidates though later omitted because of a plan convex morphology. The observation that false negatives (i.e. missed landslides) generally have smaller main scarps supports the idea of distinguishing between large and small main scarps.

Table 2: Accuracy assessment for number of landslides identified with OOA and LiDAR derivatives

	> 50% of landslide*		Main scarp but < 50% of landslide		Not identified	
	Number	%	Number	%	Number	%
Complex slide	18	69.2	1	3.8	7	26.9
Rotational slide	13	72.2	1	5.6	4	22.2
Possible	2	20	3	30	5	50

* Generally > 75%

The OOA landslide inventory contains also about 10 zones not identified as landslides by experts. These are either steep valley heads (where some slope failure might not be excluded) or zones where a road bank or earthen bank bordering a field was misclassified as a main scarp and subsequently grown into a landslide. Generally, this last group of false positives has an irregular form.

4. Discussion

4.1. LiDAR and eCognition

Compared to older versions, eCognition Developer 8 has been improved with regard to application of LiDAR data. The software now provides native LiDAR support so that LiDAR data can be loaded directly in its point cloud format (.las), and procedures to transform the original .las files in DTMs and Digital Surface Models (DSMs) can be downloaded from the community. This improvement has resulted in an increasing use of LiDAR data in OOA

studies dealing with building or tree extraction, most often in combination with passive optical images.

4.2. LiDAR and OOA

For (semi)automatic mapping of densely vegetated landslides, an alternative to passive optical sensors has to be found for production of landslide inventory maps. LiDAR derivatives are possible candidates. Their use was therefore tested in an OOA. An attempt was made to translate the human conceptualization of landslides and possible false positives into a segmentation and classification rule set. As we obtain similar accuracy results (i.e. 70%) compared to previous studies using OOA and passive optical remote-sensing data [*Martha et al.*, 2010] it is worthwhile to further exploit the possibilities of OOA with LiDAR data.

In soil covered areas such as Flanders, but also the Tualatin Mountains (Oregon), and the Puget Sound lowlands [*Booth et al.*, 2009] landslides are generally characterized by a much higher surface roughness compared to the surrounding landslide-free areas. The preliminary results suggest that slope gradient and surface roughness (standard deviation of slope gradient) provide opportunities.

In a mountainous area, such as our second study area in Vorarlberg (Austria), it is more difficult to distinguish landslides from non-landslide area as stable bed rock outcrops around landslides also have high topographic roughness. Additionally the number of false positive main scarps will be higher due to the presence of steep cliffs.

Some differences between the use of passive optical remote-sensing data and active optical remote-sensing data such as LiDAR were observed. In previous studies using passive optical remote-sensing data landslides were most often consisting of one or a few segments. However, landslides are geomorphological complex and consist of different parts with different geomorphological characteristics. Hence, they are not represented by one single segment when derived from LiDAR derivatives, and the aggregation from different segments into one final landslide segment is difficult.

So far the use of directional distributions (such as aspect or flow direction) which have no true zero and for which any designation of high or low values is arbitrary has been avoided, partly because features such as mean and standard deviation (as provided by eCognition or ArcGIS) are not correct for segments facing the north (around 0 or 360°). *Martha et al.* [2010] used flow direction in combination with main direction of segments, but only for segments representing complete objects with homogenous spectral characteristics. Hence, the main direction of the segments was really representing the main direction of the real object which is not necessarily the case for the sub-segments obtained in our analysis. Therefore features such as and main direction, aspect and flow direction, but also length/width relation are often only useful when landslides are represented as one single segment, i.e. at the end of the classification process when all landslide segments are joined.

The downslope part of a landslide often has a poor geomorphometric signature. However, this problem has also been reported for expert-based landslide inventory mapping [*Schulz*, 2004]. For delineation of landslide boundaries several edge detection procedures have been tested

but so far without great success. Edge detection requires the definition of a lower threshold defining the edge. If this value is taken too low then the image shows too many edges. On the contrary, if the value is too high then the image shows discontinuous edges, and misses edges of the lower part of the landslides. Given that the geometric signature of landslide flanks is highly variable, no optimal threshold was found so far.

Recent studies have focused on objective classification of segments. *Martha et al.* (subm.) used k-Means cluster analysis and *Stumpf and Kerle* (subm.) random forests. It should be further investigated whether one or both approaches are also useful in the context of this study. *Stumpf et al.* (subm.) distinguished between landslide segments and non-landslide segments including all types of spectrally similar objects. In our study neither all landslide segments nor all possible false positives can be put in two classes only. Therefore, similar to *Martha et al.* (2010), so far thresholds were only obtained through simple statistical analysis of limited samples selected in the test area.

5. Conclusions

The results obtained show that OOA using LiDAR derivatives (such as slope gradient, curvature and difference in elevation) and edge detection allows recognition and characterization of profound morphologic properties of deep-seated landslides. Main scarp, landslide boundary and landslide segments were successively classified. Overall about 70% of the landslides of an expert-based inventory were also included in the object-oriented inventory. Unidentified landslides were misclassified because they had a less profound or plan convex main scarp. About 10 plan concave road banks or river valley heads, on the other hand, were incorrectly classified as landslides. Based on length/width characteristics and presence of reverse slopes the landslides were further categorized as rotational or complex slides.

In the future attention should go to improvement of the segmentation and automating the classification procedure. With regard to the segmentation the detail present in the LiDAR data causes sometimes segments with a strange form or spurs. This should be avoided in the future by appropriate preprocessing (filtering) of the data, and selection of the best LiDAR derivatives and scale for segmentation and selection of the optimal scale for segmentation. Such improvements will probably automatically result in higher classification accuracy.

References

- AGIV (2005), LIDAR hoogtepunten – brondata van Digitaal Hoogtemodel Vlaanderen, MVG-LIN-AMINAL-afdeling Water en MVG-LIN-AWZ-afdeling Waterbouwkundig Laboratorium en Hydrologisch onderzoek, Brussel, Belgium, Digital file.
- Barlow, J., Y. Martin, and S.E. Franklin (2003), Detecting translational landslide scars using segmentation of Landsat ETM+ and DEM data in the northern Cascade Mountains, British Columbia, *Canadian Journal of Remote-sensing*, 29(4), 510-517.
- Blaschke, T. (2010), Object based image analysis for remote-sensing, *ISPRS J. Photogramm. Remote Sens.*, 645, 2-16.

- Booth, A.M., J.J. Roering, and J.T. Perron (2009), Automated landslide mapping using spectral analysis and high-resolution topographic data: Puget Sound lowlands, Washington, and Portland Hills, Oregon, *Geomorphology*, 109, 132-147.
- Drăguț, L., D. Tiede, and S. Levick (2010), ESP: a tool to estimate scale parameters for multiresolution image segmentation of remotely sensed data. *International Journal of Geographical Information Science*, 24, 859-871.
- GIS-Vlaanderen (2003), Nieuwsbrief GIS-Vlaanderen: Digitaal Hoogtemodel Vlaanderen. Ondersteunend Centrum GIS-Vlaanderen, Gent, Belgium.
- Haneberg, W.C., W.F. Cole, and G. Kasali (2009), High-resolution LiDAR-based landslide hazard mapping and modeling, UCSF Parnassus Campus, San Francisco, USA *Bulletin of Engineering Geology and the Environment*, 68, 263-276.
- Lang, S. (2008), Object-based image analysis for remote-sensing applications: modeling reality – dealing with complexity. In: Blaschke, T., S. Lang, and G. Hay (Eds.), *Object-Based Image Analysis Spatial Concepts for Knowledge-Driven Remote-sensing Applications*, Springer, Berlin, Heidelberg, pp. 3-27.
- Lu, P., A. Stumpf, N. Kerle, and N. Casagli (in press), Object-oriented change detection for landslide rapid mapping, *IEEE Geoscience and Remote-sensing Letters*.
- Martha, T., N. Kerle, C. J. van Westen, and K. Kumar (2010), Characterising spectral, spatial and morphometric properties of landslides for semi-automatic detection using object-oriented methods, *Geomorphology*, 116(1-2), 24-36.
- Martha, T., N. Kerle, C. J. van Westen, Jetten, V., and K. Kumar (subm.), Segment Optimisation and data-driven thresholding for knowledge-based landslide detection by object-based image analysis, *Transactions on Geoscience and Remote-sensing*.
- McKean, J., and J. Roering (2004), Objective landslide detection and surface morphology mapping using high-resolution airborne laser altimetry, *Geomorphology*, 47, 331-351.
- Minar, J., and I.S. Evans (2008), Elementary forms for land surface segmentation: the theoretical basis of terrain analysis and geomorphological mapping, *Geomorphology*, 95, 236-259.
- Schulz WH. (2004), Landslides mapped using LIDAR imagery, Seattle, Washington, *U.S. Geological Survey Open-File Report 2004-1396*. 11 pp., 1 plate.
- Stumpf, A., and N. Kerle (subm.), Object-oriented mapping of landslides using Random Forests, *Remote-sensing and Environment*.
- van Asselen, S., and A.C. Seijmonsbergen (2006) Expert-driven semi-automated geomorphological mapping for a mountainous area using a laser DTM, *Geomorphology*, 78, 309-320.
- Van Den Eeckhaut, M., J. Poesen, G. Verstraeten, V. Vanacker, J. Nyssen, J. Moeyersons, L.P.H. Van Beek, L. Vandekerckhove (2007), The use of LIDAR-derived images for mapping old landslides under forest, *Earth Surface Processes and Landforms*, 32, 754-769.

3.4. MULTI-SENSOR DATA ANALYSIS METHODS

3.4.1. Data fusion

[ITC+CNRS]

Due to the complexity and diversity of landslide processes a multitude of different instruments and analysis methods is generally desirable to investigate different landslide types and important aspects such as geometry, velocities and material properties. Similarly to data fusion approaches in geophysical investigations [Grandjean *et al.*, 2009] and early warning systems [Arnhardt *et al.*, 2010] the fusion / combination of remote-sensing datasets targets to minimize uncertainties with multiple evidences and attempts to exploit synergies from multiple sensors illuminating different aspects of the landslide. Data fusion comprises all kind of methods which systematically combine different data sources, whereas various data fusions methods are available at different processing levels. Data fusion can be applied at three different levels, including the direct combination of raw sensor signals, features extracted from the sensor data and decision methods that combine multiple inferences derived from different kinds of data and analysis methods [Hall and Llinas, 1997]. Within the remote-sensing community signal-level fusion is also often considered as pixel-level fusion and pansharpening algorithms are among the best studied methods in this domain [Zhang, 2010]. Higher-level fusion methods comprise both the extraction of combined features and (even more frequently) the consideration of multiple sensor signals in multivariate classification. The most commonly combined data sources in landslide research are at present multispectral, microwave and LiDAR sensors whereas there is theoretically no upper bound for multitude of combinable data sources. Some of those relatively new data sources still need to be explored individually in order to evaluate in depth advantages, limitations and the knowledge that can be gained. At the same time experts have already began to assimilate multi-sensor, multi-temporal and multi-scale remote-sensing data for joint-interpretation of landslide processes [Cascini *et al.*, 2010; Roering *et al.*, 2009]. The large diversity of landslide processes and observation methods makes it difficult to formalize a comprehensive framework for the combination of multiple evidences. However, multivariate statistics and object-oriented analysis appear suitable to accommodate signals, features and decisions from a multitude of sources. The studies presented in the section below demonstrate how expert interpretations can benefit of multi-sensor remote-sensing and the efficiency of OOA to formalize exploitation of object attributes from multiple sensors. We note that in a strict sense several other studies presented in this document might be considered as data-fusion as well since in most cases additional sources are considered at least for the final interpretation of the obtained results.

3.4.2. Innovative case studies

The following section demonstrates the integration of multi-sensor data via short summaries of four recently published or submitted research works carried out within SafeLand or through sister projects..

Object-oriented change detection for landslide rapid mapping

Application: Landslide inventory mapping

Technique: Passive optical spaceborne images and airborne LiDAR

Main references: Lu, P., A. Stumpf, N. Kerle and N. Casagli (2011): Object-oriented change detection for landslide rapid mapping

Contributors: ITC (A. Stumpf, N. Kerle), UNIFI (P. Lu., N. Casagli)

Abstract

A complete multi-temporal landslide inventory, ideally updated after each major event, is essential for quantitative landslide hazard assessment. However, traditional mapping methods, which rely on manual interpretation of aerial-photos and intensive field surveys, are time-consuming and accordingly not efficient for generating such event-based inventories. In this study a semi-automatic approach based on object-oriented change detection for landslide rapid mapping, and using very high resolution (VHR) optical images, is introduced. The usefulness of this methodology is demonstrated on the Messina landslide event in southern Italy that occurred on 1 October 2009. The algorithm was first developed in a training area of Altolia, and subsequently tested without modifications in an independent area of Itala. 198 newly-triggered landslides were correctly detected, with user accuracies of 81.8% for the number of landslides, and 75.9% for the extent of landslides. The principal novelty of this work is (1) a fully automatic problem-specified multi-scale optimization for image segmentation, and (2) a multi-temporal analysis at object level with several systemized spectral and textural measurements.

Keywords: OOA, change detection, landslide, rapid mapping

1. Introduction

Traditionally, landslide mapping has relied on visual interpretation of aerial-photos and intensive field surveys. However, for mapping of large areas those methods are too subjective, time-consuming and not always easy to be carried out, creating a gap that remote-sensing has been increasingly filling. Due to restrictions in spatial resolution, traditional optical satellite imagery, such as acquired by Landsat TM, has limited utility for landslide studies [*Hervás et al.*, 2003]. More recently, high resolution images and LiDAR elevation derivatives have started to offer an alternative way for effective landslide mapping. Most researches, however, have been focusing on pixel-based analysis. For example, *Borghuis et al.* [2007] employed unsupervised image classification in automated landslide mapping using SPOT-5 imagery. *McKean and Roering* [2004] also successfully delineated landslide features using statistical measures of surface roughness from LiDAR DTM. With increasing spatial resolution, however, pixel-based methods have fundamental limitations in addressing particular landslide characteristics such as shape and surface texture. Only such additional object characteristics allow landslides to be further assigned to different type classes, and other features of similar appearance to be discarded. Such methods focusing on features instead of pixels are the basis of object-oriented analysis (OOA).

The purpose of this contribution is to introduce a new approach for a rapid mapping of newly-triggered landslides using an objected-oriented change detection technique. The methodology aims at a semi-automatic and rapid analysis with a minimum of operator involvement and manual analysis steps. Compared to conventional approaches for landslide mapping, this approach benefits from (1) an image segmentation with problem-specified scale optimization, (2) a multi-temporal analysis at object level with several systemized spectral and textural metrics, and (3) the integration of pre-and post-event imagery with a post-event high resolution LiDAR DSM.

2. Data and methods

The adopted methodology includes two parts: (1) image segmentation with multi-scale optimization, and (2) classification of landslide objects. The general methodology is shown in Figure 1. Two QuickBird images were used in the study, acquired on 6 September 2006 and 8 October 2009, with respectively 0.3% and zero cloud cover. For each image, only four multispectral bands (Blue, Green, Red and NIR) with a spatial resolution of 2.4 m were used, i.e. without pansharpening with the 0.6 m panchromatic band, to avoid artefacts introduced by image fusion and to increase the efficiency of computation time. Also, the 2.4 m resolution was considered as sufficient for the scale of the targeted landslide features. Additionally, a 1 m DTM was created from airborne LiDAR data acquired during 6 to 19 October 2009, shortly after the event, with a maximum point density of 8 points/m² (vertical and horizontal accuracy: 15 cm and 40 cm, 1- σ). The spectral analysis was performed with ENVI 4.7 software. The OOA and textural analysis were implemented in eCognition Developer 8.

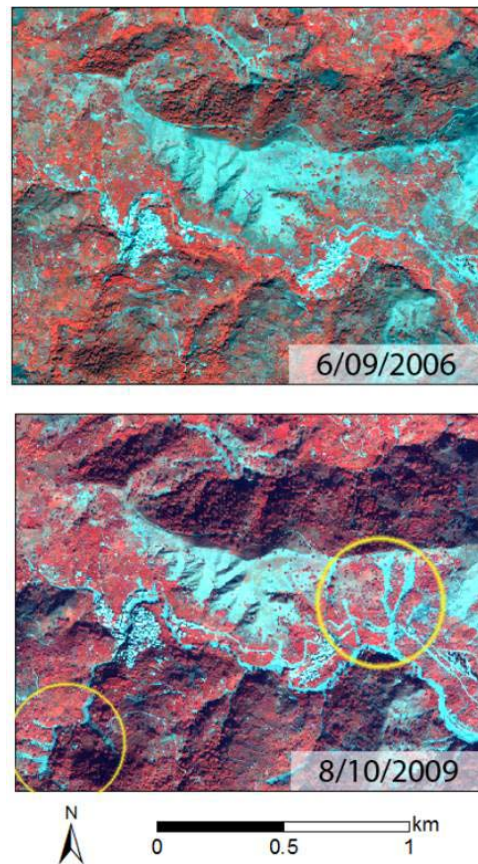


Figure 1: Training area around Altolia before and after the landslide event. Triggered landslides are highlighted exemplarily in yellow.

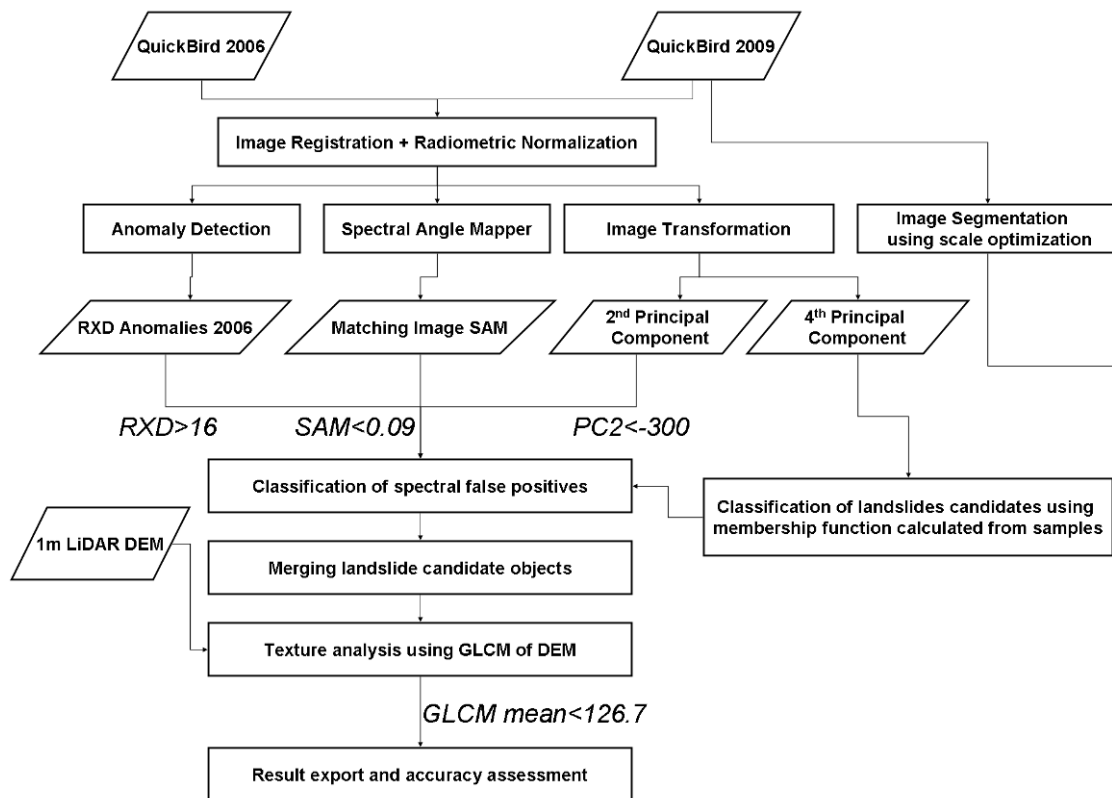


Figure 2: General flowchart of landslide mapping by OOA change detection. RXD: Reed-Xiaoli Detector; SAM: Spectral Angle Mapper; PC: Principal Component; GLCM: grey level co-occurrence matrix.

The application of this approach is demonstrated by a case study in Messina Province of Sicily, southern Italy. During the night of 1 October 2009 intensive prolonged rainfall (ca. 223 mm in 7 hours) affected several catchments south of Messina city. Numerous debris flows and shallow landslides were triggered and 31 people were reported dead. Two of the most damaged areas are studied, including a training area of Altolia (Figure 1, ca. 1.8 km²) for algorithm development, and a larger independent testing area of Itala (ca. 8.1 km²). The latter allows the robustness and transferability of the algorithm (without any change of ruleset and parameter thresholds) and the corresponding accuracy to be assessed by comparison with a manually mapped landslide inventory prepared from field works with subsequent modifications from image interpretation.

2.1. Image segmentation with scale optimization

Image segmentation defines the building blocks for object-oriented image analysis and, to ease further analysis, should aim at meaningful delineation of targeted real-world objects. However, considering the complex characteristics of landslides, including land cover variance, illumination difference, diversity of spectral behaviour and size variability, it is difficult to delineate each individual landslide as a single object [Martha *et al.*, 2010a].

Notwithstanding this difficulty, over- and under-segmentation can be reduced by means of a multi-scale optimization approach.

The multi-resolution segmentation based on Fractal Net Evolution Approach (FNEA) implemented in Definiens eCognition [Benz *et al.*, 2004] was employed for the initial segmentation, parameterized according to the specific needs of event-based rapid mapping of landslides, and incorporated in a multi-scale optimization routine. FNEA is computationally efficient, enables an analysis among various user-defined scales and has been used successfully in various remote-sensing studies. The algorithm requires the user to define weights for input layers (bands), as well as a scale parameter that defines the maximum allowed heterogeneity within individual segments. Catastrophic slope failures typically remove the vegetation, and result in high ratios between the Red and NIR bands. These bands are also the least affected by atmospheric effects and were assigned equal weights w_c . The scale parameter is consequently defined as

$$f = \sum_c w_c (n_{mrg} \cdot \sigma_{c,mrg}) - (n_{o1} \cdot \sigma_{c,o1} + n_{o2} \cdot \sigma_{c,o2}) \quad (1)$$

with n corresponding to the number of pixels within an object, and σ_c to the standard deviation of the pixel values within the band c . The subscripts indicate objects prior to merge ($o1$ and $o2$) and the respective resulting object after merging (mrg). The fact that suitable values for f usually need to be determined by the user in time consuming “trial and error” procedures, has previously been identified as one of its major limitations [Hay *et al.*, 2003]. Statistical optimization methods [Dragut and Blaschke, 2006; Espindola *et al.*, 2006a] allow the choice of the scale parameter to be made more objective, provided the targeted elements exhibit one operational scale. However, slope failures feature several orders of magnitudes in volume and area, which prohibit the definition of one single scale parameter. To overcome this difficulty, Martha *et al.* [in review] developed a modified version of Espindola *et al.* [2006a], by calculating a plateau objective function that has several scale parameter maxima to simplify segmentation parameterization and obtain a suitable multi-scale representation of satellite imagery. Esch *et al.* [2008] proposed a multi-level segmentation optimization procedure (SOP), which iteratively compares the spectral characteristics of image objects generated at multiple scales. A simplified version of this approach, which uses less spectral information and an automatically derived threshold, was used in this study.

In an initial step the image was segmented with the abovementioned settings and two hierarchical scales ($f_1=5, f_2=10$). The mean Percentage Difference (mPD) between sub-object level ($L1$) and super-object level ($L2$) was calculated as

$$mPD = \frac{|v_{L1} - v_{L2}|}{v_{L2}} \quad (2)$$

where v is the ratio of the intensities in the NIR and Red band of the respective sub- and super-object. Each sub-object whose mPD exceeds the mean mPD of all sub-objects by more

than 2σ was consequently classified as a “real” sub-object and transferred to the super-object level:

$$real\ object = \begin{cases} 1, & mPD > 2\sigma_{mPD} \\ 0, & \text{else} \end{cases} \quad (3)$$

In this sense $2\sigma_{mPD}$ replaced the user defined thresholds introduced by *Esch et al.* [2008]. In a next step the similarity of transferred adjacent sub-objects (*ob1* and *ob2*) was evaluated by their intensity difference in the NIR and Red band. Similar objects were merged according to the following condition:

$$sim_{ob1,ob2} = \begin{cases} 1, & (0.5 * |RED_{ob1} - RED_{ob2}| + 0.5 * |NIR_{ob1} - NIR_{ob2}|) < 10 \\ 0, & \text{else} \end{cases} \quad (4)$$

The procedure was repeated for a total of 11 scales (15, 20, 30, 50, 70, 100, 150, 200, 300, 500, 700), where in each step the result of the previous cycle became the sub-object level, and according to the next larger scale factor a number of objects was merged to create a super-object level above. With each iteration further objects exceeding the initially derived $2\sigma_{mPD}$ were transferred to the next level. The complete procedure aims to provide a segmentation that represents sufficiently distinct objects independent of their particular scale.

Figure 3 shows the segmentation result of the multi-scale optimization on the post-event imagery. Compared to the original FNEA with only one segmentation scale (Figure 3 a, b), image segmentation using multi-scale optimization (Figure 3 c), although still facing some difficulties to delineate every individual landslide, decreases the degree of over- and under-segmentation and is able to capture better landslides as image objects among a number of different scales. Furthermore, the optimization runs fully automatically and liberates the user from a time-consuming trial and error evaluation of the optimal parameterization for the image segmentation.

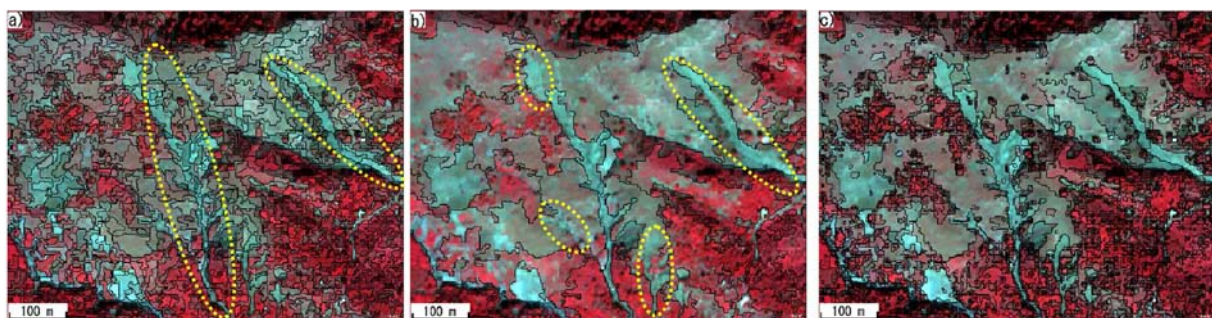


Figure 3: Detailed view of the image segmentation at: (a) a fixed scale of 30, (b) a specified scale of 200, (c) a described multi-scale optimization. Dotted ellipses are used to highlight over-segmentation (a) and under-segmentation (b) of landslides.

2.2. Classification of landslide objects

Landslide classification in previous studies has become increasingly complex. While initial works were largely restricted to DN values of multispectral bands, later indices such as NDVI, different texture measures, DEM derivatives, and externally prepared vector layers (of

flow accumulation and stream networks) or shadow masks were employed [Martha *et al.*, 2010a]. The landslide detection approach presented here makes use of additional spectral and textural measurements: change detection using temporal Principal Component Analysis (PCA), image matching through Spectral Angle Mapper (SAM), anomaly detection by Reed-Xiaoli detector (RXD), and textural analysis with grey level co-occurrence matrix (GLCM). The derivatives of PCA, SAM and RXD were calculated as separate layers and incorporated in OOA as features of each object that were derived during the hierarchical segmentation.

The change detection was first carried out using temporal PCA, an image transformation of stacked pre- and post-event images based on eigenvector analysis of their image covariance matrix [Deng *et al.*, 2008]. Temporal PCA combined all 8 bands of the pre- and post-event QuickBird images (4 bands each), and transformed these bands into 8 uncorrelated components. The components which concentrate changes have relatively smaller eigenvalues and can be determined by visual inspection [Radke *et al.*, 2005]. An assessment of the principal components in the training area revealed that the signatures of newly-triggered landslides were primarily concentrated in the 4th principal component (PC4). The minor components beyond PC4 were mainly composed of residuals of the transformation, in most cases noise. In the training area, landslide candidates were preliminarily chosen from PC4 using a membership function calculated from 10 selected samples of landslide objects. This membership function was then incorporated in the algorithm of classification and later employed without modification in the testing area. A further inspection of remaining false positives, such as roads, deforestation areas and sea, revealed relatively low values of those objects in the 2nd principal component (PC2) and values < -300 were found to be suitable threshold for their removal.

Since shadows were also possibly recorded as changes in PCA, a spectral matching image between the pre- and post-images was created using SAM [Kruse *et al.*] and then imported in OOA. The purpose of SAM is to remove the influence of these subtle spectral changes due to illumination differences and viewing angle variation. The matching image derived from SAM estimated spectral similarity by comparing spectral angle difference in terms of image space between the pre- and post-event QuickBird images. For both images each pixel was represented by a spectrum identified as a 4-dimensional vector with specified length and direction. As SAM only considers the angle between the spectral vectors but not the vector length, it is less sensitive to changes due to illumination and shadowing [Kruse *et al.*]. Excluding objects with low SAM values (SAM < 0.09) allowed a removal of spectral false positives that result from subtle spectral changes in illumination as well as shadow, which cannot always be excluded from the change component of PCA.

In addition, in order to remove false positives such as urban areas as well as existing outcrops and clear-cuts, the RXD anomaly detector [Reed and Yu, 1990] was used to estimate spectral anomalies based on the pre-event image, allowing the statistical removal of spectral noise. Assuming that urban areas, deforestation, roads and other infrastructure demonstrate spectral signatures significantly different from the background, RXD can be used to highlight those areas. In this study RXD was applied on the pre-event imagery to detect spectral anomalies

that existed already before the event, which are consequently excluded as newly-triggered landslides. A created anomaly image was then derived and employed as an additional layer in eCognition. Objects with large RXD values were considered as spectral anomalies and a threshold of $RXD > 16$ was defined to exclude these anomalous false positives.

Following the spectral processing that identified landslide candidate objects, a texture analysis of a 1 m LiDAR DTM was performed after merging those candidates. The texture analysis was performed on elevation data for the purpose of analyzing topographic variability, using second-order statistics of the widely-applied GLCM [Haralick, 1973]. The objective is to remove false positives with low-frequency elevation variation, such as undisturbed or unfractured areas, homogenous flat surfaces, and objects with low height variation (*i.e.* roads and water bodies). Texture features calculated from $GLCM_{mean}$ were used in our study. Neighbouring pixels in all directions (0° , 45° , 90° , 135°) were considered for the GLCM generation, accounting for the potential different aspects of landslide objects. Objects with low $GLCM_{mean}$ values were considered to be false positives, and a threshold of $GLCM_{mean} < 126.7$ was defined. The remaining landslide candidates were then classified as final output of newly-triggered landslides.

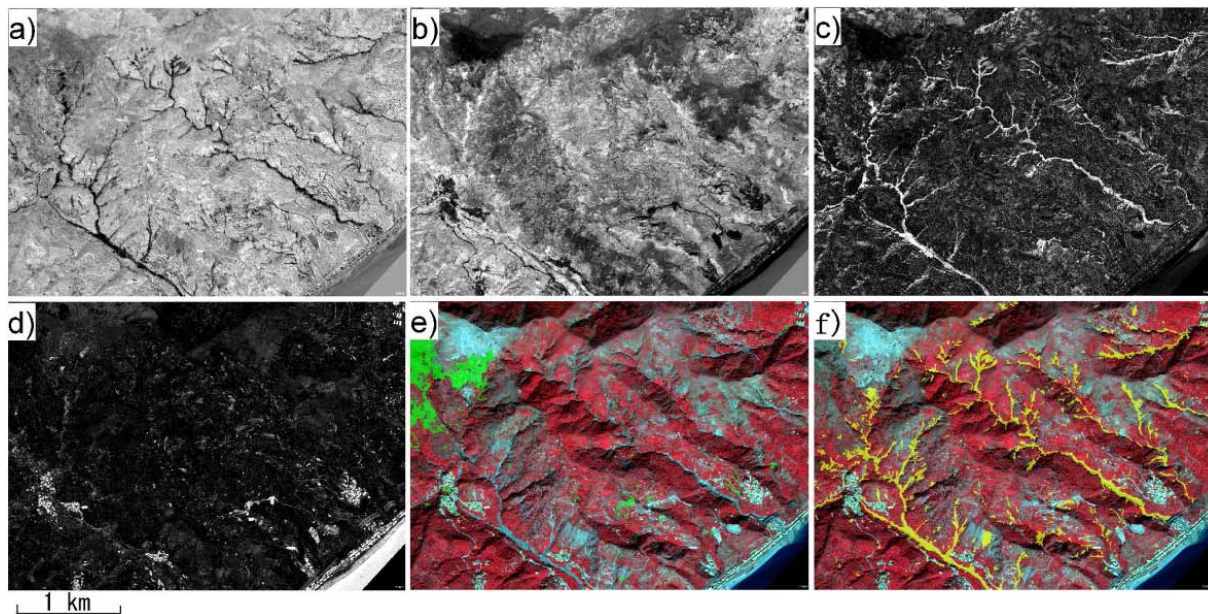


Figure 4 : The testing area of Itala: (a) 4th component of PCA, (b) 2nd component of PCA, (c) matching image of SAM, (d) result of RXD anomaly detection on pre-event image, (e) false positives (green) detected using $GLCM_{mean}$, (f) final result of newly-triggered landslides mapping (yellow).

3. Result and accuracy assessment

The algorithm developed based on the training area of Altolia was directly applied in the testing area of Itala, without any changes in membership function values and defined thresholds. The intermediate derivatives and final outputs for the testing area are shown in Figure 4. To evaluate the accuracy of this approach, OOA-derived landslides were compared

with a manually-mapped landslide inventory. The accuracy assessment was carried out for the number and the spatial extent of mapped landslides (Table 6), both of which are considered critical in a subsequent quantitative landslide hazard and risk assessment. The number of landslides is useful for a quantitative estimate of the temporal probability of landslide occurrence, whereas the spatial extent of landslide is beneficial for the estimate of probability of landslide size through the landslide frequency-area statistics [Guzzetti *et al.*, 2005].

Table 6: Accuracy assessment for the test area Itala

	Manual mapping	Auto. mapping	True positive	User Acc.	Prod. Acc.
Number	285	242	198	81.8%	69.5%
Extent (km ²)	0.602	0.555	0.421	75.9%	69.9%

The accuracy assessment calculates the commission and omission errors, which are measures of the user's and producer's accuracies of the mapped landslides, respectively. For the spatial extent of landslides a user's accuracy of 75.9% and a producer's accuracy of 69.9% were achieved. In terms of the number of landslides, user's and producer's accuracies of 81.8% and 69.5%, respectively, were reached. For both number and spatial extent of landslides the results show a lower producer's than user's accuracy: specifically, ca. 31% of all manually mapped landslides were omitted in the OOA-based detection. This indicates an overestimation of false positives during their classification, accompanied with an underestimation of true positives obtained from the membership function of the selected samples. Further improvements should include a more accurate definition of these thresholds for classifying false positives and a more careful selection of representative samples.

4. Conclusion

This study described a novel approach of object-oriented change detection for rapid mapping of newly-triggered landslides after major events, using VHR satellite images and LiDAR data. The approach used a transparent semi-automatic mapping technique that reduces the user involvement to the determination of a few thresholds for a systemized pre-designed OOA work process. First, a problem-specific multi-scale optimization of FNEA was proposed to reduce the degree of over- and under-segmentation of landslides among a number of different scales, avoiding a time-consuming trial and error evaluation of the optimal segmentation parameters that has characterised most OOA researches in the past. Second, change detection using image transformation of PCA was not only found to be useful for a preliminary selection of landslide candidates from PC4, but also enabled a removal of false positives directly from PC2. Third, the matching image derived from SAM allowed the detection of subtle spectral changes from the change of spectrum vector direction. Fourth, spectral anomalies detected by RXD in the pre-event image allowed the removal of false positives, such as landslides that already existed before the landslide event of October 2009. Finally,

surface texture measures based on a 1m LiDAR DTM were incorporated to remove false positives with low-frequency elevation variation.

For the case study in Messina, the approach achieved user's and producer's accuracies of 75.9% and 69.9%, respectively, for the extent of landslides, and 81.8% and 69.5%, respectively, for the number of landslides. Although the accuracy of the automatic approach does not entirely match what can be achieved in manual mapping, it provides an efficient supplement for traditional methods. The chosen spectral object features are expected to be useful to accommodate multispectral information from a great variety of different sensors. The proposed thresholds typically need further adjustment for the application in other cases, whereas in the presented example the visual inspection of one fifth of the study area was sufficient for this purpose. Also, it should not be forgotten that considerable time can be saved for landslide mapping because the manual drawing of landslides boundaries is replaced by image segmentation. Hence, for an effective landslide hazard assessment, the approach provides an efficient tool to retrieve lacking temporal data for an event-based landslide inventory, thus allowing the assessment of temporal probability and magnitude of landslide events for a quantitative hazard assessment.

References

- Benz, U. C., P. Hofmann, G. Willhauck, I. Lingenfelder, and M. Heynen (2004), Multi-resolution, object-oriented fuzzy analysis of remote-sensing data for GIS-ready information, *ISPRS Journal of Photogrammetry and Remote-sensing*, 58(3-4), 239-258.
- Borghuis, A. M., K. Chang, and H. Y. Lee (2007), Comparison between automated and manual mapping of typhoon-triggered landslides from SPOT-5 imagery, *International Journal of Remote-sensing*, 28, 1843–1856.
- Deng, J. S., K. Wang, Y. H. Deng, and G. J. Qi (2008), PCA-based land-use change detection and analysis using multitemporal and multisensor satellite data, *International Journal of Remote-sensing*, 29(16), 4823 - 4838.
- Dragut, L., and T. Blaschke (2006), Automated classification of landform elements using object-based image analysis, *Geomorphology*, 81(3-4), 330-344.
- Esch, T., M. Thiel, M. Bock, A. Roth, and S. Dech (2008), Improvement of Image Segmentation Accuracy Based on Multiscale Optimization Procedure, *IEEE Geoscience and Remote-sensing Letters*, 5(3), 463-467
- Espindola, G. M., G. Camara, I. A. Reis, L. S. Bins, and A. M. Monteiro (2006), Parameter selection for region-growing image segmentation algorithms using spatial autocorrelation, *International Journal of Remote-sensing*, 27(14), 3035 - 3040.
- Guzzetti, F., P. Reichenbach, M. Cardinali, M. Galli, and F. Ardizzone (2005), Probabilistic landslide hazard assessment at the basin scale, *Geomorphology*, 72(1-4), 272-299.
- Haralick, R. M., K. Shanmugam and I. H. Dinstein (1973), Textural features for image classification., *IEEE Transactions on Systems, Man and Cybernetics*, 3(6), 610-621.
- Hay, G. J., T. Blaschke, D. J. Marceau, and A. Bouchard (2003), A comparison of three image-object methods for the multiscale analysis of landscape structure, *ISPRS Journal of Photogrammetry and Remote-sensing*, 57(5-6), 327-345.
- Hervás, J., J. I. Barredo, P. L. Rosin, A. Pasuto, F. Mantovani, and S. Silvano (2003), Monitoring landslides from optical remotely sensed imagery: the case history of Tessina landslide, Italy, *Geomorphology*, 54(1-2), 63-75.
- Kruse, F. A., A. B. Lefkoff, J. W. Boardman, K. B. Heidebrecht, A. T. Shapiro, P. J. Barloon, and A. F. H. Goetz The spectral image processing system (SIPS)--interactive visualization and analysis of imaging spectrometer

- data, *Remote-sensing of Environment*, 44(2-3), 145-163.
- Martha, T., N. Kerle, C. J. van Westen, and K. Kumar (2010), Characterising spectral, spatial and morphometric properties of landslides for semi-automatic detection using object-oriented methods, *Geomorphology*, 116(1-2), 24-36
- Martha, T., N. Kerle, C. van Westen, V. Jetten, and V. Kumar (in review), Segment optimisation and data-driven thresholding for knowledge-based landslide detection by object-oriented image analysis, *Transactions on Geoscience and Remote-sensing*.
- McKean, J., and J. Roering (2004), Objective landslide detection and surface morphology mapping using high-resolution airborne laser altimetry, *Geomorphology*, 57(3-4), 331-351.
- Radke, R. J., S. Andra, O. Al-Kofahi, and B. Roysam (2005), Image change detection algorithms: a systematic survey, *Image Processing, IEEE Transactions on*, 14(3), 294-307.
- Reed, I. S., and X. Yu (1990), Adaptive multiple-band CFAR detection of an optical pattern with unknown spectral distribution, *Acoustics, Speech and Signal Processing, IEEE Transactions on*, 38(10), 1760-1770.

Combination of airborne & terrestrial LiDAR for the structural analysis of landslides

Application: Landslide characterization and monitoring

Technique: Airborne and ground-based LiDAR

Main references: Travelletti, J., J.-P. Malet, K. Samyn, G. Grandjean, M. Jaboyedoff (in press): Control of landslide retrogression by discontinuities: evidences by the integration of airborne- and ground-based geophysical information

Contributors: CNRS (J. Travelletti, J.-P. Malet), BRGM (G. Grandjean)

Abstract

The objective of this work is to present a multi-technique approach to define the geometry, the kinematic pattern and the failure mechanism of a retrogressive large landslide (upper part of the La Valette landslide, South French Alps) by the combination of airborne (ALS) and terrestrial (TLS) laser scanning data and ground-based seismic tomography data. The advantage of combining different methods is to constrain the geometrical and failure mechanism models by integrating different source of information.

ALS data are efficient to analysis the morphological structures controlling the landslide geometry at small scales. Three main discontinuities can be observed in complement to the field observations. The seismic tomography survey (P-wave and S-wave velocities) highlights the presence of a low seismic-velocity zone ($V_p < 900 \text{ m.s}^{-1}$ and $V_s < 400 \text{ m.s}^{-1}$) in the crown area which is characterized by a dense fracture network at the surface and in depth. The surface displacements calculated from TLS data over a period of two years (May 2008-May 2010) allow to quantify the landslide activity at the direct vicinity of the discontinuities. An important subsidence of the crown area with an average velocity of 3 m.year^{-1} due to a sliding along two discontinuities is determined. The displacement directions indicate that the retrogression is controlled structurally by the pre-existing discontinuities.

Keywords: slope failure, LiDAR data, seismic tomography, discontinuity, geological model

1. Introduction

In landslide investigations, a combination of several direct and indirect techniques is very often used, and several complementary ground-based and airborne-based technologies have been developed in the last decade to provide spatially-distributed information on the structure. In combination to field observations and classical geotechnical investigation, the ground-based techniques are mainly 2D and 3D electrical resistivity and seismic tomographies [Jongmans and Garambois 2007] and the airborne-based techniques are mainly radar interferometry techniques (InSAR), Light Detection and Ranging techniques (LiDAR) and correlation of optical imageries [Delacourt *et al.*, 2007; Jaboyedoff *et al.*, 2009].

Terrestrial Laser Scanning (TLS) and Airborne Laser Scanning (ALS) are very efficient techniques for characterizing the morpho-structure [Feng and Röshoff, 2004; Slob *et al.*, 2005; Jaboyedoff *et al.*, 2009] and the kinematics of landslides [Rosser *et al.* 2007; Travelletti *et al.* 2008; Prokop and Panholzer 2009] because they provide a rapid collection of field topographical data with a high density of points within a range of several hundreds of meters. Then, the possible mechanisms affecting the slope can be deduced from the displacement vectors at the ground surface [Jaboyedoff *et al.*, 2004] such as the geometry of the slip surface [Casson *et al.* 2005; Travelletti *et al.* 2008; Oppikofer *et al.* 2009].

In hard rock-types of failure, the morpho-structures identified at the ground surface often reflect the internal geometry of the deformation [Agliardi *et al.* 2001; Eberhardt *et al.* 2005]; at the opposite, in soft rock-types of failure, the extension in depth of the structures is more difficult to identify. Therefore, additional survey techniques are necessary to complement this lack of information in depth, such as seismic tomographies which allow to characterize properties such as the layering, the degree of fracturing and the stiffness of the material [Jongmans *et al.* 2009].

Still, a major difficulty consists in interpreting and integrating all the available data in a coherent framework to provide a complete picture of the landslide structure. This work presents a multi-technique approach to characterize the structure of the upper part of the La Valette landslide (South French Alps) by combining airborne and terrestrial LiDAR surveys (ALS, TLS), geomorphological analyses and seismic tomographies.

2. Data and methods

2.1. History of development of the landslide and objective of the monitoring

The La Valette landslide, triggered in 1982, is one of the most important large and complex slope movements in the South French Alps. The landslide associates two styles of activity: a mudslide type of behavior with the development of a flow tongue in the medium and lower part, and a slump type of behavior with the development of several rotational slides in the upper part. The landslide extends over a length of 2 km for a variable width of 0.2 km in the lower and medium parts, to 0.45 m in the upper part. The maximum depth varies from 25 m in the lower and middle parts [Evin 1992] to 35 m in the upper part [Le Mignon 2004]. The mean slope gradient is ca. 30° in the scarp area and ca. 20° in the mudslide area. The volume of the mudslide body is estimated at $3.5 \cdot 10^6 \text{ m}^3$.

2.2 Data acquisition and processing methods\

2.2.1 Acquisition of Airborne Laser Scanning (ALS) data

The ALS survey was performed on July 2009 with the handheld airborne mapping system of the *Helimap* company [Vallet and Skaloud 2004]. After vegetation filtering, a point density of 4.1 pt.m^{-2} has been obtained and a 0.5 m-mesh DEM from the ground surface elevation points has been generated with a Delaunay triangulation. The DEM was then used to calculate a shaded relief map and a difference map with a 10 m-mesh DEM interpolated from topographic contour lines before the landslide event (maximal elevation error of 10 m).

2.2.2 Acquisition of Terrestrial Laser Scanning (TLS) data

A displacement monitoring of the upper part of the landslide has been carried out by repeated TLS data acquisitions. The displacement monitoring device consists in a long-range terrestrial laser scan Optech ILRIS-3D, which principle is based on the time-of-flight distance

measurements using an infrared laser [Slob and Hack 2004]. Seven TLS datasets were acquired over the period 18 May 2008 to 27 May 2010 from the same base position (Fig. 1); the scanned area was orientated in the direction of the discontinuity D2 at a distance of 130 m from the base resulting in a mean point density of about 150 pts.m⁻². Only the last return pulse was registered to maximize the number of points at the ground surface.

2.2.3 Vegetation filtering, co-registration and georeferencing of the sequential TLS datasets

The TLS datasets were processed and analyzed using the *Polyworks v.11* software (InnovMetric 2009). The vegetation filter consists in an automatic selection of the points localized beyond a minimum height relative to a low-resolution square-grid DEM surface computed on the sequential point clouds. In this study, the mesh size of the low resolution DEM was fixed at 0.5 m and the minimum height at 0.1 m. A co-registration procedure is then used for aligning the sequential TLS point clouds in the same coordinate system. First a manual alignment procedure is used; then an automated Iterative Closest Point (ICP) algorithm is applied to minimize (least square method) the distance between the points belonging to the different sequential datasets. A good confidence is given to the co-registration quality because of the large size of the stable area of the image used for the co-registration (1000 m²) in reference to the size of the moving area not introduced in the co-registration procedure (4300 m²). For the absolute georeferencing, the ALS point clouds were used as a reference.

2.2.4 Accuracy of the TLS point clouds

In order to assess the accuracy associated with the TLS measurements, repetitivity measurements were realized on a planar stratum of the main scarp, and corresponding to the black marls formation (9 m²). The repetitivity analysis indicates that the measurement error of the TLS used in this study follows a normal distribution characterized with an average error u of $1.0 \cdot 10^{-3}$ m and a standard deviation σ of $1.2 \cdot 10^{-2}$.

The accuracy of co-registration procedure is given by the residual 3D misfit of the TLS of the 18 May 2008 and the ALS survey computed on the stable part. The error in the co-registration was slightly higher and mainly related to the lower point density and accuracy of the ALS datasets.

2.2.5 Displacement characterization and quantification

The displacements are calculated by comparing the TLS datasets with the reference. Two methods are used to quantify the displacements from the original point clouds. The first method is based on shortest distance comparison of point clouds. The second uses displacements of Specific Points (SPs)

The shortest distance (SD) comparison consists in computing for each point of a point cloud the shortest distance to its nearest neighbor in the reference point cloud. This method is particularly useful to detect spatially distributed changes if the direction of movement is unknown and to define zones with different displacement directions [Oppikofer et al. 2009].

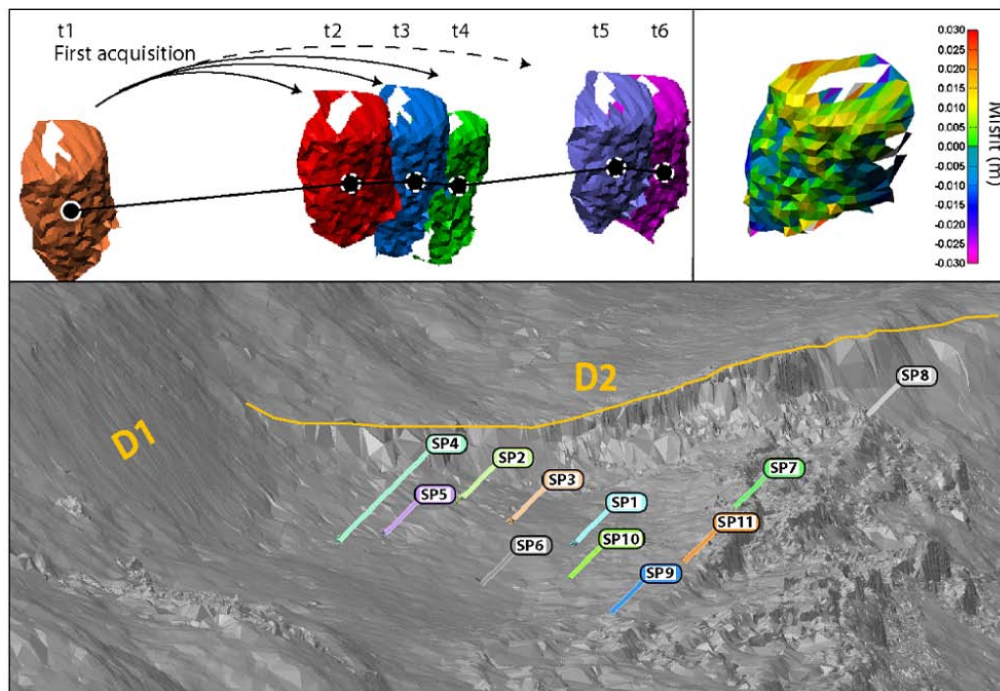


Figure 1: Location of the eleven SPs in the crown area used to calculate the displacements. The SPs of the first acquisition are aligned on their corresponding displaced SPs for each acquisition dates. The displacement of the center point of each SP of the first acquisition allows to determine the displacement vector. The average misfit between the SP of the first acquisition and the corresponding SP is estimated at ca. 0.01 m.

In order to determine the vertical displacement affecting the upper part of the landslide, the SD is constrained to compute displacement only along the vertical direction (SD_v) assuming a tolerance angle for the vertical direction of $\pm 10^\circ$. The results are therefore comparable to elevation changes computed with differential DEMs [Bitelli *et al.*, 2004]. The accuracy of the vertical displacement depends on two independent factors: (i) the co-registration accuracy, and (ii) the computed distance D according to the tolerance angle which gives a maximal error E_{\max} ($E_{\max} = D * \sin(10^\circ)$).

The observed movement of Specific Points (SPs) allows to define the direction of displacements. In this study, natural SPs were chosen (Figs. 1). They consist in tree stumps recognizable in the unfiltered sequential point clouds. In order to assess the displacements of the SPs in the crown area, a method similar to the ones proposed by *Montserrat and Crosetto* [2008] and *Oppikofer et al.* [2009] and based on a roto-translation technique is developed. Eleven SPs were triangulated in the plane normal to the laser viewing direction in order to minimize the effect of shadow zones in the interpolation (Fig. 1). To calculate the true displacement field, the center points of the SPs in the first acquisition is determined by averaging the X, Y Z positions of the points forming the SPs. Then the triangulated SPs of the reference are aligned on their corresponding triangulated SPs in the sequential point clouds (Fig. 1) Finally, the displacement vectors of the SPs are given by the initial and the final position of the center points of the first acquisition. Because the SPs are very well defined, the error mainly depends on the co-registration accuracy of the sequential point clouds.

3. Results

3.1. Morpho-structural analysis

The combined analysis of the geological field observations, the shaded relief map and the differential DEM map allows to propose a kinematic model of the landslide retrogression.

Although the highly dislocated flysch formation can be considered as a relatively soft rock, the shaded relief analysis with the differential DEM clearly demonstrate that, at small scale, the key factor controlling the failure geometry and the overall stability of the mass is not the flysch formation itself, but the spacing and the orientation of the discontinuities composed by D1, D2 and D3. The upper part of the La Valette landslide can be divided in four geological sub-units (Fig. 2a). Since the triggering date in March 1982, the sub-unit 1 has been confined between the steep discontinuities D2 and D3 that constrained the landslide retrogression to the North-East.

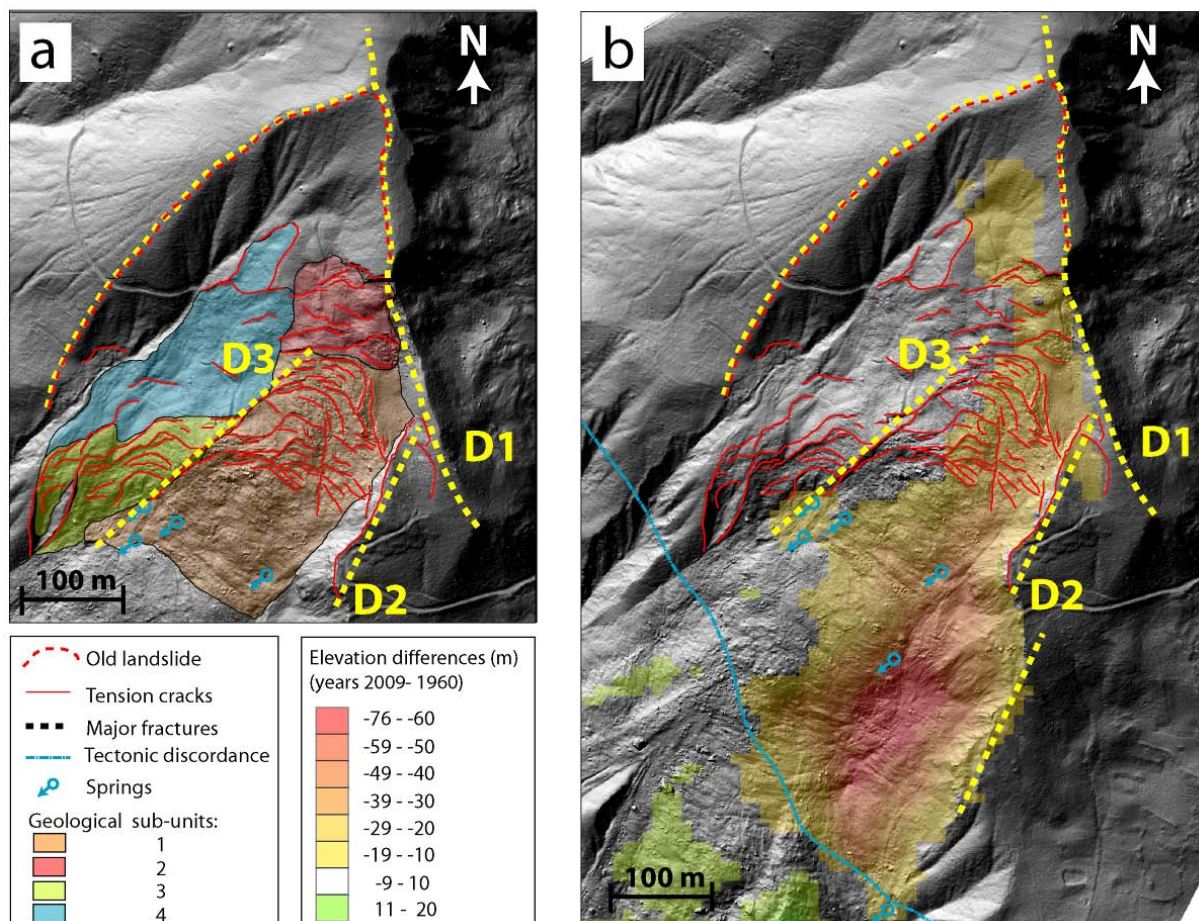


Figure 2: Morpho-structural maps derived from the interpretation of the Airbone Laser Scanning (ALS) survey. a) Major discontinuities and sub-units identified in the scarp and in the crown areas. b) Differential DEM highlighting the retrogression direction of the landslide for the period 1960-2009 constrained by the discontinuity D2 and D3.

The failed mass is composed of coherent blocks (up to 50 m wide) which are sliding towards the main slope direction. These blocks form minor counter-slopes affected by multiple open tension cracks (up to 1 m in opening and in spacing) favoring water infiltration. The blocks are progressively dislocated and incorporated in the mudslide body downhill. The negative elevation difference developing along D1 indicates that the landslide retrogression to the North-East is limited by D1 which forces the retrogression to develop laterally to the North (Fig. 2b). As a consequence of the loss of buttress given by the sub-unit 1, the sub-units 2 and 3 are progressively destabilized. The sub-unit 4 (North-West side of D3) is characterized with a hummocky morphology indicating a lower destabilization of the slope due to the loss of buttress provided by the sub-unit 3 located downhill. The downhill limit of the negative elevation remarkably coincides with the tectonic discordance of the Autapie sheet thrust and the uphill limit corresponds to the spring area. The location of the triggering area of 1982 is clearly identified where the elevation difference (50 m) is the maximum.

3.2. Kinematics analysis

Displacements calculated from the TLS datasets between the period May 2008 – May 2010 allow to quantify the landslide activity at the vicinity of D1, D2 and D3. The SDv computations on the point clouds indicate 6 m of elevation difference between July 2008 and May 2010 leading to an average vertical displacement rate of $3 \text{ m}\cdot\text{year}^{-1}$ along D1 and D2 of the top of the sub-unit 1 (Fig. 3). All the displacements in the sub-unit 1 are concentrated between D1 and D2 where tensions cracks are developing.

The vertical displacement rates allow to distinguish three coherent blocks 1a, 1b and 1c belonging in the sub-unit 1; these blocks are progressively separated by the opening of tension cracks and the sliding along D1 and D2. Uphill, the sub-unit 2 is also destabilized due to the loss of buttress provided by sub-unit 1. No displacement is detected on the South-East side of D2 with reference to the accuracy of the TLS datasets (less than 0.05 m). These observations are in agreement with the morpho-structural analysis. The displacement amplitudes of the SPs are far larger than the accuracy of the TLS datasets, thus giving a good confidence in the measurements. The SPs displacements allow to determine the true 3D displacement vectors characterized by an average velocity of about $4 \text{ m}\cdot\text{year}^{-1}$ (Fig. 4).

3.3. Identification of the failure mechanism and volume estimation

Because the upper part of the La Valette landslide is structurally controlled at small scale by planar sliding and wedge fracture configurations, a synthesis of the structural and kinematics analysis is done by the use of horizontal hemispherical projections (equal angle). Figure 5a presents the conceptual model of the failure mechanism interpreted from the integration of the ALS, TLS and seismic survey.

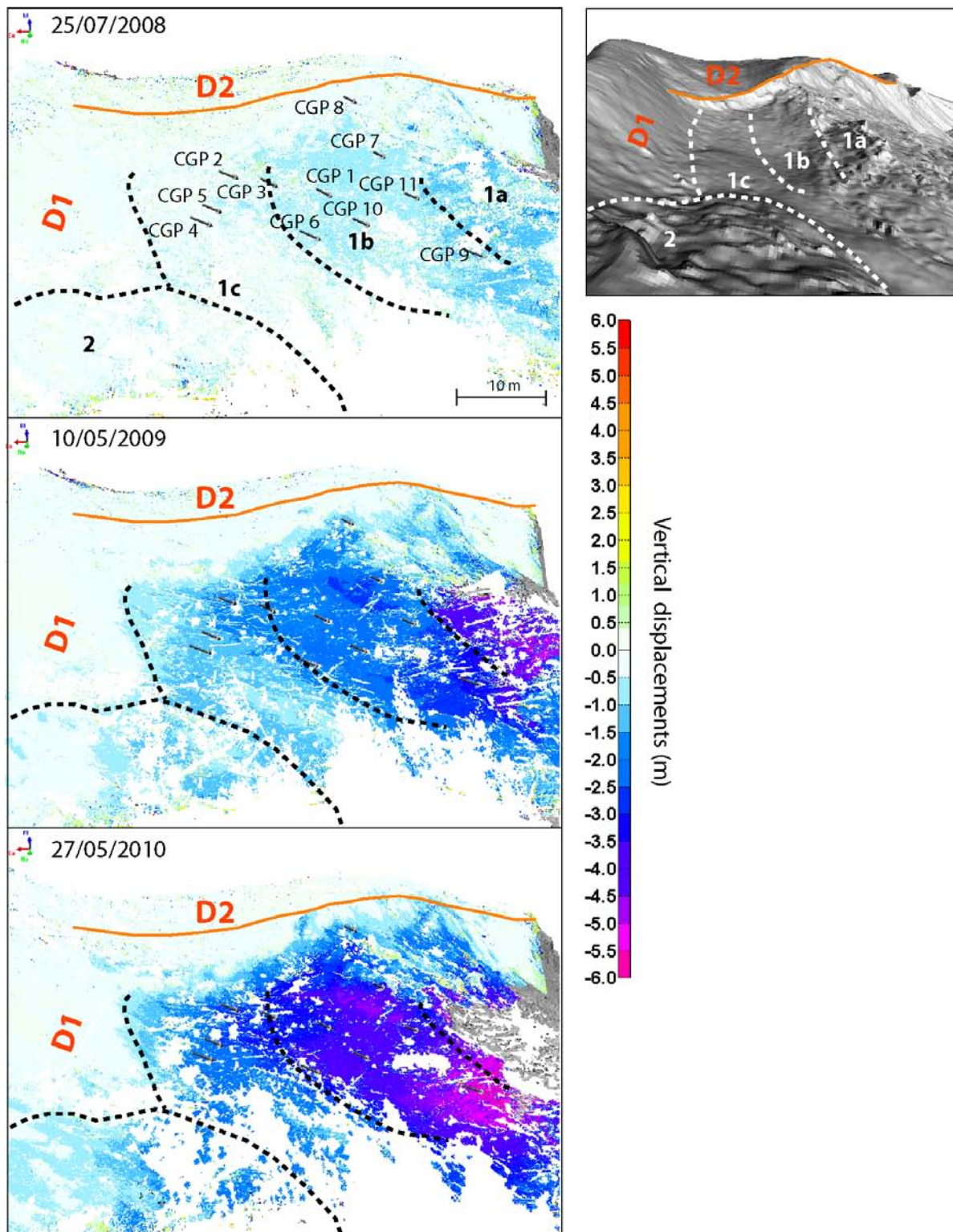


Figure 3: TLS point cloud comparisons according to the reference date of 18 May 2008. The displacements are calculated with the shortest distance comparison in the vertical direction. A negative value means that the point elevation is lower than the point of the reference. Several blocks are clearly individualized through time. The blocks 1a, 1b and 1c belong to the sub-unit 1. The block 2 belongs to the sub-unit 2. The displacement vectors of the SPs are also indicated.

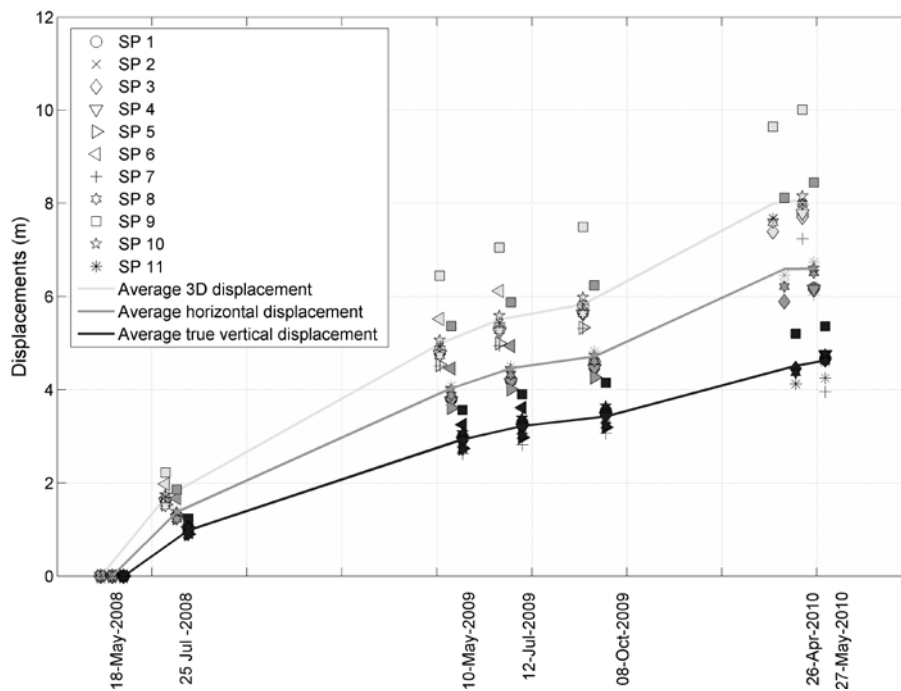


Figure 4: Cumulated displacements of the SPs calculated with the roto-translation technique.

From a kinematical point of view, D3 and D2 define a wedge geometry with an axis direction and dip of $215^{\circ}/30^{\circ} \pm 11^{\circ}/5^{\circ}$ and a maximum depth varying between 60 to 80 m which upper boundary is delimited by D1. Because the wedge axis does not ‘daylight’ in the slope face, this geometry is precluded from a strict straight-forward wedge kinematic evaluation as a single homogeneous block [Hoek and Bray 1981]. In other words, the wedge cannot move without a buttress breakout. Therefore the wedge geometry can only constrain the landslide retrogression direction between D2 and D3 to the North. Downhill, the mudslide body is acting as a buttress for the upper part. Consequently, the progression of the mudslide allows the development of dip-slope failures and coherent blocks start sliding along D4 laterally delimited by D2 and D3

To estimate the volume of the failed mass along D4 in the sub-unit 1, an interpolation is carried out using the SLBL method. The discontinuities D1 (North-East limit), D2 (South-East limit), D3 (North-West limit) and D4 (basal limit in depth) are used to constrain the calculation domain of the SLBL by assuming that D4 is continuous with a slightly curved geometry. The mechanical weak zone highlighted by the spring line at the lower limit of sub-unit 1 (Fig. 5) is used as the Southern limit for the SLBL calculation. The unstable volume is calculated using a 2 m grid DEM interpolated from the ALS data. This cell size is essentially used for computation stability and time computing purposes. A tolerance of -0.3 defining the degree of curvature of the SLBL is selected in such way that the SLBL surface fits at best the discontinuity D4. The result gives a slightly curved surface that flattens and daylight in the spring line. A volume of $500'000 \text{ m}^3$ is estimated (Fig. 5b). This volume represents the highly fractured mass mobilized by D4 which is currently loading the underlying mudslide body.

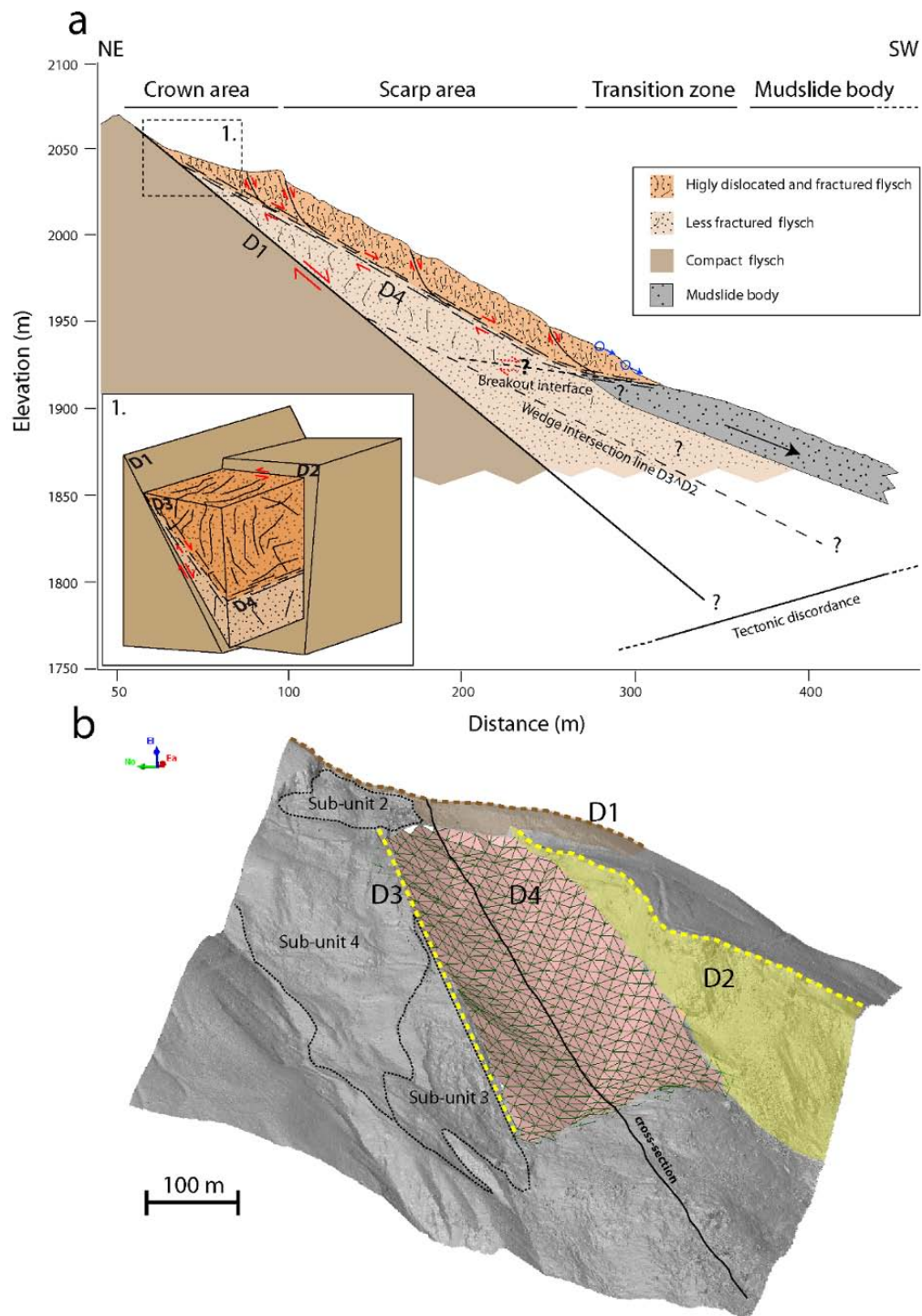


Figure 5: Conceptual geological model of development of the upper part of the La Valette landslide. a) Proposed concept of the failure mechanism affecting the scarp and the crown areas. The morpho-structural and the kinematics analyses allow to highlight a planar failure mechanism along D1 and D4 confined in a wedge geometry delimited by D2 and D3. b) 3D view of the SLBL computation carried out to estimate the volume of the failed mass and to extent D4 on the whole scarp area. The ground topography above D4 has been removed.

4. Discussion and Conclusion

The efficiency of combining ground-based (LiDAR TLS, seismic tomography) and airborne based (LiDAR ALS) geophysical information to characterize the landslide structure is demonstrated by the agreement observed between geological field observations and morpho-structural and kinematics analyses. The advantage of combining different methods is to propose an interpretation adapted to the scale of the landslide which is not possible when only punctual measurements are used. TLS data provide high resolution point clouds of the topography for large scale analysis which complements ALS data more suitable for smaller scale analysis. The seismic tomography survey provides a spatially-distributed information on how the fractures are set up in depth. The integration and the interpretation of this multi-source data allow to propose possible landslide evolution scenarios.

The upper part of the La Valette landslide is a case of reactivation of an older landslide and is characterized with a succession of individual slides as it is often observed in large deep-seated gravitational deformations [DSGSD; Agliardi *et al.* 2001]. A first slide occurs and, as a consequence of the movement of this mass, other adjacent masses starts to move thus allowing the retrogression of the landslide to the North. The opening of tension cracks in the crown area is an evidence of the initiation of a progressive failure. However, the flysch formation may already have undergone some deformation before the discontinuities start to open. The failure may have started in the weak zone D4 and along the pre-existing fractures D1, D2 and D3. Furthermore, the progressive failure of successive slides is probably a consequence of non-uniform stress and strain conditions which prevent thus the upper part to a catastrophic failure. In the same way, the dip of the SLBL is very close to the residual friction angle of the reworked flysch (30°). Therefore the stability limit is not reached in the same time in the whole mass and it would be very unlikely that the unstable mass will fail in a single event.

References

- Agliardi F, Crosta G, Zanchi A 2001 Structural constraints on deep-seated slope deformation kinematics. *Engineering Geology* 59: 83–102
- Bitelli G, Dubbini M, Zanutta A 2004 Terrestrial laser scanning and digital photogrammetry techniques to monitor landslide bodies. In: Proceedings of the XXth ISPRS Congress ‘Geo-Imagery Bridging Continents’, XXXV, Part B5, Istanbul, Turkey, 12–23 July 2004, ISPRS, pp 246–251
- Casson B, Delacourt C, Allemand P 2005 Contribution of multi-temporal sensing images to characterize landslide slip surface – Application to the La Clapière landslide (France). *Natural Hazards and Earth System Sciences* 5: 425–437
- Delacourt C, Allemand P, Berthier E, Raucoules D, Casson B, Grandjean P, Pambrun C, Varel E 2007 Remote-sensing techniques for analysing landslide kinematics: a review. *Bulletin de la Société Géologique de France* 178(2): 89–100
- Eberhardt E, Thuro K, Luginbuehl M 2005 Slope instability mechanisms in dipping interbedded conglomerates and weathered marls – the 1999 Rufi landslide, Switzerland. *Engineering Geology* 77: 35–56
- Evin M 1992 Prospection sismique en partie basse de la coulée de La Valette. Internal Report, RTM – Restauration des Terrains en Montagne, Barcelonnette, France http://eost.u-strasbg.fr/omiv/Publications_la_valette.html

- Feng QH, Röshoff K 2004 In-situ mapping and documentation of rock faces using a full-coverage 3-D laser scanning technique. *International Journal of Rock Mechanics and Mining Sciences* 41: 139–144
- Hoek E, Bray JW 1981 *Rock Slope Engineering*. Institution of Mining and Metallurgy, London, UK, 358p
- InnovMetric, 2009 *PolyWorks User's Manual - 3-D scanner and 3-D digitizer software* from InnovMetric Software Inc., <http://www.innovmetric.com/>
- Jaboyedoff M, Baillifard F, Couture R, Locat J, Locat P 2004 New insight of geomorphology and landslide prone area detection using DEM. In: Lacerda WA, Ehrlich M, Fontoura AB, Sayo A (eds.), *Landslides evaluation and stabilization*, Balkema, Rotterdam, pp 199–205
- Jaboyedoff M, Couture R, Locat P 2009 Structural analysis of Turtle Mountain (Alberta) using digital elevation model: toward a progressive failure. *Geomorphology* 103: 6–16
- Jongmans D, Garambois S 2007 Geophysical investigation of landslides: a review. *Bulletin de la Société Géologique de France* 178(2): 101–112
- Le Mignon G 2004 *Analyse de scénarios de mouvements de versants de type glissement-coulées. Application à la région de Barcelonnette (Alpes-de-Haute-Provence, France)*. PhD Thesis, Ecole Nationale des Ponts et Chaussées, Paris, France, 210 p
- Montserrat O, Crosetto M 2008 Deformation measurement using terrestrial laser scanning data and least squares 3-D surface matching. *ISPRS Journal of Photogrammetry* 63: 142–154
- Oppikofer T, Jaboyedoff M, Blikra LH, Derron MH, Metzger R 2009 Characterization and monitoring of the Aknes rockslide using terrestrial laser scanning. *Natural Hazards and Earth System Science* 9: 1003–1019
- Prokop A, Panholzer H 2009. Assessing the capability of terrestrial laser scanning for monitoring slow moving landslides. *Natural Hazards and Earth System Sciences* 9: 1921–1928
- Rosser NJ, Petley DN, Dunning SA, Lim M, Ball S 2007 The surface expression of strain accumulation in failing rock masses. In: Eberhardt E, Stead D, Morrison T (eds): *Rock mechanics: meeting Society's challenges and demands*. Proceedings of the 1st Canada–U.S. Rock Mechanics Symposium, Vancouver, Canada, 27–31 May 2007, Taylor & Francis, pp. 113–120
- Slob S, Hack R 2004 3D Terrestrial Laser Scanning as a new field measurements and monitoring technique. In: Hack R, Azzam R., Charlier R. (eds): *Engineering geology for infrastructure planning in Europe. A European perspective*. Lecture Note in Earth Sciences. Springer, Berlin-Heidelberg, pp 179–190
- Travelletti J, Oppikofer T, Delacourt C, Malet JP, Jaboyedoff M 2008 Monitoring landslides displacements during a controlled rain experiment using a long-range terrestrial laser scanning (TLS). In: *ISPRS - The International Archives of the Photogrammetry, Remote-sensing and Spatial Information Sciences*. Vol. XXXVII. Part B5, pp. 485–490
- Vallet J, Skaloud J 2004 Development and experiences with a fully-digital handheld mapping system operated from a helicopter. In: *The International Archives of the Photogrammetry, Remote-sensing and Spatial Information Sciences*, Istanbul, Vol. XXXV, Part B5.

Segment Optimization and Data-Driven Thresholding for Knowledge-Based Landslide Detection by Object-Based Image Analysis

Application: Landslide inventory mapping

Technique: Fusion of passive optical spaceborne images, spaceborne photogrammetric DSM, thematic data

Main references: Martha, T., N. Kerle, C. van Westen, V. Jetten and V. Kumar (accepted): Segment Optimization and Data-Driven Thresholding for Knowledge-Based Landslide Detection by Object-Based Image Analysis.

Contributors: ITC (T. Martha, N. Kerle, A. Stumpf)

Abstract

To detect landslides by object-based image analysis using criteria based on shape, colour, texture, and in particular contextual information and process knowledge, candidate segments must be delineated properly. This has proved challenging in the past, since segments are mainly created using spectral and size criteria that are not consistent for landslides. This paper presents an approach to select objectively parameters for a region-growing segmentation technique to outline landslides as individual segments, and also addresses the scale dependency of landslides and false positives occurring in a natural landscape. Multiple scale parameters were determined using a plateau objective function derived from the spatial autocorrelation and intrasegment variance analysis, allowing for differently sized features to be identified. While a high resolution Resourcesat-1 LISS-IV (5.8 m) multispectral image was used to create segments for landslide recognition, terrain curvature derived from a digital terrain model based on Cartosat-1 (2.5m) data was used to create segments for subsequent landslide classification. Here optimal segments were used in a knowledge-based classification approach with the thresholds of diagnostic parameters derived from K-means cluster analysis, to detect landslides of five different types, with an overall recognition accuracy of 76.9%. The approach, when tested in a geomorphologically dissimilar area, recognised landslides with an overall accuracy of 77.7%, without modification to the methodology. The multi-scale classification-based segment optimisation procedure was also able to reduce the error of commission significantly in comparison to a single optimal scale approach.

Keywords: OOA, disaster support, feature extraction, K-means cluster analysis, segmentation, India.

1. Introduction

Landslide inventories associated with a single triggering event and should be generated as soon as possible after the occurrence of the event. Satellite remote-sensing technology has proven to be the best tool for generating such landslide inventories, especially with the availability of high resolution images [Chang *et al.*, 2007; Chen *et al.*, 2007; Rau *et al.*, 2007; Voigt *et al.*, 2007]. Recent advances in computer vision and machine intelligence have led to the development of new techniques, such as object-oriented analysis (OOA, frequently also referred to as OBIA or GEOBIA) for automatic content extraction of both man-made and natural geospatial objects [Akçay and Aksoy, 2008; Holt *et al.*, 2009]. In OOA both the information content of an object, as well as process or feature knowledge, are used to classify features in a landscape. It is a step towards replicating the human cognitive process that underpins visual image interpretation. Image segmentation, a method of dividing the image

into non-overlapping regions or segments, is the first major step in OOA, and its quality controls the accuracy of subsequent land cover classification [Laliberte and Rango, 2009].

Although OOA for landslide detection has been attempted by previous workers [Barlow *et al.*, 2006; Martha *et al.*, 2010a], several critical issues have not been addressed. These concern: 1) finding reliable means to segment landslides of different shape and size, which are also internally strongly heterogeneous; 2) incorporation of relative rather than absolute contextual criteria, in addition to spectral, textural and morphometric criteria to eliminate false positives; 3) extracting suitable object characteristics that allow landslide-type specific identification; and 4) minimizing user-driven thresholding of the landslide diagnostic parameters. All of these points are essential for the development of a robust and transferable landslide detection method.

The principal objective of this study is to optimize segment boundaries with a combination of different segmentation algorithms and statistical optimization techniques to delineate automatically landslides of variable shape and size. Another objective is to apply a data-driven/unsupervised thresholding technique to the landslide diagnostic parameters to minimize human intervention.

2. Dataset, area and methodology

In this study Resourcesat-1 LISS-IV multispectral data were used for image segmentation and derivation of spectral characteristics of landslides. Along-track stereoscopic data from Cartosat-1 were used for the extraction of a 10 m gridded digital surface model (DSM) [Martha *et al.*, 2010c]. The DSM was later converted to a digital terrain model (DTM) and used for extraction of topographic parameters. We used these two primary datasets for the automatic detection of landslides in two perennially affected but geomorphologically diverse areas in the Himalayas (Table I). The methodology was developed in the Okhimath area and tested in the Darjeeling area. While summer images were used for Okhimath area, winter images were used for Darjeeling area, thus, the sensitivity of landslide detection by OOA to seasonal variability in image acquisition was also explored (Table I).

Table 1: Description of study areas

	Okhimath, Western Himalayas, India	Darjeeling, Eastern Himalayas, India
Centre location (Latitude/Longitude)	30° 33' 07" N / 79° 06' 32" E	26° 54' 06" N / 88° 15' 00" E
Date of LISS-IV scene	01 April 2007	13 January 2004
Date of Cartosat-1 scene	06 April 2006	28 January 2006
Maximum and minimum elevations	2620 m and 1047 m	2024 m and 373 m
Size of study area	29 km ²	35 km ²
Major landslide types	Rock slide, debris slide and debris flow	Rock slide, debris slide

Size of largest and smallest landslide	0.321 km ² and 0.001 km ²	0.086 km ² and 0.001 km ²
Major land use/cover categories	Barren rocky land, forest and terraced cultivation	Built-up area, forest and tea plantation
Major event	Okhimath landslide (1998) –38 fatalities	Ambootia landslide (1968) – severe loss to cash crops such as tea and oranges.

3.1. Knowledge-Based Detection of Landslide

In this study, we detected landslides by adapting the methodology proposed by [Martha *et al.*, 2010a], which identifies landslides initially along with its false positives and later eliminates them sequentially. A new sub-module for the objective determination of parameters for optimal segmentation was added existing sub-modules were modified to partially replace static thresholds with dynamic thresholding methods and relative rather than absolute criteria for identification of false positives. The modified approach for the detection of landslides was separated into four sub-modules, and implemented using eCognition (Figure 1).

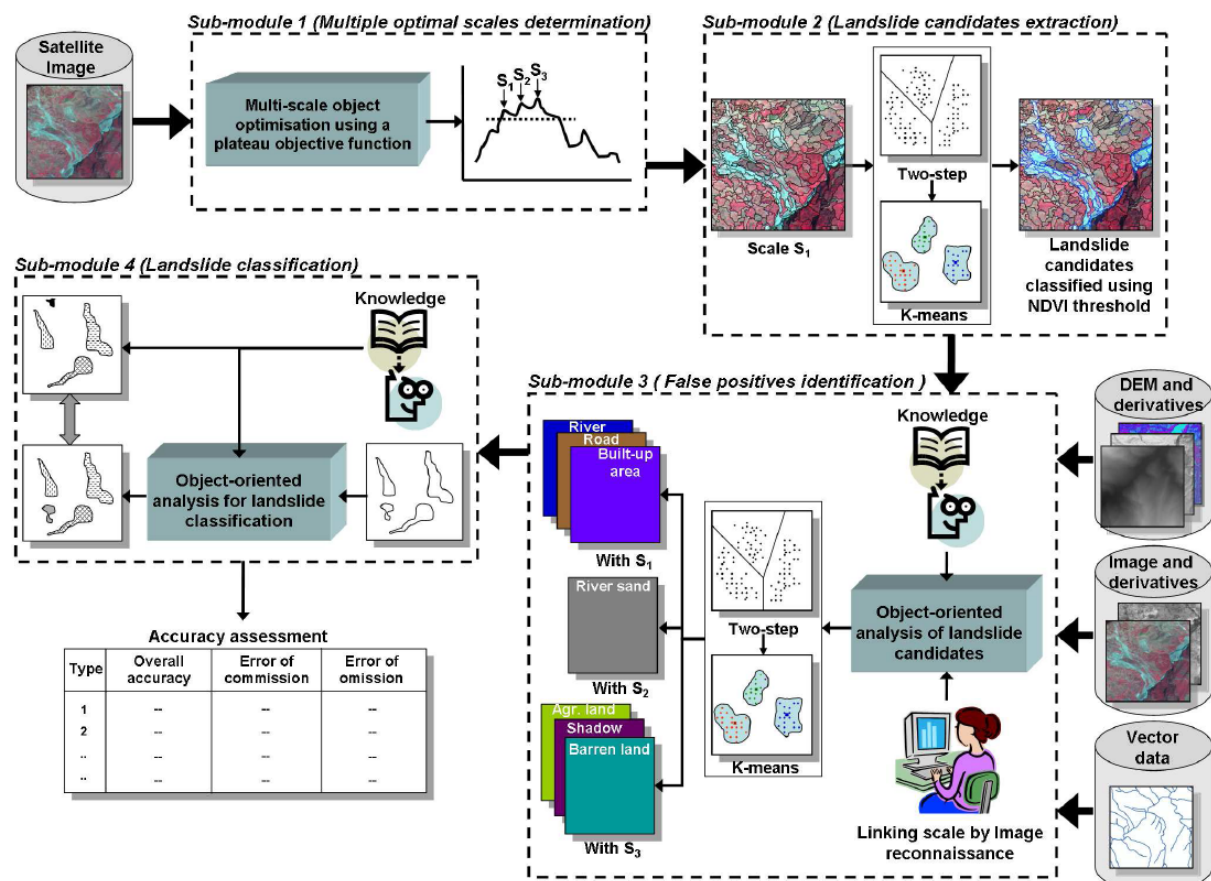


Figure 1: Concept diagram for knowledge-based detection of landslide using OOA by segment optimisation and data driven thresholding.

3.2 Optimization of Segments (Sub-module 1)

To find optimal multiple scales objectively we used Espindola *et al.*'s [Espindola *et al.*, 2006] objective function, which is a combination of intra-segment variance and Moran's I index. By varying the scale factor and maintaining uniform weights for spectral and shape heterogeneities, objects at 50 different scales were created for estimation of the objective function. Mean and variance were calculated using the brightness value of objects, which is the average of DN values of the three multispectral bands. The maximum value of the objective function is a statistical indicator of optimal image segmentation [Espindola *et al.*, 2006]. However, a single optimal scale is insufficient to address the relationship between the spatial structure of an image and the structure of a landscape, although Gao *et al.* [Gao *et al.*, In Press] reported the highest classification accuracy with single scale segments.

To obtain multiple optimal scales instead, we created a simple plateau objective function:

$$F(\text{plateau}) = F(v, I)_{\max} - \sigma \quad (1)$$

where $F(v, I)_{\max}$ is the maximum value and σ is the standard deviation of objective function calculated for 50 different scales, respectively.

The plateau objective function value was used to demarcate the lower boundary of the plateau in the curve created by plotting scale factors and objective functions in x and y axes, respectively (Figure 3). The hypothesis for the plateau objective function is that the peak values are close to the maximum value of the objective function, therefore, the balance between under- and over-segmentation still remains. Furthermore, the peaks are distinct from each other and locally optimal with respect to their immediate neighbor (Figure 3).

3.3 Extraction of Landslide Candidates (Sub-module 2)

The segments created with the scale factor corresponding to the first peak of the plateau were used to begin the landslide detection process. This scale factor has the highest potential to outline landslides of small size in comparison to other scales identified in the plateau function, and also captures the boundary of large landslides occurring in a contrast poor environment, such as within barren rocky land. Landslide candidates were extracted using a NDVI threshold. To standardize NDVI across image dates, pixel values were converted to top of the atmospheric reflectance by correcting for sensor gain and sun position [Song *et al.*, 2001].

Although an initial guess can be made about the number of existing classes by analyzing the image, we used a two-step clustering algorithm to determine the existing classes in an objective manner relying on the Schwarz Bayesian criterion [Schwarz, 1978]. The cluster centers in NDVI data obtained by K-means algorithm were used as thresholds to identify landslide candidates.

3.4. Identification of False Positives (Sub-module 3)

Generally, false positives are of different sizes and, therefore, need to be linked to one of the optimal scales (Figure 2). This increases their chances of successful classification using texture and shape-based criteria, statistical neighbourhood conditions, such as the maximum mean difference to neighbour for the identification of built-up areas, and the minimum mean difference to neighbour for identification of barren agricultural land. Small and narrow features in hills, such as roads, built-up areas and rivers, were identified with scale factor corresponding to the first peak, while larger features, such as barren rocky lands and topographic shadows, were identified with higher scale factors corresponding to subsequent peaks. The scale to feature link was established by a quick onscreen reconnaissance of the spatial structure of the segments with respect to the landscape features (Figure 2). Finally, K-means cluster analysis was used to derive thresholds for the classification of false positives.

3.5 Classification of Landslides (Sub-module 4)

At this stage further segment refinement based on chessboard segmentation was applied to eliminate small patches of vegetation and barren rocky land which had not been detected in the larger segmentation scale. Classification of landslides based on material (rock, earth or debris) was implemented using a relative border criterion. For example, landslides with high relative border to barren rocky land were classified as rock slides. Finally, landslides were segmented using terrain curvature for classification based on failure mechanism (rotational or translational). For example, rock slides with a negative curvature value represent a concave rupture surface, and thus were classified as rotational rock slides.

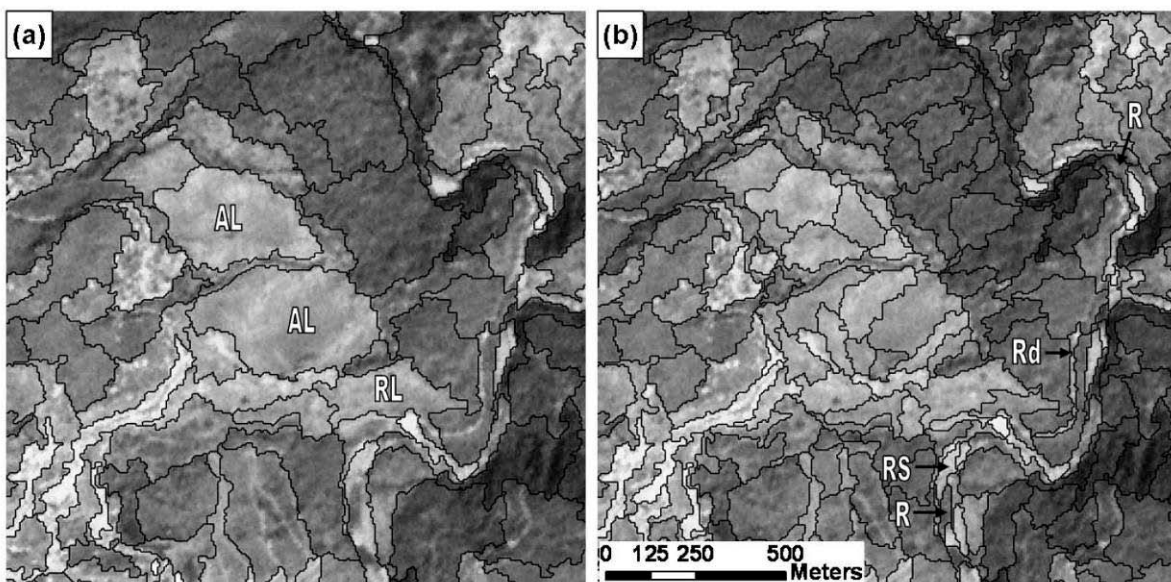


Figure 2: Spatial structure of the segments for most common landslide false positives (uncultivated agricultural terraces (AL), rocky land (RL), road (Rd), river (R) and river sand (RS)) in hilly areas. (a) and (b) show segmentation with high and low scale factors, respectively

3.6 Transferability of the Method

To verify the transferability of the proposed method to unknown areas, we tested the approach developed for Okhimath in the geomorphologically dissimilar Darjeeling area. We first calculated the accuracy in the Okhimath area to test the effectiveness of the proposed method to detect landslides, and then estimated the accuracy of the Darjeeling area to verify its transferability. Assessment of accuracy was carried out by comparing the manually and automatically prepared landslide inventory maps excluding landslides affected by shadow or vegetation cover in the satellite image and merging multiple polygons of large active landslides in the reference inventory map. The accuracy of the detected landslides was assessed in terms of their total number and areal extent.

4. Results

Using the plateau objective function value derived through eq. 1, the plateau boundaries for Okhimath and Darjeeling were determined as 1.061 and 1.078, respectively (Figure 3). These peaks exceeding the plateau correspond to the optimal scales in the respective images.

Landslides and false positives were characterised using a DEM and its derivatives (slope, flow direction, curvature and hillshade), and parameters calculated from the optical image data (NDVI, brightness). These diagnostic parameters and their thresholds obtained from K-means clustering were used to create a rule set in eCognition (Table 2). This rule set was developed using the data of the Okhimath area and the results are explained in the following section.

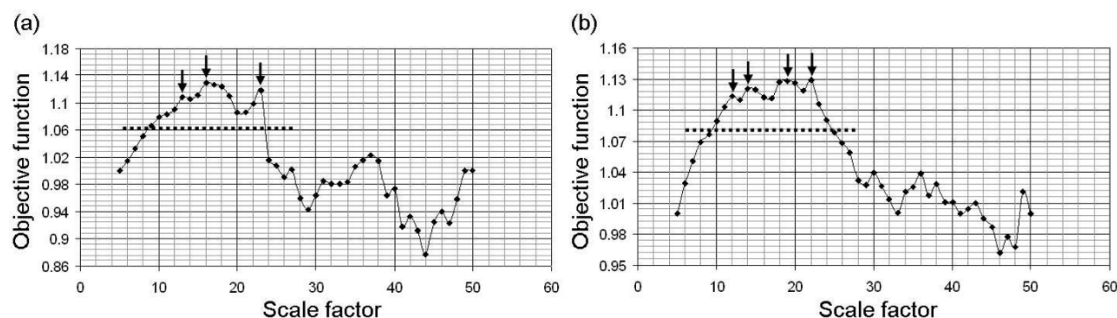


Figure 3 Objective function for Okhimath (a) and Darjeeling (b), indicating the optimal segmentation scales (the peaks shown with arrows) in the plateau area above dotted line that were used in the OOA process.

4.1 Training Area (Okhimath)

The peak scales (Figure 3a) from the objective function (13, 16 and 23) to segment the Okhimath image. Scale factor 13 was used to create objects to begin the landslide detection process. As illustrated in figure 4b, the next optimal scale factor (16) produced large size objects and was less suitable to delineate the landslide. Scale factor 13 was also used to classify false positives, such as roads, river channels and built-up areas, using the criteria given in table 2. The other two scales, 16 and 23, produced large size objects that were linked

to correspondingly larger false positives, such as river sands, barren agricultural and rocky lands, and shadow areas.

Table 2: Characteristic features, object properties and thresholds (O: Okhimath, D: Darjeeling) used for the identification of false positives and landslide types.

Target feature	Characteristic features	Object characteristics (Threshold value)	Object nature	Thresholding method
Landslide candidates	NDVI	Mean NDVI (O \leq 0.22612, D \leq 0.2455)	Spectral	K-means clustering
False positives				
Water	Drainage	Stream order (O $>$ 5, D $>$ 4)	Contextual	Spatial
	NIR band	Mean difference to neighbours (O \leq 15, D \leq 10)	Spectral	K-means clustering
	Slope	Mean angle (O and D \leq 10°)	Spatial	Existing knowledge
Built-up area	Red band	Local maxima (mean difference to neighbours)	Spectral	Statistical
	Red band	GLCM contrast (O \geq 64, D \geq 68)	Spatial	K-means clustering
	Slope	Mean angle (O and D \leq 27°)	Spectral	Existing knowledge
	Water class	Not close to river water (O and D $>$ 50 m)	Contextual	Existing knowledge
Road	All three bands	Compactness (polygon) (O and D \leq 0.2)	Shape	Existing knowledge
	Flow direction	Flow direction and Main direction difference (O and D: between 80 to 105)	Contextual	Existing knowledge
	All three bands	Length/Width (O and D \geq 3)	Shape	Existing knowledge
	Red band	GLCM contrast (O and D \geq 30)	Spatial	K-means clustering
River sand	Water class	Close to river water (O and D = 0 m)	Contextual	Existing knowledge
	DEM	Relief (O and D \leq 30 m)	Contextual	Existing knowledge
Shadow	All bands	Brightness (O \leq 40.18288, D \leq 53.91474)	Spectral	K-means clustering
	Hillshade	Mean Hillshade (O \leq 57.92239, D \leq 14.46621)	Spectral	K-means clustering
Agricultural land	Red band	Local minima (mean difference to neighbours)	Spectral	Statistical
	All three bands	Asymmetry (O and D \leq 0.9)	Shape	Existing knowledge
	Slope	Mean slope (O and D \leq 30°)	Spatial	Existing knowledge
Barren land	NDVI	Mean NDVI (O \geq 0.18425 and D \geq 0.32378)	Spectral	K-means clustering
Escarpment	NDVI	Mean NDVI (O \geq 0.22612 and \leq 0.3088, D \geq 0.32378)	Spectral	K-means clustering
	Slope	Mean slope (O and D \geq 45)	Spatial	Existing knowledge
Landslide type				
Shallow translational rock slide	All three bands	High asymmetry	Shape	Process knowledge
Debris slide	Agricultural land class	High relative border to agricultural land For Peer Review	Contextual	Statistical
Debris flow	All three bands	Large length	Shape	Process knowledge
Rotational rock slides	Barren land and escarpment classes	High relative border to barren land and escarpment	Contextual	Statistical
	Curvature	Very low mean curvature	Spatial	Process knowledge
Translational rock slides	Barren land and escarpment classes	High relative border to barren land and escarpment	Contextual	Statistical
	Curvature	Near zero mean curvature	Spatial	Process knowledge

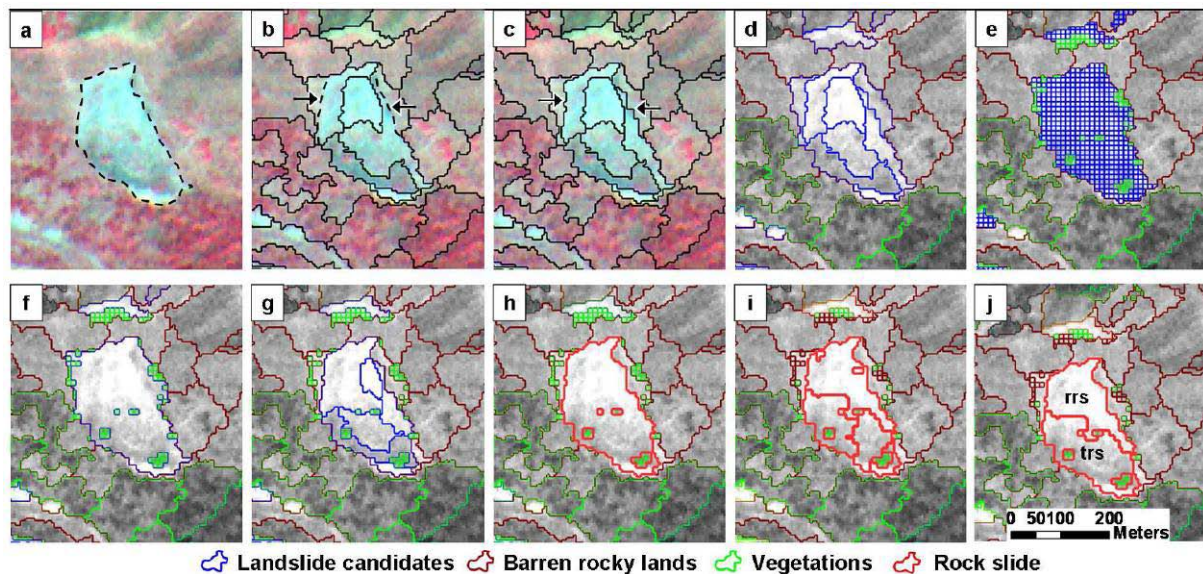


Figure 4: Important stages towards successful landslide recognition and classification illustrated for a large landslide in Okhimath. a. Actual boundary of landslide. b. Segmentation with scale factor 16 was unable to delineate the left and right flanks (shown with dashed lines) of the landslide. c. Flanks were correctly delineated with scale factor 13. d. Detection of landslide candidates with NDVI threshold. e and f. Chessboard segmentation to refine the landslide candidate objects by removing impurities such as vegetation. g. Resegmentation with scale factor 13, and elimination of barren lands from landslide candidates. h. Merging again into a single object after removal of all false positives, and classification into rock slide. i. Segmentation of rock slide using terrain curvature. j. Classification of rock slide into rotational rock slide (rrs) and translational rock slide (trs) using a curvature criteria.

Landslide candidates were identified on segment level 13 using an NDVI threshold derived from K-means clustering. This is the first and most important step in the landslide detection process, as it eliminates most of the objects from the subsequent analysis. Using a two-step auto clustering analysis, four natural clusters of NDVI were obtained. These clusters are related to the major land cover classes of this area, and are also quite distinct (Figure 4d). Subsequently, K-means clustering was carried out with $K=4$ and cluster centers were calculated. Objects classified with the cluster center value of 0.22612 could delineate all dark areas of the NDVI image. Therefore, 0.22612 was selected as the threshold for landslide candidates (Figure 4d).

Shadow is another common false positive present in all hilly areas. As opposed to the single parameter threshold used for landslide candidates, they were eliminated by simultaneous thresholding of two spectral parameters (brightness and hillshade), also derived using K-means clustering. Use of these two parameters was necessary as they complement each other, i.e. landslides originating from mafic or ultramafic rocks generally have low brightness and thus similarity with shadow. However, they have high hillshade values (if they are in shadow free area), based on which they can be differentiated from shadow.

Majority of the thresholds were determined objectively, however, those that are not scene specific but knowledge- or process-driven, were determined interactively (Table 2). It is important to classify rocky and non-rocky areas accurately, since they are used for the

classification of landslides based on material type. These features were classified using texture, brightness difference to the surrounding objects, and slope. The sub-module 2 of *Martha et al.* [2010a] was modified, and made more generic and data-driven, by removing the necessity of a threshold, and inserting a contextual information requirement, the maximum mean difference in the red band between an object and its neighbours for the detection of built-up areas, and the minimum mean difference to detect agricultural lands.

Finally, after removal of all false positives, landslides were classified based on their material and movement using shape and contextual diagnostic features as listed in table 2. In total five landslide types were identified in the Okhimath area.

4.2 Testing Area (Darjeeling)

The procedure developed using satellite data and a DEM for Okhimath was tested in the Darjeeling area without any changes to its structure. The optimal scales obtained from the plateau objective function (12, 14, 19 and 22, Figure 2b) were used for the segmentation. The analysis began by segmenting the LISS-IV image with the lowest optimal scale i.e. 12. Using K-means clustering, the NDVI threshold (0.2455) for the classification of landslide candidates was obtained. Similar to Okhimath, a small scale factor was able to delineate the boundary of all landslides completely, with the resulting oversegmentation subsequently being reduced by object merging based on NDVI thresholds (Figure 5).

Optimal scales were linked to false positives using onscreen image reconnaissance as described for Okhimath, the only subjective part left in the entire procedure. Roads and rivers were identified with scale factors 12 and 14, respectively. Scale factors 19 and 22 were used to identify river sands, shadows and barren rocky lands, respectively. All the three types of landslides present in the Darjeeling area could be detected by this procedure and are shown in figure 7.

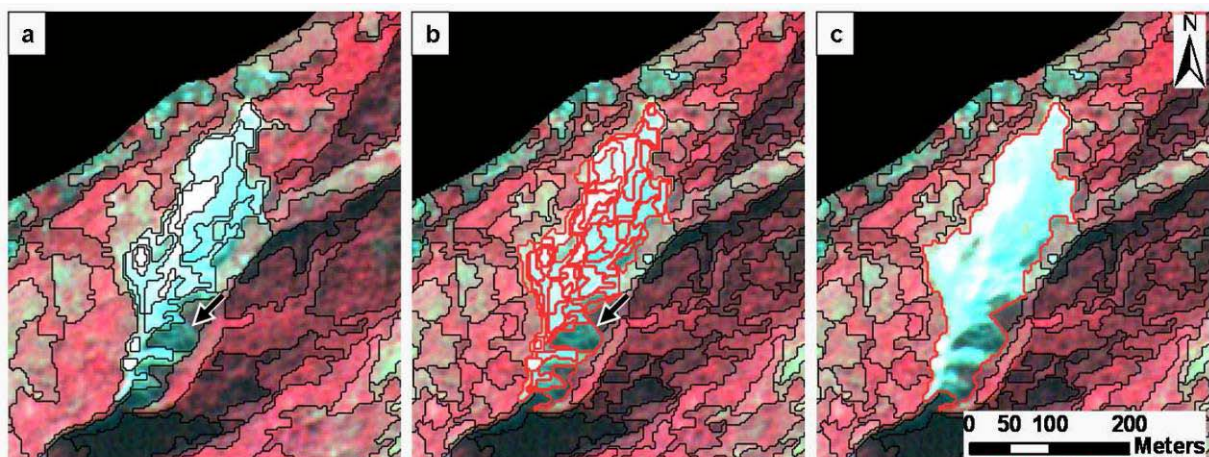


Figure 5: Effect of segment optimisation on a large landslide in the Darjeeling area. a. objects created with scale factors 19. b. objects created with scale factor 12 and classified using NDVI threshold (outlined in red) were able to outline the landslide. c. merging of segments of the large landslide into a single object, and classification into translational rock slide based on morphometry and context.

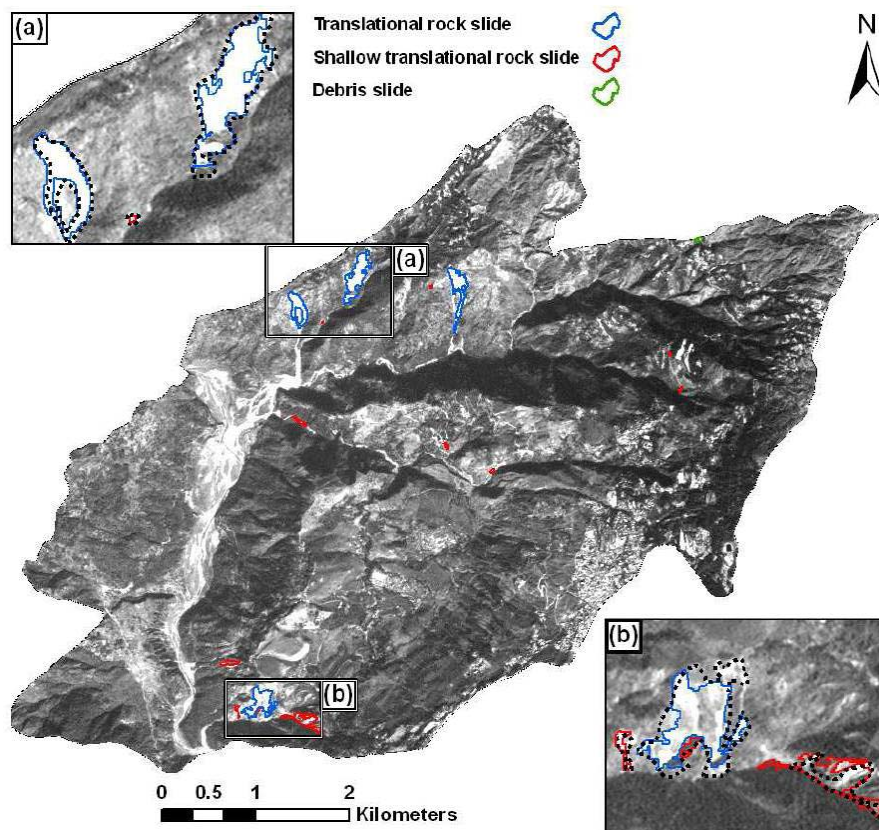


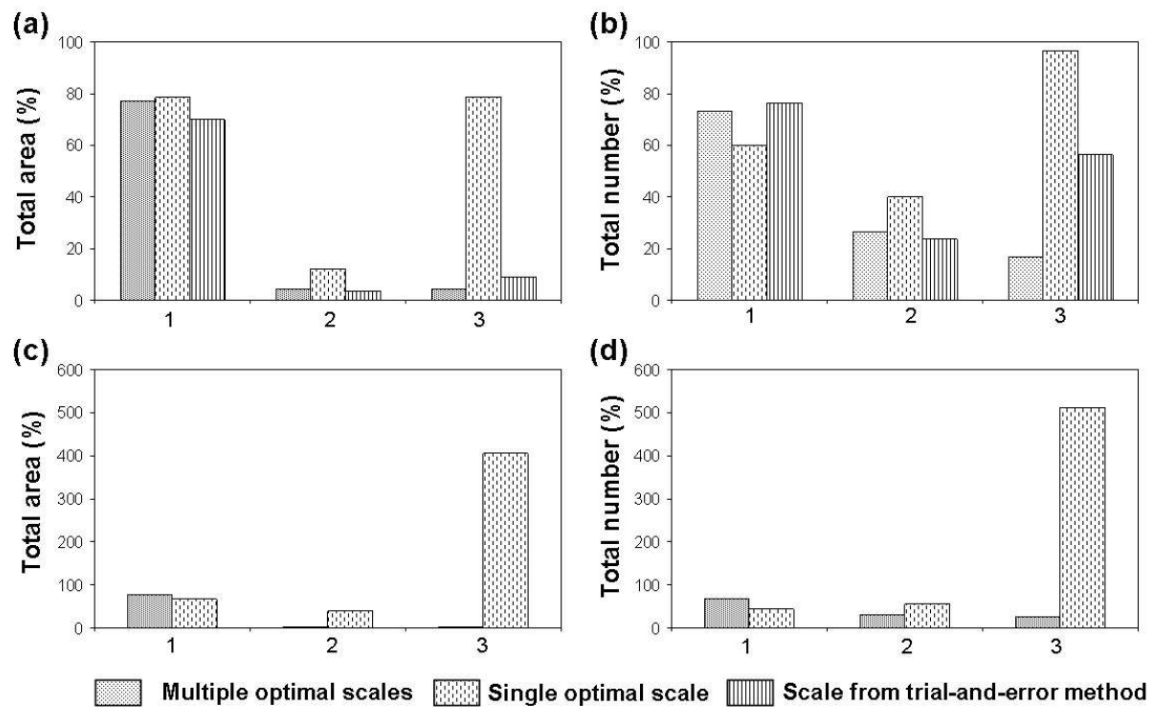
Fig. 6: In total 11 landslides of three different types were correctly recognised using OOA in the Darjeeling area. Dotted lines in insets (a) and (b) show the reference landslide inventory.

5. Accuracy assessment

The overall recognition accuracy (includes correctly and incorrectly classified landslides) for the total extent of landslides in Okhimath and Darjeeling was 76.9% and 77.7%, respectively. The accuracy in the Okhimath area is higher than that achieved (69.9%) with our previous method (refer to table 4 of Martha *et al.* [2010a], where only one scale factor selected by trial-and-error was used. The overall classification accuracy for extent of landslides in Okhimath and Darjeeling was 74.4% and 77.7 %, respectively. The higher accuracy of the landslide extent assessment, a critical parameter in landslide susceptibility analysis, resulted from better outlining of landslides and identification false positives as per their corresponding size, using multi-scale optimization.

The overall recognition accuracy for total number of landslides in the Okhimath and Darjeeling areas was 73.3% and 68.7%, respectively. Although the accuracy in Okhimath is lower than the overall recognition accuracy (76.4%) achieved in our previous work (refer to table 3 of Martha *et al.* [2010a]), it greatly reduced the percentage of incorrectly recognised landslides, i.e. error of commission (16.6%), compared to 56.4% achieved before (Figure 7b). The lower overall recognition accuracy of shallow translational rock slides (60% in both areas) mostly contributed to the 26.6% and 31.2% errors of omission of the total number of landslides in Okhimath and Darjeeling, respectively, in comparison to the contribution from

other landslide types, a trend similar to what we observed in our previous study in the Okhimath area. This is due to the fact that they are small and narrow, and commonly occur in barren rocky lands, thereby offering limited local contrast that is essential for segment delineation.



1. Landslides correctly recognised 2. Landslides not recognised 3. Wrongly recognised as landslides
Figure 7: Comparison of the accuracies obtained using segments derived from three different methods. (a) and (b) show the total area and number of landslides, respectively, recognized in Okhimath, (c) and (d) in Darjeeling.

To investigate if the enhanced accuracy figures can be attributed to the multi-scale analysis the entire analysis for both areas with segments created using only the highest single scale indicated by the objective function. The result showed that, although the overall recognition accuracy has not changed much for both areas, the error of commission has significantly increased for both the total number and the extent of landslides (Figures 7c and 7d).

6. Conclusion

In this study we created a plateau objective function using Moran's I index and intra-segment variance that allowed an objective selection of the optimal scales required for identification of false positives. Dynamic parameter thresholds estimated by K-means cluster analysis were used in several classification steps of the OOA. This work showed that multi-scale based identification of false positives helped in achieving a higher overall recognition accuracy (76.9%) of landslides compared to a single scale, and significantly reduced the error of commission affecting out earlier results. Segment optimization using the result of an intermediate classification was able to delineate small landslides and flanks of large

landslides, and outline landslides as individual objects, thereby allowing the application of process-specific criteria to classify them based on material and movement characteristics. Apart from multi-resolution segmentation, chessboard segmentation was used to remove landslide impurities, and refine landslide boundaries. To summarize, the segmentation techniques that were applied to optimize segments for landslide recognition and classification, and that in combination constitute the novelty of this research, include: 1) multi-scale segment optimization with a plateau objective function; 2) chessboard segmentation to remove landslide impurities such as vegetation within large landslides; and 3) multi-resolution segmentation with terrain curvature to classify landslides based on failure mechanism. K-means clustering proved to be effective in estimating thresholds for landslide diagnostic parameters that were used either individually or simultaneously.

The segment optimization procedure was conceived with four sub-modules, created using eCognition software, and which proved effective and robust in delineating segments for both small and large landslides embedded in different land cover units. The advantage of the methodology demonstrated in this paper is that optimal scales and thresholds were selected in an unsupervised manner. The approach could detect five and three types of landslides in Okhimath and Darjeeling areas, respectively. While the structure of sub-modules 1, 2 and 4 of the ruleset was kept unchanged for landslide detection in both the areas, a semi-supervised approach was adopted for sub-module 3, i.e. to link the optimal scales interactively to false positives through rapid image reconnaissance of the segmentation results. This remains a limitation of our method, although it was substantially improved from our previous approach by incorporating relative identification criteria and automatic thresholds.

The low recognition accuracy of total number of shallow translational rock slides (60% in both areas) is another limitation of our approach. These slides are generally small and narrow (width < 3 pixels) and could not be delineated as a segment. We address this in a separate study by further refining the objects with more shape control than colour, although insufficient resolution of the satellite image could be one of the reasons for their limited detection. Good overall recognition accuracy of the method indicates that it can be of potential use for the preparation of event-based landslide inventory maps, vital for the planning of short and long term disaster management strategies in mountainous areas. More illustrations and the rule set will be available on our website (www.itc.nl/OOA-group).

References

- Akcay, H. G., and S. Aksoy (2008), Automatic detection of geospatial objects using multiple hierarchical segmentations, *IEEE Transactions on Geoscience and Remote Sensing*, 46(7), 2097-2111.
- Barlow, J., S. Franklin, and Y. Martin (2006), High spatial resolution satellite imagery, DEM derivatives, and image segmentation for the detection of mass wasting processes, *Photogrammetric Engineering and Remote Sensing*, 72(6), 687-692.
- Chang, Y.-L., L.-S. Liang, C.-C. Han, J.-P. Fang, W.-Y. Liang, and K.-S. Chen (2007), Multisource Data Fusion for Landslide Classification Using Generalized Positive Boolean Functions, *IEEE Transactions on Geoscience and Remote Sensing*, 45(6), 1697-1708.

- Chen, K. S., M. M. Crawford, P. Gamba, and J. S. Smith (2007), Introduction for the special issue on remote-sensing for major disaster prevention, monitoring, and assessment, *IEEE Transactions on Geoscience and Remote Sensing*, 45(6), 1515-1518.
- Espindola, G. M., G. Camara, I. A. Reis, L. S. Bins, and A. M. Monteiro (2006), Parameter selection for region-growing image segmentation algorithms using spatial autocorrelation, *International Journal of Remote Sensing*, 27(14), 3035 - 3040.
- Gao, Y., J. F. Mas, N. Kerle, and A. Navarrete (In Press), Optimal region growing segmentation and its effect on classification accuracy, *International Journal of Remote Sensing*.
- Holt, A. C., E. Y. W. Seto, T. Rivard, and P. Gong (2009), Object-based detection and classification of vehicles from high-resolution aerial photography, *Photogrammetric Engineering and Remote Sensing*, 75(7), 871-880.
- Laliberte, A., and A. Rango (2009), Texture and scale in object-based analysis of subdecimeter resolution unmanned aerial vehicle (UAV) imagery, *IEEE Transactions on Geoscience and Remote Sensing*, 47(3), 761-770.
- Martha, T., N. Kerle, C. J. van Westen, and K. Kumar (2010a), Characterising spectral, spatial and morphometric properties of landslides for semi-automatic detection using object-oriented methods, *Geomorphology*, 116(1-2), 24-36
- Martha, T. R., N. Kerle, V. Jetten, C. J. van Westen, and K. Vinod Kumar (2010b), Landslide Volumetric Analysis Using Cartosat-1-Derived DEMs, *IEEE Geoscience and Remote-sensing Letters*, 7(3), 582 - 586
- Rau, J.-Y., L.-C. Chen, J.-K. Liu, and T.-H. Wu (2007), Dynamics monitoring and disaster assessment for watershed management using time-series satellite images, *Geoscience and Remote Sensing, IEEE Transactions on*, 45(6), 1641-1649.
- Schwarz, G. (1978), Estimating the dimension of a model, *Annals of Statistics*, 6(2), 461-464.
- Song, C., C. E. Woodcock, K. C. Seto, M. P. Lenney, and S. A. Macomber (2001), Classification and Change Detection Using Landsat TM Data: When and How to Correct Atmospheric Effects?, *Remote-sensing of Environment*, 75(2), 230-244.
- Voigt, S., T. Kemper, T. Riedlinger, R. Kiefl, K. Scholte, and H. Mehl (2007), Satellite Image Analysis for Disaster and Crisis-Management Support, *Geoscience and Remote Sensing, IEEE Transactions on*, 45(6), 1520-1528.

Synergetic use of UAV-based optical remote-sensing and Terrestrial LiDAR for landslide monitoring

Application: Landslide monitoring

Technique: Passive optical airborne and ground-based sensors

Main references: Niethammer, U., M. R. James, S. Rothmund, J. Travelletti, and M. Joswig (in press): UAV-based remote-sensing of the Super-Sauze landslide: Evaluation and results.

Contributors: CNRS (J. Travelletti, S. Rothmund)

Abstract

Unmanned aerial vehicles (UAVs) equipped with digital compact cameras can be used to map landslides quickly and at a high ground resolution. Images taken by a radio-controlled mini quad-rotor UAV of the Super-Sauze, France landslide have been used to produce a high-resolution ortho-mosaic of the entire landslide and digital terrain models (DTMs) of several regions. The UAV capability for imaging fissures and displacements on the landslide surface has been evaluated, and the subsequent image processing approaches for suitably georectifying the data have been assessed.

For Super-Sauze, horizontal displacements of 7 to 55 m between a high-resolution airborne ortho-photo of May 2007 and a UAV-based ortho-mosaic of October 2008 have been measured. Fixed areas of persistent deformation have been identified, producing fissures of different distributions and orientations comparable to glacial crevasses, and relating directly to the bedrock topography. The UAV has demonstrated its capability for producing valuable landslide data but improvements are required to reduce data processing time for the efficient generation of orthomosaics based on photogrammetric DTMs, in order to minimise georeferencing errors.

Keywords: landslide, remote-sensing, UAV, DTM, terrestrial LiDAR, fissures

1. Introduction

The objective of this work is to investigate the use of radio controlled unmanned aerial vehicles (UAVs) for acquiring high-resolution measurements (DTMS, orthophotographs) on landslides in order to assess their dynamics at high temporal frequency, and assess quantitatively changes in the surface texture and roughness (fissure pattern, trajectory of blocs, etc).

The mini-UAV used has the advantage over traditional methods of allowing flexible deployments capable of acquiring both high-temporal and spatial resolution data. Radio controlled UAVs are less expensive with significantly lower operational costs than manned aircraft and, in recent years, mapping and remote-sensing applications of UAV-systems have become more common [Everaerts, 2008]. In the late 1970's the use of fixed wing remote controlled aircraft was investigated for motorized UAV photogrammetry experiments [Przybilla and Wester-Ebbinghaus, 1979] and, a quarter century later, Eisenbeiss *et al.* [2005] generated the first high-resolution digital terrain models (DTMs) using autonomously controlled helicopter UAVs.

Currently, a range of UAV-systems are in use, for example, motorized paragliders [Jütte, 2008], blimps [Gomez-Lahoz and Gonzalez-Aguilera, 2009], kites [Aber *et al.*, 2002] and balloons [Fotinopoulos, 2004]. However, many such systems are strongly affected by wind

and could only be used infrequently or with difficulty in mountainous terrain. The availability of small high-quality digital cameras has now enabled radio controlled UAV-systems to represent affordable and practical remote-sensing platforms, but data analysis challenges remain. For example, in order to utilize standard aerial photogrammetric processing software, UAV-acquired photographs should be acquired in an optimal block configuration alignment, with internally stable camera-systems and minimal optical distortion. These restrictions have previously required the use of fixed-lens SLR cameras, expensive autopilot UAV navigation systems, and driven the development of dedicated photogrammetric software packages [Eisenbeiss *et al.*, 2005].

In 2006, relatively stable quad-rotor helicopter systems became available as open source public domain projects [Mikrokoetter, 2010]. These systems are suitable for adaptation for use in alpine terrain and are low-cost when compared to commercially available UAV-systems. The goal of this study was to evaluate a UAV-system developed in-house for landslide research. The potential and limitations of such a system, with preliminary results acquired at the Super-Sauze landslide, France [Weber and Herrmann, 2000; Malet, 2003] are discussed.

For the Super-Sauze landslide, a specific aim was to consider the UAV capability for imaging fissures and displacements at the surface and to assess the subsequent image processing approaches for suitably georectifying the data. For full coverage of the landslide area, a plane-rectified ortho-mosaic of UAV imagery has been constructed and comparisons were made with a previously acquired traditional aerial ortho-photo. However, the use of plane-rectification can result in significant errors in regions of rugged topography, so we explore the application of close range photogrammetry software to enhance the results with a photogrammetric DTM. The close range software can handle convergent imagery from non-metric cameras much more readily than traditional aerial photogrammetry applications, facilitating DTM generation from UAV imagery. The quality of the digital terrain model is assessed by comparison with data from a terrestrial laser scanner (TLS).

2. Data and Methods

2.1. Description of the UAV acquisition system

The UAV-system developed in-house is a low-cost quad-rotor (Figure 1) that has been previously demonstrated to be capable of flying in difficult alpine terrain. When compared to conventional helicopters, quad-rotor systems are more stable with less in-flight vibration and have the mechanical advantage of not requiring a large, variable pitch rotor-unit. Our system was derived from an open source project [Mikrokoetter, 2010] and enhanced for landslide studies. A robust aluminium flight frame was developed and the payload of the UAV-system was increased by using more powerful motors and some modifications of the flight control software. The UAV is stabilized by inertial measurement units (IMUs), including three acceleration sensors, three gyroscopes, a three-axis compass, and a pressure sensor, regulated by basic PID (proportional integral differential) loops. Flight endurance (hovering time of the

UAV-system) is up to 12 minutes using a lithium polymer battery with a capacity of ~5.0 Ah. Overall UAV-development took about one man year in order to meet all the requirements for operation in difficult alpine terrain.



Figure 1: Quad-rotor system for remote-sensing and its main characteristics.

For image acquisition, a light weight low-cost digital compact camera (Praktica Luxmedia 8213) which supports manual camera settings was used. For all flights the sensitivity, zoom and the aperture were set to fixed values in order to achieve exposure times $<1/800$ s and the largest visual angle. Without an auto-pilot navigation system to control image acquisition, all photographs were taken in an automatic image-series mode, acquiring one image every three seconds to ensure full coverage.

Our choice of a radio controlled UAV requires the presence of a highly skilled pilot and limits the operational area to the control range of a few hundreds of metres. There are also challenges related to the relatively small payloads, UAV-reliability and the restricted radio-bandwidth for ground communication [Colomina *et al.*, 2007]. Although the use of an autonomously controlled UAV could significantly increase the operational area, autonomous control is less able to cope with unpredictable conditions such as gusty winds than an experienced operator. Furthermore, the use of autonomous UAVs is tightly regulated by civil aviation and security authorities, preventing their practical deployment. Our experience is that, particularly in alpine terrain, UAV-based image acquisition requires significant technical skill and a good pilot.

2.2. Data acquisition

In October 2008 a UAV flight campaign was carried out covering the whole sliding area (850×250 m) of the Super-Sauze landslide, acquiring 1486 airborne photographs. Flight planning was carried out in-situ, where the area to be imaged could be observed and suitable locations for takeoff and landing could be identified.

After launch, the quad-rotor was guided to an imaging flight altitude of ~ 200 m to provide a ground resolution of approximately 0.06 m per pixel. However, manual control of the UAV led to deviations in flight altitude between 100 m and 250 m, with corresponding ground resolutions between 0.03 m and 0.08 m. At the imaging altitude the UAV was hovered for about 30 seconds before vertical landing was initiated. After each flight, the area covered by the acquired photographs was verified on the camera directly.

To enable the images to be georeferenced, 199 targets ($\sim 0.4 \times 0.6$ m rectangular coloured sheets to ensure visibility) were deployed over the landslide as ground control points (GCPs), and their centroid locations determined with differential GPS (DGPS). Deploying such a number of GCPs requires significant effort but was deemed an appropriate precaution for the initial assessment of UAV use over the landslide. Although long-term DGPS observations of these targets could allow for accurate displacements analysis at each GCP without the need for any UAV flight, such point data could potentially miss areas of interest and would not provide opportunity for the analysis of surface features such as fissures.

To enable a comparison of the UAV results with ground-based data, the topography of the toe-region of the slide was also mapped with a terrestrial laser scanner (TLS). The TLS instrument, an Optech ILRIS-3D, was used from a single site at a mean distance of 150 m from the toe (Fig. 2A), producing an average data density of 23,000 points per m^2 in the image plane perpendicular to the line of sight, and a total of 3×10^6 points. The laser logged the last return from each line of sight in order to minimize undesired returns from vegetation. A stable area outside of the landslide was also included within the scanned area in order to georeference the TLS data. This georeferencing was carried out using a DTM acquired by ALS on 22 May 2007 with a ground resolution of 0.2 m.

2.3. Data processing

To allow comparison of the UAV data with these other sources, two processing procedures were carried out; generation of an ortho-mosaic and DTM construction of selected areas using close range photogrammetry techniques.

2.3.1 Production of ortho-mosaic

The best 59 suitable UAV-acquired images were selected for mosaic processing. In a first step, optical (barrel) distortion was corrected using the common third degree polynomial approach [Niethammer *et al.*, 2009, 2010]. In a second processing step, each image was rectified onto the plane GCP coordinates using one of four non-parametric rectification

approaches (projective transformation, piecewise affine transformation and polynomial transformations of the 2nd and 3th order). For each image, the rectification approach was selected in order to achieve the best result and depended on the relief variation and the number of observed ground control points. In irregular terrain these approximate transformations will not fully account for the effects of relief and residual misalignments within the ortho-mosaic have to be accepted.

Finally, all rectified photographs were merged to a uniform high-resolution orthomosaic with a spatial resolution of 0.04 m. Automatic colour correction was carried out within OrthoVista software [OrthoVista, 2010] by applying a global tiling adjustment function which compares overlapping areas of images and then computes radiometric adjustment parameters for each image. All images were then merged into a seamless mosaic by an adaptive feathering image blending algorithm within OrthoVista (Fig. 2A).

2.3.2 Production of photogrammetric DTM

DTM generation was carried out using VMS close range photogrammetry software [VMS, 2010] and an image matching algorithm, GOTCHA [Gruen Otto-Chau] from the University College London [Otto and Chau, 1989]. Three regions of the Super-Sauze landslide were analyzed (Fig. 2).

For DTM creation, observations of ground control points in the selected images were used to calculate initial camera orientations (positions and pointing directions) using a preliminary estimated camera model defining principal distance only. The photogrammetric network produced was densified by incorporating additional tie points generated with GOTCHA, which is a dense matching algorithm capable of generating patch-based (rather than feature-based) matches for each pixel of an image.

The output was then reduced to a few thousand matches distributed over the images and a self-calibrating network adjustment was carried out in which the errors in the GCP positions, camera orientations and the camera model (principal distance, two radial and two tangential distortion components, principal point offsets and an affinity term) were simultaneously minimized.

The optimized locations for the 16 GCPs in the toe-region (figure 3A) showed RMS position residuals (from the original GCP coordinates) of 0.023, 0.018 and 0.019 m in x , y , and z . As is standard in rigorous close range photogrammetry procedures, VMS calculates the measurement precision within the photogrammetric network [Cooper and Robson, 2001]. Average precisions for all the GCPs were 0.079, 0.079 and 0.185 m in x , y , and z , reflecting mean image residuals of 1.4 pixels in both x and y .

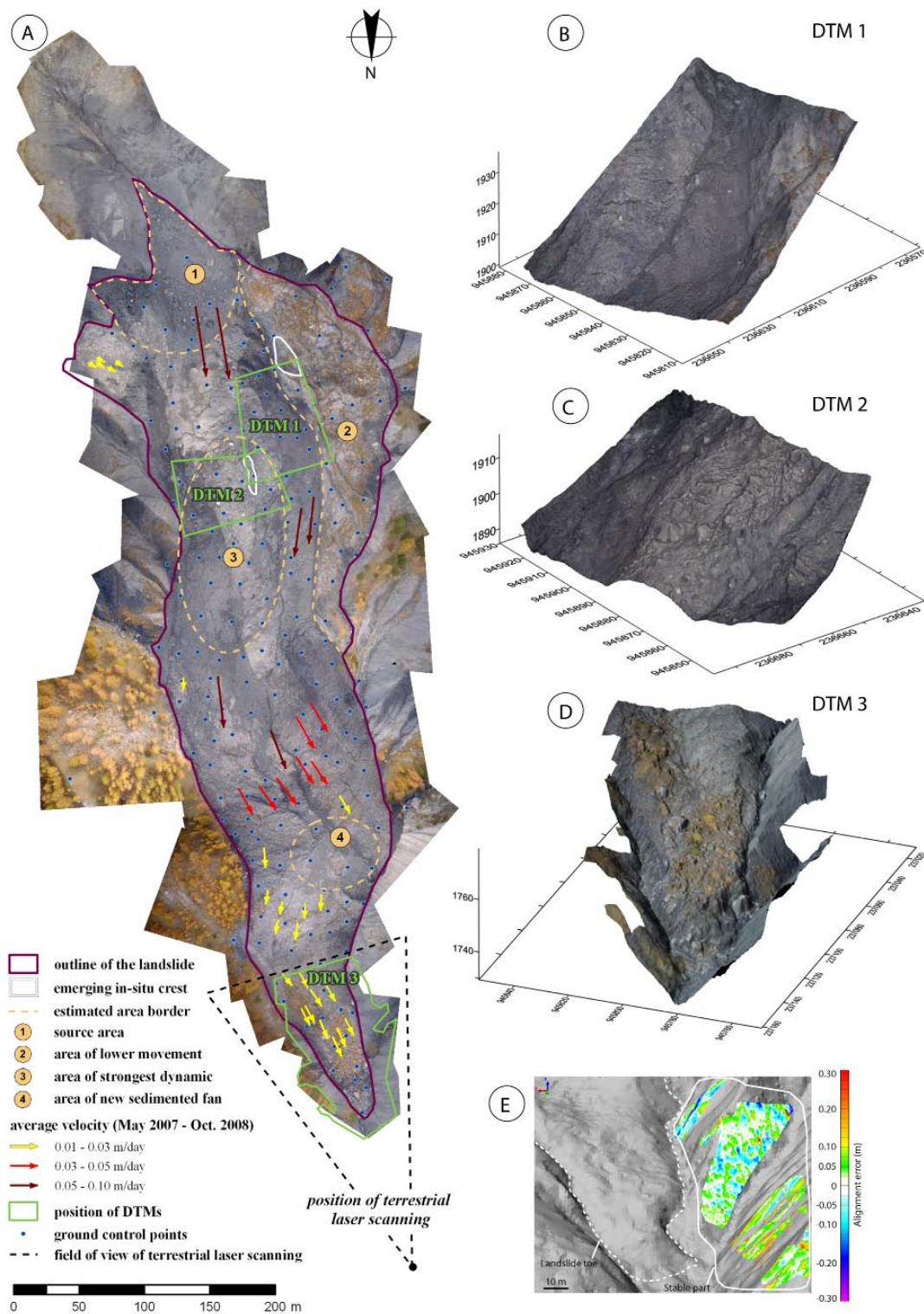


Figure 2: Ortho-mosaic of the Super-Sauze landslide of October 2008 with ground control points (GCPs), horizontal surface displacement vectors colour coded by average movement velocity (May 2007 – October 2008), different areas of dynamics and sedimentation, locations of the DTMs and the position and field of view of the terrestrial laser scanner survey. B-D: DTM 1-3 overlain with an ortho-image. E: Alignment error between the TLS DTM (October 2008) and airborne LiDAR DTM (May 2007) of the stable topography adjacent to the toe-region of the landslide.

3. Results

3.1. Ortho-mosaic and DTM quality

Errors within the georeferencing of the ortho-mosaic were quantified by comparison of all 199 GCP locations to their DGPS-measured locations. Within the boundary of the sliding area the mean error was 0.5 m, with a standard deviation of 0.57 m and a maximum misalignment of 3.9 m. However, large misalignments between 2.0 m and 3.9 m were only located at the margins of the landslide and, away from the boundary, accuracies can be considered to be ~0.5 m. In the toe-region, the ortho-mosaic could also be compared with UAV images ortho-rectified within VMS software using the photogrammetry-derived DTM 3 (Fig. 2D). Horizontal offsets were determined by image matching (using GOTCHA) and show similar magnitudes to those of the full ortho-mosaic GCPs (Fig. 3A), with the largest values located near the slide boundary.

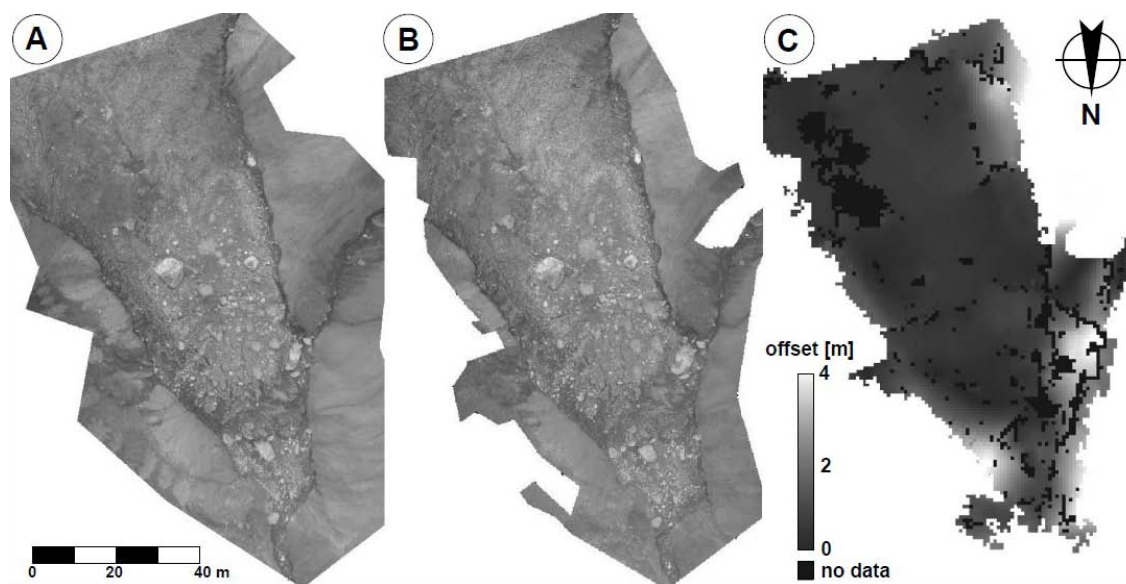


Figure 3: Comparison between the ortho-mosaic (A) and a DTM-derived ortho-photo (B) of the toe region of the landslide. Horizontal offsets determined by GOTCHA image matching.

The quality of the photogrammetric DTM was assessed by subtracting the overlapping TLS DTM (Fig. 4A, 4B). In the vertical direction the RMS difference is 0.31 m although maximum deviations reach +3.44 to -4.08 m.

The most significant errors are induced by some small trees and bushes, the effects of which could not be reliably removed from the photogrammetric DTM. However, vegetation correction on landslides has been managed by applying non-uniform vegetation-height surfaces [Martha *et al.*, 2010], but such procedures were not warranted in this work because

the most significant vegetation errors were localised and occurred only at the margins of the DTMs. Further sizable differences occur on the steepest sides of large blocks. On the northern faces, where the block surface is nearly perpendicular to the TLS line of sight (Fig. 2A), the TLS point cloud is much denser than the photogrammetric one. For example, figures 5C and 5D show that in the steep front of the toe, the point cloud of the TLS is two orders of magnitude denser than the point cloud of the photogrammetry.

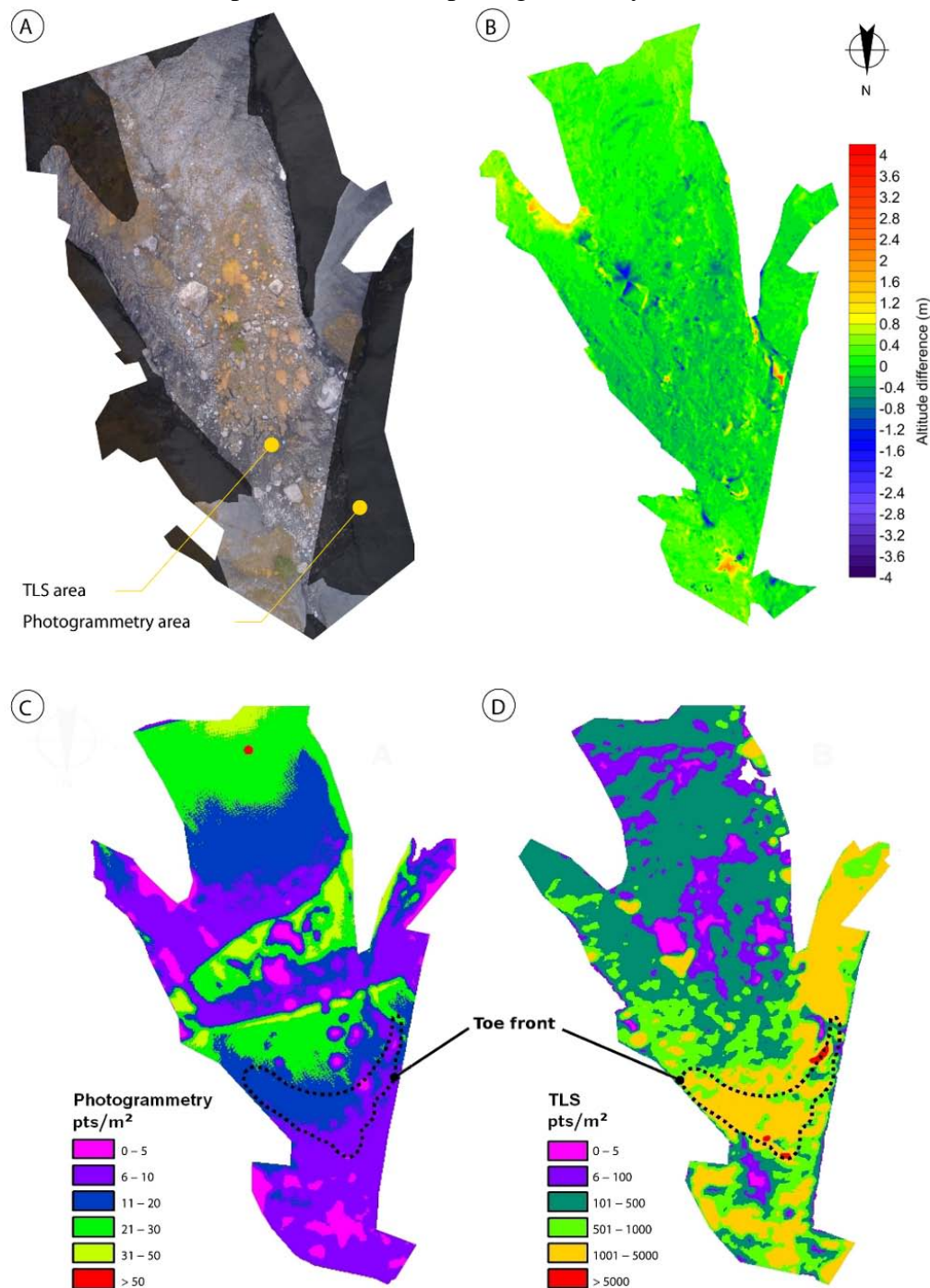


Figure 4: DTM precision analysis at the toe-region of the landslide. A: texture of the toe-region, B: elevation differences between TLS and photogrammetric DTM, C: point-density of the photogrammetry data, D: point-density of the TLS data.

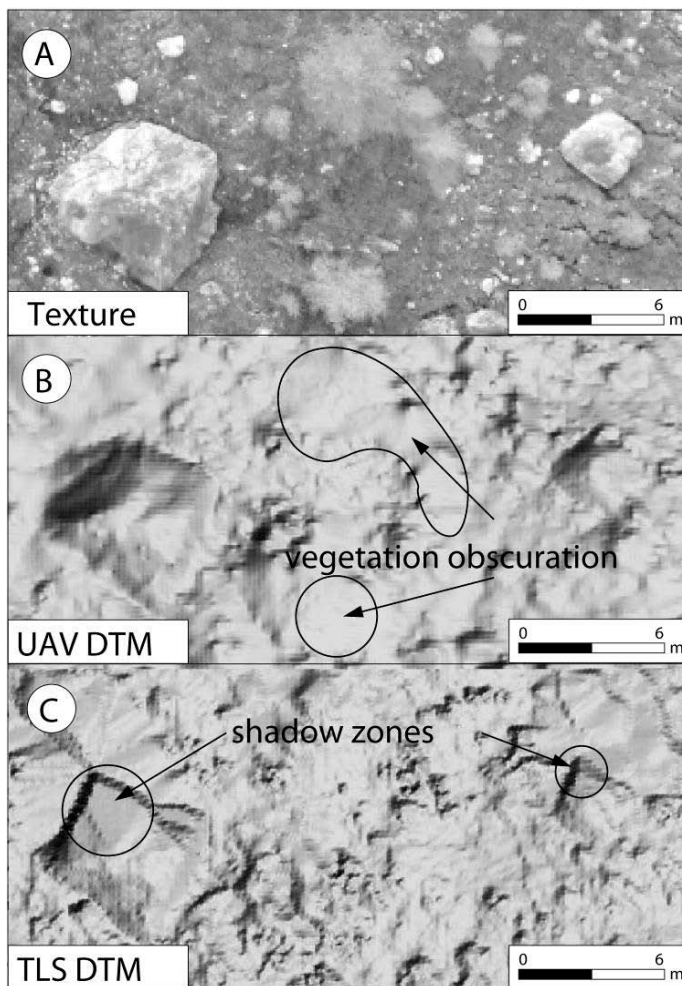


Figure 5: DTM artifacts resulting from shadow zones in TLS data and vegetation obscuration in the UAV-based DTM.

However, the TLS can only observe one side of a block and the other, shadowed, side has to be interpolated. In shadow areas, the zero point density results in predicted elevations that reflect the interpolation technique used rather than any real measurements (Fig. 5C). Nevertheless, such regions are observed fully by the UAV.

In regions of low vegetation, such as grass or small shrubs, it is difficult to completely remove vegetation returns from the TLS point cloud and this can lead to some small artifacts in the TLS DTM (Fig. 5A, 5C). On the other hand the photogrammetric approach can fail in areas of low image contrast or shadowing (for example, on some large blocks, Fig. 5A; 5B). Dense vegetation cannot be penetrated and can give poor or no results during image matching (Fig. 5A, 5B). It can be concluded that both DTMs must be regarded with caution.

3.2. Kinematics analysis

Our UAV-based displacement analysis of the Super-Sauze landslide was carried out by comparing the ortho-mosaic from October 2008 with the aerial ortho-photo from May 2007 in a geographical information system (GIS). Horizontal displacements were measured by identifying corresponding features and areas, such as rocks, stones and parts of vegetation patches in both images (Fig. 6A, 6B). In principle, such analysis could be attempted by automated image matching (using correlation-based methods), but due to the resurfacing changes over the 17-month interval, this would be ineffective with the available image pair. However, automated image matching should be possible between UAV-derived ortho-mosaics acquired at shorter interval periods, and the use of more sophisticated object- or feature-based matching like scale-invariant feature transform (SIFT) could also be investigated [Leprince, *et al.*, 2008; Lowe, 2004].

Horizontal displacements between 7 and $55\text{ m} \pm 0.5\text{ m}$, as well as varying displacement directions were detected (Fig. 2A). However, several regions could not be successfully analyzed due to a lack of clear surface features in both image sets (area 3 in Fig. 2A).

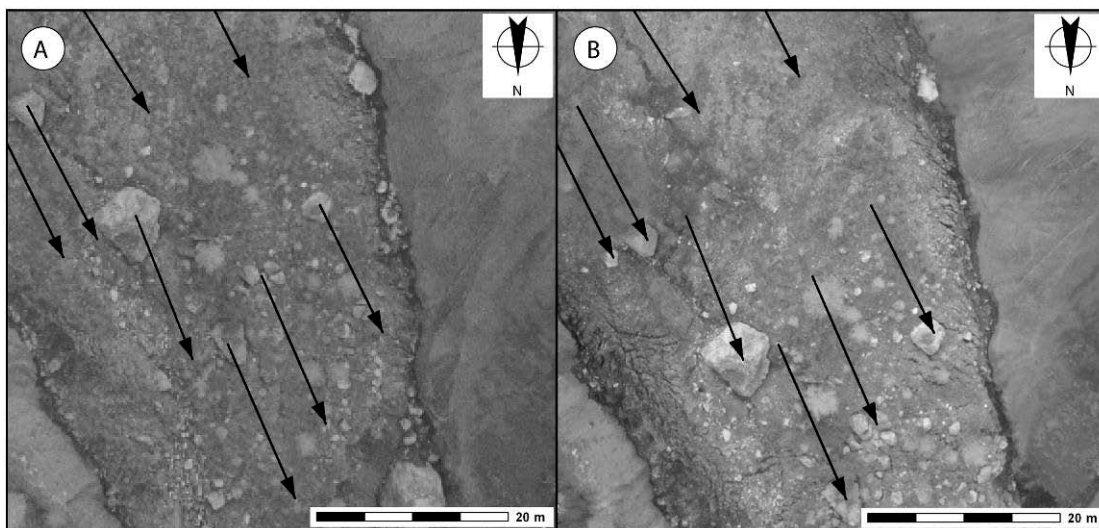


Figure 7: Horizontal displacement analysis of the toe-region between the airborne ortho-photo of May 2007 (A) and the UAV-based ortho-mosaic of October 2008 (B).

4. Discussion and conclusion

In this study it has been shown that radio controlled low-cost UAVs can deliver high resolution remote-sensing data on landslides. The proposed UAV-based remote-sensing approach shows significant potential for the production of high-resolution ortho-mosaics and DTMs that enable the analysis of fissures and surface displacements. The manual data acquisition and processing procedures used require a significant amount of time, but progress is already being made to streamline data processing by using automated targetless structure-

from-motion and multiview-stereo approaches to derive the topographic surface. Integrating such DTM generation (which includes camera model refinement), and possibly also vegetation removal, into the ortho-mosaic pipeline, will significantly reduce errors in the final ortho-mosaic.

The comparison between the plane-rectified UAV ortho-mosaic and an earlier orthophoto revealed horizontal displacements between 7 and 55 m \pm 0.5 m, representing daily average displacements rates in the range of 0.1 to 0.01 m \pm 1 mm per day, between May 2007 and October 2008. Despite the high-resolution of the imagery, errors resulting from the plane-rectification degrade the georeferencing accuracy to \sim 0.5 m over most of the landslide. Although acceptable when calculating displacement rates over periods of a year, errors of this magnitude would be restrictive for analyses over shorter intervals, and hence could limit the usefulness of the UAV's capability to regularly acquire data.

Consequently, ortho-rectification using photogrammetric DTMs is advised. A DTM of the toe-region of the Super-Sauze landslide, constructed using close range photogrammetry software, has been compared with TLS data of the same area giving an RMS of height difference values of 0.31 m. Although TLS-based point clouds are denser than photogrammetric derived point clouds, TLS data are subject to shadowing due to the oblique view point. Such shadows are minimised in nadir UAV-acquired images and a large scale data acquisition can be obtained more effectively by UAV.

References

- Aber, J.S., Aber, S.W., Pavri, F., 2002. Unmanned small-format aerial photography from kites for acquiring large scale, high-resolution, multiview-angle imagery. Proceedings of Pecora 15, Land Satellite Information IV/ISPRS Conference Commission I/FIEOS, Denver, CO, USA.
- Colomina, I., Aigner, E., Agea, A., Pereira, M., Vitoria, T., Jarauta, R., Pascual, J., Ventura, J., Sastre, J., Brechbühler, G.P., Derani, A., Hasegawa, J., 2007. The uVISION project for helicopter UAV photogrammetry and remote-sensing. Proceedings of the 7th Geomatic Week, Barcelona, Spain.
- Cooper, M.A.R., Robson, S., 2001. Theory of close range photogrammetry. In Atkinson, K. B. (Ed.) Close range photogrammetry and machine vision. Whittles Publishing, Caithness, pp. 371.
- Eisenbeiss, H., Lambers, K., Sauerbier, M., 2005. Photogrammetric recording of the archaeological site of Pinchango Alto (Palpa, Peru) using a mini helicopter (UAV). Proceedings of the 33rd CAA Conference, Tomar, Portugal, 21-24 March 2005.
- Everaerts, J., 2008. The use of unmanned aerial vehicles (UAVs) for remote-sensing and mapping. The International Archives of the Photogrammetry, Remote-sensing and Spatial Information Sciences vol. XXXVII, Part B1, Beijing 2008.
- Fotinopoulos, V., 2004. Balloon photogrammetry for archaeological surveys. International Archives of the Photogrammetry, Remote-sensing and Spatial Information Sciences, XX ISPRS Congress, Istanbul, Turkey, XXXV-B5, 504-507.
- Gomez-Lahoz, J., Gonzalez-Aguilera, D., 2009. Recovering traditions in the digital era: the use of blimps for modelling the archaeological cultural heritage. *J. Archaeol. Sci.* 36 (1), 100-109.
- Jütte, K., 2008. Vergleich verschiedener low-cost Luftbildaufnahmesysteme sowie Einsatz von Drohnen: Grenzen und Möglichkeiten. Bayerische Landesanstalt für Wald und Forstwirtschaft. Der gepixelte Wald - Fachtagung zur Forstlichen Fernerkundung.
- Leprieux, S., Berthier, E., Ayoub, F., Delacourt, C., Avouac, J.-P., 2008. Monitoring earth surface dynamics with optical imagery, *EOS Transactions, American Geophysical Union* 89 (1).
- Lowe, D., 2004. Distinctive image features from scale-invariant keypoints. *International Journal of Computer Vision* 60 (2), 91-110.

- Malet, J.-P., 2003. Les glissements de type écoulement dans les marnes noires des Alpes du Sud. Morphologie, fonctionnement et modélisation hydro-mécanique. Phd thesis, Université Louis Pasteur, Strasbourg, 364 pp.
- Martha, T.R., Kerle, N., Jetten, V.G., van Westen, C.J., Kumar, V., 2010. Landslide volumetric analysis using Cartosat - 1 - derived DEMs. *IEEE Geoscience and Remote-sensing Letters* 7 (3), 582-586.
- Mikrokopter, 2010. Official Mikrokopter open source quad-rotor homepage. <http://www.mikrokopter.com> (accessed 1 August 2010).
- Niethammer, U., Rothmund, S., Joswig, M., 2009. UAV-based remote-sensing of the slow-moving landslide Super-Sauze, in: Malet, J.-P., Remaître, A., Boogard, T.A. (Eds.), *Proceedings of the International Conference on Landslide Processes: from geomorphologic mapping to dynamic modelling*, CEREG Editions, Strasbourg, pp. 69-74.
- Niethammer, U., Rothmund, S., James, M. R., Travelletti, J., Joswig, M., 2010. UAV-based remote-sensing of landslides, *Int. Arch. Photogram. Rem. Sens. Spatial Inf. Sciences*, Vol. XXXVIII, ISPRS Comm. V., Newcastle-upon-Tyne, U.K.
- OrthoVista, 2010. Official OrthoVista software homepage. <http://www.orthovista.com> (accessed 1 August 2010).
- Otto, G.P., Chau, T.K.W., 1989. Region-growing algorithm for matching of terrain images. *Image and Vision Computing* 7 (2), 83-94.
- Przybilla, H.-J., Wester-Ebbinghaus, W., 1979. Bildflug mit ferngelenktem Kleinflugzeug. *Bildmessung und Luftbildwesen, Zeitschrift fuer Photogrammetrie und Fernerkundung* 47 (5), 137-142.
- VMS, 2010. Official Robson and Shortis VMS software homepage, <http://www.geomsoft.com> (accessed 1 August 2010).
- Weber, D., Herrmann, A., 2000. Contribution of digital photogrammetry in spatio-temporal knowledge of unstable slopes: The example of the Super-Sauze landslide (Alpes-de-Haute-Provence, France). *Bull. Soc. Géol. Fr.* 171 (6), 637-648.

4. REMOTE-SENSING DATA AS INPUT FOR QUANTITATIVE HAZARD AND RISK ASSESSMENT

4.1. DIRECT USE OF REMOTE-SENSING INFORMATION FOR HAZARD ANALYSIS

[NGU]

Landslide hazard assessment is a complex process that requires many input parameters [Aleotti and Chowdhury, 1999; Guzzetti et al., 1999; van Westen et al., 2006; van Westen et al., 2008]. Consequently it is not recommended to base hazard assessments directly and only on remote-sensing data. However, the preparation of probabilistic maps, the calibration of physically-based and deterministic models and the quantification of all involved factors can be very time consuming; emergency situations sometimes require rapid hazard assessments based on remote-sensing data only, but these have to be coupled with expert judgment. Such heuristic methods or expert evaluation approaches [Leroi, 1996] lead to qualitative landslide hazard or risk assessments. These assessments are nonetheless useful to focus more detailed investigations, make quantitative hazard assessments, initiate monitoring and eventually implement early-warning systems. Some examples of the direct use of remote-sensing data in landslide hazard analysis and early-warning are presented here.

4.1.1. Back-analysis of past landslides

Back-analyses of past landslides provide essential input parameters for investigations of present landslides, for example the geotechnical parameters of the sliding mass, the structures and mechanisms involved in past landslides, the volumes of past events, etc. The findings of such back-analyses can then be applied to present slope instabilities (for numerical simulations) and for hazard assessment using, for example, volume-frequency relationships [Dussauge-Peisser et al., 2002; Dussauge et al., 2003].

The geotechnical and geomechanical properties of the rock or soil mass involved in a past landslide event are generally assessed using numerical simulations, for landslides [Delmonaco et al., 2002], rockslides [Brideau et al., 2006; Kveldsvik et al., 2008], submarine landslides [L'Heureux et al., 2010], but also their propagation [Hungr and Evans, 1996; Jaboyedoff et al., 2009b]. Remote-sensing techniques can provide necessary input data for such back-analyses, especially airborne laser scanning (ALS) and terrestrial laser scanning (TLS) for the present topography, aerial photographs and satellite images for the extent of landslide scars and deposits, ground-based or offshore geophysical methods for the location of the sliding surface and the deposit thickness, and multi-beam echosounders for the bathymetry.

Landslide mechanisms can also be directly assessed based on the morphology of the exposed scar using high-resolution digital elevation models (DEMs) created from ALS and

TLS. This approach has proven particularly useful for landslides in hard rock slopes, structures delimiting a rockfall [Abellán *et al.*, 2006], structures forming the basal failure surface of a rockslide [Jaboyedoff *et al.*, 2009a; Pedrazzini *et al.*, 2010], surface roughness of the basal failure surface [Oppikofer *et al.*, in press], but also gives valuable information on rotational landslides ([Jaboyedoff *et al.*, 2009c].

Landslide back-analysis also includes the assessment of the landslide volume, for example by computing the difference between the pre-event topography and the post-event topography. Therefore, the pre-event topography needs to be reconstructed, which can be realized using aerial photographs [Coe *et al.*, 1997; Dewitte *et al.*, 2008; Mora *et al.*, 2003; Prokesová *et al.*, 2010] or topographic maps [Evans *et al.*, 2001] acquired before the event. Other surface reconstruction techniques are based on the continuity between the present topography outside the scar area and the pre-event topography within the landslide area. This can be achieved by following and completing the contour lines of the present-day topography over the rockslide scar [Brückl and Brückl, 2006; Rouiller *et al.*, 1998] or by interpolation methods like inverse distance weighting or kriging [Gorum *et al.*, 2008]. The sloping local base level (SLBL) technique is an alternative interpolation technique and can be applied to create the pre-event topography in the landslide scar and deposits areas [Jaboyedoff and Derron, 2005; Jaboyedoff *et al.*, 2004; Travelletti *et al.*, 2010]. Oppikofer [2009] used an ALS-DEM to reconstruct in a 3D environment the pre-event topography of large rockslides.

4.1.2. Initiation of detailed investigations and continuous monitoring

Detailed field investigations of landslides and installation of continuous monitoring systems are costly and can generally not be made on all landslides in a given region. Remote-sensing techniques help to focus detailed field investigations and monitoring on sites that show signs of activity (displacements, small shallow landslides or small rockfalls within a larger landslide, decrease in vegetation cover etc.).

Satellite-based InSAR is now widely used at regional to country scale to detect and map landslides [Lauknes *et al.*, 2010], and in some cases even to monitor their displacements [Colesanti and Wasowski, 2006; Colesanti *et al.*, 2003; Squarzoni *et al.*, 2003]. InSAR displacement maps are very useful to highlight areas with recent slope movements and supplement field investigations by focusing the work on active landslide sites [Henderson *et al.*, 2011] (see also 3.2. of this deliverable, D4.1 Part C: 4, and D4.1: Case studies 11&17).

At a more local scale, differences between multi-temporal DEMs also allow the detection of topographic changes due to slope movements [Baldi *et al.*, 2008; Casson *et al.*, 2003; Coe *et al.*, 1997; Evans *et al.*, 2001; Fischer *et al.*, 2011; Mora *et al.*, 2003; Prokesová *et al.*, 2010]. Such multi-temporal DEMs can be created from various remote-sensing datasets, especially by ALS and aerial photographs. Since ALS-DEM have only been produced regularly since the end of the 1990s, only few areas have up to now been covered twice by ALS, but their number will likely increase in the future [Jaboyedoff *et al.*, 2010]. Nonetheless, ALS-DEM can already be compared to other DEMs created from topographic maps or from aerial

photographs [Dewitte *et al.*, 2008; Fischer *et al.*, 2011]. The archive of aerial photographs allows retracing the landslide displacements in time until the 1920s to 1930s, when first surveys were made in many countries.

At local, site-specific scale, ground-based remote-sensing techniques are very appropriate to detect landslide displacements: ground-based InSAR [Casagli *et al.*, 2010; Tarchi *et al.*, 2003], terrestrial laser scanning [Abellán *et al.*, 2009; Abellán *et al.*, 2010; Jaboyedoff *et al.*, 2009c; Oppikofer, 2009; Oppikofer *et al.*, 2008; Pesci *et al.*, 2011; Teza *et al.*, 2007; Travelletti *et al.*, 2008] and terrestrial photogrammetry [Lim *et al.*, 2005]. TLS and terrestrial photogrammetry provide point clouds of the topography and enable the measurement of landslide displacements in 3D and not only along the LOS (as with InSAR) or the elevation axis (as with multi-temporal DEMs). This is one of the main advantages of these ground-based techniques together with the high spatial resolution of the data in comparison with InSAR and ALS. The interpretation of the 3D displacement pattern of a landslide allows the construction of geometric instability models, which increase the understanding of the failure mechanisms [Oppikofer *et al.*, 2008; Oppikofer *et al.*, 2009]. On the other hand, ground-based InSAR has the capability to detect smaller displacements than TLS and terrestrial photogrammetry.

Changes in vegetation cover are obvious signs of landslide activity and are readily detected on multi-temporal aerial or terrestrial photographs [Casson *et al.*, 2003; Jaboyedoff *et al.*, 2009b]. Another sign of landslide activity is rockfalls at the front or along the limits of a larger unstable slope. Such rockfall activity and precursory displacements in a rock mass are indications of possible large failures, which enable the spatial prediction of future rock slope failures based on TLS and terrestrial photogrammetry [Abellán *et al.*, 2009; Abellán *et al.*, 2010; Lim *et al.*, 2005; Oppikofer *et al.*, 2008; Pedrazzini *et al.*, 2010; Rosser *et al.*, 2007].

4.1.3. Hazard assessment in emergency situations

Emergency situations after a landslide event necessitate quick response and assessment of the new hazard situations. This is especially critical for major triggering events, such as earthquakes or extreme precipitations that can trigger dozens to thousands of landslides (Cai [Caine, 1980; Chigira *et al.*, 2010; Crosta and Frattini, 2003; Guzzetti *et al.*, 2008; Harp and Crone, 2006; Keefer, 1984; Sepúlveda *et al.*, 2010]).

At a regional scale, satellite images can be acquired shortly after a major triggering event and used to make an inventory of new landslides and landslide dams [Dunning *et al.*, 2007; Harp and Crone, 2006; Sato and Harp, 2009]. This inventory is important for the organization of emergency assistance of the affected population (extent of landslides, accessibility of communities by transportation routes etc.). The inventory is even critical for the hazard assessment of landslide dams, which could breach and flood the downstream area with potential catastrophic consequences. Due to the relatively low longevity of landslide dams [Evans, 2006], their early detection is crucial in order to initiate remedial works and to control dam breaches.

Rapid hazard assessments may be necessary following a major landslide event, especially in situations when only parts of the unstable slope failed. In such cases it is essential to assess the volume of the remaining unstable part and to measure potential displacements within it. TLS and ALS can be used to quickly create a new post-event DEM [Jaboyedoff *et al.*, 2009c], which can then be compared to pre-event DEMs in order to compute the volume of the landslide event [Oppikofer *et al.*, 2008]. Post-event DEMs are also very helpful for the design of remedial works on the landslide [Jaboyedoff *et al.*, 2009c]. Most in-situ instrumentation on a landslide will likely be destroyed by the landslide event. The installation of new in-situ instrumentation is time consuming and may not be feasible due to the danger posed by the remaining unstable mass. Therefore are remote-sensing techniques that can be operated from safe positions in the surroundings of a landslide the only suitable monitoring technique [Oppikofer *et al.*, 2008]. Ground-based InSAR and TLS can be quickly deployed and can provide measurements of the post-event displacements within a few hours to days.

4.2. INDIRECT USE OF REMOTE-SENSING INFORMATION FOR HAZARD AND RISK MODELS

4.2.1. Remote-sensing inventory maps as inputs to hazard models

[ITC+CNRS]

Quantitative assessment of landslide hazard and risk can be performed at various scales, whereas landslide inventories with sufficient spatial and temporal coverage are especially important for assessments at medium scales [Guzzetti *et al.*, 2005; van Westen *et al.*, 2006; van Westen *et al.*, 2008]. Hence, the focus is here on remote-sensing techniques that target mapping at regional scale, the quality of resulting inventory maps and remaining issues for their integration of those inventories in probabilistic hazard assessment. Landslide hazard assessment infers from knowledge about location, size and timing of the landslides [Guzzetti *et al.*, 2005] which all can be potentially derived with remote-sensing technologies.

To determine location and extent of landslide (especially after of large triggering events) aerial photographs are being progressively replaced with high and very-high resolution satellite images. The increasingly higher spatial and temporal resolution of optical satellite observations enables (i) more detailed and reliable identification of affected areas, (ii) an immediate response minimizing the risk of omission (due to landslide traces fading away with time), and (iii) repeated observations potentially leading to multi-temporal inventories, which can be easier related to specific events [Saba *et al.*, 2010]. Event-based mappings in the direct aftermath of large earthquakes also became an indispensable information source for the assessment of seismic hazards [Harp *et al.*, 2010]. For the assessment of seismic hazards (and landslide hazards similarly) it is generally desirable to map not only the landslide locations

but also the locally affected areas; a task that becomes much more feasible using VHR images.

Multi-temporal inventories are still available for relatively few thoroughly studied areas [Guzzetti *et al.*, 2009; Jaiswal and van Westen, 2009; Witt *et al.*, 2010], whereas at the same time lot of archived and continuously acquired imagery still remains unexploited to create multi-temporal inventories for other areas. Even if time-series from field-surveys are readily available VHR optical images may reveal a considerable additional number of landslides for a given area [Fiorucci *et al.*, in press] and should be considered for visual interpretation.

There is a large number of studies which proposed, applied and compared automated techniques for landslide mapping with optical data [Barlow *et al.*, 2006; Borghuis *et al.*, 2007; Cheng *et al.*, 2004; Danneels *et al.*, 2007; Di *et al.*, 2010; Gao and Maro, 2010; Hervás *et al.*, 2003; Joyce *et al.*, 2009; Lu *et al.*, 2011; Marcelino *et al.*, 2009; Martha *et al.*, 2010c; Nichol and Wong, 2005; Park and Chi, 2008; Rau *et al.*, 2007; Whitworth *et al.*, 2005; Yang and Chen, 2010] but surprisingly little work has been dedicated to the use of automatically mapped inventories as input for hazard or susceptibility assessment. One exception is a study presented by Park and Chi [2008], whereas still (presumably considerable) manual editing was involved to refine the automatically mapped landslides. Not all studies on automated mapping included proper accuracy assessments, but those who did showed mapping accuracies between approximately 30% [Marcelino *et al.*, 2009] and 90% [Yang and Chen, 2010] depending largely on the complexity of the ground conditions but also on the employed techniques and image types. It is well documented that traditional mappings comprise a large degree of subjectivity leading to sometimes incomparable inventory maps for the same area, which translate into diverging and hence uncertain spatial patterns of the slope susceptibility [Ardizzone *et al.*, 2002; Galli *et al.*, 2008; Wills and McCrink, 2002]. From this view point it might be in many cases problematic to evaluate the results of automatically derived inventories against traditional techniques and the quality of the reference data generally needs special attention. Detailed manual mappings such as presented by Galli *et al.* [2008] and Fiorucci *et al.* [in press] demonstrate that thorough interpretation of VHR images reveals many additional landslides and yields more accurate maps. However, such detailed inspections are not feasible over wide areas [Galli *et al.*, 2008] emphasizing again the need for more automated techniques. In analogy to the cited studies evaluating discrepancies among different manual mappings, an evaluation of the discrepancies and uncertainties of automated approaches, and their impact on the hazard assessment appears recommendable. To the best of our knowledge such research has not been carried out yet and integrated approaches which use satellite based inventories as input for susceptibility assessment are still rather sparse [Park and Chi, 2008; Sarkar and Kanungo, 2004].

Airborne LiDAR techniques show particular strength for the mapping of old landslides under forest [Van Den Eeckhaut *et al.*, 2007] but can also be used to support the mapping of newly triggered shallow landslides [Ardizzone *et al.*, 2007; Lu *et al.*, 2011]. There seems to be a general agreement that LiDAR based mappings yield more accurate and complete

inventories than field surveys alone [Ardizzone *et al.*, 2007; Schulz, 2007; Van Den Eeckhaut *et al.*, 2007]. Resulting inventories have been employed for efficient susceptibility models whereby the LiDAR derived terrain model provides also valuable input to extract influential topographic variables [Van Den Eeckhaut *et al.*, 2009; Van Den Eeckhaut *et al.*, 2006]. The acquisition of airborne LiDAR datasets is still rather costly and for a frequent updating of landslide inventories other techniques may remain more feasible. With an eye toward analysis of such datasets over larger areas some automated mapping techniques [Booth *et al.*, 2009; Glenn *et al.*, 2006; McKean and Roering, 2004] with partially promising accuracies [Booth *et al.*, 2009] have been proposed. It appears desirable to compare susceptibility models based on automated techniques with those based on manual mappings to assess the sensitivity of the spatial susceptibility before further inferences on the hazard are drawn.

Most remote-sensing techniques described in this section target the detection and mapping of the areal extent of landslides. The involved volumes are an important parameters for the hazard assessment, but are typically not easily available and in many cases might only be estimated as a function of the landslide area [Guzzetti *et al.*, 2009]. Direct measurements of volumes or displacements over wider areas are in principal possible with multi-temporal airborne photogrammetry and multi-temporal LiDAR [Chen *et al.*, 2006; Dewitte *et al.*, 2008; Scheidl *et al.*, 2008; Tsutsui *et al.*, 2007]. For volume estimates with multi-temporal DSM derived from SPOT stereopairs Tsutsui *et al.* [2007] reported uncertainties of around 34% and Martha *et al.* [2010c] reported a maximal deviation of 18% using stereopairs. Compared to relatively rough volume estimates based on the areal extent [c.f. Guzzetti *et al.*, 2009] this might already yield improved accuracies for further calculations such as event magnitudes. Generally, further validation studies are needed to assess the uncertainties of the volume estimates over larger areas and for specific events and initially reported volumes should be regarded with caution [Kerle, 2002].

4.2.2. Remote-sensing displacement and volume maps as inputs to hazard models

[UNISA+AMRA]

It is well known that urban planning and risk mitigation strategies may obtain a significant enhancement from landslide susceptibility and hazard zoning maps [Cascini *et al.*, 2005; Fell *et al.*, 2008]. However, the reliability of the zoning maps depends on several factors; among these the accuracy of landslide inventory plays a fundamental role. A well-developed landslide inventory involves the location, classification, volume, travel distance, state of activity and data of occurrence of landsliding in a given area. Focusing the attention on the landslide characterization, its accomplishment can be challenging when large areas are detected and no extensive monitoring systems are available. To this end, the analysis of displacement maps can provide useful information on the state of activity and on the boundaries of the affected areas; moreover, displacement measurements can also be used for the detection of unmapped phenomena.

The scientific literature reports several applications of remote-sensing derived displacement maps to be used within the landslide risk management framework [Fell *et al.*, 2008]. Hereafter some examples are described.

Many methods for landslide mapping make use of digital elevation models (DEM) of the same area from two different periods in order to visualize where displacement due to landslides has taken place. The superficial movements of unstable slopes can be derived from the comparison of various types of documents (topographic maps, aerial photographs, cadastral maps, DEMs), which represent instantaneous views of an unstable site on various dates [Malet *et al.*, 2002]. As a result, the historical development of the phenomenon on scales ranging from 1:10,000 to 1:1,000 [Engel, 1986; EPFL, 1985; Maquaire, 1990; Martin and Weber, 1996; Powers and Chiarle, 1996] can be derived. For instance, referring to terrestrial or air stereophotogrammetry, 3-D coordinates of “moving” points are provided thus allowing both the realization of morphological maps and the generation of DEMs and cross-sections along the unstable slope [Oka, 1988; Weber and Herrmann, 2000]. More recently, high resolution data from Quickbird, IKONOS, PRISM (ALOS) and CARTOSAT-1 are able to produce highly accurate DEMs that can be useful in automatic detection of large and moderately large landslides. Nowadays for many areas the use of Google Earth data is a good alternative since many parts of the world are covered by high resolution imagery which can be combined in GIS with a Digital Elevation Model to generate stereoscopic images, that are essential in landslide interpretation [van Westen *et al.*, 2008].

A further application of these techniques is the so called *change detection* that, via the exploitation of sets of digital aerial photos taken in different periods, enables a quantitative analysis of the change in slope morphology and also the retrieval of movement vectors [Chandler and Moore, 1989 ; Gili and Sendra, 1988]. In this regard, several examples can be found in the scientific literature concerning: La Clapiere landslide in France [Casson *et al.*, 2003], the Tessina landslide in Italy [van Westen and Getahun, 2003]; the Ancona landslide [Cotecchia, 2006]; the active portion of Slumgullion earthflow in Colorado [Powers *et al.*, 1996]; etc.

Remote-sensing derived displacement maps can also be obtained via repeated GPS campaigns, as a complement to geodetic methods [Gili *et al.*, 2000]. One of the first examples in literature concerned the Vallcebre landslide (Eastern Pyrenees), see Gili *et al.* [2000]. In this case data from periodic controls on 30 GPS benchmarks were used to complement measurements of inclinometers and wire extensometers. Particularly, during 14 campaigns (December 1995 to February 1998), carried out with Real Time Kinematics and Fast Static procedures [Gili *et al.*, 2000], horizontal displacements up to 1.6 m and lowering of the landslide surface of up to 0.35 m were observed [Corominas *et al.*, 2005]. Other examples of GPS monitored landslides are: the Super-Sauze earthflow (France) [Malet *et al.*, 2002]; the Sackung phenomenon affecting the urban area of Maratea (Southern Italy) [Berardino *et al.*, 2003].

Airborne Laser Scanner (ALS) can provide high resolution topographic information, depending on the flying height, point spacing and type of terrain [Glenn *et al.*, 2006; McKean

and Roering, 2004] and also the combination of ALS and Terrestrial Laser Scanner (TLS) for has been proven successfully for the quantification of landslide volumes [Hsiao, 2004]. Although there pass generally years between two ALS acquisitions it is possible reconcile displacement by tracking significant objects from one time step to another [Baldo et al., 2009; Roering et al., 2009]. Because high temporal and spatial resolutions are desirable for surveys landslide TLS is used more frequently for monitoring. A reconstruction of the 3D displacement field of individual landslides is possible via the cross-correlation of multi-date laser scans [Daehne et al., 2011; Travelletti et al., 2011]. The application of TLS displacement and volumes measurements in hazard assessment may comprise observations of increased rockfall frequency before final failures [Rosser et al., 2007], the detection of precursory displacement [Abellán et al., 2010; Oppikofer et al., 2008] or estimates of the speed rock wall retreats [Lim et al., 2010]. It has been demonstrated that the latter can also be performed with ALS if sufficiently dense time-series are available [Young et al., 2011].

When dealing with studies over large areas the use of advanced satellite techniques, which involve data achieved by Synthetic Aperture Radar (SAR) [Gabriel et al., 1989], can be extremely useful. In particular, the differential SAR interferometry (DInSAR) can complement with traditional topographic techniques as well as GPS and LiDAR to obtain measurements of ground surface displacements, providing comparable accuracy while being less expensive and time consuming. A valuable enhancement in these techniques was obtained via multipass DInSAR techniques [Ferretti et al., 2001; Lanari et al., 2004]. However, several limiting factors need to be properly taken into account [Colesanti and Wasowski, 2006] such as: displacement data represent only one dimensional projection in the Line Of Sight [Manzo et al., 2006; Rocca, 2003]; the ambiguity of phase measurements implies the possibility of using A-DInSAR data only for the measurement of displacements of landslides ranging from extremely to very slow according to the velocity classification of [Cruden and Varnes, 1996]; limited versatility in terms of (a.) positioning of the measurement points and (b.) revisiting time; very limited coverage in vegetated areas.

On the whole, the SAR case studies described in the scientific literature highlight that with reference to the detection/mapping of slow-moving landslide phenomena the main benefits regard: the definition of the boundaries of already detected mass movements; the definition of the states of activity; the detection of previously unmapped unstable areas.

Latest trends in this kind of applications pursue the development of procedures for the use of A-DInSAR data at different scales of analyses. In particular, when dealing with studies over large areas an integrated approach can be followed with the help of i) geomorphological analyses [Cascini et al., 2010; Farina et al., 2006]; ii) information derived from sensors operating at different wavelengths [Strozzi et al., 2005]; iii) the mixture with SAR remote-sensing and optical images [Casagli et al., 2005] and iv) the cross-comparison with damage survey dataset [Cascini et al., 2008]. As for studies at the scale of the single phenomenon, the integration with ground-based monitoring techniques and advanced landslide displacement monitoring as well as the use of corner reflectors [Gili et al., 2009; Novali et al., 2005] is

absolutely necessary and must be pursued in order to overcome, for instance, constraints related to the absence of natural benchmarks in vegetated areas.

4.2.3. Remote-sensing derived predisposing factors maps as inputs to hazard models

A. Topographic data and derivatives

[ITC]

The 'slope' in slope instability analysis already indicates the importance of topographical information in landslide hazard assessments, from regional studies to detailed inventories on a single landslide or hill slope. To date Digital Elevation Models (DEM) and derivative products derived from them are the main providers of topographical data used crucial as input in landslide modeling. Where originally contour lines obtained by digitizing from topographical maps provided the main source for DEM construction, today a wide variety of DEM data sources is available. This has even led to the development of a new work field in geomorphology that deals with the quantified analysis of landforms using DEMs: geomorphometry or digital terrain analysis (see website www.geomorphometry.org).

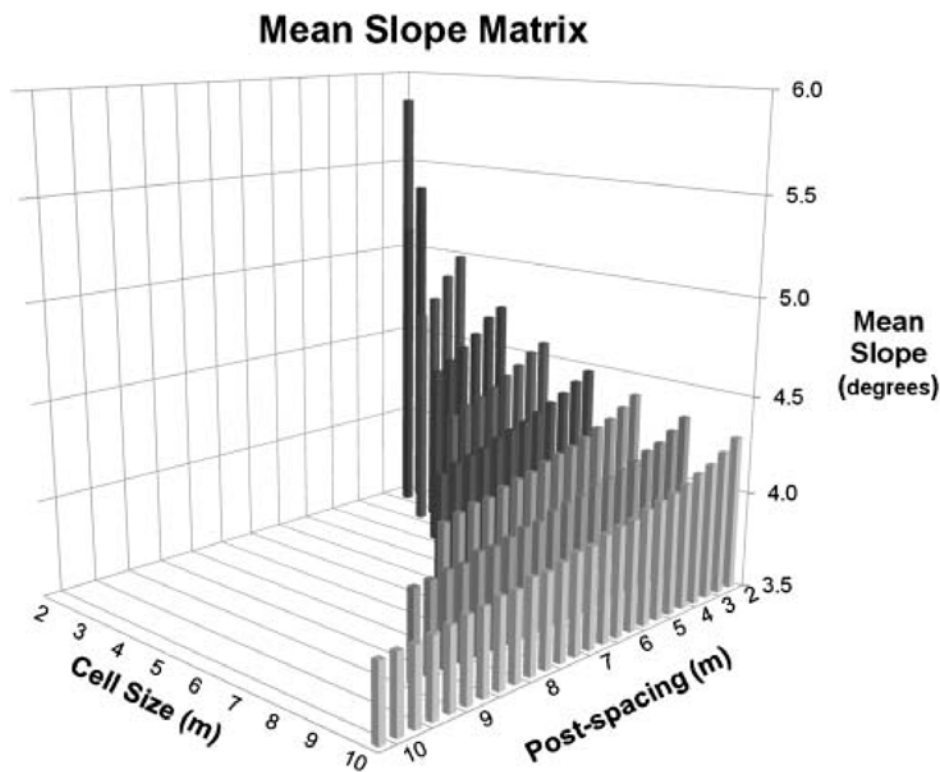


Figure 14: Relationship between the mean slope by LiDAR point-cloud spacing and resulting topographic raster [Chow and Hodgson, 2009].

- **Data sources for DEM generation**

A variety of data sources for DEM construction does exist. They range from ground-based surveys (using GPS technology), contour maps derived from topographical maps, to remote-sensing-based data sources such as stereoscopic satellite imagery, interferometric RADAR and Laser scanning (LiDAR). Focus here is on remote-sensing-based DEM data sources.

For quite some time already medium resolution DEMs can be generated from stereoscopic satellite images such as from SPOT (SPOT4-DEM is 10*10 m, SPOT5-DEM is 5*5 m) and ASTER (ASTER-DEM is 15 or 30 m spatial resolution). Higher resolution DEMs are generated from for example Quickbird and IKONOS (DEM resolution is 1- 4 m) and CARTOSAT-1 (CARTOSAT-DEM is 2.5*2.5 m). Although vertical resolution of these DEMs is typically 1 meter, the accuracy of elevation values may vary quite a bit. Especially in mountainous regions elevation value accuracy may decrease, amongst other by stereoscopic errors introduced in the DEM generation process. Furthermore, some of these systems provide DEMs free at cost and with global coverage (the ASTER Global-DEM at 30*30 m, see at <http://asterweb.jpl.nasa.gov/gdem.asp>), whereas others are expensive (IKONOS-DEM) or do not (yet) provide global coverage.

During a space shuttle mission in 2000 a DEM with near to global coverage was generated. This so called Shuttle Radar Topographic Mission (SRTM) collected elevation data at 30*30 meter spatial resolution using so called radar interferometry. To date for most part of the globe SRTM-DEM data resampled at 90*90 meter resolution are available; 30*30 meter SRTM data are available for the USA and an increasing number of regions. RADARSAT and ENVISAT are other examples of spaceborne sensor systems using radar interferometry for DEM construction.

Laser scanning or LiDAR is a relatively new technology and a data source for high resolution DEM construction. As such using LiDAR a so called 'digital surface model' (DSM) is produced that contains information of objects on the earth surface such as vegetation stands, buildings and infrastructure. Digital preprocessing and manual editing to remove these objects and surface elements is required to construct a LiDAR-DEM from such a DSM. Advantage of the DSM, however, is that it can provide relevant information about elements at risk in landslide risk assessment. A major advantage of LiDAR is that DEMs with a very high spatial resolution (up to sub meter level) can be produced. This also holds for vertical resolution (up to centimeter level). Hence, LiDAR-DEMS can be used in detailed landslide assessment. So far, mainly airborne LiDAR-DEMS are used in landslide assessment, see also below.

- **Digital elevation data in landslide hazard assessment**

Standard functionality for working with DEMs is available in almost all general purpose GIS software. In this way, DEM-derived parameters including slope gradient, slope aspect and slope shape can be computed without any problem. An overview of DEM derivative products and their applicability in landslide modeling is provided by *van Westen et al.* [2008]. In heuristic landslide analysis of larger areas at small scales hillshading maps derived from a

DEM can be used to support physiographic classification, to delineate differences in internal relief and drainage intensity. In statistical landslide modeling at medium scale DEM derivatives including slope gradient, slope direction, slope shape (profile curvature, plan curvature), and slope length serve as input parameters. Large scale deterministic modeling uses local drainage line direction, flow path, slope gradient, slope morphology and other DEM derived parameters to quantify landslide initiation and runout. DEMs derived by contour line interpolation from large scale (detailed) topographic maps are probably the most commonly used input for hazard assessment. Care should be taken in cases where the elevation model represents only the post-landslide topography. Especially for the assessment of landslide types which considerably changed the slope morphology it is recommend to use pre-failure topographic information or at least reconstruct the previous surface [Gorum *et al.*, 2008].

However high resolution DEMs generated from LiDAR data are increasingly used as input for detailed landslide studies and modeling exercises. In a landslide study in Honduras *van Westen et al.* [2008] were able to estimate the average building height of elements at risk by using the difference between elevation measurements from a LiDAR-based DEM (1.5*1.5 m resolution) and a contour line-based DEM representing the earth surface elevation (at 2.5*2.5 meter).

LiDAR data can also be used to produce high spatial resolution hillshade (shaded relief) maps. Since they provide a detailed impression of topography and topographic differences, these can be used in the detailed interpretation of landslide mechanisms [Van Den Eeckhaut *et al.*, 2007; *van Westen et al.*, 2008]. Possibilities to using more automated techniques for the exploitation of high-resolution LiDAR-DEM have been demonstrated in various studies including the automated mapping of landforms [Anders *et al.*, 2009] and of landslides in particular [Van Den Eeckhaut *et al.*, 2011]. Such methods for DEM-based semi-automated mapping of geomorphic features could well facilitate more detailed landslide studies in terrains that are difficult to access.

For shallow landslide susceptibility assessment, involving process-based modeling of soil thickness and groundwater conditions, over wider areas high-resolution topographic data are needed according to *Godt et al.* [2008]. They recognize LiDAR-DEMs as promising in this respect, also because the underlying laser scanning technology allows constructing DEMs in vegetated landscapes.

As such the use of high resolution DEMs is not intended to replace geomorphic fieldwork and geophysical site investigation. At the same time this type of DEM can be very useful in an early stage of detailed landslide investigation, when other relevant data are (still) lacking, as is illustrated by *Derron et al.* [2005] in the preliminary assessment of a large landslide are (300,000 m²) in Norway. They acquired a DEM at 1 by 1 meter spatial resolution obtained from airborne LiDAR data. This LiDAR-DEM was used in a three subsequent activities. First, the DEM was used in a structural analysis of discontinuities and faults on the landslide that are relevant to slope stability. Next, kinematic tests of planar

sliding were carried out. Thirdly, the DEM was used for a first estimation of the potential landsliding volume.

Since a DEM presents only surface data it is not an easy task to estimate a landslide volume from only a single DEM. However, if DEMs are available for different periods of the same landslide area they can be used to estimate and visualize displacement on slopes due to landslide activity. By subtracting multi-date elevation values from each other displacement and changes in volume can be computed. However, this is only feasible if the elevation data represents enough detail and precision for the targeted magnitudes of displacements and volumes [van Westen *et al.*, 2008].

- **DEM resolution and effect on landslide hazard assessments**

In theory many sources of DEM are available to date. However, which type of DEM provides adequate topographic parameters, in practice it depends on the type of landslide under study and the characteristics of the area. Still far too often the type of landslide assessment and DEM data are not properly matched. If for example coarse-resolution (90*90 m) SRTM-DEM are used for statistical landslide modeling it is mostly because finer resolution DEM maybe too costly or simply not available. In such cases, however, the method and scale of the hazard assessment must take into account the data availability restrictions. This may require that initial ambitious objectives are tempered given data availability.

DEM resolution affects for example the distribution of slopes (Figure 14; Zhang *et al.*, 1999), catchment areas and relative shallow landslide hazard, as is found by Claessens *et al.* [2005]. They experimented with DEM pixel sizes of 10, 25, 50 and 100 meters. Accepting that probably no perfect DEM resolution exists, they conclude that “Ideally, a DEM should represent the topographical and hydrological properties derived from it in such a way that neglecting features which are possibly ‘filtered out’ does not harm the quality of the model outcome”. There is still relatively few studies, which evaluated the impact of the input data resolution on probabilistic models. Lee *et al.* [2004] conducted a case study in Korea by simply resampling the original input datasets. They concluded that resolution of 30m or less are appropriate for scales larger than 1:50.000. In another study comparing different DEM resolutions and their effect on landslide assessment Tian *et al.* [2008] found that the use of a finer resolution DEM does not necessarily increase the predictive accuracy in landslide susceptibility assessment. Coarser DEM resolutions tend to have a smoothing effect on elevation values and those of derived parameters, on the topographic representation of a landscape more in general. It is often suggested that a pixel resolution between 5 and 20 meters is required for genuine analysis of landforms and of related surface processes. However, for hazard assessments over larger areas the use of coarser resolution (up to 90*90 m) may be more appropriate [Tian *et al.*, 2008].

A number general suggestions for the use of DEM derivatives in different types landslide modeling are given by van Westen *et al.* [2008]. Slope gradient, aspect, shape, length and other derivatives provide relevant input factors for medium scale heuristic and statistical landslide analysis. They advise not to use slope gradient in small scale studies. However, in

large scale and detailed deterministic modeling slope maps can be used to estimate slope hydrology and slope stability. Apart from restrictions of having DEM data of too coarse resolution according to *van Westen et al.* [2008] DEM data can also be of too fine resolution. This might be especially problematic when the maps of other environmental variables used in the hazard assessments are of much coarser resolution. It also must be stressed that for example slope values are generally increasing with higher sampling distances of the DEM [*Zhang et al.*, 1999], whereas resulting high local gradients are not necessarily relevant for the scale on which slope failures occur.

- **Object-oriented delineation of mapping units for landslide susceptibility and hazard assessment**

A basic decision that has to be made for the creation of susceptibility and hazard maps is the choice of the mapping unit whereas a multitude of different approaches reaching from pixel-based methods to the use of administrative boundaries has been proposed. Since rectangular pixel-units do not represent well natural spatial units that condition the probability of slope failures the use of slope or terrain units as mapping units is a common approach [*Rossi et al.*, 2010a; *Tian et al.*, 2010 and references therein; *Van Den Eeckhaut et al.*, 2009]. In this section we provide an overview of recent trends for the automated delineation of landforms and highlight their potential usefulness for the objective delineation of mapping units at various scales.

Information about landforms provides an important input for heuristic and probabilistic approaches to landslide hazard assessments [*van Westen et al.*, 2003]. More in general landform information is relevant in all those cases where topographic parameters are not only used as individual modeling input parameters, but where they are also considered in a landscape context.

Several recent studies in the field of geomorphometry target the (semi-)automated delineation and classification of landforms. Conventional approaches to geomorphic mapping and landform delineation are time consuming and strongly depend on a surveyor's geomorphic expertise. Approaches for (semi-)automated landform classification intend to be less time consuming and more 'objective'. At the same time it is recognized [*Anders et al.*, 2009] that, also because of the multi-scale nature of geomorphic processes, accurate delineation of landforms using these automated approaches still remains a challenge.

DEMs and DEM-derived parameters, such as slope gradient, slope orientation, profile curvature and plan curvature, for a main input for automated landform delineation and classification. So far, the types of landforms that can be classified using automatic characterization based on topographic characteristics typically include peaks and ridges, slopes, shoulders and terraces, depressions and valley bottoms.

In pixel-based approaches for automatic landform delineation and classification using expert knowledge relationships are pre-defined between selected DEM-derivatives. A thus resulting decision table is used to automatically delineate landforms in a study area by assigning landform classes to pixel values. As a simple example of such a decision rule using

input terrain parameter raster maps: “if slope gradient is low and plan curvature is high, then the assigned landform is a ridge”. The open-source software package LANDSERF (see at www.landserf.org) provides a nice example of implementation of this kind of automated landform classification.

Also non-pixel based approaches for image segmentation using object-oriented techniques for automated landform classification are being used. In fact, they are increasingly advocated for providing better accuracy and also for being more intuitive in the generation of landform information in an (semi-)automated manner [Blaschke, 2010; Dragut and Blaschke, 2006; Martha et al., 2010a]. In pixel-based approaches landform class labels are assigned to a map at pixel-by-pixel basis. On the other hand, object-oriented (non-pixel based) approaches these landform class labels are assigned to recognizable segments (objects) in the landscape that share the same attributes.

An automated landform classification using fuzzy membership classes and object-basis image analysis is introduced by Dragut and Blaschke [2006] and their approach realizes three steps. First, a number of DEM-derivatives are produced as data layers. Next, image segmentation is used to delineate homogeneous objects at different levels. Thirdly, landform elements are classified using these object primitives applying a classification model based on surface shape and topographic position of objects. By eliminating manual classification steps the authors claim to reduce human errors in landform analysis. Furthermore, their approach is less time consuming and applicable in different types of landscape using different dataset. A disadvantage of object-oriented approaches, however, is that so far the required software tools are expensive.

What both pixel-based and non-pixel based approaches share according to Stepinski and Bagaria [2009] is that they produce maps that contain unmixed (simple) well-defined landform classes. To enhance the often very granular results from pixel-based methods Stepinski and Bagaria [2009] propose a method for automated landform classification from a DEM that is capable of defining and mapping generalized landform classes. Their method first pixels in a DEM are re-classified into one of a set of pre-defined simple landform classes. The outcome of this pixel-based landform classification is used to define new landform features that also contain contextual information round each pixel. Combined image segmentation and clustering (using the so called recursive hierarchical segmentation (RHSEG) algorithm is subsequently carried out on these new features. Resulting geomorphic maps constructed by this approach are more useful for further analysis where combinations with other information such as land cover information are important. The authors note that their technique is not entirely restricted to applications on DEMs, but can also be used on other data types. Wang and Niu [2010] recently adopted an image segmentation algorithm on multiple input layers to obtain spatially homogenous mapping units and demonstrated the effectiveness of such an approach in a comparative susceptibility mapping at the Three Gorges Reservoir. Though, the authors did only adopt one specific segmentation it appears worth noting that segmentation is scalable almost seamless and might provide an interesting way forward for research to bridge between susceptibility models over multiple scales.

B. Lithology, Structure, Faults

[BRGM+ITC]

• Lithology and extraction of geological units

The geological formations in a particular area are often a key factor for the occurrence of landslides [Gerrard, 1994; Pachauri and Pant, 1992; Sarkar and Kanungo, 2004] and combined with other information layers (in particular, lineaments, faults, landuse, soil, ...) can be used to map the landslide hazard on a regional scale. The required scale for such usage is about 1:25000. We can assume that for a more local analysis (mapping monitoring an individual landslide), a more detailed map (1:5000) will be required. That has incidence on the needed data characteristics: typically the needed resolution of the remote-sensing data will be about 10m for 1:25000 regional scale hazard mapping and 2.5-5m for 1:5000.

The spectral analysis of the solar radiation backscattered by the ground surface (reflectance spectrometry) could be an important source of remote-sensing information about the chemical and mineralogical characteristics of the materials of the ground surface. In fact, the reflectance spectra (visible and near infrared) of the rocks have specific absorption bands that allow the identification of the constituent minerals, by analyzing the position, the shape and intensity of this bands.

The best results of lithological mapping were obtained on areas where surface materials are well exposed, little altered and with mineral in pure concentrations. However, recent techniques of extraction of spectral information and the improvement of the instrumental performances, we are now able to use multi-spectral and hyper-spectral images with more complex geological situations. The analysis of hyper-spectral and multi-spectral imagery is therefore a powerful tool for identifying mineralogy from space. It provides quantitative mineralogical abundancy of exposed surface materials.

The perspective of applications that could be identified in the domain of lithology, includes:

- a) the mineralogical characterization of continental surface using hyper spectral observation.
- b) pedology and soil study
- c) monitoring of dynamic geology using multi-temporal acquisitions

The main constraints for the use of hyperspectral and multi-spectral data for lithological mapping are:

- The need of images without cloud cover.
- The vegetated cover: if we are able to map mineralogy with a partial vegetation contain in the pixel, it is impossible to extract information about the ground surface with a dense vegetation (forest) masking the surface. That could be a major issue for landslides in a European contexts such those addressed by the project. Best results were obtained in arid environments [Gomez et al., 2005; Gomez et al., 2007; Harris et al., 2010].

- The complexity of the covered area in terms of rock, soil and mineral mix. In addition, reflectance spectroscopy gives typically information on the first 50 m. Any alteration of the surface (including presence of lichens) affects the analysis.
- A last issue comes from the availability of the appropriate sensor. The lack of spaceborne hyperspectral instrument is a limitation as the justification of a costly airborne campaign to complement existing geological data (at least in Europe) is valid only on sites where the surface geology knowledge is insufficient. In certain cases, the multi-spectral information from the ASTER sensor allows to produce relevant geological map [Gomez *et al.*, 2005]. However, the 30 m resolution only matches partially with the needed specifications in terms of scale.

Recently it has been demonstrated that a synergetic use of airborne hyperspectral images and high-resolution LiDAR topographic data yields the possibility to use remote-sensing as a tool for geological mapping in vegetated terrains [Grebby *et al.*, 2011]. Such applications may be regarded more frequently as the availability of advance datasets increases.

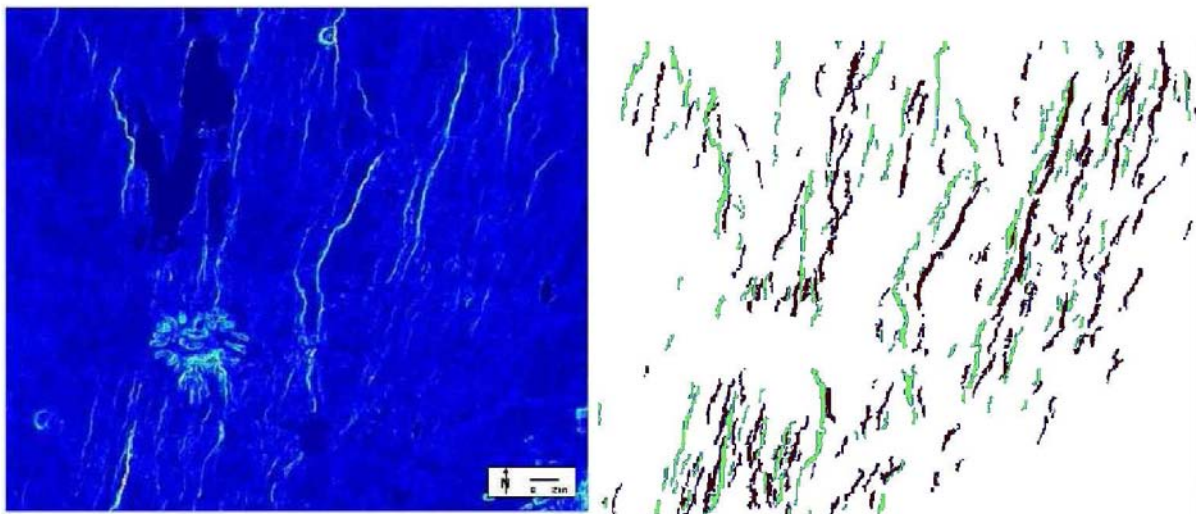


Figure 15: Derivative of a DEM and extracted fault lines [Gloaguen *et al.*, 2007]

- **Extraction of lineaments**

Extraction of linear features on Remote-sensing images (or RS Digital Elevation Models) has been widely used [O'Leary *et al.*, 1976] as indicator of the presence of specific geological objects (in particular lithological discontinuities) associated to discontinuities in the image. Classically, such extractions were conducted manually, based on the interpretation of the image by an expert. The expert visually delimitates features on the image based on his a priori knowledge of the objects on ground and their expected signature on the analyzed data.

On the one hand such approaches could be inefficient in processing time and in the other hand the interpretation is expert-dependent. To cope with these issues automatic or semi-automatic algorithms were developed for extracting of such elements [Fukue *et al.*,

1981; Gloaguen *et al.*, 2007; Koike *et al.*, 1995; Mallast *et al.*, 2011; Marghany and Hashim, 2010; Raghavan *et al.*, 1995] in order to obtain faster and more objective results (Figure 15). However, as only features representing structural elements are useful, interpretation is still required for excluding feature from other sources (anthropogenic, biological, etc.). Therefore manual component of the analyses cannot be generally fully rejected. Most commercial image processing softwares (such as PCITM, ENVITM or ERDASTM) propose tools for helping lineament extraction (including filters to pre-process the images and algorithm to extract the features).

For the landslide susceptibility mapping, lineaments associated with fractures, discontinuities and shear zones are useful information that could be combined to other data. In most cases such information will be used to refine the lithological information and fault positions. Sarkar and Kanungo [2004] for example propose a more direct use of this information by including the density of lineaments as indicator in the susceptibility computation. An extensive review of the use of lineament maps in landslide susceptibility and hazard mapping was recently undertaken by Ramli *et al.* [2010]. They concluded that lineaments maps are a vital part of landslide hazard assessment but also demonstrated that none of the reviewed studies used automated mapping techniques. The authors pointed out that manual mapping yield generally high uncertainties and only few studies apply instruments to evaluate such discrepancies of different lineament maps.

Similarly to the previous sub-section, considering the scales required for the study of the landslide phenomena (1:25000-1:5000), we recommend the use of data with resolutions better than 10 m. Spaceborne sensors such as SPOT 5, Quickbird, Geoeye, or equivalent in terms of resolution can provide valuable information.

- **Identification of faults using radar interferometry**

SAR interferometry is used on active faults deformation since the 90's for co-seismic displacements [Massonnet *et al.*, 1993]. However, on the one hand, deformation on faults affected by earthquakes with high magnitudes such as most of the earthquakes mapped by conventional differential InSAR is generally too high to allow mapping of the displacement on surface rupture due to loss of signal coherence [De Michele *et al.*, 2010; Raucoules *et al.*, 2010]. Sometimes, the lack of signal coherence in the InSAR signal of the displacement field is an indirect evidence of the seismogenic fault and can be used to detect un-mapped active faults or blind seismogenic structures [Talebian *et al.*, 2004]. On the other hand, slow (cm/yr) aseismic movements on faults are difficult to observe on single interferograms as the displacement values are lower than the displacement detection capabilities of the technique, taking into account the presence of different sources of noise in the interferometric phase.

More recently, processing of multi-temporal SAR data series provides an alternative for measuring such fault displacements by considering large sets of interferograms [Usai, 2003] or based on point wise persistent scatterers techniques [Burgmann *et al.*, 2006; Ferretti *et al.*, 2001]. Application of interferometric techniques to landslides generally targets more specifically the assessment of the location of potentially sliding areas and their activity

[Guzzetti *et al.*, 2009] than the identification of faults on the sliding area. However discontinuities in the interferogram could be in some cases identified as limits of the slide [Delacourt *et al.*, 2007].

The limitations of the technique for landslide applications are those generally admitted for SAR interferometric techniques [Raucoules *et al.*, 2007]. The quality of the InSAR information is generally poor on vegetated areas. Nevertheless, if short time span (such as obtained by the ERS tandem configuration in 95-98 or with Cosmo-skymed constellation) are possible, we could overcome this shortcoming. In addition L-band data (ALOS/PALSAR) less sensitive to vegetation than C-band data (EnviSAT/ASR, ...) when used for interferometric purposes.

In terms of resolution, the available sensors (resolution ranging from less than 1 m to about 20 m) are compatible with such deformation mapping on landslide. Higher resolution data sets can provide of course more detailed information.

Finally, we will notice that fault location would be more reliable by integrating this information with the previously described elements (i.e lithology and lineaments) that provide complementary information on the surface signature of the fault.

C. Soils

[ITC]

Spatial information about geotechnical and hydrological soil properties and about soil depth provides essential input data layers for large scale and detailed landslide studies, especially when using deterministic hazard modeling approaches. Modeling at small scale with insufficient soil input data will either lead to large simplifications in the resulting hazard and risk maps; or it will require long data collection campaigns [van Westen *et al.*, 2008].

Soil grain size distribution, soil cohesion, friction angle, and bulk density are examples of geotechnical properties that are crucial parameters in stability analysis. Dynamic modeling of spatial and temporal changes in hydrological conditions on slopes requires reliable data about soil depth (thickness) and about soil hydrological parameters such as pore volume, saturated conductivity and soil moisture. Van Westen *et al.* [2008] identify soil moisture as a main parameter in slope stability modeling, since it plays a critical role in triggering slope failure.

As the result from local differences in soil forming processes soil properties can vary considerably at local scale. This makes that they are often difficult to map at medium scale and over larger areas. Therefore, environmental correlation using topographic factors and other proxies is often applied in the medium scale mapping of soil parameters. At local scale and in detailed studies spatial interpolation using geo-statistical methods is often applied. In fact, the variation in soil properties does not only occur in 2-dimensional space (soil depth that changes from location to location'), but also in 3-dimensional space (soil moisture changes with depth in a vertical soil profile) and even in time (soil moisture conditions show seasonal differences).

This complexity of soil and soil properties makes the use of remote-sensing for soil and soil property estimation not an easy task. Furthermore, with most of the currently available sensor systems only characteristics of the soil surface can be characterized. Subsurface soil properties, however, cannot be 'seen' with remote-sensing techniques alone. A great asset of remote-sensing, on the other hand, is provided by the possibility to obtain different images of the same part of the earth surface. This allows monitoring differences in dynamic soil properties such as soil moisture content. Furthermore, remote-sensing can be used to observe land qualities that are known 'proxies' (environmental co-variables like slope gradient, topographic position) for soil properties that cannot be directly observed themselves. Authors like *McBratney et al.* [2003] even claim that these proxies together with field observations are the basis for deriving relevant soil information from remote-sensing images.

- **Remote-sensing in the visible and infrared domain**

The use of aerial photographs and medium resolution multi-spectral satellite images (from Landsat, Spot) has a long tradition in conventional general purpose soil mapping (soil survey). Stereoscopic visual image interpretation and automated image classification algorithms are used for extraction of information about landform, land cover, drainage pattern and other environmental co-variables. Together with soil surveyor's knowledge about soil forming factors and corresponding spatial variation of soils, this information is used to identify boundaries between soil classes. This type of soil estimation using remote-sensing requires a soil expert who can use what can be 'seen' on the remote-sensing image – i.e. aspects of the soil surface – to also understand the distribution of subsurface elements of the soil profile [*Campbell*, 2009]. For the National Resources Inventory (NRI) program of the United States Department of Agricultural now also IKONOS high-resolution satellite image data are applied for soil resource mapping.

Under certain circumstances, for example when vegetation cover is lacking, direct observation of surface soil properties from image data in the optical domain is possible. Some examples are: surface texture, soil moisture and organic matter [*Campbell*, 2009]. Micro-topographic differences on bare fields can show as darker image tones (lower parts, restricted drainage) that possibly correspond to higher moisture content, finer soil texture and higher organic matter content in the top soil; or as lighter image tones (higher parts, improved drainage) that can correspond to less organic matter content, somewhat coarser texture and lower soil moisture content in the top soil.

Examples of satellite sensor systems with image bands in the near infrared and the shortwave infrared image domains are Landsat, ASTER, AVIRIS. Differences in reflection and absorption features between soil materials of different mineral composition provides soil spectral reflectance curves that can be used to differentiate between mineral composition of soils. To date so called spectral libraries do exist that provide spectral reflectance curves for a large number of soil materials and minerals. See for example the USGS spectral library (<http://speclab.cr.usgs.gov/>) and the ASTER spectral library at NASA (<http://speclib.jpl.nasa.gov/>). In soil context the image bands in the shortwave infrared

(SWIR) are in particular significant for the detection of clay minerals in surface materials (as indicator for soil texture) and because of their sensitivity to surface soil moisture.

- **Remote-sensing in thermal-infrared domain (TIR)**

Emission by the earth surface of long-wave infrared (thermal) radiation provides information about differences in properties of both surface materials and subsurface geology. Absorption of this thermal energy and its re-radiation later on is controlled by the thermal properties of many factors including characteristics and depth of surface materials, differences in soil moisture condition and parent material. This makes remote-sensing in the thermal infrared domain relevant for studying soils and soil parameters.

Differences in heat capacity can be exploited in the characterization of soil texture and soil moisture conditions. The heat capacity of dry material is one fifth of that of water [Campbell, 2009]. Consequently, moist and water saturated soils have higher heat capacity as compared to dryer, often also coarser textured, soils. Also the thermal conductivity of soils increases with finer soil textures and higher soil moisture content.

Daily and seasonal variation in both air and soil temperature, including their interaction, tend to complicate the use of thermal remote-sensing for soil estimation. Soil surface temperatures vary daily with solar illumination variation between day and night; they vary seasonally with differences in solar angle and corresponding day length. On the other hand, by considering seasonal thermal image pairs the contrasting seasonal soil temperatures can be used for the observation of soil properties like soil moisture content and soil texture. However, so far this is not applied often for soil determination [Campbell, 2009]. Another example is provided by Verstraeten *et al.* [2006] who have used thermal information from METEOSAT at 10-daily intervals to estimate soil moisture conditions for European forests.

Above mentioned METEOSAT is an example of a meteorological satellite based system with thermal imaging capability. MODIS is another example of a high temporal resolution, coarse spatial resolution system. Landsat7 and ASTER are medium-resolution, operational sensor systems with image bands in in the thermal infrared domain. At NASA's Jet Propulsion Laboratory the development of HypSIRI is under study, a new spaceborne system that will also carry a thermal infrared imager of 60*60 meter spatial resolution (see at <http://hyspiri.jpl.nasa.gov/>).

- **Remote-sensing in the active microwave domain (RADAR)**

Backscatter characteristics of returned microwave signals that were purposely broadcasted by spaceborne or airborne remote-sensing systems are mainly used to determine soil moisture conditions and surface roughness.

The ability of a soil material to retain electrical charge (represented as its dielectric constant) is influenced by soil moisture [Campbell, 2009]. Overall higher soil moisture content corresponds to a higher dielectric constant, which in turn contributes to a higher radar backscatter of that soil. Depending on the RADAR system and under favorable conditions radar signals have a ground penetrating capability, enabling the estimation of soil moisture in

up to the first centimeters of the topsoil. However, interference by vegetation cover and relief can be complication factors here. Ground penetration is highest for dry soils. In a recent study *Lasne et al.* [2004] were able to detect subsurface structures up to a depth of about 5 meters below a sand dune landscape, using airborne RADAR technology and advanced data processing capability.

In the United States, RADAR systems mounted on aircraft are used in farm management to monitor soil moisture conditions of agricultural fields. So called Ground Penetrating Radar (GPR) is increasingly applied to observe and monitor soil moisture conditions in field surveys.

Passive microwave sensing presents a new development for soil determination using the microwave domain. It is described later in this chapter.

- **Hyperspectral remote-sensing**

Imaging spectroscopy is a technology that for long already is used for the identification of materials and material composition. As hyperspectral remote-sensing this technology is also widely used by geologists for the detection and mapping of minerals. In fact, it has developed as a new branch of remote-sensing, also because of the special sensor systems, image data processing methods and software tools that it involves. Based on many field and laboratory measurements on known minerals and other identified earth materials so called spectral libraries (see also above) are available. The known spectral characteristics of these materials are used in the identification of unknown materials on hyperspectral image data. An example of an operational hyperspectral imaging system is HYPERION (30*30 meter spatial resolution). AVIRIS, DAIS and HYMAP are examples of airborne systems.

To date also spectral libraries for soil materials are developed. An example is the Globally Distributed Soil Spectral Library (see at: <http://africasoils.net/data/ICRAF-ISRICspectra>). This initiative of the World Agroforestry Centre (ICRAF) and the International Soil Reference Information Centre (ISRIC) intends to present a spectral library of global soils for the sensing of soil quality.

According to *Campbell* [2009], the value of hyperspectral remote-sensing for soil studies is restricted to what he calls “rather specific situations” where a soil surface is exposed to the remote sensor. These are for example situations where there is no vegetation cover, such as in a soil salinity study in an arid region.

- **New developments in remote-sensing-based soil moisture estimation**

As has been mentioned already, the possibility of considerable variation in soil moisture content over short distance in space and also over short periods of time can make soil moisture estimation a real challenge [*Campbell*, 2009]. This may be a reason why according to *Ray et al.* [2010] soil moisture data obtained by remote-sensing so far have not been used in landslide studies.

Several satellite sensor systems measure soil moisture at a routine basis already. For example the known correlation between radar backscatter and soil moisture content is

exploited by active and passive microwave sensor systems at different spatial and temporal resolutions. Examples of sensors systems in the active microwave domain are RADARSAT 1 and ENVISAT's advanced synthetic aperture radar (ASAR). Examples of satellite-based passive microwave sensor systems are the Advanced Microwave Scanner (AMSR-E) on board of NASA's Aqua satellite, the Tropical Rainfall Measuring Mission's Microwave imager (TRIMM-TMI). Note, that many of these satellite systems play a role in global weather and climate modeling as well.

Special attention these days is paid to passive microwave sensors, since they provide higher accuracy in soil moisture measurements. The AMSR-E instrument, for example is potentially useful in the characterization of soil moisture in areas prone to landslides [Ray *et al.*, 2010].

A new development is the merging of passive and active shortwave satellite image data for soil moisture estimation. At this moment a new instrument that integrates active and passive microwave sensing is being developed by NASA. This Soil Moisture Active and Passive (SMAP) will measure both surface emission (radiometer, passive component) and backscatter (radar, active component). Its launch is scheduled for November 2014 (for sensor and mission information, see website: <http://smap.jpl.nasa.gov>).

- **RS-based soil depth estimation**

In soil-geomorphic context soil depth can be defined as the distance between the surface and the parent material of the soil. This same depth is identified by geologists and engineers as regolith depth. Depending on local conditions soil depth can vary from a few centimeters to tens of meters. Apart from characteristics of the parent material itself (lithology, weathering rate), factors such as slope gradient, slope shape, vegetation cover and land use activities result in a spatial variation in soil depth. Since the parent material underneath the regolith layer cannot be seen it is not possible to directly observe soil depth.

These are among the reasons that so far remote-sensing has not proven all that useful in obtaining relevant soil depth data for landslides studies. Furthermore, remote-sensing in the optical and microwave domain are limited to observing features at the earth surface or in a shallow subsurface layer. Field estimation and field mapping remain important for soil depth estimation.

For relatively small areas spatial estimation of soil depth from observation data from boreholes and pits can be an alternative. *Kuriakose et al.* [2009], for example, applied spatial interpolation by regression kriging on blocks of 20 by 20 meters to estimate soil depth in a catchment area of 9.5 km². As input they used 259 soil depth measurements, together with terrain parameters and land use data as environmental co-variables.

However, if larger study areas have to be covered this kind of spatial estimation is often too time-consuming and expensive. This is mainly because of the large number of soil depth observations required as input for spatial interpolation.

Geophysical survey techniques provide an alternative option for soil depth mapping. Wong *et al.* [2009], for example, have used airborne gamma-radiometry to estimate soil depth until 45 centimeters in overall sandy soils in a lateritic landscape.

D. Land cover information

[ITC]

Land cover is generally recognized as important environmental factor in hazard and risk assessment. In many cases differences in space and time in land cover conditions and land use practices play a determining role in the occurrence of landslides. Data about land cover types and about temporal changes in land cover are identified by van Westen *et al.* [2008] as highly important, from small scale to detailed landslide hazard assessments. Land cover data are even considered as critical for probabilistic approaches to landslide hazard modelling. Vegetation related characteristics such as aerial (canopy) cover and rooting depth, but also the presence of different vertical layers (of trees, shrubs, herbs) influence slope stability.

However, different land cover types and changes in land cover do not only play a role as landslide causing factors. They can as well be the effect of landslide activity. Then they should also be considered as potential elements at risk, being affected by occurring landslides. The ecological value of a forest area, for example, may be seriously affected by landslide activity. Or the harvest of agricultural fields may be lost after being covered by soil, rock and debris transported by a landslide.

The relationship between landslide occurrence, land use activities and land cover is not necessarily that simple and straightforward. For a study area in Cambodia Lee and Sambath [2006] found lower landslide occurrence in urban, agricultural and grassland areas, and higher occurrence of landslides under forest and shrub land. Here landslides simply correlated to the slopes occurring in mountainous terrain. With changes in land use this situation can of course change with time; urban expansion and an increase of land use activities on sloping land may well establish a strong and direct relationship between landslide occurrence and (changed) land cover. New Zealand provides a good example in this respect [Glade, 2003]. With the arrival of European settlers in a relatively short period of time the native forest and bush vegetation was cleared from extensive hill areas and converted into farm land and pasture for sheep herding. This has resulted in a permanent new situation of landscapes that are much more sensitive to disturbance and with hill slopes much more susceptible to landslide occurrence.

Land cover has to be handled with care as a predictive variable for landslide susceptibility assessment using bivariate approaches such as weight of evidence modeling. These approaches assume the use of a priori independent variables, whereas the above mentioned example from Cambodia shows that such is not necessarily the case for land cover. Thiery *et al.* [2007] present a statistical bivariate approach for large scale (1:10,000) landslide susceptibility assessment that includes a procedure to identify which are the best predictive variables in a given area. As an advantageous additional effect application of this procedure

also allows to limit the number of landslide and thematic data to be collected. The proposed procedure consist of four successive steps: (1) definition of the best landslide inventory ('response variable') to be introduced in the statistical model; (2) identification of the best predictive variables (the class of predictive variables that are influencing the location of landslides) to be used, by minimizing conditional dependence via statistical tests; (3) using a combination of statistical tests and expert knowledge to test the model performance in a 'sampling area'; (4) application of identified neo-predictive variables and weights to the total study area. According to this procedure expert knowledge is needed in statistical models in order to produce reliable landslide susceptibility maps [Thiery *et al.*, 2007].

Remote-sensing technology has been used for decades already for the generation of information about land cover, especially vegetation cover types, and changes in land cover. Especially for remote-sensing sensor systems in the optical and near infrared domain a wealth of well documented approaches and techniques exist that can be applied for image manipulation and feature extraction. The re-visiting capability of well-known medium-resolution satellite-based sensors such as Landsat-TM, SPOT, and ASTER has also resulted in an array of techniques for remote-sensing-based land cover change analysis. Where above mentioned remote-sensing systems re-visit an area every 2-3 (SPOT5) to 16 (Landsat7) days other sensor systems such as the NOAA-AVHRR, MODIS, and SPOT-vegetation systems provide global daily revisiting capability. This has led to the development of hyper-temporal image analysis. By applying images of many different time periods of the same area the seasonal behavior of vegetation can be monitored, see for example the application for crop mapping by *de Bie et al.* [2008].

Despite the availability of relevant remote-sensing technology (see above), in landslide studies land cover data are far too often considered as a static factor only [van Westen *et al.*, 2008]. But activities and events such as tree logging, wildfires, deforestation for road construction and crop cultivation clearly influence landslide activity. Quite a number approaches for remote-sensing-based detection of changes in land cover are applied on a routine basis. Examples are post-classification comparison, the use of multi-temporal colour composites, temporal image ratioing. However, the resulting land cover change information is barely considered in landslide hazard studies. Even more so, sometimes even outdated land cover information is used in landslide hazard studies. An example in this context is the CORINE 2000 land cover map of Europe. Land cover information of this map produced in 2000 is still sometimes used, without being updated, as input variable in national scale landslide susceptibility assessments.

Since “landslide hazard and risk maps are generated for the future”, as *van Westen et al.* [2008] put it, not only detected changes in land cover are important. Also expected land cover changes in the future should play a relevant role in landslide hazard and risk studies, for example in the form of the modeling of change scenarios.

Land cover also plays a role in landslide hazard assessment at global level. *Hong and Adler [2008]* have developed a preliminary satellite-based global landslide hazard algorithm for near real-time prediction of areas with increased potential for the occurrence of rainfall

triggered landslides. This algorithm uses rainfall data obtained using the Tropical Rainfall Measuring Mission (TRMM) satellite to compute a rainfall duration-intensity threshold that is combined with 6 surface parameters, including land cover.

In their evaluation study of above mentioned algorithm *Kirschbaum et al.* [2009] use the Moderate Resolution Imaging Spectroradiometer (MODIS) to identify general land cover classes as input to this algorithm. Although MODIS offers land cover information with near to global coverage, they find that classification of land cover pixels into distinct land cover categories can be subjective. MODIS pixel resolution restricts accurate characterization of landslide susceptibility. According to this study for effective operational global level landslide forecasting remote-sensing products at higher resolution would be required to represent variation in land cover and other surface characteristics.

Deforestation is generally recognized as a main factor contributing to the development of landslides. Rapid deforestation of hillslope areas often causes a sudden increase in hill slope instability. The removal of the forest vegetation results in changes in soil hydrology. And even more important, the decreased root cohesion reduces soil strength and consequently increases the probability of landslide occurrence in response of rainfall or other triggers. Especially the deforestation of extensive areas in mountainous terrain over relatively short periods of time and the substitution by crop land and managed grasslands often results in development of a chain in time of erosion, landslides, and debris flows. This not only has a permanent destabilizing effect on the hill slope landscape but also will result in the development of new environmental problems for communities living in downstream areas. Examples for such issues can be found worldwide from the Spanish Pyrenees [*Garcia-Ruiz et al.*, 2010] to New Zealand [*Glade*, 2003]. In both areas rapid deforestation over larger areas and subsequent conversion into grassland for sheep herding has resulted in a clear increase in slope instability and corresponding increase in landslide susceptibility.

Wildfires form another factor contributing to the development of landslides. Wildfire is in many regions a recurrent process. Depending on its intensity the effect of a wildfire ranges from a reduction in vegetation cover to a complete removal of the vegetation cover. A hillslope burnt by a wildfire will suffer strong erosion, with its impact onsite but also downslope. Since the wildfire results in (partial) removal of vegetation cover the soil hydrological conditions will change, up to a number of years afterwards. As a result the hazard that rainfall triggered landslides occur will considerably increase. If an area is only affected once by a wildfire the vegetation cover will re-establish with time and conditions may return 'back to normal'. However, in case of recurring wild fires in the same area they can result in a significant long-term destabilization of a landscape. The increase in dry periods and resulting wildfires coupled with an increase in the occurrence of high intensity rainfall in different Mediterranean and semi-arid regions in the world increase the risk for landslides. *Bisson et al.* [2005] have developed an approach for rapid appraisal of landslide hazard in wildfire affected areas. This approach consists of the following steps: (1) identification of burned areas using multi-temporal multi-spectral satellite image data; (2) evaluation of the

potential for landslide development in identified burnt areas using morphometric parameters; (3) evaluation of elements at risk (buildings, roads, a.o.) exposed to landslide hazard; Thus this method seeks to identify those wild fire affected (burnt) areas that are most prone to landslide development.

4.2.4. Remote-sensing derived elements at risk maps as inputs to risk models

[ITC]

A. Elements at risk in the landslide hazard context

Landslide risk can only be meaningfully assessed and modeled if suitable information on all aspects central to the risk concept is available. Specifically, this means that current, accurate and comprehensive information on the actual hazard, all relevant elements at risk (EaR) and their value and vulnerability is required ($\text{Risk} = \text{hazard} * \text{vulnerability} * \text{amount}$). This then allows an estimation of the expected losses for a given time unit [*van Westen et al.*, 2008; *Zeze et al.*, 2008]. Several SafeLand deliverables review how landslide hazard can be assessed (D2.1 and D2.2), focusing on landslide inventorization and characterization (D4.1, D4.3), slope susceptibility assessment (D2.4), landslide triggers (D1.1) and frequency calculations (D3.7), and on landslide runout modeling (D1.9). Once the actual hazard of mass movements is understood, including what types of movements can occur, and what the magnitude and spatial extent of such events is going to be, it needs to be analyzed what damage they can cause. EaR are defined as “population, properties, economic activities, including public services, or any other defined values exposed to hazards in a given area” [*Varnes*, 1984], frequently also referred to as “assets”. The amount of elements at risk can be quantified either in numbers (of buildings or people), in monetary value (replacement costs, market costs etc.), affected area or importance of the EaR.

Landslides are only of consequence and interest when damage can be caused, i.e. where elements that can suffer damage are present. This implies that we require information on the presence of EaR, but also whether they are truly at risk given the present landslide hazard. For example, a bridge and an adjacent building may both be destroyed in a debris avalanche, while in a less energetic debris flow only the weaker building might be damaged or destroyed. Those differences in performance are evaluated via their vulnerability to present mass movement types and their magnitude [*Papathoma-Kohle et al.*, 2007]. It is, therefore, meaningful to begin with a complete inventory of all EaR of importance in a landslide hazard zone, even if some of them turn out to be unaffected by certain events (vulnerability, $V, = 0$).

Landslide-prone areas that are inhabited tend to be characterized by different EaR types, not all of which are physical and can be quantified in monetary terms. The typical physical elements include buildings, roads, railways, bridges, land used for production

(agriculture or forestry), and industrial facilities [see for example *Abella and van Westen*, 2008]. Also people are in principle physical EaR, although a loss quantification similar to the other classes, i.e. in financial terms, is less meaningful. They also differ fundamentally in terms of physical presence, showing a dynamic that is comparable to vehicles, another important physical EaR. Even cattle led on landslide-affected roads in some countries are dynamic EaR of economic value. Current landslide risk assessment work tends to focus on the permanent physical infrastructure categories, in particular buildings and roads. In addition to direct physical damage, however, infrastructure also serves an important economic function that may suffer due to a hazardous event. It is possible to calculate the economic effect of a temporary or permanent disruption of a transport corridor due to landsliding, considering actual amounts and values of transported goods or services, alternative routes, etc. However, this type of economic study is rare and rather local [*Guzzetti et al.*, 2004; *Jaiswal et al.*, 2010; *Zeze et al.*, 2008]. Similarly, it is very difficult to model or calculate the potential or actual losses to protected areas (national parks), wildlife, biodiversity, or other such EaR, not least because of potential secondary effects, such as on tourism [*Delmonaco et al.*, 2009]. These different aspects can be investigated in terms of the specific physical, social, environmental, economic or political vulnerability of the present EaR (see Safeland deliverable D2.5.). In case of excessive complexity due to the number of diverse EaR, it is also possible to focus on their functional linkages within a system instead [*Pascale et al.*, 2010].

B. Inventorization of EaR

A number of ways exists to map and characterize the different EaR, with methods and data sources depending on their type. Existing cadastral data provide information on buildings, while transport authority records contribute infrastructure information, and census data add information on people living in a hazardous area. Other government records may reveal additional information, also on the non-physical EaR mentioned above. Where those records are missing or incomplete, thematic maps may be able to fill or reduce the gap. For example, information on buildings or settlements, bridges, railways, roads, or agricultural lands can be extracted from topographic maps. However, to be of use, the above data sources need to be current and complete, and of sufficient detail, all of which is frequently not the case. While it is possible to create such EaR inventories or update existing ones through field-based mapping [with GPS; *Montoya*, 2003], the most efficient way is via remote-sensing (RS) methods. This is easiest for stationary, physical EaR, and many RS datasets and processing methods can be used to map them.

- **Suitable data**

Appropriate data types and methods need to be identified in the context of the EaR of interest, in particular their size and spectral properties. Relatively easy to detect are buildings and industrial facilities, roads, railways and bridges, and fields and forest stands. It has to be noted that the vulnerability of different building types can vary dramatically, with the building type

also being a proxy for the type of persons present in the building (i.e. not directly visible EaR), and their respective social vulnerability [a school, hospital or factory; *Ebert et al.*, 2009]. However, distinguishing the type of building based only on RS data may not be possible; hence the EaR database may only include information on a building of a given size being present, without including more detailed information on type and occupants, i.e. little to work with for a vulnerability assessment.

The principal RS data types to be used for EaR inventorisation are aerial photographs, satellite images, and airborne laser scanning. Satellite data useful in this context can be further broadly separated into optical and radar images. For all data types the spatial resolution largely determines the minimum size of an EaR to be detectable, while the spectral characteristics (number and wavelength of spectral bands) inform which types of EaR can be mapped, which is further a function of the local spectral contrast. In principle three different image interpretation levels are distinguished: (i) EaR detection, which only discerns separate objects, (ii) recognition of what those EaR are (distinguishing a building from a parking lot, or a field from a forest stand), and (iii) identification, whether a building is residential or industrial. For risk assessment this gradation is clearly of critical importance as it determines the amount of information on value and vulnerability available.

Aerial photographs (AP), in addition to having the highest spatial resolution, have the longest record of any RS data type. Consequently, they have been used in numerous projects to map physical EaR. In fact, given that *any* landcover element that is detectable remotely may also be an EaR in some hazard context, any RS methodology explored or developed in the past to map or characterize landcover features can also be used to map EaR in landslide areas. For AP this has been done visually or (semi-)automatically, and using monoscopic and stereo imagery. For current landslide EaR inventory work traditional analogue aerial photos have been losing importance, though modern digital aerial images remain a viable data source. The latter allow more rapid data processing, real-time georeferencing and photogrammetric processing, direct integration of raw data and derivatives in a GIS environment, and better spectral performance. For example, Microsofts UltraCam camera captures 4 spectral bands, including near infrared (NIR) at resolutions of up to a few cm. Both the high amount of detail and the availability of a NIR band allow not only traditional physical EaR to be mapped, but also accurate distinction of different vegetation types (different forest or crop types). Given the relatively low flying height, AP often have problems with occlusion, which can pose problems in densely build up areas or steep terrain, where EaR (roads along cut slopes) may be obscured. In wooded areas, AP, like all optical image data types, also suffer from lacking penetration, which readily obscures roads and other important features. The increasing amount of detail of AP, and the increasing availability of digital data, have also caused changes in processing. Historically, AP analysis was focused on visual analysis and photogrammetry, while subsequent digital processing (at first of scanned images) was limited to pixel-based processing, i.e. using per-pixel spectral information only. More recently this has been replaced by more advanced methods, including neural networks, texture-based pattern recognition, change detection [*Chang et al.*, 2010] or object-based

analysis [Perea *et al.*, 2009; Tuominen and Pekkarinen, 2005]. The principal disadvantages of aerial photography are their relatively high cost per area unit and lack of regular repeat observations. Most parts of the world's land areas have not been imaged by AP in recent decades, hence for updating EaR databases AP are of limited use.

Optical satellite images provide information similar to AP, but also offer many critical advantages. In the past decade spatial image resolution has been increasingly approaching those of AP. Moving to meter- and submeter resolutions, i.e. to Ikonos, Quickbird, Worldview-2 and Geoeye-1 with pan-chromatic resolutions of 1m, 0.61m, 0.5m and 0.41 m, respectively, identification of small EaR, such as individual buildings or bridges, has become possible. The principal advantages of satellite data over airborne imagery are (i) access also to remote areas, (ii) lower cost per area unit, (iii) regular repeat coverage of the same scene with identical viewing geometry, and (iv) completely digital acquisition and sophisticated data calibration. Modern satellite sensors, such as Quickbird and Ikonos, and more recently Worldview-1 and Geoeye-1, have also been offering stereo coverage, as well as pointable sensors that allow more flexible coverage away from nadir. In principle the same processing methods explained for AP are applicable to optical satellite images. One important difference, however, is that satellite sensors frequently have more spectral bands (for example, Worldview-2 has 8 bands), providing more spectral discrimination, and information from spectral ranges not covered by AP.

Radar satellite images provide information that differs fundamentally from the optical domain. Radar data primarily reflect the surface physics (structure/roughness, moisture, topography), compared to the surface chemistry that optical data correspond to (mineral type, chlorophyll content in leaves, etc.). The data are therefore well suited to identify landcover objects/EaR that differ physically from their surroundings [identification of individual forest stands; Grover *et al.*, 1999], or have sharp geometric contrast. In particular buildings and bridges are straightforwardly mapped with radar [Ferraioli, 2010; Gamba *et al.*, 2000; Wang and Zheng, 1998]. The typically smooth surface of roads also aids their detection with radar [Dell'Acqua and Gamba, 2001; Tupin *et al.*, 1998]. Like all image types, radar data have disadvantages. The oblique viewing angle leads to severe geometric distortion, especially in mountainous areas: foreshortening, layover, and radar shadow. This means that features that are visible from a vertical perspective, such as narrow roads in forests or roads cuts along steeper slopes, may not be visible. Also features that are chemically (and thus visually) distinct but similar in terms of roughness (unsurfaced roads surrounded by rough, unvegetated terrain) may not be visible in radar imagery. Recent generations of spaceborne radar sensors, such as TerraSar-x and Tandem-X, reach spatial resolutions on 1 m (in small-coverage spotlight mode), allowing also small features to be resolved.

Airborne laser scanning, or LiDAR, constitutes a distinctly different RS type from the above. Like radar, it is an active sensing methodology, where the instrument emits a laser signal and measures the return information. Due to signal attenuation and laser beam divergence, it is currently only practically used in ground-based instruments and mounted on aircraft operating at altitudes of up to approximately 8000 m. LiDAR measures directly and

efficiently 3D coordinates (x, y, z) of points on surfaces, including the terrain but also buildings, vegetation (leaves) and above-ground utility lines, with data being referenced to a global coordinate system. Other information, such as object reflectivity, can also be recorded for each point. LiDAR directly delivers so-called point-clouds, i.e. directly without laborious manual processing steps. While LiDAR does not produce photographic images, it has other advantages, such as (i) penetration of vegetation and thus recording of the ground surface also in wooded areas, (ii) the high degree of automation, ranging from data acquisition to digital terrain model (DTM) generation, (iii) a high point density of up to several tens of points per m² that allows a very detailed terrain description, (iv) a vertical accuracy of up to approximately ± 5 cm, and (v) as an active system allowing measurements at night or over areas without texture (snow). Penetration of haze, smoke, water vapour clouds, rain, and snow-fall is only possible for short ranges or limited atmospheric disturbance by these effects [Jelalian, 1992]. Thus data acquisition during rain or fog or through clouds is not possible.

In the landslide context LiDAR has shown great promise. This is because (i) the typically local scale of (especially active) landslides matches well the local, but high resolution coverage of LiDAR, (ii) LiDAR data can provide information on minute morphological changes (though only with multi-temporal data), (iii) LiDAR data do not suffer from the occlusion that poses problems in radar and low-altitude aerial imagery, and (iv) multiple signals returns can be recorded [for more background information on lidar see also Kerle *et al.*, 2008]. Point (iv) is of particular interest. It means that a single LiDAR signal emitted from the sensor leads to height information from different levels, i.e. the ground, major tree branches, and tree tops. This allows vegetation to be identified and characterised [tree vegetation type, height and density; Blair *et al.*, 1999; Harding *et al.*, 2001; Reutebuch *et al.*, 2005], or digital terrain models (without above-ground features such as vegetation) to be calculated [Kobler *et al.*, 2007]. It also allows landslides underneath vegetation to be identified [Van Den Eeckhaut *et al.*, 2011; Van Den Eeckhaut *et al.*, 2007]. Similarly, also buildings (Figure 16) and roads (Figure 17) can be readily identified in LiDAR data using such filtering [Forlani *et al.*, 2006; Razak *et al.*, 2011a]. Depending on the detail of the LiDAR survey, a comprehensive description of buildings is possible, including height, size, shape, type (based on building footprint and roof structure). Compared with airborne and satellite images discussed above, LiDAR provides a useful combination of many of their advantages, and is thus able to provide very elaborate data on a number of landslide risk related parameters. Current disadvantages are the relatively high cost of LiDAR instruments and LiDAR-ready aircraft, resulting in high survey cost and typically relatively small survey areas. Like with aerial photographs, most of the world's terrestrial areas have not been mapped with LiDAR. However, LiDAR no longer remains a niche, and the amount of systems in use is rising rapidly.

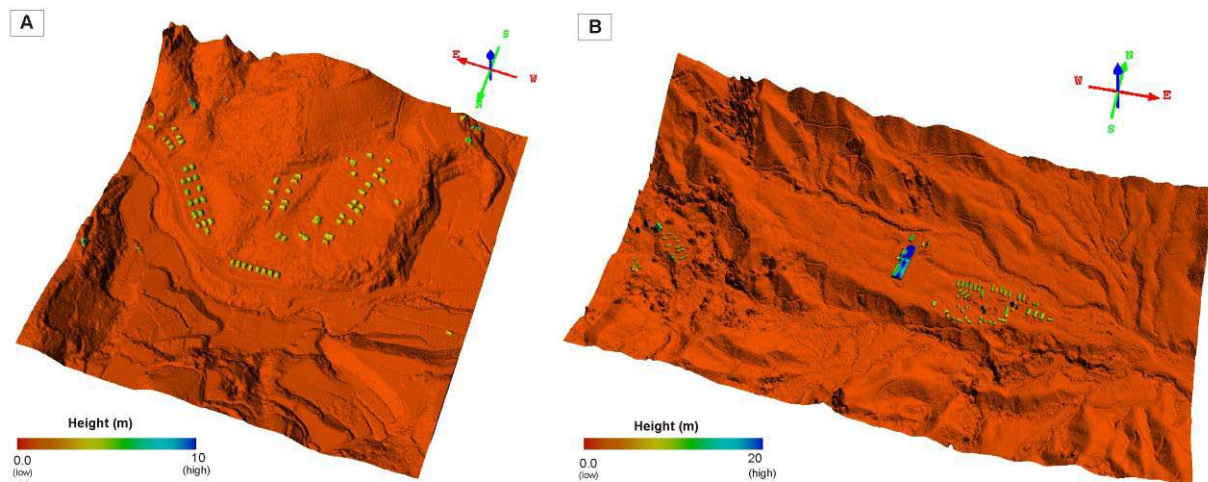


Figure 16: Locations and heights of buildings in landslide prone areas as extracted from a high-resolution ALS dataset. 88.6% of the buildings were correctly detected and the map includes only 10% false positives [Razak *et al.*, 2011a].

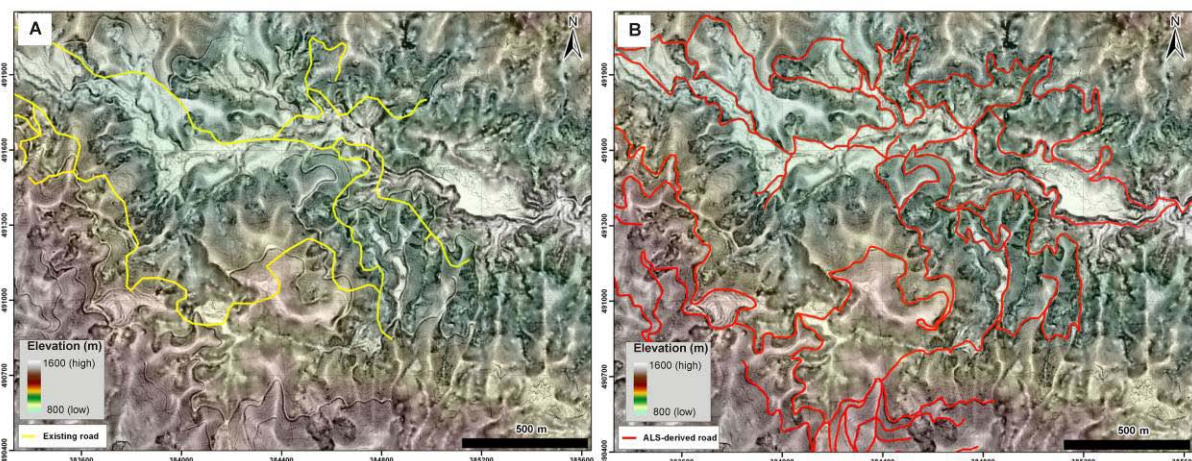


Figure 17: Existing roads (yellow lines in A) and ALS-derived road network (red lines in B) overlaid on the topographic openness with elevation variation [Razak *et al.*, 2011a].

• Data processing

A number of methods to process the above data have already been mentioned. Many are unique to a given data type (to filter buildings from LiDAR data, or to correct geometric distortion in radar imagery). However, it was already mentioned that traditional image processing was largely based on pixel-based methods, i.e. where each square-shaped pixel would contain one or more data values (one for each spectral band). Processing individual pixels was also computationally efficient. However, with increasing image resolution, better availability of auxiliary spatial information (other thematic layers), and better process and feature knowledge, those methods have become less suitable. For decades there has been research already in texture-based processing (i.e. the consideration of pixel in their context). This has been very useful to identify landslides [Chang *et al.*, 2006], as well as other EaR.

However, comprehensive identification and characterization of landcover and landuse (a plantation vs. a natural tree stand) features, distinction of objects with similar appearance (a road segment vs. a debris flow), and a contextual consideration of all EaR in an areas with respect to each other and present hazards, is better achieved with so-called object-oriented image analysis (OOA).

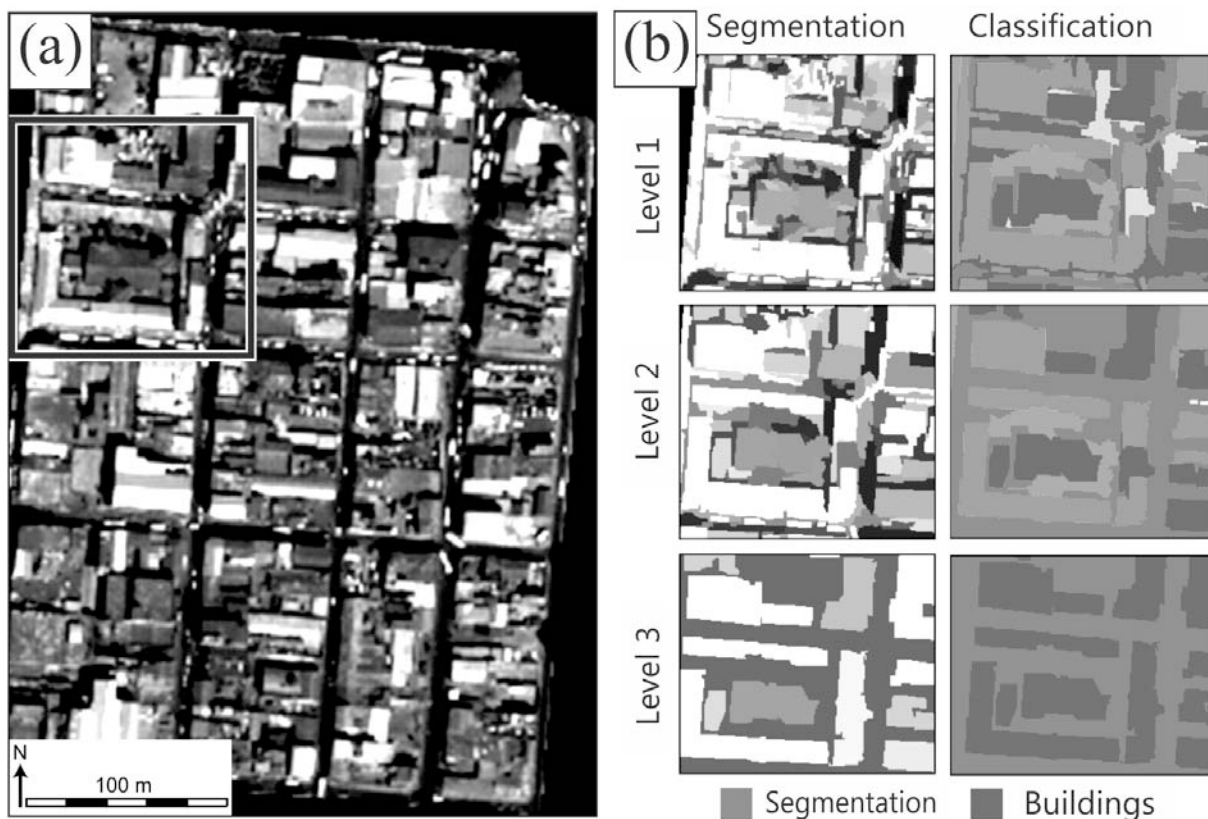


Figure 18: (a) Building footprint extraction for parts of Tegucigalpa, Honduras, and (b) three segmentation and classification levels (close-up area indicated by box in (a)). Small objects, such as cars, are gradually removed in the rule-based classification stage, while at level 3 only whole buildings as semantic groups remain. (Source: Kerle 2011, unpublished material)

OOA is based on the segmentation of any kind of spatial data (i.e. also radar images or digital elevation models) into homogenous units, in terms of variation in values used in a particular data set. In optical images this allows, for example, road sections, building elements or water features to be segmented, while in a DEM areas with little elevation change will result in segments. Those segments, which can be calculated at different spatial scales and which are hierarchically linked, are then classified [Blaschke, 2010]. In this step additional data layers (elevation, thematic datasets) and available feature or process knowledge is used. This allows roads to be separated from debris flows, or artificial from natural water features, or buildings from other urban elements. Not only do the results are more meaningful than in pixel-based analysis (a building is identified as such, instead of a group of unconnected pixel that are spectrally identified as concrete or clay, depending on the roof material). The

resulting objects (Figure 18) also implicitly contain object attributes, such as building size, or possibly type, if the knowledge inserted into the classification process allows such distinction. In landslide hazard assessment OOA has already been used to detect landslides [Martha *et al.*, 2010a], but also EaR detection has benefited. Shamaoma *et al.* [2006] developed an OOA methodology in eCognition software that extracted buildings from a Quickbird image (ca. 1.6 m multispectral resolution) of a complex urban landscape. The same approach was used to identify also different neighborhood types (formal, informal, central business district, etc.). The same dataset, together with LiDAR data, was used by Ebert *et al.* [2009], who used physical proxies (buildings) to extract information on not directly visible EaR (people) and to derive information on their social vulnerability.

OOA is gradually becoming a widely-used tool in risk research, also being applied to radar images [Cruz *et al.*, 2010], LiDAR data [Aubrecht *et al.*, 2009] and scanned thematic maps [Kerle and Leeuw, 2009], which can be a useful source of EaR data. It is a powerful approach to map any kind of EaR that are imaged in a given dataset, or also the not directly visible ones via physical proxies. There are, however, also disadvantages. Currently only one commercial OOA software package, eCognition, exists, with availability not yet being very widespread. Additionally, eCognition operates with so-called process trees, where in programming-fashion a potentially large number of steps is executed, frequently also involving loops. Those steps enter the process or feature knowledge of the analyst into the analysis, and are frequently directly based on the actual image information. This means that most rulesets contain a large number of specific data thresholds and are tailored towards a specific case study. This severely limits their transferability to other areas or datasets. Additionally, for all segments created by the software a large number (>100) of spectral, geometric and contextual features are automatically created, which are then used in the knowledge-driven classification. Identifying the most useful of those features for a specific landcover class identification is not easy, again limiting ready implementation of existing research results in an operational context. However, research is ongoing on more objective segmentation and deriving thresholds automatically from the image data [Martha *et al.*, in press-a], and on statistics-based identification of optimal feature [Stumpf and Kerle, in press].

4.3. REMOTE-SENSING DERIVED DATA FOR MODEL ASSESMENT AND VALIDATION

[UPC]

For the development of an analysis of the landslide risk, it is appropriate to follow several stages which result in different outcomes, usually landslide inventories, susceptibility maps, hazard maps and risk maps at several scales. Staging of the risk analysis may reduce the costs by limiting the most detailed zoning only to areas where is necessary [Fell *et al.*, 2008]. Moving from a stage to the next one requires increasing amount and quality of data, and analytical effort.

In the last two decades, there has been a significant improvement of the techniques for data capture (remote-sensing), of the methodologies for data analysis and treatment, and in the availability of the computational resources. Thanks to these improvements it is nowadays possible to perform the quantitative risk assessment of landslides (QRA). Rapid development of new remote-sensing techniques (as LiDAR and SAR interferometry) and innovation of existing ones (satellite imaging with very high resolution) has multiplied the chance of landslide detection and characterisation over large areas, which has allowed increasing the amount and quality of landslide data (as it has been shown in the previous chapters).

Recent development of remote-sensing is also extending to the modelling of landslides and to the validation of models. Analysis carried out a regional and local scale are typically performed using a statistical approach (particularly for the preparation of susceptibility maps) whilst physically-based models have been mostly used to estimate landslide hazard and risk at site-specific scale.

Validation of models is essential for obtaining reliable predictions. There are a number of potential sources of error in the landslide zoning process. These include, for example, limitations in the landslide inventory upon which the susceptibility and hazard zoning maps are based; model uncertainty, meaning the limitations of the methods used to relate the inventory, topography, geology, geomorphology and triggering events such as rainfall to predicting landslide susceptibility, hazard and risk [Fell *et al.*, 2008].

Model uncertainty is a fact of landslide zoning and none of the methods are particularly accurate [Fell *et al.*, 2008]. Physically-based models are advanced methods which are suitable for site-specific risk assessment. However, the parameter uncertainty is large due to limitations in the knowledge of the stability conditions of the landslide (such as shear strength and pore pressures or boundary conditions) [Fell *et al.*, 2008]. At regional or local scale, the assessment of susceptibility, hazard and risk maps involves a strong empirical component and a looser physical basis. Empirical models require a more rigorous testing of hypothesis, and, indeed, a continuous validation with new observations.

The following lines intend to highlight how remote-sensing techniques can contribute to the assessment and to the validation of landslide models for quantitative risks analysis, both at the regional-local scale and at the site specific scale.

4.3.1. Remote-sensing for the assessment of susceptibility/hazard maps at regional-local scale

The purpose to which the landslide zoning is to be applied, and the funds available, determine the scale of the risk analysis and the type and level of detail of the zoning [Fell *et al.*, 2008]. The lowest level of analysis corresponds to susceptibility zoning, which usually involves developing an inventory of landslides which have occurred in the past together with an assessment of the areas with a potential to experience landsliding in the future [Fell *et al.*, 2008].

As it was mentioned above, recent developments of remote-sensing derived in an improvement on the data capture of landslides. Any improvement on the landslide inventories, including the run out distance and the intensity, should obviously enhance the accuracy of assessment of the landslide susceptibility. Landslide intensity may be expressed either as a displacement (total or differential) or as the velocity (or the kinetic energy) of the moving mass. Detection and characterization of new moving landslides is, however, difficult by using of airborne or spaceborne remote sensors, which are the most suitable at regional or local scales (see Deliverable 4.5).

Quantitative analysis of landslide hazard is only feasible when (where) accurate data on frequency of landslides exists. To obtain landslide frequency a complete record of past landsliding events in the study area is required. Data on landslide occurrence are usually scarce. The most reliable records are those based on direct sources such as landslide inventories gathered by technical units. In many cases, however, the records have to be prepared using indirect sources (by dating landslides). The latter often produces incomplete landslide series that have to be combined with other sources of information, as the frequency of triggers. Where complete temporal series of landslides inventories are available, hazard assessment may not require prior landslide susceptibility analysis [Corominas and Moya, 2008]. Nevertheless, landslide hazard maps are more commonly developed from susceptibility map with the areas classified according to the frequency of landsliding [Fell *et al.*, 2008].

Aerial photographs have been routinely employed for landslide inventories and for mapping new slope failures. Landslide inventories over defined time intervals may be derived from series of consecutive images. These series are particularly suited for the inventory of landslides associated to specific triggering events.

Two sets of consecutive photographs bracket the age of landslides. The frequency of landslides may be calculated by counting the number of new landslides between consecutive sets of images and dividing by the time span separating the sets. This method provides valid estimates of the short term average frequency, though can seldom be used for a mid and long-term because the average frequency may change with time.

An image is a cumulative record of landslide occurrence over an undefined period of time before the image was taken. Thus, when using these data sets one must keep in mind that: (a) depending on the spatial resolution of the images, the smallest landslides may not be detected unless parallel field work is carried out, and (b) the time span is not the same for all the landslide types and sizes [Corominas and Moya, 2008]. On one hand, the deposits of smaller landslides are short-lived and they are easily eroded. Consequently, although several events triggering small-size landslides may have occurred since the occurrence of the largest landslides, they may have been overlooked during the interpretation of images because their deposits have been removed or are not discernible. Due to the censoring produced by the erosion, the observed small-size landslides represent only a small percentage of the original population. On the other hand, the landslide inventory might not reflect the activity in the past

of the existing landslides. The history of landslide reactivation events cannot be inferred from the image interpretation unless the displacement was large.

Satellite optical images of very high resolution and radar images and airborne LiDAR images are being increasingly used for landslide detection. On one hand, spatial resolution has raised significantly with these three techniques. On the other hand, temporal resolution has increased from every few years, which is the typical of aerial photographs, to about a month of satellite SAR images, and to some days in the case high resolution satellite optical images. The spectacular increase of the revisiting time allows reducing the chance of landslide erosion or covering by vegetation, and, hence, allows for a more accurate assessment of the frequency of very recent landslides. In this sense, it is noteworthy that images should be obtained as soon as possible after a major landsliding event [van Westen *et al.*, 2008].

Very high resolution imagery with stereo capabilities and resolution of 3 m or better (QuickBird, IKONOS, CARTOSAT-1, CARTOSAT-2) has become the best option now for landslide mapping from satellite images. However, the high costs may still be a limitation for obtaining these very high resolution images for particular study areas, especially for multiple dates after the occurrence of main triggering events [van Westen *et al.*, 2008].

The increase of amount of images available encourages automatic analysis to detect landslides. Many developments have taken place in the last decade related to methods for the automatic detection of landslides (van Westen *et al.*, 2008). Many methods for landslide mapping make use of digital elevation models of the same area from two different periods. The subtraction of the DEMs allows visualizing where displacement due to landslides has taken place, and the quantification of displacement volumes [Dewitte *et al.*, 2008; Oka, 1988; van Westen and Getahun, 2003]. High resolution data from Quickbird, IKONOS, PRISM (ALOS) and CARTOSAT-1 are able to produce highly accurate digital elevation models that might be useful in automatic detection of large and moderately large landslides.

It must be recognized that landslide zoning is not a precise science and the results are only a prediction of performance of the slopes based on the available data [Fell *et al.*, 2008]. The greatest source of error in landslide susceptibility and hazard maps comes from limitations in the landslide inventory. Van Westen *et al.* [1999] and Ardizzone *et al.* [2002] point out that the greatest errors occur when inventories rely on air photo interpretation, particularly of small scale photography. These errors are in part due to the subjective nature of aerial photo interpretation but also to vegetation covering the areas to be mapped. Aerial photographic mapping should be supported by a surface mapping of selected areas to calibrate the mapping [Fell *et al.*, 2008]. Obviously, surveys should be systematic. By visual interpretation of TerraItaly aerial ortho-photographs and Ikonos satellite images of an area of Umbria (central Italy), Fiorucci *et al.* [in press] obtained 145% more landslides and 85% more landslide area than a pre-existing non-systematic field inventory, made driving and walking along main, secondary and farm roads.

Susceptibility, hazard and risk maps must be validated to be reliable. A rigorous validation implies statistical test of hypothesis and checking of the predicted landslides. Validation should include review of the type, magnitude, intensity, location and occurrence

time of the predicted landslides. Susceptibility and hazard maps usually are carried out for specific types of landslides, in such way that volume and, to a lesser degree, intensity (i.e. susceptibility map of shallow landslides, susceptibility map of deep landslides, hazard map of rockfalls) are implicit in the map, and, therefore, these parameters can be considered as validated implicitly with the map (it seems acceptable at a regional scale of work up to a certain level, particularly for rapid landslides, for which the intensity is the velocity or a derived variable).

For the validation of the location of landslides (spatial validation), the landslide inventory of the study area is randomly split in two samples. One of the samples is the used for the calibration of the model, that is to say for the preparation of the map, and the other is used for the validation. This type of validation is the currently applied for susceptibility maps, which does not include information on landslide frequency.

The validation of hazard maps requires an additional test of the landslide frequency. In this case, the landslides of the two samples of the inventory must correspond to different periods. This type of validation is not as common as the spatial validation, due to the difficulty to obtain enough data on temporal occurrence to calibrate the model, but also to validate it. Some data of landslide occurrence can be incorporated by dating (particularly, using techniques of high temporal resolution, i.e., dendrogeomorphology) [Corominas and Moya, 2008] but it can seldom be applied to many of the landslides existing in a large study area. At this point is where the increased temporal resolution of satellite SAR imaging and satellite very high resolution optical imaging may contribute to hazard validation. Accurate data on occurrence of new landslides (both first-time and reactivations) can be gathered after the hazard map was completed, especially if imaging is obtained soon after major landsliding events, which may include hundreds to thousands of landslides. This approach is really only practical in areas with high frequency of landsliding because of the time frame required to gather performance data [Fell et al., 2008].

Finally, there is a growing knowledge of climate change and the effects of this on rainfall and snowfall regime and on thickness of permafrost. For example, an increase of frequency of heavy rainfalls will probably increase the frequency of shallow landslides and debris flows in susceptible zones. This might also increase the susceptibility of some sites to shallow landsliding triggered by rainfall, this is because susceptibility levels are estimated empirically for a given area, within a given period of time and, consequently, for given climatic conditions. Change of frequency rainfalls triggering landslides due to a climatic change is possible in the future; this means this approach might not be applicable for temporal validation of hazard maps, but also means that remote-sensing monitoring for detection of new landslides is particularly necessary in areas where a change of landslide frequency can be foreseen. In this zones hazard maps should be updated every certain period to avoid underestimation of the risk but also overestimation.

4.3.2. Remote-sensing for the assessment of site-specific physically-based models

Physically-based models of landslides may target to predict displacement rates, timing of final failures or the zones affected by long-distance runout deposition. Dependent on the model complexity typically several physical parameters are needed including in most cases the local geometry and parameters which characterize the material properties. The determination often requires model calibration that involves field work and laboratory work, whereas remote-sensing data is only of secondary importance. Effectively, the soil properties and the slope hydrology, which are capital in physical modelling are also the most difficult to obtain, and remote-sensing has not proven to be a very important tool for these [van Westen *et al.*, 2008]. Not surprisingly, the assessment and validation of these local and physically based models is performed also mainly in the field. However, for example debris flow runout modelling can benefit from remote-sensing derived DTMs with high resolutions [Stolz and Huggel, 2008] and remote-sensing data recorded shortly after the event may help to constrain the areas of the initial failure, runout distances or involved volumes [Scheidl *et al.*, 2008].

Other remote-sensing methods might help in certain cases for the assessment and validation of the models. Usually, the check can be focused in the comparison between displacements (or velocities) predicted by the model and the actual values measured in the field. In this last point, remote-sensing techniques such as DInSAR, GB-InSAR or LiDAR may help, expanding the classical techniques (surveying, GPS, inclinometers, wire extensometers, etc) and among several available studies the few examples are quoted here. The first one is the Vallcebre landslide [Gili, 2011]. In this translational complex slide, it has been demonstrated that the DInSAR gives reliable point movements that should be used as validation. Also the GB-InSAR technique has been applied to the measurement of a set of special corner reflectors spread in the lower part of the hill slope. These displacements can confirm the model that has been build up for Vallcebre [Corominas *et al.*, 2005]. Another case is located in Portalet [Herrera *et al.*, 2009], where terrestrial laser scanning, and GBSAR surveys have been carried out in order to calibrate and validate the forecasting model. The remote-sensing techniques present some clear advantages and some drawbacks that have been highlighted elsewhere. Only to note here that the temporal resolution (revisiting time) must be high enough in order to accurately follow the slide. As quoted before, the SAR techniques are suitable for slow to very slow movements, except if we can install a GB-InSAR continuous setup. The LiDAR and the High Resolution imagery can be used to follow slow movements as well. When the remote-sensing methods are adequate, one general advantage is the wide and almost continuous coverage of the phenomena. More recently *Travelletti et al.* [2011] presented a system based on multi-temporal photographs taken by a fixed terrestrial camera. They used a digital image correlation technique to gain detailed displacement vectors of the Super-Sauze mudslide. Compared to traditional in-situ measurements the technique has the advantage that it enables to reconstruct the movement of the complete surface and provides better base for model calibration and validation than point-wise measurements.

5. DISCUSSION

5.1. UPDATING STRATEGIES OF REMOTE-SENSING PRODUCTS

5.1.1. For event-based landslide inventory mapping

[ITC]

Among (or within) landslide inventories we can typically distinguish three types of information sources, which are (1) event-based inventory mappings associated with a specific triggering event [Gorum *et al.*, in press; Guzzetti *et al.*, 2002; Lee *et al.*, 2008; Malamud *et al.*, 2004], (2) historical (geomorphological) landslide inventories [Korup *et al.*, 2004; Stark and Hovius, 2001; Van Den Eeckhaut *et al.*, 2007], and recently more common (3) frequent updates to determine location and activity status of slow moving landslide that are not necessarily associated with a specific triggering event [Cascini *et al.*, 2009; Cigna *et al.*, 2010; Farina *et al.*, 2006].

Event-based landslide inventory mappings are crucial to understand relationships between triggers and landslides in terms of spatial patterns, intensity and temporal recurrence [Gorum *et al.*, in press; Harp *et al.*, 2010; Keefer, 1984; Rossi *et al.*, 2010b; Witt *et al.*, 2010]. They are generally more complete than paleo-landslide inventories and considered to be more reliable if remote-sensing data acquired immediately after the triggering event has been incorporated in their elaboration [Ardizzone *et al.*, 2007; Fiorucci *et al.*, in press; Galli *et al.*, 2008; Malamud *et al.*, 2004].

Large triggering events typically induce significant surface changes at landslide-affected and non-affected areas leading to a loss of signal coherence and restricting largely the use of interferometry and digital image correlation. Airborne LiDAR has demonstrated considerable added value for landslide mappings in the aftermath of large events [Ardizzone *et al.*, 2007; Joyce *et al.*, 2009; Lu *et al.*, 2011] but is relatively costly to acquire for frequent updates. At present mainly optical remote-sensing, and increasingly VHR satellite images [Fiorucci *et al.*, in press; Gorum *et al.*, in press; Lee *et al.*, 2008], are used for event-based mappings through visual interpretation. Submeter image resolution can be considered as sufficient for the preparation and updating of inventory maps at 1:10.000 and due to the increasing number of operational and scheduled platforms (Rapid Eye, Geoeye-1, Pleiades) imagery can be acquired quickly after any given event. Especially for rainfall induced landslides cloud cover is still a limiting factor in many cases (Figure 19). In the European context the performance of optical image acquisition can be optimized using weather forecast information on cloud cover, and for the Pleiades mission it has been considered to further implement an onboard system which reacts in near-real time upon the actual observed cloud cover [Beaumont *et al.*, 2011].

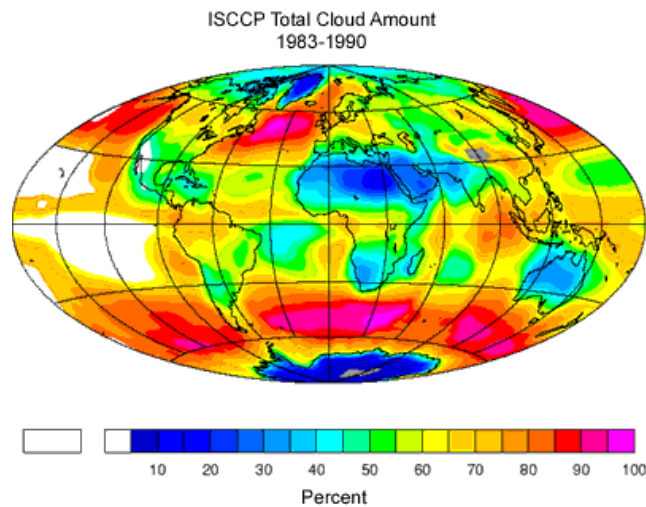


Figure 19: Total fractional cloud cover annual averaged from 1983-1990 according to the database of the International Satellite Cloud Climatology Project (ISCCP).

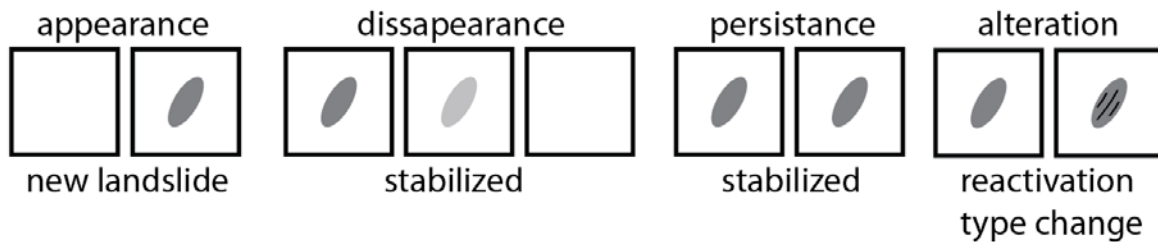
Source: <http://terra.nasa.gov/FactSheets/Clouds/>

Though necessary image material becomes increasingly available its visual interpretation remains generally very time-consuming and is far from optimal for operational updating over large areas [comp. *Ardizzone et al.*, 2007; *Galli et al.*, 2008]. A number of recent studies on semi-automated image analysis and change detection methods have already focused on the development of more efficient ways for the creation of event-based landslide inventories [*Di et al.*, 2010; *Lu et al.*, 2011; *Martha et al.*, 2010a; *Martha et al.*, in press-b; *Mondini et al.*, 2011; *Stumpf and Kerle*, accepted; *Yang and Chen*, 2010]. Though change detection methods consider implicitly the pre-event distribution of landslides, to the best of our knowledge none of those studies incorporated explicitly pre-existing landslide inventories in the analysis. For the semi-automated updating of inventories with interferometry a concept has already been laid out and tested [*Cigna et al.*, 2010] but it is only partially applicable for event-based updates from optical data.

Among other parameters inventories should ideally comprise information on the areal extent of each landslide and polygon-based representations of individual landslides are commonly used in European countries (see D. 2.3 for further details). The representation and updating of landslides as objects has a common ground with the concepts and issues encountered for the object-based updating of land cover information [*McDermid et al.*, 2008]. The remainder of this section highlights some current issues and challenges for a conceptual framework toward a consistent fusion of pre-existing inventories and post-event information.

Fig. 15 shows abstract types of change that can be encountered in event-based mappings, whereas pre-event information may arise from an earlier acquired image or a pre-existing inventory. For event-based mappings we are particularly interested in newly triggered landslides and reactivations, which may manifest as the appearance, expansion and deformation, and alterations at the surface of a defined object (a landslide).

a, existence / state



b, size and shape

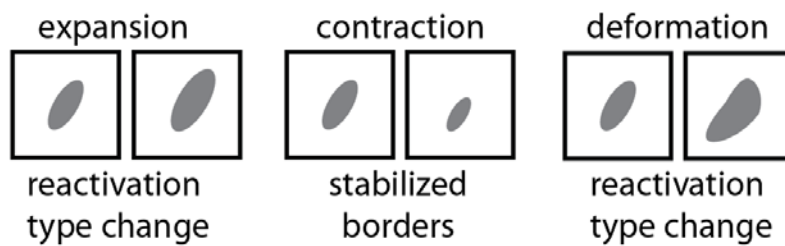


Figure 20: Abstract types of two-dimensional object changes and typical significance in the context of event-based landslide mapping. In reality the abstract types may often overlap or occur in parallel at different parts of a landslide.

Blaschke [2004] also suggested to incorporate dislocation of objects as a general type of change. Though, the displacement of mass is inherent to slope failures, a landslide as a whole does generally not completely change its location and hence we leave this unconsidered here.

Appearance, disappearance or persistence (Figure 20) are the typical types of changes which are addressed in most of the proposed change detection by analyzing changes in the spectral values of individual pixels or objects [*Hazel*, 2001; *Radke et al.*, 2005].

Surface alterations in terms of displacement can be measured with interferometry, multi-temporal airborne LiDAR or and photogrammetry but - for abovementioned reasons - they are of limited applicability for event-based updates. In this context it is interesting to note that multi-temporal VHR optical images contain a significant amount of information about textural changes as indicators of recent activities. Such changes in the surface texture can generally be exploited well by an image interpreter even if color information remains similar (Figure 16). The complementary integration into automated change detection has been previously suggested [*Li and Leung*, 2002] but has been explored relatively little in the context of remote-sensing [*Bovolo*, 2009; *Lefebvre et al.*, 2008].

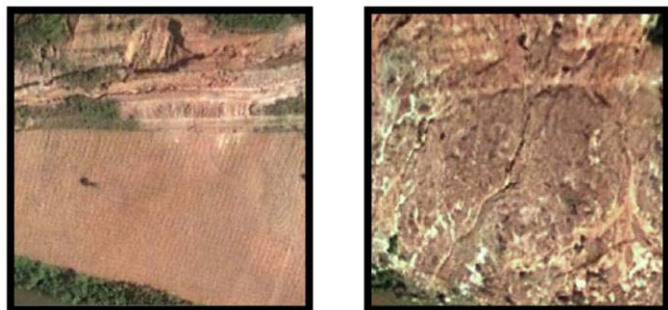


Figure 21: Example for changes in surface texture indicating the occurrence of a landslide while the color information remains very similar.

There is still, however, a general difficulty to reliably define and extract individual slope failures with remote-sensing aided event-based mappings. A common issue is for example the convergence of landslide along their travel path (Figure 1, 2). In many cases it might still be possible to estimate the number of individual source areas, whereas the attribution of an area to each source poses serious conceptual problems. At present there is no common agreement if the magnitude of a landslide event is better expressed in terms of number, area or volume of the landslides. Via an empirical relationship *Guzzetti et al.*, [2009] derived volumes from the landslide area and used this measure to indicate the event-magnitude, whereas other researchers preferred the use of the number of landslides [*Malamud et al.*, 2004]. Similarly for susceptibility models the landslide density is often introduced in terms of number of landslide per unit [*Guzzetti et al.*, 2006; *Van Den Eeckhaut et al.*, 2009], whereas the relative area per spatial unit appears to be an at least equally well suited descriptor [*Lee et al.*, 2008]. Recently it has been suggested that for co-seismic landslides, the area density shows better correlation with the trigger than the landslide number, and that the landslide number in fact contains less information than the affected area [*Meunier et al.*, 2011]. For the derivation of magnitude-frequency curves it remains essential to obtain reliable estimates of landslide numbers and object-oriented methods have shown their potential to extract meaningful quantities from VHR images [*Barlow et al.*, 2006; *Lu et al.*, 2011; *Martha et al.*, 2010a]. The success of such methods still depends to a large degree on the appropriate parameterization according to the image type and the respective study areas. In situations where the task of remote-sensing is mainly the detection of affected areas more generic sample-based approaches can be employed [*Mondini et al.*, 2011; *Stumpf and Kerle*, accepted].

5.1.2. For long-term landslide monitoring at hot spot areas

[UNIFI]

Monitoring means the comparison of landslide conditions like areal extent, speed of movement, surface topography, soil humidity from different periods in order to assess landslide activity [*Mantovani et al.*, 1996]. The measurement of superficial displacements induced by a slope movement often represents the most effective method for defining its behavior, allowing the observation of response to triggering factors and the assessment of effectiveness of corrective measures [*Farina et al.*, 2006].

Different techniques are available for measurements of the ground displacements, starting from the traditional inclinometers, extensometers, topographic surveys, until more recent applications such as GPS, aerial photogrammetry, LiDAR measurements [*Angeli et al.*, 2000; *Gili et al.*, 2000; *Kääb and Vollmer*, 2000; *Malet et al.*, 2002; *McKean and Roering*, 2004].

Remote-sensing images represent a powerful tool to measure landslide displacement as they offer a synoptic view that can be repeated at different time intervals and available at various scales. In *Delacourt et al.* [2007] a DInSAR technique and optical correlation method

for displacement measurements are described. Interferometric SAR is the techniques most researched during the last decade for slope motion monitoring [Metternicht *et al.*, 2005].

The monitoring of landslides by means of optical imagery can be performed correlating optical data. This methodology has been used to measure displacements not only for landslides [Casson *et al.*, 2005; Delacourt *et al.*, 2004] but also for earthquakes [Van Puymbroeck *et al.*, 2000] and glacier flow [Berthier *et al.*, 2005; Käüb, 2002; 2005; Scambos *et al.*, 1992].

The correlated images have to share a common (ground or image) geometry which is obtained either by orthorectifying both images (the correlation is performed in the ground geometry) or by resampling a secondary image in the geometry of a reference image (correlation performed in the image geometry) and the availability of a DEM with high accuracy is mandatory and the measured shift in the two optical images is linked to the ground displacement by the pixel size [Delacourt *et al.*, 2007].

Application of the image correlation technique can be found in in Delacourt *et al.* [2004] which propose to use aerial photographs and Quickbird imagery to monitor landslide displacements. In particular in Delacourt *et al.* [2004] a very interesting technique based on optical correlation of aerial photographs (for time baselines that require imagery previous to the launch of the Quickbird satellite) and Quickbird imagery is presented. In Hervas *et al.* [2003] an image-processing method to map and monitor landslide activity using multitemporal optical imagery has been proposed. Basically this approach proposes the use of very high resolution images (e.g., Ikonos or Quickbird type) acquired at different dates. The method consists on image orthorectification, relative radiometric normalisation, change detection using image difference, thresholding and spatial filtering to eliminate pixel clusters that could correspond to man-made land use changes. In Yamaguchi *et al.* [2003] SPOT imagery have been used to detect the rate of movement of an active slow landslide located in Itaya area in Northern Japan.

Main limitation on the use of optical satellite images in landslides monitoring rely on the atmospheric effects, meteorological condition, sun illumination and orbital parameters; moreover the availability of archived VHR acquisitions is very limited and the temporal resolution is not always suitable as it around 20 days and only in specific conditions it can be reduced to few days on demand, moreover the different solar conditions of the two acquisitions and on the variation of surface state due to vegetation growth and anthropic modifications can invalidate the results.

Both Differential SAR intererferomtry (DInSAR) and multi interferograms SAR Interferometry (A-DInSAR) such as PS [Ferretti *et al.*, 2001] can be used for landslide monitoring. Rott [2004], Paganini [2004] and Singhroy [2002] summarize the potentials and opportunities of space-borne SAR sensors for monitoring slope instability as follows:

- a) detailed motion maps produced from C-band, whether using techniques such as PSI (Persistent Scatterers Interferometry), DInSAR or InSAR, can assist in more accurate slope stability studies. When the conditions are favourable (e.g., coherence, imaging

- geometry) C-band SAR interferometry is a useful tool for mapping and monitoring mass movements;
- b) if SAR time series are available, accurate analysis of displacement is possible using PSI technique. Successful mapping of continuous slow landslide movements has been achieved using multi-temporal DInSAR techniques. Movements of -5 to 5 mm/year have been detected;
 - c) the access to archived SAR data (e.g., in excess of 10 years) is useful to study temporal variations of motion that enable assessing slope stability, complementary to other information;
 - d) future SAR systems with higher spatial resolution (e.g., Radarsat-2, TerraSat-X, COSMO-SkyMed) will enable the mapping of smaller slides. With the PSI technique, the movement of small objects (e.g., down to about one square meter) can be monitored.

Though it looks promising as a technique for monitoring landslides, the characteristics of the currently operational satellites put strong constraints on the use of DInSAR as a monitoring instrument. In particular the spatial resolution of the SAR images, the time-interval between the successive passages of satellites and the wavelength of the radiation are unsuitable for a systematic monitoring of relatively rapid movements, concentrated in small areas and on steep slopes or narrow valleys [Reñice *et al.*, 2001; Rott *et al.*, 2000]. Quantitative information on landslide activity can be obtained in the case of extremely slow movements (velocity less than a few centimeters per month), affecting large areas with sparse vegetation [Fruneau *et al.*, 1996; Kimura and Yamaguchi, 2000; Rizzo and Tesauro, 2000; Rott and Siegel, 1999].

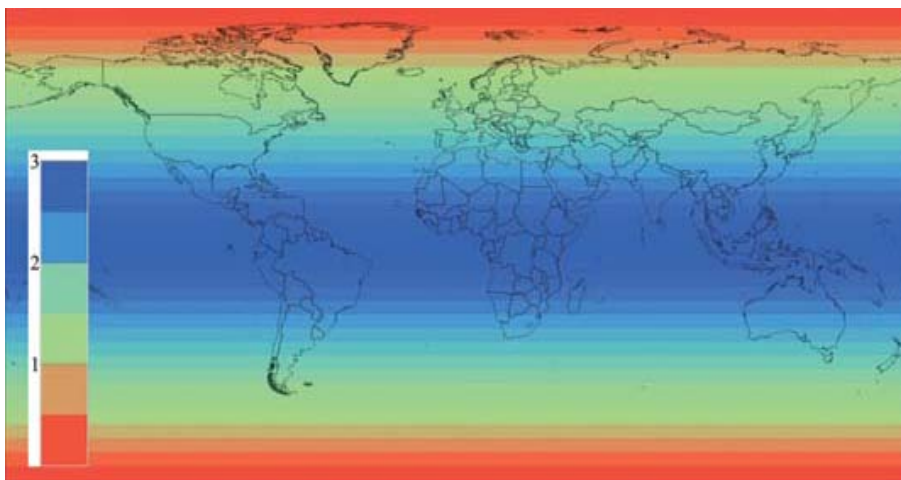


Figure 23: Average revisit time (in days) across the world for the Sentinel-1 constellation: Two satellites in 12-day repeat orbits with 250 km swath widths. The blue around the equator reflects the 3-day revisit period, improving towards the poles. Source: esa bulletin 131 - august 2007

The temporal scale is controlled by the time interval between the successive acquisitions. The passage rate of the present satellites over the same area range between 11 days for TerraSAR-X, 24 days for RADARSAT and 35 days for ENVISAT. Recently launched SAR missions such as the Japanese ALOS, the German TerraSAR-X or the Italian

COSMO-SkyMed program, seem to meet the operational requirements for an effective and systematic monitoring of slope movements. Furthermore, within ESAs GMES Sentinel program the launch of the first of two SAR satellite is scheduled for 2013. This should ensure the continuity of C-band SAR observation from ERS-1, ERS-2, Envisat and Radarsat and up to daily revisit intervals (Figure 23). The complete database will be available free online and may provide an inexpensive alternative for many long-term monitoring tasks.

An extensive body of studies documents the use of DInSAR and PS-InSAR for landslide monitoring [Berardino *et al.*, 2003; Colesanti *et al.*, 2003; Farina *et al.*, 2006; Meisina *et al.*, 2007; Singhroy and Molch, 2004; Strozzi *et al.*, 2005] and in many cases the A-DInSAR data have been integrated with in-situ monitoring instrumentation (Pancioli [Farina *et al.*, 2006; Pancioli *et al.*, 2008]. The joint use of satellite and ground-based data assists the geological interpretation of the landslide and allow the better understanding of landslide geometry and kinematics.

5.1.3. For hazard and risk assessment

[UPC]

As quoted in section 4.3.1, the empirical models require a more rigorous testing of hypothesis, and, indeed, a continuous validation with new observations. This will make the models more robust, and permits to follow the temporal evolution of the risk. On the other hand, when the remote-sensing methods are suitable for a given model assessment, it is mandatory to obtain the new images as soon as possible after a new critical situation has occurred. In this sense, the development or adaptation of some sensors to airborne platforms would permit to fly over a given area short after the landsliding event. For the long term assessment of detailed zones with SAR techniques, the installation of corner reflectors should be considered. A more detailed analysis of these strategies and the current restrictions on the use of remote-sensing data is provided in the deliverable D4.5.

5.2. REINFORCING THE LINKS BETWEEN QRA AND REMOTE SENSING

Remote-sensing has already become an indispensable source to create and update landslide inventory and deformation maps, and especially on regional scale provides valuable inputs for hazards and risk assessment. A multitude of studies has focused on the validation of remotely sensed inventory and displacement maps against manual image interpretation and field surveys. As a general conclusion it can be stated that remote-sensing techniques complement and enhance existing maps and typically yield higher mapping accuracies and coverage than could be achieved with field work and in-situ measurements alone. However, to which degree the enhanced map products affect the outcome of hazard and risk assessments

remains to be investigated in a systematic manner and could not be addressed in the work package so far.

When using remotely sensed inventory and displacement information as an input for QRA it is important to understand the potential spatial and/or temporal biases that each sensor technology comprises. This includes issues such as the occlusion of particular terrain parts, lower detection rate with certain land cover types or thresholds on terrain parameters used in the detection workflow. Technological limitations can be partially compensated using multiple complementary sensor systems for the same area, or by adjusting the risk assessment strategy according to the known biases of the mapping methods. For a general overview of the potential uncertainties in input datasets we also wish to refer to chapter 2 of the SafeLand Deliverable D2.8 (Recommended Procedures for Validating Landslide Hazard and Risk Models and Maps) and to fact sheets in SafeLand Deliverable D4.4 that summarizes the advantages and limitations of the available techniques.

To enable an informed use of remote-sensing based maps it is generally desirable to provide remote-sensing products together with uncertainty estimates to the potential users. Information about the spatio-temporal coverage and accuracy of inventory and deformation maps may be expressed in additional visibility maps (Cascini et al. 2009), standard errors of the measurements or similar uncertainty measures. Evidence from multiple sensors and/or image classification techniques can also be combined and yield probability maps instead of binary inventories. In this context it might be interesting to test if a seamless integration of such probability maps in QRA is feasible and useful.

As deformation maps and inventory maps become available at increasing temporal resolution the question arises at which frequencies hazard and risk assessment should be repeated and how an optimal repetition rate can be determined in the regional context. Space-borne derived deformation maps are at present mainly used to complement existing inventories and to better understand the ongoing processes in active landslides. In hot-spot areas where the landslide associated risks justify continuously repeated acquisitions of new microwave and optical images available time-series can be extended. Frequent image acquisition campaigns, however, should be accompanied by the installation of operational systems that implement data analysis techniques such as described in this document largely automated. Resulting frequently updated map products can then be used for QRA as an intermediate tool between static maps and early warning systems.

Vice versa the quantitative outputs of hazard and risk assessment should guide the elaboration of observational campaigns. From socio-economic standpoint considering short- and medium term developments the observations should certainly be focused on areas where landslide related risks are highest (see in this context D2.10 Identification of landslide hazard and risk "hotspots" in Europe). However, also low risk areas (i.e. areas with low socio-economic values) should be considered in the planning of satellite missions and flights campaigns to support further investigations toward a better process understanding and hold information available for areas that are relevant for environmental protection and long-term socio-economic activities.

Concerning the updating frequencies of the data input for QRA chapter 5 in D2.4 (Guidelines for landslide susceptibility, hazard and risk assessment and zoning) provides a general overview desirable updating intervals for regional assessments. In general it must be noted that more dynamic factors and/or more dynamic environmental conditions require also higher observation frequencies.

6. CONCLUSION

[ALL]

This deliverable provides a comprehensive view on the latest developments of remote-sensing technologies as applied for the creation and updating of landslide inventory and deformation maps by the members of the SafeLand workpackage 4.2. Furthermore, chapter 4 gives a broad overview of input datasets for hazard and risk assessment that can be obtained through remote sensing, and in chapter 5 suitable updating strategies as well as steps toward a better linkage between the recent technological developments and QRA methods are discussed.

Considering the increasingly large fleet of remote-sensing satellites operated by space agencies and private companies, and the increasing widespread of aerial and terrestrial sensors at constantly decreasing costs, the remote-sensing of landslides and risk related information encounters generally favourable data availability. One exception is currently the segment of L-band spaceborne SAR that has been demonstrated as a valuable tool for the monitoring surfaces that induce a loss of coherence with C- and X-band techniques [Strozzi *et al.*, 2005]. With the failure of the ALOS satellite earlier this year no L-band satellite is currently operational and the launch of ALOS 2 with similar capabilities will take place in 2013 earliest. Meanwhile more frequent observations of constellations of C-band and X-band satellites may be able to fill this gap.

It is expected that LiDAR sensors will become a standard tool for landslide investigations, and if the current trend persists most of the industrialized countries will obtain full coverage aerial LiDAR DEMs within the next 10 years. While it can be expected that remaining computational issues arising from large point cloud analyses will be solved as computational time becomes cheaper, but many conceptual questions on the integration of HRDEMs in hazard and risk assessment remain [Jaboyedoff *et al.*, 2010].

A full exploitation of the daily recorded images will not only depend on the implementation of operational processing systems but also on an easy data access and exchange via European and international networks such as GMES and GEOSS. The International Charter on Space and Major Disasters has already demonstrated the advantages of a more liberal data exchange in the aftermath of major disasters. Analogous initiatives to open data archives including comprehensive time-series to a broader group of potential users appear desirable. Similarly to issues concerning easy data access, the availability of high quality software tools for the extraction of the required information is of at least equal importance. Besides proprietary software and in-house algorithms of private companies, many of such tools are also freely available on the web. This includes software for SAR interferometry (ROI_PAC), open source projects with general GIS and raster processing capabilities (ILWIS). One of the most remarkable examples is probably the ORFEO (Optical and Radar Federated Earth Observation) toolbox which includes wide range of state of the art image processing tools and sensor specifications.

Major challenges for the further development of analysis methods are the intergration of multi-modal and multi-temporal remote-sensing datasets with existing inventory databases and in situ measurements. The four case studies in chapter 3.4.2 specifically address the combined use of data from different platforms and sensor types and further studies in this direction would most certainly benefit from the complemenatry information recorded by different sensor technologies. Modern spaceborne DInSAR techniques and many terrestrial techniques already rely on the analysis of longer time series, whereas only recently optical satellite images become more frequently used for the assesment of long-term landscape dynamics in landslide affected areas [Chuang *et al.*, 2011; Lin *et al.*, 2010a; Lin *et al.*, 2010b; Liu *et al.*, 2010]. Constantly growing image archives also lead to an increased research interest in algorithms for the systematic mining of satellite image time series and spatio-temporal clustering [Petitjean *et al.*, 2010].

Finally it should also be mentioned that the great success of collaborative mapping projects such OpenStreetMap has raised a broad public and academic interest in the application of crowd-sourcing for many applications such as the monitoring of transportation networks, the collection of information during disaster response phases or conflict management [Goodchild, 2010; Heinzelman *et al.*, 2011; Heipke, 2010]. Examples for the application of such community based platforms during landslide disaster already start to appear on the internet (<http://www.gawana.com/peru/ushahidi/>). They should be explored as they could yield a valuable information source that may complement “traditional” remote-sensing techniques.

REFERENCES

- Abella, E. C., and C. J. van Westen (2008), Spatial landslide risk assessment in Guantanamo province, Cuba, in *Landslides and Engineered Slopes: From the Past to the Future, Vols 1 and 2*, edited by Z. Chen, J. M. Zhang, Z. K. Li, F. Q. Wu and K. Ho, pp. 1879-1885.
- Abellán, A., J. M. Vilaplana, and J. Martínez (2006), Application of a long-range Terrestrial Laser Scanner to a detailed rockfall study at Vall de Núria (Eastern Pyrenees, Spain), *Engineering Geology*, 88(3-4), 136-148.
- Abellán, A., M. Jaboyedoff, T. Oppikofer, and J. M. Vilaplana (2009), Detection of millimetric deformation using a terrestrial laser scanner: experiment and application to a rockfall event, *Nat. Hazards Earth Syst. Sci.*, 9(2), 365-372.
- Abellán, A., J. Calvet, J. M. Vilaplana, and J. Blanchard (2010), Detection and spatial prediction of rockfalls by means of terrestrial laser scanner monitoring, *Geomorphology*, 119(3-4), 162-171.
- Akçay, H. G., and S. Aksoy (2008), Automatic detection of geospatial objects using multiple hierarchical segmentations, *IEEE Transactions on Geoscience and Remote Sensing*, 46(7), 2097-2111.
- Aleotti, P., and R. Chowdhury (1999), Landslide hazard assessment: summary review and new perspectives, *Bulletin of Engineering Geology and the Environment*, 58(1), 21-44.
- Anders, N. S., A. C. Seijmonsbergen, and W. Bouten (2009), Multi-scale and object-oriented image analysis of high-resolution LiDAR data for geomorphological mapping in Alpine mountains., in *Geomorphometry* edited, Zurich, Switzerland.
- Anderson, K., and H. Croft (2009), Remote-sensing of soil surface properties, *Progress in Physical Geography*, 33(4), 457-473.
- Angeli, M.-G., A. Pasuto, and S. Silvano (2000), A critical review of landslide monitoring experiences, *Engineering Geology*, 55(3), 133-147.
- Ardizzone, F., M. Cardinali, A. Carrara, F. Guzzetti, and P. Reichenbach (2002), Impact of mapping errors on the reliability of landslide hazard maps, *Nat. Hazards Earth Syst. Sci.*, 2(1/2), 3-14.
- Ardizzone, F., M. Cardinali, M. Galli, F. Guzzetti, and P. Reichenbach (2007), Identification and mapping of recent rainfall-induced landslides using elevation data collected by airborne Lidar, *Nat. Hazards Earth Syst. Sci.*, 7(6), 637-650.
- Arnhardt, C., T. M. Fernandez-Steeger, and R. Azzam (2010), Sensor Fusion of Position- and Micro-Sensors (MEMS) integrated in a Wireless Sensor Network for movement detection in landslide areas., in *General Assembly of the European Geosciences Union*, edited, Geophysical Research Abstracts, Vienna, Austria.
- ASTER-GDEM-VALIDATION-TEAM (2009), ASTER Global DEM Validation Summary ReportRep., 28 pp, METI/ERSDAC, NASA/LPDAAC, USGS/EROS.
- Aubrecht, C., K. Steinnocher, M. Hollaus, and W. Wagner (2009), Integrating earth observation and GIScience for high resolution spatial and functional modeling of urban land use, *Computers, Environment and Urban Systems*, 33(1), 15-25.
- Baldi, P., N. Cenni, M. Fabris, and A. Zanutta (2008), Kinematics of a landslide derived from archival photogrammetry and GPS data, *Geomorphology*, 102(3-4), 435-444.
- Baldo, M., C. Bicocchi, U. Chiochini, D. Giordan, and G. Lollino (2009), LIDAR monitoring of mass wasting processes: The Radicofani landslide, Province of Siena, Central Italy, *Geomorphology*, 105(3-4), 193-201.

- Barlow, J., Y. Martin, and S. E. Franklin (2003), Detecting translational landslide scars using segmentation of Landsat ETM+ and DEM data in the northern Cascade Mountains, British Columbia, *Canadian Journal of Remote Sensing*, 29(4), 510–517.
- Barlow, J., S. Franklin, and Y. Martin (2006), High spatial resolution satellite imagery, DEM derivatives, and image segmentation for the detection of mass wasting processes, *Photogrammetric Engineering and Remote Sensing*, 72(6), 687-692.
- Beaumont, G., G. Verfaillie, and M.-C. Charneau (2011), FEASIBILITY OF AUTONOMOUS DECISION MAKING ON BOARD AN AGILE EARTH-OBSERVING SATELLITE, *Computational Intelligence*, 27(1), 123-139.
- Berardino, P., M. Costantini, G. Franceschetti, A. Iodice, L. Pietranera, and V. Rizzo (2003), Use of differential SAR interferometry in monitoring and modelling large slope instability at Maratea (Basilicata, Italy), *Engineering Geology*, 68(1-2), 31-51.
- Berthier, E., H. Vadon, D. Baratoux, Y. Arnaud, C. Vincent, K. L. Feigl, F. Rémy, and B. Legrézy (2005), Surface motion of mountain glaciers derived from satellite optical imagery, *Remote-sensing of Environment*, 95(1), 14-28.
- Besl, P., and N. McKay (1992), A method for registration of 3-D shapes, *IEEE Trans Pattern Anal Mach Intell*, 14, 239–256.
- Bevis, M., S. Businger, T. A. Herring, C. Rocken, R. A. Anthes, and R. H. Ware (1992), GPS Meteorology: Remote-sensing of Atmospheric Water Vapor Using the Global Positioning System, *J. Geophys. Res.*, 97(D14), 15787-15801.
- Bisson, M., M. Favalli, A. Fornaciai, F. Mazzarini, I. Isola, G. Zanchetta, and M. T. Pareschi (2005), A rapid method to assess fire-related debris flow hazard in the Mediterranean region: An example from Sicily (southern Italy), *International Journal of Applied Earth Observation and Geoinformation*, 7(3), 217-231.
- Bitelli, G., M. Dubbini, and A. Zanutta (2004), Terrestrial Laser Scanning and Digital Photogrammetry techniques to monitor landslide bodies, in *ISPRS*, edited, Istanbul.
- Blair, J. B., D. L. Rabine, and M. A. Hofton (1999), The Laser Vegetation Imaging Sensor: a medium-altitude, digitisation-only, airborne laser altimeter for mapping vegetation and topography, *ISPRS Journal of Photogrammetry and Remote Sensing*, 54(2-3), 115-122.
- Blaschke, T. (2004), Towards a framework for change detection based on image objects., in *Göttinger Geographische Abhandlungen*, edited by S. Erasmi, B. Cyffka and M. Kappas, pp. 1-9.
- Blaschke, T. (2010), Object based image analysis for remote sensing, *ISPRS Journal of Photogrammetry and Remote Sensing*, 65(1), 2-16.
- Booth, A. M., J. J. Roering, and J. T. Perron (2009), Automated landslide mapping using spectral analysis and high-resolution topographic data: Puget Sound lowlands, Washington, and Portland Hills, Oregon, *Geomorphology*, 109(3-4), 132-147.
- Borghuis, A. M., K. Chang, and H. Y. Lee (2007), Comparison between automated and manual mapping of typhoon-triggered landslides from SPOT-5 imagery, *International Journal of Remote Sensing*, 28, 1843–1856.
- Bovolo, F. (2009), A Multilevel Parcel-Based Approach to Change Detection in Very High Resolution Multitemporal Images, *IEEE Geoscience and Remote-sensing Letters*, 6(1), 33-37.
- Bovolo, F., L. Bruzzone, S. Member, and S. Marchesi (2009), Analysis and Adaptive Estimation of the Registration Noise Distribution in Multitemporal VHR Images, *IEEE Trans. Geosci. Remote Sens.*, 47(8).

- Brardinoni, F., O. Slaymaker, and M. A. Hassan (2003), Landslide inventory in a rugged forested watershed: a comparison between air-photo and field survey data, *Geomorphology*, 54(3-4), 179-196.
- Breiman, L. (2001), Random Forests, *Machine Learning*, 45(1), 5-32.
- Brenning, A. (2009), Benchmarking classifiers to optimally integrate terrain analysis and multispectral remote-sensing in automatic rock glacier detection, *Remote-sensing of Environment*, 113 239–247.
- Brideau, M.-A., D. Stead, and R. Couture (2006), Structural and engineering geology of the East Gate Landslide, Purcell Mountains, British Columbia, Canada, *Engineering Geology*, 84(3-4), 183-206.
- Brückl, E., and J. Brückl (2006), Geophysical models of the Lesachriegel and Gradenbach deep-seated mass-movements (Schober range, Austria), *Engineering Geology*, 83(1-3), 254-272.
- Burgmann, R., G. Hilley, A. Ferretti, and F. Novali (2006), Resolving vertical tectonics in the San Francisco Bay Area from permanent scatterer InSAR and GPS analysis, *Geology*, 34(3), 221-224.
- Burns, W. J., J. A. Coe, B. S. Kaya, and L. Ma (2010), Analysis of Elevation Changes Detected from Multi-Temporal LiDAR Surveys in Forested Landslide Terrain in Western Oregon, *Environmental Engineering Geoscience*, 16(4), 315-341.
- Caine, N. (1980), The Rainfall Intensity: Duration Control of Shallow Landslides and Debris Flows, *Geografiska Annaler. Series A, Physical Geography*, 62(1/2), 23-27.
- Campbell, J. B. (2009), Remote-sensing of soils, in *The SAGE handbook of remote sensing*, edited by G. M. Foody, T. A. Warner and M. D. Nellis, pp. 341-353, SAGE, London, UK.
- Canuti, P., N. Casagli, L. Ermini, R. Fanti, and P. Farina (2004), Landslide activity as a geoinicator in Italy: Significance and new perspectives from remote sensing., *Environmental Geology*, 45(7), 907-919.
- Carnec, C., D. Massonnet, and C. King (1996), Two examples of the use of SAR interferometry on displacement fields of small spatial extent, *Geophys. Res. Lett.*, 23(24), 3579-3582.
- Casagli, N., F. Catani, C. Del Ventisette, and G. Luzi (2010), Monitoring, prediction, and early warning using ground-based radar interferometry, *Landslides*, 7(3), 291-301.
- Casagli, N., L. Guerri, G. Righini, A. Ferretti, D. Colombo, and C. Prati (2005), Integrated use of PS and very high resolution optical images for supporting landslide risk management., in *Symposium on Microwave Remote-sensing of the Earth, Oceans, Ice and Atmosphere*, edited, Ispra, Italy.
- Cascini, L., G. Fornaro, and D. Peduto (2009), Analysis at medium scale of low-resolution DInSAR data in slow-moving landslide-affected areas, *ISPRS Journal of Photogrammetry and Remote Sensing*, 64(6), 598-611.
- Cascini, L., G. Fornaro, and D. Peduto (2010), Advanced low- and full-resolution DInSAR map generation for slow-moving landslide analysis at different scales, *Engineering Geology*, 112(1-4), 29-42.
- Cascini, L., C. Bonnard, J. Corominas, R. Jibson, and J. Montero-Olarte (2005), Landslide hazard and risk zoning for urban planning and development. State of the Art Report (SOA7). paper presented at International Conference on “Landslide Risk Management”, Taylor and Francis, London, Vancouver / Canada.

- Cascini, L., S. Ferlisi, D. Peduto, G. Pisciotta, D. N. S., and F. G. (2008), Multitemporal DInSAR data and damages to facilities as indicators for the activity of slow-moving landslides., in *10th International Symposium on Landslides and Engineered Slopes. Landslides and Engineered Slopes. From the Past to the Future*, edited by Z. Chen, J. Zhang, Z. Li, F. Wu and K. Ho, pp. 1103-1109, Taylor and Francis Group, London, Xian, China.
- Casson, B., C. Delacourt, and P. Allemand (2005), Contribution of multi-temporal remote-sensing images to characterize landslide slip surface. Application to the La Clapière landslide (France), *Nat. Hazards Earth Syst. Sci.*, 5(3), 425-437.
- Casson, B., C. Delacourt, D. Baratoux, and P. Allemand (2003), Seventeen years of the "La Clapière" landslide evolution analysed from ortho-rectified aerial photographs, *Engineering Geology*, 68(1-2), 123-139.
- Catani, F., P. Farina, S. Moretti, G. Nico, and T. Strozzi (2005), On the application of SAR interferometry to geomorphological studies: estimation of landform attributes and mass movements, *Geomorphology*, 66(1-4), 119-131.
- Chandler, J. H., and R. Moore (1989), Analytical photogrammetry: a method for monitoring slope instability. , *Quarterly Journal of Engineering Geology and Hydrogeology*, 22, 97-110.
- Chang, K.-t., S.-H. Chiang, and F. Lei (2008), Analysing the Relationship Between Typhoon-Triggered Landslides and Critical Rainfall Conditions, *Earth Surface Processes and Landforms*, 33(8), 1261-1271.
- Chang, K. T., S. A. Wan, and T. C. Lei (2010), Development of a spatial decision support system for monitoring earthquake-induced landslides based on aerial photographs and the finite element method, *International Journal of Applied Earth Observation and Geoinformation*, 12(6), 448-456.
- Chang, L. W., P. F. Hsieh, C. W. Lin, and Ieee (2006), Landslide identification based on FORMOSAT-2 multispectral imagery by wavelet-based texture feature extraction, in *2006 IEEE International Geoscience and Remote-sensing Symposium, Vols 1-8*, edited, pp. 3317-3320.
- Chang, Y.-L., L.-S. Liang, C.-C. Han, J.-P. Fang, W.-Y. Liang, and K.-S. Chen (2007), Multisource Data Fusion for Landslide Classification Using Generalized Positive Boolean Functions, *IEEE Transactions on Geoscience and Remote Sensing*, 45(6), 1697-1708.
- Chen, K. S., M. M. Crawford, P. Gamba, and J. S. Smith (2007), Introduction for the special issue on remote-sensing for major disaster prevention, monitoring, and assessment, *IEEE Transactions on Geoscience and Remote Sensing*, 45(6), 1515-1518.
- Chen, R.-F., K.-J. Chang, J. Angelier, Y.-C. Chan, B. Deffontaines, C.-T. Lee, and M.-L. Lin (2006), Topographical changes revealed by high-resolution airborne LiDAR data: The 1999 Tsaoling landslide induced by the Chi-Chi earthquake, *Engineering Geology*, 88(3-4), 160-172.
- Cheng, K. S., C. Wei, and S. C. Chang (2004), Locating landslides using multi-temporal satellite images, *Advances in Space Research*, 33(3), 296-301.
- Chigira, M., X. Wu, T. Inokuchi, and G. Wang (2010), Landslides induced by the 2008 Wenchuan earthquake, Sichuan, China, *Geomorphology*, 118(3-4), 225-238.
- Chou, T.-Y., M.-L. Yeh, Y.-C. Chen, and Y.-H. Chen (2010), Disaster monitoring and management by the unmanned aerial vehicle technology, in *ISPRS TC VII Symposium – 100 Years ISPRS*, edited by W. W. and B. Székely, p. Part 7B, IAPRS, Vienna, Austria.

- Chow, T. E., and M. E. Hodgson (2009), Effects of lidar post-spacing and DEM resolution to mean slope estimation, *International Journal of Geographical Information Science*, 23(10), 1277 - 1295.
- Chuang, C.-W., C.-Y. Lin, C.-H. Chien, and W.-C. Chou (2011), Application of Markov-chain model for vegetation restoration assessment at landslide areas caused by a catastrophic earthquake in Central Taiwan, *Ecological Modelling*, 222(3), 835-845.
- Cigna, F., S. Bianchini, G. Righini, C. Proietti, and C. N. (2010), Updating landslide inventory maps in mountain areas by means of Persistent Scatterer Interferometry (PSI) and photo-interpretation: Central Calabria (Italy) case study., in *International Conference on Mountain Risks: Bringing Science to Society*, edited by J.-P. Malet, T. Glade and N. Casagli, pp. 3-9, CERGI Editions, Florence, Italy.
- Claessens, L., G. B. M. Heuvelink, J. M. Schoorl, and A. Veldkamp (2005), DEM resolution effects on shallow landslide hazard and soil redistribution modelling., *Earth Surface Processes and Landforms*, 30, 461-477.
- Coe, J. A., P. A. Glancy, and J. W. Whitney (1997), Volumetric analysis and hydrologic characterization of a modern debris flow near Yucca Mountain, Nevada, *Geomorphology*, 20(1-2), 11-28.
- Colesanti, C., and J. Wasowski (2006), Investigating landslides with space-borne Synthetic Aperture Radar (SAR) interferometry, *Engineering Geology*, 88(3-4), 173-199.
- Colesanti, C., A. Ferretti, C. Prati, and F. Rocca (2003), Monitoring landslides and tectonic motions with the Permanent Scatterers Technique, *Engineering Geology*, 68(1), 3-14.
- Corominas, J., and J. Moya (2008), A review of assessing landslide frequency for hazard zoning purposes, *Engineering Geology*, 102(3-4), 193-213.
- Corominas, J., J. Moya, A. Ledesma, A. Lloret, and J. Gili (2005), Prediction of ground displacements and velocities from groundwater level changes at the Vallcebre landslide (Eastern Pyrenees, Spain), *Landslides*, 2(2), 83-96.
- Corominas, J., J. Moya, A. Lloret, J. A. Gili, M. G. Angeli, A. Pasuto, and S. Silvano (2000), Measurement of landslide displacements using a wire extensometer, *Engineering Geology*, 55, 149-166.
- Cotecchia, V. (2006), The Second Hans Cloos Lecture. Experience drawn from the great Ancona landslide of 1982, *Bulletin of Engineering Geology and the Environment*, 65(1), 1-41.
- Crippen, R. E., and R. G. Blom (1991), Measurement of Subresolution Terrain Displacements Using Spot Panchromatic Imagery, paper presented at Geoscience and Remote-sensing Symposium, 1991. IGARSS '91. Remote Sensing: Global Monitoring for Earth Management., International, 3-6 Jun 1991.
- Crosta, G. B., and P. Frattini (2003), Distributed modelling of shallow landslides triggered by intense rainfall, *Nat. Hazards Earth Syst. Sci.*, 3(1/2), 81-93.
- Cruden, D. M., and D. J. Varnes (1996), Landslides Types and Processes, in *Landslides: Investigation and Mitigation.*, edited by A. K. Turner and R. L. Schuster, pp. 36-75, Transportation Research Board, National Academy of Sciences, Washington D.C.
- Cruz, V. H., M. Muller, and C. Weise (2010), Flood extent mapping based on TerraSar-X data, *Photogrammetrie Fernerkundung Geoinformation*(6), 475-488.
- Daehne, A., A. Corsini, and F. Ronchetti (2011), Correlation image velocimetry applied to multitemporal LiDAR data for automated landslide movement assessment, in *EGU General Assembly 2011*, edited, Copernicus, Vienna, Austria.

- Dai, F. C., and C. F. Lee (2003), A spatiotemporal probabilistic modelling of storm-induced shallow landsliding using aerial photographs and logistic regression, *Earth Surface Processes and Landforms*, 28(5), 527-545.
- Dalla-Mura, M., J. A. Benediktsson, F. Bovolo, and L. Bruzzone (2008), An Unsupervised Technique Based on Morphological Filters for Change Detection in Very High Resolution Images, *IEEE Geoscience and Remote-sensing Letters*, 5(3), 433.
- Danneels, G., E. Pirard, and H.-B. Havenith (2007), Automatic landslide detection from remote-sensing images using supervised classification methods, in *Geoscience and Remote-sensing Symposium*, edited, IGARSS, Barcelona, Spain.
- de Bie, C. A. J. M., Khan, M.R., Toxopeus, A.G., Venus, V. and Skidmore, A.K. pp. 803-812 (2008), Hypertemporal image analysis for crop mapping and change detection., in *ISPRS 2008 : Proceedings of the XXI congress: Silk road for information from imagery : the International Society for Photogrammetry and Remote Sensing*, edited by W. V. Comm. VII, ISPRS, Beijing, China.
- De Michele, M., D. Raucoules, J. De Sigoyer, M. Pubellier, and N. Chamot-Rooke (2010), Three-dimensional surface displacement of the 2008 May 12 Sichuan earthquake (China) derived from Synthetic Aperture Radar: evidence for rupture on a blind thrust, *Geophysical Journal International*, 183(3), 1097-1103.
- Delacourt, C., P. Allemand, B. Casson, and H. Vadon (2004), Velocity field of the “La Clapière” landslide measured by the correlation of aerial and QuickBird satellite images, *Geophys. Res. Lett.*, 31.
- Delacourt, C., P. Allemand, E. Berthier, D. Raucoules, B. Casson, P. Grandjean, C. Pambrun, and E. Varel (2007), Remote-sensing techniques for analysing landslide kinematics: a review, *Bulletin de la Societe Geologique de France*, 178(2), 89-100.
- Dell'Acqua, F., and P. Gamba (2001), Detection of urban structures in SAR images by robust fuzzy clustering algorithms: The example of street tracking, *IEEE Transactions on Geoscience and Remote Sensing*, 39(10), 2287-2297.
- Delmonaco, G., C. Margottini, D. Spizzichiono, and L. Falconi (2009), *Exposure and vulnerability of cultural heritage affected by geomorphological hazard: The Machu Picchu case study*, 905-909 pp.
- Delmonaco, G., G. Leoni, C. Margottini, C. Puglisi, and D. Spizzichino (2002), Large scale debris-flow hazard assessment: a geotechnical approach and GIS modelling, *Nat. Hazards Earth Syst. Sci.*, 3(5), 443-455.
- Derron, M. H., L. H. Blikra, and M. Jaboyedoff (2005), High resolution digital elevation model analysis for landslide hazard assessment (Åkerneset, Norway). in *Landslide and avalanches*, edited by K. Senneset, K. Flaate and J. A. Larsen, pp. 101–106, ICFL.
- Dewitte, O., J. C. Jasselette, Y. Cornet, M. Van Den Eeckhaut, A. Collignon, J. Poesen, and A. Demoulin (2008), Tracking landslide displacements by multi-temporal DTMs: A combined aerial stereophotogrammetric and LIDAR approach in western Belgium, *Engineering Geology*, 99(1-2), 11-22.
- Di, B., H. Zeng, M. Zhang, S. L. Ustin, Y. Tang, Z. Wang, N. Chen, and B. Zhang (2010), Quantifying the spatial distribution of soil mass wasting processes after the 2008 earthquake in Wenchuan, China: A case study of the Longmenshan area, *Remote-sensing of Environment*, 114(4), 761-771.
- Diaz-Uriarte, R., and S. Alvarez de Andres (2006), Gene selection and classification of microarray data using random forest, *BMC Bioinformatics*, 7(1), 3.

- Dragut, L., and T. Blaschke (2006), Automated classification of landform elements using object-based image analysis, *Geomorphology*, 81(3-4), 330-344.
- Dunning, S. A., W. A. Mitchell, N. J. Rosser, and D. N. Petley (2007), The Hattian Bala rock avalanche and associated landslides triggered by the Kashmir Earthquake of 8 October 2005, *Engineering Geology*, 93(3-4), 130-144.
- Dussauge-Peisser, C., A. Helmstetter, J. R. Grasso, D. Hantz, P. Desvarreux, M. Jeannin, and A. Giraud (2002), Probabilistic approach to rock fall hazard assessment: potential of historical data analysis, *Nat. Hazards Earth Syst. Sci.*, 2(1/2), 15-26.
- Dussauge, C., J.-R. Grasso, and A. Helmstetter (2003), Statistical analysis of rockfall volume distributions: Implications for rockfall dynamics. , *Journal of Geophysical Research (Solid Earth)* 108(B6).
- Ebert, A., N. Kerle, and A. Stein (2009), Urban social vulnerability assessment with physical proxies and spatial metrics derived from air- and spaceborne imagery and GIS data, *Natural Hazards*, 48(2), 275-294.
- Eisenbeiss, H. (2010), UAV-borne Laser Scanning, in *DFG-Rundgespräch „Unbemannte autonom navigierende Flugsysteme (UAS) – Technologische Herausforderungen und Chancen für die Geodatengewinnung“* edited, Rostock.
- Engel, T. (1986), Nouvelles methodes de mesure et d'analyse pour l'etudes des mouvements de sol en terrains instables, 108 pp, Ecole Polytechnique Fédérale de Lausanne, Lausanne, Switzerland.
- EPFL (1985), Les travaux de mensuration en terrain instable. Projet d'ecole "Detection et Utilisation des Terrains Instables", DUTI. *Rep.*, 27 pp, Ecole Polytechnique Federale de Lausanne (EPFL).
- Erten, E., A. Reigber, O. Hellwich, and P. Prats (2009), Glacier Velocity Monitoring by Maximum Likelihood Texture Tracking, *IEEE Transactions on Geoscience and Remote Sensing*, 47(2.), 394–405.
- Espindola, G. M., G. Camara, I. A. Reis, L. S. Bins, and A. M. Monteiro (2006), Parameter selection for region-growing image segmentation algorithms using spatial autocorrelation, *International Journal of Remote Sensing*, 27(14), 3035 - 3040.
- Evans, S. G. (2006), The formation and failure of landslide dams: an approach to risk assessment. , *Italian Journal of Engineering Geology and Environment*(Special issue 1), 15-20.
- Evans, S. G., O. Hungr, and J. J. Clague (2001), Dynamics of the 1984 rock avalanche and associated distal debris flow on Mount Cayley, British Columbia, Canada; implications for landslide hazard assessment on dissected volcanoes, *Engineering Geology*, 61(1), 29-51.
- Fallourd, R., F. Vernier, J.-M. Friedt, G. Martinc, E. Trouvé, L. Moreau, and J.-M. Nicolas (2010), Monitoring temperate glacier with high resolution automated digital cameras application to the argentière glacier, in *IAPRS*, edited by N. Paparoditis, M. Pierrot-Deseilligny, C. Mallet and O. Tournaire, Saint-Mandé, France.
- Farina, P., D. Colombo, A. Fumagalli, F. Marks, and S. Moretti (2006), Permanent Scatterers for landslide investigations: outcomes from the ESA-SLAM project, *Engineering Geology*, 88(3-4), 200-217.
- Favalli, M., A. Fornaciai, F. Mazzarini, A. Harris, M. Neri, B. Behncke, M. T. Pareschi, S. Tarquini, and E. Boschi (2010), Evolution of an active lava flow field using a multitemporal LIDAR acquisition, *J. Geophys. Res.*, 115(B11), B11203.

- Fell, R., J. Corominas, C. Bonnard, L. Cascini, E. Leroi, and W. Z. Savage (2008), Guidelines for landslide susceptibility, hazard and risk zoning for land use planning, *Engineering Geology*, 102(3-4), 85-98.
- Ferraioli, G. (2010), Multichannel InSAR Building Edge Detection, *IEEE Transactions on Geoscience and Remote Sensing*, 48(3), 1224-1231.
- Ferretti, A., C. Prati, and F. Rocca (1999), Permanent scatterers in SAR interferometry, paper presented at Geoscience and Remote-sensing Symposium, 1999. IGARSS '99 Proceedings. IEEE 1999 International, 1999.
- Ferretti, A., C. Prati, and F. Rocca (2000), Nonlinear subsidence rate estimation using permanent scatterers in differential SAR interferometry, *Geoscience and Remote Sensing, IEEE Transactions on*, 38(5), 2202-2212.
- Ferretti, A., C. Prati, and F. Rocca (2001), Permanent scatterers in SAR interferometry, *Geoscience and Remote Sensing, IEEE Transactions on*, 39(1), 8-20.
- Ferretti, A., A. Monti-Guarnieri, C. Prati, F. Rocca, D. Massonnet, and J. Lichtenegger (2007), *InSAR principles: Guidelines for SAR Interferometry Processing and Interpretation*, ESA Publications.
- Fiorucci, F., M. Cardinali, R. Carlà, M. Rossi, A. C. Mondini, L. Santurri, F. Ardizzone, and F. Guzzetti (in press), Seasonal landslide mapping and estimation of landslide mobilization rates using aerial and satellite images, *Geomorphology, In Press, Corrected Proof*.
- Fischer, L., H. Eisenbeiss, A. Käab, C. Huggel, and W. Haeberli (2011), Monitoring topographic changes in a periglacial high-mountain face using high-resolution DTMs, Monte Rosa East Face, Italian Alps, *Permafrost and Periglacial Processes*, n/a-n/a.
- Forlani, G., C. Nardinocchi, M. Scaioni, and P. Zingaretti (2006), Complete classification of raw LIDAR data and 3D reconstruction of buildings, *Pattern Analysis and Applications*, 8(4), 357-374.
- Fruneau, B., J. Achache, and C. Delacourt (1996), Observation and modelling of the Saint-Etienne-de-Tinee landslide using SAR interferometry, *Tectonophysics*, 265(181-190).
- Fukue, K., H. Shimoda, and T. Sakata (1981), Complete Lineament Extraction with the Aid of Shadow-Free LANDSAT Image, in *Seventh International Symposium Machine Processing of Remotely Sensed Data with special emphasis on Range, Forest and Wetlands Assessment*, edited, pp. 94-102, Purdue e-Pubs, Purdue, USA.
- Gabriel, A. K., R. M. Goldstein, and H. A. Zebker (1989), Mapping Small Elevation Changes Over Large Areas: Differential Radar Interferometry, *J. Geophys. Res.*, 94(B7), 9183-9191.
- Galli, M., F. Ardizzone, M. Cardinali, F. Guzzetti, and P. Reichenbach (2008), Comparing landslide inventory maps, *Geomorphology*, 94(3-4), 268-289.
- Gamba, P., B. Houshmand, and M. Saccani (2000), Detection and extraction of buildings from interferometric SAR data, *IEEE Transactions on Geoscience and Remote Sensing*, 38(1), 611-618.
- Gao, J., and J. Maro (2010), Topographic controls on evolution of shallow landslides in pastoral Wairarapa, New Zealand, 1979-2003, *Geomorphology*, 114(3), 373-381.
- Gao, Y., J. F. Mas, N. Kerle, and A. Navarrete (In Press), Optimal region growing segmentation and its effect on classification accuracy, *International Journal of Remote Sensing*.

- Garcia-Ruiz, J. M., S. Begueria, L. C. Alatorre, and J. Puigdefabregas (2010), Land cover changes and shallow landsliding in the flysch sector of the Spanish Pyrenees, *Geomorphology*, 124(3-4), 250-259.
- Gerrard, J. (1994), The landslide hazard in the Himalayas: geological control and human action, *Geomorphology*, 10(1-4), 221-230.
- Gili, J. (2011), Monitoring the Vallcebre landslide, Spain: from wire extensometers to GB-InSAR. *Rep.*, 339-344 pp, UNIL, Lausanne, Switzerland.
- Gili, J. A., and J. Sendra (1988), Aplicacion de la fotogrametria terrestre al control de taludes. , in *II Simposio Nacional de Taludes y Laderas Inestables*, edited, pp. 407-418, (in Spanish). Andorra.
- Gili, J. A., J. Corominas, and J. Rius (2000), Using Global Positioning System techniques in landslide monitoring, *Engineering Geology*, 55(3), 167-192.
- Gili, J. A., M. Crosetto, and D. Serral (2009), Reflectores Radar en el deslizamiento de Vallcebre. Validación y primeros resultados (in Spanish), in *VII Simposio Nacional sobre Taludes y Laderas Inestables*, edited, Barcelona, Spain.
- Glade, T. (2003), Landslide occurrence as a response to land use change: a review of evidence from New Zealand, *CATENA*, 51(3-4), 297-314.
- Glenn, N. F., D. R. Streutker, D. J. Chadwick, G. D. Thackray, and S. J. Dorsch (2006), Analysis of LiDAR-derived topographic information for characterizing and differentiating landslide morphology and activity, *Geomorphology*, 73(1-2), 131-148.
- Gloaguen, R., P. R. Marpu, and I. Niemeyer (2007), Automatic extraction of faults and fractal analysis from remote-sensing data, *Nonlin. Processes Geophys.*, 14(2), 131-138.
- Godt, J. W., R. L. Baum, W. Z. Savage, D. Salciarni, W. H. Schulz, and E. L. Harp (2008), Transient deterministic shallow landslide modeling: Requirement for susceptibility and hazard assessments in a GIS framework, *Engineering Geology*, 102, 214-226.
- Gomez, C., C. Delacourt, P. Allemand, P. Ledru, and R. Wackerle (2005), Using Aster remote-sensing data set for geological mapping in Namibia., *Physics and Chemistry of the Earth*, 30, 97-108.
- Gomez, C., H. L. Borgne, P. Allemand, C. Delacourt, and P. Ledru (2007), N-FindR method versus independent component analysis for lithological identification in hyperspectral imagery, *International Journal of Remote Sensing*, 28(23), 5315 - 5338.
- Gómez, H., and T. Kavzoglu (2005), Assessment of shallow landslide susceptibility using artificial neural networks in Jabonosa River Basin, Venezuela, *Engineering Geology*, 78(1-2), 11-27.
- Goodchild, M. F. (2010), Crowdsourcing geographic information for disaster response: a research frontier, *International Journal of Digital Earth*, 3(3), 231-241.
- Gordon, S., D. Lichti, and M. Stewart (2001), Application of a high-resolution, ground-based laser scanner for deformation measurements., in *10th international FIG symposium on deformation measurements*, edited, pp. 23-32, Orange, California, USA.
- Gorum, T., B. Gonencgil, C. Gokceoglu, and H. Nefeslioglu (2008), Implementation of reconstructed geomorphologic units in landslide susceptibility mapping: the Melen Gorge (NW Turkey), *Natural Hazards*, 46(3), 323-351.
- Gorum, T., X. Fan, C. J. van Westen, R. Q. Huang, Q. Xu, C. Tang, and G. Wang (in press), Distribution pattern of earthquake-induced landslides triggered by the 12 May 2008 Wenchuan Earthquake. , *Geomorphology*.
- Grandjean, G., C. Hibert, A. Bitri, J. Travelletti, and J.-P. Malet (2009), Geophysical data fusion applied to the characterization of the La Valette landslide, in *International*

- Conference 'Landslide Processes', edited by J.-P. Malet, A. Remaître and T. Bogaard, pp. 119-124, Strasbourg, France.
- Gray, A., N. Short, K. Matter, and K. Jezek (2001), Velocities and Ice Flux of the Filchner Ice Shelf and its Tributaries Determined from Speckle Tracking Interferometry, *Canadian Journal of Remote Sensing*, 27(3), 193–206.
- Grebby, S., J. Naden, D. Cunningham, and K. Tansey (2011), Integrating airborne multispectral imagery and airborne LiDAR data for enhanced lithological mapping in vegetated terrain, *Remote-sensing of Environment*, 115(1), 214-226.
- Grover, K., S. Quegan, and C. D. Freitas (1999), Quantitative estimation of tropical forest cover by SAR, *IEEE Transactions on Geoscience and Remote Sensing*, 37(1), 479-490.
- Gruen, A., E. Baltsavias, and O. Henricsson (1997), *Automatic Extraction of Man-made Objects from Aerial and Space Images*, Birkhauser Verlag, Basel.
- Guzzetti, F., P. Reichenbach, and S. Ghigi (2004), Rockfall hazard and risk assessment along a transportation corridor in the Nera Valley, central Italy, *Environmental Management*, 34(2), 191-208.
- Guzzetti, F., A. Carrara, M. Cardinali, and P. Reichenbach (1999), Landslide hazard evaluation: a review of current techniques and their application in a multi-scale study, Central Italy, *Geomorphology*, 31(1-4), 181-216.
- Guzzetti, F., B. D. Malamud, D. L. Turcotte, and P. Reichenbach (2002), Power-law correlations of landslide areas in central Italy, *Earth and Planetary Science Letters*, 195(3-4), 169-183.
- Guzzetti, F., S. Peruccacci, M. Rossi, and C. Stark (2008), The rainfall intensity–duration control of shallow landslides and debris flows: an update, *Landslides*, 5(1), 3-17.
- Guzzetti, F., P. Reichenbach, M. Cardinali, M. Galli, and F. Ardizzone (2005), Probabilistic landslide hazard assessment at the basin scale, *Geomorphology*, 72(1-4), 272-299.
- Guzzetti, F., P. Reichenbach, F. Ardizzone, M. Cardinali, and M. Galli (2006), Estimating the quality of landslide susceptibility models, *Geomorphology*, 81(1-2), 166-184.
- Guzzetti, F., F. Ardizzone, M. Cardinali, M. Rossi, and D. Valigi (2009), Landslide volumes and landslide mobilization rates in Umbria, central Italy, *Earth and Planetary Science Letters*, 279(3-4), 222-229.
- Haala, N., and M. Kada (2010), An update on automatic 3D building reconstruction, *ISPRS Journal of Photogrammetry and Remote Sensing*, 65(6), 570-580.
- Haala, N., H. Hastedt, C. Ressel, and K. Wolf (2010), DGPF Projekt: Evaluierung digitaler photogrammetrischer Luftbildkamerasysteme - Themenschwerpunkt Höhenmodelle, paper presented at Dreiländertagung OVG, DGPF und SGPF
- Hall, D. L., and J. Llinas (1997), An introduction to multisensor data fusion, *Proceedings of the IEEE*, 85(1), 6-23.
- Hanssen, R. F. (2001), *Radar Interferometry: Data Interpretation and Error Analysis*, Kluwer Academic Publishers.
- Haralick, R. M., K. Shanmugam and I. H. Dinstein (1973), Textural features for image classification, *IEEE Transactions on Systems, Man and Cybernetics*, 3(6), 610-621.
- Harant, O., L. Bombrun, G. Vasile, L. Ferro-Famil, and M. Gay (2011), Displacement Estimation by Maximum Likelihood Texture Tracking, *IEEE Journal of Selected Topics in Applied Earth Observations and Remote Sensing*.
- Harding, D. J., M. A. Lefsky, G. G. Parker, and J. B. Blair (2001), Laser altimeter canopy height profiles - Methods and validation for closed-canopy, broadleaf forests, *Remote-sensing of Environment*, 76(3), 283-297.

- Harp, E. L., and A. J. Crone (2006), Landslides Triggered by the October 8, 2005, Pakistan Earthquake and Associated Landslide-dammed Reservoirs. *Rep.*, U.S. Geological Survey.
- Harp, E. L., D. K. Keefer, H. P. Sato, and H. Yagi (2010), Landslide inventories: The essential part of seismic landslide hazard analyses, *Engineering Geology*.
- Harris, J. R., R. McGregor, and P. Budkewitsch (2010), Geological analysis of hyperspectral data over southwest Baffin Island: methods for producing spectral maps that relate to variations in surface lithologies, *Canadian Journal of Remote Sensing*, 36, 412-443.
- Hazel, G. G. (2001), Object-level change detection in spectral imagery, *IEEE Trans. Geosci. Remote Sens.*, 39(3), 553-561.
- Heinzelman, J., R. Brown, and P. Meier (2011), Mobile Technology, Crowdsourcing and Peace Mapping: New Theory and Applications for Conflict Management, in *Mobile Technologies for Conflict Management*, edited by M. Poblet, pp. 39-53, Springer Netherlands.
- Heipke, C. (2010), Crowdsourcing geospatial data, *ISPRS Journal of Photogrammetry and Remote Sensing*, 65(6), 550-557.
- Henderson, I. H. C., T. R. Lauknes, P. T. Osmundsen, J. Dehls, Y. Larsen, and T. F. Redfield (2011), A structural, geomorphological and InSAR study of an active rock slope failure development., in *Slope Tectonics*, edited by M. Jaboyedoff, pp. 185-199.
- Herrera, G., J. A. Fernández-Merodo, J. Mulas, M. Pastor, G. Luzi, and O. Monserrat (2009), A landslide forecasting model using ground based SAR data: The Portalet case study, *Engineering Geology*, 105(3-4), 220-230.
- Hervás, J., and P. Bobrowsky (2009), Mapping: inventories, susceptibility, hazard and risk, in *Landslides – Disaster Risk Reduction*, edited by K. Sassa and P. Canuti, pp. 321-349, Springer, Heidelberg.
- Hervás, J., J. I. Barredo, P. L. Rosin, A. Pasuto, F. Mantovani, and S. Silvano (2003), Monitoring landslides from optical remotely sensed imagery: the case history of Tessina landslide, Italy, *Geomorphology*, 54(1-2), 63-75.
- Hofmann, P., J. Strobl, T. Blaschke, and H. Kux (2008), Detecting informal settlements from QuickBird data in Rio de Janeiro using an object based approach, in *Object-Based Image Analysis*, edited by T. Blaschke, S. Lang and G. J. Hay, pp. 531-553, Springer Berlin Heidelberg.
- Holt, A. C., E. Y. W. Seto, T. Rivard, and P. Gong (2009), Object-based detection and classification of vehicles from high-resolution aerial photography, *Photogrammetric Engineering and Remote Sensing*, 75(7), 871-880.
- Honda, K., and M. Nagai (2002), Real-time volcano activity mapping using ground-based digital imagery, *ISPRS Journal of Photogrammetry and Remote Sensing*, 57(1-2), 159-168.
- Hong, Y., and R. F. Adler (2008), Predicting global landslide spatiotemporal distribution: Integrating landslide susceptibility zoning techniques and real-time satellite rainfall estimates, *International Journal of Sediment Research*, 23(3), 249-257
- Hovius, N., C. P. Stark, and P. A. Allen (1997), Sediment flux from a mountain belt derived by landslide mapping, *Geology*, 25(3), 231-234.
- Howe, E. (1909), Landslides in the San Juan Mountains, Colorado, *U.S. Geological Survey Professional Paper*, 67, 58.

- Hsiao, K. H., Liu, J.K., Yu, M.F., Tseng, Y.H. (2004), Change detection of landslide terrains using ground-based LiDAR data., in *XXth ISPRS Congress*, edited by W. V. Commission VII, p. 5, Istanbul, Turkey.
- Huang, R., and W. Li (2009), Analysis of the geo-hazards triggered by the 12 May 2008 Wenchuan Earthquake, China, *Bulletin of Engineering Geology and the Environment*, 68(3), 363-371.
- Hungr, O., and S. G. Evans (1996), Rock avalanche runout prediction using a dynamic model, in *Landslides*, edited by K. Senneset, pp. 233-238, Balkema, Rotterdam.
- Im, J., and J. R. Jensen (2005), A change detection model based on neighborhood correlation image analysis and decision tree classification, *Remote-sensing of Environment*, 99(3), 326-340.
- Jaboyedoff, M., and M.-H. Derron (2005), A new method to estimate the infilling of alluvial sediment of glacial valleys using a sloping local base level, *Geografica Fisica e Dinamica Quaternaria* 28, 37-46.
- Jaboyedoff, M., R. Couture, and P. Locat (2009a), Structural analysis of Turtle Mountain (Alberta) using digital elevation model: Toward a progressive failure, *Geomorphology*, 103(1), 5-16.
- Jaboyedoff, M., F. Baillifard, R. Couture, J. Locat, and P. Locat (2004), Toward preliminary hazard assessment using DEM topographic analysis and simple mechanical modeling by means of sloping local base level., in *Landslides: Evaluation and Stabilization*, edited by W. A. Lacerda, M. Ehrlich, A. B. Fontoura and A. Sayão, pp. 199-205, Taylor & Francis Group, London, UK.
- Jaboyedoff, M., A. Pedrazzini, A. Loye, T. Oppikofer, and M. Güell i Pons (2009b), Earth flow in a complex geological environment: the example of Pont Bourquin, Les Diablerets (Western Switzerland), in *Landslides Processes – From Geomorphologic mapping to dynamic modeling*, edited by J.-P. Malet, A. Remaître and T. A. Bogaard, pp. 131-137, Strasbourg, France.
- Jaboyedoff, M., T. Oppikofer, A. Abellán, M.-H. Derron, A. Loye, R. Metzger, and A. Pedrazzini (2010), Use of LIDAR in landslide investigations: a review, *Natural Hazards*, 1-24.
- Jaboyedoff, M., D. Demers, J. Locat, A. Locat, P. Locat, T. Oppikofer, D. Robitaille, and D. Turmel (2009c), Use of terrestrial laser scanning for the characterization of retrogressive landslides in sensitive clay and rotational landslides in river banks. , *Canadian Geotechnical Journal* 46, 1379-1390.
- Jaiswal, P., and C. J. van Westen (2009), Estimating temporal probability for landslide initiation along transportation routes based on rainfall thresholds, *Geomorphology*, 112(1-2), 96-105.
- Jaiswal, P., C. J. van Westen, and V. Jetten (2010), Quantitative assessment of direct and indirect landslide risk along transportation lines in southern India, *Natural Hazards and Earth System Sciences*, 10(6), 1253-1267.
- Jarvis, A., H. I. Reuter, A. Nelson, and E. Guevara (2008), Hole-filled SRTM for the globe Version 4, available from the CGIAR-CSI SRTM 90m Database, edited.
- Jelalian, A. V. (1992), *Laser Radar Systems*, 308 pp., Artech House Books.
- Jones, F. O., D. R. Embody, W. L. Peterson, and R. M. Hazelwood (1961), Landslides along the Columbia River valley, northeastern Washington, with a section on seismic surveys:, *U.S. Geological Survey Professional Paper*, 367, 98.

- Joyce, K. E., S. Samsonov, V. Manville, R. Jongens, A. Graettinger, and S. J. Cronin (2009), Remote-sensing data types and techniques for lahar path detection: A case study at Mt Ruapehu, New Zealand, *Remote-sensing of Environment*, 113(8), 1778-1786.
- Kääb, A. (2002), Monitoring high-mountain terrain deformation from repeated air- and spaceborne optical data: examples using digital aerial imagery and ASTER data, *ISPRS Journal of Photogrammetry and Remote Sensing*, 57(1-2), 39-52.
- Kääb, A. (2005), Combination of SRTM3 and repeat ASTER data for deriving alpine glacier flow velocities in the Bhutan Himalaya, *Remote-sensing of Environment*, 94(4), 463-474.
- Kääb, A., and M. Vollmer (2000), Surface Geometry, Thickness Changes and Flow Fields on Creeping Mountain Permafrost: Automatic Extraction by Digital Image Analysis, *Permafrost and Periglacial Processes*, 11, 315–326.
- Karnieli, A., A. Meisels, L. Fisher, and Y. Arkin (1996), Automatic extraction and evaluation of geological linear features from digital remote-sensing data using a Hough transform, *Photogrammetric Engineering and Remote Sensing*, 62(5), 525–531.
- Kasai, M., M. Ikeda, T. Asahina, and K. Fujisawa (2009), LiDAR-derived DEM evaluation of deep-seated landslides in a steep and rocky region of Japan, *Geomorphology*, 113(1-2), 57-69.
- Keefer, D. K. (1984), Landslides caused by earthquakes. , *Geological Society of America Bulletin*, 95, 406-421.
- Kerle, N. (2002), Volume estimation of the 1998 flank collapse at Casita volcano, Nicaragua: a comparison of photogrammetric and conventional techniques, *Earth Surface Processes and Landforms*, 27(7), 759-772.
- Kerle, N., and J. d. Leeuw (2009), Reviving Legacy Population Maps With Object-Oriented Image Processing Techniques, *IEEE Transaction on Geoscience and Remote Sensing*, 47(7), 2392-2402.
- Kerle, N., S. Heuel, and N. Pfeifer (2008), Real-time data collection and information generation using airborne sensors, in *Geospatial Information Technology for Emergency Response*, edited by S. Zlatanova and J. Li, pp. 43-74, Taylor & Francis, London.
- Kimura, H., and Y. Yamaguchi (2000), Detection of landslide areas using radar interferometry, *Photogrammetric Engineering & Remote Sensing*, 66(3), 337–344
- Kirschbaum, D. B., R. Adler, Y. Hong, and A. Lerner-Lam (2009), Evaluation of a preliminary satellite-based landslide hazard algorithm using global landslide inventories, *Nat. Hazards Earth Syst. Sci.*, 9(3), 673-686.
- Kobler, A., N. Pfeifer, P. Ogrinc, L. Todorovski, K. Ostir, and S. Dzeroski (2007), Repetitive interpolation: A robust algorithm for DTM generation from Aerial Laser Scanner Data in forested terrain, *Remote-sensing of Environment*, 108(1), 9-23.
- Koike, K., S. Nagano, and M. Ohmi (1995), Lineament analysis of satellite images using a Segment Tracing Algorithm (STA), *Computers & Geosciences*, 21(9), 1091-1104.
- Korup, O., M. J. McSaveney, and T. R. H. Davies (2004), Sediment generation and delivery from large historic landslides in the Southern Alps, New Zealand, *Geomorphology*, 61(1-2), 189-207.
- Krieger, G., A. Moreira, H. Fiedler, I. Hajnsek, M. Werner, M. Younis, and M. Zink (2007), TanDEM-X: A Satellite Formation for High-Resolution SAR Interferometry, *Geoscience and Remote Sensing, IEEE Transactions on*, 45(11), 3317-3341.

- Kuriakose, S. L., S. Devkota, D. G. Rossiter, and V. G. Jetten (2009), Prediction of soil depth using environmental variables in an anthropogenic landscape, a case study in the Western Ghats of Kerala, India, *CATENA*, 79(1), 27-38.
- Kveldsvik, V., B. Nilsen, H. Einstein, and F. Nadim (2008), Alternative approaches for analyses of a 100,000 m³ rock slide based on Barton–Bandis shear strength criterion, *Landslides*, 5(2), 161-176.
- L’Heureux, J. S., L. Hansen, O. Longva, A. Emdal, and L. O. Grande (2010), A multidisciplinary study of submarine landslides at the Nidelva fjord delta, Central Norway—implications for geohazards assessment., *Norw.J.Geol*, 90, 1-20.
- Lagacherie, P., F. Baret, J.-B. Feret, J. Madeira Netto, and J. M. Robbez-Masson (2008), Estimation of soil clay and calcium carbonate using laboratory, field and airborne hyperspectral measurements, *Remote-sensing of Environment*, 112(3), 825-835.
- Laliberte, A., and A. Rango (2009), Texture and scale in object-based analysis of subdecimeter resolution unmanned aerial vehicle (UAV) imagery, *IEEE Transactions on Geoscience and Remote Sensing*, 47(3), 761-770.
- Lanari, R., O. Mora, M. Manunta, J. J. Mallorqui, P. Berardino, and E. Sansosti (2004), A small-baseline approach for investigating deformations on full-resolution differential SAR interferograms, *Geoscience and Remote Sensing, IEEE Transactions on*, 42(7), 1377-1386.
- Lasne, Y., P. Paillou, T. August-Bernex, G. Ruffie, and G. Grandjean (2004), A phase signature for detecting wet subsurface structures using polarimetric L-band SAR, *IEEE Trans. Geosci. Remote Sens.*, 42(8), 1683 - 1694
- Lauknes, T. R. (2004), Long-Term Surface Deformation Mapping using Small-Baseline Differential SAR Interferograms, 88 pp, University of Tromsø, Norway.
- Lauknes, T. R., A. Piyush Shanker, J. F. Dehls, H. A. Zebker, I. H. C. Henderson, and Y. Larsen (2010), Detailed rockslide mapping in northern Norway with small baseline and persistent scatterer interferometric SAR time series methods, *Remote-sensing of Environment*, 114(9), 2097-2109.
- Lee, C.-T., C.-C. Huang, J.-F. Lee, K.-L. Pan, M.-L. Lin, and J.-J. Dong (2008), Statistical approach to earthquake-induced landslide susceptibility, *Engineering Geology*, 100(1-2), 43-58.
- Lee, S., and T. Sambath (2006), Landslide susceptibility mapping in the Damrei Romel area, Cambodia using frequency ratio and logistic regression models, *Environmental Geology*, 50, 847-855.
- Lee, S., J. Choi, and I. Woo (2004), The effect of spatial resolution on the accuracy of landslide susceptibility mapping: a case study in Boun, Korea, *Geosciences Journal*, 8(1), 51-60.
- Lefebvre, A., T. Corpetti, and L. Hubert-Moy (2008), Object-Oriented Approach and Texture Analysis for Change Detection in Very High Resolution Images, paper presented at Geoscience and Remote-sensing Symposium, 2008. IGARSS 2008. IEEE International, 7-11 July 2008.
- Leprince, S. (2008), Monitoring Earth Surface Dynamics With Optical Imagery, 252 pp, California Institute of Technology, Pasadena.
- Leroi, E. (1996), Landslide hazard-risk maps at different scales: objectives, tools and developments, in *7th International Symposium on Landslides*, edited by Anonymous, 17-21, Trondheim, Norway.

- Li, J. (2010), Using ICT to Reduce Flood Risk in China, in *UN-ESCAP Regional Workshop on ICT Applications for Disaster Risk Reduction and Sustainable Economic Development*, edited, Astana, Kazakhstan.
- Li, L., and M. K. H. Leung (2002), Integrating intensity and texture differences for robust change detection, *IEEE Trans. Image Process*, 11, 105–112.
- Liaw, A. (2010), randomForest: Breiman and Cutler's random forests for classification and regression, Version 4.5-36.
- Lillesand, T. M., and R. W. Kiefer (1987), *Remote-sensing and image interpretation. Second edition*, Medium: X; Size: Pages: 650 pp.
- Lillesand, T. M., R. W. Kiefer, and J. W. Chipman (2008), *Remote-sensing and Image Interpretation*, 756 pp., John Wiley & Sons.
- Lim, M., N. J. Rosser, R. J. Allison, and D. N. Petley (2010), Erosional processes in the hard rock coastal cliffs at Staithes, North Yorkshire, *Geomorphology*, 114(1-2), 12-21.
- Lim, M., D. N. Petley, N. J. Rosser, R. J. Allison, A. J. Long, and D. Pybus (2005), Combined Digital Photogrammetry and Time-of-Flight Laser Scanning for Monitoring Cliff Evolution, *The Photogrammetric Record*, 20(110), 109-129.
- Lin, C.-Y., C.-W. Chuang, W.-T. Lin, and W.-C. Chou (2010a), Vegetation recovery and landscape change assessment at Chiufenershan landslide area caused by Chichi earthquake in central Taiwan, *Natural Hazards*, 53(1), 175-194.
- Lin, Y. P., H. J. Chu, and C. F. Wu (2010b), Spatial pattern analysis of landslide using landscape metrics and logistic regression: a case study in Central Taiwan, *Hydrol. Earth Syst. Sci. Discuss.*, 7(3), 3423-3451.
- Linke, J., and G. J. McDermid (2010), A Conceptual Model for Multi-Temporal Landscape Monitoring in an Object-Based Environment, *Selected Topics in Applied Earth Observations and Remote Sensing, IEEE Journal of*, PP(99), 1-7.
- Liu, Y., R. Liu, and Q. Ge (2010), Evaluating the vegetation destruction and recovery of Wenchuan earthquake using MODIS data, *Natural Hazards*, 54(3), 851-862.
- Lu, P., A. Stumpf, N. Kerle, and N. Casagli (2011), Object-Oriented Change Detection for Landslide Rapid Mapping, *Geoscience and Remote-sensing Letters, IEEE, PP(99)*, 701-705.
- Lu, P., A. Stumpf, N. Kerle, and N. Casagli (in press), Object-oriented change detection for landslide rapid mapping, *IEEE Geoscience and Remote-sensing Letters*.
- Malamud, B. D., D. L. Turcotte, F. Guzzetti, and P. Reichenbach (2004), Landslide inventories and their statistical properties, *Earth Surface Processes and Landforms*, 29(6), 687-711.
- Malet, J. P., O. Maquaire, and E. Calais (2002), The use of Global Positioning System techniques for the continuous monitoring of landslides: application to the Super-Sauze earthflow (Alpes-de-Haute-Provence, France), *Geomorphology*, 43(1-2), 33-54.
- Mallast, U., R. Gloaguen, S. Geyer, T. Rödiger, and C. Siebert (2011), Semi-automatic extraction of lineaments from remote-sensing data and the derivation of groundwater flow-paths, *Hydrol. Earth Syst. Sci. Discuss.*, 8(1), 1399-1431.
- Mantovani, F., R. Soeters, and C. J. Van Westen (1996), Remote-sensing techniques for landslide studies and hazard zonation in Europe, *Geomorphology*, 15(3-4), 213-225.
- Manzo, M., G. P. Ricciardi, F. Casu, G. Ventura, G. Zeni, S. Borgström, P. Berardino, C. Del Gaudio, and R. Lanari (2006), Surface deformation analysis in the Ischia Island (Italy) based on spaceborne radar interferometry, *Journal of Volcanology and Geothermal Research*, 151(4), 399-416.

- Maquaire, O. (1990), Les mouvements de terrain de la cote du Calvados. Recherche et prevention. *Rep.*, 431 pp.
- Marcelino, E. V., A. R. Formaggio, and E. E. Maed (2009), Landslide inventory using image fusion techniques in Brazil, *International Journal of Applied Earth Observation and Geoinformation*, 11(3), 181-191.
- Marghany, M., and M. Hashim (2010), Lineament mapping using multispectral remote-sensing satellite data, *Research Journal of Applied Sciences*, 5(2), 126-130.
- Martha, T., N. Kerle, C. J. van Westen, and K. Kumar (2010a), Characterising spectral, spatial and morphometric properties of landslides for semi-automatic detection using object-oriented methods, *Geomorphology*, 116(1-2), 24-36
- Martha, T., N. Kerle, C. van Westen, V. Jetten, and K. Vinod Kumar (2010b), Effect of Sun Elevation Angle on DSMs Derived from Cartosat-1 Data. , *Photogrammetry and Remote Sensing*, Article In Press.
- Martha, T., N. Kerle, C. J. van Westen, V. Jetten, and K. Vinod Kumar (in press-a), Segment optimisation and data-driven thresholding for knowledge-based landslide detection by object-based image analysis, *IEEE Transactions on Geoscience and Remote Sensing*.
- Martha, T., N. Kerle, C. van Westen, V. Jetten, and V. Kumar (in press-b), Segment optimisation and data-driven thresholding for knowledge-based landslide detection by object-oriented image analysis, *IEEE Transactions on Geoscience and Remote Sensing*.
- Martha, T. R., N. Kerle, V. Jetten, C. J. van Westen, and K. Vinod Kumar (2010c), Landslide Volumetric Analysis Using Cartosat-1-Derived DEMs, *IEEE Geoscience and Remote-sensing Letters*, 7(3), 582 - 586
- Martin, B., and D. Weber (1996), Vitesses de déplacement des mouvements de terrain à Vars (Hautes-Alpes, France): le recours aux archives et à la topométrie. , *Revue de Géographie Alpine* 2, 57– 66.
- Massonnet, D. (1985), Etude de Principe d'une Détection de Mouvements Tectoniques par Radar. *Rep.*, Centre National d'Etude Spatial (CNES), Toulouse, France.
- Massonnet, D., and K. L. Feigl (1998), Radar interferometry and its application to changes in the Earth's surface, *Rev. Geophys.*, 36(4), 441-500.
- Massonnet, D., W. Thatcher, and H. Vadon (1996), Detection of postseismic fault zone collapse following the Landers earthquake, *Nature*, 382, 612-616.
- Massonnet, D., M. Rossi, C. Carmona, F. Adragna, G. Peltzer, K. Feigl, and T. Rabaute (1993), The displacement field of the Landers earthquake mapped by radar interferometry, *Nature*, 364(6433), 138-142.
- Mavrantza, O., and D. Argialas (2008), An object-oriented image analysis approach for the identification of geologic lineaments in a sedimentary geotectonic environment, edited, pp. 383-398.
- McBratney, A. B., M. I. M. Santos, and B. Minasny (2003), On digital soil mapping, *Geoderma*, 117, 3-52.
- McDermid, G. J., J. Linke, A. Pape, D. N. Laskin, A. J. McLane, and S. E. Franklin (2008), Object-based approaches to change detection and thematic map update: Challenges and limitations., *Canadian Journal of Remote Sensing*, 34(5), 462–466.
- McKean, J., and J. Roering (2004), Objective landslide detection and surface morphology mapping using high-resolution airborne laser altimetry, *Geomorphology*, 57(3-4), 331-351.

- Meisina, C., F. Zucca, F. Conconi, F. Verri, D. Fossati, M. Ceriani, and J. Allievi (2007), Use of Permanent Scatterers technique for large-scale mass movement investigation, *Quaternary International*, 171-172, 90-107.
- Metternicht, G., L. Hurni, and R. Gogu (2005), Remote-sensing of landslides: An analysis of the potential contribution to geo-spatial systems for hazard assessment in mountainous environments, *Remote-sensing of Environment*, 98(2-3), 284-303.
- Meunier, P., T. Ushida, and N. Hovius (2011), What controls the size of earthquake-triggered landslides?, *Geophysical Research Abstracts*, Vol. 13(EGU2011-11165).
- Meusburger, K., and C. Alewell (2008), Impacts of anthropogenic and environmental factors on the occurrence of shallow landslides in an alpine catchment (Urseren Valley, Switzerland), *Nat. Hazards Earth Syst. Sci.*, 8(3), 509-520.
- Meusburger, K., and C. Alewell (2009), On the influence of temporal change on the validity of landslide susceptibility maps, *Nat. Hazards Earth Syst. Sci.*, 9(4), 1495-1507.
- Michoud, C., A. Abellán, M.-H. Derron, and M. Jaboyedoff (Eds.) (2010), *SafeLand deliverable 4.1: Review of Techniques for Landslide Detection, Fast Characterization, Rapid Mapping and Long-Term Monitoring*, 401 pp.
- Moine, M., A. Puissant, and J.-P. Malet (2009), Detection of landslides from aerial and satellite images with a semi-automatic method. Application to the Barcelonnette basin (Alpes-de-Haute-Provence, France), in *International Conference 'Landslide Processes'*, edited by J.-P. Malet, A. Remaître and T. Bogaard, pp. 63-68, Strasbourg, France.
- Mondini, A. C., F. Guzzetti, P. Reichenbach, M. Rossi, M. Cardinali, and F. Ardizzone (2011), Semi-automatic recognition and mapping of rainfall induced shallow landslides using optical satellite images, *Remote-sensing of Environment*, 115(7), 1743-1757.
- Monserrat, O., and M. Crosetto (2008), Deformation measurement using terrestrial laser scanning data and least squares 3D surface matching., *ISPRS J Photogramm Remote Sens*, 63, 142-154.
- Montoya, L. (2003), Geo-data acquisition through mobile GIS and digital video: an urban disaster management perspective, *Environmental Modelling & Software*, 18(10), 869-876.
- Mora, P., P. Baldi, G. Casula, M. Fabris, M. Ghirotti, E. Mazzini, and A. Pesci (2003), Global Positioning Systems and digital photogrammetry for the monitoring of mass movements: application to the Ca' di Malta landslide (northern Apennines, Italy), *Engineering Geology*, 68(1-2), 103-121.
- Mueller, R., and S. Loew (2009), Predisposition and Cause of the Catastrophic Landslides of August 2005 in Brienz (Switzerland)., *Swiss J Geosci*, 102(2), 331-344.
- Nagai, M., T. Chen, R. Shibasaki, H. Kumagai, and A. Ahmed (2009), UAV-Borne 3-D Mapping System by Multisensor Integration, *IEEE Transactions on Geoscience and Remote Sensing*, 47(3), 701-708.
- Nichol, J., and M. S. Wong (2005), Satellite remote-sensing for detailed landslide inventories using change detection and image fusion, *International Journal of Remote Sensing*, 26(9), 1913 - 1926.
- Niethammer, U., S. Rothmund, and M. Joswig (2009), UAV-based remote-sensing of the slow-moving landslide Super-Sauze, paper presented at International Conference Landslide Processes: from geomorphologic mapping to dynamic modelling, CERG Editions, Strasbourg, February 6 to 7, 2009.

- Niethammer, U., M. R. James, S. Rothmund, J. Travelletti, and M. Joswig (forthcoming), Very high spatial resolution monitoring of the Super-Sauze landslide with an UAV-based remote-sensing technique, *Engineering Geology*.
- Novali, F., A. Ferretti, C. Prati, F. Rocca, G. Savio, and S. Musazzi (2005), PSInSAR Validation by Means of a Blind Experiment Using Dihedral Reflectors., in *FRINGE 2005*, edited, Frascati, Italy.
- O'Leary, D. W., J. D. Friedman, and H. A. Pohn (1976), Lineament, linear, lineation: Some proposed new standards for old terms, *Geological Society of America Bulletin*, 87(10), 1463-1469.
- Oka, N. (1988), Applications of photogrammetry to the field observation of failed slopes, *Engineering Geology* 50, 85-100.
- Oppikofer, T. (2009), Detection, analysis and monitoring of slope movements by high-resolution digital elevation models. , University of Lausanne, Lausanne, Switzerland. .
- Oppikofer, T., M. Jaboyedoff, and H.-R. Keusen (2008), Collapse at the eastern Eiger flank in the Swiss Alps, *Nature Geosci*, 1(8), 531-535.
- Oppikofer, T., M. Jaboyedoff, L. Blikra, M. H. Derron, and R. Metzger (2009), Characterization and monitoring of the Åknes rockslide using terrestrial laser scanning, *Nat. Hazards Earth Syst. Sci.*, 9(3), 1003-1019.
- Oppikofer, T., M. Jaboyedoff, A. Pedrazzini, M. H. Derron, and L. H. Blikra (in press), Detailed DEM analysis of a rockslide scar to improve the basal failure surface model of active rockslides, *Journal of Geophysical Research*.
- Pachauri, A. K., and M. Pant (1992), Landslide hazard mapping based on geological attributes, *Engineering Geology*, 32(1-2), 81-100.
- Paganini, M. (2004), The use of space-borne sensors for the monitoring of slope instability: Present potentialities and future opportunities, in *Workshop on risk mitigation of slope instability*, edited, JRC, Institute for the Protection and Security of the Citizen, Ispra, Italy.
- Pancioli, V., H. Raetzo, T. Campolmi, and N. Casagli (2008), Terrafirma Landslide Services for Europe based on Space-borne InSAR Data, in *First World Landslide Forum*, edited, pp. 81-84, Tokyo, Japan.
- Papathoma-Kohle, M., B. Neuhauser, K. Ratzinger, H. Wenzel, and D. Dominey-Howes (2007), Elements at risk as a framework for assessing the vulnerability of communities to landslides, *Natural Hazards and Earth System Sciences*, 7(6), 765-779.
- Park, N.-W., and K.-H. Chi (2008), Quantitative assessment of landslide susceptibility using high-resolution remote-sensing data and a generalized additive model, *Int. J. Remote Sens.*, 29(1), 247-264.
- Pascale, S., F. Sdao, and A. Sole (2010), A model for assessing the systemic vulnerability in landslide prone areas, *Natural Hazards and Earth System Sciences*, 10(7), 1575-1590.
- Pedrazzini, A., T. Oppikofer, M. Jaboyedoff, M. Guell i Pons, R. Chantry, and E. Stampfli (2010), Assessment of rockslide and rockfall problems in an active quarry: case study of the Arvel quarry (Western Switzerland), in *Rock Mechanics in Civil and Environmental Engineering*, edited by J. Zhao, V. Labiouse, J.-P. Dudt and J.-F. Mathier, pp. 593-596, CPC/Balkema.
- Perea, A. J., J. E. Merono, and M. J. Aguilera (2009), Object-based classification in aerial digital photography for land-use discrimination, *Interciencia*, 34(9), 612-616.
- Pesci, A., G. Teza, G. Casula, F. Loddo, P. De Martino, M. Dolce, F. Obrizzo, and F. Pingue (2011), Multitemporal laser scanner-based observation of the Mt. Vesuvius crater:

- Characterization of overall geometry and recognition of landslide events, *ISPRS Journal of Photogrammetry and Remote Sensing*, 66(3), 327-336.
- Petitjean, F., P. Gançarski, F. Masegla, and G. Forestier (2010), Analysing Satellite Image Time Series by Means of Pattern Mining, in *Intelligent Data Engineering and Automated Learning – IDEAL 2010*, edited by C. Fyfe, P. Tino, D. Charles, C. Garcia-Osorio and H. Yin, pp. 45-52, Springer Berlin / Heidelberg.
- Petrie, G., and C. K. Toth (2009), Airborne and Spaceborne Laser Profilers and Scanners, in *Topographic Laser Ranging and Scanning, Principles and Processing*, edited by J. a. C. K. T. Shan, pp. 1-27, CRC Press, Taylor and Francis Group.
- Poli, D., E. Angiuli, and F. Remondino (2010), Radiometric and geometric analysis of WorldView-2 stereo scenes paper presented at International Archives of Photogrammetry and Remote-sensing and Spatial Information Sciences, ISPRS, Calgary, Canada, 15-18 June 2010,.
- Powers, P. S., and M. Chiarle (1996), A digital photogrammetric method to measure horizontal surficial movements on the Slumgullion landslide, Hinsdale County, Colorado, *Bulletin of the U.S. Geological Survey* 2130, 51-55.
- Powers, P. S., M. Chiarle, and W. Z. Savage (1996), A digital photogrammetric method for measuring horizontal surficial movements on the Slumgullion earthflow, Hinsdale County, Colorado, *Computers & Geosciences*, 22(6), 651-663.
- Pradhan, B., R. P. Singh, and M. F. Buchroithner (2006), Estimation of stress and its use in evaluation of landslide prone regions using remote-sensing data, *Advances in Space Research*, 37(4), 698-709.
- Prats, P., R. Scheiber, A. Reigber, C. Andres, and R. Horn (2009), Estimation of the Surface Velocity Field of the Aletsch Glacier Using Multibaseline Airborne SAR Interferometry, *IEEE Transactions on Geoscience and Remote Sensing*, 47(2), 419-430.
- Prokesová, R., M. Kardos, and A. Medvedová (2010), Landslide dynamics from high-resolution aerial photographs: A case study from the Western Carpathians, Slovakia, *Geomorphology*, 115(1-2), 90-101.
- Radke, R. J., S. Andra, O. Al-Kofahi, and B. Roysam (2005), Image change detection algorithms: a systematic survey, *Image Processing, IEEE Transactions on*, 14(3), 294-307.
- Raghavan, V., S. Masumoto, K. Koike, and S. Nagano (1995), Automatic lineament extraction from digital images using a segment tracing and rotation transformation approach, *Computers & Geosciences*, 21(4), 555-591.
- Ramli, M., N. Yusof, M. Yusoff, H. Juahir, and H. Shafri (2010), Lineament mapping and its application in landslide hazard assessment: a review, *Bulletin of Engineering Geology and the Environment*, 69(2), 215-233.
- Rau, J.-Y., L.-C. Chen, J.-K. Liu, and T.-H. Wu (2007), Dynamics monitoring and disaster assessment for watershed management using time-series satellite images, *Geoscience and Remote Sensing, IEEE Transactions on*, 45(6), 1641-1649.
- Raucoules, D., C. Colesanti, and C. Carnec (2007), Use of SAR interferometry for detecting and assessing ground subsidence, *Comptes Rendus Geosciences*, 339(5), 289-302.
- Raucoules, D., B. Ristori, M. de Michele, and P. Briole (2010), Surface displacement of the Mw 7 Machaze earthquake (Mozambique): Complementary use of multiband InSAR and radar amplitude image correlation with elastic modelling, *Remote-sensing of Environment*, 114(10), 2211-2218.

- Ray, R. L., J. M. Jacobs, and M. H. Cosh (2010), Landslide susceptibility mapping using downscaled AMSR-E soil moisture: A case study from Cleveland Corral, California, US, *Remote-sensing of Environment*, 114(11), 2624-2636.
- Razak, K. A., C. v. Westen, M. Straatsma, and S. d. Jong (2011a), Mapping of Elements at Risk for Landslides in the Tropics Using Airborne Laser Scanning, in *FIG Working Week 2011 - Bridging the Gap between Cultures*, edited, Marrakech, Morocco.
- Razak, K. A., M. W. Straatsma, C. J. van Westen, J. P. Malet, and S. M. de Jong (2011b), Airborne laser scanning of forested landslides characterization: Terrain model quality and visualization, *Geomorphology*, 126(1-2), 186-200.
- Refice, A., L. Guerriero, F. Bovenga, J. Wasowski, S. Atzori, R. Ferrari, and M. Marsella (2001), Detecting landslide activity by SAR interferometry, in *ERS-ENVISAT Symposium*, edited, Goteborg, Sweden.
- Reinartz, P., P. d'Angelo, T. Krauß, D. Poli, K. Jacobsen, and G. Buyuksalih (2010), Benchmarking and quality analysis of DEM generated from high and very high resolution optical stereo satellite data., paper presented at International Archives of Photogrammetry and Remote-sensing and Spatial Information Sciences., ISPRS, Calgary, Canada, 15-18 June 2010.
- Reutebuch, S. E., H. E. Andersen, and R. J. McGaughey (2005), Light detection and ranging (LIDAR): An emerging tool for multiple resource inventory, *Journal of Forestry*, 103(6), 286-292.
- Rib, H. T., and T. Liang (1978), Recognition and identification, in *Landslide Analysis and Control* edited by R. L. Schuster and R. J. Krizek, pp. 34–80, National Academy of Sciences, Washington DC.
- Rizzo, V., and M. Tesauro (2000), SAR interferometry and field data of Randazzo landslide (Eastern Sicily, Italy), *Physics and Chemistry of the Earth, (B)* 25(9), 771–780.
- Rocca, F. (2003), 3D Motion recovery with multi-angle and/or left right Interferometry., in *3rd International Workshop on ERS SAR Interferometry (FRINGE 2003)*, edited, Frascati, Italy.
- Roering, J. J., J. W. Kirchner, and W. E. Dietrich (2005), Characterizing structural and lithologic controls on deep-seated landsliding: implications for topographic relief and landscape evolution in the Oregon Coast Range, USA, *GSA Bulletin* 117, 654-668.
- Roering, J. J., L. L. Stimely, B. H. Mackey, and D. A. Schmidt (2009), Using DInSAR, airborne LiDAR, and archival air photos to quantify landsliding and sediment transport, *Geophys. Res. Lett.*, 36(19), L19402.
- Rosser, N., M. Lim, D. Petley, S. Dunning, and R. Allison (2007), Patterns of precursory rockfall prior to slope failure, *J. Geophys. Res.*, 112(F4), F04014.
- Rossi, M., F. Guzzetti, P. Reichenbach, A. C. Mondini, and S. Peruccacci (2010a), Optimal landslide susceptibility zonation based on multiple forecasts, *Geomorphology*, 114(3), 129-142.
- Rossi, M., A. Witt, F. Guzzetti, B. D. Malamud, and S. Peruccacci (2010b), Analysis of historical landslide time series in the Emilia-Romagna region, northern Italy, *Earth Surface Processes and Landforms*, 35(10), 1123-1137.
- Rott, H. (2004), Requirements and applications of satellite techniques for monitoring slope instability in Alpine areas., in *Workshop on risk mitigation of slope instability.*, edited, JRC-Institute for the Protection and Security of the Citizen, Ispra, Italy'.
- Rott, H., and A. Siegel (1999), Analysis of mass movements in alpine terrain by means of SAR interferometry., in *IGARSS'99*, edited, pp. 1993–1939, Hamburg, Germany.

- Rott, H., C. Mayer, and A. Siegel (2000), On the operational potential of SAR interferometry for monitoring mass movements in alpine areas, in *EUSAR 2000*, edited, pp. 43–46, Munchen, Germany.
- Rouiller, J., M. Jaboyedoff, C. Marro, F. Phlipposian, and M. Mamin (1998), Pentes instables dans le Pennique valaisan. Matterock: une méthodologie d'auscultation des falaises et de détection des éboulements majeurs potentiels *Rep.*, VDF Hochschulverlag AG an der ETH Zürich, Zürich, Switzerland.
- Rybár, J., J. Pasek, and L. Repka (1965), Dokumentation der systematischen untersuchung der rutschungsgebiete in der tschechoslowakei, *Engineering Geology*, 1(1), 21-29.
- Saba, S. B., M. van der Meijde, and H. van der Werff (2010), Spatiotemporal landslide detection for the 2005 Kashmir earthquake region, *Geomorphology*, 124(1-2), 17-25.
- Sarkar, S., and D. P. Kanungo (2004), An Integrated Approach for Landslide Susceptibility Mapping using Remote-sensing and GIS, *Photogrammetric Engineering & Remote Sensing*, 70(5), 617–625.
- Sato, H., and E. Harp (2009), Interpretation of earthquake-induced landslides triggered by the 12 May 2008, M7.9 Wenchuan earthquake in the Beichuan area, Sichuan Province, China using satellite imagery and Google Earth, *Landslides*, 6(2), 153-159.
- Scambos, T. A., M. J. Dutkiewicz, J. C. Wilson, and R. A. Bindschadler (1992), Application of image cross-correlation to the measurement of glacier velocity using satellite image data, *Remote-sensing of Environment*, 42(3), 177-186.
- Scheiber, R., and A. Moreira (2000), Coregistration of interferometric SAR images using spectral diversity, *IEEE Trans. Geoscience and Remote Sensing*, 38(5).
- Scheidl, C., D. Rickenmann, and M. Chiari (2008), The use of airborne LiDAR data for the analysis of debris flow events in Switzerland, *Nat. Hazards Earth Syst. Sci.*, 8(5), 1113-1127.
- Schulz, W. H. (2007), Landslide susceptibility revealed by LIDAR imagery and historical records, Seattle, Washington, *Engineering Geology*, 89(1-2), 67-87.
- Schwarz, G. (1978), Estimating the dimension of a model, *Annals of Statistics*, 6(2), 461-464.
- Sepúlveda, S., A. Serey, M. Lara, A. Pavez, and S. Rebolledo (2010), Landslides induced by the April 2007 Aysén Fjord earthquake, Chilean Patagonia, *Landslides*, 7(4), 483-492.
- Serafino, F. (2006), Sar Image Coregistration Based on Isolated Point Scatterers, *IEEE Geoscience and Remote-sensing Letters*, 3(3), 354–358.
- Shamaoma, H., N. Kerle, and D. Alkema (2006), Extraction of flood-modelling related base-data from multi-source remote-sensing imagery, in *ISPRS Mid-term Symposium 2006: from Pixels to Processes*, edited by N. Kerle and A. K. Skidmore, pp. 643-649, Enschede, The Netherlands.
- Shan, J., and C. K. Toth (Eds.) (2009), *Topographic Laser Ranging and Scanning, Principles and Processing*, 590 pp., CRC Press, Taylor and Francis Group.
- Shen, Z.-K., J. Sun, P. Zhang, Y. Wan, M. Wang, R. Burgmann, Y. Zeng, W. Gan, H. Liao, and Q. Wang (2009), Slip maxima at fault junctions and rupturing of barriers during the 2008 Wenchuan earthquake, *Nature Geosci*, 2(10), 718-724.
- Shepherd, E. C. (1965), Laser to watch height, *New Scientist*, 26(437), 33.
- Singhroy, V. (2002), Landslide hazards: CEOS, The use of earth observing satellites for hazard support: Assessments and scenarios. *Rep.*, 98 pp, NOAA.
- Singhroy, V., and K. Molch (2004), Characterizing and monitoring rockslides from SAR techniques, *Advances in Space Research*, 30(3), 290-295.

- Soeters, R., and C. Van Westen (1996), Slope instability recognition, analysis and zonation, in *Landslides, investigation and mitigation.*, edited by A. K. Turner and R. L. Schuster, pp. 129-177, Transportation Research Board, National Research Council, National Academy Press, Washington, USA.
- Song, C., C. E. Woodcock, K. C. Seto, M. P. Lenney, and S. A. Macomber (2001), Classification and Change Detection Using Landsat TM Data: When and How to Correct Atmospheric Effects?, *Remote-sensing of Environment*, 75(2), 230-244.
- Squarzoni, C., C. Delacourt, and P. Allemand (2003), Nine years of spatial and temporal evolution of the La Valette landslide observed by SAR interferometry, *Engineering Geology*, 68(1-2), 53-66.
- Stark, C. P., and N. Hovius (2001), The characterization of landslide size distributions, *Geophys. Res. Lett.*, 28(6), 1091-1094.
- STATENS-JÄRNVGARS (1922), Slutbetänkande angivet till Kungl. Järnvägsstyrelsen *Rep.*, 174-180 pp, Geotekniska "Kommission, Stockholm.
- Stepinski, T. F., and C. Bagaria (2009), Segmentation-based unsupervised terrain classification for generation of physiographic maps, in: IEEE Geoscience and Remote-sensing Letters, , *IEEE Geoscience and Remote-sensing Letters*, 6(4), 733-737
- Stolz, A., and C. Huggel (2008), Debris flows in the Swiss National Park: the influence of different flow models and varying DEM grid size on modeling results, *Landslides*, 5(3), 311-319.
- Strozzi, T., A. Luckman, T. Murray, U. Wegmuller, and C. Werner (2002), Glacier Motion Estimation using SAR Offset- Tracking Procedures, *IEEE Transactions on Geoscience and Remote Sensing*, 40(11), 2384–2391.
- Strozzi, T., R. Delaloye, A. Käab, C. Ambrosi, E. Perruchoud, and U. Wegmüller (2010), Combined observations of rock mass movements using satellite SAR interferometry, differential GPS, airborne digital photogrammetry, and airborne photography interpretation, *Journal of Geophysical Research*, 115(F01014).
- Strozzi, T., P. Farina, A. Corsini, C. Ambrosi, M. Thüring, J. Zilger, A. Wiesmann, U. Wegmüller, and C. Werner (2005), Survey and monitoring of landslide displacements by means of L-band satellite SAR interferometry, *Landslides*, 2(3), 193-201.
- Stumpf, A., and N. Kerle (accepted), Object-oriented mapping of landslides using Random Forests., *Remote-sensing of Environment*.
- Stumpf, A., and N. Kerle (in press), Object-oriented mapping of landslides using Random Forests, *Remote-sensing of Environment*.
- Talebian, M., et al. (2004), The 2003 Bam (Iran) earthquake: Rupture of a blind strike-slip fault, *Geophys. Res. Lett.*, 31(11), L11611.
- Tarchi, D., N. Casagli, R. Fanti, D. D. Leva, G. Luzi, A. Pasuto, M. Pieraccini, and S. Silvano (2003), Landslide monitoring by using ground-based SAR interferometry: an example of application to the Tessina landslide in Italy, *Engineering Geology*, 68(1-2), 15-30.
- Tesfa, T. K., D. G. Tarboton, D. G. Chandler, and J. P. McNamara (2009), Modeling soil depth from topographic and land cover attributes, *Water Resour. Res.*, 45(10), W10438.
- Teza, G., A. Galgaro, N. Zaltron, and R. Genevois (2007), Terrestrial laser scanner to detect landslide displacement fields: a new approach, *International Journal of Remote Sensing*, 28(16), 3425 - 3446.
- Thiery, Y., J. P. Malet, S. Sterlacchini, A. Puissant, and O. Maquaire (2007), Landslide susceptibility assessment by bivariate methods at large scales: Application to a complex mountainous environment, *Geomorphology*, 92(1-2), 38-59.

- Tian, Y., C. Xiao, and L. Wu (2010), Slope unit-based landslide susceptibility zonation, in *18th International Conference on Geoinformatics*, edited, pp. 18-20 June 2010, Beijing, China.
- Tian, Y., C. Xiao, Y. Liu, and L. Wu (2008), Effects of raster resolution on landslide susceptibility mapping: A case study of Shenzhen, *Science in China Series E: Technological Sciences*, 51(0), 188-198.
- Tofani, V., F. Catani, V. Pancioli, S. Moretti, and N. Casagli (2010), Integration of PSI technique and conventional ground-based methods for characterization and monitoring of Santo Stefano d'Aveto landslide (Central Italy), in *Mountain Risks: bringing Science to Society*, edited by J.-P. Manet, T. Glade and N. Casagli, pp. 301 - 330, Cerg Editions, Strasburgo, Strasbourg.
- Travelletti, J., J.-P. Malet, and C. Delacourt (2011), Characterization of the 3D displacement field of landslides from Terrestrial Laser Scanning using 2D cross-correlation technique, in *EGU General Assembly 2011*, edited, Copernicus, Vienna, Austria.
- Travelletti, J., C. Delacourt, and J.-P. Malet (in review), Multi-date correlation of Terrestrial Laser Scanning data for the characterization of landslide kinematics, *Geomorphology*, 15.
- Travelletti, J., Delacourt, C., Allemand, P., Malet, J.-P., Schmittbuhl, J., Toussaint, R., Bastard, M. (in press). A multi-temporal image correlation method to characterize landslide displacements with a terrestrial camera. *International Journal of Photogrammetry & Remote-Sensing*, 23p. (in press).
- Travelletti, J., J. Demand, M. Jaboyedoff, and F. Marillier (2010), Mass movement characterization using a reflexion and refraction seismic survey with the sloping local base level concept, *Geomorphology*, 116(1-2), 1-10.
- Travelletti, J., T. Oppikofer, C. Delacourt, J.-P. Malet, and M. Jaboyedoff (2008), Monitoring landslide displacements during a controlled rain experiment using a long-range terrestrial laser scanning (TLS). *International Archives of Photogrammetry and Remote-sensing* 37(Part B5), 485-490.
- Travelletti, J., Malet, J.-P., Samyn, K., Grandjean, G., Jaboyedoff, M. 2011. Control of landslide retrogression by discontinuities: evidences by the integration of airborne- and ground-based geophysical information. *Landslides, Journal of the International Consortium on Landslides*, 21p. (in press).
- Tsutsui, K., S. Rokugawa, H. Nakagawa, S. Miyazaki, T. Chin-Tung Cheng Shiraishi, and S.-D. Yang (2007), Detection and Volume Estimation of Large-Scale Landslides Based on Elevation-Change Analysis Using DEMs Extracted From High-Resolution Satellite Stereo Imagery *IEEE Transactions on Geoscience and Remote-sensing Letters*, 45(6), 1681 - 1696
- Tuominen, S., and A. Pekkarinen (2005), Performance of different spectral and textural aerial photograph features in multi-source forest inventory, *Remote-sensing of Environment*, 94(2), 256-268.
- Tupin, F., H. Maitre, J. F. Mangin, J. M. Nicolas, and E. Pechersky (1998), Detection of linear features in SAR images: Application to road network extraction, *IEEE Transactions on Geoscience and Remote Sensing*, 36(2), 434-453.
- Usai, S. (2003), A least squares database approach for SAR interferometric data, *Geoscience and Remote Sensing, IEEE Transactions on*, 41(4), 753-760.

- van Asselen, S., and A. C. Seijmonsbergen (2006), Expert-driven semi-automated geomorphological mapping for a mountainous area using a laser DTM, *Geomorphology*, 78(3-4), 309-320.
- Van Den Eeckhaut, M., J. Hervás, N. Kerle, and R. Supper (2011), Mapping of landslides under dense vegetation cover using object-oriented analysis and LiDAR derivatives, in *The Second World Landslide Forum* edited, Rome, Italy.
- Van Den Eeckhaut, M., P. Reichenbach, F. Guzzetti, M. Rossi, and J. Poesen (2009), Combined landslide inventory and susceptibility assessment based on different mapping units: an example from the Flemish Ardennes, Belgium, *Nat. Hazards Earth Syst. Sci.*, 9(2), 507-521.
- Van Den Eeckhaut, M., J. Hervás, C. Jaedicke, J.-P. Malet, and L. Picarelli (2010), Calibration of logistic regression coefficients from limited landslide inventory data for European-wide landslide susceptibility modelling, paper presented at Int. Conference Mountain Risks: Bringing Science to Society, , CERIG Editions, Strasbourg, Florence, Italy, 24-26 November 2010.
- Van Den Eeckhaut, M., T. Vanwallegem, J. Poesen, G. Govers, G. Verstraeten, and L. Vandekerckhove (2006), Prediction of landslide susceptibility using rare events logistic regression: A case-study in the Flemish Ardennes (Belgium), *Geomorphology*, 76(3-4), 392-410.
- Van Den Eeckhaut, M., J. Poesen, G. Verstraeten, V. Vanacker, J. Nyssen, J. Moeyersons, L. P. H. v. Beek, and L. Vandekerckhove (2007), Use of LIDAR-derived images for mapping old landslides under forest, *Earth Surface Processes and Landforms*, 32(5), 754-769.
- Van Puymbroeck, N., R. Michel, R. Binet, J.-P. Avouac, and J. Taboury (2000), Measuring Earthquakes from Optical Satellite Images, *Appl. Opt.*, 39(20), 3486-3494.
- van Westen, C. J., and F. L. Getahun (2003), Analyzing the evolution of the Tessina landslide using aerial photographs and digital elevation models, *Geomorphology* 54(1-2), 77-89.
- Van Westen, C. J., A. C. Seijmonsbergen, and F. Mantovani (1999), Comparing Landslide Hazard Maps, *Natural Hazards*, 20(2), 137-158.
- van Westen, C. J., N. Rengers, and R. Soeters (2003), Use of Geomorphological Information in Indirect Landslide Susceptibility Assessment, *Natural Hazards*, 30(3), 399-419.
- van Westen, C. J., T. W. J. van Asch, and R. Soeters (2006), Landslide hazard and risk zonation—why is it still so difficult?, *Bulletin of Engineering Geology and the Environment*, 65(2), 167-184.
- van Westen, C. J., E. Castellanos, and S. L. Kuriakose (2008), Spatial data for landslide susceptibility, hazard, and vulnerability assessment: An overview, *Engineering Geology*, 102(3-4), 112-131.
- Varnes, D. J. (1984), Landslide Hazard Zonation: a review of principles and practice *Rep.*, 61 pp, Commission on landslides of the IAEG, UNESCO, 61 pp.
- Verstraeten, W. W., F. Veroustrate, C. J. Van der Sande, I. Grootaerts, and L. Feyen (2006), Soil moisture retrieval using thermal inertia, determined with visible and thermal spaceborne data, validated for European forests, *Remote-sensing of Environment*, 101(3), 299-314.
- Voigt, S., T. Kemper, T. Riedlinger, R. Kiefl, K. Scholte, and H. Mehl (2007), Satellite Image Analysis for Disaster and Crisis-Management Support, *Geoscience and Remote Sensing, IEEE Transactions on*, 45(6), 1520-1528.

- Vosselman, G., and H.-G. Maas (2010), *Airborne and Terrestrial Laser Scanning*, 318 pp., CRC Press, Taylor and Francis Group.
- Wang, X., and R. Niu (2010), Landslide intelligent prediction using object-oriented method, *Soil Dynamics and Earthquake Engineering*, 30(12), 1478-1486.
- Wang, Y., and Q. F. Zheng (1998), Recognition of roads and bridges in SAR images, *Pattern Recognition*, 31(7), 953-962.
- Weber, D., and A. Herrmann (2000), Contribution de la photogrammétrie numérique à l'étude spatio-temporelle de versants instables: l'exemple du glissement de Super-Sauze (Alpes-de-Haute-Provence). , *Bulletin de la Société géologique de France*, 171(6), 637-648.
- Whiton, R. C., P. L. Smith, S. G. Bigler, K. E. Wilk, and A. C. Harbuck (1998), History of Operational Use of Weather Radar by U.S. Weather Services. Part I: The Pre-NEXRAD Era, *Weather and Forecasting*, 13(2), 219-243.
- Whitworth, M., D. Giles, and W. Murphy (2005), Airborne remote-sensing for landslide hazard assessment: a case study on the Jurassic escarpment slopes of Worcestershire, UK, *Quarterly Journal of Engineering Geology and Hydrogeology*, 38(3), 285-300.
- Wieczorek, G. F., P. L. Gori, and L. M. Highland (2005), Reducing landslide hazards and risk in the United States: The role of the U.S.. Geological Survey., in *Landslide Hazard and Risk*, edited by T. Glade, M. Anderson and M. J. Crozier, pp. 351- 373, Wiley, Chichester.
- Wiley, C. A. (1954), *Pulsed Doppler Radar Methods and Apparatus*, edited.
- Wills, C. J., and T. P. McCrink (2002), Comparing Landslide Inventories: The Map Depends on the Method, *Environmental and Engineering Geoscience*, 8(4), 279-293.
- Witt, A., B. D. Malamud, M. Rossi, F. Guzzetti, and S. Peruccacci (2010), Temporal correlations and clustering of landslides, *Earth Surface Processes and Landforms*, 35(10), 1138-1156.
- Wong, M. T. K., Y. M. Oliver, and M. J. Robertson (2009), Gamma-radiometric assessment of soil depth across a landscape not measurable using electromagnetic surveys, *Soil Science Society of America Journal*, 73(4), 1261-1267.
- Woodhouse, I. H. (2006), *Introduction to Microwaves Remote Sensing*, CRC Taylor & Francis.
- Yamaguchi, Y., S. Tanaka, T. Odajima, T. Kamai, and S. Tsuchida (2003), Detection of a landslide movement as geometric misregistration in image matching of SPOT HRV data of two different dates, *International Journal of Remote Sensing*, 24(18), 3523-3534.
- Yang, X., and L. Chen (2010), Using multi-temporal remote sensor imagery to detect earthquake-triggered landslides, *International Journal of Applied Earth Observation and Geoinformation*, 12(6), 487-495.
- Yin, Y., W. Zheng, Y. Liu, J. Zhang, and X. Li (2010), Integration of GPS with InSAR to monitoring of the Jiayu landslide in Sichuan, China, *Landslides*, 7(3), 359-365.
- Young, A. P., R. T. Guza, W. C. O'Reilly, R. E. Flick, and R. Gutierrez (2011), Short-term retreat statistics of a slowly eroding coastal cliff, *Nat. Hazards Earth Syst. Sci.*, 11(1), 205-217.
- Zebker, H. A., P. A. Rosen, and S. Hensley (1997), Atmospheric effects in interferometry synthetic aperture radar surface deformation and topographic maps, *Journal of Geophysical research*, 102, 7547-7563.
- Zezeze, J. L., R. A. C. Garcia, S. C. Oliveira, and E. Reis (2008), Probabilistic landslide risk analysis considering direct costs in the area north of Lisbon (Portugal), *Geomorphology*, 94(3-4), 467-495.

- Zhang, J. (2010), Multi-source remote-sensing data fusion: status and trends, *International Journal of Image and Data Fusion*, 1(1), 5 - 24.
- Zhang, X., N. A. Drake, J. Wainwright, and M. Mulligan (1999), Comparison of slope estimates from low resolution DEMs: scaling issues and a fractal method for their solution, *Earth Surface Processes and Landforms*, 24(9), 763-779.